

MASSIVE RUNAWAY STARS INSIDE SUPERNOVA REMNANTS

MASSEREICHE SCHNELLÄUFERSTERNE IN SUPERNOVA-ÜBERRESTEN

A thesis submitted for the degree of
doctor rerum naturalium (Dr. rer. nat.)
2017 January 26th

presented to the council of
Physikalisch-Astronomische-Fakultät
Friedrich-Schiller-Universität Jena (FSU)

MSc. BAHA DİNÇEL
born on July 29th 1983 in Salihli, Turkey

ASTROPHYSIKALISCHES INSTITUT UND UNIVERSITÄTS-STERNWARTE (AIU)

1st Reviewer: Prof. Dr. Ralph Neuhäuser

Astrophysical Institute and University Observatory, FSU-Jena

2nd Reviewer: Prof. Dr. Ulrich Heber

Dr. Remeis-Sternwarte Bamberg Astronomisches Institut, FAU-Erlangen-Nürnberg

3rd Reviewer: Prof. Dr. Edward Peter Jacobus van den Heuvel

Anton Pannekoek Institute for Astronomy, University of Amsterdam (Retired)

Date of Defense: 11.05.2017

ABSTRACT

Binarity is an important factor affecting the evolution of a star. The fundamental properties of a star such as mass, rotation rate, magnetic field, lifetime and the end-product are strongly influenced by binary parameters and their evolution. Most of the massive stars, which undergo a supernova explosion in the end of their lives, reside in close binary systems in which the components experience mass transfer or mass loss. Therefore, during their evolution, their stellar parameters are significantly altered. This also affects the type of the supernova they experience as well as the type of their compact stellar remnants, neutron stars and black holes. By disrupting the gravitational bound of the system, the supernova leaves the companion as a runaway star which shows a high space velocity owing to its former orbital motion. The distribution of binary system mass ratios shows that the pre-supernova companion should also be a massive or an intermediate mass star. Although many massive runaway stars have been found so far, none of them could be linked to a supernova remnant or a neutron star with high accuracy. Thus, their origins are doubtful. By finding massive runaway stars which can be associated to a supernova remnant and a neutron star, firstly, the theoretical case of binary supernova ejection of a star can be proven. Secondly, the relation between the binary evolution and the observational properties of neutron stars and supernova remnants can be found. Thirdly, the effects of the binary evolution on the stellar parameters of the pre-supernova companion can be identified. Lastly, the supernova remnant parameters such as distance and age can be determined more precisely.

In this thesis, the massive runaway stars are searched inside the supernova remnants. As long as the observational conditions are available, intermediate mass stars are also studied. The blue stars are selected from their color magnitudes published in the literature. To confirm their temperature type and the radial velocities through Doppler shift, their spectra are taken. The association with the supernova remnant and the neutron star is shown by tracing

back their motions on the sky. Out of 27 supernova remnants which are visible in the northern hemisphere, inside one of them, a massive runaway star is found and the association is confirmed by kinematics.

HD 37424 inside the supernova remnant S 147 is the first massive runaway star discovered which can be directly linked to a neutron star and a supernova remnant. The space velocity of the star is $74.0 \pm 8 \text{ km s}^{-1}$. The surface temperature of the star is $30000 \pm 1000 \text{ K}$ and the logarithm of surface gravity is 4.0 ± 0.25 in cgs. The star has a moderate projected rotational velocity, $140 \pm 20 \text{ km s}^{-1}$. Tracing back the past trajectories via Monte Carlo simulations, it is found that HD 37424 was located at the same position as the central source PSR J0538+2817 30 ± 4 kyr ago. This position is only ~ 4 arcminutes away from the geometrical center of the SNR. So, it is suggested that HD 37424 was the pre-supernova binary companion to the progenitor of the neutron star and the supernova remnant. Furthermore, the pre-supernova binary is also constructed and the parameters are shown. The progenitor of S 147 had experienced a close binary evolution with HD 37424. The SNR distance and age is specified precisely as $1333_{-112}^{+103} \text{ pc}$ and 30 ± 4 kyr.

Two massive runaway stars HD 184927 and HD 254577 are also detected inside the supernova remnants G065.3+5.7 and IC 443 respectively, their association with the remnants are discussed. Eight other stars inside different supernova remnants are found as potential runaway stars which further evidences and better quality data are needed for a complete proof. The remaining 16 SNRs host no OB runaway stars. They are either from single star progenitors or the runaway star is out of the detection limit.

Binarität ist ein wichtiger Faktor für die Evolution von Sternen. Die grundlegenden Eigenschaften eines Sternes wie Masse, Rotationsdauer, Magnetfeld, seine Lebensdauer und sein Endprodukt sind stark von binären Parametern und ihrer Evolution geprägt. Die meisten massiven Sterne, die am Ende ihres Lebens in einer Supernova enden, befinden sich in engen Binärsystemen, in denen die Komponenten einen Massentransfer oder Massenverlust erfahren. Daher gibt es signifikante Veränderungen der stellaren Parameter während ihrer Entwicklung. Dies beeinflusst auch, in welchem Typus Supernova sie enden sowie die Art ihrer kompakten Sternreste: Neutronensterne oder Schwarze Löcher. Das Zerreißen des Systems führt dazu, dass sich der Begleitstern als Schnellläuferstern mit einer hohen Raumgeschwindigkeit fortbewegt, die von seiner hohen Orbitalgeschwindigkeit herrührt.

Die Verteilung der binären Massenverhältnisse zeigt, dass der Begleiter des Supernova-Vorläufersterns ebenfalls ein massereicher oder zumindest ein mittelschwerer Stern sein müsste. Obgleich bisher viele massereiche Schnellläufersterne gefunden worden sind, konnte keiner von ihnen mit einem Supernova-Überrest oder einem Neutronenstern mit einer ausreichenden Genauigkeit in Verbindung gebracht werden. Daher ist ihr Entstehungsmechanismus noch unklar. Durch das Auffinden solcher Schnellläufersterne, kann erstens die theoretische Möglichkeit ihrer Entstehung nachgewiesen werden. Zweitens kann die Relation zwischen der binären Evolution und den beobachteten Eigenschaften von Neutronensternen und Supernova-Überresten gefunden werden. Drittens können die Einflüsse der binären Evolution auf die stellaren Parameter des Begleitsterns nachverfolgt werden. Schließlich können Parameter des Supernova-Überrests, wie seine Entfernung und das Alter, präziser bestimmt werden.

In dieser Arbeit wird nach massereichen Schnellläufersternen in Supernova-Überresten gesucht. Falls die Beobachtungsbedingungen es zugelassen haben, wurden auch mittelschwere Sterne untersucht. Die Auswahl der Sterne erfolgte anhand ihrer Farbmagnituden, bekannt aus der Literatur. Für die Ermittlung ihrer genauen Temperatur und der Radialgeschwindigkeiten durch Dopplerverschiebung wurden ihre Spektren aufgenommen. Die Assoziation mit dem Supernova-Überrest und dem Neutronenstern wurde durch das Zurückverfolgen ihrer Bahnen rekonstruiert. Von 27 untersuchten Supernova-Überresten in der nördlichen Hemisphäre wurde in einem von ihnen ein massereicher Schnellläuferstern gefunden und die zugehörige Assoziation wurde durch kinematische Untersuchungen bestätigt.

Der Stern HD 37424 innerhalb des Supernova-Überrestes S 147 ist die erste Entdeckung eines massereichen Schnellläufersterns, welcher direkt mit einem Neutronenstern und einem Supernova-Überrest in Zusammenhang gebracht werden kann. Die Raumgeschwindigkeit des Sterns beträgt $74.0 \pm 8 \text{ km s}^{-1}$ die Oberflächentemperatur ist $30000 \pm 1000 \text{ K}$ und die Oberflächengravitation beträgt $4.00 \pm 0.25 \text{ dex}$. Der Stern hat eine moderate Rotationsgeschwindigkeit von $140 \pm 20 \text{ km s}^{-1}$. Die Rückverfolgung der Bahntrajektorien mittels Monte-Carlo-Simulationen ergab für HD 37424, dass er sich zusammen mit dem zentralen Pulsar PSR J0538+2817 vor $30 \pm 4 \text{ kyr}$ an der selben Position befand. Diese Position ist nur ~ 4 Bogenminuten vom geometrischen Zentrum des Supernova-Überrestes entfernt. Daher wird angenommen, dass HD 37424 der Begleiter des Supernova-Vorläufersterns ist. Des Weiteren wurde auch das System vor der Supernovaexplosion rekonstruiert und dessen Pa-

parameter dargestellt. Der Vorläuferstern von S 147 entwickelte sich in einem engen Binärsystem mit HD 37424. Die Entfernung des Überrestes und sein Alter wurden sehr genau ermittelt und betragen 1333_{-112}^{+103} pc and 30 ± 4 kyr. Des Weiteren wurden potentielle Schnellläufersterne in sechs weiteren Supernova-Überresten gefunden. Für einen eindeutigen Nachweis ihrer Natur werden jedoch Beobachtungsdaten mit höherer Qualität benötigt.

In den Supernova-Überresten G065.3 + 5.7 und IC 443 wurden ebenfalls zwei massereiche Schnellläufersterne HD 184927 und HD 254577 detektiert, ihre Zugehörigkeit zu den Überresten wird dargestellt. Ihre Assoziation mit den Resten wird diskutiert. Acht weitere Sterne in anderen Supernova-Überresten wurden als potentielle Schnellläufersterne identifiziert. Für einen vollständigen Nachweis sind weitere Daten mit einer höheren Qualität notwendig. Die restlichen 16 SNRs beherbergen keine OB Schnellläufersterne. Sie entstanden entweder von einem einzelnen Stern als Vorläufer oder der Schnellläuferstern liegt außerhalb der Nachweisgrenze.

To my Mum

ACKNOWLEDGMENTS

I would like to thank my supervisor Prof. Dr. Ralph Neuhaeuser for giving me the chance to work on this project, guidance and friendship. It was a great honor to work with him for the four years and our cooperation influenced my academical and world view highly. I also would like to thank Assoc. Prof. Sinan Kaan Yerli and Assoc. Prof. Askin Ankey for their support on my research through the guidance of late Oktay Hüseyin Guseinov. His contribution to the science will be missed.

Sincere thanks are given to my dear colleague Anna Pannicke for supporting me during the most difficult times during my studies and for fruitful discussions

A lot of people influenced and supported this work scientifically and their contribution were most valuable for me. Here, I thank Nina Tetzlaff, Markus Hohle and Ludwig Trepl, the neutron star group, for their friendship and their contributions to my knowledge. Special thanks are given to Dr. Manami Sasaki for her teaching, support and patience. I also learned a lot from Prof. Dr. Alexander Krivov, Dr. Valeri Hambaryan, Dr. Markus Mugrauer, Dr. Christian Ginski, Dr. Tobias Schmidt.

I would like to thank Dr. Nina Tetzlaff for her contribution with Monte Carlo simulations and its results and figures, Dr. Guillermo Torres for providing me with important observational data from TRES instrument, Dr. Ronny Errmann for his python code to select the candidate stars of this work, Dr. Markus Mugrauer for making the mosaic picture of S 147 and all the observers of University observatory of Jena, for observing for this work.

Very special thanks to my friends; Can Güngör, Christian Adam, Janos Schmidt, Martin Seeliger, Jonas Greif, Ronny Errmann and Sara Saeedi.

My family also provided invaluable support for this work. I would like to thank specially to my mum Vildan Pişirgen and my sisters Berna Çağlayan and Gülden Dinçel.

This work is supported by Deutsche Forschungsemainschaft (DFG), under the project, SFB/TR7–

C7 Gravitational Wave Astronomy.

This work has made use of SIMBAD¹ and *Vizier*² catalogue access tools, CDS, Strasbourg, France, Australia Telescope National Facility (ATNF)³ database and *Skyview*⁴ online virtual observatory. The model atmospheres are constructed by the program *Spectrum*⁵ and synthetic spectra were retrieved from *Sterne/Spectrum Model Grids*⁶ and standard star spectra were obtained from *A digital Spectral Classification Atlas*⁷. The observations were carried out in the following observatories; TBİTAK National Space Observatory, Turkey, Calar Alto Observatory, Spain, University Observatory of Jena and Smithsonian Astronomical Observatory, U.S.A.

Finally, I would like to thank all the observers, night assistants and staff astronomers of GSH, TUG and Calar Alto.

¹ <http://simbad.u-strasbg.fr/simbad/>

² <http://vizier.u-strasbg.fr/viz-bin/VizieR>

³ <http://www.atnf.csiro.au/people/pulsar/psrcat/>

⁴ <http://skyview.gsfc.nasa.gov/current/cgi/titlepage.pl>

⁵ <http://www.appstate.edu/~grayro/spectrum/spectrum.html>

⁶ <http://www.arm.ac.uk/~csj/models/Grid.html>

⁷ <https://ned.ipac.caltech.edu/level5/Gray/Gray1.html>

TABLE OF CONTENTS

ABSTRACT	iii
ACKNOWLEDGMENTS	viii
TABLE OF CONTENTS	x
LIST OF TABLES	xiv
LIST OF FIGURES	xvi
LIST OF ABBREVIATIONS	xxvi

CHAPTERS

1	INTRODUCTION	1
1.1	Massive Stars	1
1.2	Neutron Stars and Supernova Remnants	3
1.3	OB Runaway Stars	6
1.4	Motivation	7
2	THE SAMPLE	9
2.1	Supernova Remnants	9
2.2	Candidate Selection	12
3	OBSERVATIONAL	17
3.1	Observations	17
3.1.1	Calar Alto	18
3.1.2	TUG	19
3.1.3	University Observatory of Jena	20

3.1.4	SAO	21
3.2	Data reduction	22
3.3	Analyses	24
3.3.1	Continuum Subtraction	24
3.3.2	Spectral Type Identification	26
3.3.3	Radial Velocity Measurement	29
3.3.4	Interstellar Medium Lines	32
3.3.5	Stellar Parameters	32
4	RESULTS AND DISCUSSION	35
4.1	The Massive Runaway Star Inside SNR G180.0-1.7 (S 147)	35
4.1.1	Observational Results	37
4.1.2	Kinematics	40
4.1.3	Associations	40
4.1.4	Full Picture of an OB Runaway	43
4.2	SNRs With Possible OB Runaway Stars	46
4.2.1	G189.1+3.0 (IC 443)	46
4.2.2	G065.3+5.7	54
4.3	SNRs with Potential OB Runaway Stars	58
4.3.1	G078.2+2.1 (DR 4)	58
4.3.2	G093.7-0.2 (CTB 104A)	61
4.3.3	G109.1-1.0 (CTB 109)	62
4.3.4	G114.3+0.3	66
4.3.5	G116.9+0.2 (CTB 1)	68
4.3.6	G126.2+1.6	70
4.3.7	G127.1+0.5 (R 5)	72
4.3.8	G132.7+1.3 (HB 3)	73

4.4	SNRs With No OB Runaways Stars	76
4.4.1	G034.7-0.4 (W 44)	76
4.4.2	G054.4-0.3 (HC 40)	76
4.4.3	G069.0+2.7 (CTB 80)	77
4.4.4	G074.0-8.5 (Cygnus Loop)	78
4.4.5	G082.2+5.3 (W 63)	79
4.4.6	G089.0+4.7 (HB 21)	80
4.4.7	G106.3+2.7	81
4.4.8	G111.7-2.1 (Cas A)	83
4.4.9	G093.3+6.9 (DA 530)	83
4.4.10	G119.5+10.2 (CTA 1)	84
4.4.11	G120.1+1.4 (Tycho SNR)	85
4.4.12	G130.7+3.1 (SN 1181)	85
4.4.13	G156.2+5.7	86
4.4.14	G160.9+2.6 (HB 9)	87
4.4.15	G166.0+4.3 (VRO 65.05.01)	88
4.4.16	G184.6-5.8 (Crab Nebula)	90
4.4.17	The General Picture	91
5	CONCLUSION	95
	REFERENCES	97
A	IMAGES OF SUPERNOVA REMNANTS	119
A.1	1420 MHz Images	119
A.2	Different Wavebands	122
B	HIGH VELOCITY ISM GAS	125

C	LOW RESOLUTION SPECTRA	133
C.1	G069.0+2.7	140
C.2	G078.2+2.1	142
C.3	G082.2+5.3	146
C.4	G089.0+4.7	160
C.5	G093.7-0.2	173
C.6	G109.1-1.0	193
C.7	G114.3+0.3	200
C.8	G116.9+0.2	206
C.9	G126.2+1.6	226
C.10	G127.1+0.5	238
C.11	G132.7+1.3	245
C.12	G156.2+5.7	258
C.13	G160.9+2.6	265
C.14	G166.0+4.3	271
C.15	G180.0-1.7	286
C.16	G189.1+3.0	299

LIST OF TABLES

TABLES

Table 2.1	The NSs of the SNRs in the sample	11
Table 2.2	The SNRs in the sample	13
Table 3.1	List of observations	18
Table 3.2	Fxcor results	29
Table 3.3	Radial velocity measurements of HD 37424	31
Table 4.2	Velocities of IS Lines in the HD 37424 Spectrum	39
Table 4.3	Members of possible OB association of HD 37424	43
Table 4.4	Visual absolute magnitudes of massive stars nearby HD 37424	44
Table 4.5	19 stars around HD 37424 with common proper motion	45
Table 4.7	Early type stars identified inside IC 443	49
Table 4.8	Radial velocity of HD 254577 w.r.t. Gem OB1	53
Table 4.9	Binary parameters of HD 254577	53
Table 4.10	Members and kinematics of Gem OB1	55
Table 4.11	Binary parameters of HD 184927	58
Table 4.12	Early type stars identified inside SNR γ -Cygni	60
Table 4.13	Early type stars identified inside SNR γ -Cygni	63

Table 4.14 Early type stars identified inside CTB 109	65
Table 4.15 Early type stars identified inside SNR G114.3+0.3	68
Table 4.16 Early type stars identified inside CTB 1	71
Table 4.17 Early type stars identified inside SNR G126.2+1.6	72
Table 4.18 Early type stars identified inside R 5	73
Table 4.19 Early type stars identified inside HB 3	75
Table 4.20 Early type stars identified inside SNR G082.2+5.3	80
Table 4.21 Early type stars identified inside SNR HB 21	81
Table 4.22 Early type stars identified inside SNR G156.2+5.7	87
Table 4.23 Early type stars identified inside SNR HB 9	88
Table 4.24 Early type stars identified inside SNR VRO 42.05.01	90
Table 4.25 Results of Search for runaway stars	92
Table 4.26 Updated distances of SNRs	94
Table B.1 High velocity gas of IC 443	125
Table B.2 High velocity gas of SNR G166.0+4.3	125
Table B.3 High velocity gas of HB 21	126
Table B.4 High velocity gas of R 5	126
Table B.5 Velocities w.r.t the normal ISM component	127
Table C.1 Spectral types determined from low resolution spectroscopy.	133

LIST OF FIGURES

FIGURES

Figure 2.1	Galactic distribution of the SNRs	12
Figure 2.2	The OB runaway search region assigned for SNR S 147	14
Figure 2.3	Deviation vs. spectral type graph: observational	15
Figure 2.4	Deviation vs. spectral type graph: theoretical	16
Figure 3.1	The bump in CAFOS flat spectrum	25
Figure 3.2	Fxcor of TYC 3572-00017-1 vs F0V	27
Figure 3.3	Fxcor of TYC 3572-00017-1 vs B2V	28
Figure 3.5	Radial velocity measurement by Gaussian fit.	31
Figure 3.6	Measurement of surface gravity	32
Figure 3.7	Measurement of effective temperature	33
Figure 3.8	Measurement of rotational velocity	34
Figure 4.1	Image of HD 37424, S 147 and the pulsar	38
Figure 4.2	Interstellar Absorption Lines of HD 37424	39
Figure 4.3	Distribution of encounters of the pulsar and HD 37424	41
Figure 4.4	IC 443 and the possible OB runaway star	47
Figure 4.5	PWN inside IC 443	50

Figure 4.6	Stellar parameters of HD 254577	51
Figure 4.7	Comparison of HD 254577 with HD 43818	52
Figure 4.8	Possible true dimensions of IC 443 and SNR CTB 80	54
Figure 4.9	Possible extent of IC 443	55
Figure 4.10	SNR G065.3+5.7 with HD 184927	56
Figure 4.11	SNR γ -Cygni with the strong candidates	58
Figure 4.12	Stellar parameters of a candidate in γ -Cyg	61
Figure 4.13	X-ray and IR image of CTB 109	63
Figure 4.14	4850 MHz image of SNR G114.3+0.3	66
Figure 4.15	SNRs R 5 and CTB 1	69
Figure 4.16	Spectra of HD 278115	90
Figure A.1	SNRs W 63 and HB 21	119
Figure A.2	SNRs CTB 104A and DA 530	119
Figure A.3	SNRs G106.3+2.7 and Tycho	120
Figure A.4	SNRs SN 1181 and HB 9	120
Figure A.5	1420 MHz images of W 63 and HB 3	121
Figure A.6	SNRs W 44 and CTA 1	122
Figure A.7	SNRs HC 40 and Cygnus Loop	122
Figure A.8	SNRs Cas A and G156.2+5.7	123
Figure A.9	Crab Nebula in red band	123
Figure B.1	High velocity gas of IC 443	128
Figure B.2	High velocity gas towards the stars behind IC 443	129

Figure B.3	High velocity gas of R 5	129
Figure B.4	High velocity gas of SNR G166.0+4.3	130
Figure B.5	High velocity gas of HB 21	131
Figure C.1	CAFOS Spectrum of 615-089671	140
Figure C.2	CAFOS Spectrum of 615-089063	141
Figure C.3	CAFOS Spectrum of 653-092525	142
Figure C.4	CAFOS Spectrum of 653-092507	143
Figure C.5	CAFOS Spectrum of 653-092521	144
Figure C.6	CAFOS Spectrum of 653-092554	145
Figure C.7	CAFOS Spectrum of 678-083025	146
Figure C.8	CAFOS Spectrum of 679-080132	147
Figure C.9	CAFOS Spectrum of 679-080240	148
Figure C.10	CAFOS Spectrum of 678-083187	149
Figure C.11	CAFOS Spectrum of 679-080191	150
Figure C.12	CAFOS Spectrum of 678-083207	151
Figure C.13	CAFOS Spectrum of 677-080274	152
Figure C.14	CAFOS Spectrum of 679-080132	153
Figure C.15	CAFOS Spectrum of 678-083011	154
Figure C.16	CAFOS Spectrum of 678-083198	155
Figure C.17	CAFOS Spectrum of 678-083187	156
Figure C.18	CAFOS Spectrum of 678-083207	157
Figure C.19	CAFOS Spectrum of 678-083036	158

Figure C.20	TFOSC Spectrum of 677-080274	159
Figure C.21	CAFOS Spectrum of 703-081098	160
Figure C.22	CAFOS Spectrum of 703-081110	161
Figure C.23	CAFOS Spectrum of 704-078261	162
Figure C.24	CAFOS Spectrum of 703-081075	163
Figure C.25	CAFOS Spectrum of 703-080795	164
Figure C.26	CAFOS Spectrum of 704-078114	165
Figure C.27	CAFOS Spectrum of 704-077723	166
Figure C.28	CAFOS Spectrum of 703-080556	167
Figure C.29	CAFOS Spectrum of 704-077771	168
Figure C.30	CAFOS Spectrum of 704-078268	169
Figure C.31	CAFOS Spectrum of 703-080682	170
Figure C.32	TFOSC Spectrum of 703-080938	171
Figure C.33	TFOSC Spectrum of 703-081110	172
Figure C.34	CAFOS Spectrum of 704-083954	173
Figure C.35	CAFOS Spectrum of 704-083954	174
Figure C.36	CAFOS Spectrum of 704-083954	175
Figure C.37	CAFOS Spectrum of 704-083954	176
Figure C.38	CAFOS Spectrum of 704-083954	177
Figure C.39	CAFOS Spectrum of 704-083954	178
Figure C.40	CAFOS Spectrum of 704-083954	179
Figure C.41	CAFOS Spectrum of 704-083954	180

Figure C.42	CAFOS Spectrum of 704-083954	181
Figure C.43	CAFOS Spectrum of 704-083954	182
Figure C.44	CAFOS Spectrum of 704-083954	183
Figure C.45	CAFOS Spectrum of 704-083954	184
Figure C.46	CAFOS Spectrum of 704-083954	185
Figure C.47	CAFOS Spectrum of 704-083954	186
Figure C.48	CAFOS Spectrum of 704-084001	187
Figure C.49	CAFOS Spectrum of 705-085540	188
Figure C.50	CAFOS Spectrum of 705-085587	189
Figure C.51	CAFOS Spectrum of 705-085590	190
Figure C.52	CAFOS Spectrum of 705-085595	191
Figure C.53	TFOSC Spectrum of 705-085474	192
Figure C.54	CAFOS Spectrum of	193
Figure C.55	CAFOS Spectrum of 745-080787	194
Figure C.56	CAFOS Spectrum of 745-080774	195
Figure C.57	CAFOS Spectrum of 745-080963	196
Figure C.58	CAFOS Spectrum of 745-080963	197
Figure C.59	TFOSC Spectrum of 745-080772	198
Figure C.60	TFOSC Spectrum of 745-080935	199
Figure C.61	CAFOS Spectrum of 761-072876	200
Figure C.62	CAFOS Spectrum of 760-074536	201
Figure C.63	CAFOS Spectrum of 760-074418	202

Figure C.64	TFOSC Spectrum of 761-072674	203
Figure C.65	TFOSC Spectrum of 759-074519	204
Figure C.66	TFOSC Spectrum of 761-072827	205
Figure C.67	CAFOS Spectrum of 763-077202	206
Figure C.68	CAFOS Spectrum of 762-000129	207
Figure C.69	CAFOS Spectrum of 763-076740	208
Figure C.70	CAFOS Spectrum of 762-000278	209
Figure C.71	CAFOS Spectrum of 763-000154	210
Figure C.72	CAFOS Spectrum of 762-075659	211
Figure C.73	CAFOS Spectrum of 762-075495	212
Figure C.74	CAFOS Spectrum of 763-076928	213
Figure C.75	CAFOS Spectrum of 763-077172	214
Figure C.76	CAFOS Spectrum of 762-075534	215
Figure C.77	CAFOS Spectrum of 762-075377	216
Figure C.78	CAFOS Spectrum of 763-077093	217
Figure C.79	CAFOS Spectrum of 763-077125	218
Figure C.80	CAFOS Spectrum of 763-077195	219
Figure C.81	CAFOS Spectrum of 763-077148	220
Figure C.82	CAFOS Spectrum of 762-075588	221
Figure C.83	CAFOS Spectrum of 763-077153	222
Figure C.84	CAFOS Spectrum of 763-077012	223
Figure C.85	TFOSC Spectrum of 763-077199	224

Figure C.86	TFOSC Spectrum of 762-075426	225
Figure C.87	CAFOS Spectrum of 772-009418	226
Figure C.88	CAFOS Spectrum of 772-009343	227
Figure C.89	CAFOS Spectrum of 772-009430	228
Figure C.90	CAFOS Spectrum of 772-009483	229
Figure C.91	CAFOS Spectrum of 772-009467	230
Figure C.92	CAFOS Spectrum of 771-009610	231
Figure C.93	CAFOS Spectrum of 772-009227	232
Figure C.94	CAFOS Spectrum of 771-009642	233
Figure C.95	CAFOS Spectrum of 772-009224	234
Figure C.96	CAFOS Spectrum of 772-009499	235
Figure C.97	CAFOS Spectrum of 772-009451	236
Figure C.98	TFOSC Spectrum of 772-009430	237
Figure C.99	CAFOS Spectrum of 767-013562	238
Figure C.100	CAFOS Spectrum of 766-013622	239
Figure C.101	CAFOS Spectrum of 766-013684	240
Figure C.102	CAFOS Spectrum of 767-013623	241
Figure C.103	CAFOS Spectrum of 767-013673	242
Figure C.104	CAFOS Spectrum of 766-013734	243
Figure C.105	TFOSC Spectrum of 767-013623	244
Figure C.106	CAFOS Spectrum of 765-021781	245
Figure C.107	CAFOS Spectrum of 765-021812	246

Figure C.108	CAFOS Spectrum of 764-021488	247
Figure C.109	CAFOS Spectrum of 764-021273	248
Figure C.110	CAFOS Spectrum of 764-021254	249
Figure C.111	CAFOS Spectrum of 764-021397	250
Figure C.112	CAFOS Spectrum of 765-021722	251
Figure C.113	CAFOS Spectrum of 764-021210	252
Figure C.114	CAFOS Spectrum of 765-021792	253
Figure C.115	CAFOS Spectrum of 764-021329	254
Figure C.116	CAFOS Spectrum of 764-021331	255
Figure C.117	CAFOS Spectrum of 764-021370	256
Figure C.118	CAFOS Spectrum of 764-021388	257
Figure C.119	CAFOS Spectrum of 710-035795	258
Figure C.120	CAFOS Spectrum of 710-035809	259
Figure C.121	CAFOS Spectrum of 710-035810	260
Figure C.122	CAFOS Spectrum of 710-035713	261
Figure C.123	CAFOS Spectrum of 710-035782	262
Figure C.124	CAFOS Spectrum of 709-034542	263
Figure C.125	CAFOS Spectrum of 710-035744	264
Figure C.126	CAFOS Spectrum of 683-034093	265
Figure C.127	CAFOS Spectrum of 683-034211	266
Figure C.128	CAFOS Spectrum of 683-034148	267
Figure C.129	CAFOS Spectrum of 685-033089	268

Figure C.130	CAFOS Spectrum of 684-032395	269
Figure C.131	CAFOS Spectrum of 684-032951	270
Figure C.132	CAFOS Spectrum of 666-037743	271
Figure C.133	CAFOS Spectrum of 665-037654	272
Figure C.134	CAFOS Spectrum of 665-037919	273
Figure C.135	CAFOS Spectrum of 666-037784	274
Figure C.136	CAFOS Spectrum of 666-037842	275
Figure C.137	CAFOS Spectrum of 665-037914	276
Figure C.138	CAFOS Spectrum of 665-037807	277
Figure C.139	CAFOS Spectrum of 665-037801	278
Figure C.140	CAFOS Spectrum of 665-037911	279
Figure C.141	CAFOS Spectrum of 666-037753	280
Figure C.142	CAFOS Spectrum of 665-037712	281
Figure C.143	CAFOS Spectrum of 665-037733	282
Figure C.144	CAFOS Spectrum of 666-037857	283
Figure C.145	CAFOS Spectrum of 590-020323	284
Figure C.146	TFOSC Spectrum of 666-037743	285
Figure C.147	CAFOS Spectrum of 590-020323	286
Figure C.148	CAFOS Spectrum of 590-020251	287
Figure C.149	CAFOS Spectrum of 591-020517	288
Figure C.150	CAFOS Spectrum of 587-019374	289
Figure C.151	CAFOS Spectrum of 588-020228	290

Figure C.152	CAFOS Spectrum of 590-020733	291
Figure C.153	CAFOS Spectrum of 592-020035	292
Figure C.154	CAFOS Spectrum of 589-019826	293
Figure C.155	CAFOS Spectrum of 592-020103	294
Figure C.156	CAFOS Spectrum of 589-019783	295
Figure C.157	CAFOS Spectrum of 589-020390	296
Figure C.158	CAFOS Spectrum of 591-020513	297
Figure C.159	TFOSC Spectrum of 589-020158	298
Figure C.160	CAFOS Spectrum of 563-026583	299
Figure C.161	CAFOS Spectrum of 562-026666	300
Figure C.162	CAFOS Spectrum of 564-025656	301
Figure C.163	CAFOS Spectrum of 564-025691	302
Figure C.164	CAFOS Spectrum of 564-025754	303
Figure C.165	CAFOS Spectrum of 563-026606	304
Figure C.166	CAFOS Spectrum of 563-026625	305
Figure C.167	CAFOS Spectrum of 563-026556	306
Figure C.168	CAFOS Spectrum of 563-026710	307
Figure C.169	CAFOS Spectrum of 564-025691	308
Figure C.170	CAFOS Spectrum of 563-026587	309
Figure C.171	CAFOS Spectrum of 564-025653	310

LIST OF ABBREVIATIONS

SN	Supernova
HN	Hypernova
T	Temperature
T_{eff}	Effective temperature
τ	Age
NS	Neutron star
BH	Black Hole
SNR	Supernova remnant
PWN	Pulsar wind nebula
MMSNR	Mixed morphology supernova remnant
F	Plerion type supernova remnant
C	Composit type supernova remnant
S	Shell type supernova remnant
P	Period
RPP	Rotationally powered pulsar
CCO	Central compact object
MSP	Milli second pulsar
Σ	Surface brightness
v_{bw}	Blast wave velocity
DM	Dispersion measure
τ	Characteristic age
n_0	Number density
WD	White Dwarf
AIC	Accretion Induced Collapse
BSS	Binary Supernova Scenario
DES	Dynamical Ejection Scenario
PWN	Pulsar Wind Nebula
LSR	Local Standard of Rest

LIST OF UNITS

In astronomy cgs units are used rather than mks units. Furthermore, astronomical quantities are commonly in use. Here, a list of units that is used throughout this thesis is given.

- $L_{\odot} = 3.83 \times 10^{26} \text{ J s}^{-1}$ (Solar Luminosity)
- $M_{\odot} = 1.99 \times 10^{30} \text{ kg}$ (Solar Mass)
- $R_{\odot} = 6.96 \times 10^8 \text{ m}$ (Solar Radius)
- $1 \text{ erg} = 1 \text{ g cm}^2 \text{ s}^{-2} = 10^{-7} \text{ J}$
- $1 \text{ eV} = 1.6 \times 10^{-19} \text{ J}$
- $1 \text{ G} = 1 \text{ V s cm}^{-2} = 10^{-4} \text{ T}$
- $1 \text{ au} = 149.6 \times 10^9 \text{ m}$
(astronomical unit: the distance between the Earth and the Sun)
- $1 \text{ pc} = 30.857 \times 10^{15} \text{ m}$
(parsec: an object at 1 pc distance has a parallax of one arcsec with respect to 1 au)

CHAPTER 1

INTRODUCTION

1.1 Massive Stars

We owe our lives to massive stars of which masses are > 8 Solar mass (M_{\odot}). They are the engines of the universe, synthesizing heavy elements and spreading them to the interstellar medium (ISM) by supernova (SN) explosions. Both the stellar nucleosynthesis and the SN are responsible for the production of majority of the metals (elements heavier than He) in the Universe. Besides nurturing the ISM with metals, SN also trigger star formation by compressing the nearby molecular clouds. Massive stars also do the same with their strong winds throughout their lives. Then, the fresh formed low mass stars develop proto-planetary disks where the metal content precipitates and forms the planets and finally the living forms may appear under appropriate conditions. Massive stars are destructive as well as they are constructive. The SN and the hypernova (HN) destroy the molecular clouds nearby until the shock velocity decreases down to 45 km s^{-1} [288]. Also, the gamma ray bursts (GRBs) formed in the spin poles of the exploding star during a HN, can be destructive for the delicate zones of the Universe like the Earth if targeted by the γ -ray beam with high flux [217]. Hence, studying the massive stars is vitally important to understand the chemical evolution and the life cycle of micro and macro structures throughout a galaxy.

Mass is the fundamental parameter of a star. In hydrogen burning phase, the luminosity (L) of a star is proportional to the mass by $L \propto M^{3.5}$. Massive stars are the hottest ones with a temperature of $T_{\text{eff}} > 20000 \text{ K}$, as $L \propto T^4$. They are classified as O and B type stars in the Hertzsprung–Russell diagram which shows the relation between the temperature and the luminosity of the stars [240]. Furthermore, they have the shortest lifetime due to the high rate of energy dissipation. Considering the nuclear timescale, $\tau = 0.0007 \times c^2 \times M/L$, the

lifetime of a star is inversely proportional to the mass, $\tau \propto M^{-2.5}$.

The lifetime of a single non-rotating massive star having solar metallicity is calculated as < 25 Myr [190]. After the consumption of hydrogen, the core contracts and reaches the temperature at which the He-burning (fusion) will take place. Unlike low mass stars, massive star cores have enough pressure to contract to synthesize further elements through CNO cycle up to iron group and their lives end with a catastrophic explosion, a SN. As well as mass, rotation and metallicity are the conditions which must always be taken into account in analysis of the evolution of a massive star. Metallicity increase the impact cross-section of the elements on average, hence the opacity of the photosphere, so the radiation pressure is more effective to apply force on the stellar layers against the gravity which results in mass loss [162]. Rotation rate plays an important role in mixing the synthesized material through the layers as well as in mass loss [176]. For example, while a massive star can evolve to a red supergiant through all of the fusion phases and undergoes a SN, one having the same initial mass but higher metallicity, can experience huge mass loss to lose its hydrogen envelope and never evolve to a red supergiant phase. It may even fail to make a SN if the core cannot reach the critical mass ($1.4 M_{\odot}$) to overcome the electron degeneracy pressure to collapse to a neutron star (NS) or a black hole (BH) [97].

Binarity is the situation which can directly affect all of these factors. In a binary system, the stars can exchange mass via accretion on to each other through the first Lagrangian point when they fill their Roche lobe where the material is no more gravitationally bound to the star. The dimensions of Roche lobe depend on the binary separation and stellar mass ratios [207] The smaller the Roche lobe is, the earlier the star can fill it. Depending on the evolutionary stage of the star, the mass transfer stages are classified as Case A, B and C, where the star fills its Roche lobe in the main sequence (H-burning), in the red giant (He-burning) and in the supergiant (further synthesis) phases respectively. The binary evolution affects not only the fate of a star, but also the end-products such as the initial energy and the type of SN (the light curve and the emitting elements) [56], the linear momentum gained by the NS [219] and possibly the initial spin period [291]. A massive star of which zero age main-sequence mass is $> 10 M_{\odot}$, undergoes a SN as a result of the collapse of its iron core. Those which have masses $8 < M < 10 M_{\odot}$ experience the same by electron capture of their degenerate O+Ne+Mg cores [204]. These mass limits can be even lower considering binary interactions [218]. In both cases a NS is likely to be born.

1.2 Neutron Stars and Supernova Remnants

A NS is a compact object which is supported by neutron degeneracy pressure against gravitational contraction. The typical mass of an NS is $1.4 M_{\odot}$, which is the Chandrasekhar limit. The mass of a NS can be slightly less considering possible mass losses during the core collapse. The upper limit is still not known, but estimated as $2-3 M_{\odot}$. A typical theoretical radius of a NS is only 10 km, so from conservation of angular momentum the initial spin period (P_0) is at the order of ms. They typically show very high dipole magnetic field strength (B_{dip}) vary between $10^{10}-10^{16}$ G. The magnetic field strength depends on the age of the NS and some initial conditions at birth. The surface temperature of a young NS is estimated as $> 10^7$ K. As they cool down, they are observed in a wide range of temperatures down to 10^5 K. Owing to their very short radius, their luminosities are low, so it is not easy to detect. However, there are ~ 2000 [178] detected NS as they manifest themselves with their regular pulses formed by their magnetospheres. They are called pulsars [80].

Pulsars show a characteristic synchrotron radiation of accelerated electrons along the magnetic field lines. As long as the spin and magnetic field axes are not aligned, the rotating magnetic dipole generates an electric field followed by the electrons on the surface. Therefore, the magnetospheric activity causes the pulsar to spin down owing to the conservation of angular momentum. This is called magnetic braking. Thus, by measuring the period (P) and period derivative (\dot{P}), the dipole magnetic field strength B_{dip} , the dissipation of rotational energy (\dot{E}) and an upper limit of the age of the pulsar (the characteristic age (τ)) can be found. These relations are given as follows;

$$B_{\text{dip}} = \sqrt{\frac{3c^3 I P \dot{P}}{8\pi^2 R^6}} \quad (1.1)$$

$$\dot{E} = \frac{4\pi^2 I \dot{P}}{P^3} \quad (1.2)$$

$$\tau = \frac{P}{(n-1)\dot{P}} \left[1 - \left(\frac{P_0}{P} \right)^{n-1} \right] \quad (1.3)$$

where c is the speed of light in km s^{-1} , I is the moment of inertia in $\text{kg} \cdot \text{km}^2$ and R is the radius of the NS in km and B_{dip} is in G, τ in s and \dot{E} in W. [80].

Owing to their extreme properties, NSs are observed mainly in Radio and X-ray bands due to their strong magnetic fields and hot surfaces. The observational properties of NS imply

a variation among these objects. Alongside the typical middle aged rotationally powered pulsars (RPPs) with a magnetic field of $B_{\text{dip}}=10^{12}$ G, there are other classifications or sub-classifications such as dim thermal NS which are nearby the Earth and observed as thermal soft X-ray–UV radiators [123], central compact objects (CCOs) which are young NSs inside supernova remnants (SNRs) with large P , low B_{dip} and much higher τ compared to their real ages [50], magnetars which are RPPs with very high B_{dip} showing characteristic X-ray outbursts [54] and milli-second pulsars which are powered by the accretion from their non-degenerate binary companions [15].

To understand the variation among different types of NS, exploring the history of the progenitor can bring invaluable contribution.

A NS is not the only remnant of the core collapse SN. SNe manifest themselves also as supernova remnants (SNR) for up to 10^5 yr by interacting with the ISM. SN shines on the sky and is observable for some months to over a year [13]. Later on, it loses its optical depth and fades away until it interacts with the dense circumstellar material [74] or to the walls of the cavity which was generated by the progenitor’s wind [37]. The expansion of the shell can be as fast as 10000 km s^{-1} in the beginning. This velocity decreases down to $\sim 100 \text{ km s}^{-1}$ and even less in the observable lifetime of the SNR. The expansion of a SNR is divided into three phases; free expansion, Sedov-Taylor (adiabatic) expansion and snowplough (radiative) expansion.

The free expansion phase is the stage where the mass of the swept up IS material by the blast wave is negligible compared to the ejecta mass. In this stage, the relation between the expansion velocity of the blast wave and the elapsed time is linear; $v_{\text{bw}} = R/t$ where v_{bw} is the velocity, R is the radius of the SNR and t is the age of the SNR in SI units. This phase lasts for a few hundred years.

When the swept up mass is comparable with the ejecta mass, then the SNR enters the Sedov phase. In this phase, the reverse shock is strong and determinative. The inner medium is heated and the expansion is dominated by the pressure from inside the SNR. This phase is also called adiabatic, because the shell is not radiative enough, in other words, the SNR is still dissipating its energy into expansion rather than radiation. In this stage, the radius of the SNR at the age of t is; $R(t) = 14(E_{51}/n_0)^{\frac{1}{5}} t_4^{\frac{2}{5}}$ pc where E_{51} is the initial explosion energy (E_0) in 10^{51} erg, n_0 is the ambient medium density in cm^{-3} and t_4 is the age in 10^4 yr. The

expansion velocity can be calculated as, $v_{\text{bw}} = \frac{2}{5} R/t$. The shock temperature (T_{sh}) which can be detected in X-ray observations is $T_{\text{sh}} = 1.0 \times 10^{10} (E_{51}/n_0) R^{-3}$ K. The Sedov expansion phase lasts for 10000–20000 yr.

The last stage of the observable life of a SNR is the snowplough phase. In this stage, the swept up mass is much larger than the ejecta mass. The hot interior cools down to 10^5 K, so the inflation of the SN bubble fades away, the shell expands only by conservation of momentum. The expansion velocity of the shell in this stage can be found by the relation; $v_{\text{bw}} = \frac{2}{7} R/t$ (for further details, see [230]).

The SNRs are divided into three classes regarding their observational properties. Majority of them are shell type SNRs (S) having a bright shell owing to the interaction of the shock front with the ISM. Especially young SNRs' radiation can be dominated by the pulsar wind nebula (PWN), a powerful wind of electrons due to the fast rotation and high magnetic field strength. The shell, in these SNRs are faint compared to the PWN, so they are called plerionic type SNRs (F). When the shell is also bright enough together with the PWN, then the SNR is of composite type (C) [86]. Lastly, while some SNRs show shell type morphology in radio bands, centrally peaked thermal X-ray emission is detected within the boundary of the shell. They are called mixed morphology (MM) SNRs. Although the mechanism behind the MM is not clearly known, most of these remnants are thought to be in interaction with dense molecular clouds [231]. Therefore F, C and MM type morphologies may be a good tool to distinguish the SNRs born with a core collapse of a massive star from those having different origins; a white dwarf (WD) merger or an accretion induced collapse (AIC) (carbon detonation as a result of accretion on to a WD) origin.

The greatest challenge to work with SNRs is to estimate their distances. It is necessary as all of the parameters depend on the SNR radius which can be found by translating the angular dimension into physical one. There are several ways to estimate the distance of a SNR. The most widely used is to find the HI clouds shaped by the SNR by 1420 MHz observations and to measure their velocity. This represents the velocity of Galactic rotation w.r.t. the observer. Applying i. e. flat rotation model, the distance of the SNR can be found. The error of this method is assumed as 30 to 50 per cent. Another way is placing the SNR in the Σ -D diagram which shows the relation between the surface brightness (Σ) of the SNRs in 5 GHz and their diameters (D) ([88], Thereafter G03). As the SNR evolves the Σ value decreases.

However, E_0 and n_0 are free variables and may effect the solution dramatically. Furthermore, the number of well studied SNRs of which the distance determination is accurate may not be enough for high accuracy. Another method is detecting an OB association which implies that the progenitor belongs this family, hence the distance of the association can be assigned. Determining the distance from more than one sources (OB stars in this case) reduces the error statistically. The radio or optical parallax of the NS is one of the precise way to determine the SNR distance. However, most of the SNRs cannot be linked to an association or a NS because of the observational limits such as high absorption or beaming fraction. Finally, as the ISM is disturbed by the SNR, the ISM features in the optical and UV band of the stellar spectra show blue and red-shifted components. Therefore, from the distances of these background stars, the SNR distance can be limited.

When a massive star undergoes a SN within a binary system, the companion star can either remain gravitationally bounded to the compact object or released from the system with a velocity which is comparable with its pre-supernova orbital velocity. The companion star is expected to be a massive or an intermediate mass star. These two groups of stars can be classified as one by calling them OB runaway stars. Henceforth, this term will be used.

1.3 OB Runaway Stars

High space velocities of OB runaway stars are explained by two independent mechanisms: dynamical ejection due to gravitational interactions of massive stars in cluster cores [220] and binary disruption as a result of a supernova explosion of the initially more massive component [16]. Both scenarios are viable, but whether one of the mechanisms is dominant is still uncertain. According to the virial theorem, through a symmetric supernova explosion in a binary system, if more than half of the total mass of the system is released, then the new born NS (or BH) and the non-degenerate component are no more gravitationally bound [16]. However, the energy stored in the orbit, in most cases, is not sufficient to produce the neutron star kick velocities that are typically in the range of $300\text{--}500 \text{ km s}^{-1}$ [4, 102, 173]. There is also a group of NS with low space velocities, but most of the pulsars are in isolation implying the high kick mechanism is dominant [11]. The asymmetry in supernova explosions is responsible for such high velocities [297]. Therefore, there are no pulsar companions to many of the OB runaway stars [247]. In some cases, the compact object does not receive

a significant kick and/or the majority of the total mass is stored on the secondary through conservative mass transfer, hence, the compact object remains bound to the companion star [285, 286]. The runaway high mass X-ray binaries like 4U1700-37 [8] and Vela X-1 [122] are such examples.

Yet, the low rate of X-ray binaries and the high rate of isolated neutron stars by taking into consideration the selection effects, the binary disruption is likely to occur in most cases ([90]; hereafter G05). The kinematics of the binary disruption due to an asymmetric supernova explosion is widely discussed in [263]. However, a sample of observationally confirmed OB runaway-NS couples is needed for a better understanding of the problem.

1.4 Motivation

The observational efforts are concentrated on runaway-NS coupling and abundance investigations of runaway stars. Some examples of the runaway-NS pairs (components are separated) are PSR B1929+10 – ζ Oph [20, 105, 268], PSR J0630-2834 – HIP 47155 [270] and PSR J0826+2637 – HIP 13962 [266]. Based on their motions in space, the pulsars and the corresponding runaway stars were traced back in time by using 3-D Monte Carlo simulations. They were found at the same position and the same time inside a young open cluster. The PSR J0630-2834 – HIP 47155 pair is thought to be ejected from very old SNR Antlia.

There are considerable uncertainties in these cases as the supernova events took place more than 10^5 yr ago. The separation between the objects is very large and the SNR has faded away long ago and/or the components are outside of the SNR (the Antlia case). Other important observational evidence is detecting the enhancement of α -process elements on the photosphere of the runaway stars; e. g. the hyper-velocity star HD 271791. The star is proposed to be ejected from a massive close binary system due to a SN that enriches its photosphere in elements which can be synthesized in large amounts during the evolution of the progenitor [221].

The importance of searching for OB runaway stars inside SNRs was first mentioned in [284]. However, the kinematical study of known OB stars inside SNRs was concluded with a lack of OB runaways due to the poor sample of SNRs and OB stars. Still, there is no known O or B-type runaway star that can be directly linked to an SNR given in the literature.

Exploring OB runaway stars inside the SNRs brings valuable outcomes. Firstly, the identification of the explosion positions more precisely will be useful for determining the velocities of young NSs of which proper motion measurements have high uncertainties. Thus, the kick that is gained by the NS due to the asymmetry of the SN can be determined more precisely. Secondly, the distance to the remnant can be measured more accurately by studying the runaway star, as it cannot be largely separated from the explosion center in the observational lifetime of the SNR. Finally, possible effects of a close binary system on the observational properties of the NS can also be examined. Additionally, it would be a direct evidence of the binary supernova scenario (BSS).

The method followed in our work is a direct study of possible runaway stars inside SNRs as described in G05. The stars close to the SNR geometrical centers are selected. OB-type star candidates are determined by a careful study of their BVJHK magnitudes obtained from the literature. The distance moduli are calculated for all sources within this region, and the sources having extinctions and radial distances consistent with those of the SNRs are considered as "candidates". Measuring the radial velocities and identifying the precise spectral types of these objects via spectroscopy reveal their runaway nature, their youth and the exact spatial relations with the SNRs, in other words, the genetic connections.

The space velocity of an OB runaway star is thought to be larger than $30\text{--}40\text{ km s}^{-1}$ [58, 247]. A more precise value is proposed in [267]; 28 km s^{-1} in 3-D and 20 km s^{-1} in 2-D. To summarize, a main-sequence OB-type star of which at least one component of the velocity vector is greater than 20 km s^{-1} is searched in selected SNRs.

In chapter 2, the selected sample of SNRs with or without NSs are introduced and the selection of OB-type star candidates are explained. In chapter 3, the observations carried out and data analysis are explained in details. The results of the observations and candidate selection for each SNR are shared in chapter 4 with the evaluation of the general picture. The OB-type stars and their SNRs are classified regarding their level of confirmation of their runaway nature and associations with the SNRs. Lastly, findings of this thesis will be summarized in the conclusion part.

CHAPTER 2

THE SAMPLE

The regions and the stars to study should have been selected carefully to avoid time consumption. Mostly, the distances to both SNRs and stars cannot be measured precisely. So the background and foreground contamination from other OB stars and even other SNRs or H II regions must be taken care of. Also, in general, shape of a shock front expanding through the ISM is not perfectly symmetric, so the geometrical center of SNRs can be different from the true explosion center. In each search region there are many stars, even one hundred in some cases. This is too big number of stars to take spectra as the telescope time is valuable and limited. Hence, the SNRs and the OB runaway candidates were selected by a careful study. In this chapter, the details of the sample selection is explained.

2.1 Supernova Remnants

There are 300 extended objects which were identified as SNRs [86]. Many others were once claimed to be a SNR, but were then excluded as bidentified as an H II region, another extended object which is a plasma shell due to the ionization of the ISM by the fast winds and UV radiation of a massive star. This is the first challenge to select the fields to work on. For example SNR G206.9+2.3, were removed from the sample due to the possible origin of H II.

Another important point in sample selection is that the observational facilities utilized for this work are located in the northern hemisphere of the Earth. Due to the telescope time pressure of the instruments fitting the purpose of this work in the southern hemisphere observatories, the sample was restricted to the northern sky sources. Hence, although the southern sky

SNRs were studied for candidate selection, it is excluded from this work as the spectral type identification through spectroscopy is strongly needed.

As mentioned in chapter (1), SNR distances have typical uncertainties vary between 30 and 50 per cent. Based on different techniques and observation wavebands, the uncertainty may be even larger. For SNR–OB runaway association, the distance should be known as precisely as possible. As the SNRs are further away than 1 kpc from the Sun in general, the optical parallax of stars cannot be used. The distances to the stars found are then measured as spectro–photometric distance (spectroscopic parallax). Considering the large errors in the absolute magnitudes of massive stars, their distance measurements would also be far from being precise. The distances both to the stars and the SNRs can be confirmed by an OB association or a young cluster. The error in the measurement can be statistically reduced as long as the star found or the SNR can be suggested to belong to this family. However, very few SNR is directly linked to OB associations. For example, in our sample, only three of them have been previously suggested to have genetic connection with an OB association. As SNRs are extended objects with large angular dimensions, they can be projected on to some other young clusters. But each such association needs further proofs and discussions. Besides the distance, the reddening towards the SNR should also be known as it directly affects the OB star candidate selection. Therefore, only the SNRs which are extensively studied in the literature were selected to the sample.

The observing facilities used in this work also limit the SNR selection to the sample. The stars fainter than 14 mag would cost too much time to complete the sample. Given the allocated observing time for this project, the visual magnitude of a candidate was limited to 14 mag, which costs 20 minutes integration time with low resolution spectrographs (see 3). So, this brought a distance limit to the SNR sample, 5 kpc. Assuming 1 mag/kpc global distribution of the A_V , roughly an O9V ($\sim 20 M_\odot$) type star at 5 kpc, reddened by 5 mag can have an apparent magnitude (m_v) of 14 mag. Considering the additional reddening due to the molecular clouds towards the SNR direction, this might be an even lower limit. As the OB runaway stars from SNe are the secondary stars in the binary system and such very massive binaries are rare, the OB runaway mass is expected to be lower. Here, the statistical effect of the conservative mass transfer is neglected. So, a distance limit of 5 kpc was assigned to the SNR sample.

The SNR shock wave expands spherically symmetric in a homogeneous medium, yet the

Table 2.1: The NSs of the SNRs in the sample are shown with their host SNRs and observational properties; period, period derivative, dipole magnetic field strength and characteristic ages respectively.

SNR	Name	P (s)	\dot{P} ($s\ s^{-1}$)	B (Gauss)	τ (yr)
069.0+2.7	B1951+32	0.040	5.844×10^{-15}	4.86×10^{11}	107000
078.2+2.1	J2021+4026	0.265	5.468×10^{-14}	3.85×10^{12}	76900
106.3+2.7	J2229+6114	0.052	7.827×10^{-14}	2.03×10^{12}	10470
109.1-1.0	1E 2259+586	6.979	4.712×10^{-13}	5.80×10^{13}	235000
111.7-2.1	J2315+58	1.061	-	-	-
114.3+0.3	B2334+61	0.495	1.934×10^{-13}	9.91×10^{12}	40600
119.5+10.2	J0007+7303	0.316	3.604×10^{-13}	1.08×10^{13}	13900
130.7+3.1	J0205+6449	0.066	1.938×10^{-13}	3.61×10^{12}	5370
180.0-1.7	J0538+2817	0.143	3.669×10^{-15}	7.33×10^{11}	618000
184.6-5.8	B0531+21	0.033	4.210×10^{-13}	3.79×10^{12}	1260

ambient medium may have different densities in different directions. Therefore, the SNR shape can be highly distorted by the ISM. This makes the geometrical center shift from the true center where the explosion had occurred. The best example for this case is Vela SNR. The geometrical center of Vela mentioned in [86] based on the radio observations, is $\sim 40'$ separated from the explosion center. The explosion center can be found accurately, as Vela SNR hosts the Vela pulsar of which the proper motion is precisely known. Tracing back this proper motion back in time; for 11000 yr, shows the position of the SN precisely. Note that the tracing back is to the opposite direction from the geometrical center, so increasing time is not in the advantage of the explosion center. Due to ambiguity in SNR shape, SNR G205.5+0.5 and SNR G192.8-1.1 was removed from the sample. Also, CTB 80 was not completed for runaway search due to the same reason. On the other hand, in this work, a new explosion center was proposed for two SNRs.

Similar to the physically asymmetric ones, SNRs with strong galactic background may not be resolved regarding the complete shape of their shock front. For this reason, SNRs closer to the Galactic center more than 30° in our point of view were omitted (Figure 2.1). Another reason for this criterion is the large number of background massive stars towards the Galactic center. The chance projection possibility should be very high. But, the only SNR satisfying the distance criteria between the galactic longitudes (l,b); 30° and 60° , are SNR G34.7-0.4. No OB star candidate was found for this SNR. Hence, the majority of this study is the SNRs located at the galactic region between $60^\circ-180^\circ$, which means they are mostly Perseus arm objects. Through these selection criteria, 27 SNRs were selected for OB runaway search.

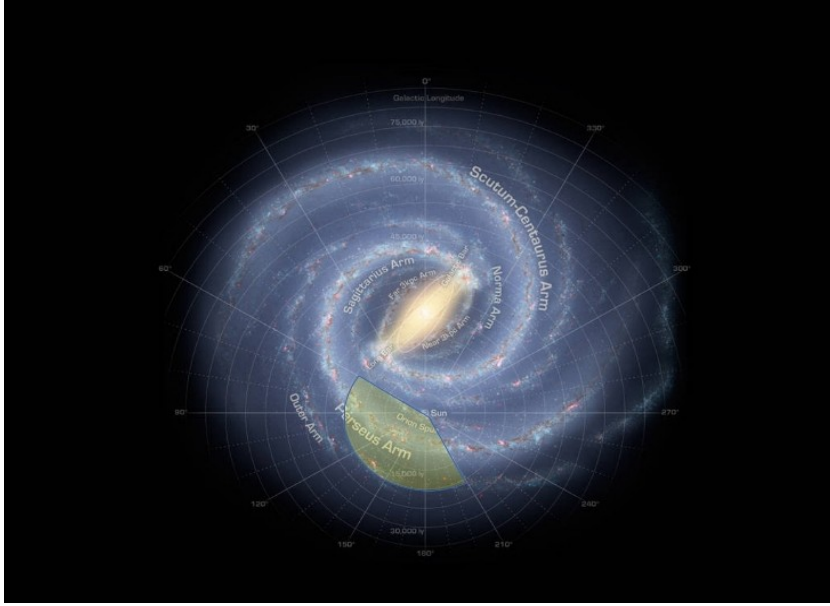


Figure 2.1: The SNRs in the sample are distributed over the region between $l=60^\circ-180^\circ$. The only SNR selected for this work out of the region shown is SNR G34.7-0.4. No OB star candidate was found in this SNR.

These SNRs are northern sky objects in a well defined shape, well studied in the literature, at least 30° separated from the galactic center, and within 5 kpc from the Sun.

The SNRs are mostly shell type and evolved. Crab and SN 1181 are the only two plerion type SNRs. Six of them are MMSNR. Cas A, Crab, Tycho and SN 1181 are younger than 1000 yr. Ten of the SNRs are linked to a NS, a magnetar and a CCO are the different type of NS in the sample (Table 2.2). Two of the 7 rotationally powered pulsars show characteristic ages very high compared to their kinematical ages (Table 2.1). One neutron star having a bright PWN was thermally detected in X-rays, but no pulses was observed in any wavebands. Overall, the SNR sample represents the large variety of types and compact objects (Table 2.2).

2.2 Candidate Selection

SNRs are large objects in an angular diameter varying from $5'$ to 4° . Some are projected on to thousands of stars. Hence, the search region must have been restricted. The observed velocities of the OB runaway stars vary between $(30 - 80) \text{ km s}^{-1}$ [82]. In this work, the upper limit is taken as 100 km s^{-1} . Considering the SNR expansion starts with a speed of 10000 km s^{-1} and slows down to a few hundred km s^{-1} as it sweeps up IS material, the

Table 2.2: The SNRs in the sample. Column 1:Galactic coordinates, Column 2: Type of SNR (Shell type (S), mixed morphology (MMSNR), Composite (C), Plerion (P)) Column 3:Distances from the literature in kpc (referances are in chapter 4) Column 4: Angular diameter in arcminutes Column 5: Search radius in arcminutes Column 6: Type of related NS, PWN is mentioned if the period is not known

SNR	Type	Dist. (kpc)	D	S.R.	NS
034.7−0.4	S	1.6-3.0	35 × 27	3	−
054.4−0.3	S	3.0-6.0	40	4	−
065.3+5.7	S	0.6−1.0	310 × 240	25	−
069.0+2.7	S	1.5−2.5	80	7	RPP
074.0−8.5	S	0.4−0.8	230 × 160	20	−
078.2+2.1	S	1.2-1.8	60	5	RPP
082.2+5.3	S	1.5-2.5	95 × 65	8	−
089.0+4.7	MMSNR	0.8-1.8	120 × 90	10	−
093.7−0.2	S	1.5-3.2	80	7	−
093.3+6.9	S	2.2-5.8	27 × 20	3	PWN?
106.3+2.7	C?	0.8-4.0	60 × 24	5	RPP
109.1−1.0	S	2.8-5.0	28	3	Magnetar
111.7−2.1	S	3.0-3.7	5	1	CCO
114.3+0.3	S	0.7-3.8	90 × 55	8	RPP
116.9+0.2	MMSNR	1.6-4.5	34	3	−
119.5+10.2	S	1.0-1.8	90	8	RPP
120.1+1.4	S	2.0-5.0	8	4	−
126.2+1.6	S	2.0-5.0	70	6	−
127.1+0.5	S	1.0-3.5	45	4	−
130.7+3.1	C	2.2-3.6	9 × 5	1	RPP
132.7+1.3	MMSNR	1.9-4.0	80	7	−
156.2+5.7	S/MMSNR	1.0-3.0	110	10	−
160.9+2.6	MMSNR	0.8-3.2	140 × 120	12	−
166.0+4.3	MMSNR	3.0-6.0	55 × 35	5	−
180.0−1.7	S	0.8-1.8	180	15	RPP
184.6−5.8	P	1.5-2.5	7 × 5	1	RPP
189.1+3.0	MMSNR	1.0-2.0	45	4	PWN

average velocity can be considered as 1000 km s^{-1} . Hence, the runaway star should be found in a circular region with a radius of one tenth of the SNR radius. However, the uncertainties in geometrical centers cannot be empirically determined. Also, the old SNRs in snowplough phase has significantly slowed down, and a fast runaway star may have enough time to exceed this limit. Therefore, following G05, the search region is restricted by one sixth of the SNR radius.

In general, for stars fainter than 10.0 mag, there is no spectral type determination mentioned

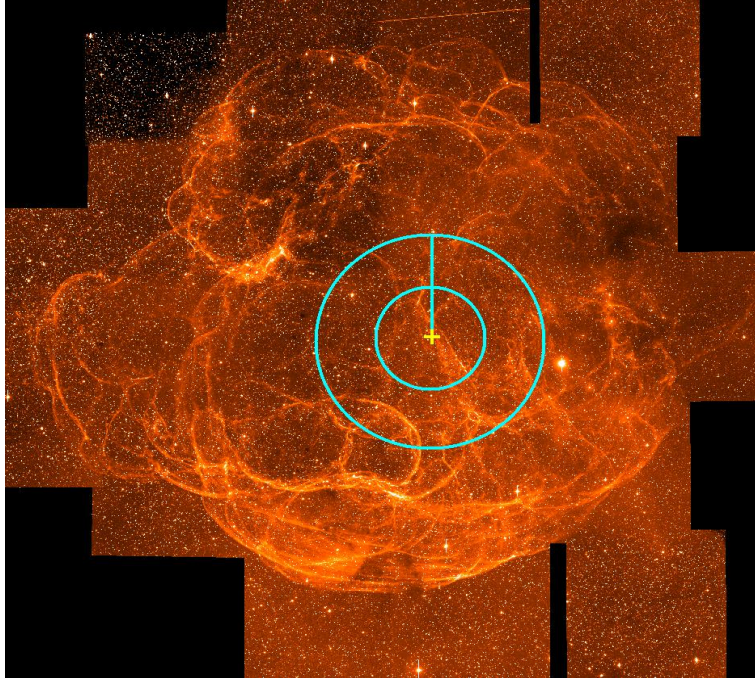


Figure 2.2: The OB runaway search region assigned for SNR S 147. The small circle with a radius of $R/6$, is the one where the runaway star is most expected to be found. The larger circle has a radius of $R/3$, in which the OB type star candidates, runaway or not, was searched. Here, R represents the radius of the SNR, and it is $15'$.

in the literature. For brighter targets, the *Catalogue of Stellar Spectral Classifications* [252] was checked. Then, all of the stars brighter than 14 mag were studied by means of spectral type estimation through their photometric colors to identify the early type stars.

The BVJHK magnitudes of the stars were retrieved from the *UCAC4* catalog [305]. The errors of the colors are between 0.02 and 0.05 mag. For some important bright stars, the photometric magnitudes are also obtained from the *ASCC-2.5 V3* catalog [130]. For each star, the A_V value was calculated for all of the spectral types through all of the color excess combinations; B-V, B-J, B-H, B-K, V-J, V-H, V-K, J-H, J-K, H-K. For calculating the A_V from each color difference, the following equation was used;

$$A_V = \frac{(\lambda_1 - \lambda_2) - (\lambda_1 - \lambda_2)_0}{A_{\lambda_1}/A_V - A_{\lambda_2}/A_V}, \quad (2.1)$$

Where λ_{num} represents the color magnitude in a waveband different from the visual, the A_{λ_1} stands for the absorption value in that band and $(\lambda_1 - \lambda_2)_0$ is the intrinsic color difference. The intrinsic values and A_{λ_1}/A_V coefficients were obtained from [233].

For each star, each spectral type (from O6 to M0) gives 10 A_V values. The true spectral type of the star is the one which yields the minimum standard deviation of the 10 A_V values.

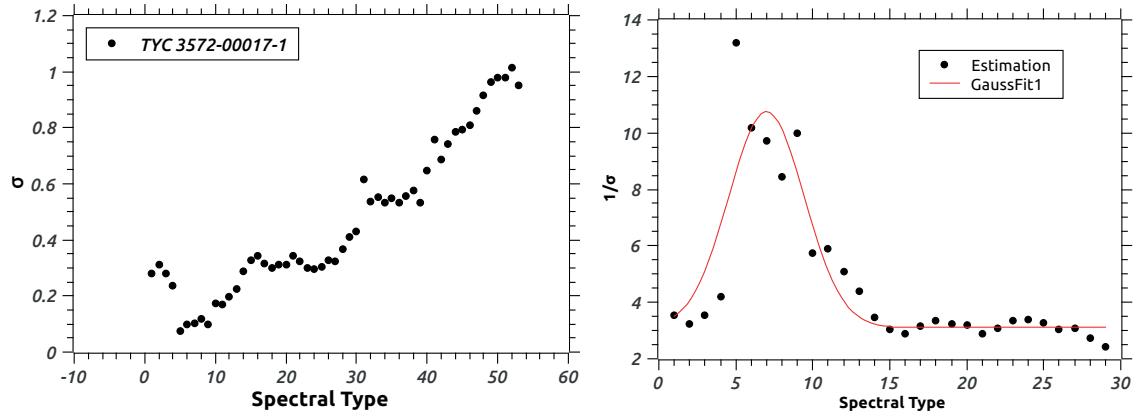


Figure 2.3: *Left:* Deviation (σ) vs. spectral type graph of one of the candidates; TYC 3572-00017-1. The numbers in the x-axis represents the spectral types; 1 is O6 and 53 is M0. The best spectral type is B2V which yields the lowest value of σ of the absorption calculated through whole colors. *Right:* The Gaussian fit to the distribution with a reduced chi square of 0.815. The best spectral type is found to be 7, which is the B2V. In 5σ , the spectral types up to A4 are included.

When calculating this deviation, the individual errors of each color differences was also taken into account. So, the weighted mean of A_V of each spectral type was obtained. The true spectral type is assumed to have the smallest deviation, but due to the uncertainties of the measurements, the model and the accuracy of the calculation approach, the result was taken as a distribution centered on the *best* spectral type and fitted by a Gaussian curve. Stars were checked whether they show OB spectral type in 5σ (Figure 2.3). Those which do not satisfy were removed. Hence, the possible OB type star candidates within were found in this way. In (Figure 2.4), the distribution of the deviations for an F-type star; HD 27524 is shown together with the theoretical one.

The method was also tested with 202 highly reddened ($A_V = 2 - 5$ mag) OB-type stars of which the spectral types were confirmed by spectroscopy [44]. Twenty-two stars were neglected owing to the lack of accurate color measurements in some bands. Out of 180 stars, 160 of them was estimated as OB type star by using the *python* script written by Dr. Ronny Errmann. Given the success of the method, the stars inside the SNR search regions were assigned as the OB type star candidates as long as they yielded an OB-type as the *best* spectral type.

High proper motion was not assigned as a strict criterion, as the measurement accuracy is low for the stars fainter than 13 mag and also a star could be kicked by the orbital energy only in the radial direction. The proper motion values were obtained from *UCAC4* catalog [305]. For

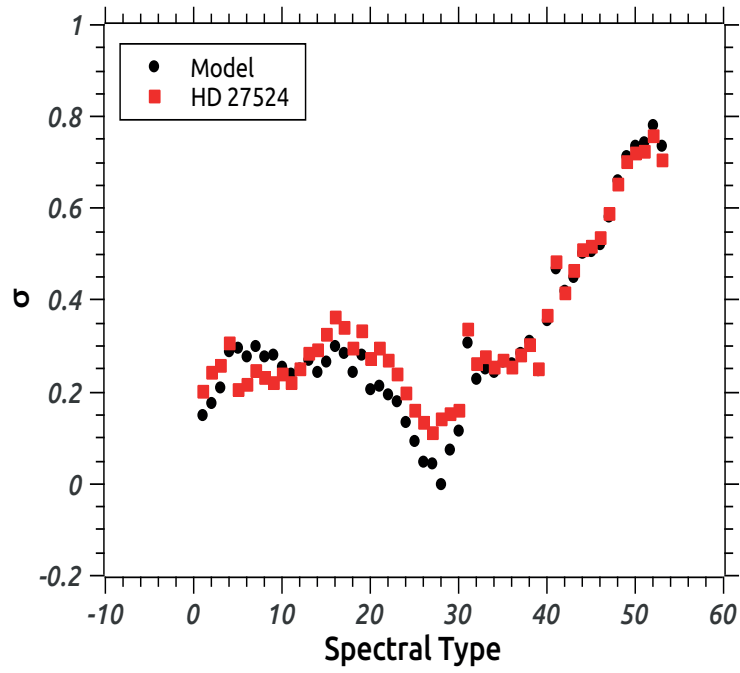


Figure 2.4: Deviation (σ) vs. spectral type graph of an F4V type star (red) and the model values given for the same star in [129]

bright stars, the values were also compared with the ones from *ASCC-2.5 V3* catalog [130].

In total, 176 candidates were determined as potential OB-type stars. These stars were observed for further confirmation of the spectral type.

CHAPTER 3

OBSERVATIONAL

To confirm the OB runaway nature of the candidates, their spectra were obtained and studied. The systematic observations were carried out in two parts; low resolution spectroscopy for spectral type identification and medium and high resolution observations for radial velocity determination. Low resolution observations for the systematic search for the OB type stars were performed at Calar Alto Observatory in Almeria and at TÜBİTAK National Space Observatory (TUG) in Antalya. Fifteen bright targets (not necessarily to be a candidate) up to 11 mag (except for one star with 11.7 mag) were observed at University Observatory of Jena. Four strong candidates were observed at Fredd L. Whipple Observatory in Arizona, for high resolution spectroscopy. In this chapter, the observations, data reduction and analyses are explained in details.

3.1 Observations

The information on the instruments and the number of the stars observed are given in Table (3.1). Spectral type identification had been planned to be done through line strength ratios of continuum subtracted spectra not to consume allocated time with standard star observations. Only a few standard stars were observed at the beginning and at the end of the night, for checking the possible instrumental problems and instabilities, not for calibration. For spectral type identification, the wavelength range chosen in this work is λ 3850–5000 Å following the Morgan–Keenan standards [196]. FLECHAS and TRES providing a resolving power of $R \sim 9000$ and $R \sim 44000$ respectively, were adequate for radial velocity measurements. But, the limiting m_v for both instruments are 11–12 mag. On the other hand, the strong candidates were brighter than 12 mag. Therefore, the observatories mentioned above

Table 3.1: List of observations. The dates of observations, observatories, instruments, their resolving powers, success rate of the night and the number of the stars are given.

Date	Observatory	Inst.	Res. Pow	Success	Stars
Sep 12–13, 2012	TUG	TFOSC	1300	100	10
Jan 29, 2013	Calar Alto	CAFOS	550	100	34
Feb 11–12, 2013	TUG	TFOSC	1300	0	0
Jul 18–19, 2013	Calar Alto	CAFOS	550	90	42
Aug 09–10, 2013	TUG	TFOSC	1300	100	17
Summer 2013	SAO	TRES	44000	100	3
Jan 12–13, 2014	Calar Alto	CAFOS	550	0	0
Oct, 19 2015	TUG	TFOSC	1300	10	2
Jan 07–08, 2015	Calar Alto	CAFOS	550	80	58
Winter 2015	SAO	TRES	44000	100	1
2014–2015	Uni–Jena	FLECHAS	9200	100	15

supplied instrument configurations suitable for the purposes of this work.

3.1.1 Calar Alto

CAFOS (Calar Alto Faint Object Spectrograph) is a low resolution spectrograph with a CCD detector, mounted on 2.2 meter telescope at Calar Alto Observatory. It offers different grism options for long slit spectroscopy in the full optical range B–100, B–200 and B–400 includes the wavelength range of $\lambda\lambda$ 3850–5000 Å. B–200 was preferred because, while B–400 offers very low resolving power, ~ 250 and B–100 offers a higher resolution, but a narrower wavelength range. Although it covers the intended range, grism B–100 excludes two important HeI absorption lines at $\lambda\lambda$ 5876 and 6678 Å, which are not blended and can be distinctive in the OB type star spectra. Furthermore, higher resolution requires longer integration times. Fifty minutes integration time is expected to reach 50 S/N value for a 14 mag star. Considering the observing time allocated to this project is 2 nights per semester, a lower resolution option was more convenient to complete the full sample. The grism B–200 offers a wide wavelength range, $\lambda\lambda$ 3200–8000 Å with a resolving power of 505 at the blaze wavelength ¹, (Accessed on November 01, 2016). ~ 50 S/N was achieved in a 20 minutes integration time for a 13.99 mag target. Hence, the grism B–200 was used in all of the CAFOS observations of this project.

¹ <https://www.caha.es/alises/cafos/cafos.html>

CAFOS observations are the main source of this work. The systematic identification of spectral types was done with this instrument. The moderate resolving power and the larger diameter of the mirror was the optimum choice to take the maximum number of the star spectra.

The proper slit width, $2''$ in all of the observations, was chosen depending on the seeing measured at the beginning of the night. The CCD used in CAFOS is cooled down and fixed to -100°C to avoid count variations due to the temperature. As no dark current was expected, no dark frames, which are the images taken without any light source in a certain exposure time, were taken. Ten bias frames, the instantaneous images taken in an infinitely small exposure time were taken. Biases were sufficient to remove the background counts of the CCD. To calibrate the wavelength scale of the CCD, three HgHeRb lamp (arc) spectra were taken both at the beginning and at the end of each night. An arc is an emission spectrum of the monochromatic light. Each emission line has a certain wavelength, so the corresponding pixel is assigned to have that value. To correct the science spectra regarding the energy dependence of the CCD, five spectra of a halogen lamp (flats) were taken at the beginning and at the end of each night. In 5 successive nights out of 7 allocated, 153 stars were observed.

3.1.2 TUG

TFOSC (TUG Faint Object Spectrograph and Camera) mounted on RTT-150 (150 cm Russian-Turkish Telescope) at TUG, is another low resolution spectrograph with nine grism choices² (Accessed on November 06, 2016). The grism G14, $R\sim 1337$, serves a wavelength range of $3270\text{--}6120\text{ \AA}$. The grism G7 is the only alternative for this project, however, the wavelengths shorter than 4300 \AA are out of range, so the Ca II-K $\lambda\lambda 3934, 3968$ absorption line which is very important in spectral type identification of A-F type stars, is not included. G9 is used for echelle spectroscopy and it serves both a wide wavelength range and a higher resolution, but the integration time needed is much larger. So, the grism G14 is the optimum choice of this instrument.

To keep the resolving power at ~ 1300 , 67 micron slit was preferred to 100 micron one. The TFOSC CCD is also cooled down to -100°C which provides a stable background. Bias, arc and flat frames were taken following the procedure in Calar Alto observations. For the arc

² <http://tug.tubitak.gov.tr/tr/teleskoplar/tfosc>

spectrum, the suitable lamp for this wavelength range is the helium. An alternative is the iron–argon lamp. However, these elements have a high number of transition stages within this range, whereas the resolving power is not enough to resolve these lines. Therefore, due to the line blending, the spectrum has a continuum shape besides the emission lines. So, the helium lamp was preferred. For flat correction, halogen lamp spectra were taken.

Out of eight awarded nights in TUG, 18 targets were observed in four successful nights.

3.1.3 University Observatory of Jena

Fibre Linked Echelle Astronomical Spectrograph (FLECHAS) is an echelle spectrograph on 90 cm Schmidt Telescope at University Observatory of Jena. [197]. This is the only choice for spectroscopy. The covered wavelength range through 29 orders, is 3900–8100 Å. The resolving power is satisfactory, ~ 9200 . The FLECHAS CCD does not have a cooling system with liquid nitrogen. Depending on the season, it is cooled down to a temperature between -35°C and -25°C . Therefore, three dark exposures with an integration time of the science spectra are taken at the beginning of the night. Immediately before the darks, the CCD was illuminated by the tungsten lamp to simulate the remnant counts from the stimulated pixels along the orders. This effect must be taken into account for exposures with an integration longer than 30 s, far less than the science exposures of this work. The FLECHAS data is used for radial velocity determination, hence, the wavelength calibration must be done carefully. Three tungsten and Th–Ar lamp spectra were taken immediately before each science spectrum for flat–fielding and wavelength calibration.

The mirror diameter of the Schmidt telescope is relatively small and the resolution of the instrument is pretty high. This causes the limiting magnitude is low, 11–12 mag. The targets observed here have a brightness of 7.0–11.7 mag in visual band. However, the integration times are quite long, ~ 1800 s. In addition, the CCD quantum efficiency is the highest in the visual part and is significantly low in the wavelengths shorter than 4000 Å [197]. But, there are important features in this part, such as CaII–K absorption. So, to increase the S/N level, three stars were observed by using pixel binnings different from 1×1 . For one star the CCD pixels were binned by 2×2 , while for the other two, it was binned by 1×4 . The dispersion axis is the x–axis. By 1×4 binning, the losses in the resolution was minimized. However, the high binning rate in the y–axis resulted in the complete loss of the last order which is

closer to the edge. Nevertheless, the wavelength range of the last order is not significant as it is mostly dominated by the atmospheric absorption. A 1×8 binning is not useful for the current purposes as all of the orders in the blue part merge with the adjacent one. The science spectra were also taken as three exposures consecutively to remove the cosmic rays and other possible instabilities.

University Observatory of Jena is at 400 m altitude and located in Central Europe. Thus, the weather conditions are mostly not stable. Although the S/N was expected to be doubled, the variations in the weather conditions and possible tracking problems caused less counts to be obtained.

Three OB runaway candidates and 6 neighboring stars were observed by FLECHAS. Spectral type confirmation, stellar parameter determinations and radial velocity measurements were done successfully.

3.1.4 SAO

TRES (Tillinghast Reflector Echelle Spectrograph) is a two fiber (sky and object) optical echelle spectrograph on the 1.5-meter Tillinghast telescope at the Smithsonian Astrophysical Observatory's Fred L. Whipple Observatory on Mt. Hopkins in Arizona. Four important OB runaway candidates were observed here. The observations and data reduction were carried out by Guillermo Torres. The resolving power is high, ~ 44000 , and the wavelength range is broad, 3800–9100 Å. A typical exposure time is 300 s.

Same as CAFOS and TFOSC, the CCD is cooled down to -100°C , so no dark exposure is taken. Biases, flats and arcs taken at the beginning and at the end of each night as a standard, were used. The arc lamp is a Th–Ar and the flat lamp is a halogen. The sky spectrum is also taken simultaneously with the object to remove the effects of the Earth's atmosphere.

The maximum S/N in the blue part is ~ 50 . With TRES spectra, the stellar parameters and radial velocities were determined. Also, ISM absorption lines which are very important to reveal the star–SNR relation were studied.

3.2 Data reduction

The reduction of TRES data were done by Guillermo Torres by using TRES IDL pipeline. The other data obtained were reduced in IRAF environment [274].

TFOSC and CAFOS instruments are similar to each other and both used for long slit spectroscopy. So, the data processing is also similar. Ten bias frames were combined to have an average CCD background. This was subtracted from all other frames. For TFOSC data, in addition to the bias subtraction, all of the frames were over-scanned. This is an additional subtraction of the counts in the over-scan region of the CCD which is a narrow stripe (i. e. 10 pixels wide) along the y-axis, kept dark during the observations. Later, this region is scanned through the whole x-axis and subtracted. This was done in case of additional counts which were not simulated by the bias frames. After bias subtraction, the flats were also combined to a single frame. Unlike CAFOS data, TFOSC flats were combined into two frames as the evening and the morning flats to check possible deviations. However, the division of these two flats by each other yielded only some variations at its noise level, 5/1000. For all of the science spectra, the S/N is much lower than those of the flats. The bias subtracted arcs were also combined for the average. As long as the science frames were taken in two exposures, they are also combined.

The combination processes was done by the combination tasks of IRAF. The main operation is to scale and to take the average of the input frames. But, the important point is the rejection algorithms. For example, the cosmic rays randomly shine the pixels, and it is highly unlikely that the cosmic rays excite exactly the same pixel in two or more exposures of the same. Hence, such artificial counts can be detected and rejected while taking the average. Furthermore, the noise can also be removed to some extent, depending on the rejection sigma. In this work, all of the combination processes was done by using the IRAF parameter; *ccdclip*. The pixel values larger than 3σ of the average were rejected. In this rejection algorithm, each pixels are evaluated independently from the neighbors of the same frame. Another possible choice, *avsigclip* (average σ clipping) takes the average of 10 neighboring pixels into account and then makes the rejection.

After having a unique flat, arc and science frames, the further reduction was applied. The science frames were divided by the flats by the IRAF task *ccdproc*. This task first scale the

flats with the science frame and then applies the division. In other words, the flat is first divided by its median count before flat-fielding to keep the original counts of the science frame. By flat-fielding the wavelength dependence of the CCDs, which is red sensitive, was removed. Then, the science spectra and arcs were ready to be extracted.

For the extraction, the IRAF task *apall* was used. First, the aperture was assigned and the sky background was subtracted interactively. The sky was taken as the average of two portions (left and right) which are 10 pixel long and slightly separated from the gaussian wings (the separation from the center differ for each spectra). As the aperture deviate along the horizontal or vertical axis, one must determine the pixels to follow for extraction. The aperture tracing can be done interactively in *apall*. CAFOS and TFOSC apertures can be fit by third order Legendre polynomials. This traced aperture information is kept in a database folder, so the arcs can be traced and extracted. For each science spectrum, the arc was extracted by tracing its aperture. So, each science spectrum has a different tracing, hence a different arc spectrum.

The emission lines in the arc spectra were identified one by one with the task *identify* by using the atlases in the instruments web pages ref. HgHeRb lamp of CAFOS presents 10 lines to be assigned. The non-linearity in extrapolation through the whole pixel-wavelength scale was overcome by fitting a *legendre* polynomial in the fourth order. However, the number of the lines are not enough. The root mean square value of the variations is around 0.6 pixels for both instruments. For CAFOS, this corresponds to $\sim 3 \text{ \AA}$. In CAFOS spectra, the dispersion is lower around H_{β} . So the difference between stellar absorption line and the laboratory wavelength widens towards the blue and the red end of the spectrum Nevertheless, as long as the radial velocity measurements are not intended, the dispersion is in adequate quality. Spectral type identification can successfully be done. He lamp of TFOSC presents only six lines to be assigned. The dispersion of assignment is $\sim 1.2 \text{ \AA}$. Lastly, the bias subtracted, flat-fielded and extracted science spectra were settled to the wavelength scale.

A similar procedure was applied for the FLECHAS data Instead of biases, the dark exposures in the same integration time with the corresponding spectra were combined and subtracted from the rest. Each sets of flats and arcs taken just before each of the science spectrum were also combined for the average values with rejecting extra-ordinary counts. The flat-fielded science spectra were extracted for all of the 29 orders. The arcs were extracted as again tracing the apertures of the corresponding science spectra. Because of that FLECHAS

was mounted on July 2013, during this project, the calibration atlas for the arcs was not available. Over 200 emission lines in the Th–Ar lamp spectra were identified by the author one by one, using the Th–Ar atlases from National Optical Astronomy Observatory (NOAO), USA ³ (Accessed on November 8, 2014). Later on, the calibration atlas was published by the observatory. Yet, in this work, the dispersion solution made by the author was used. The difference between two solutions is that while one was done by using fewer but deblended lines (this work), the other was done by more lines but also including the blended ones. Nevertheless, the rms value is 0.02 Å and the whole spectral range, especially the blue part was covered sufficiently to avoid non–linearity. Finally, the dispersion corrected spectra were ready for analyses.

3.3 Analyses

The reduced spectra were analyzed for the spectral type identification, determination of stellar atmosphere parameters and radial velocity measurements. First, the spectra were normalized, then were cross correlated with standard stars or synthetic spectra. The line intensities and/or EWs were measured, Doppler shifts were determined. The analyses were also performed in IRAF environment.

3.3.1 Continuum Subtraction

As the spectral type identification was not done through the flux calibrated spectra, the continuum radiation was subtracted to measure the intensity ratios and radial velocities. Hence, all of the spectra were normalized to an arbitrary flux around the value; 1.

Before normalization, each long slit (low resolution) spectrum was trimmed and a spectrum in the wavelength range of 3850–5000 Å was maintained. The red part of the spectrum was also used for several spectra which are mentioned in the next section. Also, the continuum can be fitted more easily for a smaller portion of the spectrum. The echelle spectra, TRES and FLECHAS were also also trimmed in each orders to remove the overlapping regions. For example, the wavelength range of the second and the third order of FLECHAS is 3945–4119 and 4018–4196 Å respectively [197]. After trimming, the orders had the ranges of 4000–

³ <http://iraf.noao.edu/specatlas/thar-photron/thar-photron.html>

4080 Å and 4080–4160 Å respectively. Then, each order was normalized individually and then merged together to make a single spectrum in the range of 3900–8000 Å.

Low resolving power of CAFOS caused difficulties in continuum subtraction. Late type star spectra show many absorption lines and molecular bands so that tracing the continuum radiation curve is very difficult. This effect, called line-blanketing, becomes more efficient with decreasing resolving power. Also, early B type stars show wide absorption lines and more than A and late B type stars in number. Although it is not as effective as the late type stars, a similar difficulty can be mentioned. The flat-fielded spectra of the first Calar-Alto campaign showed an unexpected band-like feature in absorption between ~ 4170 and ~ 4600 Å. It was found out that the reason was a bump in the flat spectra (Figure 3.1). The flats from the other campaigns do not show such structures (3.1). Therefore, these data were trimmed further into two at 4195 Å, keeping the same range, before normalization. Such normalization has removed this effect.

To avoid underestimation of the errors in measurements due to the normalization, firstly, the strength of a line was compared with the closest hydrogen line in the wavelength scale, secondly, the strength was measured from different continuum levels, typically ± 0.02 .

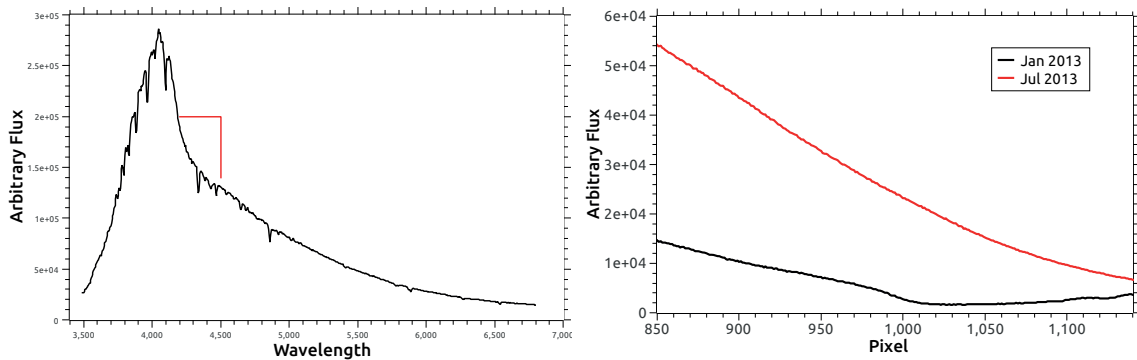


Figure 3.1: *Left:* A flat-fielded spectrum taken by CAFOS on 2013, January. The fall in flux in the range of 4185–4500 Å (Shown by red lines) is artificial. *Right:* Comparison between the flat spectra taken in January (black) and in July (red) of the same year. The bump between the pixels 920 and 1010, is the reason of the ambiguity in the science spectrum.

3.3.2 Spectral Type Identification

For spectral type identification of the CAFOS and TFOSC data, the spectra of Morgan–Keenan standard stars observed at Dark Sky Observatory with a dispersion of $1.8 \text{ \AA}/\text{px}$, were retrieved from ⁴ (Accessed on 2012, September). The standard spectra were smoothed via boxcar by values 7 and 3 respectively, due to its higher dispersion. Each spectrum was cross correlated with all of the standard spectra from B to K type by using the IRAF task *fxcor* (Figure 3.2). The spectral type yielding the largest correlation height was assigned (Figure 3.3). However, a fine tune was also needed to improve the accuracy of the determination. So, the intensities of some indicator features was measured manually and compared to the related lines. For example the spectral type assigned for TYC 3572-00017-1 is B2V by *fxcor*, while the He/H strength ratios suggest B1V temperature type. The error in spectral identification is ± 1 spectral digit (e. g. $B2 \pm 1$).

To test the method used, two of the candidates, which are early B type stars; HD 278115 and TYC 3572-00017-1 were observed by both TFOSC and CAFOS. The spectral type of the stars are B1V and B2V respectively. The standard spectra were smoothed and cross-correlated with the observed data. Also, TFOSC spectra were smoothed and cross-correlated with CAFOS spectra of the same stars. The cross-correlation heights for both spectra are the largest between B1–B3 spectral types . The resolving power of TFOSC is sufficient to limit the error to 0.5 in HR scale through intensity ratios, and the results of correlation with different spectral types significantly differs from each other within ± 1 spectral type digit. On the other hand, the results for CAFOS data are very close to each other in an interval of 1 spectral type. For CAFOS data, an error of 1 spectral type was kept for the entire sample. In addition, with CAFOS spectra the luminosity class V may not be distinguished from the luminosity class III. But, supergiants show significantly different spectrum and can be distinguished All of the low resolution spectra are given in Appendix (C) with their comparison spectra.

The FLECHAS data were again cross-correlated with MK standard star spectra retrieved from [290] and also with OBA type stars of which the spectral types are known and observed by FLECHAS. Given the high resolution, the important spectral type indicators are measured for their EWs and compared to the standards.

⁴ <https://ned.ipac.caltech.edu/level5/Gray/Gray1.html>

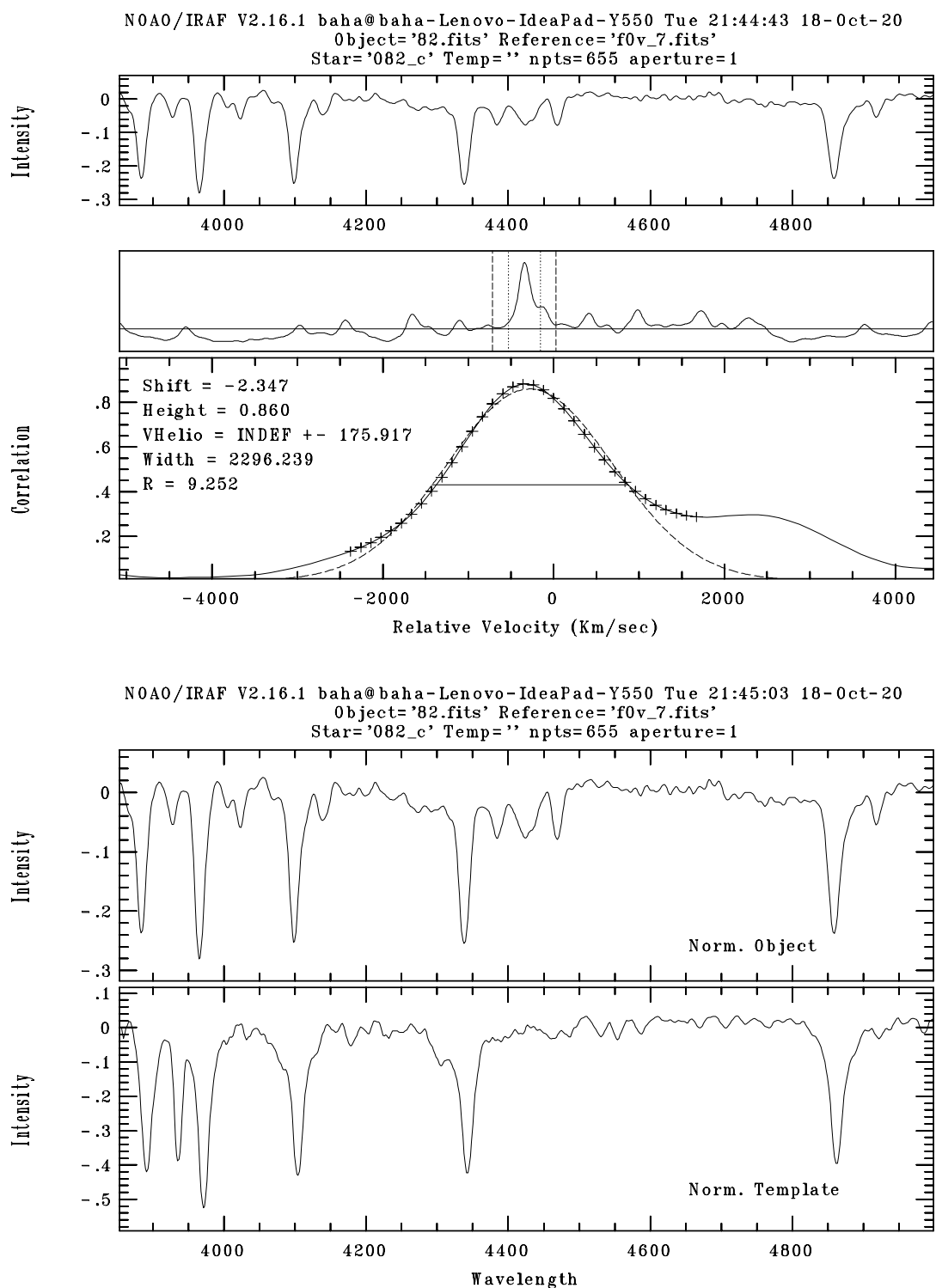


Figure 3.2: Above: Fourier cross-correlation of TYC 3572-00017-1 with an F0V type star. Below: Scaled spectra of the star and the template.

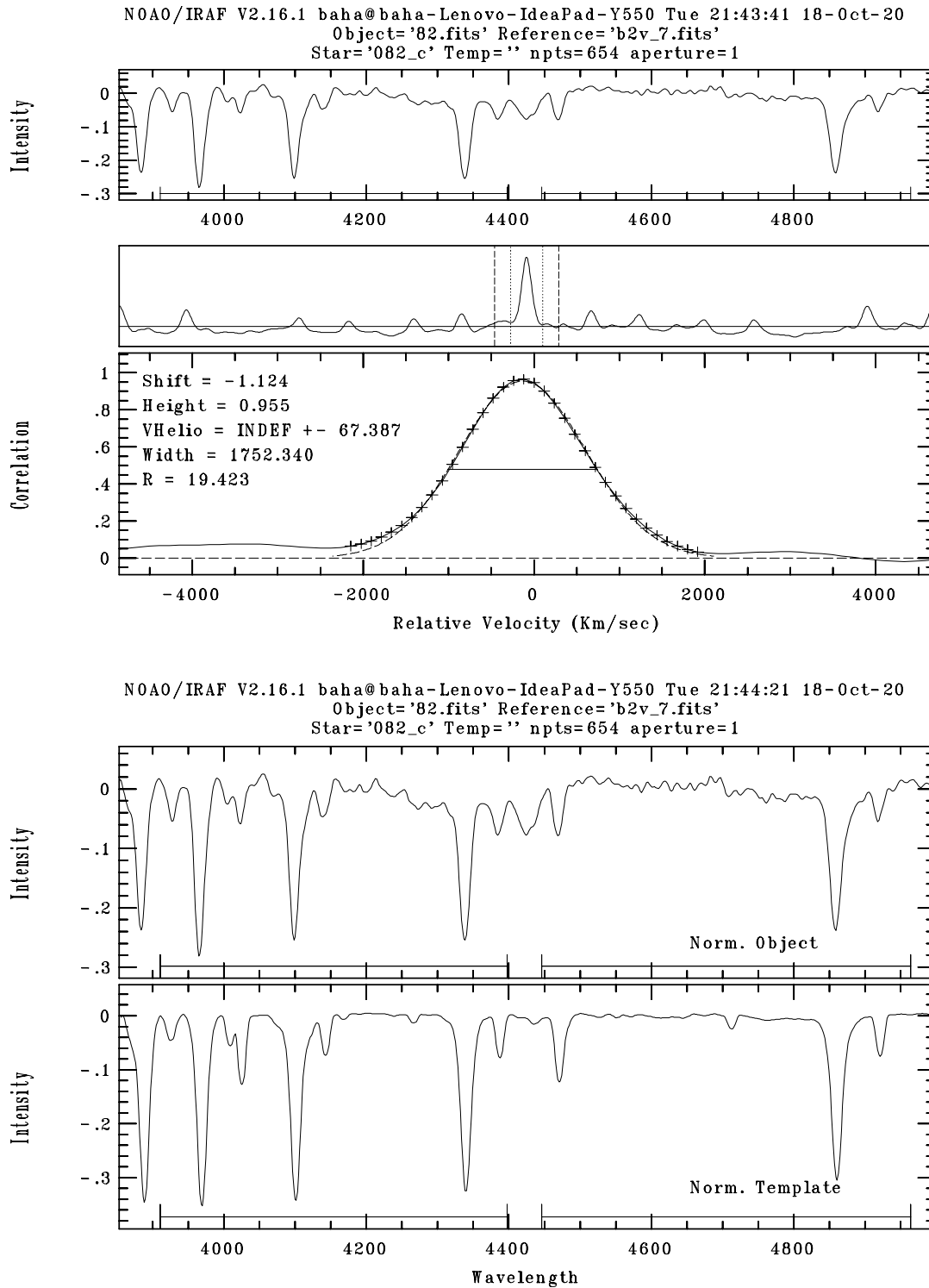


Figure 3.3: Above: Fourier cross-correlation of the same with a smoothed B2V type MK standard star. Below: Scaled spectra of the star and the template.

Table 3.2: Results of Fourier cross correlation of CAFOS spectra of HD 278115 and TYC 3572-00017-1 with their own TFOSC spectra (last column) and with standard stars of various spectral types

Star	F0V	A0V	B5V	B3V	B2V	B1V	O9V	TFOSC
TYC 0017	0.844	0.876	0.921	0.933	0.955	0.933	0.906	0.963
HD 278115	0.815	0.872	0.888	0.891	0.925	0.937	0.927	0.973

In early B type star spectra, ionized helium, highly ionized oxygen and silicon are the main indicators. More ionized species become dominant with the increasing temperature. For the mid-B type stars, the number of the lines becomes fewer as the ionized features vanish. The main indicator becomes ionized magnesium and neutral helium. Their spectra are hydrogen and neutral helium dominated. The strength of the helium with respect to hydrogen decreases with decreasing temperature.

Here, the spectral type identification of the OB runaway star HD 37424, discovered in this work, is shown: HD 37424 shows He II $\lambda 4686$ absorption indicating that the spectral type is earlier than B1. This feature is not seen in stars with a spectral type later than B0.7. On the other hand, He I lines (i.e. He I $\lambda 4713$) are not as weak as in O type stars compared to He II lines; $\lambda 4200$, $\lambda 4686$. The Si IV $\lambda 4116$ line is totally blended and unmeasurable. Si III $\lambda 4552$ is in low strength compared to Si IV $\lambda 4089$ like in the B0V type spectrum. This ratio decreases towards higher temperatures, but He I $\lambda 4541$ is not stronger than Si III $\lambda 4552$ as seen in B0V and O9.5V spectra. Given the equal strengths of O II $\lambda 4640$, He II $\lambda 4686$, He I $\lambda 4713$ and more intense C III+O II $\lambda 4650$ blends, HD 37424 matches best with B0.2V. Considering the slightly stronger He I $\lambda 4713$, B0.5 would be the best approach to the temperature class of the star. Si IV $\lambda 4089$ strength increases against He I $\lambda 4026$ – 4144 as the luminosity class goes higher. However, neutral helium lines are strong enough to judge that HD 37424 is a main sequence star; B0.5V (3.4). The spectral type is between B0.2V–B0.7V, but it is assumed as $B0.5 \pm 0.5V$ in the distance and extinction calculations to avoid underestimation of the errors.

3.3.3 Radial Velocity Measurement

Due to the poor resolution, no radial velocity was measured from TFOSC and CAFOS spectra. After heliocentric corrections were applied to the spectra, radial velocities of TRES and FLECHAS spectra were measured in two ways: fitting one or more Gaussian functions to

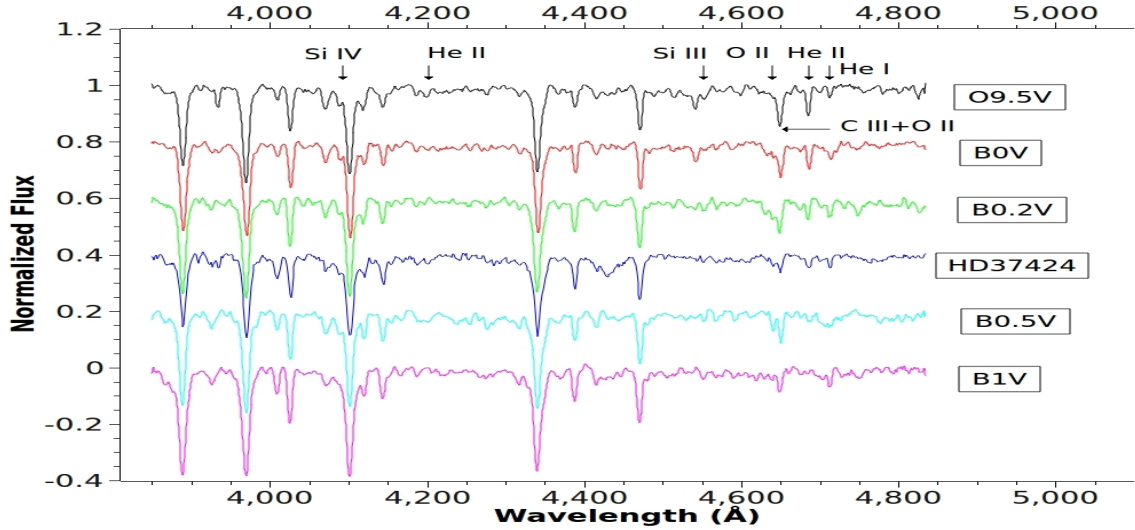


Figure 3.4: TFOSC spectrum of HD 37424 compared to main sequence B type stars. Distinctive features are marked. From left to right; Si IV λ 4089, He II λ 4200, Si III λ 4552, O II λ 4640, C III+O II λ 4650 blend, He II λ 4686, He I λ 4713

the individual lines and/or cross-correlating with a template spectrum.

Because the TRES data were noisy, $S/N < 50$ and the stars were early type, maximum 10 lines were used for the measurement. The doublets and triplets were also avoided, so this may not be enough statistics. On the other hand, radial velocity measurements of early type stars are already far from being accurate and precise. There is still no approved OB-type radial velocity standard star. Few lines, fast rotation, line asymmetries and also binarities are the reasons for this. Not to underestimate the errors, each absorption line were fitted by a Gaussian function fitting the central core. For each line, another two Gaussian fits were applied: one fits the outer edge of the noise of the blue side while fitting the inner edge of the red and the other fits the outer edge of the red and the inner edge of the blue (Figure 3.5). Hence, each line gave a velocity with the central fit and its absolute upper and lower errors from the other two fits. By measuring more lines, the error was reduced to a mean value. As an example, the results for one of the stars observed by TRES are given in Table (3.3). The radial velocity of HD 37424 is measured as $-9.2 \pm 6.5 \text{ km s}^{-1}$.

TRES spectra of HD 37424 was cross-correlated with synthetic spectra. However, the IRAF task *fxcor* calculates a statistical error based on the dispersion of results from the individual lines. As the number of the lines are few, cross-correlation may not be a reliable technique in the OB star case. On the other hand, the results from cross-correlation are perfectly consistent with those from the Gaussian fittings: $-9.6 \pm 4.7 \text{ km s}^{-1}$.

Table 3.3: Radial velocity measurements of HD 37424. The laboratory wavelength of the features, the Gaussian width (σ) of the fit, the wavelength shift obtained by the best fitting (BF) Gaussian, upper (UL) and lower limits (LL) of the shift from different Gaussian fits and the final error are presented. The average of errors of the individual lines is 16 km s^{-1} . The features are given in \AA while all other columns are in km s^{-1} . Subscript 1 and 2 denotes that the measurements are from spectra taken in two different nights.

Feature	σ	BF ₁	UL ₁	LL ₁	E ₁	BF ₂	UL ₂	LL ₂	E ₂
3889.051	164	-10.1	19.3	-29.2	29.4	-12.6	6.2	-28.2	18.8
3970.074	137	-0.5	21.4	-22.3	21.9	-1.4	18.0	-19.8	19.4
4101.737	144	-9.4	12.2	-32.3	22.9	-5.1	14.9	-21.2	20.0
4143.759	98	+4.0	17.1	-10.9	14.9	-1.9	7.2	-8.7	9.1
4340.468	142	-10.6	6.2	-28.8	18.2	-11.5	11.9	-36.6	25.1
4387.928	81	-13.1	-7.1	-24.1	11.0	-8.8	-4.1	-19.3	10.5
4861.332	139	-13.8	0.9	-18.9	14.7	-11.7	-3.0	-19.5	8.7
4921.929	89	-16.5	-1.6	-32.4	15.9	-17.2	-4.9	-31.6	14.4
6562.817	115	-14.7	0.3	-21.5	15.0	-14.4	1.4	-29.7	15.8
6678.149	82	-7.5	0.3	-14.5	7.8	-6.7	3.3	-15.1	10.0

Gaussian fittings were also applied to the FLECHAS data. However, the resolution of this instrument corresponds to 32 km s^{-1} , requiring a good statistics, many more lines to measure to yield a low error. Due to the stellar structure and low S/N, in some cases, this was not possible. The FLECHAS data were cross-correlated with each other, not with a synthetic spectrum. An important runaway candidate HD 254577 in SNR IC 443 was observed together with other members of its OB association. The radial velocity was measured w.r.t. the association members.

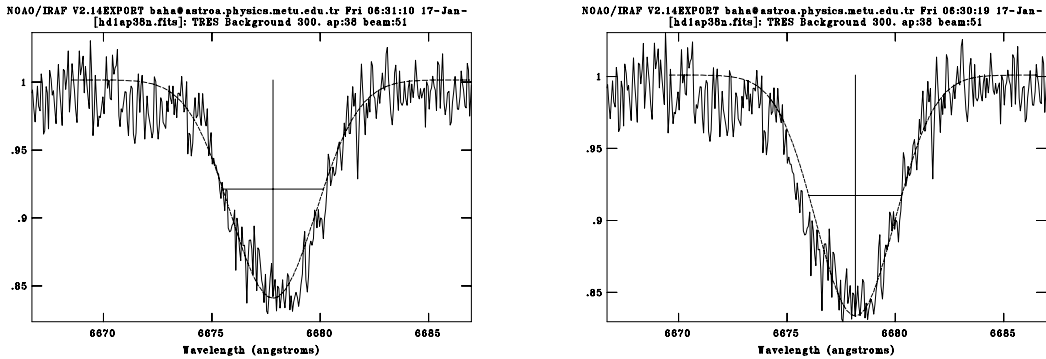


Figure 3.5: Radial velocity measurement by Gaussian fit starting with the blue and the red wings of He I λ 6678 respectively.

3.3.4 Interstellar Medium Lines

Detecting high velocity component of the ISM absorption features may directly prove the connection between the SNR and the OB runaway star. Both TRES and FLECHAS spectra are studied for the ISM features. Gaussian fitting is sufficient to measure the radial velocities and the EWs accurately as the width of these features are mainly due to the Gaussian distribution of the particle velocities. In case of blending due to the high velocity component, double Gaussian function was used. However, in general, the accelerated clouds from the SN are fragmented by the shock wave and they have different discrete velocities despite the narrow range. So originally more than two Gaussian fittings might be necessary, but this is a matter of resolving power of the instrument. Gaussian fits and the results are shown in chapter (B)

3.3.5 Stellar Parameters

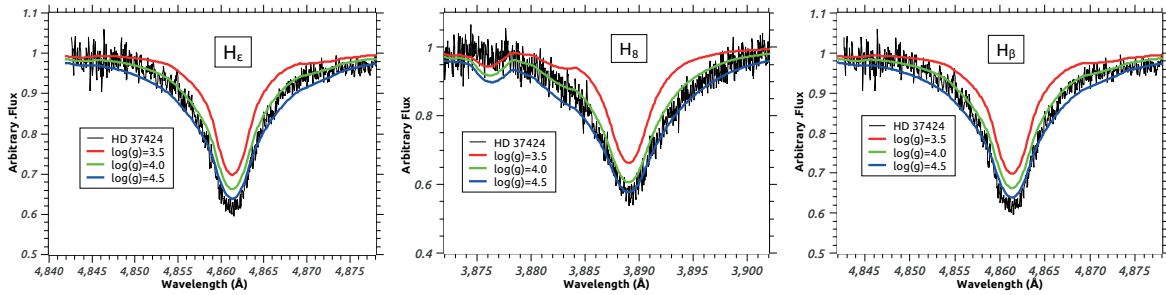


Figure 3.6: H_{ϵ} (left) and H_{δ} (middle) and H_{β} lines of HD 37424 are compared with the synthetic spectra of $\log(g) = 3.5, 4.0, 4.5$ in cgs. The wings of the hydrogen lines are in best correlation with $\log(g) = 4.0$.

For three of the OB runaway candidates observed by TRES and FLECHAS, model spectra were synthesized by using the program *Spectrum* [85]. Stellar atmosphere data files were retrieved from [33, 147]. These grids are modeled for photospheres which are assumed to be plane parallel and in local thermodynamic equilibrium (LTE). For massive stars which mostly show strong winds, non-LTE departures for the chemical abundances are significant. However, owing to the noisy data, here, the aim of this work is restricted to determination of fundamental parameters; effective temperature (T_{eff}), surface gravity ($\log(g)$) and projected rotational velocity ($v \sin(i)$). Also the abundances of He are measured. The low S/N ratio does not allow to measure the microturbulent velocity which can be measured from the lines with several tens of $\text{m}\text{\AA}$ EW. For all the spectra, it was set to 2.0 km s^{-1} . The rotational

velocities found in this work, can only set an upper limit as the spectral line broadening is also due to the macroturbulent velocity.

The atmosphere model, line lists, intended wavelength range, resolution and microturbulence velocity were provided as input parameters. The disadvantage of the program is that it cannot calculate the features of some of the ionized elements like He II and Si IV which are important for early B type stars. Therefore, the observed spectra were also cross-correlated with model spectra synthesized by the code, *Sterne* [113, 114]. The model atmospheres are synthesized by *Spectrum* for 0.1 Å resolution to simulate the instrumental broadening. Then, the outcome spectra of certain temperature, surface gravity and microturbulence velocity are smoothed by using *avsini* task of *Spectrum* for different projected rotational velocities.

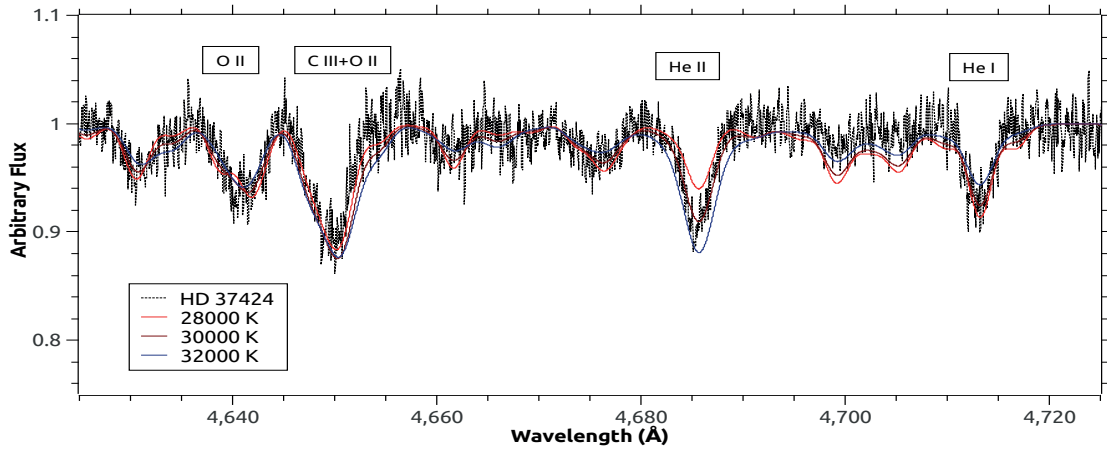


Figure 3.7: The spectrum of HD 37424 is compared with synthetic spectra of different temperatures; 28000 K (in Red), 30000 K (in Brown) and 32000 K (in Blue). He II / He I ratio, ~ 1 , favors 30000 K. *Sterne* spectrum: $[\text{He}/\text{H}]=0.1$ dex, CNO is solar.

For example, for the OB runaway star HD 37424, to determine the T_{eff} , He II $\lambda 4686$ to He I $\lambda 4713$ EW ratio is used. 28000, 30000 and 32000 K spectra with $\log(g)=4.0$ in cgs and smoothed for 120 km s^{-1} of $v_{\text{sin}(i)}$ from *Sterne* are compared with TRES spectrum of HD 37424 (Figure 3.7). This ratio of ~ 1 , clearly shows the star has a T_{eff} of 30000 ± 1000 K. As 29000 and 31000 K models do not exist, 1000 K error can be assigned. The surface gravity is found by comparison with the spectra of $T_{\text{eff}} = 30000$ K with $\log(g)$ of 3.5, 4.0 and 4.5 in cgs. The logarithm of surface gravity of HD 37424 is $\log(g) = 4.0$ in cgs (Figure 3.6). Finally, to determine $v_{\text{sin}(i)}$, a spectrum with T_{eff} of 30000 K and a $\log(g)$ of 4.0 was reproduced for $v_{\text{sin}(i)}$ from 80 to 200 km s^{-1} with steps of 20 km s^{-1} (Figure 3.8). As a result, the stellar parameters of HD 37424 is as follows: $T_{\text{eff}} = 30000 \pm 1000$ K, $\log(g) = 4.0 \pm 0.25$ in cgs and $v_{\text{sin}(i)} = 140 \pm 20 \text{ km s}^{-1}$. Although chemical abundances cannot

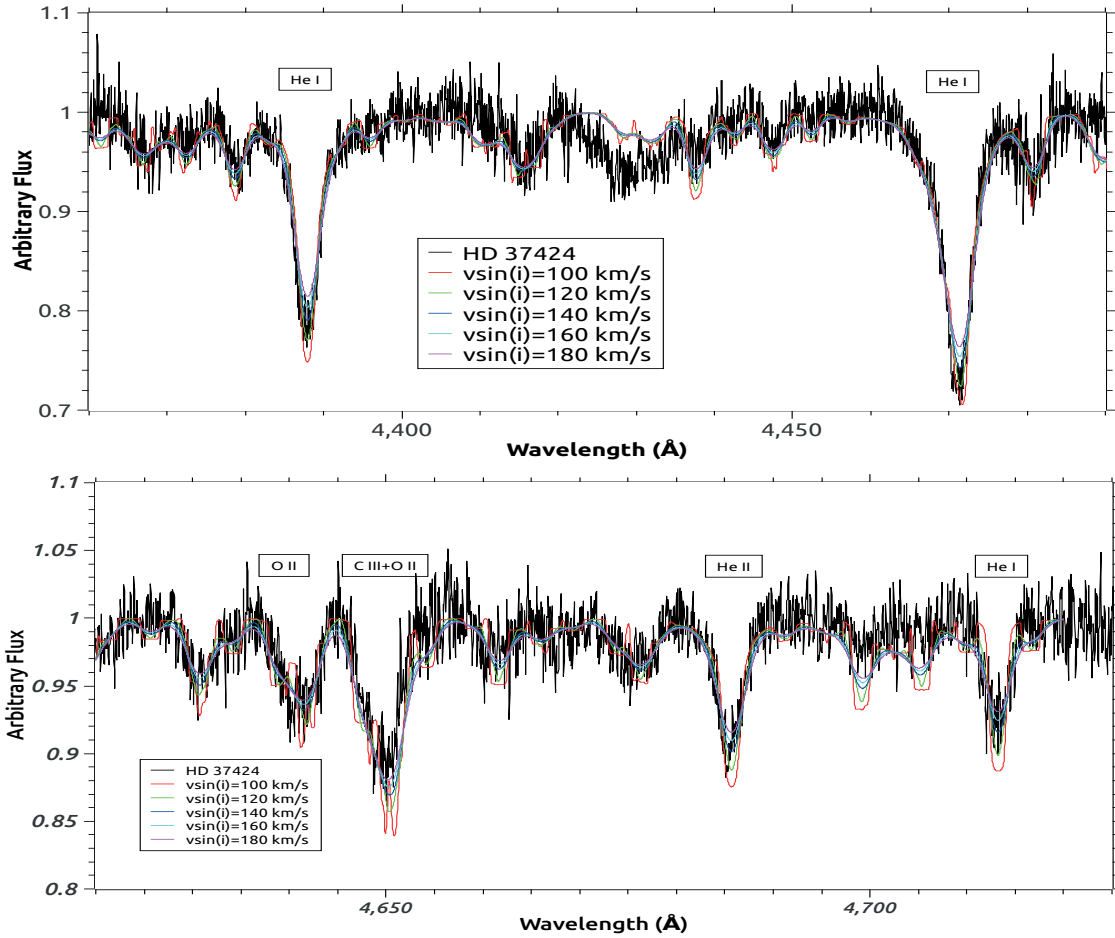


Figure 3.8: Comparison of HD 37424 spectrum with a synthetic spectra of $T_{\text{eff}} = 30000$ K and $\log(g)=4.0$ smoothed for a $v \sin(i)$ of 100 to 180 km s^{-1} . 120 (in Green), 140 (in Dark blue) and 160 (in Light blue) km s^{-1} remains the least residuals comparable with the noise level. Hence $v \sin(i)$ for HD 37424 is $140 \pm 20 \text{ km s}^{-1}$. Above; *Sterne* spectrum with $[\text{He}/\text{H}]=0.3$ dex, Below; $[\text{He}/\text{H}]=0.1$ dex w.r.t. solar

measured be measured precisely, the star is likely to be a He-rich star. For comparison, the *Sterne* spectra of 0.3 and 0.1 dex enhanced He is used. Comparison with *Spectrum* models, 0.22 dex with a high σ of 0.06 dex He abundance is measured.

CHAPTER 4

RESULTS AND DISCUSSION

OB runaway stars were searched inside 27 SNRs and spectroscopic observations were carried out for 170 candidates inside 16 SNRs. The sample was completed for almost all of the SNRs. There are exceptions which are mentioned in Section 4.4.17.

In this chapter, firstly, the full picture of the only confirmed OB runaway star HD 37424 and its association with the SNR S 147 and the pulsar will be demonstrated. Secondly, two possible OB runaway stars inside IC 443 and G065.3+5.7 will be discussed regarding their association with the SNRs. Thirdly, the potential OB runaway stars inside six SNRs will be shown and future studies will be explained. Lastly, the SNRs in which no OB runaway star found will be reported and the general picture of the study will be drawn.

The fundamental parameters of SNRs are mentioned and discussed in detail, as a convincing association between the stars and the SNRs is necessary to be demonstrated. For each SNR, stars observed and found to have spectral types earlier than A3 are listed with their distances and A_V values calculated. The later type stars are foreground stars without any exception. The kinematics of the stars are studied relative to the host OB association if exists. As, for many SNRs, the associations are not very well known, the neighboring stars are also discussed regarding a genetic connection with the OB runaway and the progenitor of the SNR.

4.1 The Massive Runaway Star Inside SNR G180.0-1.7 (S 147)

S147 is a shell type SNR located in the Galactic anti-center direction with a diameter of 180'. [86]. Its compact object is a radio pulsar, PSR J0538+2817 [7]. The filamentary shell

Table 4.1: Distance estimates for S147. (R^l) denotes the radius lower limit of the SNR.

Distance (kpc)	Method	Reference
1.6 ± 0.3	$\Sigma - D$	[256]
0.8–1.37	$R^l, \Sigma - D$	[146]
0.6	R^l	[133]
0.9	$\Sigma - D$	[40]
0.8 ± 0.1	A_V	[62]
1.06	$\Sigma - D$	[88]
0.88>	High Vel Gas	[242]
1.2	Pulsar DM	[143]
$1.47^{+0.42}_{-0.27}$	Pulsar Plx	[203]
$1.3^{+0.22}_{-0.16}$	Pulsar Plx	[35]

is bright in H_α and spherically symmetric. (Figure 4.1). Based on optical observations, the total absorption in the V band is $A_V = 0.7 \pm 0.2$ mag [62]. The shell structure is also well defined in radio wavelengths which coincide with that in the optical bands [75]. The remnant has not been studied in X-rays [246]. The distance estimations vary from 0.6 to 1.9 kpc (Table 4.1). Four of these are based on $\Sigma - D$ relation proposed in [40, 88, 192]. The radius lower limit calculated through SNR dynamics based on the model of [36] sets another constraint on the SNR distance. The distance derived from the pulsar’s parallax or dispersion measure is larger than the distance suggested for the background stars of which spectra show high velocity gas which might be related to the SNR.

The age was estimated as 100–200 kyr from the Sedov solution by using a shock velocity $\sim 80\text{--}100 \text{ km s}^{-1}$ [146, 256] which was derived from the radial velocity of the filamentary knots [133, 169]. However, the travel time of the pulsar from the geometrical center of the SNR indicates an age of 30 ± 4 kyr [143, 203]. For a distance of 1.3 kpc, and an angular diameter of $200'$, the radius (R) of the SNR is 38 pc. Then, for 30 kyr age, the SNR must have a blast wave velocity of 500 km s^{-1} considering that it is still in the Sedov phase. The blast wave velocity can be measured by X-ray observations in the future. The estimated explosion energy and the ambient medium density are $E_0 = (1 - 3) \times 10^{51}$ erg and $n_0 = 0.03 - 0.1 \text{ cm}^{-3}$ respectively [127]. The SNR is expanding in a low density medium, probably in the cavity generated by the progenitor.

The central source, PSR J0538+2817, is an extensively studied radio and X-ray pulsar lo-

cated $\sim 28'$ away from the geometrical center towards north. The 143.16 ms period and $3.6710^{-15} \text{ s s}^{-1}$ period derivative [7] imply a characteristic age of $\tau = \sim 620 \text{ kyr}$ which is ~ 20 times larger than its kinematic age of 30 kyr. This discrepancy is explained by either a long initial spin period of $P_0 = 139 \text{ ms}$ [143] or strong magnetic field decay [89]. The parallax distance was measured as $1.47_{-0.27}^{+0.42} \text{ kpc}$ [203] and $1.3_{-0.16}^{+0.22} \text{ kpc}$ [35] and the distance derived from the dispersion measure (DM) by using the NE2001 model of [45] is 1.2 kpc [143] which are consistent with each other. The most precise proper motion is $\mu_\alpha^* = -23.57_{-0.10}^{+0.10} \text{ mas yr}^{-1}$, $\mu_\delta = 52.87_{-0.10}^{+0.09} \text{ mas yr}^{-1}$ corresponding to a transverse velocity of $357_{-43}^{+59} \text{ km s}^{-1}$ at $1.3_{-0.16}^{+0.22} \text{ kpc}$ [35]. The pulsar does not show a clear γ -ray emission [127], but it is observable in soft X-rays due to thermal emission. PSR J0538+2817 is one of the few thermal pulsars. Based on a blackbody model, the surface temperature and the emitting radius are given as $T = 2.1210^6 \text{ K}$ and $R = 1.68 \pm 0.05 \text{ km}$ [185]. The hydrogen atmosphere model with $B = 10^{12} \text{ G}$ gives $T = 2.1210^6 \text{ K}$ and $R \simeq 10 \text{ km}$ [306]. A faint pulsar wind nebula is observed in X-rays but not in radio [77]. It is not known whether the observed elongated structure is the torus or the jets of the PWN. But assuming that it is due to the torus, it provides valuable information on the spin-kick alignment.

HD 37424 is a sound OB runaway star at $10.3'$ away from the geometrical center to the west. It is a relatively bright star, $m_V = 9.0 \text{ mag}$. The proper motion of the star is much larger than each of the neighboring massive stars, $\mu_\alpha^* = 10.8 \pm 0.8$, $\mu_\delta = -10.2 \pm 0.6 \text{ mas yr}^{-1}$. While proper motion values were retrieved from the *UCAC 4*- catalog [305], the photometric magnitudes are obtained from the *ASCC-2.5 V3* catalog [130]. Its spectral type was previously identified as B0.5/1 IV/V [42]. As there was no public data nor a visualized spectrum, the spectral type is established again in this work. There is no variability or binarity reported for the star in the literature. Hence, HD 37424 is a good OB runaway star candidate.

4.1.1 Observational Results

The spectral type identification of the star is explained in detail in Section and 3.3.5. The sources observed by CAFOS are foreground stars with a maximum distance of $671_{-56}^{+96} \text{ pc}$. Two sources observed by TFOSC are B9–A0V type stars which are probably closer to the SNR. The possible background star HD 36665 showing high velocity gas components of the ISM features was observed by FLECHAS. The spectral type of HD 36665 is confirmed to be

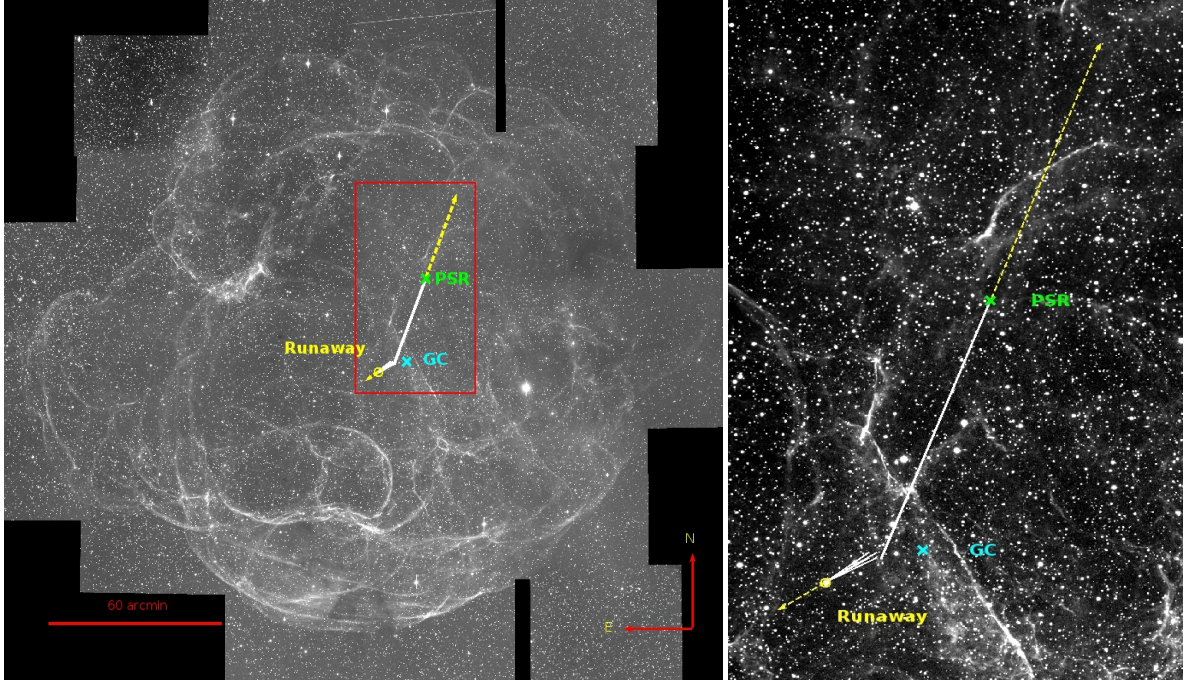


Figure 4.1: The $4.8^\circ \times 4.1^\circ$ H_α image of SNR S147 taken at the University Observatory Jena. The green cross represents the pulsar, the cyan cross shows the geometrical center of the SNR and the yellow circle is HD 37424. The yellow vectors show the proper motion of the objects. The red box is the zoom-in area shown in the right panel. The white arrows are the tracing back cones of the proper motion for 29300 yr. The angle between the pm vectors is $139^\circ - 148^\circ$. In 2-D calculations, both objects come towards each other as close as 0.126 pc which means that they have a common origin; binary supernova disruption.

$B1 \pm 0.5V$ type star (Dinçel, et al. 2015 [53]).

As long as HD 37424 is inside the SNR, its spectrum is expected to show blue-shifted components to ISM absorption features, Ca II-K and H and/or Na I-D1 and D2, which are due to the expanding SNR. The spectra of HD 37424 show no clear high velocity features (Figure 4.2). This is because, the star is not projected onto any dense filaments. The high velocity gas is found where the filaments are concentrated [169]. The average heliocentric radial velocity of the IS gas is $12.1 \pm 0.5 \text{ km s}^{-1}$ (Table 4.2) (Dinçel, et al. 2015 [53]). This is typical for the neighboring stars [250]. It represents the local standard of rest.

Using the absolute visual magnitude from [5], for a spectral type $B0.5V \pm 0.5$, the distance modulus yields 1868_{-403}^{+410} pc for HD 37424. Using the bolometric luminosity of the same spectral type from [104], the distance is found to be 1318 ± 119 pc which is well consistent with the distance of the pulsar. The A_V was taken into account in both calculations. The distance determination was further confirmed by the IS Ca II-K and H lines. By using the

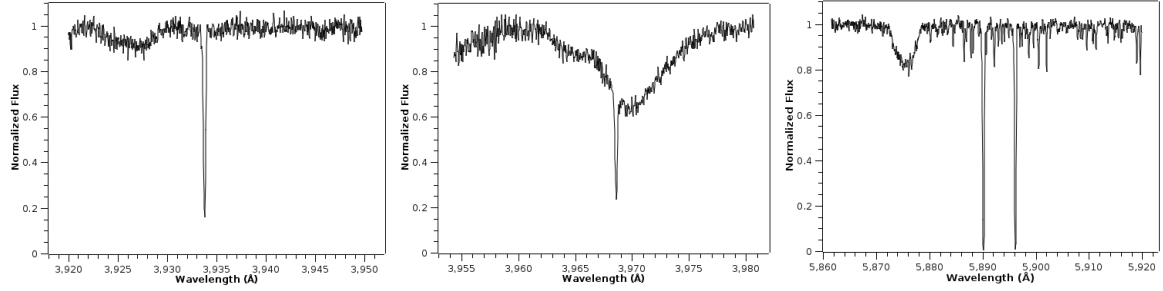


Figure 4.2: The strong interstellar lines of HD37424. *Left:* Ca II–K line from TRES spectrum. Despite a weak blended feature at -13 km s^{-1} , there is no clear high velocity component. *Middle:* Ca II–H line (H_{ϵ} as a background) from the same spectrum. Again there is no clear high velocity gas component. *Right:* IS Na I–D1 and D2 lines. The broad feature is He I $\lambda 5875$ triplet. Those around Na I doublet are all tellurics (absorption due to the atmosphere of the Earth) (Dinçel, et al. 2015 [53]).

Table 4.2: Measured velocities for IS Ca II–K and H and Na I–D1 and D2 lines. These lines have a low Gaussian width unlike the intrinsic features of the star. The average velocity is 12.1 km s^{-1} with a standard deviation of 0.5 km s^{-1} in each observation. The data in the first column are in (\AA) while the others are in km s^{-1} (Dinçel, et al. 2015 [53]).

Feature	σ	Velocity (Day 1)	Velocity (Day 2)
3933.664	7.5	12.3	11.8
3968.47	5.9	12.8	12.7
5889.953	9.0	11.6	11.6
5895.923	8.3	11.9	12.0

Day 1: Sep. 16th, 2013; Day 2: Sep 21st, 2013.

following relation from [187],

$$D = 77 + \left(2.78 + \frac{2.60}{\frac{EW(K)}{EW(H)} - 0.932} \right) EW(H) \quad (4.1)$$

the distance to HD 37424 is found as $1288_{-193}^{+304} \text{ pc}$ which is almost in the same range as the pulsar. The EW's are $EW = 243 \pm 7$ and $EW = 160 \pm 15 \text{ m\AA}$ for Ca II–K and H respectively (Dinçel, et al. 2015 [53]).

High resolution observations show that HD 37424 is a hot star ($T_{\text{eff}} = 30000 \pm 1000 \text{ K}$) with slightly lower surface gravity ($\log(g) = 4.0 \pm 0.25$ in cgs) star with a normal rotational velocity of $v \sin(i) = 140 \pm 20 \text{ km s}^{-1}$ (see Section 3.3.5).

4.1.2 Kinematics

HD 37424 and PSR J0538+2817 have proper motions receding away from each other and departing from the same location on the sky (Figure 4.1). The proper motion of both objects are corrected for Galactic rotation and solar motion. The distance of the Sun to the center of the Galaxy is taken as 8.5 kpc and the solar orbital velocity as 220 km s^{-1} . The local standard of rest is obtained from [267] as $(U_{\odot}, V_{\odot}, W_{\odot}) = (10.4 \pm 0.4, 11.6 \pm 0.2, 6.1 \pm 0.2) \text{ km s}^{-1}$. The resultant values for HD 37424 are $\mu_{\alpha}^* = 10.0 \pm 0.8 \text{ mas yr}^{-1}$, $\mu_{\delta} = -5.9 \pm 0.6 \text{ mas yr}^{-1}$ and for the pulsar, $\mu_{\alpha}^* = -24.4 \pm 0.1 \text{ mas yr}^{-1}$, $\mu_{\delta} = 57.2 \pm 0.1 \text{ mas yr}^{-1}$. Together with the $-20.0 \pm 6.5 \text{ km s}^{-1}$ peculiar radial velocity, HD 37424 has a space velocity of $74 \pm 8 \text{ km s}^{-1}$ at 1.3 kpc. HD 37424 is a runaway star of which velocity is higher than typical runaway velocities $40\text{--}50 \text{ km s}^{-1}$. The 2-D space velocity of the pulsar at the same distance is $382.2 \pm 0.8 \text{ km s}^{-1}$.

The past 3D trajectories of PSR J0538+2817 and the runaway star HD 37424 were constructed to evaluate whether these two objects had been at the same position at the same time in the past. Three million past trajectories of two objects were constructed via Monte Carlo simulations for varying parameters distance, proper motion and radial velocity within their errors. The radial velocities of NS cannot be measured, so it is assumed to be in an interval of -1500 to $+1500 \text{ km s}^{-1}$. The galactic gravitational potential on the vertical motion is also taken into account. The vertical acceleration from [212] is applied for a fixed time-step of 1000 yr by Euler–Cauchy numerical method. For all pairs of trajectory, the smallest separation d_{min} and the time elapsed τ are determined following the procedure in [268, 269]. The simulations were made and results were obtained by Dr. Nina Tetzlaff.

HD 37424 and PSR J0538+2817 are found to be at the same position at $\alpha, \delta = 84.82^{\circ} \pm 0.01^{\circ}, 27.84^{\circ} \pm 0.01^{\circ}$ at $30 \pm 4 \text{ kyr}$ (Figure 4.3). This predicted position of the SN is $4.2_{-0.6}^{+0.8}$ arcminutes offset from the nominal geometric center. The predicted distance of the supernova (as it is seen from the Earth today) is $1333_{-112}^{+103} \text{ pc}$.

4.1.3 Associations

There is no known OB association within 4.5° ($\sim 100 \text{ pc}$ at 1300 pc) from SNR S147. Owing to the large angular separations and inconsistent radial distances, HD 37424 cannot be linked

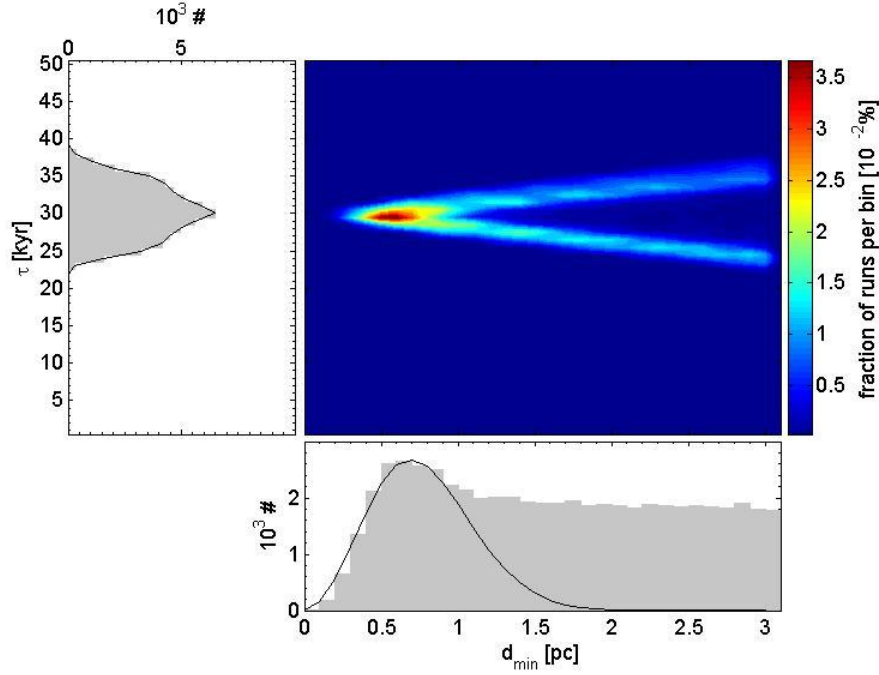


Figure 4.3: Distributions of minimum separations d_{\min} and corresponding flight times τ for encounters between PSR J0538+2817 and HD 37424. The solid curves drawn in the d_{\min} histogram (bottom panel) represent the theoretically expected distribution with $\mu = 0$ and $\sigma = 0.35$ pc, adapted to the first part of the histogram. Credit: Dr. Nina Tetzlaff

to any of the known young open cluster around. Hence, the progenitor of S 147 is considered to be a runaway star ejected e. g. from the cluster NGC 1960, which is 217 pc away from the SNR, several millions years ago [203]. However, binarity among cluster ejected runaway stars are rare [82]. So, as the progenitor was the previous binary companion to HD 37424, it may be unlikely that they were ejected from a cluster. Therefore, the neighboring stars are investigated to search for an association.

All of the OB-type stars within 4.5° from the geometrical center of the SNR are selected from *The Catalogue of Stellar Spectral Classifications* [251] where the spectral types are known through spectroscopic observations. There are some discrepancies in spectral types reported by different papers. In such cases, the latest reference was chosen. Together with two B-type stars from our observations at TUG, 99 stars are used. The photometric data are obtained from the catalog *ASCC-2.5 V3* [130] except for UCAC 4-589-020390 of which photometric data are retrieved from the *UCAC4* catalog. For each star having an integer spectral subclass, distance and extinction are calculated in an interval between one spectral subclass above and below, e. g. B0V–B2V for a B1V type star. For those having half integer subclass, half spectral subclass above and below are used e. g. B0V–B1V for a B0.5V type

star. The A_V value was determined as mentioned in section (2.2).

The intrinsic colors are obtained from [129] and [293], while A_λ/A_V ratios are from [233]. Color differences of short intervals, e. g. H–K yield high errors as they are multiplied by higher coefficients. Hence, these are not used. The color excess $E(B-V)$ is mentioned separately (Table 4.3). The values obtained from six color differences are averaged and their standard deviation are calculated for the individual spectral type interval. As long as the error due to the spectral type uncertainty is larger than the standard deviation of the color differences, it is assigned to be the final error. When the error is asymmetric due to the intrinsic colors of different spectral types, the larger one is accepted. In some cases, the uncertainty is dominated by the error in color differences. Then, these are preferred to be the final error for such sources. $E(B-V)$ versus A_V fit yields a total to selective absorption ratio is 3.24 ± 0.06 . In individual cases, $E(B-V)$ deviates strongly from A_V . However, the large sample reveals that the ratio of total to selective absorption has a usual value. The distances were derived from distance moduli using the absolute magnitudes from [5]. Errors in distances are due to the uncertainty in spectral type and the error in A_V were also taken into account.

The spectro–photometric distance alone is not enough to propose or to reject an association due to the high dispersion in the brightness of OB–type stars [294] (Thereafter W06). Assuming the stars beyond 1 kpc are within 100 pc from the SNR geometrical center, the absolute visual magnitudes are (m_V) calculated. Although the dispersion mentioned in W06 is high, 24 of the stars fit well in the comparison with the W06 values. Hence, here, it is suggested that these stars are members of an OB association (Table 4.3, Table 4.4). Nineteen of them have similar proper motion values. The average proper motion in R.A. and dec. is $\mu_\alpha^* = -1.39 \text{ mas yr}^{-1}$ and $\mu_\delta = -4.17 \text{ mas yr}^{-1}$ with 0.99 mas yr^{-1} and 1.45 mas yr^{-1} standard deviation respectively (Table 4.5). At 1.3 kpc, 5 of them are runaway stars exceeding 20 km s^{-1} 2–D peculiar velocity. This is consistent with the general ratio of the runaway stars to the normal stars which is 10–30 per cent [81].

To summarize, it is expected that the massive pre–supernova binary was born here, as a member of this possible OB association.

Table 4.3: 24 stars beyond 1 kpc are presented. Angular distances are given in degrees, distances in parsecs, extinctions and brightness in visual band in magnitudes. In the column; SpT adopted, the average spectral types that are used in distance calibrations are given.

Ang. Sep.	Name	SpT	SpT (adopted)	A_V	A_V (Err)	E(B-V)	E(B-V) (Err)	Distance	Distance (Err)	V	Ref#*
0.09	TYC 1869-01317-1	B9.5V	B9.5V	0.83	0.1	0.26	0.090	1013	+183 / -174	11.258	tw
0.09	TYC 1869-01642-1	B9.5V	B9.5V	1.00	0.1	0.3	0.090	952	+172 / -163	11.293	tw
0.17	HD 37424	B0.5V	B0.5V	1.28	0.06	0.35	0.036	1868	+410 / -403	8.989	tw
0.52	HD 36993	B0.5/III/IV	B0.5III-IV	1.35	0.06	0.39	0.028	1961	+636 / -628	8.248	1
0.63	HD 37318	B0.5Ve	B0.5V	2.29	0.15	0.59	0.026	903	+231 / -228	8.399	1
1.00	BD+27 797	B0.5Ve	B0.5V	2.50	0.14	0.62	0.094	1788	+485 / -465	10.095	2
1.35	HD 37696	B0.5IV/V	B0.5IV-V	1.12	0.06	0.29	0.023	1549	+565 / -558	7.973	1
1.35	BD+27 850	B1.5IVe	B1.5V	1.31	0.04	0.35	0.056	1525	+313 / -305	9.362	2
1.52	HD 245770	O9/B0III/Ve	B0III-V	2.11	0.13	0.79	0.053	2595	+1090 / -1066	9.187	3
1.76	HD 36441	B0.5/1.5V	B1V	1.13	0.13	0.33	0.058	1153	+628 / -389	8.239	1
1.97	BD+26 943	B2V	B1.5V	1.41	0.14	0.37	0.040	1357	+723 / -511	9.623	8
2.61	HD 38010	B1III	B1III	1.29	0.1	0.22	0.028	967	+437 / -236	6.817	4
2.95	BD+30 938	B3III	B3III	1.44	0.04	0.45	0.030	1332	+741 / -255	9.062	7
2.98	Sh2-242 1	B0V	B0V	2.17	0.13	0.78	0.056	2318	+853 / -842	9.996	5
3.06	HD 37366	O9.5V	O9.5V	1.22	0.06	0.35	0.016	1375	+201 / -199	7.640	6
3.07	BD+30 987	B5III:	B5III	0.73	0.08	0.25	0.044	1523	+398 / -287	9.444	7
3.24	BD+30 976	B7V	B7V	0.89	0.17	0.18	0.020	994	+264 / -226	10.277	7
3.45	BD+25 989	B1Vn	B1V	1.59	0.13	0.43	0.082	1872	+1061 / -649	9.751	8
3.61	BD+27 909	B2III	B2III	1.87	0.1	0.55	0.076	2004	+683 / -761	9.479	8
4.05	BD+31 1065	B3III	B3III	0.67	0.04	0.27	0.043	2304	+1286 / -442	9.482	7
4.07	BD+31 1050	B3III	B3III	1.01	0.03	0.35	0.047	1791	+988 / -338	9.276	7
4.09	HD 38909	B3II-III	B3II-III	0.56	0.03	0.17	0.033	2057	+1007 / -992	8.145	9
4.28	BD+31 1021	B7V	B7V	1.05	0.12	0.14	0.106	1007	+250 / -218	10.465	7
4.46	HD 40297	B9.5Ib/II	B9.5Ib/II	1.07	0.13	0.25	0.015	1337	+693 / -688	7.270	1

* Ref#: 1: [42]; 2: [257]; 3: [292]; 4: [48]; 5: [110]; 6: [289]; 7: [24]; 8: [39]; 9: [195]; 10: [39]; tw: This work.

4.1.4 Full Picture of an OB Runaway

The runaway nature of HD 37424 is clear. The star is proven to be at the same position on the sky with the NS of the SNR at the same time, so a chance projection possibility must be very low. HD 37424 is clearly the pre-supernova binary companion of the progenitor of SNR S 147 and PSR J0538+2817.

HD 37424 is an early B-type massive star ($T_{\text{eff}} = 30000 \pm 1000$ K, $\log(g) = 4.0 \pm 0.25$ in cgs, $v \sin(i) = 140 \pm 20$ km s⁻¹). The uncertainty in stellar parameters are high to calculate the mass and the radius of the star. Taking the distance 1350 pc, the logarithm of the bolometric luminosity in terms of solar luminosity is found as $\log(L) = 4.24$ in L_{\odot} . For 29000 K, the radius is $R = 5.23 R_{\odot}$, hence for $\log(g) = 4.0$, the mass of the star is $10 M_{\odot}$, and for $\log(g) = 4.1$, $13 M_{\odot}$ and for $\log(g) = 4.2$, the mass is $16 M_{\odot}$. To show the possible pre-supernova binary parameters, $13 M_{\odot}$ is adopted. The progenitor of the pulsar must have

Table 4.4: Visual absolute magnitudes at 1.3 ± 0.1 kpc for the stars of the possible OB association of which HD 37424 is a member. Errors are mainly due to the distance range 1.2–1.4 kpc. The expected M_V for the corresponding spectral types and its dispersion from [294] (W06) are given. All values are in mag.

Name	M_V (@1.3±0.1 kpc)	error	M_V (W06)	Disp. (W06)
TYC 1869-01317-1	-0.14	+0.26 / -0.27	+0.29	1.40
TYC 1869-01642-1	-0.28	+0.26 / -0.27	+0.29	1.40
HD 37424	-2.86	+0.22 / -0.23	-3.34	2.40
HD 36993	-3.67	+0.22 / -0.23	-4.02	2.30
HD 37318	-4.46	+0.31 / -0.32	-3.34	2.40
BD+27 797	-2.97	+0.30 / -0.31	-3.34	2.40
HD 37696	-3.72	+0.22 / -0.23	-3.34	2.40
BD+27 850	-2.52	+0.20 / -0.21	-2.95	1.16
HD 245770	-3.49	+0.29 / -0.30	-3.34	2.40
HD 36441	-3.46	+0.29 / -0.30	-2.95	1.16
BD+26 943	-2.36	+0.30 / -0.31	-2.64	1.40
HD 38010	-5.04	+0.26 / -0.27	-4.10	2.20
BD+30 938	-2.95	+0.20 / -0.21	-2.32	1.50
Sh 2-242 1	-2.74	+0.29 / -0.30	-3.34	2.40
HD 37366	-4.15	+0.22 / -0.23	-4.49	2.27
BD+30 987	-1.86	+0.24 / -0.25	-1.49	2.00
BD+30 976	-1.18	+0.33 / -0.34	-0.63	1.40
BD+25 989	-2.41	+0.29 / -0.30	-2.95	1.16
BD+27 909	-2.96	+0.26 / -0.27	-2.63	2.20
BD+31 1065	-1.76	+0.20 / -0.21	-2.32	1.50
BD+31 1050	-2.30	+0.19 / -0.20	-2.32	1.50
HD 38909	-2.98	+0.19 / -0.20	-2.32	1.50
BD+31 1021	-1.15	+0.28 / -0.29	-0.63	1.40
HD 40297	-4.37	+0.29 / -0.30	-3.75	1.30

a higher mass. Based on the lack of O–type stars in the field (see Table 4.3) An upper mass limit of 20–25 M_\odot is set. The Roche Lobe radii calculated for 15, 20 and 25 M_\odot vary between 91 and 311 R_\odot which shows that the system might have been an interacting binary. In the late evolution stages, the progenitor can fill a Roche lobe with these dimensions. Hence, the progenitor star should be a naked helium star at the final stage of its evolution with a mass even as low as 2 M_\odot [285], [298]. However, how conservative the mass transfer was, will be understood after further observations. Assuming a circular orbit, pre–supernova binary parameters are calculated for 2, 5, 10, 15, 20 and 25 M_\odot (Table 4.6) progenitor masses.

The period of the star for the same parameters and for the rotational velocity of $v_{\text{rot}} = 140 \pm 20 \text{ km s}^{-1}$, is 1.9 ± 0.2 days. If HD 37424 and the progenitor was tidally locked to each other, then the final progenitor mass would be $2.7 \pm 0.3 M_\odot$ as in the case of tidal locking, the spin period of the star equals to the orbital period.

As discussed in the previous section, the OB stars around might be members of an uniden-

Table 4.5: 19 stars with common proper motion are presented. The average proper motion is $\mu_\alpha^* = -1.39 \pm 0.99 \text{ mas yr}^{-1}$ and $\mu_\delta = -4.17 \pm 1.45 \text{ mas yr}^{-1}$. The last three columns represent the 2-D space velocity of the stars w.r.t. the average motion of the group with maximum and minimum values in km s^{-1} . All the values of proper motions are in mas yr^{-1} .

Name	μ_α^*	err	μ_δ	err	V_{REL}	max	min
HD 37318	-0.8	0.6	-5.9	0.6	11.2	16.1	6.9
TYC 1869-01642-1	-1.5	1.1	-2.4	1.2	11.0	19.8	7.1
HD 38010	-1.7	1.0	-3.3	1.0	5.7	14.1	0.0
BD+30 976	-3.5	0.9	-5.3	0.5	14.7	21.1	8.4
BD+31 1021	-2.8	0.7	-5.5	0.8	11.9	18.4	5.4
TYC 1869-01317-1	-0.9	0.9	-5.1	0.9	6.5	14.2	0.0
HD 36441	-2.0	0.6	-6.6	0.6	15.4	20.1	11.2
BD+30 938	-1.7	0.8	-3.6	0.6	4.0	9.9	0.0
HD 40297	-1.4	1.0	-3.7	1.0	2.9	11.0	0.0
BD+26 943	-0.9	0.8	-3.7	0.8	4.2	11.2	0.0
BD+30 987	-2.0	0.6	-4.7	1.2	4.9	13.0	0.0
BD+27 797	-0.1	0.7	-3.1	1.4	10.4	19.6	4.2
BD+31 1050	-1.0	0.6	-4.0	0.6	2.7	7.8	0.0
BD+25 989	-1.5	0.9	-2.5	1.6	10.3	21.1	4.9
HD 36993	-0.2	0.9	-5.8	0.6	12.4	18.8	6.6
HD 38909	+0.7	0.5	-4.2	1.5	12.9	18.4	0.0
BD+31 1065	-1.0	0.6	-1.3	0.5	17.9	21.7	14.7
Sh 2-242 1	-0.1	0.7	-1.8	1.0	16.7	24.2	9.2
HD 245770	-2.0	0.5	-4.3	1.1	3.8	10.2	0.0

tified old OB association of which all of the O type stars underwent supernova explosions. This also makes a plausible explanation for the low density medium in which the SNR expands symmetrically. A membership to an OB association or to a cluster is important also regarding the distance determination. In this work, the distance derived from pulsar parallax ($1.3_{-0.16}^{+0.20}$ kpc) is accepted as the most reliable estimation. Also, the distance to the star measured from interstellar lines is in the same range, 1288_{-193}^{+304} (see section 3). The spectro-photometric distance is much larger by using absolute magnitudes from [5]. Yet, by using typical luminosities for B0.5V type suggested in [104], it is 1318 ± 119 pc. Hence, the distance to the star and the SNR can be assumed to be 1.3 kpc. However, the A_V measured directly towards S147 is much lower than the A_V towards the stars beyond 1 kpc. Furthermore, two stars, HD 36665 and HD 37318, show shifted IS CaII and NaI lines related to the SNR implying that these objects are background sources [242]. Their distances based on the reported spectral types are closer to the Sun than HD 37424 is. HD 36665 has 837_{-285}^{+347} pc for B1V type and HD 37318 is 903_{-228}^{+231} pc far away adopting B0.5V. On the other hand, the distance for HD 36665 is identified as 1860 pc in [199] through H_β measurements. It has a high A_V of 1.74 mag. If it is assumed that HD 36665 is also at 1.3 ± 0.1 kpc, then it must be a bright B1V type star which is 1–1.5 mag brighter than the average value given in W06.

Table 4.6: The binary separations, the orbital velocities of the progenitor, the orbital periods and the Roche Lobe radii of the pre-supernova binary for various final masses of the progenitor with $13 M_{\odot}$ HD 37424 are given. Roche Lobe radii are calculated based on [55].

Progenitor Mass (M_{\odot})	2	5	10	15	20	25
Bin. Sep. (R_{\odot})	9^{+1}_{-3}	49^{+9}_{-11}	152^{+26}_{-37}	281^{+49}_{-68}	425^{+75}_{-101}	576^{+101}_{-137}
Orb. Vel. (km s^{-1})	481 ± 49	192 ± 20	96 ± 10	64 ± 7	48 ± 5	38 ± 4
Orb. P. (days)	$0.85^{+0.22}_{-0.32}$	9^{+2}_{-4}	45^{+11}_{-17}	103^{+26}_{-39}	176^{+44}_{-66}	259^{+65}_{-98}
RL Rad. (R_{\odot})				110^{+19}_{-27}	177^{+31}_{-42}	251^{+44}_{-60}

HD 37318 can be a member of the possible OB association. HD 36665 can be a variable star of which the spectro-photometric distance is not reliable. Also, the IS lines can belong to another HII region.

The supernova event had occurred quite nearby in a fairly reddened medium. Assuming a very faint SN ($m_V = -14$ mag), the apparent visual magnitude is -2.1 mag, and for a bright SN with $m_V = -21$ mag, the apparent visual magnitude is -9.1 mag; as bright as SN 1006. The event might have also caused the ^{10}Be peak at 35 ± 2 kyr measured in [222] from the deep ice cores from Dome C and Vostok Antarctica.

4.2 SNRs With Possible OB Runaway Stars

Two OB-type stars, HD 254577 and HD 184927 are found as possible pre-supernova companion star of the progenitors of IC 443 and G065.3+5.7. Although both stars show peculiar motion, they are far away from the geometrical centers, out of search regions. Thus, both cases need further confirmation. Nevertheless, they are very strong candidates.

4.2.1 G189.1+3.0 (IC 443)

IC 443 is a MMSNR [231] with an angular diameter of $45'$ located at the Galactic anti-center direction [86]. The SNR shell is bright and show the same morphology in radio, X-ray and optical wavebands. [12,60,157]. It also shows centrally peaked morphology in X-rays [213].

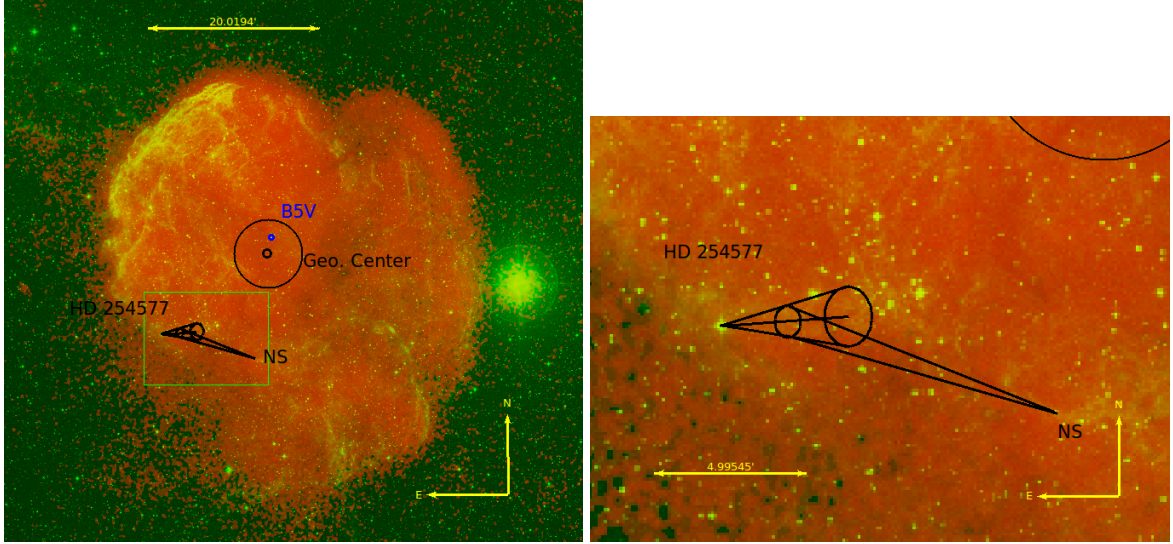


Figure 4.4: *Left:* Color composite image of IC 443. ROSAT PSPC (0.1–2.4 keV) image is in red and DSS2 (R–band) in green. The black circle shows the search region around the geometrical center (small black circle). The B5V type star UCAC4-563-026625 is represented by blue dot. Due to the very large errors in proper motion of this star, the kinematics is not studied. *Right:* Close up view of the possible OB runaway–NS system. The error cone of the proper motion tracing back of the massive star HD 254577, for 30 and 60 kyr, is shown. The proper motion of the NS derived here, for 30 kyr elapsed time, is $\mu_{\alpha}^* = -16.1 \pm 1.1$, $\mu_{\delta} = -5.1 \pm 1.9$ mas yr⁻¹, consistent with the measured value.

Unlike other MMSNRs, the central X–ray emission originates from two different positions, in the north and in the center [277], suggesting a cloud evaporation origin. The shock wave is interacting with the surrounding dense atomic and molecular clouds [43, 254] and expanding in a highly inhomogeneous environment. Hence, it is comprised of two semi–spheres sharing the same horizontal plane but having different radii and centroids (Figure 4.4).

Based on the genetic connection with Gem OB1 association [109] and Sh 2–249 HII region [78], the distance estimation to the SNR is ~ 1.5 kpc. The age estimates vary from 3 to 60 kyr. Due to the high temperature (10^7 K) of the plasma in the NE rim, the suggested age is 3 kyr [213]. Another young age, 4 – 10 kyr, was derived based on the radius comparison of the southern shell and the possible ejecta ring [277]. It is suggested as 10 – 20 kyr considering its mixed morphology nature [128].

The shock velocities measured from the filaments in the optical band are in the range of $60 - 100$ km s⁻¹ [65, 168]. Also, velocities up to 350 km s⁻¹ from diffuse H α emission was detected by long–slit spectroscopy. Taking the projection effects into account, a shock velocity of 400 km s⁻¹ was suggested [165]. Sedov solution gives an age of 60 and 10 kyr for the low and high velocities measured. Considering an SNR evolution within the low

density bubble owing to the fast winds of the progenitor and the neighboring stars, the age was estimated as 30 kyr [37]. On the other hand, the angular diameter is as small as $45'$, one fourth of the SNR S147 which is lying at a similar distance, 1.3 kpc from the Sun and having an age of 30 kyr (Dinçel et. al, 2015 [53]).

The A_V value measured from H_β/H_α strength ratios is $2.5 - 3.4$ mag [60] which is consistent with the $N_H \sim 6.2 \times 10^{21} \text{ cm}^{-2}$ measured from X-ray spectral fit [277]. Owing to the dense clouds, this value is quite high with respect to the global distribution, 1 mag/kpc [199]. Furthermore, from NIR Fe II line intensities, it is found that A_V varies from 2 to 6 mag within the northeastern shell [135].

The compact object of the SNR is NS CXOU J61705.3+222127. Although it shows no radio emission, its PWN and blackbody radiation are observable in X-rays [22, 206]. No pulse has been detected so far. From the hydrogen atmosphere model, the effective temperature was found as $T_{\text{eff}} \approx 6.8 \times 10^5$ K. The blackbody model yields a higher temperature, $T_{\text{eff}} \approx 1.6 \times 10^6$ K close to that of Vela pulsar [260], a 10 – 30 kyr old NS. The cooling age is consistent with the SNR age of 30 kyr [76]. The X-ray bolometric luminosity of the PWN is $L_{\text{PWN}} \approx 1.4 \times 10^{33} \text{ erg s}^{-1}$. Based on this value, the predicted period of the pulsar is $P = 250$ ms with a relatively high magnetic field strength, $B_{\text{dip}} = 2.0 \times 10^{13}$ G. Overall, it is an energetic pulsar with a possible spin down luminosity of $\dot{E} = (1 - 30) \times 10^{36} \text{ erg s}^{-1}$. The position of the NS is $\sim 12'$ separated from the geometrical center of IC 443 to the south. The proper motion in R.A. and Dec. was measured as $\mu_\alpha^* = -18.1 \pm 33.4$, $\mu_\delta = -1.2 \pm 33.4$ mas yr $^{-1}$. [260].

Fourteen stars were observed by CAFOS to find an OB runaway star of IC 443. Three of them were in the search region. Others were observed to have clearer picture of the association regarding kinematics, distance and extinction. Four mid-early B-type stars were found (Table 4.7). One of these stars, UCAC 4-563-026625, is a B5V type star of which the visual absorption and the distance values are consistent with those of the SNRs. The star must be a member of Gem OB1 and most probably physically inside the SNR. The proper motion values are well above the average motion of the association (4.10). However, the star is faint, $m_V = 13.4$ mag, and the proper motion measurements have very large errors. Although they are within the large errors, the values in UCAC 4, $\mu_\alpha^* = 5.1 \pm 3.7$ and $\mu_\delta = -0.8 \pm 2.0$ mas yr $^{-1}$, is significantly different from those in PPMXL [235], $\mu_\alpha^* = -4.1 \pm 3.9$ mas yr $^{-1}$, $\mu_\delta = 1.4 \pm 3.9$ mas yr $^{-1}$. As there is no consistency between the measurements, the runaway

Table 4.7: Early type stars identified inside IC 443. First column is the name of the star in the *UCAC 4* catalog. Second column shows the separation between the star and the geometrical center of the remnant in arcminutes. Third column is the visual apparent magnitude of the star in mag, with a maximum error of 0.07 mag. The fourth and the fifth column are the proper motion values at R.A. and Dec. in mas yr^{-1} . The errors of the proper motion is shown in the sixth column again in mas yr^{-1} . The spectral types identified in this work are given in the seventh column together with the derived A_V in magnitude and the distances in parsecs in the eighth and the ninth columns. Lastly, the instrument used in spectral type identification is given in the column ten. While C represents CAFOS, T stands for TFOSC. The radius of the search region of IC 443 is $4.0'$.

Name	Ang	V	μ_α^*	μ_δ	err	SpT	A_V	Dist	Tel
563-026625	1.99	13.42	5.4	-0.8	3.7 / 2.0	B5V	3.48	1691^{+101}_{-190}	C
563-026599	3.35	12.65	-1.9	-3.3	1.1 / 1.2	A2V	0.97	1192^{+125}_{-58}	T
563-026616	4.31	12.56	-2.1	-6.9	2.3 / 1.1	A1V	1.07	1220^{+195}_{-80}	T
564-025691	8.53	13.00	0.3	-4.2	1.5 / 1.7	B6V	2.66	1711^{+188}_{-140}	C
564-025653	10.56	11.70	-1.2	-1.1	2.6 / 3.7	B2V	3.22	1550^{+552}_{-436}	C
563-026556	11.10	12.24	-2.9	-3.1	1.0 / 0.9	A1V	0.87	1255^{+167}_{-119}	C
563-026710	11.64	13.42	0.7	-2.3	1.9 / 1.2	B6V	2.20	2226^{+439}_{-166}	C

nature of the star is doubtful. To reveal the true nature, the proper motion must be measured more accurately. As it is faint, also the high resolution spectroscopy could not have been carried out. It needs long integration time.

On the other hand, the bow-shock PWN which can show the direction of the motion of the pulsar as it is created by its supersonic motion, does not show the geometrical center as the origin [206] (Figure 4.5). The parallactic angle of the cometary tail is measured as $71 \pm 5^\circ$. By tracing back the direction of the bow-shock accompanied by the cometary tail, a B0II–III [47] type star, HD 254577 was found $\sim 10'$ separated from the NS to the east. Although the proper motion measurements of the NS are not precise, the best fit is well consistent with the position of the runaway star. On the other hand, the proper motion can still be traced back to the IC 443 geometrical center within 5σ error (Figure 4.5).

HD 254577 is a runaway star of Gem OB1 association. The average proper motion of the members of Gem OB1 is $\mu_\alpha^* = -0.5 \pm 0.8$, $\mu_\delta = 2.2 \pm 1.1 \text{ mas yr}^{-1}$, while HD 254577 has a proper motion of $\mu_\alpha^* = 4.0 \pm 0.8$, $\mu_\delta = -2.5 \pm 1.0 \text{ mas yr}^{-1}$ which is larger than that of the association in R.A. considering the standard deviation of $\sigma = 0.8 \text{ mas yr}^{-1}$. Compared to the parent association, the 2-D peculiar velocity of the star is $28.4 \pm 5.8 \text{ km s}^{-1}$. Therefore, this star was also investigated as a potential pre-supernova companion of the progenitor of IC 443. The star was observed by FLECHAS on 2015, February 22, March 16 and 18. The observations were held as described in section (3.1). The spectra of the last date was taken

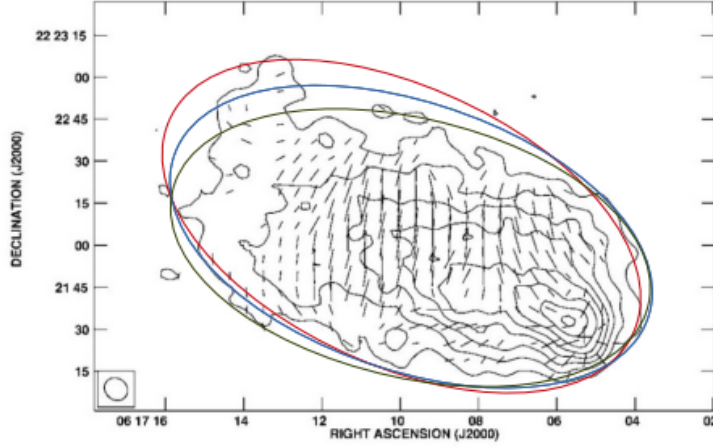


Figure 4.5: PWN inside IC 443, the geometry points back to another direction of origin, not the geometrical center.

by using a higher binning 1×4 to increase the S/N to 75. The spectra were cross correlated through entire range within each other to check possible radial velocity variations indicating binarity. The maximum relative velocity was measured to be 3 km s^{-1} well within the error of 8 km s^{-1} . No clear evidence of binarity was found. Also, no such information, i.e. variability was mentioned in the literature. The star seems to be a single star.

The spectrum best matches with that of B0III–B1III type stars observed by FLECHAS. The effective temperature of HD 186994 (B0III) is $\sim 29000 \text{ K}$ and of HD 218376 is $24135 \pm 600 \text{ K}$ [104]. From HeII $\lambda 4686$ to HeI $\lambda 4713$ ratio and H-line profiles and cross correlation with the synthetic spectra from *Sterne*, gives an effective temperature, $T_{\text{eff}} = 25000 \pm 1000 \text{ K}$ and a surface gravity of $\log(g) = 3.0 \pm 0.25$ in cgs for HD 254577 (Figure 4.6). On the other hand, "C+O" lines are very strong compared to the synthetic spectrum (Figure 4.6). The model used here has solar abundances for CNO, while $[\text{He}/\text{H}] = 0.3$.

Together with HD 254577, seven other members [189] of Gem OB1 were also observed. Among these stars, HD 43818 (B0II–III [255]) showed EW ratios perfectly matching with HD 254577. But the cross correlation gave somewhat lower values of correlation height (~ 0.6) due to the difference in rotational velocities. HD 254577 has very similar spectral parameters with HD 43818, but smoothed over rotation. A boxcar smoothing of 29 was applied to HD 43818 and compared with the runaway star (Figure 4.7) Rotational smoothing by *avsini* task of *Spectrum* was also performed on HD 43818 spectrum (Figure 4.7). Applying a 140 km s^{-1} rotational velocity, cross correlation yields a value of 0.818 which

is the best value obtained for the runaway star. The contribution of the intrinsic rotation of HD 43818 (70 km s^{-1} [83]) is low. By $v_{\text{tot}} = \sqrt{v_{\text{rot1}}^2 + v_{\text{rot2}}^2}$, the resultant velocity is $156 \pm 10 \text{ km s}^{-1}$. The error is enough to cause the intensity variation of ± 0.01 among the helium lines. Together with the results from synthetic spectrum comparison, the rotational velocity is $v_{\text{rot}} = 150 \pm 20 \text{ km s}^{-1}$.

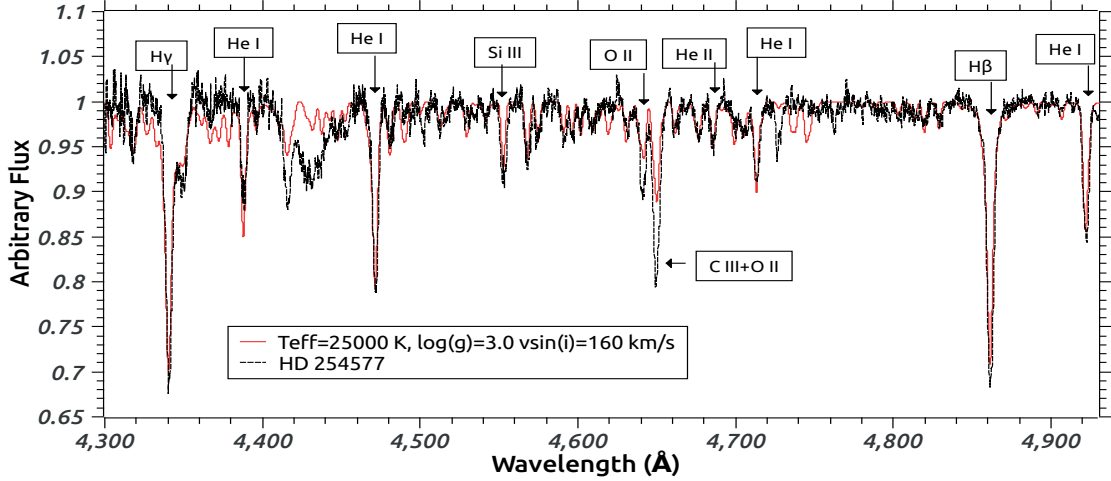


Figure 4.6: The spectrum of HD 254577 compared with the synthetic spectrum from *Sterne*.

The radial velocity of the star from cross correlation with the synthetic spectrum is $18 \pm 11 \text{ km s}^{-1}$. The relative radial velocities with respect to six members of Gem OB1 are given in Table (4.8). The peculiar radial velocity of HD 254577 w.r.t. the average of these members is $6 \pm 6 \text{ km s}^{-1}$. Although the star does not show a peculiar radial velocity, the proper motion which is clearly deviated from the average of the association and the direction of the PWN suggests that HD 254577 is the OB runaway star of IC 443. For a 3-D peculiar velocity of $29 \pm 6 \text{ km s}^{-1}$ and a mass of $12 M_{\odot}$, the pre-supernova binary parameters are calculated (Table 4.9).

Owing to the high values of Roche lobe radii, only a post-case C mass transfer seems to be possible. The rotation period of HD 254577 is $\sim 6 \text{ d}$, hence the synchronous rotation (tidal lock) is not possible. As the rotation velocity is not extra-ordinary, it is not likely to reveal that the star has been spun up as a result of the steady accretion.

Considering the star is the massive runaway of this SNR, the location of the explosion center has large separation from the geometrical center and is close to the edge of the remnant. Such an asymmetric shape might be possible for SNRs expanding inside inhomogeneous medium. CTB 80 might be another example for this kind (Figure 4.8).

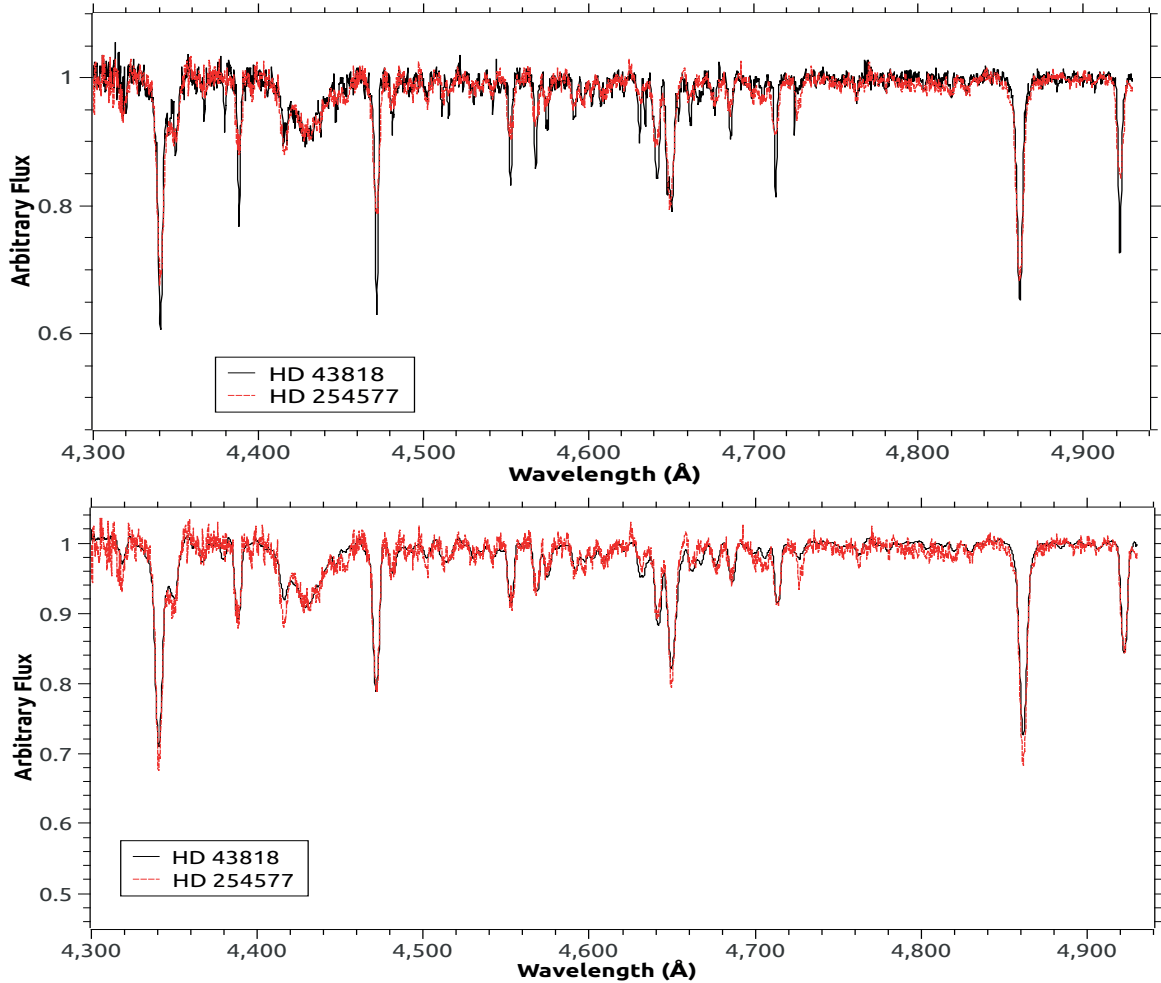


Figure 4.7: Comparison of HD 254577 (red) with HD 43818 (black). *Above:* Stars poorly match ($h=0.62$) but show close EW ratios. *Below:* Stars match ($h=0.82$) after smoothing HD 43818. The added rotational velocity here is 140 km s^{-1} .

The north eastern limb of the shell is significantly brighter than the southern and the western parts in all wavebands. The southern shell is incomplete in the eastern direction (Figure 4.4). This was interpreted as the breakout region of the remnant [37]. However, the SNR may have a third component in the east, which is larger ($\sim 70'$) and fainter than the other two shells. The northern part of this shell is well defined and distinguished from the HII region Sh 2 – 229 regarding its high velocity and S III/ H_{α} ratio [60]. Braun et al. (1986 [28]) has shown the complete picture through IR and radio observations, suggesting the SNR is comprised of three subshells (named A,B, and C) as a result of expansion into wind blown cavities (Figure 4.8). There are massive enough stars to make strong winds like HD 254755 (SpT; O8IV) within the subshells on the sky plane. Based on ROSAT observations, the subshell C was also defined by faint soft X-ray radiation. However, the subshell C was excluded

Table 4.8: Radial velocity (RV) of HD 254577 relative to six other members of Gem OB1 in km s^{-1} , found by cross correlation. Excluding HD 43703, the potential runaway star does not show a high peculiar radial velocity. The correlation height, h , show the resemblance of the correlated spectra. The value ranges between 0 (the worst) and 1 (the best)

Quantity	HD 43348	HD 43582	HD 43703	HD 43753	HD 254755	HD 43818
RV	12 ± 13	0 ± 11	-18 ± 11	9 ± 5	9 ± 26	0 ± 5
h	0.639	0.613	0.581	0.674	0.420	0.662

Table 4.9: The binary separations, the orbital velocities of the progenitor, the orbital periods and the Roche Lobe radii of the pre-supernova binary for various final masses of the progenitor with $12 M_{\odot}$ HD 254577 are given. Roche Lobe radii are calculated based on [55].

Pro. Mass (M_{\odot})	2	5	10	15	20	25
Bin. Sep. (R_{\odot})	65^{+39}_{-20}	335^{+198}_{-105}	1037^{+611}_{-325}	1901^{+1120}_{-596}	2851^{+1681}_{-894}	3852^{+2273}_{-1207}
Orb. Vel. (km s^{-1})	174 ± 36	70 ± 15	35 ± 7	23 ± 5	17 ± 4	14 ± 3
Orb. P (days)	16^{+17}_{-7}	172^{+173}_{-74}	822^{+825}_{-355}	1842^{+1849}_{-794}	3108^{+3121}_{-1340}	4540^{+4560}_{-1958}
RL Rad (R_{\odot})	16^{+9}_{-5}	103^{+60}_{-32}	377^{+222}_{-118}	757^{+447}_{-237}	1208^{+713}_{-379}	1709^{+1008}_{-536}

to be a part of the SNR [12]. A belt-like structure from the north to the south of IC443 was found out to be responsible for an additional absorption of the SNR emission while it is also positionally consistent to be a possible western limb of the sub-shell C. Hence, the sub-shell C has been accepted as a old, faint, foreground SNR [12]. Yet, such an X-ray absorption from the belt was excluded by XMM-Newton observations [277]. On the other hand, a dense molecular cloud belt from east to west, explaining the two-shell structure of the SNR, was suggested [278].

FLECHAS observation showed that three stars behind the SNR, HD 43582 HD 254477 and HD 254577, display high velocity component for the IS CaII-H&K and NaI-D1&D2 (Figure B.2). All these components are blue-shifted and very strong. Especially in the spectrum of HD 254477, the high velocity component is nearly at the same strength with the component at $V_{\text{LSR}} \approx 0 \text{ km s}^{-1}$ (Table B.3). Other investigations in the literature has reported that the components at negative velocities are much more intense than those at positive velocities [101, 295]. Therefore, the dense medium is one-sided, between the explosion center and the observer. The bright sub-shells A and B can hardly be suggested to be expanding in both directions. So, it is natural to expect that the SNR has different dimensions in other directions. This supports the expansion of a SNR inside the bubbles in various dimensions and

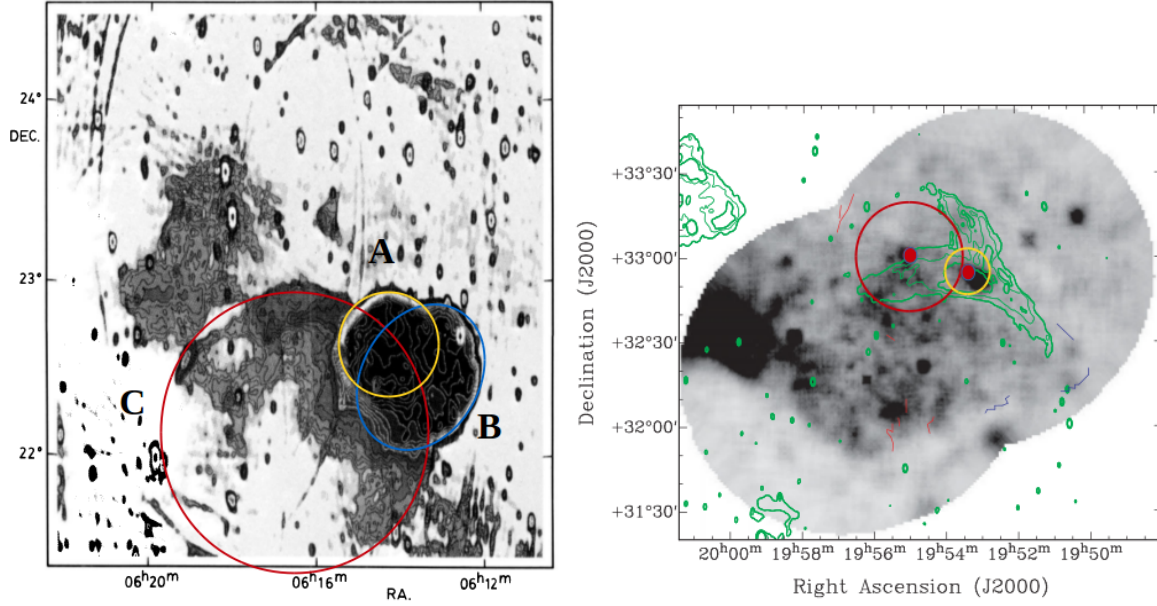


Figure 4.8: *Left:* Possible true dimensions of IC 443. Shell A and B show the ordinary borders of the SNR, like in Figure 4.4, while the extension towards the east in 408 MHz image, should be a part of the remnant. The image is adapted from Braun et al. (1986 [28]) *Right:* Such an example. SNR CTB 80 has highly asymmetric morphology. The search region is represented by yellow circle, the red circle is to demonstrate roughly the dimensions of the IR shell. The ROSAT data is seen as an X-ray shell extending to the south and southwest. The picture is adapted from [160]

densities. The archival ROSAT image supports the brightness gradient from the sub-shells A+B to the sub-shell C (Figure 4.9) observed in radio observations [28]. In conclusion, HD 254577 can be the runaway star of SNR IC 443 and NS CXOU J61705.3+222127 as long as the asymmetric shape is explained. For a conclusive result, a more precise measurement of the proper motion of the NS is needed.

4.2.2 G065.3+5.7

SNR G065.3+5.7 is an evolved MMSNR having the largest angular diameter in the sample; 300' [86]. The shell is bright in optical and radio bands and accompanied by centrally peaked X-ray emission. The distances proposed for this remnant, from $\Sigma - D$ relation, vary between 0.6 and 1.5 kpc [226]. 0.8 kpc is determined by the $\Sigma - D$ relation of G03. Based on the HI velocity ($V_{\text{LSR}} = 11 \text{ km s}^{-1}$) [84], the distance is derived as 1.3 kpc. The heliocentric velocity of -7 km s^{-1} from O III emission, the distance is derived as 1.0 kpc. Also considering the expansion velocity found from O III emitting filaments, the suggested dis-

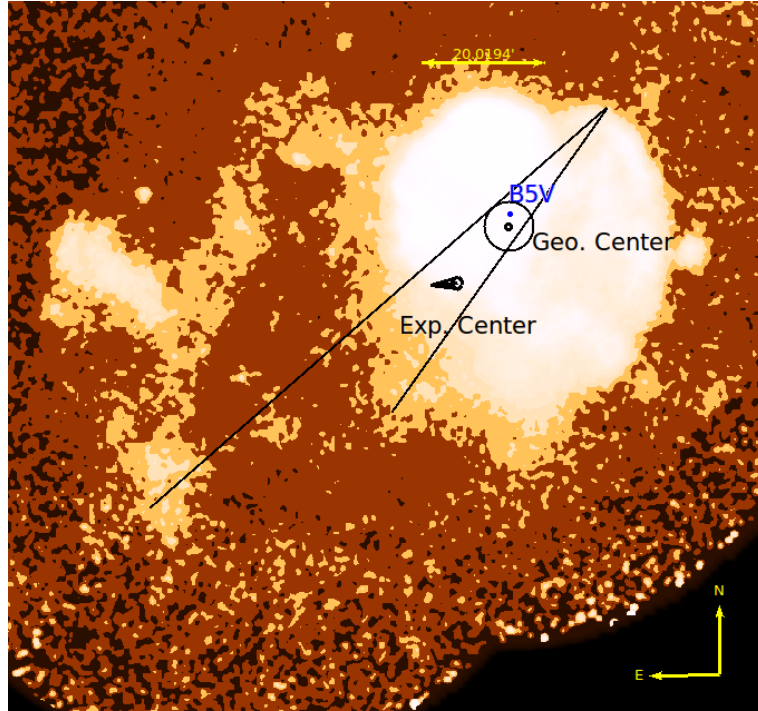


Figure 4.9: ROSAT PSPC (0.1–2.4 keV) archival image retrieved from *Skyview*. The image is smoothed by a factor of 5. The explosion center is within the error cone of the proper motion tracing back. The longer line represents the possible maximum diameter of the true extent, 90'. The shorter line covers the relatively bright region in 60' long.

Table 4.10: Observational and kinematic properties of the members of Gem OB1. HD 254577 has significantly different proper motion value in R.A. compared to the other stars.

Name	V	Ang	μ_{α}^*	μ_{δ}	err $\mu_{\alpha}^*/\mu_{\delta}$	SpT	SpT Ref
HDE 254577	9.08	15.72	4.0	-2.5	0.8/1.0	B0.5 II-III	[47]
HD 43582	9.12	14.97	-0.5	-1.8	0.7/0.7	B0IIIInk	[195]
HDE 254755	8.84	22.22	-0.7	-3.4	0.8/0.7	O9V	[201]
HD 43703	8.62	35.01	0.0	-1.6	0.5/0.6	B1IV:p	[163]
HD 43078	8.78	28.94	0.0	-1.3	0.7/0.9	B0.5III	[289]
HD 43753	7.90	37.95	0.6	-1.1	0.6/0.6	B0.5II-III	[116]
HD 44139	8.79	62.16	-0.3	-2.7	0.6/0.8	B0.5V	[205]
HDE 255134	9.17	57.93	-1.4	-2.4	1.1/0.7	B1IV:p	[47]
HD 43818	6.92	62.93	-0.6	-1.6	1.0/1.0	B0II	[195]
HD 43384	6.25	70.45	-0.4	-1.3	1.0/1.0	B2Ib	[201]
HDE 255091	9.54	85.14	-2.4	-4.1	1.0/1.3	B2V	[163]
HDE 254042	8.92	91.14	-0.1	-2.8	1.4/0.7	B0.5:IV:nn	[289]

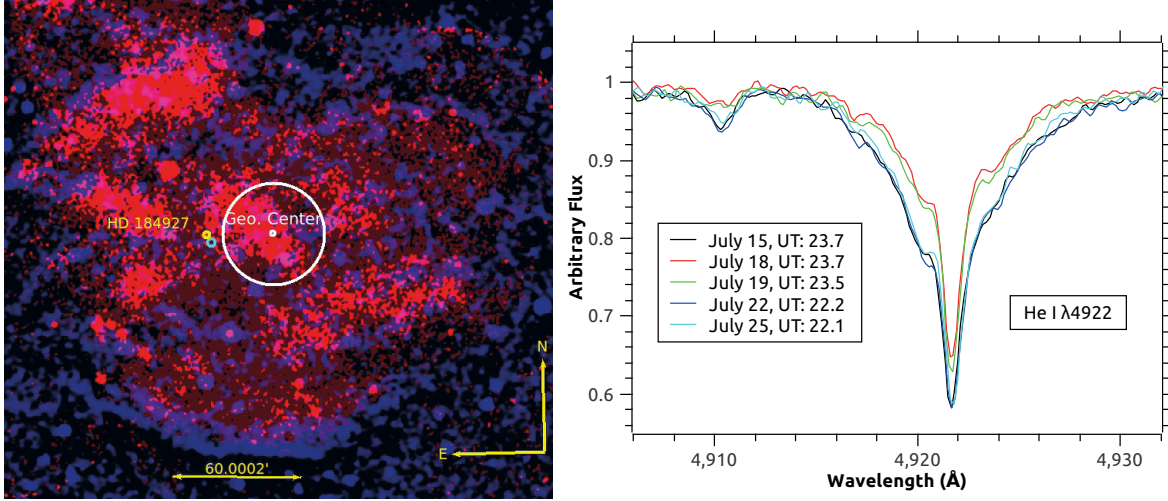


Figure 4.10: *Left:* X-ray (red) and radio (blue) composite image of SNR G065.3+5.7. The massive star HD 184927 is shown by yellow circle. The cyan circle represents the possible explosion center found by the tracing back the star’s proper motion. The geometrical center and the search region is shown by white circles. The ROSAT (X-ray) data are smoothed by Gaussian function for 3 pixels. The OB runaway candidate is out of search region. *Right:* He I λ 4922 line from the FLECHAS spectra covering 10 days. The EW changes are clearly seen. But no clear radial velocity variation was found.

tance is 0.8 ± 0.2 kpc [26]. The A_V value is very low; ~ 0.05 mag based UV and X-ray observations [131, 249]. However, it is spatially varying and increases up to 0.75 mag [183].

Because of the large search area of the SNR with a $25'$ radius, the distance is limited up to 0.6 kpc. Assuming a 0.6 mag of A_V , a B9V type star should be 9.5 mag at that distance. So, the search for OB runaway in this SNR is limited up to 9.5 mag. Otherwise the number of the candidates to be observed would be 72, which is not feasible. No OB runaway candidate was found in the search region.

The bright ($V = 7.4$ mag) B2V type star HD 184927 located in the R/3 region, is a strong candidate to be the OB runaway star of SNR G065.3+5.7. Its distance measured from optical parallax is 0.6 ± 0.2 kpc [287]. This star is slightly out of the search region ($R_{S.R.} = 25'$), $33'$ separated from the geometrical center. But, it was previously mentioned as a potential OB runaway [267]. Hence, despite its large separation from the geometrical center, it is studied in this work.

The SNR and the star are far from OB associations and young clusters. Therefore, there is no clear reference for the space velocity measurements. Within 5° (~ 50 pc), six massive stars possibly at the same distance were found in [251]. BD+31 3685, HD 332624, V379 Vul, HD 183561, HD 187851, HD 187688 are stars having spectral types B2V–B3V at a distance

of 0.7 ± 0.3 kpc. Many other OB stars within this region are background to HD 184927. The average proper motion of all of the stars are $\mu_{\alpha}^* = -1.5$, $\mu_{\delta} = -4.9$ mas yr $^{-1}$ with a high standard deviation, $\sigma = 3.3$ & 4.0 mas yr $^{-1}$ respectively. But, BD+31 3685, HD 183561 and HD 187851 have an average proper motion of, $\mu_{\alpha}^* = -2.4$, $\mu_{\delta} = -5.9$ mas yr $^{-1}$. with a reasonable deviation, $\sigma = 0.7$ & 1.1 mas yr $^{-1}$ respectively. HD 184927 has a highly different proper motion, $\mu_{\alpha}^* = 5.0 \pm 1.0$, $\mu_{\delta} = 3.4 \pm 1.0$ mas yr $^{-1}$. Hence, despite its large separation from the geometrical center it might be the OB runaway star from SNR G065.3+5.7. The proper motion of the star after the correction of galactic rotation and solar motion is $\mu_{\alpha}^* = 4.9 \pm 1.0$, $\mu_{\delta} = 7.0 \pm 1.0$ mas yr $^{-1}$, hence the 2-D space velocity of HD 184927 is 24.5 ± 2.5 km s $^{-1}$.

The star is well studied in the literature. It is a helium strong peculiar star showing rotational variabilities. Especially, the helium abundance vary between 0.2–0.4 dex w.r.t the solar values. [99]. The stellar parameters are as follows; the surface temperature is $T_{\text{eff}} = 22000$ K, the logarithm of the surface gravity is $\log(g) = 4.0 \pm 0.2$ in cgs, the projected rotational velocity is $v \sin(i) = 10 \pm 2$ km s $^{-1}$ with an inclination angle of $25 \pm 5^\circ$ which corresponds to a rotational velocity of $v_{\text{rot}} = 25$ km s $^{-1}$. The mass was derived as $M = 8.3 \pm 0.7 M_{\odot}$. As the period was found from the variation in He abundance, $P = 9.53102 \pm 0.0007$ d, so the radius can be independently found; $R = 4.4_{1.0}^{1.9} R_{\odot}$. Typically as an oblique rotator, the magnetic field strength is high, $B_{\text{dip}} \simeq 9.7$ kG [301].

HD 184927 was observed by FLECHAS on 2014, July 15 to 25, In five different nights as mentioned in Figure 4.10. The radial velocity is measured by gaussian fitting to the core of each line. As the projected rotational velocity is low, the result is accurate. The heliocentric radial velocity is found as -21 ± 3 km s $^{-1}$. Its maximum variation through the dates based on Fourier cross correlation is 1.6 km s $^{-1}$ with an error of 2.2. The value is well within the error, so it is not significant. Therefore, the star is thought to be a single star. However, the peculiar radial velocity w.r.t. ISM velocity field is very low, -3 km s $^{-1}$.

Unlike typical runaway stars, HD 184927 does not rotate fast. The rotational velocity is low. For the runaway mass of $9 M_{\odot}$, the binary parameters is calculated. All of the combinations point out a wide binary (Table 4.11) and tidal lock cannot be maintained.

Table 4.11: The binary separations, the orbital velocities of the progenitor, the orbital periods and the Roche Lobe radii of the pre-supernova binary for various final masses of the progenitor with $9 M_{\odot}$ HD 184927 are given. Roche Lobe radii are calculated based on [55].

Pro. Mass (M_{\odot})	2	5	10	15	20	25
Bin. Sep. (R_{\odot})	112^{+32}_{-23}	548^{+160}_{-111}	1615^{+471}_{-327}	2877^{+838}_{-583}	4233^{+1233}_{-859}	5641^{+1644}_{-1144}
Orb. Vel. (km s^{-1})	113 ± 14	45 ± 5	23 ± 3	15 ± 2	11 ± 1	9 ± 1
Orb. P (days)	41^{+19}_{-12}	396^{+185}_{-114}	1720^{+804}_{-496}	3638^{+1700}_{-1049}	5906^{+2761}_{-1702}	8392^{+3922}_{-2419}
RL Rad (R_{\odot})	29^{+8}_{-6}	180^{+53}_{-36}	627^{+182}_{-127}	1219^{+355}_{-247}	1902^{+554}_{-386}	2647^{+771}_{-537}

4.3 SNRs with Potential OB Runaway Stars

In 8 SNRs, there are OB-type stars which cannot be either proven or rejected to be the runaway star. There are also some evidences like peculiar motion or X-ray counterpart which make them deserve to be studied in the future projects.

4.3.1 G078.2+2.1 (DR 4)

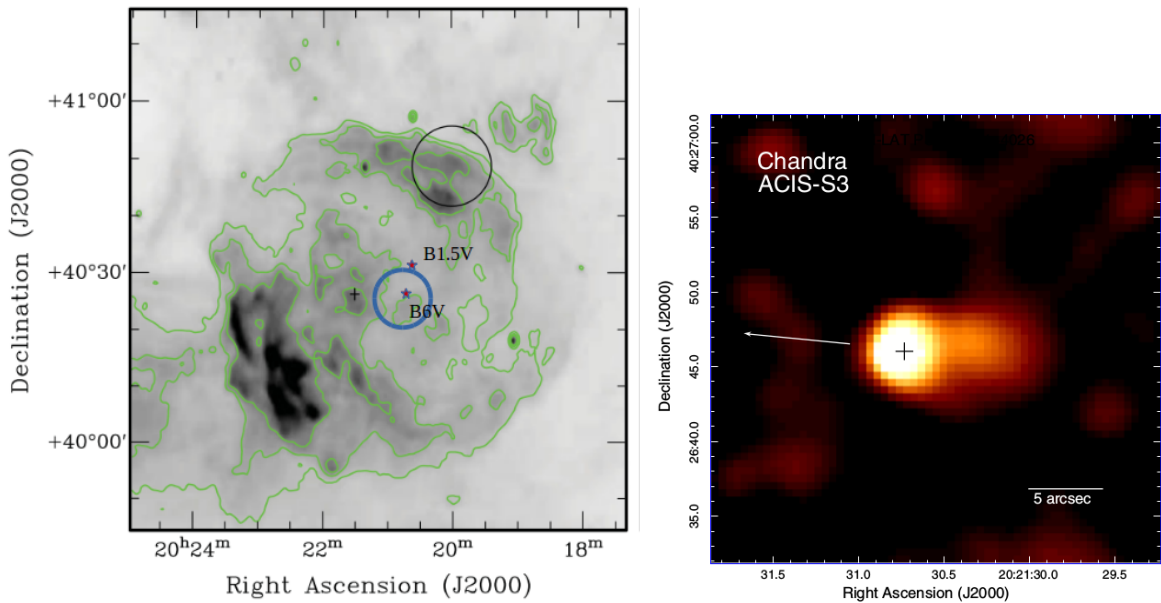


Figure 4.11: *Left:* The search region and the strong candidates of γ -Cygni. UCAC 4-653-092531, the B1.5V type star is slightly outside of the search region [159]. Due to the peculiar proper motion, it is a massive runaway candidate of γ -Cygni. *Right:* The PWN in X-rays. The elongated shape may indicate the direction of the motion. The pulsar must be originated from the geometrical center of the SNR [107].

γ -Cygni is a shell type SNR in a complex region with a diameter of $60'$ [86]. Due to the possible relation with Cyg OB9 association, the distance was suggested as ~ 1.3 kpc. A distance of 1.5 ± 0.5 kpc, is assigned by studying the systematic velocity of HI surrounding the SNR [151]. This is consistent with the one derived from the $\Sigma - D$ diagram, 1.2 kpc [88]. The remnant is in its adiabatic expansion phase. Due to the spectral observations by ASCA, the shock-cloud interaction manifest itself via soft X-ray emission with a temperature of ~ 0.6 keV from the north to the southeast of the remnant. The SNR is expanding inside the low density inter-cloud medium swept up by the progenitor's wind and has recently started interacting with dense clouds, especially at the southeast. Therefore the age is derived from Sedov-Taylor solution by using a shock velocity of ~ 800 km s $^{-1}$ derived from plasma temperature. For 1.5 kpc, the age is 6600 yr [281]. The total mass swept up by the SNR is 50–100 M_{\odot} [171]. The spectral index is measured as 0.54 ± 0.02 with an rms value of spatial variation; ± 0.17 [308]. and a steeper averaged spectrum of ~ 0.7 spatially varying between 0.4 – 0.8 [148]. The steepest values are reached at the southeast. The large spatial variations in spectral index may indicate that the shell is expanding in an inhomogeneous medium. This is also confirmed by the clumpy hard X-ray emission through non-thermal Bremsstrahlung. The expanding shell may be interacting with the H II region in the south and compressing the ISM to form a possible star formation region [100].

The O9V type star; GSC 03156–00657 [144] is claimed to be the exciting star of γ -Cygni Nebula located in the dense southeastern part of the SNR [10]. The spectro-photometric distance to the star is 1.47 kpc [9], consistent with that of the SNR and Cyg OB9. The shape of the SNR shell, in this region, has a planar geometry implying the interaction.

Based on optical observations, the $E(B - V)$ and derived distances are; $E(B - V) = 0.8 \pm 0.2$ mag, $d = 1.0$ kpc and for $E(B - V) = 1.0 \pm 0.2$ mag, $d = 1.5$ kpc [180].

The central source of the SNR is a γ -ray pulsar PSR J2021+4026. The object was previously known as the EGRET source RX J2020.6+4026 [29]. Finally, it was detected with 16 other pulsars by Fermi LAT. The timing properties were revealed as; $P = 265$ ms, $\dot{P} = 5.48 \times 10^{-14}$ s s $^{-1}$ which yields a characteristic age of $\tau = 77$ kyr and surface dipole magnetic field; $B_{\text{dip}} = 4 \times 10^{12}$ G and spin down luminosity $\dot{E} = 1.16 \times 10^{35}$ erg s $^{-1}$ [1].

The X-ray counterpart, hence the precise pointing and X-ray emission properties was discussed extensively [275]. The source is probably an isolated NS with a possible extended

feature implying PWN [107]. The γ -ray luminosity of the pulsar is $L_\gamma = 2.6 \pm 1.5 \times 10^{35}$ erg s $^{-1}$ at 1.5 kpc, 2.2 ± 1.3 times greater than spin down luminosity. At 1 kpc, the γ -ray efficiency is comparable with that of Geminga pulsar [275]. To summarize, γ -Cygni is a middle-age SNR with a γ -ray pulsar at a distance of 1.3 ± 0.3 kpc.

Table 4.12: Early type stars identified inside SNR γ -Cygni. The star name (1), the angular separation from the center ($'$) (2), m_V (mag) (3), the proper motion in α and δ (mas yr $^{-1}$) (4 and 5), their errors (mas yr $^{-1}$) (6), the spectral types (7), the A_V (mag) and the distance found (pc) (8 and 9) and the instrument of observation (10) are given respectively. The radius of the search region of is $5'$. While C represents CAFOS, T stands for TFOSC. Detailed information can be found in Table (4.7)

Name	Ang	V	μ_α^*	μ_δ	err	SpT	A_V	Dist	Tel
653-092531	1.6817	11.1	-1.9	-7.7	0.9/1.0	B6V	$1.94^{+0.04}_{-0.05}$	1017^{+128}_{-112}	C
653-092521	4.3181	13.9	-2.9	-3.2	2.6/1.9	B7V	$3.38^{+0.05}_{-0.04}$	1647^{+204}_{-215}	C
653-092525	5.6691	12.6	-6.4	-0.9	3.7/2.4	B1V	$5.08^{+0.13}_{-0.09}$	1388^{+505}_{-364}	C

Two B-type stars are found in the search region. Their proper motion does not show any significant peculiarity w.r.t Cyg OB9 association (4.12). One of them, UCAC 4-653-092531, is a B6V type star and located very close to the geometrical center. By matching with the synthetic spectra produced with *Spectrum*, the stellar parameters were found. The star has an effective temperature of $T_{\text{eff}} = 15000 \pm 1000$ K, and a surface gravity, $\log(g) = 4.0 \pm 0.25$ in cgs. It is a fast rotator with a projected rotational velocity, $v \sin(i) = 200 \pm 30$ km s $^{-1}$ (Figure 4.12). By cross correlation with the synthetic spectrum, the radial velocity of the star is found as $V_{\text{rad}} = -15 \pm 7$ km s $^{-1}$ which is hardly peculiar compared to the velocity measured from the ISM lines (-11 km s $^{-1}$) and to the average radial velocity of Cyg OB9 (-19 ± 8 km s $^{-1}$) [188]. The average proper motion of Cyg OB9 is $\mu_\alpha^* = -2.4 \pm 0.5$, $\mu_\delta = -5.9 \pm 1.4$ mas yr $^{-1}$ [188]. In this work, by using *UCAC4* data of the members mentioned by [44], it is found as $\mu_\alpha^* = -3.1 \pm 1.6$, $\mu_\delta = -5.4 \pm 1.6$ mas yr $^{-1}$. The maximum peculiar velocity of the star derived from both reference frames is 18 km s $^{-1}$. Hence, UCAC 4-653-092531 is not considered as a runaway star. Also, the A_V value is considerably lower than the members of Cyg OB9 behind the SNR. Three of these members, UCAC 4-653-092525 (B1.5V), UCAC 4-653-092539 (B1.5V) and UCAC 4-652-090023 (B2III) are inside the R/3 region. The A_V value towards these stars are 4.7 ± 0.3 mag [44]. With an A_V of 1.94, the star is considered as a foreground star as there are evidences for that the SNR is expanding in the cavity surrounded by dense molecular clouds which cause high A_V values.

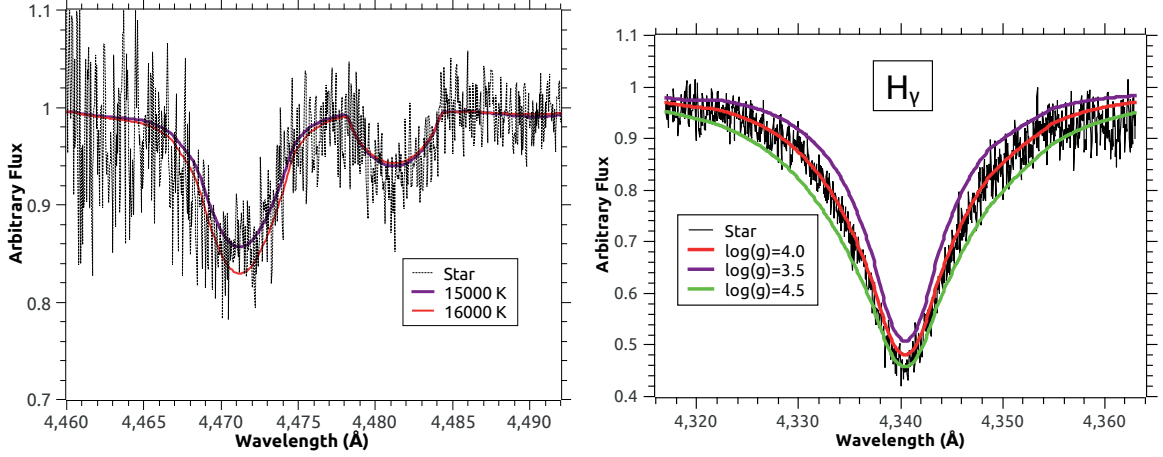


Figure 4.12: *Left:* He I and Mg I lines of the TRES spectrum of UCAC4-653-092531. They are fit well by 15000 K model smoothed for 200 km s^{-1} . *Right:* Comparison with the same spectrum for $\log(g)$. The $\log(g)$ of the star is found to be 4.0 in cgs.

UCAC 4-653-092525, one of these three stars close to the search region, was also observed by CAFOS. Because, unlike others, the proper motion of the star is higher than the average (Table 4.12). However, the errors are very large and the values are not consistent with those in *PPMXL*. On the other hand, it is only $0.6'$ outside of the search region (Figure 4.11). Thus, there is a possibility that it is the runaway star of γ -Cygni and PSR J2021+4026. To prove this, a precise proper motion measurement and radial velocity determination is needed.

4.3.2 G093.7-0.2 (CTB 104A)

CTB 104A is a shell type SNR with a diameter of $80'$. Although it is not extensively studied in the literature, it is discussed in this work owing to its unusual morphology. Similar to SNR G166.0+4.7 (Section 4.4.15), CTB 104A has two hemispheres in different radii (Figure A.2). The SNR was suggested to be a MMSNR [231], but no details were published.

The V_{LSR} of HI clouds related to the SNR is $\sim -6 \text{ km s}^{-1}$ [282]. This corresponds to a distance of 1.5 kpc. However, based on 1720 MHz OH MASER emission, the suggested V_{LSR} of the clouds is -45 km s^{-1} [138] which gives a $> 5 \text{ kpc}$ distance. Because there is no discussion on the details in the latter work, the distance is accepted to be 1.5 kpc. The HII region nearby, Sh2 - 124, is located at $2.6 \pm 0.6 \text{ kpc}$ [27]. $\Sigma - D$ diagram suggests 1.8 kpc [88].

There is no known massive star within the borders of the SNR. For 1.5 kpc and 2.5 mag A_V ,

three massive stars around the H II region, V645 Cyg (O6e [38], LS III +50 24 (B0V [46]) and LS III +50 27 (B0Ve [96]), are at ~ 3.5 [179], ~ 4.0 and ~ 2.5 kpc spectro–photometric distances. The proper motion of the stars are; $\mu_{\alpha}^* = -5.0 \pm 0.8$, $\mu_{\delta} = -3.0 \pm 1.2$ mas yr $^{-1}$, $\mu_{\alpha}^* = -5.9 \pm 0.9$, $\mu_{\delta} = -5.9 \pm 0.7$ mas yr $^{-1}$, $\mu_{\alpha}^* = -5.6 \pm 0.8$, $\mu_{\delta} = -4.5 \pm 0.7$ mas yr $^{-1}$. Although these values are higher than expected from the galactic rotation, they are consistent with those of the stars found in this work (Table 4.13). The SNR is highly separated from the known OB associations.

Twenty OB runaway candidates were observed by CAFOS and TFOSC. Ten of the stars are in early A spectral types or hotter (Table 4.13). A group of late B–type stars at 1.2 – 1.8 kpc are found. UCAC 4-705-085427 and 705-085563 are B8V and B6V type stars showing a common proper motion; $\mu_{\alpha}^* = -5.75 \pm 0.05$, $\mu_{\delta} = -2.35 \pm 0.35$ mas yr $^{-1}$. which is consistent with that of V645 Cyg. The B4V type star UCAC 4-705-085564 is located $\sim 1.5'$ out of the search area. It shows a peculiar proper motion with high errors (Table 4.13). However, like in the case of γ –Cygni and IC 443, the accuracy of this measurement is doubtful. This star lies at a distance of 3.3 ± 0.2 kpc, most probably from the same generation with V 645 Cyg.

The extinction towards the stars are high. Even for the nearby stars ~ 600 pc, $A_V = 1.5$ mag. For some of the stars, it is as high as 2.5 mag, beyond 1.0 kpc.

To summarize, no OB runaway star is found for CTB 104 A. The visual absorption is mostly due to the foreground clouds. UCAC 4-705-085564 is a B4 type massive star, located out of the search region, Due to the high errors of its proper motion, a possible runaway nature cannot proven. On the other hand, it might be from the same stellar group with the progenitor, so the distance to the SNR might be 3.0 – 4.0 kpc.

4.3.3 G109.1-1.0 (CTB 109)

CTB 109 is a shell type SNR, having relatively small angular diameter, $27'$. It is one of the most important remnant in the sample, as it is one of the few SNRs hosting a magnetar. Although the magnetars are young pulsars, their association to the SNRs are not clear. Hence, discovering the origin of CTB 109 and its magnetar can supply evidences for the relation between the stellar evolution and the end product.

Table 4.13: Early type stars identified inside SNR γ -Cygni. The star name (1), the angular separation from the center (') (2), m_v (mag) (3), the proper motion in α and δ (mas yr $^{-1}$) (4 and 5), their errors (mas yr $^{-1}$) (6), the spectral types (7), the A_V (mag) and the distance found (pc) (8 and 9) and the instrument of observation (10) are given respectively. The radius of the search region of is $7'$. While C represents CAFOS, T stands for TFOSC. Detailed information can be found in Table (4.7)

Name	Ang	V	μ_α^*	μ_δ	err	SpT	A_V	Dist	Tel
705-085474	2.31	13.23	-4.5	-1.5	1.3/1.7	B9V	$2.53^{+0.16}_{-0.20}$	1257^{+177}_{-139}	T
705-085427	3.24	13.23	-5.8	-2.6	2.4/0.9	B8V	$2.56^{+0.05}_{-0.21}$	1556^{+234}_{-192}	C
704-084001	4.33	13.24	-0.4	-2.6	1.8/1.6	A0V	$1.56^{+0.20}_{-0.08}$	1608^{+200}_{-187}	C
705-085431	5.98	13.91	3.8	-0.6	3.4/5.1	A0V	$2.44^{+0.12}_{-0.16}$	1402^{+214}_{-125}	C
705-085595	6.54	12.13	-3.5	-4.3	1.1/0.7	B9V	$1.26^{+0.17}_{-0.20}$	1362^{+191}_{-151}	C
705-085563	6.60	12.76	-5.7	-2.1	0.9/1.1	B6V	$2.11^{+0.04}_{-0.04}$	2037^{+257}_{-225}	C
705-085587	6.92	10.12	-4.5	-5.7	1.0/0.6	B8V	$1.51^{+0.04}_{-0.17}$	599^{+91}_{-73}	C
705-085564	7.81	13.79	0.1	0.3	3.5/1.9	B4V	$2.61^{+0.08}_{-0.07}$	3396^{+203}_{-185}	C
704-084117	8.33	13.42	0.1	-1.1	3.5/3.0	B7V	$2.57^{+0.05}_{-0.05}$	1948^{+243}_{-256}	C
704-083991	8.63	11.60	-2.1	-3.2	0.7/0.7	B9V	$1.92^{+0.17}_{-0.19}$	784^{+110}_{-87}	C
705-085447	8.76	11.43	2.7	2.0	0.6/0.8	A1V	$1.55^{+0.08}_{-0.09}$	597^{+79}_{-57}	C

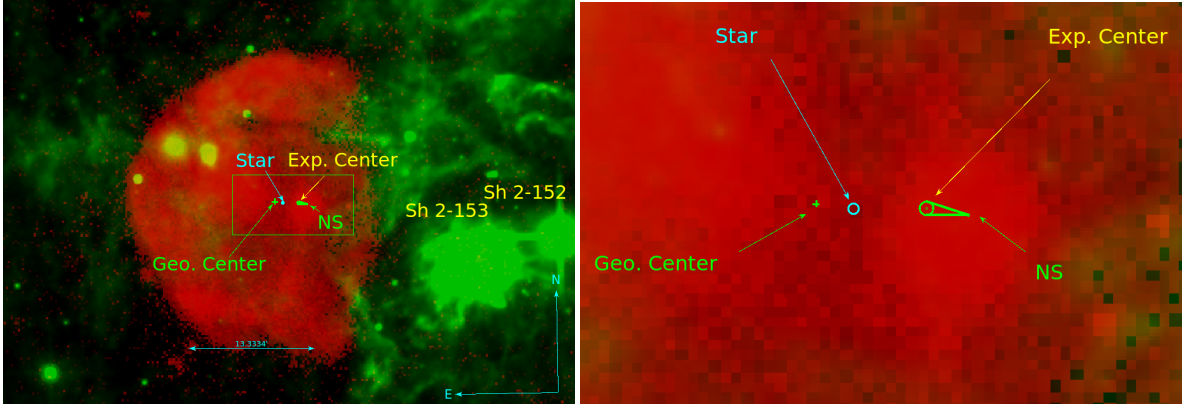


Figure 4.13: *Left:* Color composite image of CTB 109 and the surroundings. ROSAT PSPC (0.1–2.4 keV) image is in red while WISE (22 μ) image is in green. Both are retrieved from *Skyview*. *Right:* Close up to the system. The magnetar (green) proper motion was traced back for 15000 yr. The tracing back can reach the possible OB star (cyan) in 40000 yr. Both objects are close to the geometrical center.

The position of AXP 1E2259+586, which is close to the center of CTB 109 is the main evidence for an association. This is also supported by the direction of the proper motion, away from the center, to the west (Figure 4.13). It can give rise to X-ray outbursts with an energy release of 5×10^{36} erg s $^{-1}$ [125]. The magnetar distinguishes from the others by its low surface dipole magnetic field strength, $B_{\text{dip}} = 5.9 \times 10^{13}$ G. Its period and period derivative ($P = 6.98\text{s}$, $\dot{P} = 4.837 \times 10^{-13}$ s s $^{-1}$) [52] yield a characteristic age of 230 kyr

which is very high compared to the age of the remnant, and a low $\dot{E} \approx 10^{31} \text{ erg s}^{-1}$.

CTB 109 is interacting with a giant molecular cloud in the west. The shock front has completely lost its energy due to this interaction, so the shell has a semi-circular shape. The systematic velocity of the molecular clouds related to the SNR were measured as $-50 \pm 3 \text{ km s}^{-1}$ [261]. and $-55 \pm 3 \text{ km s}^{-1}$ was also measured from 408 MHz observations [243]. Both were derived from 408 MHz observations of CO molecules. Although this velocity corresponds to a $5.0 \pm 0.5 \text{ kpc}$ kinematic distance, the velocity dispersion in Perseus arm due to the density wave shock brings other alternatives from 2.8 to 4.0 kpc [72, 273]. The H II regions Sh 2 – 152 and Sh 2 – 153 are located in the southeast of the SNR have a distance of $\sim 3.21 \pm 0.21$ [223]. These star forming regions is thought to be a part of the giant molecular cloud which in interaction with CTB 109. Hence, the suggested distance is $3.2 \pm 0.2 \text{ kpc}$ [141].

Based on XMM–Newton and Chandra observations, the X–ray emitting plasma was found to be at a temperature of $T = 0.25 \pm 0.03 \text{ keV}$. This translates to a blast wave velocity of $v_{\text{bw}} = 460 \pm 30 \text{ km s}^{-1}$. From Sedov solution, the age was derived as $14000 \pm 2000 \text{ yr}$. This is way below the characteristic age of the magnetar which is 230 kyr. The detection of a $> 20 M_{\odot}$ SN ejecta shows that the SNR has a core collapse origin. This is supported by the enhancement in Si abundance [244, 245]. The spatial variation of N_{H} is high; $(0.5 - 1.5) \times 10^{22} \text{ cm}^{-2}$ ($A_{\text{V}} = 2 - 7 \text{ mag}$), consistent with the values found for the magnetar [309].

Based on the X–ray images, the proper motion of the magnetar is $\mu_{\alpha}^* = -6.4 \pm 0.6 \text{ mas yr}^{-1}$, $\mu_{\delta} = -2.3 \pm 0.6 \text{ mas yr}^{-1}$ [265]. The authors calculated the space motion of the magnetar as $\mu_{\alpha}^* = -9.9 \pm 1.1$, $\mu_{\delta} = -3.0 \pm 1.1 \text{ mas yr}^{-1}$ with respect to the average proper motion of the field stars nearby. The space velocity of the magnetar is then, $v = 157 \pm 17 \text{ km s}^{-1}$ at 3.2 kpc.

However, the correction made for solar peculiar motion and the galactic rotation in this work yielded a space motion of a $\mu_{\alpha}^* = -3.87 \pm 0.62$, $\mu_{\delta} = -0.65 \pm 0.62 \text{ mas yr}^{-1}$, which is equal to a space velocity of $59 \pm 9 \text{ km s}^{-1}$ at 3.2 kpc, and $85 \pm 12 \text{ km s}^{-1}$ at 4.5 kpc. These values are way below the global distribution of pulsar space velocities [173]. It is in the range of the velocities of slow pulsar minority [11]. To avoid a mistake, the proposed value can be confirmed by the proper motions of the stars or stellar groups nearby.

CTB 109 lies on the galactic plane, but due to the large distance, it is difficult to resolve

Table 4.14: Early type stars identified inside CTB 109. The star name (1), the angular separation from the center ($'$) (2), m_v (mag) (3), the proper motion in α and δ (mas yr^{-1}) (4 and 5), their errors (mas yr^{-1}) (6), the spectral types (7), the A_V (mag) and the distance found (pc) (8 and 9) and the instrument of observation (10) are given respectively. The radius of the search region of is $2.5'$. While C represents CAFOS, T stands for TFOOSC. Detailed information can be found in Table (4.7)

Name	Ang	V	μ_α^*	μ_δ	err	SpT	A_V	Dist	Tel
745-080772	0.85	13.99	-3.2	0.6	2.1/2.7	B7V	$2.63_{0.04}^{+0.04}$	2469_{325}^{+311}	T
745-080881	2.03	12.75	2.2	1.7	2.2/2.5	A1V	$1.32_{0.08}^{+0.08}$	1219_{116}^{+162}	C
745-080935	3.81	11.77	-3.5	-3.2	1.2/0.7	B7V	$1.34_{0.05}^{+0.04}$	1611_{213}^{+202}	C

the associations nearby. However, the massive young stars lying in the southwest of the SNR, in the H II regions, can set a reference frame. The stars LS III +58 70 (O9.5V [239]) and LS III +58 70 (B0V [200]) have proper motions as $\mu_\alpha^* = -4.3 \pm 0.7$, $\mu_\delta = -2.3 \pm 0.6$ mas yr^{-1} and $\mu_\alpha^* = -3.6 \pm 1.1$, $\mu_\delta = -1.5 \pm 1.3$ mas yr^{-1} respectively. At 3.2 kpc, the SNR is ~ 20 pc away from this star forming region. The space motion of the magnetar is then $\mu_\alpha^* \sim -2.5$ $\mu_\delta \sim -0.4$ mas yr^{-1} which is more consistent with the value suggested in this work. So, the magnetar space velocity with respect to the physically neighboring stars is only ~ 40 km s^{-1} .

Such a low velocity pulsar can be proposed to have a e^- capture SN origin. The magnetar is an isolated NS [108], so the companion star should be a runaway, or the progenitor itself must be a runaway star. Hence, it is very important to find a possible OB runaway inside CTB 109.

Two of the three early type stars found in the search region are obviously foreground stars (Table 4.14). UCAC 4-745-080772 is a possible B7V type star, very close to the geometrical center (Figure 4.13). Owing to its low brightness, the proper motion values are not measured precisely. Furthermore, although it was observed both by CAFOS and TFOOSC, the spectral type identification could not be done accurately due to the high noise level, $S/N = 40$. Nevertheless, it is the only OB runaway candidate for the system considering 3.2 kpc distance with an A_V of 3 mag. Further observations are needed to reveal the true nature of the star.

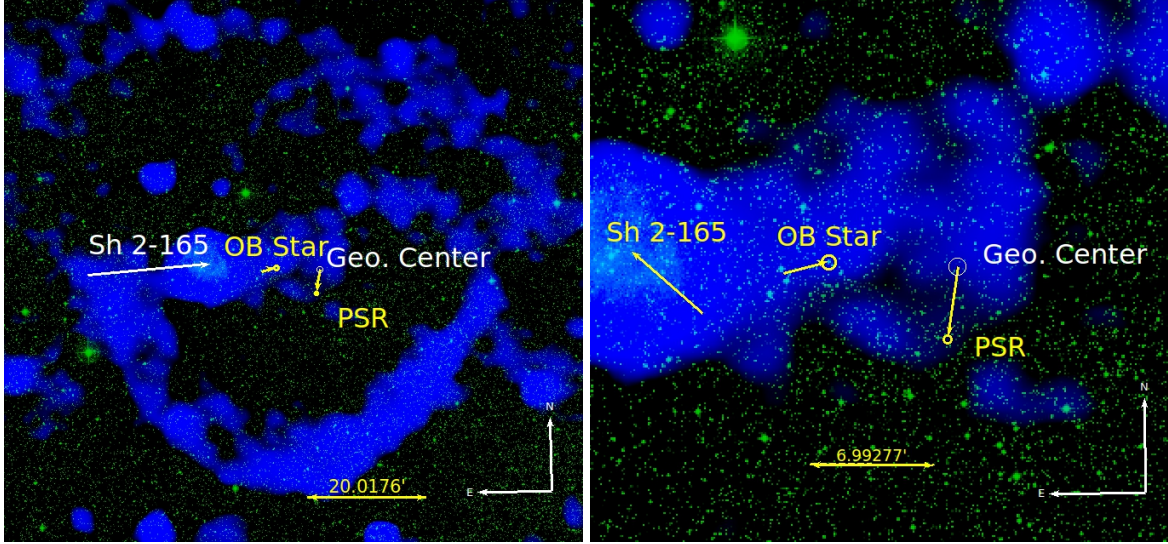


Figure 4.14: *Left:* Color composite image of SNR G114.3+0.3 and the surroundings. GB6/PMN image is in blue while DSS2 (R-band) image is in green. Both are retrieved from *Skyview*. The spherical radio and optical bright source is the HII region Sh 2-165. *Right:* Close up to the system. The proper motion (yellow vector towards the pulsar) implies that the pulsar originates from the geometrical center. The arrival time at the current position is 15000 yr. However, the tracing back of OB runaway candidate (yellow vector from OB star to the east) points out a different origin.

4.3.4 G114.3+0.3

G114.3+0.3 is a shell type SNR with $90' \times 55'$ angular size [86]. The radio shell has a circular shape in the south and mostly diffuse in the north 4.14. The shell is diffuse and faint in optical bands. The velocity of the shocked filaments is $\sim 100 \text{ km s}^{-1}$. No X-ray emission was detected from the SNR. G114.3+0.3 is an evolved SNR in radiative phase [182].

The SNR hosts a radio pulsar, PSR B2334+61. Similar to PSR J0538+2817 in S 147, it is a thermal X-ray pulsar with radio pulsations at a period of 495 ms. The period derivative is $\dot{P} = 1.93 \times 10^{-13} \text{ s s}^{-1}$, so the $\tau = 40600 \text{ yr}$. Yet, unlike PSR J0538+2817, PSR B2334+61 has an ordinary dipole magnetic field strength of $B_{\text{dip}} = 9.9 \times 10^{12} \text{ G}$. A dispersion measure of $DM = 58.38 \pm 0.09 \text{ pc cm}^{-3}$ for the pulsar yields a distance of $3.15 \pm 0.5 \text{ kpc}$ [194] based on galactic electron distribution from [45]. It is, however, $2.5 \pm 0.5 \text{ kpc}$ with using the previous electron distribution from [264]. From the ROSAT data, the upper limit of the surface temperature of the NS was determined as $T = 1.2 \times 10^6 \text{ K}$ [14]. Based on XMM-Newton observations, the X-ray spectrum is well consistent with a hydrogen atmosphere at a temperature of $T = 0.65 \times 10^6 \text{ K}$ with a N_{H} of $3.3 \times 10^{21} \text{ cm}^{-2}$ [186]. This equals to a A_{V} of 1.5 mag. Although it is lower than expected from the distance, low A_{V} values were

also measured towards SNR G116.9+0.2 (Section 4.3.5) This shows that there might be a window in these galactic directions up to 2.0–3.0 kpc. For the given temperature and model, the distance is 3.2 ± 1.7 kpc.

The HI related to the SNR is at -35 & -45 km s^{-1} velocities [227]. This corresponds to 3.2 and 4.2 kpc respectively. The HI cloud at -6.5 km s^{-1} , which translates to a 550 pc, was proposed to be related to the SNR. Based on this value, a distance of 700 pc was suggested [304]. The $\Sigma - D$ diagram suggests a distance of 2.94 kpc [88]. CTB 1, G116.5+1.1 and G114.3+0.3 was proposed to be located in a giant HI bubble of 280 pc diameter [68]. But, a recent work excludes the G114.3+0.3 from the super bubble, GS 118 + 01 – 44 [259].

An important indicator for the distance is the HII region Sh 2 – 165. Based on the polarisation studies at 2.7 GHz, it was found that the SNR is foreground to Sh 2 – 165 [227] which is at a distance of 1.96 ± 0.39 kpc [71].

The progenitor of the SNR can be a member of Cas OB5 association which is at 2.5 kpc (spectro–photometric distance). The association is 2° separated from the SNR which is 87 pc. The average radial velocity of 16 members is -45.8 km s^{-1} with a dispersion of 7.2 km s^{-1} and the average proper motion of 52 members is $\mu_\alpha^* = -3.4 \pm 1.2$, $\mu_\delta = -2.2 \pm 0.8$ mas yr^{-1} [188].

The early type stars found in this work are given in Table (4.15). Among these stars, UCAC 4-760-074536 is a B1V type star inside the runaway search region (Figure 4.14). The distance to the star is 2.5 ± 0.8 kpc like Cas OB5 association. Its proper motion is well above the average of Cas OB5 and the one derived from the galactic rotation ($\mu_\alpha^* = -2.2$, $\mu_\delta = -1.2$ mas yr^{-1} at 2.5 kpc). The space velocity of the star 65 ± 24 km s^{-1} at 2.5 kpc.

The fact which does not favor the link between the star and the SNR is the proper motion of the pulsar, $\mu_\alpha^* = -1.0 \pm 15.0$, $\mu_\delta = -15 \pm 16.0$ mas yr^{-1} . Although it is poorly measured, the direction of the pulsar’s motion is well consistent with the direction of the SNR geometrical center from the position of the pulsar. However, the potential runaway star approaches the geometrical center while it is expected to recede away from it (Figure 4.14). Furthermore, the B6V type star, UCAC 4-761-072827, found well outside the search region shows a similar proper motion with the runaway candidate. Yet, these two stars have large difference in distance. The latter seems to be a foreground star at 1.2 kpc. UCAC 4-760-074536 spectrum shows a strong H_α emission line which may indicate a Herbig Be star nature. The star

Table 4.15: Early type stars identified inside SNR G114.3+0.3. The star name (1), the angular separation from the center (') (2), m_V (mag) (3), the proper motion in α and δ (mas yr^{-1}) (4 and 5), their errors (mas yr^{-1}) (6), the spectral types (7), the A_V (mag) and the distance found (pc) (8 and 9) and the instrument of observation (10) are given respectively. The radius of the search region of is $8'$. While C represents CAFOS, T stands for TFOSC. Detailed information can be found in Table (4.7)

Name	Ang	V	μ_α^*	μ_δ	err	SpT	A_V	Dist	Tel
760-074536	7.45	12.53	-7.5	0.4	2.1/2.1	B1V	$3.77^{+0.13}_{-0.06}$	2457^{+891}_{-641}	C
761-072876	9.75	11.77	0.8	-1.3	0.8/0.7	A0V	$0.72^{+0.20}_{-0.08}$	1339^{+166}_{-157}	C
761-072674	9.82	11.94	-1.8	-2.3	1.4/1.4	B8V	$2.27^{+0.05}_{-0.16}$	1298^{+196}_{-161}	T
761-072827	14.47	13.40	-6.0	-1.1	1.6/0.9	B6V	$3.82^{+0.05}_{-0.04}$	1249^{+154}_{-136}	T
759-074519	14.85	10.86	-2.1	-1.8	0.8/0.8	B2V	$2.31^{+0.09}_{-0.15}$	1590^{+562}_{-453}	T

might be a young DES runaway accelerated by a cluster. The flight time ~ 100 kyr is much lower than the age of Sh 2 – 165. As the Sh 2 – 165 was not affected by the shock wave it is difficult to suggest it as the origin.

To summarize, UCAC 4-760-074536 is a massive star which is potentially the massive runaway star of SNR G114.3+0.3. To confirm this relation, a precise proper motion measurement of the pulsar is necessary.

4.3.5 G116.9+0.2 (CTB 1)

CTB 1 is a shell type MMSNR with a diameter of $34'$ [86]. The morphology in H_α band is almost spherical symmetric except for the breakout region in the northeast (Figure 4.15). X-ray emission lies along the breakout region and completed with the radio shell bright in the southwest. Considering a filament density of 10 cm^{-3} and an average velocity of the shocked filaments, $\sim 100 \text{ km s}^{-1}$, the age and the explosion energy is 16 kyr and $E_0 = 1.0 \times 10^{50}$ erg at 3.0kpc [67]. For 4.5kpc, the initial explosion energy is $E_0 = 3.5 \times 10^{50}$ erg. Based on Chandra observations, the temperature of the expanding plasma is $0.2 \pm 0.02 \text{ keV}$. This translates to an expansion velocity of $410 \pm 70 \text{ km s}^{-1}$. By Sedov or evaporating cloud models, the age was found as $13000 \pm 1500 \text{ yr}$ for 3.0 kpc distance. The suggested explosion energy is even lower, $E_0 = (3.4 \pm 1.2) \times 10^{49}$ erg from Sedov model and $E_0 = (1.5 \pm 0.7) \times 10^{50}$ erg from evaporating clouds model [154]. Based on CHANDRA and ASCA spectra, CTB 1 is rich in O and Mg. This shows that it must have a core collapse origin. From the abundances the predicted progenitor mass is $13 - 15 M_\odot$. [209].

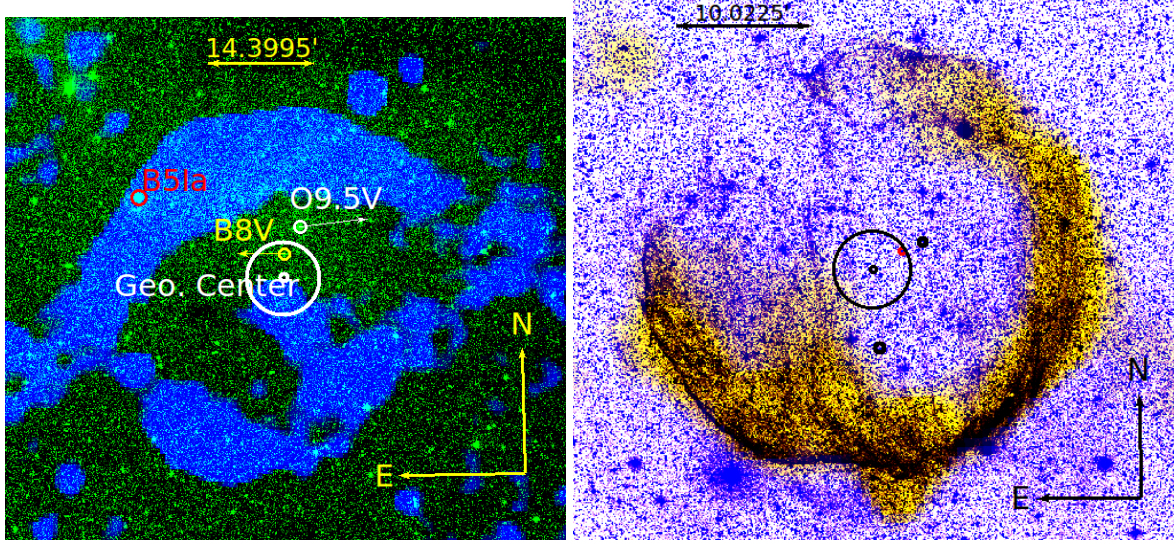


Figure 4.15: *Left:* 4850 MHz image of R 5 from GB6/PMN survey. The search region and the geometrical center are shown by white circles. Small white circle in the north indicates the position of HD 8768 with its proper motion vector w.r.t. the Galactic rotation. The small yellow circle is a possible B8V type runaway star inside the search region. The proper motion w.r.t. the average motion of the other observed stars is shown in yellow. Another massive star HD 9105 is marked as small red circle. *Right:* Color composite image of CTB 1. 4850 MHz from GB6/PMN survey is represented by green while R-band image from DSS2 by blue. The two small black circles show the position of two massive star out of the search region (big circle). The red dot shows the position of the B8V type star which is linked to an X-ray source which might be a NS. All of the frames were retrieved from *Skyview*

The systematic velocity derived from HI measurements vary between -27 and -33 km s^{-1} . This is confirmed by the average radial velocity of the $\text{H}\alpha$ filaments at -35 km s^{-1} [167,304]. Together with the interpretations of the surroundings, the suggested distance is 2.4 ± 0.8 kpc [92,150,304]. $\Sigma - D$ diagram suggests a higher value, 4.5 kpc [88]. If 3.0 kpc is adopted, then the SNR is either expanding in a very low density medium or the initial explosion energy is very low. The A_V was found as 1.64 mag [62]. However, in Fesen et. al, (1997 [67]), larger values were measured; 2.2 – 3.1 mag. The N_H measured by fitting the X-ray spectrum vary between $(4.0 - 6.0) \times 10^{21} \text{ cm}^{-2}$ [209]. Even higher N_H values, up to $8 \times 10^{21} \text{ cm}^{-2}$ was suggested gain from X-ray spectra [154].

The HI velocities are consistent with those of the OB associations in this direction, Cas OB4 (-37.0 km s^{-1}) and Cas OB5 (-45.4 km s^{-1}). The spectro-photometric distances of the associations are 2.9 and 2.5 kpc respectively. While the SNR is inside the borders of Cas OB5, $\sim 2^\circ$ separated from Cas OB4. The progenitor might be a member of Cas OB5. It is possible that three SNRs are thought to be close to each other and together with the possible faint SNR G117.7+0.6, they are all located inside the giant HI bubble mentioned in (Section

4.3.4). The breakout morphology of CTB 1 can be explained by the possible interaction with a very faint SNR G117.7+0.6 [93]. Most probably the shock is expanding freely in this direction to the low density medium formed by this SNR. This new SNR might be faint due to its location in the center of the super bubble where ambient medium density is low.

UCAC 4-763-077012 is a B8V type star and is the only OB-type star located inside the search region. Because of that it is faint, $V = 13.75$ mag, the proper motion is not precise enough to find out the possible runaway nature. However, the star is linked to an X-ray source CXOG J235851.8+622725 [69]. The X-ray source was found by CHANDRA imaging, but nothing was mentioned about its nature. Instead, 1WGA J0001.4+6229, close to the northeastern edge was pointed out as a potential NS [209]. RX J0002+6246 is also an X-ray source proposed to be a pulsar located in the breakout region [93]. But, later observations showed that the source of the emission is a foreground star [57]. The B-type star is at 3.2 ± 0.5 kpc distance with $A_V = 1.45$ mag (4.16). It might be further away than the OB associations. Eight more stars located in the R/3 region were observed. The A_V value varies between 0.8 – 1.5 kpc and the variation does not depend on the distance. Two B3V type stars were found with similar proper motion at an approximate distance of 4.0 kpc (4.16). These stars seem to be background to the potential runaway and the associations. They have a peculiar proper motion of ~ 4 mas yr⁻¹ in Dec. As it is highly unlikely to find two OB runaway star inside a SNR moving in the same direction. So, these stars should be located at a different velocity field which cannot be explained by a uniform galactic rotation curve. Therefore, the SNR might belong to Cas OB5 at 2.5 kpc, but if the B8V type star is the runaway, then the distance would be ~ 3.0 kpc or ~ 4.0 kpc assuming the progenitor had a genetic connection with the neighboring massive stars.

4.3.6 G126.2+1.6

G126+1.6 is a SNR with a poorly defined shell, partially showing filamentary emission A.5. The angular diameter is 70' [86]. OIII/ H_β ratio gives a shock velocity of 120 km s⁻¹ [25]. The V_{LSR} of the HI related to the clouds vary between -33 and -55 km s⁻¹. Hence, the estimated distances show large variation; 2.0 to 5.6 kpc [117, 271]. For 5.0 kpc, the physical diameter of the SNR is 128 pc with a Sedov age of 210 kyr. $\Sigma - D$ diagram yields a lower value; 2.88 kpc [88]. The A_V towards the SNR is ~ 1.4 mag [19].

Table 4.16: Early type stars identified inside CTB 1. The star name (1), the angular separation from the center ($'$) (2), m_V (mag) (3), the proper motion in α and δ (mas yr^{-1}) (4 and 5), their errors (mas yr^{-1}) (6), the spectral types (7), the A_V (mag) and the distance found (pc) (8 and 9) and the instrument of observation (10) are given respectively. The radius of the search region of is $3'$. While C represents CAFOS, T stands for TFOSC. Detailed information can be found in Table (4.7)

Name	Ang	V	μ_α^*	μ_δ	err	SpT	A_V	Dist	Tel
763-077012	2.55	13.75	0.7	6.4	3.8/4.3	B8V	$1.45^{+0.05}_{-0.17}$	3234^{+487}_{-394}	C
763-077153	3.52	13.25	-6.4	-2.0	0.5/2.1	B9V	$1.19^{+0.17}_{-0.20}$	2352^{+327}_{-260}	C
763-076928	4.25	12.62	-3.4	2.0	0.9/1.2	B3V	$1.07^{+0.14}_{-0.07}$	4262^{+1663}_{-240}	C
763-077148	4.67	13.33	-4.4	7.4	2.2/2.4	A2V	$0.78^{+0.08}_{-0.09}$	1777^{+186}_{-86}	C
763-077093	4.83	13.84	-6.3	8.6	3.4/3.8	A2V	$1.06^{+0.08}_{-0.09}$	1979^{+208}_{-96}	C
763-077172	5.24	12.30	0.9	-0.4	1.6/0.6	A0V	$0.90^{+0.20}_{-0.08}$	1408^{+174}_{-165}	C
763-077199	5.65	10.61	-6.6	0.1	1.5/0.7	A0V	$0.75^{+0.20}_{-0.08}$	695^{+86}_{-81}	T
762-075377	5.79	13.73	2.1	3.5	2.9/3.6	A3V	$1.07^{+0.09}_{-0.09}$	1708^{+87}_{-107}	C
762-075495	5.99	12.87	-4.0	2.2	1.3/2.4	B3V	$1.48^{+0.14}_{-0.07}$	3953^{+1542}_{-222}	C

TYC 4038-1657-1 is A0Ib type star [95] which is only $50''$ separated from the geometrical center (Figure A.5). Its spectro-photometric distance is 5495 pc where the errors are extremely large $\sim 2-5$ kpc considering an uncertainty in the luminosity class. On the other hand, based on m_V values from W06, the distance is calculated as 4.0 kpc which is perfectly consistent with the distance of UCAC 4-772-009430 (B1V) of which the spectro-photometric distance is also 4.0 kpc (Table 4.17).

Both stars do not show a clear peculiar velocity. The proper motion values are $\mu_\alpha^* = -2.2 \pm 0.9$, $\mu_\delta = -1.0 \pm 0.8 \text{ mas yr}^{-1}$ and $\mu_\alpha^* = -1.2 \pm 1.0$, $\mu_\delta = -0.5 \pm 2.2 \text{ mas yr}^{-1}$ respectively. The expected proper motion in this direction at 4.0 kpc is $\mu_\alpha^* = -1.5$, $\mu_\delta = -0.3 \text{ mas yr}^{-1}$. While the B2 type star UCAC 4-772-009430, perfectly represents the velocity field, TYC 4038-1657-1 seems to be slightly faster. The peculiar velocity of the star is $20 \pm 14 \text{ km s}^{-1}$, which is not convincing to confirm its runaway nature. Nevertheless, as it is very close to the geometrical center, it is considered as a potential OB runaway. Also, the progenitor star should be a part of this possible cluster.

Here, the distance to the SNR G126.2+1.6 is suggested to be $4.0^{+1.45}_{-1.16}$ kpc and it should have a core collapse origin with a progenitor mass of $12 - 15 M_\odot$.

SNR G126.2+1.6 is too distant (4.0 kpc) for OB runaway search. Radial velocities of TYC 4038-1657-1 must be measured to show its possible runaway nature. On the other

Table 4.17: Early type stars identified inside SNR G126.2+1.6. The star name (1), the angular separation from the center (') (2), m_V (mag) (3), the proper motion in α and δ (mas yr^{-1}) (4 and 5), their errors (mas yr^{-1}) (6), the spectral types (7), the A_V (mag) and the distance found (pc) (8 and 9) and the instrument of observation (10) are given respectively. The radius of the search region of is $6'$. While C represents CAFOS, T stands for TFOSC. Detailed information can be found in Table (4.7)

Name	Ang	V	μ_α^*	μ_δ	err	SpT	A_V	Dist	Tel
772-009430	3.35	12.78	-1.2	-0.5	1.0/2.2	B1V	$2.96^{+0.20}_{-0.09}$	4035^{+1453}_{-1160}	T
772-009343	3.40	13.03	-4.6	-0.3	1.8/1.7	A1V	$2.71^{+0.08}_{-0.09}$	733^{+97}_{-70}	C
772-009467	4.67	13.64	0.9	1.6	2.9/5.9	B1V	$2.99^{+0.13}_{-0.08}$	5891^{+2138}_{-1550}	C
772-009227	11.98	11.61	-5.0	-1.0	1.1/1.5	B9V	$1.80^{+0.07}_{-0.08}$	948^{+52}_{-130}	C

hand, the intermediate mass stars are above the magnitude limit. The SNR is highly evolved and has a physical diameter of $D=81$ pc. A core collapse origin is suggested due to the neighboring massive stars.

4.3.7 G127.1+0.5 (R 5)

R 5 is a shell type SNR with a $45'$ diameter and spherical symmetric shape [86, 140]. The shell is bright and complete in radio, while it is not recognized in optical bands. The H_α emission is diffuse and [299] hardly related to the SNR. The central compact radio sources are confirmed to be extra-galactic objects [134].

The kinematic distance derived from -12 to -16 km s^{-1} velocities [156] is 1.15 kpc. The distance was also confirmed by the open cluster NGC 559 [19]. However, more recent age and distance measurements for this cluster is 224 ± 24 Myr and 2.43 ± 0.23 kpc respectively [118]. Due to the low surface brightness of the SNR, $\Sigma - D$ diagram gives a distance of 3.5 kpc [88].

At the distance of 1.15 kpc, assuming that the initial explosion energy is $E_0 = 0.5 \times 10^{51}$ erg, the age was found as 20 – 30 kyr [156].

The O9.5IV type [195] star, HD 8768, which is slightly out of the search region, was observed by FLECHAS. In the FLECHAS spectrum, blue-shifted component for the Na I–D1 & D2 lines is detected (Table B.4). This is a sign that the star is either inside or behind the SNR, so it is a good distance indicator for R 5. For O9.5IV spectral type, its spectro-

photometric distance is 1525 ± 220 pc. For the spectral type found by CAFOS observations, B0V, the distance is 1309^{+435}_{-348} kpc (Table 4.18). Due to the high noise level in FLECHAS data, spectral type identification could not be done precisely. Overall, here, it is suggested that the SNR distance is closer than 1.5 kpc.

UCAC 4-767-013623 is the only OB-type star found in the search region of R 5. However, its runaway nature is somewhat dubious. Compared to the other candidates, the proper motion is highly different in R.A. This peculiar motion corresponds to a 2-D space velocity of ~ 15 km s⁻¹ at 0.8 kpc, which is not sufficient to propose a runaway nature. On the other hand, the star shows no peculiar velocity w. r. t. the galactic rotation or the nearest OB association Cas OB8 (70 pc away at 2.0 kpc). In addition, a B5Iab ([195]) type star, HD 9105 (Figure 4.15) might have a genetic connection to other OB stars and the progenitor star. The proper motion of this star is, $\mu_{\alpha}^* = -1.6 \pm 1.0$, $\mu_{\delta} = -0.2 \pm 1.0$ mas yr⁻¹, representing the local standards. On the same reference frame, HD 8768 has a peculiar velocity of 37 ± 6 km s⁻¹ at 1.5 kpc. The reason of the peculiar velocity might be binarity. The star has a binary companion [177] which is possibly a B5V type star. Due to the binarity, its separation from the geometric center and the direction of the proper motion (Figure 4.15), HD 8768 is not considered as the runaway star of R 5. Further evidences are needed.

Table 4.18: Early type stars identified inside R 5. The star name (1), the angular separation from the center (′) (2), m_V (mag) (3), the proper motion in α and δ (mas yr⁻¹) (4 and 5), their errors (mas yr⁻¹) (6), the spectral types (7), the A_V (mag) and the distance found (pc) (8 and 9) and the instrument of observation (10) are given respectively. The radius of the search region of is 4′. While C represents CAFOS, T stands for TFOSC. Detailed information can be found in Table (4.7)

Name	Ang	V	μ_{α}^*	μ_{δ}	err	SpT	A_V	Dist	Tel
767-013623	3.21	11.08	-0.9	1.7	0.7/0.6	B8V	$1.70^{+0.04}_{-0.17}$	801^{+121}_{-98}	C
766-013684	6.42	12.14	-5.1	2.2	0.8/1.0	B8V	$2.32^{+0.05}_{-0.19}$	949^{+143}_{-108}	C
766-013622	7.21	11.54	-4.4	1.5	0.6/0.7	B8V	$2.40^{+0.05}_{-0.17}$	729^{+110}_{-87}	T
767-013562	7.21	9.13	-5.9	0.3	0.7/1.4	B0V	$2.04^{+0.12}_{-0.01}$	1309^{+435}_{-348}	C

4.3.8 G132.7+1.3 (HB 3)

HB 3 is a MMSNR with an angular diameter of 80′ [86]. It resides in a complex region with an asymmetric shape in radio bands (Figure A.5). It is possibly interacting with the molecular clouds of W 3 in the southeast [237]. The shell is faint in optical bands and not

observable in X-rays. The expansion velocity derived from diffuse H_α emission is $150 - 180 \text{ km s}^{-1}$ [167]. The dense filaments have velocities lower than 100 km s^{-1} indicating that HB 3 is an evolved SNR. The A_V measured from optical filaments is $2.2 \pm 0.1 \text{ mag}$ [63], while the N_H derived from the X-ray spectrum is $(3.2 \pm 0.1) \times 10^{22}$ which is equal to $\sim 1.5 \text{ mag } A_V$ [154]. The X-ray radiating plasma is at relatively low temperature, $0.14 \pm 0.04 \text{ keV}$ which translates to $v_{\text{bw}} = 340 - 400 \text{ km s}^{-1}$. Based on Sedov or evaporating cloud models, $E_0 = (0.3 - 2.0) \times 10^{51} \text{ erg}$ and $\tau = 30000 \pm 5000 \text{ yr}$ at 2.2 kpc . The diameter of HB 3 at this distance is 51 pc . Enhanced abundances in Mg is possible, but not clear. Hence, HB 3 is an old SNR which is most likely to have a core collapse origin.

The systematic velocity of H I related to the SNR was found as -30 km s^{-1} [224, 237]. The CO clouds detected in 408 MHz observations, which might be shocked by the SNR has -43 km s^{-1} velocity, while the systematic velocity of W 3 from 1720 MHz OH Maser yields $-40 \pm 5 \text{ km s}^{-1}$ [138]. The average velocity of H_α filaments is $-45 \pm 3 \text{ km s}^{-1}$ [170]. The corresponding distances are 2.3 (from H I), 3.4 (from W 3) and 4.0 (from H_α) kpc. The distance of the full extent of the complex, $l = 132^\circ - 138^\circ$ considering the OB stars and H II regions, is $2.0 \pm 0.05 \text{ kpc}$ [132, 300]. The distance derived from $\Sigma - D$ diagram is 1.93 kpc [88].

The spectro-photometric distance of OB-type stars inside W 3 and the host OB association Cas OB6 is $\sim 2.3 \text{ kpc}$ [189] and $\sim 2.2 \text{ kpc}$ [17]. It was suggested that optical parallax would yield 1.8 kpc [188].

Due to the high reddening, the OB stars inside W 3 complex are faint ($> 14 \text{ mag}$). So, the proper motion values have high errors ($> 2.0 \text{ mas yr}^{-1}$). In the given sample of 18 stars [132], the average proper motion calculated with using *UCAC 4* data is $\mu_\alpha^* = -2.3 \pm 7.4$ and $\mu_\delta = -2.3 \pm 9.8 \text{ mas yr}^{-1}$. Nine stars with proper motion errors of $< 3.0 \text{ mas yr}^{-1}$ show an average of $\mu_\alpha^* = -2.4 \pm 1.3$ and $\mu_\delta = -1.2 \pm 1.9 \text{ mas yr}^{-1}$,

The progenitor of HB 3 should be a member of Cas OB6 association. The average proper motion of $\mu_\alpha^* = -1.3 \pm 1.8$ and $\mu_\delta = -0.6 \pm 1.6 \text{ mas yr}^{-1}$. For consistency, this was also calculated with using *UCAC 4* data for the same 13 stars and it is found to be $\mu_\alpha^* = -1.5 \pm 0.6$ and $\mu_\delta = -0.6 \pm 0.7 \text{ mas yr}^{-1}$. This is taken as the reference motion for runaway candidates of HB 3. The average radial velocity of Cas OB6 is $-42 \pm 8 \text{ km s}^{-1}$.

It is difficult to judge that the stars inside the search region are runaways or not due to the

Table 4.19: Early type stars identified inside HB 3. The star name (1), the angular separation from the center ($'$) (2), m_V (mag) (3), the proper motion in α and δ (mas yr^{-1}) (4 and 5), their errors (mas yr^{-1}) (6), the spectral types (7), the A_V (mag) and the distance found (pc) (8 and 9) and the instrument of observation (10) are given respectively. The radius of the search region of is $7'$. While C represents CAFOS, T stands for TFOSC. Detailed information can be found in Table (4.7)

Name	Ang	V	μ_α^*	μ_δ	err	SpT	A_V	Dist	Tel
764-021331	4.36	13.74	-1.6	-0.2	2.2/1.6	A0V	$2.15^{+0.20}_{-0.08}$	1541^{+191}_{-180}	C
764-021370	5.24	13.65	-3.7	-1.3	2.4/2.4	B8V	$2.45^{+0.05}_{-0.16}$	1946^{+293}_{-237}	C
764-021388	6.49	12.37	-1.8	-1.4	1.0/1.0	B9V	$1.59^{+0.16}_{-0.20}$	1306^{+182}_{-144}	C
765-021792	7.54	13.59	2.6	0.1	3.8/1.7	B8V	$1.80^{+0.17}_{-0.20}$	2083^{+289}_{-230}	C
765-021812	9.10	12.38	-4.0	0.4	0.6/0.8	B2V	$2.62^{+0.08}_{-0.15}$	2763^{+1003}_{-764}	C
765-021781	12.83	11.50	-3.0	2.2	0.5/0.6	B8V	$1.53^{+0.04}_{-0.17}$	1108^{+167}_{-135}	C
765-021729	13.42	9.201	-5.0	4.1	0.8/0.7	B8V	$1.50^{+0.05}_{-0.17}$	689^{+191}_{-124}	T

high high errors of proper motion and late spectral types. For example, the B8V type star UCAC 4-764-021370 has a distance consistent with that of the SNR and the OB association and has higher proper motion than the references (Table 4.19). The relative proper motion is $\mu_\alpha^* = -2.2 \pm 2.4$ and $\mu_\delta = -0.7 \pm 2.4 \text{ mas yr}^{-1}$ which can be purely due to the poor measurement.

The massive star UCAC 4- 765-021812 (B2V) is $2'$ outside of the search region. The proper motion is precise and higher than the reference. The relative proper motion and corresponding transverse velocity are; $\mu_\alpha^* = -2.5 \pm 0.6$ and $\mu_\delta = 1.0 \pm 0.8 \text{ mas yr}^{-1}$ and $V_{\text{tr}} = 25.5 \pm 5.3 \text{ km s}^{-1}$. Owing to the asymmetric shape of the remnant, this star is a potential runaway of HB 3. The explosion center found from tracing back for 15000 yr is shown in Figure (A.5). It is $\sim 10'$ separated from the geometrical center. On the other hand tracing back the star for $\sim 1 \text{ Myr}$, it coincides with W 3 star forming region. 1 Myr flight time is consistent with the age of W 3, so this star can also be the cluster ejected runaway star. Even, the progenitor of HB 3 can be a massive ($> 30 M_\odot$), cluster ejected runaway star from W 3 region. The SNR morphology which looks like to be vacuumed by W 3 might be an evidence (Figure A.5). The SNR expands freely inside the tunnel which had been carved by the progenitor during the escape from the cluster.

4.4 SNRs With No OB Runaways Stars

In 16 SNRs, no OB-type stars in the search regions were found. They are the remnants of an explosion of a single star or the OB runaway star is above our detection limit. Also, there are no OB-type stars which are not projected on the runaway search region. Three of these are very young SNRs having a small angular diameter, so the chance projection possibility is low. One of them, Cygnus Loop is relatively close to the Sun. Hence, due to the distance restriction in the candidate selection, the background massive stars were avoided. Cas A, HC 40 and W 44 suffer from high values of extinction. Another four are far away from the star forming regions and young stellar associations.

4.4.1 G034.7-0.4 (W 44)

Among the SNRs within 5 kpc, W 44 is one of the two extensively studied SNR, located between the galactic longitudes 30° and 60° (Figure A.6). The angular diameter of the SNR is $35'$ [86]. The star formation regions in these directions must be further away than at least 3 kpc. W 44 is a MMSNR [232] which shows a high abundance of metals [128]. Based on measurements of HI absorption and 1720 MHz maser lines, the kinematical distance was estimated as 2.8 ± 0.2 kpc [34, 43]. Although the SNR is interacting with the dense clouds [103, 248], there is no known OB star within 1° from the geometrical center. Also, there is no known OB association within 5° (~ 260 pc at 3.0 kpc) projected onto the SNR. The minimum N_{H} measured from CHANDRA observations is relatively high, $9.2 \times 10^{21} \text{ cm}^{-2}$. Based on the relation given in [91], this corresponds to a A_{V} of 4.0 mag. Taking the lowest values of the A_{V} and the distance (4.0 mag and 2.6 kpc), stars having the spectral types later than B2.5–B3 is fainter than 14 mag. So, in W 44, there is no OB runaway star with a spectral type earlier than B3V.

4.4.2 G054.4-0.3 (HC 40)

HC 40 is an evolved shell type SNR in a complex region with a diameter of $40'$ [86] (Figure A.7). The radio and IR studies show that it is expanding inside the cavity of a molecular cloud. The HI column density measured from ROSAT observations is $N_{\text{H}} = 1.0 \sim 10^{22} \text{ cm}^{-2}$ [119]. This corresponds to a A_{V} of 4.7 mag. The filamentary shell of the SNR is

faint, so no extinction could have been derived from the optical studies [25]. Based on CO observations, the kinematical distance is 3.0 ± 1.0 kpc [120, 121].

The progenitor star of HC 40 is probably a member of a possible distant OB association [70]. Among the listed OB associations, the closest one is Vul OB1 which is $\sim 5^\circ$ (260 pc at 3.0 kpc) separated. This is very large distance to propose an association. Additionally, the distances derived for Vul OB1 are 2.54 and 1.6 kpc [189, 268]. There is also no OB star identified so far within $30'$ (26 pc) from the geometrical center [251]. Similar to SNR W44 (Section 4.4.1), HC 40 must be from the SN of a massive star. However, the large distance and the extinction make it difficult to study the stars related to the SNR. Considering a distance of 3.0 kpc and a A_V of 4.0 mag, there is no OB runaway star with a spectral type earlier than B2V.

4.4.3 G069.0+2.7 (CTB 80)

CTB 80 is a shell type SNR with an incomplete morphology in a complex region. It hosts a pulsar, PSR B1951+32 of which the proper motion is well defined; $\mu_\alpha^* = -28.8 \pm 0.9$ and $\mu_\delta = -14.7 \pm 0.9$ mas yr $^{-1}$ [307]. Tracing back the pulsar towards the center of the northern IR shell at $\alpha = 19\text{h}54\text{m}50\text{s}$, $\delta = +33^\circ 00' 30''$ [137] (Figure 4.8), gives an age of 51 kyr. This suggests that it is an evolved SNR. However, another suggestion for the geometrical center is the center of the triangular shaped region which is bright at 1420 MHz (Figure 4.8) at $\alpha = 19\text{h}53\text{m}20\text{s}$, $\delta = +32^\circ 55' 00''$ [86]. This location is also consistent with the pulsar proper motion, yet the tracing back yields a lower value; ~ 10 kyr. The SNR has a highly peculiar shape. It is expanding in a medium having significantly different densities in different directions. This can only be seen in the combination of optical, [184] IR [136] and X-ray [160] images (Figure 4.8).

Based on ROSAT data, the N_H value is 3.0×10^{21} cm $^{-2}$ [241], which corresponds to a A_V of 1.4 mag. The distance was estimated as 2.5 kpc. From HI velocities around 8 km s $^{-1}$, the kinematic distance was suggested as 1.5 ± 0.5 kpc [160]. The extinction based on optical studies gives a higher value, ~ 2.5 mag [98].

PSR B1951+32 has a spin period and a period derivative of $P = 39.5$ ms and $\dot{P} = 5.92 \times 10^{-14}$ s s $^{-1}$ respectively. This corresponds to a dipole magnetic field, $B = 4.86 \times 10^{11}$ G, a

spin down luminosity, $\dot{E} = 3.7 \times 10^{36} \text{ erg s}^{-1}$ and a characteristic age, $\tau = 107000 \text{ yr}$. The pulsar is accompanied by a bow shock PWN. The DM of the pulsar is $50 \pm 8 \text{ cm}^{-3}$ which suggests a distance of 1.4 kpc [145]. At 2.0 kpc, the pulsar space velocity is 274 km s^{-1} , which is expected considering the pulsar space velocity distribution (see Section 1.3).

The SNR cannot be directly linked to an OB association. The Cyg OB3 is 125 pc away at 1.8 kpc [188]. Considering the association extension of 106 pc [268], there should be no relation. But, there are two massive stars as close to the remnant as 25 pc, HD 225985 (B1V) and HD 226111 (B1Ib). Both stars are variable and the former shows a significant NIR excess implying a recent formation. The J – H and H – K values are 0.1 and 0.28 mag respectively. The A_V values and distances are 0.8 mag and 1.5 kpc, 1.9 mag and 1.5 kpc respectively. The distances are consistent with that of proposed in [160].

In the central search region there is no OB runaway candidates. The geometrical center of the IR shell was not covered. As to define a reliable geometrical center for this SNR is difficult, the OB runaway search was done only for the center proposed by [86] (Figure 4.8).

4.4.4 G074.0-8.5 (Cygnus Loop)

Cygnus loop is one of the largest SNR ($240' \times 160'$) with well defined shell bright in all wavebands. Yet, the breakout region in the south makes two different centers at $\alpha = 20\text{h}51\text{m}00\text{s}$, $\delta = +30^\circ 40' 00''$ [86] and $\alpha = 20\text{h}51\text{m}00\text{s}$, $\delta = +31^\circ 03' 00''$ [283] A.7. It is located at the low galactic latitude owing to its possible nearness to the Sun. The distance estimates do not place the SNR further away than 0.6 kpc. It is restricted by 0.9 kpc by the B9V type star HD 198946 which shows an intermediate velocity, 29 km s^{-1} component, for the Na I–D1 ISM line [296]. The distance to the star by optical parallax is 550_{-150}^{+350} [287]. The shock velocity derived from UV observations is $180 \pm 10 \text{ km s}^{-1}$. The proper motion of the filaments correspond to this velocity at 540_{-80}^{+100} pc [18]. The expansion infer an age of 10000 yr. The low N_H value of $(1 - 6) \times 10^{20} \text{ cm}^{-2}$ [155] confirms the low A_V values of 0.22 ± 0.08 mag [61, 210].

The metal abundances which are 5 times of the solar values indicate the core collapse origin. Based on the radial discontinuity at nine tenth of the shock radius, it was found that the SNR has encountered the cavity wall 1000 yr ago. The dimension of the cavity imply a progenitor

mass of $15 M_{\odot}$ [164]. The abundances also indicate a $15 M_{\odot}$ progenitor [279].

The large dimensions and the asymmetric shape bring necessity of observation of hundreds of stars. Thus, similar to the SNR G65.3+5.7, the distance is restricted to 0.6 kpc to search for OB runaway stars. At this distance and a highest possible A_V of 0.6 mag, a B9 type star is not fainter than 9.0 mag. Around both geometrical centers, no OB runaways were found. The progenitor of the Cygnus loop was a single star, a merger or a star with a low mass companion.

There are five early B-type stars within 5° from the geometrical center. They show various distances from 0.3 to 2.3 kpc. However, the A_V does not change with distance owing to the direction which is out of the galactic plane. No OB association is also found.

4.4.5 G082.2+5.3 (W 63)

SNR G082.2+5.3 is a MMSNR [231] lying in the Cygnus region, having an angular size of $95' \times 55'$ [86] (Figure A.1). Various $\Sigma - D$ relations suggest a distance of 1.6 ± 0.3 kpc [88, 236]. Based on ROSAT observations, the HI column density was found as $N_H = (1.0 - 8.0) \times 10^{21} \text{ cm}^{-2}$ [231] and $N_H = (2.2 - 5.0) \times 10^{21} \text{ cm}^{-2}$ [181]. The equivalent A_V value is 1.0 – 2.4 mag.

The maximum velocity of the shocked filaments are around 100 km s^{-1} [181]. Slower shock velocities, from 35 km s^{-1} to 70 km s^{-1} were also suggested [236]. From the ASCA spectrum, two temperatures for the X-ray emitting plasma can be derived; 0.2 and 0.6 keV. The latter component imply a 720 km s^{-1} expansion velocity. At 1.6 kpc, considering a 720 km s^{-1} shock velocity, the initial explosion energy is $E_0 = 0.17 \times 10^{51}$ erg, the ambient medium density is $n_0 = 0.012 \text{ cm}^{-3}$ and the age is 13500 yr [181].

W 63 cannot be linked to an OB association. The nearby associations, their angular separations and physical distances at 1.6 kpc are Cyg OB8–280' (130 pc), OB2–290' (134 pc) and OB9 335' (155 pc). The distances to the associations are 1.8, 1.5 and 1.0 kpc respectively [188].

UCAC 4-677-080274 (B2V) and UCAC 4-679-080132 (B9V) are the candidates of which the distances are consistent with that of the SNR (Table 4.20). The proper motion of UCAC 4-

Table 4.20: Early type stars identified inside SNR G082.2+5.3. The star name (1), the angular separation from the center (') (2), m_v (mag) (3), the proper motion in α and δ (mas yr $^{-1}$) (4 and 5), their errors (mas yr $^{-1}$) (6), the spectral types (7), the A_V (mag) and the distance found (pc) (8 and 9) and the instrument of observation (10) are given respectively. The radius of the search region of is 8'. While C represents CAFOS, T stands for TFOSC. Detailed information can be found in Table (4.7)

Name	Ang	V	μ_α^*	μ_δ	err	SpT	A_V	Dist	Tel
678-083198	4.63	12.67	-5.1	-6.2	0.8 / 1.7	A1V	1.81 $^{+0.08}_{-0.09}$	942 $^{+124}_{-89}$	C
678-083207	4.86	11.36	-2.9	-5.0	0.7 / 0.7	A0V	1.68 $^{+0.20}_{-0.08}$	640 $^{+80}_{-74}$	C
678-083011	7.04	10.18	4.5	1.7	0.5 / 0.6	A2V	0.30 $^{+0.09}_{-0.09}$	519 $^{+55}_{-25}$	C
678-083025	7.43	13.86	9.0	-0.7	2.4 / 3.0	A1V	3.08 $^{+0.08}_{-0.08}$	905 $^{+119}_{-86}$	C
677-080274	7.73	12.18	-3.1	-5.4	0.6 / 0.7	B2V	3.33 $^{+0.08}_{-0.14}$	1823 $^{+652}_{-511}$	T
679-080132	9.86	12.95	-6.3	-1.3	1.9 / 6.2	B9V	2.36 $^{+0.05}_{-0.08}$	1472 $^{+220}_{-261}$	C

677-080274 is well consistent with that of Cyg OB9, $\mu_\alpha^* = -3.1 \pm 1.6$, $\mu_\delta = -5.4 \pm 1.6$ mas yr $^{-1}$ (see Section 4.3.1). So it is not considered as a runaway star. The proper motion of UCAC 4-679-080132 suffer from poor measurement. As it is also out of the search region, it is also not a runaway star of W 63. To summarize there is no OB runaway star of W 63

4.4.6 G089.0+4.7 (HB 21)

HB 21 is another MMSNR in Cygnus region (Figure A.1). It is suggested to be in interaction with molecular clouds [31] owing to its morphology which was shaped by the density variations in the ISM. While having a semi-spherical shape in the south, the shell was bent in the north. Clumpy and dense environment implies that the SNR has a core-collapse origin which was also confirmed by Si and S enhancement found by the X-ray spectroscopy [154] The SNR has an elliptic shape in 120' \times 90' angular size. The pulsar PSR J2047+5029 was studied for a possible relation with the SNR, but owing to its very old characteristic age of 53 Myr [112], such a relation was ruled out. Considering the progenitor star is a member of Cyg OB7 association, the distance suggested for the SNR is 0.8 kpc [262]. But, a distance of 1.7 \pm 0.5 kpc was also proposed based on cloud velocities and X-ray properties [31].

As the OB runaway search inside HB 21 is not completed, no further details on the SNR is given here. Five candidates inside the search region was observed together with another five inside R/3 portion (Table 4.21). Owing to the large dimensions of the SNR and possible young open clusters, there are still ten more candidates inside the search region to observe

Table 4.21: Early type stars identified inside SNR HB 21. The star name (1), the angular separation from the center ($'$) (2), m_v (mag) (3), the proper motion in α and δ (mas yr^{-1}) (4 and 5), their errors (mas yr^{-1}) (6), the spectral types (7), the A_V (mag) and the distance found (pc) (8 and 9) and the instrument of observation (10) are given respectively. The radius of the search region of is $10'$. While C represents CAFOS, T stands for TFOSC. Detailed information can be found in Table (4.7).

Name	Ang	V	μ_α^*	μ_δ	err	SpT	A_V	Dist	Tel
703-080938	2.43	10.22	-2.1	-6.4	0.8/0.9	B2Ve	$2.07^{+0.09}_{-0.14}$	1470^{+525}_{-413}	T
704-078114	7.19	10.91	3.5	-1.4	0.9/0.8	A0V	$0.55^{+0.12}_{-0.07}$	978^{+124}_{-76}	C
703-081075	9.02	12.44	-2.2	-3.6	1.7/1.1	A1V	$1.47^{+0.21}_{-0.07}$	1159^{+141}_{-137}	C
703-081098	9.87	12.18	-0.9	-4.5	2.4/1.0	A1V	$1.51^{+0.22}_{-0.10}$	1079^{+109}_{-121}	C
703-081110	9.93	11.74	-1.1	-4.2	1.9/0.8	B8V	$1.92^{+0.04}_{-0.11}$	1036^{+155}_{-134}	T
703-080680	10.31	13.04	0.2	9.3	1.9/2.8	A0V	$1.95^{+0.20}_{-0.08}$	1226^{+153}_{-142}	C
703-080795	11.60	13.75	-4.4	3.7	2.1/2.5	A0V	$1.26^{+0.20}_{-0.07}$	2333^{+288}_{-274}	C
704-078268	12.18	12.13	-2.2	-3.1	1.1/0.7	A0V	$1.12^{+0.20}_{-0.08}$	1169^{+139}_{-139}	C
704-078280	12.46	10.02	4.3	-3.6	0.7/0.6	B8V	$1.30^{+0.10}_{-0.09}$	607^{+91}_{-86}	C
704-077771	17.26	10.52	-2.7	-7.8	1.4/0.7	B9V	$0.58^{+0.16}_{-0.20}$	803^{+112}_{-89}	C

to confirm the spectral type.

The B2Ve type star UCAC 4-703-080938 (BD+50 3188) is very close to the SNR geometrical center (Table 4.21). However, the TRES spectrum of the star shows both blue and red-shifted components of the ISM lines (see Appendix B). As the gas receding away from us can be detected in the spectrum, the star is confirmed to be behind the SNR, not inside. So, it cannot be the OB runaway star from this SNR.

4.4.7 G106.3+2.7

SNR G106.3+2.7 is a composite type SNR hosting an energetic pulsar; PSR J2229+6114. It has a cometary shape with $40' \times 24'$ dimensions (Figure A.3). The PWN is on the northeastern edge of the SNR and interacting with the dense ambient medium, while the southwestern part is fainter and is expanding into a low density medium, a breakout region [215] causing the elongated shape.

PSR J2229+6114 is a radio pulsar with a period of $P = 51.6$ ms and a spin down rate of $\dot{P} = 7.83 \times 10^{-14} \text{ s s}^{-1}$. From the measured P and \dot{P} , the derived spin down power is quite high; $\dot{E} = 2.2 \times 10^{37} \text{ erg s}^{-1}$. The dipole magnetic field is $B_{\text{dip}} = 2.0 \times 10^{12} \text{ G}$ and the

characteristic age is $\tau = 10460$ yr [94]. The pulsar also shows γ -ray emission, but no pulses have been detected at this waveband yet [3]. The high dispersion measure, 200 cm^{-3} yields a distance of 12 kpc. The N_{H} derived from the CHANDRA X-ray images of the pulsar is $(6.3 \pm 1.3) \times 10^{21} \text{ cm}^{-2}$. This corresponds to a A_{V} of 3.1 mag. Hence the distance estimated for the SNR is 3.0 ± 1.0 kpc [94]. However, based on HI velocity, it was proposed to be 800 pc [142].

For 3.0 kpc distance, the closest OB associations are NGC 7235 and Cep OB1 with $240'$ and $255'$ (209 and 222 pc) separation respectively. These distances are too large for a possible association. Yet, for a 0.8 kpc distance, the remnant is 50 and 56 pc away from the Cep OB3 and Cep OB2 associations. The extension of Cep OB3 is only 29 pc while Cep OB2 has a diameter of 105 pc. So, the progenitor star could be a member of Cep OB2.

Although there is no OB-type star candidates inside the search region (R/6), two candidates out of the region were observed. UCAC 4-754-073561 and UCAC 4-754-073653 are found to be A6V and A9V type stars. They are at the distances of 539_{-16}^{+12} and 477_{-51}^{+14} pc respectively. Despite the short separation between them, $7.5'$, the A_{V} values are highly different, 2.29 ± 0.08 and 0.76 ± 0.09 mag respectively. This is the clear evidence of a nearby dense cloud partially covering the line of sight of the remnant. The B5 type emission star EM GGR 71 located at $20'$ to the west of the pulsar, also show high absorption, $A_{\text{V}} = 3.3$ mag, [193] compared to its spectro-photometric distance of 0.8 ± 0.1 kpc. Owing to NIR excess, $J - H = 0.95$ / $H - K = 1.32$, and the nebulosity, EM GGR 71 should be a Herbig Be star, recently formed in this cloud. Therefore, the distance derived from the N_{H} values are not reliable as there is a dense cloud at a distance of ~ 500 pc.

Owing to the asymmetric shape of the SNR, an OB runaway search was also done within $5'$ from the pulsar. Also in this region, no OB-type candidate was found. Considering 3.0 kpc distance and 3.0 mag A_{V} , there is no OB runaway star to the SNR, earlier than B5V type. For 0.8 kpc and the same A_{V} , there is no OB runaway star inside the SNR. The stars observed showed the existence of a dense foreground cloud which makes the closer distance estimates for this SNR also possible.

4.4.8 G111.7-2.1 (Cas A)

Cas A is a very young SNR with a very bright shell in radio (Figure A.8) [6]. The age was measured from the optical expansion of the dense knots and found as 353 ± 27 yr [64]. Probably due to the high reddening, the explosion could not be seen by any observers. A $5 - 6$ mag of A_V value is suggested [111]. However, the N_H values measured from the X-ray observations corresponds to $8 - 9$ mag of A_V [106]. The estimated distance towards the SNR is $3.4^{+0.3}_{-0.1}$ kpc [225]

Cas A has a core collapse origin which resulted in a type IIb SN. It is a typical O rich SNR hosting a neutron star, right in the geometrical center, observable in X-rays [153]. Although the thermal radiation can be observed, no pulsations were detected so far. Furthermore, no non-thermal emission which could be a sign of a PWN, was also seen. Thus, the NS is thought to be a CCO with a very slow spin and low B_{dip} [211]. Given the properties, Cas A progenitor must be a massive star.

No OB-type star was found inside Cas A probably due to high extinction. At 3.4 kpc and with a A_V of 6 mag, an O9–O8 type runaway star would have an apparent magnitude of $m_v = 14$ mag. Considering a higher extinction, the possible OB runaway star in Cas A is even fainter. As the SNR is young, the position of the geometrical center is precisely known. The HST images of the NS taken in a time span of three years in the HST archive should be studied by means of proper motion determinations. There is also no known young stellar associations around like in the case of W 44. For Cas A, there is no clear conclusion for the search for massive runaway star.

4.4.9 G093.3+6.9 (DA 530)

DA 530 is a SNR with a symmetric bilateral shape (Figure A.2) and is located far away from star formation regions. The closest OB Association NGC 6991 is 7.9° separated from the SNR. This is more than 200 pc at the given distance of the cluster, 1.4 kpc [188]. Some members of the Cyg OB7 and Cep OB2 are projected within 1° of the remnant. The parallax measurements for early B-type stars, HD 198895, HD 199308 and HD 198512 yield a < 1.0 kpc distance. Both associations are within 1.0 kpc [188], while the distance estimates for the SNR are 2.2 and 3.5 kpc.

From HI column densities, the distance to the remnant was proposed to be 2.2 ± 0.5 kpc [73]. This was also confirmed by [152], based on HI velocities with larger errors. The authors of the latter work, suggested 3.5 kpc, the maximum distance within the errors, as the closer distances result in a very low explosion energy for the SN. The explosion energy for 2.2 kpc is $(1 - 4) \times 10^{49}$ erg [73]. So, a possible relation between the nearby associations and DA 530 is ruled out. For the given distances, the galactic height is 300 and 420 pc respectively, which are both very large values for a core collapse origin. However, based on XMM–Newton observations, a PWN candidate was proposed by [21]. By following Chandra observations, the possible source can be a faint PWN with a soft X–ray (0.2 – 4.0 keV) luminosity of 1.6×10^{31} erg s⁻¹ [115]. The $\Sigma - D$ diagram gives an even higher distance, 5.75 kpc. The N_{H} value is 5.7×10^{21} cm⁻², due to [91], this corresponds to an A_{V} of ~ 2.7 mag. A B8V type star in the region is expected to be brighter than 14 mag. Such a candidate was found neither in the search region nor within a region with 16 pc radius including the entire SNR. Although DA 530 is proposed to be expanding in a wind bubble and hosting a PWN candidate, core–collapse origin is challenged by the distance from star forming regions and the large values of Galactic height. Some CO clouds were detected towards the remnant, yet any interaction or relation could not be proved [115].

There is no OB runaway star for this SNR.

4.4.10 G119.5+10.2 (CTA 1)

CTA 1 is a large SNR with a diameter of $120'$, located at high galactic latitude [86] (Figure A.6). However, a type Ia (WD) origin is ruled out as it hosts a γ –ray pulsar; RX J0007.0+7303. The period and the period derivative are $P = 316$ ms and $\dot{P} = 3.6 \times 10^{-13}$ ss⁻¹ respectively [2]. This yields a characteristic age of $\tau = 14$ kyr, which is consistent with the proposed ages of the SNR. The SNR is located far away from the OB associations. Cep OB4 is 3° separated, but its distance is given as 0.7 kpc [188], while the SNR is at 1.4 kpc. There is no other known potential SN progenitor nearby the SNR. Given the distance and the reddening, a star with absolute magnitude of $M_{\text{V}} = -2.0$ mag (B2V–B3V), must have an apparent magnitude of $m_{\text{V}} = 10.4$ mag. Within the borders of the SNR on the sky frame, there are nine stars with an m_{V} between 10.0 – 10.7 mag, which can be early B–type stars. It is worth to take their spectra in the future. The only OB star candidate UCAC 4-814-000374 could not

be observed. For B9V spectral type, the A_V is 1.54 ± 0.1 and the distance is 1.7 ± 0.5 kpc.

There is no OB runaway star with a spectral type earlier than B8V found inside CTA 1.

4.4.11 G120.1+1.4 (Tycho SNR)

Tycho is an extensively studied historical SNR of which explosion was observed by Tycho Brahe in 1572 A.D (Figure A.3). From light echo observations it is known to be from a type Ia SN (WD origin) [229]. The distance from HI velocities is 2.5 ± 0.5 kpc [272]. It was previously investigated for a runaway donor star, assuming the origin is an accretion induced collapse (AIC). Tycho-G, a G0IV type star, was found to be the only possible companion star of the pre-supernova WD [238]. The mechanism and the progenitor for this type SN is still unclear. The origin can also be a merging of two WD in a binary system. Nevertheless, OB runaway star was searched assuming that the donor star was more massive than $3 M_{\odot}$. No OB star candidate was found within $5'$ which includes the entire SNR.

4.4.12 G130.7+3.1 (SN 1181)

SN 1181 is a plerion type SNR with an angular dimensions of $9' \times 5'$ [86]. The SNR is very faint while the emission is dominated by the energetic PWN (Figure A.4). It is most probably the remnant of the SN recorded in 1181 A.D. [258]. However, 3000 – 5000 yr age is also strongly suggested for the nebula [59]. A neutral hydrogen column density of $N_H = (3.75 \pm 0.11) \times 10^{21} \text{ cm}^{-2}$ [253] was derived from CHANDRA observations of the pulsar 3.2 kpc was suggested from HI velocity of -35 km s^{-1} [234] Considering the density wave pressure in this direction, similar to HB 3, the distance was estimated as 2.0 kpc [139]. A DM of $140.7 \pm 0.3 \text{ pc cm}^{-3}$ [32] suggests a distance of 2.8 kpc [303]. The total visual absorption is $A_V = (1.6 - 2.3) \text{ mag}$ which is consistent with the N_H [59].

The spin period and period derivative of the pulsar is $P = 65.68 \text{ ms}$ and $\dot{P} = 1.93 \times 10^{-13} \text{ s s}^{-1}$. this corresponds to a characteristic age of $\tau = 5380 \text{ yr}$ and $B_{\text{dip}} = 3.6 \times 10^{12} \text{ G}$. Yet the SNR age is $\tau \sim 840 \text{ yr}$ assuming the historical record belongs to this SNR. The age discrepancy can be explained by high initial spin period [198]. However, as mentioned above, the SNR can also be at a comparable age with $\sim 5000 \text{ yr}$.

No candidate was found inside the SNR up to a A_V of 3 mag for the distance of 3 kpc. However, a B-type star IPHAS J020618.67+644945.1, showing H_α emission in its spectrum, was found $4'$ to the east of the pulsar. Due to its low brightness, it was not included in the sample. Nevertheless, the photometric spectral type estimation done in this work results in an F type star, not a B-type star. Furthermore, the proper motion given in the literature results in a 200 km s^{-1} space velocity at 3 kpc distance. Such high velocity runaways should not be common. Hence, the spectral type is doubtful. Also, the direction of its proper motion is towards the SNR geometrical center and the pulsar, not away from them. So, even if this star is an OB runaway, it can not be linked to SN 1181. Further spectroscopic observations should be done for this target.

SN 1181 is also far away from known OB associations and star formation regions. There is no OB runaway star associated to this SNR.

4.4.13 G156.2+5.7

SNR G156.2+5.7 is a shell type SNR discovered in X-rays [214]. The shell is bright in X-ray and optical bands (Figure A.8) while very faint in radio. The angular diameter of the optical shell is $110'$ [86]. From ROSAT X-ray observations, the blast wave velocity was determined as $v_{\text{bw}} = 651 \text{ km s}^{-1}$. The SNR was found to be in adiabatic expansion phase. Adopting $E_0 = 10^{51}$ erg, Sedov solution yields a distance of 3 kpc, an age of 26000 yr and very low ambient medium density, $n_0 = 0.01 \text{ cm}^{-3}$. The N_{H} value is quite high, $(0.96 - 2.2) \times 10^{22} \text{ cm}^{-2}$ [214]. A lower value of $N_{\text{H}} = (0.5 \pm 0.25) \times 10^{22} \text{ cm}^{-2}$ was found from ASCA spectrum [302]. 1.3 kpc distance and 15000 yr age was suggested for $E_0 = 10^{51}$ erg and $n_0 = 0.2 \text{ cm}^{-3}$ [208], Based on SUZAKU observations, $614 - 960 \text{ km s}^{-1}$ blast wave velocity was found. At 1.1 kpc, the age is 7000 – 15000 yr. Based on spectral fitting, lower N_{H} values were also found, $(3.3 \pm 0.8) \times 10^{21} \text{ cm}^{-2}$ with lower temperature corresponding to a $v_{\text{bw}} = 500 \text{ km s}^{-1}$ and $t = 8000 \text{ yr}$ [280]. The chemical abundances showed that the SNR has a core-collapse origin with a progenitor mass of $< 15 M_\odot$ [126].

Due to the faintness in radio, the kinematic distance measurements are doubtful. The measured velocity, -45 km s^{-1} corresponds to a distance of 7 kpc, yet, based on the dynamics of the SNR, the suggested distance is 1 – 3 kpc. The low brightness in radio is explained by the expansion into a low density medium, probably in the wind blown cavity of the progeni-

Table 4.22: Early type stars identified inside SNR G156.2+5.7. The star name (1), the angular separation from the center ($'$) (2), m_v (mag) (3), the proper motion in α and δ (mas yr^{-1}) (4 and 5), their errors (mas yr^{-1}) (6), the spectral types (7), the A_V (mag) and the distance found (pc) (8 and 9) and the instrument of observation (10) are given respectively. The radius of the search region of is $10'$. While C represents CAFOS, T stands for TFOOSC. Detailed information can be found in Table (4.7)

Name	Ang	V	μ_α^*	μ_δ	err	SpT	A_V	Dist	Tel
710-035713	3.54	13.67	-0.5	0.7	2.6/2.1	A2V	$2.62^{+0.09}_{-0.09}$	889^{+93}_{-44}	C
710-035795	12.14	11.28	-4.0	-1.3	1.1/0.6	A0V	$1.32^{+0.19}_{-0.09}$	729^{+91}_{-85}	C
710-035809	16.64	12.90	-2.4	-0.3	3.0/2.0	B8V	$1.78^{+0.05}_{-0.07}$	1875^{+281}_{-272}	C
710-035810	15.98	12.57	1.5	-4.7	1.5/1.9	A0V	$1.71^{+0.20}_{-0.08}$	1096^{+137}_{-127}	C

tor [228].

Based on possible interaction with the dense clouds in the southwest, the distance was proposed to be 0.5 kpc. Due to these clouds which are at 0.3 – 0.6 kpc, the spatial variation of A_V is high and peaked at 3 mag [79]. This also explains the highly variable N_H measurements of X–ray observations.

The SNR is far from known OB associations and star forming regions. There are no massive stars inside the SNR considering a distance of 1.1 ± 0.5 kpc. SNR G156.2+5.7 has no OB runaway star up to a distance limit of 2.0 kpc and $A_V = 3.0$ mag.

4.4.14 G160.9+2.6 (HB 9)

HB 9 is a MMSNR with an angular size of $140' \times 120'$ [86]. It is centrally filled in X–rays, while the shell is bright in radio (Figure A.4) and partially bright in optical bands. The systematic velocities found are -3 to -9 km s^{-1} based on HI [161], and $-18 \pm 10 \text{ km s}^{-1}$ based on H_α observations. Therefore, the kinematic distance varies from 0.5 to 3.2 kpc. The N_H determined from ROSAT X–ray observations is very low, $2.7 \times 10^{20} \text{ cm}^{-2}$ [158]. This is even lower than the A_V derived from the optical filaments, which is 0.6 ± 0.25 mag [62].

The stars found in this work are early A type stars some of which share the same distance with the SNR. None of them are runaway stars. Finding stars at that distance showed the expected visual magnitudes for B–type stars. At 0.8 kpc, a B–type star has an m_v of 7 – 12 mag. No such bright object over the entire nebula, is a candidate of OB–type star. Therefore, if 0.8 kpc is the real distance, then the SNR must have a relatively low mass progenitor. However, three candidates, in the entire search region, show B–type colors. These are faint stars which

Table 4.23: Early type stars identified inside SNR HB 9. The star name (1), the angular separation from the center ($'$) (2), m_v (mag) (3), the proper motion in α and δ (mas yr^{-1}) (4 and 5), their errors (mas yr^{-1}) (6), the spectral types (7), the A_v (mag) and the distance found (pc) (8 and 9) and the instrument of observation (10) are given respectively. The radius of the search region of is $12'$. While C represents CAFOS, T stands for TFOOSC. Detailed information can be found in Table (4.7)

Name	Ang	V	μ_α^*	μ_δ	err	SpT	A_v	Dist	Tel
683-034211	7.18	10.93	-4.0	-7.9	0.9/0.9	A3V	$0.89^{+0.10}_{-0.09}$	510^{+26}_{-32}	C
683-034093	8.19	11.19	-0.3	-1.3	0.7/0.9	A1V	$1.54^{+0.08}_{-0.08}$	538^{+71}_{-51}	C
683-034148	10.04	11.53	-0.1	-4.1	1.1/1.2	A3V	$1.45^{+0.09}_{-0.09}$	520^{+26}_{-33}	C

have a spectro–photometric distance of > 3 kpc at early spectral types (Table 4.23). Their possible runaway nature cannot be found from their proper motion measurements. Finding early type stars at that distance obviously expected considering the distances to the young H II regions Sh2 – 219 and Sh2 – 217 in this direction. Furthermore, the SGR 0501+4516 located at $\sim 2^\circ$ to the south of HB 9, is also at a distance of > 2.0 kpc. However, for 3 – 4 kpc, the SNR would be physically the largest and the oldest of all. It must be 100 pc in diameter.

For the nearby distances such as 0.8 kpc, there is no OB runaway star for HB 9. For the distances > 3 kpc, there are 3 candidates left to be observed.

4.4.15 G166.0+4.3 (VRO 65.05.01)

VRO 42.05.01 is a MMSNR composed of two hemispheres with great differences in diameter, $55' \times 35'$ [86] A.9. The shell is bright in radio and optical bands, while centrally filled in X–rays. This peculiar morphology is explained by breakout to the low density medium in the west [216]. In the X–ray spectrum from XMM–Newton observations, no enhanced chemical abundance was found. The blast wave velocity inferred from the plasma temperature of $T = 8.5 \times 10^6$ K is $v_{\text{bw}} = 680 \text{ km s}^{-1}$ [23]. Based on H_α radial velocities, the expansion velocity was measured as 200 km s^{-1} [166].

V_{LSR} of HI clouds was measured as $-31 \pm 5 \text{ km s}^{-1}$. But, due to the Perseus arm velocity anomaly (see Section 4.3.8), the systematic velocity is not a good indicator in this direction, it only shows that the distance is above 1.8 kpc [149]. For a flat rotation curve, such a high negative velocity do not exist. The SNR was thought to be an outer–arm object with a distance of 4.5 ± 1.5 kpc [149]. The $\Sigma - D$ diagram gives a distance of 3.9 kpc [88].

The A_V is 1.68 mag [62]. The N_H derived from X-ray spectrum are also low, $2.9 \times 10^{21} \text{ cm}^{-2}$ [87] and $(1.3 - 2.6) \times 10^{21} \text{ cm}^{-2}$ [30].

Nine early type stars were found in the R/3 region of the SNR (Table 4.24). Two A0V type star in the search region are foreground stars. No OB runaway star was found.

HD 278115 is a massive star (B1V) $0.3'$ outside of the search region. The relative proper motion with respect to the neighbouring star UCAC 4-665-037733, 666-037784 and 665-037914 is large; 60 km s^{-1} and pointing back to the geometrical center (Figure A.9). Therefore it was observed with TRES. The TRES spectrum shows highly red-shifted and blue-shifted components for CaII-K & H lines (see appendix B, Figure B.4). of which radial velocities vary between -114 and $+109 \text{ km s}^{-1}$ (Table B.2). Such high velocities can be explained only by SNR expansion. So, the star is definitely a background object to VRO 42.05.01. This is surely a good tool to set an upper limit to the SNR distance. The spectro-photometric distance of the star is 2089_{-550}^{+760} . However, the star is inside a binary system which is observed as double-line spectroscopic binary (Figure 4.16). The binary parameters are poorly determined. The period is < 13 days. The EW ratio of the HeI $\lambda 5876$ of the components is $\sim 1:2$. So, the companion star is a $B5 \pm 1$ type star. Taking M_V values of the components as -3.0 and -1.5 mag, the contribution of the secondary is found as 0.5 mag. So, assuming $m_V = 10.1$ mag as mentioned in the UCAC 4 catalog, is due to the brightest phase, HD 278115 must have an apparent magnitude which is originally 0.5 mag fainter. For $m_V = 10.6$ mag, the spectro-photometric distance is 2.5 kpc, instead of 2.1 , which is already within the large errors due to the overestimated spectral type uncertainty. Therefore, a distance upper limit of 2.9 kpc for VRO 42.05.01 is confident. Furthermore, despite the measured H I velocity of -35 km s^{-1} and the Perseus arm velocity anomaly, the main component of NaI-D1 and D2 lines show a radial velocity -3.0 km s^{-1} which yields a kinematic distance of 2.0 kpc. The suggested distance of VRO 42.05.01 in this work is 2.0 kpc, far closer than the previous distance estimates. At this distance, the radius of the SNR is 10 and 15.5 pc. The new distance gives 8800 yr age for the expansion velocity of 680 km s^{-1} and for the 15.5 pc radius.

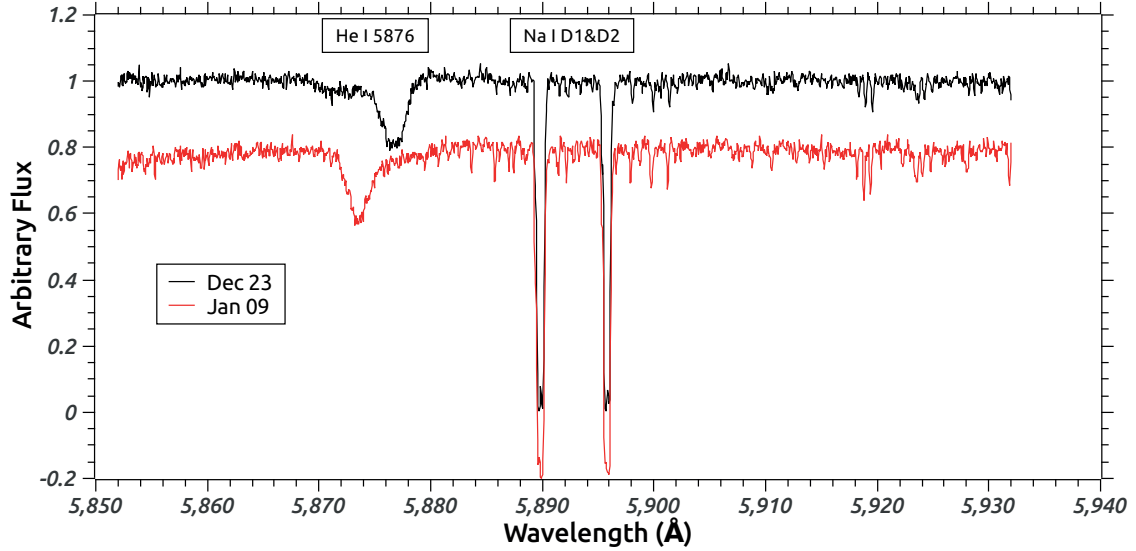


Figure 4.16: Spectra of HD 278115 taken on 2014, December 23, and on 2015 January 09. While ISM lines are not shifted relative to each other as expected, He I λ 5876 feature shows double-line nature.

Table 4.24: Early type stars identified inside VRO 42.05.01. The star name (1), the angular separation from the center ($'$) (2), m_v (mag) (3), the proper motion in α and δ (mas yr^{-1}) (4 and 5), their errors (mas yr^{-1}) (6), the spectral types (7), the A_V (mag) and the distance found (pc) (8 and 9) and the instrument of observation (10) are given respectively. The radius of the search region of is $5'$. While C represents CAFOS, T stands for TFOOSC. Detailed information can be found in Table (4.7)

Name	Ang	V	μ_α^*	μ_δ	err	SpT	A_V	Dist	Tel
665-037801	2.3628	12.21	-2.1	-1.2	1.6/0.6	A0V	$1.39^{0.20}_{0.07}$	1077^{+133}_{-126}	C
665-037807	4.4987	11.94	0.3	-5.0	0.9/1.0	A0V	$1.31^{0.19}_{0.08}$	991^{+122}_{-116}	C
666-037743	5.3617	10.12	-2.5	-0.3	0.5/0.6	B1V	$1.72^{0.13}_{0.09}$	2089^{+760}_{-550}	C
665-037733	5.6344	13.60	-5.8	-4.9	1.4/1.7	B9V	$1.82^{0.17}_{0.17}$	2064^{+289}_{-228}	C
666-037784	5.805	12.35	-5.1	-2.9	2.6/1.0	B8V	$1.21^{0.05}_{0.17}$	1895^{+286}_{-227}	C
665-037914	6.3072	13.62	-4.2	-3.1	1.4/1.7	B9V	$1.04^{0.17}_{0.20}$	2999^{+414}_{-331}	T
666-037842	8.935	12.73	-4.2	0.6	2.2/2.2	B9V	$0.94^{0.17}_{0.12}$	2075^{+285}_{-181}	C
665-037654	9.705	13.63	3.1	-3.8	1.5/1.7	A1V	$1.21^{0.13}_{0.08}$	1925^{+177}_{-182}	C
665-037712	9.8113	13.37	-3.9	-0.7	1.3/1.6	A1V	$1.51^{0.08}_{0.08}$	1486^{+196}_{-141}	C

4.4.16 G184.6-5.8 (Crab Nebula)

Crab Nebula is another plerion type SNR in the sample with a small angular diameter of $9'$ [86] (Figure A.9). It is the only candidate for the historical SN in 1054 A.D. [258]. The shock front is very faint and the ejected mass is $1 - 2 M_\odot$ [175]. The swept up mass is still comparable with the mass of the ejecta, $2 - 3 M_\odot$. Although the SNR is in the free expansion phase, the measured velocities from bright filaments are $< 2000 \text{ km s}^{-1}$ [41]. Hence, the suggested explosion energy is very low, $E_0 = 3.2 \times 10^{49} \text{ erg}$ [66]. The visual absorption

measured from optical nebula is $A_V = 1.6 \pm 0.2$ mag [191]. Based on the abundances derived from the optical spectra, the progenitor zero-age main sequence mass is proposed to be $> 9.5 M_\odot$ [174]. [191] and $8 - 10 M_\odot$ [49].

The NS is Crab Pulsar, one of the best studied NS in the literature. The period and period derivative are $P = 33$ ms and $\dot{P} = 4.21 \times 10^{-13}$ s s $^{-1}$ [172]. The corresponding magnetic field and characteristic age are $B_{\text{dip}} = 3.79 \times 10^{12}$ G and $\tau = 1260$ yr. Hence it is a pulsar with moderate magnetic field and it does not show any characteristic age anomaly. Although, it was extensively studied, the distance to the Crab Nebula and the pulsar cannot be measured precisely. Various indicators suggest a distance of 2.0 ± 0.5 kpc [124, 276]. The total proper motion of the pulsar is 14.8 mas yr $^{-1}$ [202] which translates to a space velocity of $v_{\text{sp}} = 140.3$ km s $^{-1}$.

Crab Nebula has a large separation from the known OB associations. There is no OB association within 300 pc from the remnant. There is also no OB stars inside or in the close vicinity of the SNR. There are a number of late type stars close to the SNR geometrical center. They can be related to the system, but they are much fainter than 14 mag.

It is clear that the progenitor of Crab was formed in isolation or migrated to the current position, and gave birth to an energetic pulsar by a weak SN. In this regard, it is very similar to SN 1181 (see Section 4.4.12).

4.4.17 The General Picture

Out of 27, only one star HD 37424 is proven as a sound OB runaway of an SNR. Two stars inside SNRs G065.3+5.7 and IC 443 showed strong evidences to be the OB runaway of these SNRs, while there are another eight which can neither be proven nor be rejected to be OB runaway stars. In 16 SNRs, there is no massive runaway star whereas 8 of them can still be hosting an intermediate mass runaway star. Except for 6 SNRs, the results depend on certain conditions which are mentioned in the individual sections and summarized on Table (4.25).

The majority are OB runaways only if the geometrical center is highly separated from the explosion center. This is not surprising considering a $\sim 40'$ (one third of the radius) separation between the geometrical center and the explosion center found from the pulsar kinematics in Vela SNR. The origin of the pulsar shows that the SN happened in relatively dense en-

Table 4.25: The results of search for OB runaway stars. Col 1: The number given to the SNR for practical purposes, Col 2: The name of the SNR, Col 3: SNR type Col 4: What is left to be done. Col 5: The result of the runaway search Col 6: The condition of the result. For the SNR number 1) There is no OB runaway with an earlier spectral type B3V. 2) The same result with 1, but earlier than B2V. 3) It has an OB runaway if the expansion is asymmetric and the distance is limited to 0.6 kpc. 4) No satisfactory result, due to highly asymmetric shape. 5) There is no OB runaway star up to a distance limit of 0.6 kpc. 6) The stars fainter than B5V cannot be studied. There is a potential OB runaway if the direction shown by the PWN is ignored. 7) There is no OB runaway star earlier than B5V. Later types can suffer from extinction. 8) Not completed, no result 9) There is a potential OB runaway star considering an asymmetric expansion. 10) There is no OB runaway star. 11) There is no OB runaway star. 12) There is no OB runaway star earlier than B5V type. 13) There is no OB runaway star earlier than O9V type. 14) OB runaway found if the pulsar proper motion is highly incorrect. 15) OB runaway found if the X-ray source linked to this star is the NS. 16) There is no OB runaway star earlier than B8V type. 17) There is no OB runaway star. 18) Potential OB runaway stars are confirmed OB runaways if they show high radial velocity. 19) OB runaway star found if the correct reference frame is found. 20) There is no OB runaway star. 21) OB runaway star found if the expansion is asymmetric and the velocity references are correct. 22) There is no OB runaway star up to a distance limit of 3.0 kpc. 23) There is no OB runaway star up to a distance limit of 3.0 kpc. 24) There is no OB runaway star. 25) OB runaway star is found and confirmed 26) There is no OB runaway star. 27) OB runaway is found if the expansion is highly asymmetric.

Num.	SNR	Type	NS	Statue	Finding	Condition
1	034.7-0.4	S	-	No Cand. Found (Extinction)	No OB Runaway	Earlier than B3V
2	054.4-0.3	S	-	No Cand. Found (Extinction)	No OB Runaway	Earlier than B2V
3	065.3+5.7	S	-	No Cand. Left up to 0.6 kpc	Poss. OB Runaway	Asymmetric Expansion
4	069.0+2.7	S	RPP	Not Completed (Asymmetry)	-	-
5	074.0-8.5	S	-	No Cand. Found up to 0.6 kpc	No OB Runaway	up to 0.6 kpc
6	078.2+2.1	S	RPP	No Cand. Left up to B5V	Pot. OB Runaway	Neglecting PWN direction
7	082.2+5.3	S	-	No Cand. Left	No OB Runaway	Earlier than B5V
8	089.0+4.7	MM	-	10 Cand. Left	-	-
9	093.7-0.2	S	-	No Cand. Left	Pot. OB Runaway	Asymmetric expansion
10	093.3+6.9	S	PWN?	No Cand. Found	No OB Runaway	-
11	106.3+2.7	C	RPP	No Cand. Found?	No OB Runaway	-
12	109.1-1.0	S	Magnetar	No Cand Left up to B5V	No OB Runaway	Earlier than B5V
13	111.7-2.1	S	CCO	No Cand. Found (Extinction)	No OB Runaway	Earlier than O9V
14	114.3+0.3	S	RPP	No Cand. Left	Pot. OB Runaway	Pulsar proper motion
15	116.9+0.2	MM	-	No Cand. Left	Pot. OB Runaway	Nature of the X-ray source
16	119.5+10.2	S	RPP	1 Cand. Left	No OB Runaway	Earlier than B8V
17	120.1+1.4	S	-	No Cand. Found	No OB Runaway	-
18	126.2+1.6	S	-	No Cand. Left	Pot. OB Runaway	RV needed
19	127.1+0.5	S	-	No Cand. Left	Pot. OB Runaway	Reference Frame needed
20	130.7+3.1	C	RPP	No Cand. Found	No OB Runaway	-
21	132.7+1.3	MM	-	No Cand. Left	Pot. OB Runaway	Asymmetric expansion, RF
22	156.2+5.7	S/MM	-	No Cand. Left	No OB Runaway	up to 3.0 kpc
23	160.9+2.6	MM	-	No Cand. Left for Dist<2 kpc	No OB Runaway	up to 3.0 kpc
24	166.0+4.3	MM	-	No Cand. Left	No OB Runaway	-
25	180.0-1.7	S	RPP	No Cand. Left	OB Runaway	Definite
26	184.6-5.8	P	RPP	No Cand. Found	No OB Runaway	-
27	189.1+3.0	MM	PWN	No Cand. Left up to B5V	Poss. OB Runaway	Asymmetric expansion

vironment and then penetrated to a lower density medium which results in an asymmetric shape like in the case of SNR G166.0+4.3 (Figure A.9) or in IC 443 (Shells A & B). The

differences between these remnants can just be the viewing angle which is possibly edge-on for SNR G166.0+4.3. Expansion into an inhomogeneous ambient medium can be more effective than previously thought. This will be proven by the completion of the kinematic study of the NS and the runaway star inside IC 443. If such a large separation between the centers is possible, then OB runaway stars must be searched for the entire SNR. On the other hand, in the case of S 147, the explosion center is very close to the geometrical center taking the large diameter of the SNR into account.

If an SNR's geometrical center represents the true explosion center for every SNRs, then the conclusion of this work might be that the binary supernova is not an efficient mechanism in producing massive ($> 8M_{\odot}$) runaway stars. Within the search region, for 22 SNRs, there is definitely no massive runaway star (Table 4.25). Another four are highly reddened for searching for a runaway star, so HD 37424 is the unique object. As massive stars are rare objects, this should be expected. Furthermore, the progenitors of observable SNRs might be already runaway stars. A SNR is observable only if the shock front interacts with the ISM. Local progenitors may be losing this chance because they evolve inside the super bubble of the host OB association. But the runaway stars can migrate to the walls of the super bubble where the SNR formation is more likely. Then, a significant number of BSS runaways from SNe expanding inside low density medium is still possible. The binary merger (see [51]) also explains the separation between the SNRs and the star forming regions and the lack of massive runaways in large populations.

OB runaway search also provided invaluable information about NSs. PSR J0538+2817 is the only isolated NS in the literature, of which the pre-supernova history of the progenitor is known. It is a thermal RPP showing a large age discrepancy (see Section 4.1) which is less than CCOs, but more than ordinary pulsars. Here, it is shown that PSR J0538+2817 had a massive progenitor which experienced a close binary evolution and severe mass loss. Loss of angular momentum during the binary evolution might be the reason for large initial spin period of the NS. Young RPPs with strong PWN; Crab Pulsar, J0205+6449 (SN 1181) and J2229+6114 (G106.3+2.7) are not linked to an OB runaway star. Together with the γ -ray pulsar J0007+7303 (CTA 1), these pulsars experience the age discrepancy the least and their progenitors did not experience a massive binary evolution (excluding possible merger events). To see the clear picture, the possible and potential OB runaway stars which are linked to the pulsars with high age discrepancy must be studied in depth and their nature

Table 4.26: The SNR distance estimates of this work. Name of the SNRs, distances from the literature in kpc and the distance estimation of this work are given respectively. the distance estimates are based on confirmed runaway stars, possible (Poss.) and potential (Pot.) runaway stars, massive stars (Assoc.) and ISM lines detected in the star’s spectrum.

SNR	Dist. (lit)	Dist. (tw) / Source	SNR	Dist. (lit)	Dist. (tw)
034.7–0.4	1.6 – 3.0	–	114.3+0.3	0.7 – 3.8	2.5±0.8 / Assoc.
054.4–0.3	3.0 – 6.0	–	116.9+0.2	1.6 – 4.5	3.0±0.5 / Pot. Run.
065.3+5.7	0.6 – 1.0	0.6±0.2 / Poss. Run.	119.5+10.2	1.0 – 1.8	–
069.0+2.7	1.5 – 2.5	–	120.1+1.4	2.0 – 5.0	–
074.0–8.5	0.4 – 0.8	–	126.2+1.6	2.0 – 5.0	4.0±1.0 / Assoc.
078.2+2.1	1.2 – 1.8	1.4+0.4 / Pot. Run.	127.1+0.5	1.0 – 3.5	<1.3 / ISM Lines
082.2+5.3	1.5 – 2.5	2.0±0.5 / Assoc.	130.7+3.1	2.2 – 3.6	–
089.0+4.7	0.8 – 1.8	<1.4 / ISM Lines	132.7+1.3	1.9 – 4.0	2.2±0.3 / Pot. Run.
093.7–0.2	1.5 – 3.2	3.4±0.2 / Assoc.	156.2+5.7	1.0 – 3.0	–
093.3+6.9	2.2 – 5.8	–	160.9+2.6	0.8 – 3.2	–
106.3+2.7	0.8 – 4.0	–	166.0+4.3	3.0 – 6.0	<3.0 kpc / ISM Lines
109.1–1.0	2.8 – 5.0	2.8±0.3 / Pot. Run.	180.0–1.7	0.8 – 1.8	1.3±0.1 kpc / Run.
111.7–2.1	3.0 – 3.7	–	184.6–5.8	1.5 – 2.5	–
			189.1+3.0	1.0 – 2.0	1.75 ± 0.5 / Poss.Run.

must be revealed.

Three of the MMSNR have no OB runaway stars whereas another three have candidates. The only clear finding about the SNR–OB runaway relation is that the plerion or composite types (those with powerful PWNe) are not linked to OB runaway stars (Table 4.25), even maybe to any massive star association. Finding massive stars around the SNRs contributes the SNR distance estimations. In this thesis, distances are estimated for 14 SNRs by detecting high velocity ISM gas in the spectra of the background stars, by finding possible associations to massive stars which might have a genetic connection with the SNR, or by finding even closer family members OB runaway stars (Table 4.26). In two cases, S 147 and IC 443, the age of the SNR is also found or restricted independently. The most striking example for distance estimation is SNR G166.0+4.3 of which previous estimate was 4.5 ± 1.5 kpc. By detecting ISM features at velocities up to 114 km s^{-1} in the spectrum of HD 278115, the distance to the SNR is found to be 2.5 ± 0.5 kpc 4.4.15. However, majority of the estimations in this work is to confirm or restrict the previous estimates rather than suggesting a revolutionary change.

CHAPTER 5

CONCLUSION

Out of 27 SNRs, only S 147 is found to be hosting an OB runaway star. HD 37424 is a massive runaway star from a binary ejection due to the supernova which gave birth to SNR S 147 and PSR J0538+2817. The star has a 3-D peculiar velocity of $74 \pm 8 \text{ km s}^{-1}$. The distance calculated from IS Ca II lines is 1288_{-193}^{+304} pc and from spectro-photometry 1318 ± 119 pc. The past trajectories of the pulsar and HD 37424 are reconstructed throughout Monte Carlo simulations. It is found that both stars were at the same position at $\alpha, \delta = 84.82^\circ \pm 0.01^\circ, 27.84^\circ \pm 0.01^\circ$) 30 ± 4 kyr ago. The position of the explosion is $4.2_{-0.6}^{+0.8}$ arcminutes away from the geometrical center. The distance of the SNR is found as 1333_{-112}^{+103} pc. Total visual absorption towards the SNR is 1.28 ± 0.06 mag.

By high resolution spectroscopy the stellar parameters are determined as; the effective temperature is $T_{\text{eff}} = 30000 \pm 1000$ K, the logarithm of the surface gravity is $\log(g) = 4.0 \pm 0.25$ in cgs, and the projected rotational velocity is $v \sin(i) = 140 \pm 20 \text{ km s}^{-1}$. For a mass of $13 M_{\odot}$ for HD 37424, the pre-supernova binary parameters are found. Assuming a circular orbit, the pre-supernova binary separation is in the range of 8 to $711 R_{\odot}$ for 2 to $25 M_{\odot}$ final mass of the progenitor. The corresponding Roche Lobe radii for 15 to $25 M_{\odot}$ masses vary from 91 to $311 R_{\odot}$. It must have been an interacting binary. Considering the possible one to one synchronous rotation, if the rotation period of the star equals to the orbital period, then the final mass of the progenitor was $2.7 \pm 0.3 M_{\odot}$.

HD 37424 is the direct evidence of binary supernova ejection of a massive star, and it showed that a $15 - 20 M_{\odot}$ star experienced a close binary interaction, lost the majority of its mass and remained to be a $2.7 M_{\odot}$ and gave birth to a pulsar which can be classified between a RPP and a CCO owing to the large difference between the characteristic and kinematic (real)

ages.

Two massive runaway stars found inside the SNRs IC 443 and G65.3+5.7 are assigned as possible runaways due to their large separation from the geometrical center. HD 254577 inside IC 443 is an evolved star with the physical parameters; $T_{\text{eff}} = 25000 \pm 1000$ K, $\log(g) = 3.0 \pm 0.25$ in cgs, and $v \sin(i) = 150 \pm 20$ km s⁻¹. The 3-D peculiar velocity is 29 ± 6 km s⁻¹. The He rich star HD 184927 inside SNR G65.3+5.7 is also out of the search region. The previously found stellar parameters are $T_{\text{eff}} = 22000 \pm 2000$ K, $\log(g) = 4.25 \pm 0.25$ in cgs, and $v_{\text{rot}} = 25 \pm 5$ km s⁻¹. Considering masses of 12 and 9 M_{\odot} for the stars, pre-supernova binary parameters are found. Both stars had much larger separation than HD 37424 had, and binary interaction is not for sure. Also, a possible synchronous rotation by tidal lock is not possible. For HD 254577, owing to its relatively high angular momentum, it can be suggested that the system experienced a steady accretion which leads to increase the binary separation. While the companion of HD 37424 experienced a common envelope phase with a non-conservative mass loss, the companion of HD 254577 has experienced stable and conservative mass transfer.

For other 8 SNRs, there are potential OB runaway stars while for 16 SNRs no OB runaway stars are found for certain conditions. Further observations and measurements are necessary to reveal the true nature of the potential OB runaway stars. In some cases, the stars are highly separated from the geometrical centers. If the SNR expansion is highly asymmetric in most of the cases, then a further search for OB runaway stars must be performed. HD 254577 inside IC 443 is a good example for such a case and it will bring a new sight on the expansion of SNRs to inhomogeneous medium. However, if the majority of the SNRs expand symmetrically to some extent, like in the case of HD 37424, then the result of this thesis might be that the BSS is not an effective mechanism in producing massive runaway stars.

REFERENCES

- [1] A. A. Abdo, M. Ackermann, M. Ajello, W. B. Atwood, M. Axelsson, L. Baldini, J. Ballet, G. Barbiellini, M. G. Baring, D. Bastieri, and et al. The First Fermi Large Area Telescope Catalog of Gamma-ray Pulsars. *ApJ*, 187:460–494, Apr. 2010.
- [2] A. A. Abdo, K. S. Wood, M. E. DeCesar, F. Gargano, F. Giordano, P. S. Ray, D. Parent, A. K. Harding, M. C. Miller, D. L. Wood, and M. T. Wolff. PSR J0007+7303 in the CTA1 Supernova Remnant: New Gamma-Ray Results from Two Years of Fermi Large Area Telescope Observations. *ApJ*, 744:146, Jan. 2012.
- [3] V. A. Acciari, E. Aliu, T. Arlen, T. Aune, M. Bautista, M. Beilicke, W. Benbow, D. Boltuch, S. M. Bradbury, J. H. Buckley, V. Bugaev, Y. Butt, K. Byrum, A. Cannon, A. Cesarini, Y. C. Chow, L. Ciupik, P. Cogan, W. Cui, R. Dickherber, T. Ergin, S. J. Fegan, J. P. Finley, P. Fortin, L. Fortson, A. Furniss, D. Gall, G. H. Gillanders, E. V. Gotthelf, J. Grube, R. Guenette, G. Gyuk, D. Hanna, J. Holder, D. Horan, C. M. Hui, T. B. Humensky, P. Kaaret, N. Karlsson, M. Kertzman, D. Kieda, A. Konopelko, H. Krawczynski, F. Krennrich, M. J. Lang, S. LeBohec, G. Maier, A. McCann, M. McCutcheon, J. Millis, P. Moriarty, R. Mukherjee, R. A. Ong, A. N. Otte, D. Pandel, J. S. Perkins, M. Pohl, J. Quinn, K. Ragan, L. C. Reyes, P. T. Reynolds, E. Roache, H. J. Rose, M. Schroedter, G. H. Sembroski, A. W. Smith, D. Steele, S. P. Swordy, M. Theiling, J. A. Toner, V. V. Vassiliev, S. Vincent, R. G. Wagner, S. P. Wakely, J. E. Ward, T. C. Weekes, A. Weinstein, T. Weisgarber, D. A. Williams, S. Wissel, M. Wood, and B. Zitzer. Detection of Extended VHE Gamma Ray Emission from G106.3+2.7 with Veritas. *ApJ*, 703:L6–L9, Sept. 2009.
- [4] A. O. Allakhverdiev, O. H. Guseinov, S. O. Tagieva, and I. M. Yusifov. Velocities of pulsars: A new approach. *Astronomy Reports*, 41:257–261, Mar. 1997.
- [5] L. H. Aller, I. Appenzeller, B. Baschek, H. W. Duerbeck, T. Herczeg, E. Lamla, E. Meyer-Hofmeister, T. Schmidt-Kaler, M. Scholz, W. Seggewiss, W. C. Seitter, and V. Weidemann, editors. *Landolt-Börnstein: Numerical Data and Functional Relationships in Science and Technology - New Series " Gruppe/Group 6 Astronomy and Astrophysics " Volume 2 Schaifers/Voigt: Astronomy and Astrophysics / Astronomie und Astrophysik " Stars and Star Clusters / Sterne und Sternhaufen*, 1982.
- [6] M. Anderson, L. Rudnick, P. Leppik, R. Perley, and R. Braun. Relativistic electron populations in Cassiopeia A. *ApJ*, 373:146–157, May 1991.
- [7] S. B. Anderson, B. J. Cadwell, B. A. Jacoby, A. Wolszczan, R. S. Foster, and

- M. Kramer. A 143 Millisecond Radio Pulsar in the Supernova Remnant S147. *ApJ*, 468:L55, Sept. 1996.
- [8] A. Ankay, L. Kaper, J. H. J. de Bruijne, J. Dewi, R. Hoogerwerf, and G. J. Savonije. The origin of the runaway high-mass X-ray binary HD 153919/4U1700-37. *A&A*, 370:170–175, Apr. 2001.
- [9] I. Appenzeller and H. J. Wendker. The Cygnus X region. XII - On the excitation and distance of the Gamma Cygni H II region. *A&A*, 89:239, Sept. 1980.
- [10] V. P. Arkhipova and T. A. Lozinskaia. The exciting star of the nebula near Gamma CYG is found. *Soviet Ast*, 22:751, Dec. 1978.
- [11] Z. Arzoumanian, D. F. Chernoff, and J. M. Cordes. The Velocity Distribution of Isolated Radio Pulsars. *ApJ*, 568:289–301, Mar. 2002.
- [12] I. Asaoka and B. Aschenbach. An X-ray study of IC443 and the discovery of a new supernova remnant by ROSAT. *A&A*, 284:573–582, Apr. 1994.
- [13] W. Baade. B Cassiopeiae as a Supernova of Type I. *ApJ*, 102:309, Nov. 1945.
- [14] W. Becker, K. T. S. Brazier, and J. Truemper. ROSAT observations of PSR 2334+61 in the supernova remnant G 114.3+0.3. *A&A*, 306:464, Feb. 1996.
- [15] D. Bhattacharya and E. P. J. van den Heuvel. Formation and evolution of binary and millisecond radio pulsars. *Phys. Rep.*, 203:1–124, 1991.
- [16] A. Blaauw. On the origin of the O- and B-type stars with high velocities (the "runaway" stars), and some related problems. *Bull. Astron. Inst. Netherlands*, 15:265, May 1961.
- [17] C. Blaha and R. M. Humphreys. A comparison of the luminosity functions in U, B, and V and their relationship to the initial mass function for the Galaxy and the Magellanic Clouds. *AJ*, 98:1598–1608, Nov. 1989.
- [18] W. P. Blair, R. Sankrit, and J. C. Raymond. Hubble Space Telescope Imaging of the Primary Shock Front in the Cygnus Loop Supernova Remnant. *AJ*, 129:2268–2280, May 2005.
- [19] W. P. Blair, D. L. Sawyer, R. P. Kirshner, T. R. Gull, and R. A. R. Parker. The discovery of optical emission from the SNR G126.2 + 1.6. *ApJ*, 242:592–595, Dec. 1980.
- [20] V. V. Bobylev. Open clusters IC 4665 and Cr 359 and a probable birthplace of the pulsar PSR B1929+10. *Astronomy Letters*, 34:686–698, Oct. 2008.
- [21] F. Bocchino, R. Bandiera, and Y. Gallant. XMM-Newton survey of non-thermal shell candidates: Preliminary results on DA 530. *Advances in Space Research*, 41:407–410, 2008.

- [22] F. Bocchino and A. M. Bykov. The plerion nebula in IC 443: The XMM-Newton view. *A&A*, 376:248–253, Sept. 2001.
- [23] F. Bocchino, M. Miceli, and E. Troja. On the metal abundances inside mixed-morphology supernova remnants: the case of IC 443 and G166.0+4.3. *A&A*, 498:139–145, Apr. 2009.
- [24] R. Bouigue, J. Boulon, and A. Pedoussaut. Contribution aux recherches de photométrie photoélectrique dans la Galaxie. VII. Mesure d'étoiles brillantes dans les champs galactiques. *Annales de l'Observatoire Astron. et Meteo. de Toulouse*, 28:33, 1961.
- [25] P. Boumis, F. Mavromatakis, E. M. Xilouris, J. Alikakos, M. P. Redman, and C. D. Goudis. Deep optical observations of the supernova remnants G 126.2+1.6, G 59.8+1.2 and G 54.4-0.3. *A&A*, 443:175–183, Nov. 2005.
- [26] P. Boumis, J. Meaburn, J. A. López, F. Mavromatakis, M. P. Redman, D. J. Harman, and C. D. Goudis. The kinematics of the bi-lobal supernova remnant G 65.3+5.7. II. *A&A*, 424:583–588, Sept. 2004.
- [27] J. Brand and L. Blitz. The Velocity Field of the Outer Galaxy. *A&A*, 275:67, Aug. 1993.
- [28] R. Braun and R. G. Strom. The structure and dynamics of evolved supernova remnants - The IC 443 complex. *A&A*, 164:193–207, Aug. 1986.
- [29] K. T. S. Brazier, G. Kanbach, A. Carramiñana, J. Guichard, and M. Merck. The nature of the γ -ray source 2EG J2020+4026 (2CG 078+2). *MNRAS*, 281:1033–1037, Aug. 1996.
- [30] D. N. Burrows and Z. Guo. ROSAT observations of VRO 42.05.01. *ApJ*, 421:L19–L22, Jan. 1994.
- [31] D.-Y. Byun, B.-C. Koo, K. Tatematsu, and K. Sunada. Interaction between the Supernova Remnant HB 21 and Molecular Clouds. *ApJ*, 637:283–295, Jan. 2006.
- [32] F. Camilo, I. H. Stairs, D. R. Lorimer, D. C. Backer, S. M. Ransom, B. Klein, R. Wielebinski, M. Kramer, M. A. McLaughlin, Z. Arzoumanian, and P. Müller. Discovery of Radio Pulsations from the X-Ray Pulsar J0205+6449 in Supernova Remnant 3C 58 with the Green Bank Telescope. *ApJ*, 571:L41–L44, May 2002.
- [33] F. Castelli and R. L. Kurucz. New Grids of ATLAS9 Model Atmospheres. *ArXiv Astrophysics e-prints*, May 2004.
- [34] J. L. Caswell, J. D. Murray, R. S. Roger, D. J. Cole, and D. J. Cooke. Neutral hydrogen absorption measurements yielding kinematic distances for 42 continuum sources in the galactic plane. *A&A*, 45:239–258, Dec. 1975.

- [35] S. Chatterjee, W. F. Brisken, W. H. T. Vlemmings, W. M. Goss, T. J. W. Lazio, J. M. Cordes, S. E. Thorsett, E. B. Fomalont, A. G. Lyne, and M. Kramer. Precision Astrometry with the Very Long Baseline Array: Parallaxes and Proper Motions for 14 Pulsars. *ApJ*, 698:250–265, June 2009.
- [36] R. A. Chevalier. The Evolution of Supernova Remnants. Spherically Symmetric Models. *ApJ*, 188:501–516, Mar. 1974.
- [37] R. A. Chevalier. Supernova Remnants in Molecular Clouds. *ApJ*, 511:798–811, Feb. 1999.
- [38] R. Chini and J. E. Wink. The galactic rotation outside the solar circle. *A&A*, 139:L5–L8, Oct. 1984.
- [39] J. W. Christy. The radial velocities of early-type stars within six degrees of the galactic anticenter direction. *ApJ*, 217:127–133, Oct. 1977.
- [40] D. H. Clark and J. L. Caswell. A study of galactic supernova remnants, based on Molonglo-Parkes observational data. *MNRAS*, 174:267–305, Feb. 1976.
- [41] D. H. Clark, P. Murdin, R. Wood, R. Gilmozzi, J. Danziger, and A. W. Furr. Three-dimensional structure of the Crab Nebula. *MNRAS*, 204:415–431, July 1983.
- [42] J. V. Clausen and K. S. Jensen. Classification Based on 102/A/mm Objective Prism Spectra. In M. F. McCarthy, A. G. D. Philip, and G. V. Coyne, editors, *IAU Colloq. 47: Spectral Classification of the Future*, volume 9 of *Ricerche Astronomiche*, page 479, 1979.
- [43] M. J. Claussen, D. A. Frail, W. M. Goss, and R. A. Gaume. Polarization Observations of 1720 MHz OH Masers toward the Three Supernova Remnants W28, W44, and IC 443. *ApJ*, 489:143–159, Nov. 1997.
- [44] F. Comerón and A. Pasquali. New members of the massive stellar population in Cygnus. *A&A*, 543:A101, July 2012.
- [45] J. M. Cordes and T. J. W. Lazio. NE2001.I. A New Model for the Galactic Distribution of Free Electrons and its Fluctuations. *ArXiv Astrophysics e-prints*, July 2002.
- [46] D. Crampton, Y. M. Georgelin, and Y. P. Georgelin. First optical detection of W51 and observations of new H II regions and exciting stars. *A&A*, 66:1–11, May 1978.
- [47] D. Crawford, D. N. Limber, E. Mendoza, D. Schulte, H. Steinman, and T. Swihart. The Association i Geminorum. *ApJ*, 121:24, Jan. 1955.
- [48] A. Cucchiaro, M. Jaschek, C. Jaschek, and D. Macau-Hercot. Spectral classification from the ultraviolet line features of S2/68 spectra. I. Early B-type stars. *A&AS*, 26:241, Nov. 1976.
- [49] K. Davidson and R. A. Fesen. Recent developments concerning the Crab Nebula. *ARA&A*, 23:119–146, 1985.

- [50] A. de Luca. Central Compact Objects in Supernova Remnants. In C. Bassa, Z. Wang, A. Cumming, and V. M. Kaspi, editors, *40 Years of Pulsars: Millisecond Pulsars, Magnetars and More*, volume 983 of *American Institute of Physics Conference Series*, pages 311–319, Feb. 2008.
- [51] S. E. de Mink, N. Langer, R. G. Izzard, H. Sana, and A. de Koter. The Rotation Rates of Massive Stars: The Role of Binary Interaction through Tides, Mass Transfer, and Mergers. *ApJ*, 764:166, Feb. 2013.
- [52] R. Dib and V. M. Kaspi. 16 yr of RXTE Monitoring of Five Anomalous X-Ray Pulsars. *ApJ*, 784:37, Mar. 2014.
- [53] B. Dinçel, R. Neuhäuser, S. K. Yerli, A. Ankaý, N. Tetzlaff, G. Torres, and M. Mugaer. Discovery of an OB runaway star inside SNR S147. *MNRAS*, 448:3196–3205, Apr. 2015.
- [54] R. C. Duncan and C. Thompson. Formation of very strongly magnetized neutron stars - Implications for gamma-ray bursts. *ApJ*, 392:L9–L13, June 1992.
- [55] P. P. Eggleton. Approximations to the radii of Roche lobes. *ApJ*, 268:368, May 1983.
- [56] J. J. Eldridge, M. Fraser, S. J. Smartt, J. R. Maund, and R. M. Crockett. The death of massive stars - II. Observational constraints on the progenitors of Type Ibc supernovae. *MNRAS*, 436:774–795, Nov. 2013.
- [57] P. Esposito, A. de Luca, A. Tiengo, A. Paizis, S. Mereghetti, and P. A. Caraveo. Unveiling the nature of RXJ0002+6246 with XMM-Newton. *MNRAS*, 384:225–229, Feb. 2008.
- [58] M. W. Feast and M. Shuttleworth. The kinematics of B stars, cepheids, galactic clusters and interstellar gas in the Galaxy. *MNRAS*, 130:245, 1965.
- [59] R. Fesen, G. Rudie, A. Hurford, and A. Soto. Optical Imaging and Spectroscopy of the Galactic Supernova Remnant 3C 58 (G130.7+3.1). *ApJ*, 174:379–395, Feb. 2008.
- [60] R. A. Fesen. The nature of the filaments northeast of the supernova remnant IC 443. *ApJ*, 281:658–664, June 1984.
- [61] R. A. Fesen, W. P. Blair, and R. P. Kirshner. Spectrophotometry of the Cygnus Loop. *ApJ*, 262:171–188, Nov. 1982.
- [62] R. A. Fesen, W. P. Blair, and R. P. Kirshner. Optical emission-line properties of evolved galactic supernova remnants. *ApJ*, 292:29–48, May 1985.
- [63] R. A. Fesen, R. A. Downes, D. Wallace, and M. Normandeau. Optical and Radio Emission from the Galactic Supernova Remnant HB 3(G132.6 +1.5). *AJ*, 110:2876, Dec. 1995.

- [64] R. A. Fesen, M. C. Hammell, J. Morse, R. A. Chevalier, K. J. Borkowski, M. A. Dopita, C. L. Gerardy, S. S. Lawrence, J. C. Raymond, and S. van den Bergh. The Expansion Asymmetry and Age of the Cassiopeia A Supernova Remnant. *ApJ*, 645:283–292, July 2006.
- [65] R. A. Fesen and R. P. Kirshner. Spectrophotometry of the supernova remnant IC 443. *ApJ*, 242:1023–1040, Dec. 1980.
- [66] R. A. Fesen, J. M. Shull, and A. P. Hurford. An Optical Study of the Circumstellar Environment Around the Crab Nebula. *AJ*, 113:354–363, Jan. 1997.
- [67] R. A. Fesen, F. Winkler, Y. Rathore, R. A. Downes, D. Wallace, and R. W. Tweedy. Optical Imaging and Spectroscopy of the Galactic Supernova Remnants CTB 1 (G116.9+0.2), G116.5+1.1, and G114.3+0.3. *AJ*, 113:767–779, Feb. 1997.
- [68] M. Fich. Supernova remnants associated with an H I ‘supershell’ in the Perseus spiral arm. *ApJ*, 303:465–469, Apr. 1986.
- [69] E. W. Fleisch. The Million Optical - Radio/X-ray Associations (MORX) Catalogue. *Publ. Astron. Soc. Australia*, 33:e052, Oct. 2016.
- [70] D. Forbes. Possible membership for the 51-day Cepheid GY Sagittae in a new OB association. *AJ*, 87:1022–1028, July 1982.
- [71] T. Foster and C. M. Brunt. A CGPS Look at the Spiral Structure of the Outer Milky Way. I. Distances and Velocities to Star-forming Regions. *AJ*, 150:147, Nov. 2015.
- [72] T. Foster and J. MacWilliams. Modeling the Neutral Hydrogen Interstellar Medium: A Better Kinematic Distance Tool. *ApJ*, 644:214–228, June 2006.
- [73] T. Foster and D. Routledge. A New Distance Technique for Galactic Plane Objects. *ApJ*, 598:1005–1016, Dec. 2003.
- [74] C. Fransson, R. Gilmozzi, P. Groeningsson, R. Hanuschik, K. Kjaer, B. Leibundgut, and J. Spyromilio. Twenty Years of Supernova 1987A. *The Messenger*, 127, Mar. 2007.
- [75] E. Fuerst and W. Reich. Multifrequency radio observations of S 147. *A&A*, 163:185–193, July 1986.
- [76] B. M. Gaensler and P. O. Slane. The Evolution and Structure of Pulsar Wind Nebulae. *ARA&A*, 44:17–47, Sept. 2006.
- [77] B. M. Gaensler, B. W. Stappers, D. A. Frail, D. A. Moffett, S. Johnston, and S. Chatterjee. Limits on radio emission from pulsar wind nebulae. *MNRAS*, 318:58–66, Oct. 2000.
- [78] J. A. Galt and J. E. D. Kennedy. Survey of radio sources observed in the continuum near 1420 MHz, declinations -5 to +70. *AJ*, 73:135–151, Apr. 1968.

- [79] C. L. Gerardy and R. A. Fesen. Discovery of extensive optical emission associated with the X-ray bright, radio faint Galactic SNR G156.2+5.7. *MNRAS*, 376:929–938, Apr. 2007.
- [80] P. Ghosh. *Rotation and Accretion Powered Pulsars*. World Scientific Publishing Co, 2007.
- [81] D. R. Gies. The kinematical and binary properties of association and field O stars. *ApJS*, 64:545–563, July 1987.
- [82] D. R. Gies and C. T. Bolton. The binary frequency and origin of the OB runaway stars. *ApJS*, 61:419–454, June 1986.
- [83] R. Głębocki and P. Gnaciński. Systematic errors in the determination of stellar rotational velocities. In F. Favata, G. A. J. Hussain, and B. Battrick, editors, *13th Cambridge Workshop on Cool Stars, Stellar Systems and the Sun*, volume 560 of *ESA Special Publication*, page 571, Mar. 2005.
- [84] I. V. Gosachinskii. Association of the supernova remnant G 65.3+5.7 with ambient neutral hydrogen and a possible nature of the remnant. *Astronomy Letters*, 36:260–268, Apr. 2010.
- [85] R. O. Gray and C. J. Corbally. The calibration of MK spectral classes using spectral synthesis. 1: The effective temperature calibration of dwarf stars. *AJ*, 107:742–746, Feb. 1994.
- [86] D. A. Green. A Catalogue of Galactic Supernova Remnants (Green, 2009). *VizieR Online Data Catalog*, 7253:0, June 2009.
- [87] Z. Guo and D. N. Burrows. ASCA Observations of the Supernova Remnant VRO 42.05.01. *ApJ*, 480:L51–L54, May 1997.
- [88] O. H. Guseinov, A. Ankay, A. Sezer, and S. O. Tagieva. The relation between the surface brightness and the diameter for galactic supernova remnants. *Astronomical and Astrophysical Transactions*, 22:273, Mar. 2003.
- [89] O. H. Guseinov, A. Ankay, and S. O. Tagieva. The Strong Magnetic Field Decay and Evolution of Radio Pulsars on the P-a' Diagram. *International Journal of Modern Physics D*, 13:1805–1815, Oct. 2004.
- [90] O. H. Guseinov, A. Ankay, and S. O. Tagieva. Searching for Runaway OB Stars in Supernova Remnants. *Astrophysics*, 48:330–343, July 2005.
- [91] T. Güver and F. Özel. The relation between optical extinction and hydrogen column density in the Galaxy. *MNRAS*, 400:2050–2053, Dec. 2009.
- [92] C. J. Hailey and W. W. Craig. Spectroscopy of the supernova remnant CTB 1. *ApJ*, 434:635–640, Oct. 1994.

- [93] C. J. Hailey and W. W. Craig. Discovery of a Candidate Isolated Neutron Star in a New Supernova Remnant near CTB 1. *ApJ*, 455:L151, Dec. 1995.
- [94] J. P. Halpern, F. Camilo, E. V. Gotthelf, D. J. Helfand, M. Kramer, A. G. Lyne, K. M. Leighly, and M. Eracleous. PSR J2229+6114: Discovery of an Energetic Young Pulsar in the Error Box of the EGRET Source 3EG J2227+6122. *ApJ*, 552:L125–L128, May 2001.
- [95] J. Hardorp, K. Rohlf, A. Slettebak, and J. Stock. Luminous stars in the Northern Milky Way. Part I. *Hamburger Sternw. Warner & Swasey Obs.*, 1959.
- [96] J. Hardorp, I. Theile, and H. H. Voigt. Luminous Stars in the Northern Milky Way. *Hamburger Sternw. Warner & Swasey Obs.*, 1964.
- [97] A. Heger, C. L. Fryer, S. E. Woosley, N. Langer, and D. H. Hartmann. How Massive Single Stars End Their Life. *ApJ*, 591:288–300, July 2003.
- [98] J. J. Hester and S. R. Kulkarni. Optical imagery and spectrophotometry of CTB 80. *ApJ*, 340:362–378, May 1989.
- [99] N. A. Higginbotham and P. Lee. The helium-rich star HD 184927. *PASP*, 85:215, Apr. 1973.
- [100] L. A. Higgs, T. L. Landecker, and R. S. Roger. The true extent of the Gamma Cygni supernova remnant. *AJ*, 82:718–724, Sept. 1977.
- [101] A. Hirschauer, S. R. Federman, G. Wallerstein, and T. Means. Diffuse Atomic and Molecular Gas Near IC 443. *ApJ*, 696:1533–1542, May 2009.
- [102] G. Hobbs, D. R. Lorimer, A. G. Lyne, and M. Kramer. A statistical study of 233 pulsar proper motions. *MNRAS*, 360:974–992, July 2005.
- [103] I. M. Hoffman, W. M. Goss, C. L. Brogan, and M. J. Claussen. The OH (1720 MHz) Supernova Remnant Masers in W44: MERLIN and VLBA Polarization Observations. *ApJ*, 627:803–812, July 2005.
- [104] M. M. Hohle, R. Neuhäuser, and B. F. Schutz. Masses and luminosities of O- and B-type stars and red supergiants. *Astronomische Nachrichten*, 331:349, Apr. 2010.
- [105] R. Hoogerwerf, J. H. J. de Bruijne, and P. T. de Zeeuw. On the origin of the O and B-type stars with high velocities. II. Runaway stars and pulsars ejected from the nearby young stellar groups. *A&A*, 365:49–77, Jan. 2001.
- [106] J. P. Hughes, C. E. Rakowski, D. N. Burrows, and P. O. Slane. Nucleosynthesis and Mixing in Cassiopeia A. *ApJ*, 528:L109–L113, Jan. 2000.
- [107] C. Y. Hui, K. A. Seo, L. C. C. Lin, R. H. H. Huang, C. P. Hu, J. H. K. Wu, L. Treppl, J. Takata, Y. Wang, Y. Chou, K. S. Cheng, and A. K. H. Kong. A Detailed X-Ray Investigation of PSR J2021+4026 and the γ -Cygni Supernova Remnant. *ApJ*, 799:76, Jan. 2015.

- [108] F. Hulleman, M. H. van Kerkwijk, F. W. M. Verbunt, and S. R. Kulkarni. A deep search for the optical counterpart to the anomalous X-ray pulsar 1E 2259+58.6. *A&A*, 358:605–611, June 2000.
- [109] R. M. Humphreys. Studies of luminous stars in nearby galaxies. I. Supergiants and O stars in the Milky Way. *ApJS*, 38:309–350, Dec. 1978.
- [110] D. A. Hunter and P. Massey. Small Galactic H II regions. I - Spectral classifications of massive stars. *AJ*, 99:846–856, Mar. 1990.
- [111] A. P. Hurford and R. A. Fesen. Reddening Measurements and Physical Conditions for Cassiopeia A from Optical and Near-Infrared Spectra. *ApJ*, 469:246, Sept. 1996.
- [112] G. H. Janssen, B. W. Stappers, R. Braun, W. van Straten, R. T. Edwards, E. Rubio-Herrera, J. van Leeuwen, and P. Weltevrede. Discovery and timing of the first 8gr8 Cygnus survey pulsars. *A&A*, 498:223–231, Apr. 2009.
- [113] C. S. Jeffery and U. Heber. The extreme helium star BD-9 deg 4395. *A&A*, 260:133–150, July 1992.
- [114] C. S. Jeffery, V. M. Woolf, and D. L. Pollacco. Time-resolved spectral analysis of the pulsating helium star V652 Her. *A&A*.
- [115] B. Jiang, Y. Chen, and Q. D. Wang. The Chandra View of DA 530: A Subenergetic Supernova Remnant with a Pulsar Wind Nebula? *ApJ*, 670:1142–1148, Dec. 2007.
- [116] H. L. Johnson and W. W. Morgan. Fundamental stellar photometry for standards of spectral type on the revised system of the Yerkes spectral atlas. *ApJ*, 117:313, May 1953.
- [117] G. Joncas, R. S. Roger, and P. E. Dewdney. New radio observations of two supernova remnants in Cassiopeia - G 126.2 + 1.6 and G 127.1 + 0.5. *A&A*, 219:303–307, July 1989.
- [118] Y. C. Joshi, L. A. Balona, S. Joshi, and B. Kumar. Photometric study of the open cluster - II. Stellar population and dynamical evolution in NGC 559. *MNRAS*, 437:804–815, Jan. 2014.
- [119] N. Junkes. G54.4-0.3 - Multi-Frequency Investigation of an SNR in Interaction with the ISM. In L. Blitz and P. J. Teuben, editors, *Unsolved Problems of the Milky Way*, volume 169 of *IAU Symposium*, page 627, 1996.
- [120] N. Junkes, E. Fuerst, and W. Reich. G54.4-0.3: CO shell and star formation region surrounding a shell-type supernova remnant. I - Properties of the CO shell. *A&As*, 96:1–21, Nov. 1992.
- [121] N. Junkes, E. Fuerst, and W. Reich. G54.4-0.3: CO shell and star formation region surrounding a shell-type supernova remnant. II - Compact CO clouds and the star formation scenario. *A&A*, 261:289–300, July 1992.

- [122] L. Kaper, J. T. van Loon, T. Augusteijn, P. Goudfrooij, F. Patat, L. B. F. M. Waters, and A. A. Zijlstra. Discovery of a Bow Shock around VELA X-1. *ApJ*, 475:L37–L40, Jan. 1997.
- [123] D. L. Kaplan. Nearby, Thermally Emitting Neutron Stars. In Y.-F. Yuan, X.-D. Li, and D. Lai, editors, *Astrophysics of Compact Objects*, volume 968 of *American Institute of Physics Conference Series*, pages 129–136, Jan. 2008.
- [124] D. L. Kaplan, S. Chatterjee, B. M. Gaensler, and J. Anderson. A Precise Proper Motion for the Crab Pulsar, and the Difficulty of Testing Spin-Kick Alignment for Young Neutron Stars. *ApJ*, 677:1201–1215, Apr. 2008.
- [125] V. M. Kaspi, F. P. Gavriil, P. M. Woods, J. B. Jensen, M. S. E. Roberts, and D. Chakrabarty. A Major Soft Gamma Repeater-like Outburst and Rotation Glitch in the No-longer-so-anomalous X-Ray Pulsar 1E 2259+586. *ApJ*, 588:L93–L96, May 2003.
- [126] S. Katsuda, R. Petre, U. Hwang, H. Yamaguchi, K. Mori, and H. Tsunemi. Suzaku Observations of Thermal and Non-Thermal X-Ray Emission from the Middle-Aged Supernova Remnant G156.2+5.7. *PASJ*, 61:S155–S165, Jan. 2009.
- [127] J. Katsuta, Y. Uchiyama, T. Tanaka, H. Tajima, K. Bechtol, S. Funk, J. Lande, J. Ballet, Y. Hanabata, M. Lemoine-Goumard, and T. Takahashi. Fermi Large Area Telescope Observation of Supernova Remnant S147. *ApJ*, 752:135, June 2012.
- [128] M. Kawasaki, M. Ozaki, F. Nagase, H. Inoue, and R. Petre. Ionization States and Plasma Structures of Mixed-Morphology Supernova Remnants Observed with ASCA. *ApJ*, 631:935–946, Oct. 2005.
- [129] S. J. Kenyon and L. Hartmann. Pre-Main-Sequence Evolution in the Taurus-Auriga Molecular Cloud. *ApJS*, 101:117, Nov. 1995.
- [130] N. V. Kharchenko. All-sky compiled catalogue of 2.5 million stars. *Kinematika i Fizika Nebesnykh Tel*, 17:409–423, Oct. 2001.
- [131] I.-J. Kim, K.-I. Seon, K.-W. Min, J.-H. Shinn, W. Han, and J. Edelstein. Far-ultraviolet Emission-line Morphologies of the Supernova Remnant G65.3+5.7. *ApJ*, 722:388–394, Oct. 2010.
- [132] M. M. Kiminki, J. S. Kim, M. B. Bagley, W. H. Sherry, and G. H. Rieke. The O- and B-Type Stellar Population in W3: Beyond the High-Density Layer. *ApJ*, 813:42, Nov. 2015.
- [133] R. P. Kirshner and C. N. Arnold. Kinematics of the supernova remnant S147. *ApJ*, 229:147–152, Apr. 1979.
- [134] R. P. Kirshner and R. A. Chevalier. The central source in the supernova remnant G127.1+0.5. *Nature*, 276:480, Nov. 1978.

- [135] T. Kokusho, T. Nagayama, H. Kaneda, D. Ishihara, H.-G. Lee, and T. Onaka. Large-area [Fe II] Line Mapping of the Supernova Remnant IC 443 with the IRSF/SIRIUS. *ApJ*, 768:L8, May 2013.
- [136] B.-C. Koo, W. T. Reach, C. Heiles, R. A. Fesen, and J. M. Shull. Detection of an expanding H I shell in the old supernova remnant CTB 80. *ApJ*, 364:178–186, Nov. 1990.
- [137] B.-C. Koo, M.-S. Yun, P. T. P. Ho, and Y. Lee. Interaction between the Supernova Remnant CTB 80 and the Ambient Interstellar Medium: H i and CO Observations. *ApJ*, 417:196, Nov. 1993.
- [138] B. Koralesky, D. A. Frail, W. M. Goss, M. J. Claussen, and A. J. Green. Shock-excited Maser Emission from Supernova Remnants: G32.8-0.1, G337.8-0.1, G346.6-0.2, and the HB 3/W3 Complex. *AJ*, 116:1323–1331, Sept. 1998.
- [139] R. Kothes. Distance and age of the pulsar wind nebula 3C 58. *A&A*, 560:A18, Dec. 2013.
- [140] R. Kothes, K. Fedotov, T. J. Foster, and B. Uyaniker. A catalogue of Galactic supernova remnants from the Canadian Galactic plane survey. I. Flux densities, spectra, and polarization characteristics. *A&A*, 457:1081–1093, Oct. 2006.
- [141] R. Kothes and T. Foster. A Thorough Investigation of the Distance to the Supernova Remnant CTB109 and Its Pulsar AXP J2301+5852. *ApJ*, 746:L4, Feb. 2012.
- [142] R. Kothes, B. Uyaniker, and S. Pineault. The Supernova Remnant G106.3+2.7 and Its Pulsar-Wind Nebula: Relics of Triggered Star Formation in a Complex Environment. *ApJ*, 560:236–243, Oct. 2001.
- [143] M. Kramer, A. G. Lyne, G. Hobbs, O. Löhmer, P. Carr, C. Jordan, and A. Wolszczan. The Proper Motion, Age, and Initial Spin Period of PSR J0538+2817 in S147. *ApJ*, 593:L31–L34, Aug. 2003.
- [144] J. Kubát, D. Korčáková, A. Kawka, A. Pigulski, M. Šlechta, and P. Škoda. The H α stellar and interstellar emission in the open cluster NGC 6910. *A&A*, 472:163–167, Sept. 2007.
- [145] S. R. Kulkarni, T. C. Clifton, D. C. Backer, R. S. Foster, and A. S. Fruchter. A fast pulsar in radio nebula CTB80. *Nature*, 331:50–53, Jan. 1988.
- [146] M. R. Kundu, P. E. Angerhofer, E. Fuerst, and W. Hirth. Observations of the old supernova remnant S 147 at 11.1 and 18.2 CM wavelengths. *A&A*, 92:225–229, Dec. 1980.
- [147] R. L. Kurucz. Model Atmospheres for Population Synthesis. In B. Barbuy and A. Renzini, editors, *The Stellar Populations of Galaxies*, volume 149 of *IAU Symposium*, page 225, 1992.

- [148] Y. Ladouceur and S. Pineault. New perspectives on the supernova remnant G78.2+2.1. *A&A*, 490:197–211, Oct. 2008.
- [149] T. L. Landecker, S. Pineault, D. Routledge, and J. F. Vaneldik. The interaction of the supernova remnant VRO 42.05.01 with its H I environment. *MNRAS*, 237:277–297, Mar. 1989.
- [150] T. L. Landecker, R. S. Roger, and P. E. Dewdney. The supernova remnant G116.9+0.2 /CTB 1/ - 21-cm continuum and H I emission. *AJ*, 87:1379–1389, Oct. 1982.
- [151] T. L. Landecker, R. S. Roger, and L. A. Higgs. Atomic hydrogen in a field in Cygnus X containing the supernova remnant G78.2+2.1. *A&AS*, 39:133–151, Feb. 1980.
- [152] T. L. Landecker, D. Routledge, S. P. Reynolds, R. J. Smegal, K. J. Borkowski, and F. D. Seward. DA 530: A Supernova Remnant in a Stellar Wind Bubble. *ApJ*, 527:866–878, Dec. 1999.
- [153] J. S. Lazendic, D. Dewey, N. S. Schulz, and C. R. Canizares. The Kinematic and Plasma Properties of X-Ray Knots in Cassiopeia A from the Chandra HETGS. *ApJ*, 651:250–267, Nov. 2006.
- [154] J. S. Lazendic and P. O. Slane. Enhanced Abundances in Three Large-Diameter Mixed-Morphology Supernova Remnants. *ApJ*, 647:350–366, Aug. 2006.
- [155] D. Leahy and M. Hassan. Joint Suzaku and XMM-Newton Spectral Analysis of the Southwest Cygnus Loop. *ApJ*, 764:55, Feb. 2013.
- [156] D. Leahy and W. Tian. Radio observations and spectrum of the SNR G127.1+0.5 and its central source 0125+628. *A&A*, 451:251–257, May 2006.
- [157] D. A. Leahy. 1420 and 408 MHz Continuum Observations of the IC 443/G189.6+3.3 Region. *AJ*, 127:2277–2283, Apr. 2004.
- [158] D. A. Leahy and B. Aschenbach. ROSAT X-ray observations of the supernova remnant HB 9. *A&A*, 293:853–858, Jan. 1995.
- [159] D. A. Leahy, K. Green, and S. Ranasinghe. X-ray and radio observations of the γ Cygni supernova remnant G78.2+2.1. *MNRAS*, 436:968–977, Dec. 2013.
- [160] D. A. Leahy and S. Ranasinghe. Radio observations of CTB80: detection of the snowplough in an old supernova remnant. *MNRAS*, 423:718–724, June 2012.
- [161] D. A. Leahy and W. W. Tian. Radio spectrum and distance of the SNR HB9. *A&A*, 461:1013–1018, Jan. 2007.
- [162] C. Leitherer, C. Robert, and L. Drissen. Deposition of mass, momentum, and energy by massive stars into the interstellar medium. *ApJ*, 401:596–617, Dec. 1992.

- [163] J. R. Lesh and M. L. Aizenman. The spectral classification of the beta Cephei stars and their location in the theoretical Hertzsprung-Russell diagram. *A&A*, 22:229–237, Jan. 1973.
- [164] N. A. Levenson, J. R. Graham, L. D. Keller, and M. J. Richter. Panoramic Views of the Cygnus Loop. *ApJS*, 118:541–561, Oct. 1998.
- [165] T. A. Lozinskaia. Supernova remnant IC 443 - Fast filaments and high-velocity gas. *A&A*, 71:29–35, Jan. 1979.
- [166] T. A. Lozinskaia. The supernova remnants IC 443 and VRO 42.05.01 - Fast filaments and high-velocity gas. *Australian Journal of Physics*, 32:113–121, Mar. 1979.
- [167] T. A. Lozinskaia. Kinematics of old supernova remnants. *A&A*, 84:26–35, Apr. 1980.
- [168] T. A. Lozinskaya. Observations of the Filamentary Nebula IC 443 in the H α Line with a Fabry-Perot Interferometer. *Soviet Ast.*, 13:192, Oct. 1969.
- [169] T. A. Lozinskaya. Optical observations of supernova remnants: the filamentary nebula Simeiz 147. *Soviet Ast.*, 20:19, Feb. 1976.
- [170] T. A. Lozinskaya. The radio brightness-diameter relation for supernova remnants - Some new distance calibrators. *Soviet Astronomy Letters*, 7:29–32, Feb. 1981.
- [171] T. A. Lozinskaya, V. V. Pravdikova, and A. V. Finoguenov. The Supernova Remnant G78.2+2.1: New Optical and X-ray Observations. *Astronomy Letters*, 26:77–87, Feb. 2000.
- [172] A. G. Lyne, C. A. Jordan, F. Graham-Smith, C. M. Espinoza, B. W. Stappers, and P. Weltevrede. 45 years of rotation of the Crab pulsar. *MNRAS*, 446:857–864, Jan. 2015.
- [173] A. G. Lyne and D. R. Lorimer. High birth velocities of radio pulsars. *Nature*, 369:127–129, May 1994.
- [174] G. M. MacAlpine and T. J. Satterfield. The Crab Nebula’s Composition and Precursor Star Mass. *AJ*, 136:2152–2157, Nov. 2008.
- [175] G. M. MacAlpine and A. Uomoto. Photometry of the Crab Nebula - Variability and the mass of emitting gas. *AJ*, 102:218–223, July 1991.
- [176] A. Maeder and G. Meynet. Evolution of massive stars with mass loss and rotation. *New Astron. Rev.*, 54:32–38, Mar. 2010.
- [177] J. Maíz Apellániz.
- [178] R. N. Manchester, G. B. Hobbs, A. Teoh, and M. Hobbs. The Australia Telescope National Facility Pulsar Catalogue. *AJ*, 129:1993–2006, Apr. 2005.
- [179] P. Manoj, H. C. Bhatt, G. Maheswar, and S. Muneer. Evolution of Emission-Line Activity in Intermediate-Mass Young Stars. *ApJ*, 653:657–674, Dec. 2006.

- [180] F. Mavromatakis. Deep optical observations of the supernova remnant G 78.2+2.1. *A&A*, 408:237–243, Sept. 2003.
- [181] F. Mavromatakis, B. Aschenbach, P. Boumis, and J. Papamastorakis. Multi-wavelength study of the {G 82.2+5.3} supernova remnant. *A&A*, 415:1051–1063, Mar. 2004.
- [182] F. Mavromatakis, P. Boumis, and E. V. Paleologou. Imaging and spectroscopy of the faint remnant G 114.3+0.3. *A&A*, 383:1011–1017, Mar. 2002.
- [183] F. Mavromatakis, P. Boumis, J. Papamastorakis, and J. Ventura. Deep optical observations of G 65.3+5.7. *A&A*, 388:355–362, June 2002.
- [184] F. Mavromatakis, J. Ventura, E. V. Paleologou, and J. Papamastorakis. The peculiar supernova remnant CTB 80. *A&A*, 371:300–311, May 2001.
- [185] K. E. McGowan, J. A. Kennea, S. Zane, F. A. Córdova, M. Cropper, C. Ho, T. Sasseen, and W. T. Vestrand. Detection of Pulsed X-Ray Emission from XMM-Newton Observations of PSR J0538+2817. *ApJ*, 591:380–387, July 2003.
- [186] K. E. McGowan, S. Zane, M. Cropper, W. T. Vestrand, and C. Ho. Evidence for Surface Cooling Emission in the XMM-Newton Spectrum of the X-Ray Pulsar PSR B2334+61. *ApJ*, 639:377–381, Mar. 2006.
- [187] A. Megier, A. Strobel, G. A. Galazutdinov, and J. Krelowski. The interstellar Ca II distance scale. *A&A*, 507:833–840, Nov. 2009.
- [188] A. M. Mel’Nik and A. K. Dambis. Kinematics of OB-associations and the new reduction of the Hipparcos data. *MNRAS*, 400:518–523, Nov. 2009.
- [189] A. M. Mel’Nik and Y. N. Efremov. A new list of OB associations in our galaxy. *Astronomy Letters*, 21:10–26, Jan. 1995.
- [190] G. Meynet and A. Maeder. Stellar evolution with rotation. V. Changes in all the outputs of massive star models. *A&A*, 361:101–120, Sept. 2000.
- [191] J. S. Miller. Reddening of the Crab Nebula from Observations of [s II] Lines. *ApJ*, 180:L83, Mar. 1973.
- [192] D. K. Milne. A new catalogue of galactic SNRs corrected for distance from the galactic plane. *Australian Journal of Physics*, 32:83–92, Mar. 1979.
- [193] A. S. Miroshnichenko, K. S. Bjorkman, E. L. Chentsov, V. G. Klochkova, N. Manset, P. García-Lario, J. V. Perea Calderón, R. J. Rudy, D. K. Lynch, J. C. Wilson, and T. L. Gandet. V669 Cep: A new binary system with a B[e] star. *A&A*, 388:563–572, June 2002.
- [194] D. Mitra, R. Wielebinski, M. Kramer, and A. Jessner. The effect of HII regions on rotation measure of pulsars. *A&A*, 398:993–1005, Feb. 2003.

- [195] W. W. Morgan, A. D. Code, and A. E. Whitford. Studies in Galactic STRUCTURE.II.LUMINOSITY Classification for 1270 Blue Giant Stars. *ApJS*, 2:41, July 1955.
- [196] W. W. Morgan, P. C. Keenan, and E. Kellman. *An atlas of stellar spectra, with an outline of spectral classification*. 1943.
- [197] M. Mugrauer, G. Avila, and C. Guirao. FLECHAS A new Echelle spectrograph at the University Observatory Jena. *Astronomische Nachrichten*, 335:417, 2014.
- [198] S. S. Murray, P. O. Slane, F. D. Seward, S. M. Ransom, and B. M. Gaensler. Discovery of X-Ray Pulsations from the Compact Central Source in the Supernova Remnant 3C 58. *ApJ*, 568:226–231, Mar. 2002.
- [199] T. Neckel, G. Klare, and M. Sarcander. Catalogue of Extinction Data of 12547 O-Stars to F-Stars Galactic Clusters and Delta-Cephei Stars. *Bulletin d’Information du Centre de Donnees Stellaires*, 19:61, July 1980.
- [200] I. Negueruela and A. Marco. Stellar tracers of the Cygnus Arm. I. Spectroscopic study of bright photometric candidates. *A&A*, 406:119–130, July 2003.
- [201] I. Negueruela, I. A. Steele, and G. Bernabeu. On the class of Oe stars. *Astronomische Nachrichten*, 325:749–760, Dec. 2004.
- [202] C.-Y. Ng and R. W. Romani. Proper Motion of the Crab Pulsar Revisited. *ApJ*, 644:445–450, June 2006.
- [203] C.-Y. Ng, R. W. Romani, W. F. Brisken, S. Chatterjee, and M. Kramer. The Origin and Motion of PSR J0538+2817 in S147. *ApJ*, 654:487–493, Jan. 2007.
- [204] K. Nomoto. Evolution of 8-10 solar mass stars toward electron capture supernovae. I - Formation of electron-degenerate O + NE + MG cores. *ApJ*, 277:791–805, Feb. 1984.
- [205] J. A. O’Keefe. The Distances of the Reddined B Stars. *ApJ*, 94:353, Sept. 1941.
- [206] C. M. Olbert, C. R. Clearfield, N. E. Williams, J. W. Keohane, and D. A. Frail. A Bow Shock Nebula around a Compact X-Ray Source in the Supernova Remnant IC 443. *ApJ*, 554:L205–L208, June 2001.
- [207] B. Paczyński. Evolutionary Processes in Close Binary Systems. *ARA&A*, 9:183, 1971.
- [208] T. G. Pannuti and G. E. Allen. ASCA and RXTE observations of non-thermal X-ray emission from galactic supernova remnants: G156.2+5.7. *Advances in Space Research*, 33:434–439, 2004.
- [209] T. G. Pannuti, J. Rho, K. J. Borkowski, and P. B. Cameron. Mixed-morphology Supernova Remnants in X-rays: Isothermal Plasma in HB21 and Probable Oxygen-rich Ejecta in CTB 1. *AJ*, 140:1787–1805, Dec. 2010.

- [210] R. A. R. Parker. A Model for the "filaments" in the Cygnus Loop. *ApJ*, 149:363, Aug. 1967.
- [211] G. G. Pavlov and G. J. M. Luna. A Dedicated Chandra ACIS Observation of the Central Compact Object in the Cassiopeia A Supernova Remnant. *ApJ*, 703:910–921, Sept. 2009.
- [212] C. A. Perrot and I. A. Grenier. 3D dynamical evolution of the interstellar gas in the Gould Belt. *A&A*, 404:519–531, June 2003.
- [213] R. Petre, A. E. Szymkowiak, F. D. Seward, and R. Willingale. A comprehensive study of the X-ray structure and spectrum of IC 443. *ApJ*, 335:215–238, Dec. 1988.
- [214] E. Pfeffermann, B. Aschenbach, and P. Predehl. Discovery of a galactic supernova remnant with ROSAT. *A&A*, 246:L28–L31, June 1991.
- [215] S. Pineault and G. Joncas. G106.3+2.7: A Supernova Remnant in a Late Stage of Evolution. *AJ*, 120:3218–3225, Dec. 2000.
- [216] S. Pineault, T. L. Landecker, and D. Routledge. VRO 42.05.01 - A supernova remnant reenergizing an interstellar cavity. *ApJ*, 315:580–587, Apr. 1987.
- [217] T. Piran and R. Jimenez. Possible Role of Gamma Ray Bursts on Life Extinction in the Universe. *Physical Review Letters*, 113(23):231102, Dec. 2014.
- [218] P. Podsiadlowski, P. C. Joss, and J. J. L. Hsu. Presupernova evolution in massive interacting binaries. *ApJ*, 391:246–264, May 1992.
- [219] P. Podsiadlowski, N. Langer, A. J. T. Poelarends, S. Rappaport, A. Heger, and E. Pfahl. The Effects of Binary Evolution on the Dynamics of Core Collapse and Neutron Star Kicks. *ApJ*.
- [220] A. Poveda, J. Ruiz, and C. Allen. Run-away Stars as the Result of the Gravitational Collapse of Proto-stellar Clusters. *Boletín de los Observatorios Tonantzintla y Tacubaya*, 4:86–90, Apr. 1967.
- [221] N. Przybilla, M. F. Nieva, U. Heber, and K. Butler. HD 271791: An Extreme Supernova Runaway B Star Escaping from the Galaxy. *ApJ*, 684:L103–L106, Sept. 2008.
- [222] G. M. Raisbeck, F. Yiou, D. Bourles, C. Lorius, and J. Jouzel. Evidence for two intervals of enhanced Be-10 deposition in Antarctic ice during the last glacial period. *Nature*, 326:273–277, Mar. 1987.
- [223] S. Ramírez Alegría, A. Herrero, A. Marín-Franch, E. Puga, F. Najarro, J. A. Acosta Pulido, S. L. Hidalgo, and S. Simón-Díaz. Near-infrared study of the stellar population of Sh2-152. *A&A*, 535:A8, Nov. 2011.
- [224] P. L. Read. H I aperture synthesis observations towards galactic H II regions. II - W3. *MNRAS*, 194:863–878, Mar. 1981.

- [225] J. E. Reed, J. J. Hester, A. C. Fabian, and P. F. Winkler. The Three-dimensional Structure of the Cassiopeia A Supernova Remnant. I. The Spherical Shell. *ApJ*, 440:706, Feb. 1995.
- [226] W. Reich, E. M. Berkhuijsen, and Y. Sofue. Radio continuum observations at 1420 MHz of the new SNR G65.2+5.7 in Cygnus. *A&A*, 72:270–276, Feb. 1979.
- [227] W. Reich and E. Braunsfurth. 2.7 GHz observations of the three old supernova remnants CTB1, G116.5+1.1, and G114.3+0.3 with the Effelsberg 100-m telescope. *A&A*, 99:17–26, June 1981.
- [228] W. Reich, E. Fuerst, and E. M. Arnal. Radio observations of the bright X-ray supernova remnant G156.2+5.7. *A&A*, 256:214–224, Mar. 1992.
- [229] A. Rest, D. L. Welch, N. B. Suntzeff, L. Ooster, H. Lanning, K. Olsen, R. C. Smith, A. C. Becker, M. Bergmann, P. Challis, A. Clocchiatti, K. H. Cook, G. Damke, A. Garg, M. E. Huber, T. Matheson, D. Minniti, J. L. Prieto, and W. M. Wood-Vasey. Scattered-Light Echoes from the Historical Galactic Supernovae Cassiopeia A and Tycho (SN 1572). *ApJ*, 681:L81, July 2008.
- [230] S. P. Reynolds. Supernova Remnants at High Energy. *ARA&A*, 46:89–126, Sept. 2008.
- [231] J. Rho and R. Petre. Mixed-Morphology Supernova Remnants. *ApJ*, 503:L167–L170, Aug. 1998.
- [232] J. Rho, R. Petre, E. M. Schlegel, and J. J. Hester. An X-ray and optical study of the supernova remnant W44. *ApJ*, 430:757–773, Aug. 1994.
- [233] G. H. Rieke and M. J. Lebofsky. The interstellar extinction law from 1 to 13 microns. *ApJ*, 288:618–621, Jan. 1985.
- [234] D. A. Roberts, W. M. Goss, P. M. W. Kalberla, U. Herbstmeier, and U. J. Schwarz. High Resolution HI Observations of 3C58. *A&A*, 274:427, July 1993.
- [235] S. Roeser, M. Demleitner, and E. Schilbach. The PPMXL Catalog of Positions and Proper Motions on the ICRS. Combining USNO-B1.0 and the Two Micron All Sky Survey (2MASS). *AJ*, 139:2440–2447, June 2010.
- [236] M. Rosado and J. Gonzalez. The Radial Velocity Field of the Optical Filaments Associated with the Supernova Remnant W63. *Rev. Mex. Astron. Astrofis.*, 5:93, June 1981.
- [237] D. Routledge, P. E. Dewdney, T. L. Landecker, and J. F. Vaneldik. The structure of atomic and molecular gas in the vicinity of the supernova remnant HB3. *A&A*, 247:529–544, July 1991.
- [238] P. Ruiz-Lapuente, F. Comeron, J. Méndez, R. Canal, S. J. Smartt, A. V. Filippenko, R. L. Kurucz, R. Chornock, R. J. Foley, V. Stanishev, and R. Ibata. The binary progenitor of Tycho Brahe’s 1572 supernova. *Nature*, 431:1069–1072, Oct. 2004.

- [239] D. Russeil, C. Adami, and Y. M. Georgelin. Revised distances of Northern HII regions. *A&A*, 470:161–171, July 2007.
- [240] H. N. Russell. Relations Between the Spectra and Other Characteristics of the Stars. *Popular Astronomy*, 22:275–294, May 1914.
- [241] S. Safi-Harb, H. Ogelman, and J. P. Finley. ROSAT observations of the unusual supernova remnant CTB 80 containing the pulsar PSR 1951 + 32. *ApJ*, 439:722–729, Feb. 1995.
- [242] S. Sallmen and B. Y. Welsh. Intermediate-velocity gas observed towards the Shajn 147 SNR. *A&A*, 426:555–565, Nov. 2004.
- [243] M. Sasaki, R. Kothes, P. P. Plucinsky, T. J. Gaetz, and C. M. Brunt. Evidence for Shocked Molecular Gas in the Galactic Supernova Remnant CTB 109 (G109.1-1.0). *ApJ*, 642:L149–L152, May 2006.
- [244] M. Sasaki, P. P. Plucinsky, T. J. Gaetz, and F. Bocchino. Chandra observation of the Galactic supernova remnant CTB 109 (G109.1-1.0). *A&A*, 552:A45, Apr. 2013.
- [245] M. Sasaki, P. P. Plucinsky, T. J. Gaetz, R. K. Smith, R. J. Edgar, and P. O. Slane. XMM-Newton Observations of the Galactic Supernova Remnant CTB 109 (G109.1-1.0). *ApJ*, 617:322–338, Dec. 2004.
- [246] J. L. Sauvageot, J. Ballet, and R. Rothenflug. EXOSAT observation toward S147 and A0535 + 26. *A&A*, 227:183–187, Jan. 1990.
- [247] R. W. Sayer, D. J. Nice, and V. M. Kaspi. A Search for Pulsar Companions to OB Runaway Stars. *ApJ*, 461:357, Apr. 1996.
- [248] R. L. Shelton, K. D. Kuntz, and R. Petre. Chandra Observations and Models of the Mixed-Morphology Supernova Remnant W44: Global Trends. *ApJ*, 611:906–918, Aug. 2004.
- [249] R. L. Shelton, K. D. Kuntz, and R. Petre. G65.2+5.7: A Thermal Composite Supernova Remnant with a Cool Shell. *ApJ*, 615:275–279, Nov. 2004.
- [250] J. Silk and G. Wallerstein. High-velocity gas in supernova remnants. II. Shajn 147. *ApJ*, 181:799–804, May 1973.
- [251] B. A. Skiff. General Catalogue of Stellar Spectral Classifications. *VizieR Online Data Catalog*, 1:2023, 2013.
- [252] B. A. Skiff. VizieR Online Data Catalog: Catalogue of Stellar Spectral Classifications (Skiff, 2009-2016). *VizieR Online Data Catalog*, 1, Oct. 2014.
- [253] P. O. Slane, D. J. Helfand, and S. S. Murray. New Constraints on Neutron Star Cooling from Chandra Observations of 3C 58. *ApJ*, 571:L45–L49, May 2002.

- [254] R. L. Snell, D. Hollenbach, J. E. Howe, D. A. Neufeld, M. J. Kaufman, G. J. Melnick, E. A. Bergin, and Z. Wang. Detection of Water in the Shocked Gas Associated with IC 443: Constraints on Shock Models. *ApJ*, 620:758–773, Feb. 2005.
- [255] T. P. Snow, H. J. G. L. M. Lamers, D. M. Lindholm, and A. P. Odell. An atlas of ultraviolet P Cygni profiles. *ApJ*, 95:163–299, Nov. 1994.
- [256] Y. Sofue, E. Furst, and W. Hirth. Radio Continuum Observations at 5-GHZ of the Supernova Remnant S147. *PASJ*, 32:1, 1980.
- [257] I. A. Steele, I. Negueruela, and J. S. Clark. A representative sample of Be stars . I. Sample selection, spectral classification and rotational velocities. *A&AS*, 137:147–156, May 1999.
- [258] F. R. Stephenson and D. A. Green. Historical supernovae and their remnants. *Historical supernovae and their remnants, by F. Richard Stephenson and David A. Green. International series in astronomy and astrophysics, vol. 5. Oxford: Clarendon Press, 2002, ISBN 0198507666, 5, 2002.*
- [259] L. A. Suad, S. Cichowolski, A. Noriega-Crespo, E. M. Arnal, J. C. Testori, and N. Flagey. The H I supershell GS 118+01-44 and its role in the interstellar medium. *A&A*, 585:A154, Jan. 2016.
- [260] D. A. Swartz, G. G. Pavlov, T. Clarke, G. Castelletti, V. E. Zavlin, N. Bucciantini, M. Karovska, A. J. van der Horst, M. Yukita, and M. C. Weisskopf. High Spatial Resolution X-Ray Spectroscopy of the IC 443 Pulsar Wind Nebula and Environs. *ApJ*, 808:84, July 2015.
- [261] K. Tatematsu, Y. Fukui, T. Iwata, F. D. Seward, and M. Nakano. A further study of the molecular cloud associated with the supernova remnant G109.1-1.0. *ApJ*, 351:157–164, Mar. 1990.
- [262] K. Tatematsu, Y. Fukui, T. L. Landecker, and R. S. Roger. The interaction of the supernova remnant HB 21 with the interstellar medium - CO, H I, and radio continuum observations. *A&A*, 237:189–200, Oct. 1990.
- [263] T. M. Tauris and R. J. Takens. Runaway velocities of stellar components originating from disrupted binaries via asymmetric supernova explosions. *A&A*, 330:1047–1059, Feb. 1998.
- [264] J. H. Taylor and J. M. Cordes. Pulsar distances and the galactic distribution of free electrons. *ApJ*, 411:674–684, July 1993.
- [265] S. P. Tendulkar, P. B. Cameron, and S. R. Kulkarni. Proper Motions and Origins of AXP 1E 2259+586 and AXP 4U 0142+61. *ApJ*, 772:31, July 2013.
- [266] N. Tetzlaff, B. Dinçel, R. Neuhäuser, and V. V. Kovtyukh. The origin of the young pulsar PSR J0826+2637 and its possible former companion HIP 13962. *MNRAS*, 438:3587–3593, Mar. 2014.

- [267] N. Tetzlaff, R. Neuhäuser, and M. M. Hohle. A catalogue of young runaway Hipparcos stars within 3 kpc from the Sun. *MNRAS*, 410:190–200, Jan. 2011.
- [268] N. Tetzlaff, R. Neuhäuser, M. M. Hohle, and G. Maciejewski. Identifying birth places of young isolated neutron stars. *MNRAS*, 402:2369–2387, Mar. 2010.
- [269] N. Tetzlaff, J. G. Schmidt, M. M. Hohle, and R. Neuhäuser. Neutron Stars From Young Nearby Associations: The Origin of RX J1605.3+3249. *Publ. Astron. Soc. Australia*, 29:98–108, Mar. 2012.
- [270] N. Tetzlaff, G. Torres, R. Neuhäuser, and M. M. Hohle. The neutron star born in the Antlia supernova remnant. *MNRAS*, 435:879–884, Oct. 2013.
- [271] W. W. Tian and D. A. Leahy. Radio observations and spectral index study of the SNR G126.2+1.6. *A&A*, 447:205–211, Feb. 2006.
- [272] W. W. Tian and D. A. Leahy. Tycho SN 1572: A Naked Ia Supernova Remnant Without an Associated Ambient Molecular Cloud. *ApJ*, 729:L15, Mar. 2011.
- [273] W. W. Tian, D. A. Leahy, and D. Li. Distance to the SNR CTB109/AXP1E2259+586 by HI absorption and self-absorption. *MNRAS*, 404:L1–L5, May 2010.
- [274] D. Tody. The IRAF Data Reduction and Analysis System. In D. L. Crawford, editor, *Instrumentation in astronomy VI*, volume 627 of *Proc. SPIE*, page 733, Jan. 1986.
- [275] L. Trepl, C. Y. Hui, K. S. Cheng, J. Takata, Y. Wang, Z. Y. Liu, and N. Wang. Multiwavelength properties of a new Geminga-like pulsar: PSRJ2021+4026. *MNRAS*, 405:1339–1348, June 2010.
- [276] V. Trimble. The Distance to the Crab Nebula and NP 0532. *PASP*, 85:579, Oct. 1973.
- [277] E. Troja, F. Bocchino, M. Miceli, and F. Reale. XMM-Newton observations of the supernova remnant IC 443. II. Evidence of stellar ejecta in the inner regions. *A&A*, 485:777–785, July 2008.
- [278] E. Troja, F. Bocchino, and F. Reale. XMM-Newton Observations of the Supernova Remnant IC 443. I. Soft X-Ray Emission from Shocked Interstellar Medium. *ApJ*, 649:258–267, Sept. 2006.
- [279] H. Tsunemi, S. Katsuda, N. Nemes, and E. D. Miller. The Plasma Structure of the Cygnus Loop from the Northeastern Rim to the Southwestern Rim. *ApJ*, 671:1717–1725, Dec. 2007.
- [280] H. Uchida, H. Tsunemi, S. Katsuda, K. Mori, R. Petre, and H. Yamaguchi. A Suzaku Study of Ejecta Structure and Origin of Hard X-Ray Emission in the Supernova Remnant G156.2+5.7. *PASJ*, 64:61, June 2012.
- [281] Y. Uchiyama, T. Takahashi, F. A. Aharonian, and J. R. Mattox. ASCA View of the Supernova Remnant γ Cygni (G78.2+2.1): Bremsstrahlung X-Ray Spectrum from Loss-flattened Electron Distribution. *ApJ*, 571:866–875, June 2002.

- [282] B. Uyaniker, R. Kothes, and C. M. Brunt. The Supernova Remnant CTB 104A: Magnetic Field Structure and Interaction with the Environment. *ApJ*, 565:1022–1034, Feb. 2002.
- [283] B. Uyaniker, W. Reich, A. Yar, R. Kothes, and E. Fürst. Is the Cygnus Loop two supernova remnants? *A&A*, 389:L61–L64, July 2002.
- [284] S. van den Bergh. A Search for OB Stars in Supernova Remnants. *Journal of Astrophysics and Astronomy*, 1:67–70, Sept. 1980.
- [285] E. P. J. van den Heuvel. Massive close binaries: Observational characteristics. *Space Sci. Rev.*, 66:309–322, Mar. 1993.
- [286] E. P. J. van den Heuvel and J. van Paradijs. Intrinsic Kicks at Birth Are Required to Explain the Observed Properties of Single and Binary Neutron Stars. *ApJ*, 483:399–401, July 1997.
- [287] F. van Leeuwen. Validation of the new Hipparcos reduction. *A&A*, 474:653–664, Nov. 2007.
- [288] H. A. T. Vanhala and A. G. W. Cameron. Numerical Simulations of Triggered Star Formation. I. Collapse of Dense Molecular Cloud Cores. *ApJ*, 508:291–307, Nov. 1998.
- [289] N. R. Walborn. Some Spectroscopic Characteristics of the OB Stars: an Investigation of the Space Distribution of Certain OB Stars and the Reference Frame of the Classification. *ApJS*, 23:257, Aug. 1971.
- [290] N. R. Walborn and E. L. Fitzpatrick. Contemporary optical spectral classification of the OB stars - A digital atlas. *PASP*, 102:379–411, Apr. 1990.
- [291] C. Wang, D. Lai, and J. L. Han. Neutron Star Kicks in Isolated and Binary Pulsars: Observational Constraints and Implications for Kick Mechanisms. *ApJ*, 639:1007–1017, Mar. 2006.
- [292] Z. X. Wang and D. R. Gies. Constraints on the Radial Velocity Curve of HDE 245770 = A0535+26. *PASP*, 110:1310–1314, Nov. 1998.
- [293] W. Wegner. Intrinsic Colour Indices of OB Supergiants Giants and Dwarfs in the UBVRIJHKLM System. *MNRAS*, 270:229, Sept. 1994.
- [294] W. Wegner. Absolute magnitudes of OB and Be stars based on Hipparcos parallaxes - II. *MNRAS*, 371:185–192, Sept. 2006.
- [295] B. Y. Welsh and S. Sallmen. High-velocity NaI and CaII absorption components observed towards the IC 443 SNR. *A&A*, 408:545–551, Sept. 2003.
- [296] B. Y. Welsh, S. Sallmen, D. Sfeir, and R. Lallement. Interstellar NaI and CaII absorption observed towards the Cygnus Loop SNR. *A&A*, 391:705–711, Aug. 2002.

- [297] A. Wongwathanarat, H.-T. Janka, and E. Müller. Three-dimensional neutrino-driven supernovae: Neutron star kicks, spins, and asymmetric ejection of nucleosynthesis products. *A&A*, 552:A126, Apr. 2013.
- [298] S. E. Woosley, N. Langer, and T. A. Weaver. The Presupernova Evolution and Explosion of Helium Stars That Experience Mass Loss. *ApJ*, 448:315, July 1995.
- [299] K. M. Xilouris, J. Papamastorakis, E. V. Paleologou, Y. Andredakis, and G. Haerendel. Detection of optical emission in the area of G127.1+0.5. *A&A*, 270:393–396, Mar. 1993.
- [300] Y. Xu, M. J. Reid, X. W. Zheng, and K. M. Menten. The Distance to the Perseus Spiral Arm in the Milky Way. *Science*, 311:54–57, Jan. 2006.
- [301] I. Yakunin, G. Wade, D. Bohlender, O. Kochukhov, W. Marcolino, M. Shultz, D. Monin, J. Grunhut, T. Sitnova, V. Tsymbal, and MiMeS Collaboration. The surface magnetic field and chemical abundance distributions of the B2V helium-strong star HD 184927. *MNRAS*, 447:1418–1438, Feb. 2015.
- [302] S. Yamauchi, K. Koyama, H. Tomida, J. Yokogawa, and K. Tamura. ASCA Observations of the Supernova Remnant G156.2+5.7. *PASJ*, 51:13–22, Feb. 1999.
- [303] J. M. Yao, R. N. Manchester, and N. Wang. A New Electron Density Model for Estimation of Pulsar and FRB Distances. *ArXiv e-prints*, Oct. 2016.
- [304] A. Yar-Uyaniker, B. Uyaniker, and R. Kothes. Distance of Three Supernova Remnants from H I Line Observations in a Complex Region: G114.3+0.3, G116.5+1.1, and CTB 1 (G116.9+0.2). *ApJ*, 616:247–256, Nov. 2004.
- [305] N. Zacharias, C. T. Finch, T. M. Girard, A. Henden, J. L. Bartlett, D. G. Monet, and M. I. Zacharias. UCAC4 Catalogue (Zacharias+, 2012). *VizieR Online Data Catalog*, 1322:0, July 2012.
- [306] V. E. Zavlin and G. G. Pavlov. XMM observations of three middle-aged pulsars. *Mem. Soc. Astron. Italiana*, 75:458, 2004.
- [307] B. R. Zeiger, W. F. Brisken, S. Chatterjee, and W. M. Goss. Proper Motions of PSRs B1757-24 and B1951+32: Implications for Ages and Associations. *ApJ*, 674:271–277, Feb. 2008.
- [308] X. Zhang, Y. Zheng, T. L. Landecker, and L. A. Higgs. Multi-frequency radio spectral studies of the supernova remnant G 78.2+2.1. *A&A*, 324:641–650, Aug. 1997.
- [309] W. Zhu, V. M. Kaspi, R. Dib, P. M. Woods, F. P. Gavriil, and A. M. Archibald. The Long-Term Radiative Evolution of Anomalous X-Ray Pulsar 1E 2259+586 After Its 2002 Outburst. *ApJ*, 686:520–527, Oct. 2008.

APPENDIX A

IMAGES OF SUPERNOVA REMNANTS

A.1 1420 MHz Images

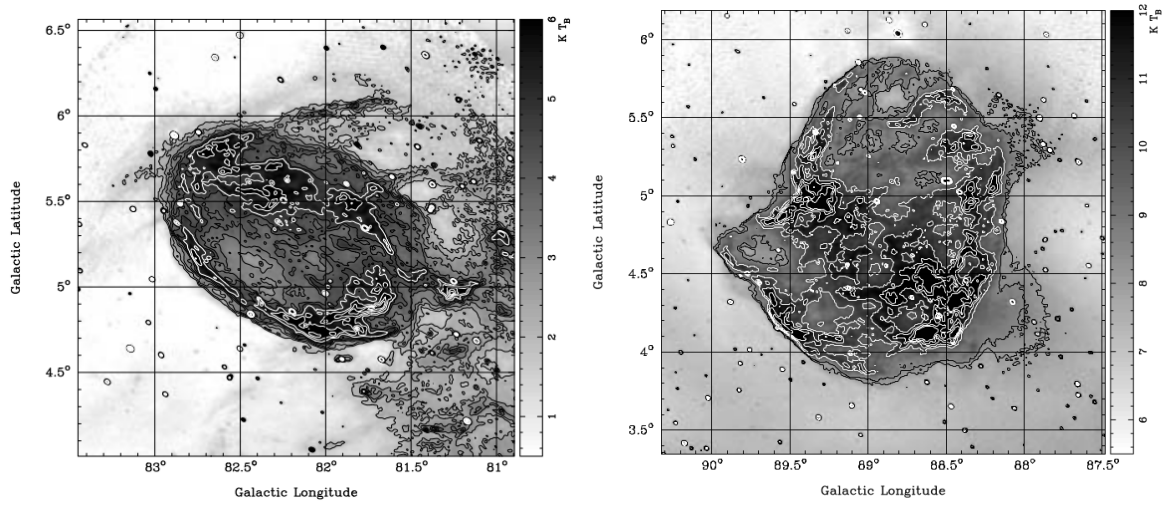


Figure A.1: 1420 MHz images of SNRs W 63 (Left) and HB 21 [140]

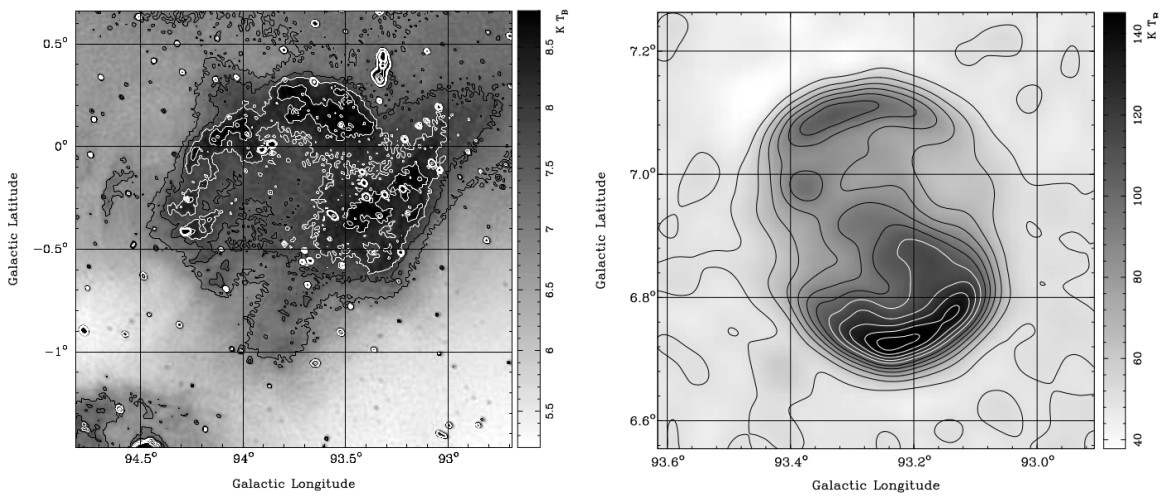


Figure A.2: 1420 MHz images of SNRs HC 40 (Left) and DA 530 [140]

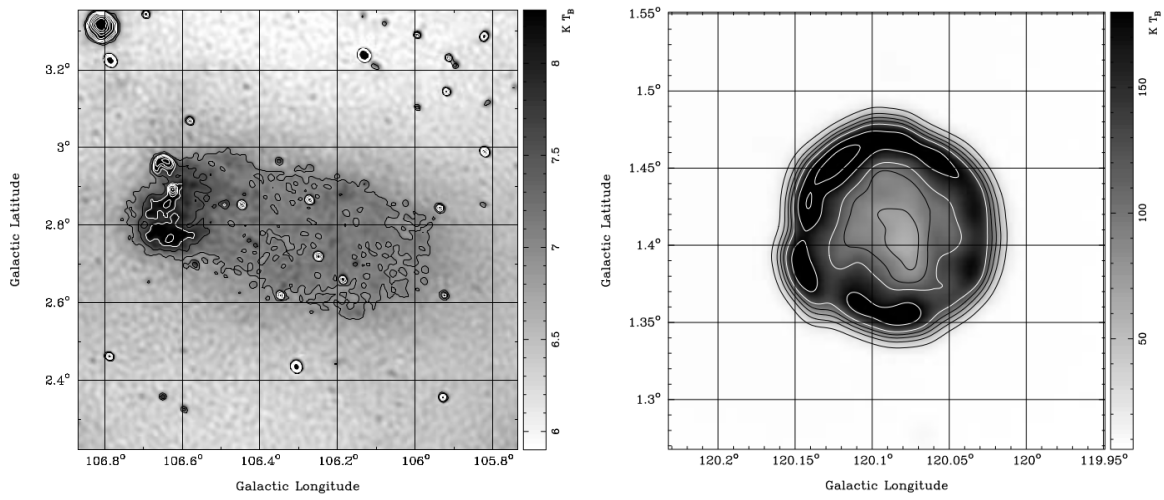


Figure A.3: 1420 MHz images of SNRs G106.3+2.7 (Left) and Tycho [140]

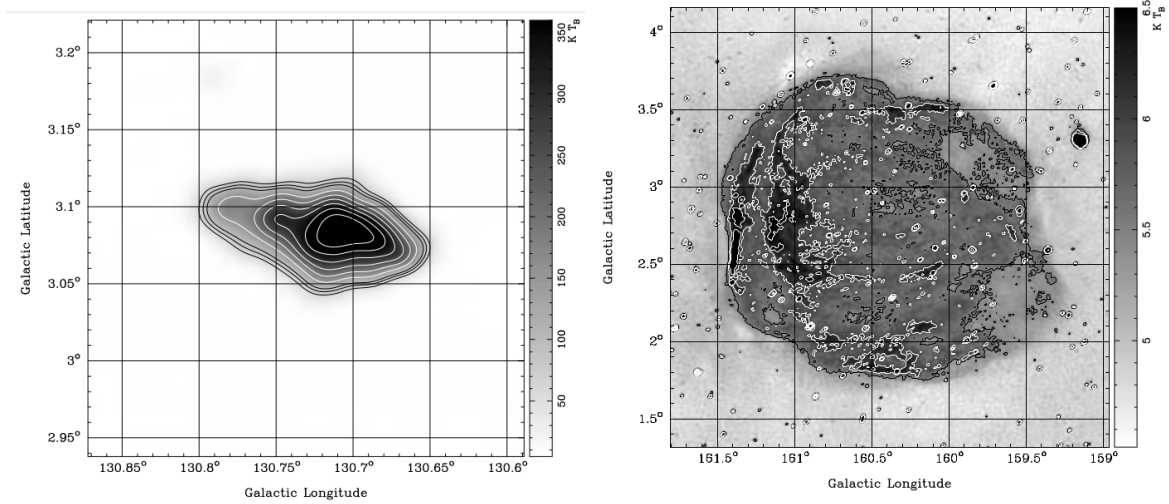


Figure A.4: 1420 MHz images of SNRs SN 1181 (Left) and HB 9 (Right) [140]

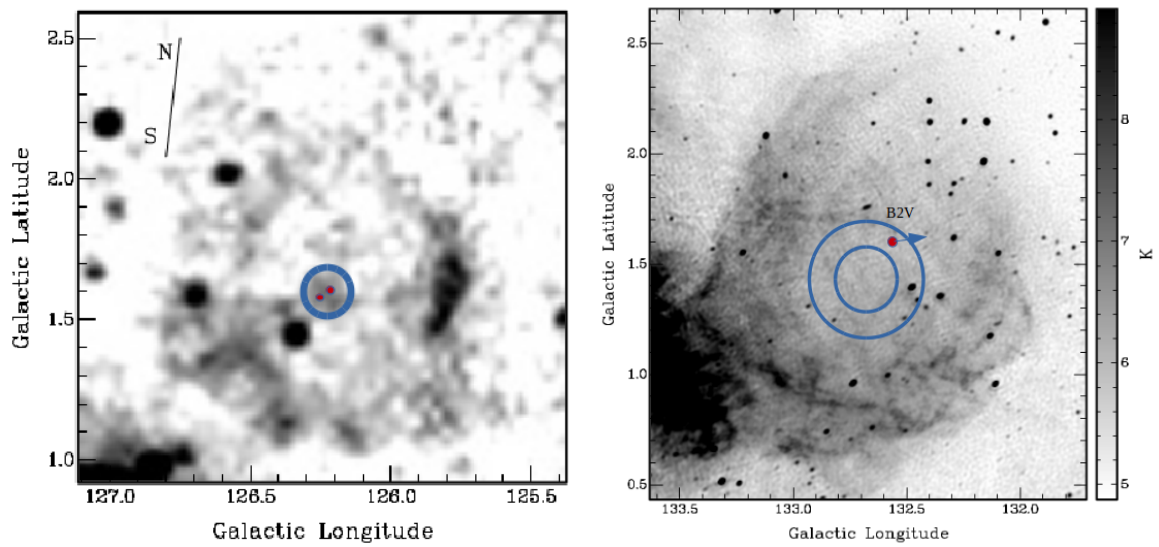


Figure A.5: 1420 MHz images of SNR G126.2+1.6 (Left) and HB 3 (Right). Adapted from [271] and [?] respectively. The blue circles demonstrate the search region. The larger circle on HB 3 is the R/3 region. The B2V potential runaway star is found here. The peculiar motion of the star also points an origin from W 3 massive star forming region. The red dots show the positions of the massive stars TYC 4038-1657-1 (A0Ib) (close to the center) and UCAC 4-772-009430 (B1V) (separated from the center).

A.2 Different Wavebands

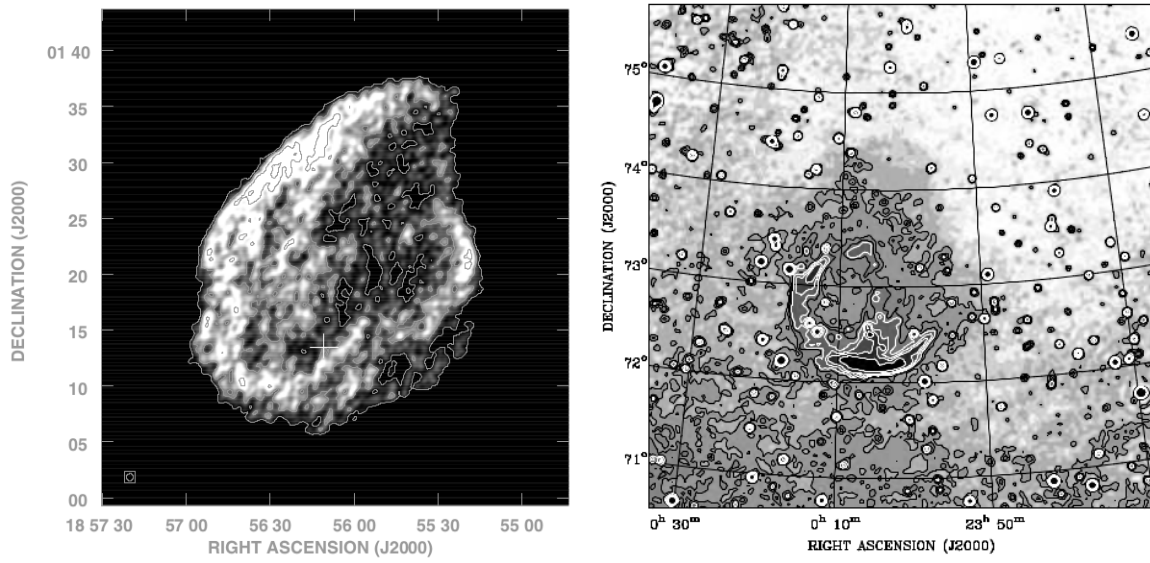


Figure A.6: 74 MHz image of W 44 [?] (Left) and 408 MHz image of CTA 1 [?] (Right)

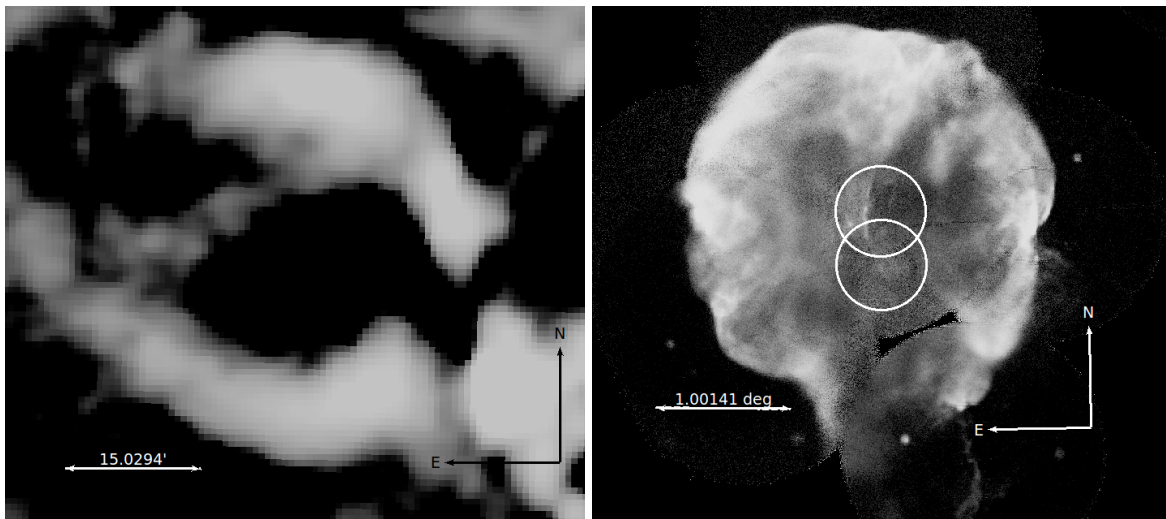


Figure A.7: 4850 MHz image of HC 40 (Left) from GB6/PMN survey and ROSAT PSPC (0.1–2.4 keV) image of Cygnus Loop (Right). Both are obtained from *Skyview*.

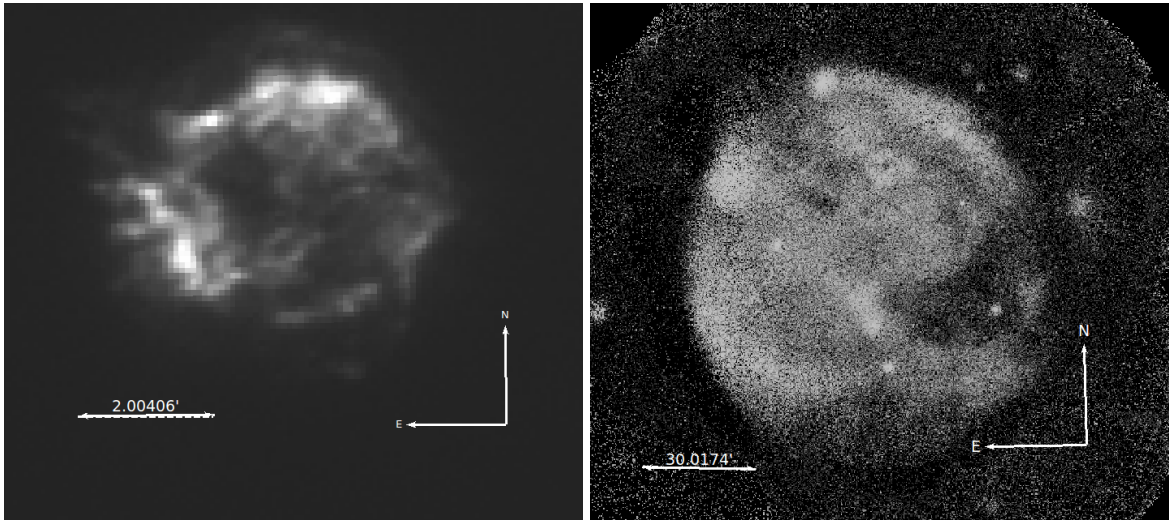


Figure A.8: ROSAT PSPC (0.1–2.4 keV) images of SNRs Cas A (Left) and G156.2+5.7 (Right) retrieved from *Skyview*

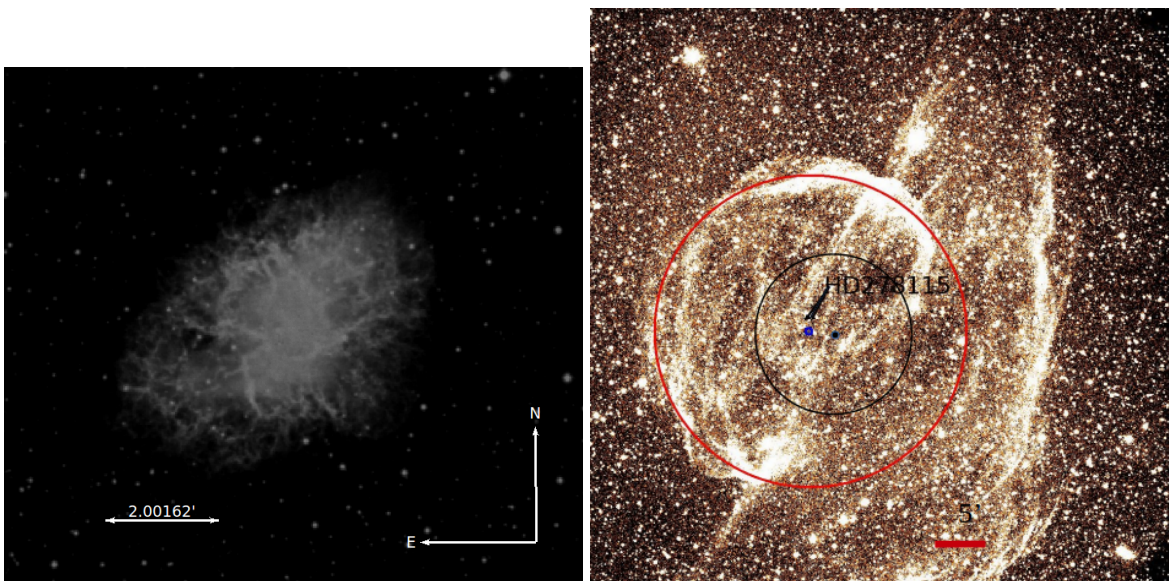


Figure A.9: Crab Nebula (Left) in red band obtained from *Skyview*. H_{α} image of SNR G166.0+4.3 taken at University Observatory of Jena (Right). Black triangle–arrow shows the position of HD 278115. The blue circle shows the geometrical center derived by fitting circles (i.e. the red circle) to the spherical symmetric smaller shell. The black dot is the geometrical center from [86]. The runaway star is search inside R/3 region (black circle) for this remnant. No OB runaway was found.

APPENDIX B

HIGH VELOCITY ISM GAS

In this chapter, the high velocity gas owing to the SNR expansion, detected in the spectra of the stars which are inside or behind the SNRs are demonstrated. The local standard of rest velocities, the EWs and the FWHMs are measured.

Table B.1: High velocity components of the ISM absorption lines owing to SNR IC 443.

Star	Feature	V_{LSR} (km s ⁻¹)	EW (Å)	FWHM (Å)
HD 254577	NaI–D1	20.9	0.86	0.94
	NaI–D1	-23.9	0.44	0.72
	NaI–D2	20.9	0.78	0.86
	NaI–D2	-24.9	0.39	0.69
HD 254477	NaI–D1	24.0	0.69	0.87
	NaI–D1	-43.8	0.88	0.93
	NaI–D2	22.9	0.62	0.74
	NaI–D2	-45.2	0.74	0.84

Table B.2: High velocity components of the ISM absorption lines owing to SNR G166.0+4.3.

Star	Feature	V_{LSR} (km s ⁻¹)	EW (Å)	FWHM (Å)
HD 278115	CaII–K	-84.3	0.075	0.24
	CaII–K	-104.9	0.083	0.17
	CaII–K	-4.2	0.32	0.35
	CaII–K	14.9	0.11	0.2
	CaII–K	118.6	0.15	0.23
	CaII–K	137.7	0.02	0.19
	CaII–H	-105.1	0.03	0.13
	CaII–H	14.4	0.068	0.17
	CaII–H	-3.8	0.21	0.29
	CaII–H	118.7	0.09	0.23

Table B.3: High velocity components of the ISM absorption lines owing to HB 21.

Star	Feature	V_{LSR} (km s $^{-1}$)	EW (\AA)	FWHM (\AA)
TYC 3582-00211-1	Na I–D1	-11.1	0.17	0.22
	Na I–D1	-74.3	0.06	0.16
	Na I–D1	-107.3	0.30	0.30
	Na I–D2	-10.5	0.13	0.19
	Na I–D2	-107.2	0.25	0.29
	Na I–D2	-72.9	0.03	0.15
	Ca II–K	-102	0.15	0.24
	Ca II–K	-72.3	0.06	0.16
	Ca II–K	42.1	0.09	0.2
	Ca II–K	72.6	0.15	0.3
	Ca II–K	59.6	0.04	0.12
	Ca II–H	-103.2	0.08	0.2
	Ca II–H	40.4	0.06	0.24
	Ca II–H	63.1	0.08	0.217
	Ca II–H	79.7	0.08	0.26
	Ca II–H	-73.0	0.02	0.1

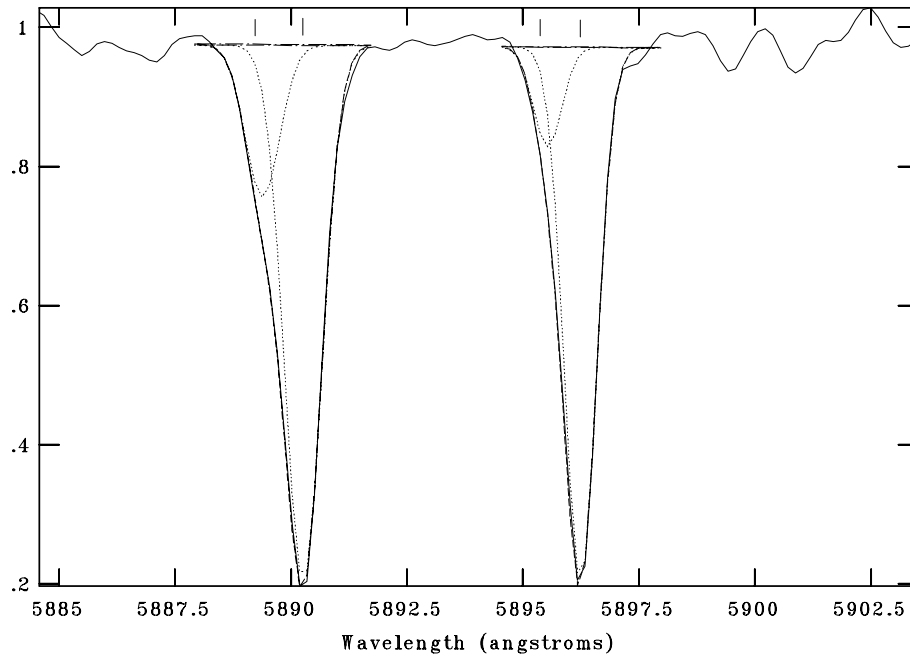
Table B.4: High velocity components of the ISM absorption lines owing to R 5.

Star	Feature	V_{LSR} (km s $^{-1}$)	EW (\AA)	FWHM (\AA)
HD 8768	Na I–D1	-26.0	0.89	1.11
	Na I–D1	-79.9	0.18	0.80
	Na I–D2	-26.9	0.63	0.89
	Na I–D2	-75.8	0.16	0.76

Table B.5: The velocity of the shifted components of the ISM w.r.t the normal ISM component.

Star	Feature	V_{LSR} (km s $^{-1}$)	EW (\AA)	FWHM (\AA)
HD 278115	CaII-K	-80.1	0.075	0.24
	CaII-K	-100.7	0.083	0.17
	CaII-K	19.1	0.11	0.2
	CaII-K	122.8	0.15	0.23
	CaII-K	141.9	0.02	0.19
	CaII-H	-101.3	0.03	0.13
	CaII-H	18.1	0.068	0.17
	CaII-H	122.5	0.09	0.23
TYC 3582-00211-1	NaI-D1	-13.0	0.17	0.22
	NaI-D1	-109.7	0.06	0.16
	NaI-D1	-75.4	0.30	0.30
	NaI-D2	-13.6	0.13	0.19
	NaI-D2	-76.8	0.25	0.29
	NaI-D2	-109.8	0.03	0.15
	CaII-K	-104.5	0.15	0.24
	CaII-K	-74.8	0.06	0.16
	CaII-K	39.6	0.09	0.2
	CaII-K	70.1	0.15	0.3
	CaII-K	57.1	0.04	0.12
	CaII-H	-105.7	0.08	0.2
	CaII-H	37.9	0.06	0.24
	CaII-H	60.6	0.08	0.217
	CaII-H	77.2	0.08	0.26
	CaII-H	-75.5	0.02	0.1
HD 8768	NaI-D1	-53.9	0.18	0.80
	NaI-D2	-49.9	0.16	0.76
HD 254577	NaI-D1	-44.8	0.44	0.72
	NaI-D2	-45.8	0.39	0.69
HD 254477	NaI-D1	-67.7	0.88	0.93
	NaI-D2	-68.2	0.74	0.84

NOAO/IRAF V2.16.1 baha@baha-Lenovo-IdeaPad-Y550 Wed 00:09:22 14-Dec-2016
[hd43582_1703v.fits.0001.fits]: Unknown 1200. ap:1 beam:56



NOAO/IRAF V2.16.1 baha@baha-Lenovo-IdeaPad-Y550 Wed 00:02:33 14-Dec-2016
[hd477.fits]: Unknown 1200. ap:1 beam:56

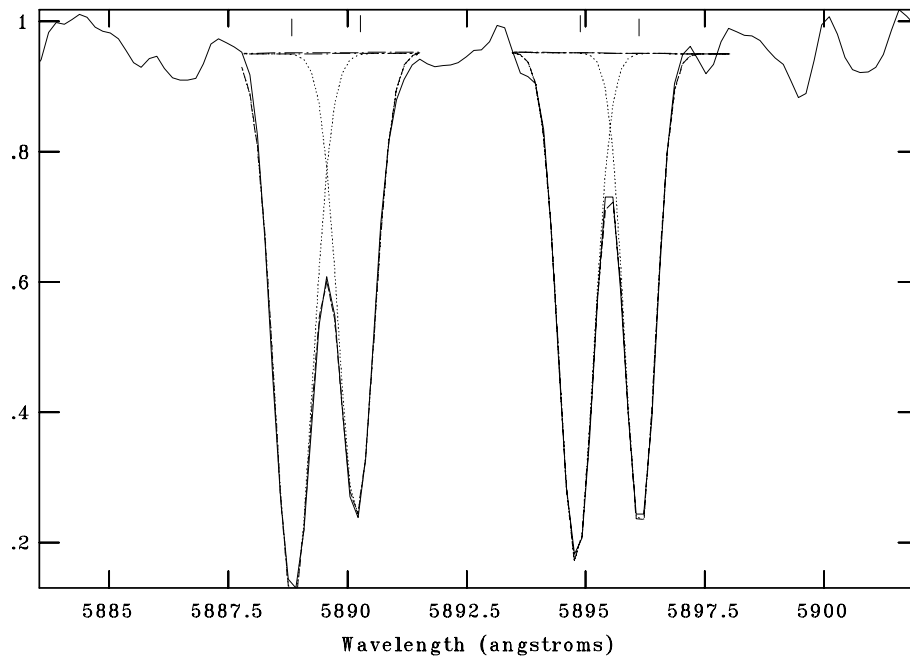


Figure B.1: High velocity gas of IC 443. The NaI lines of HD 43582 and HD 254477 respectively.

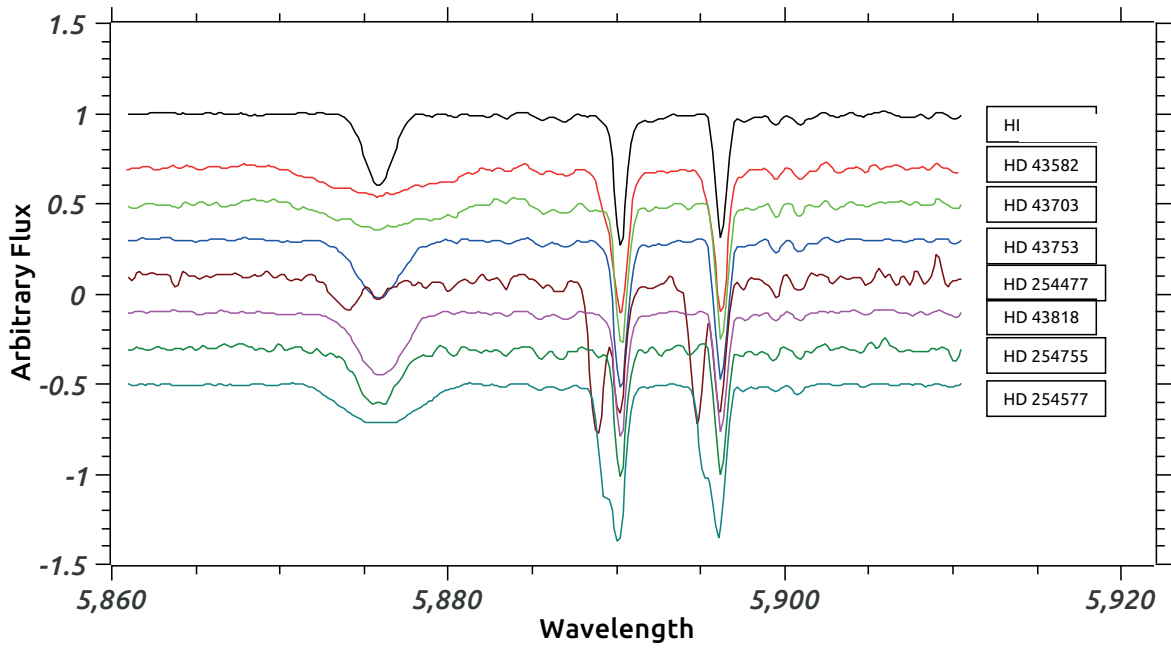


Figure B.2: Stars behind or inside IC 443 shows strong high velocity ISM gas. The broad feature is stellar He I λ 5876. The deeper lines are Na I–D1 & D2.

N/AO/IRAF V2.16.1 baha@baha-Lenovo-IdeaPad-Y550 Tue 22:31:02 13-Dec-2016
 [hd8]: Unknown 600. ap:1 beam:47

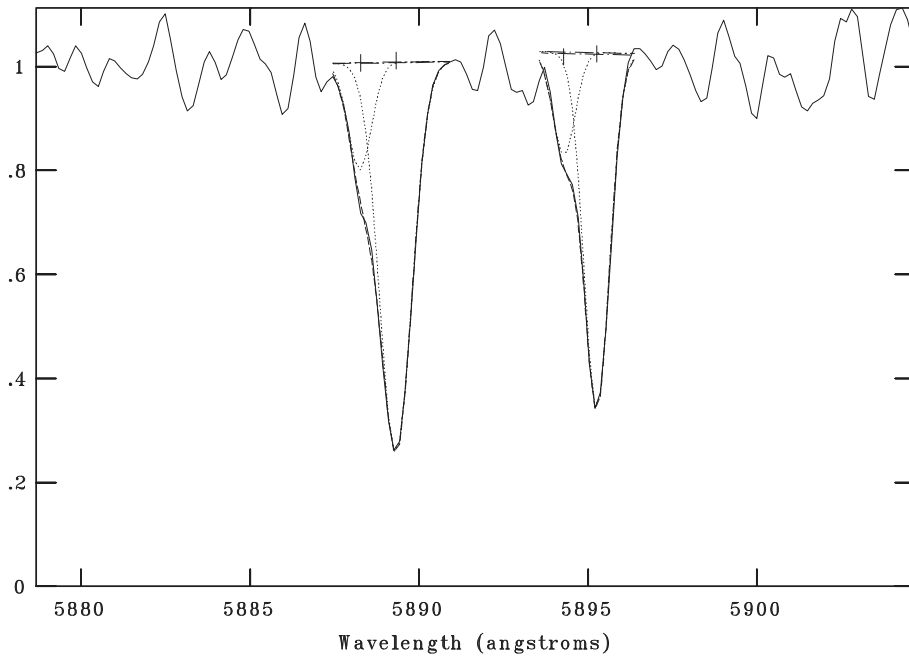
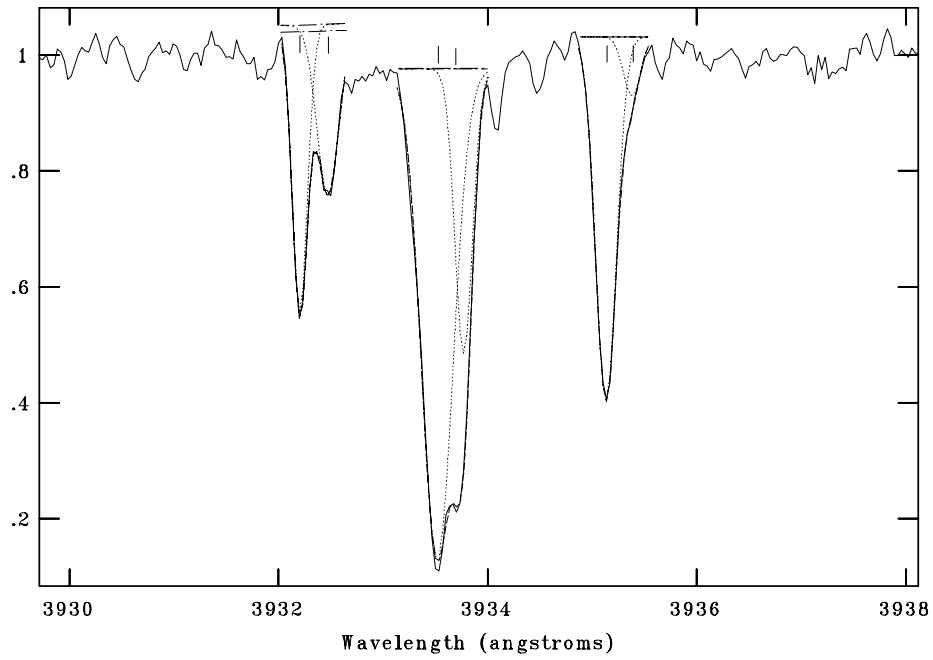


Figure B.3: High velocity gas of R 5. The Na I lines of HD 8768.

NOAO/IRAF V2.16.1 baha@baha-Lenovo-IdeaPad-Y550 Tue 22:45:58 13-Dec-2016
[z2dn.fits[*],2]: TRES Background 1350. ap:2 beam:87



NOAO/IRAF V2.16.1 baha@baha-Lenovo-IdeaPad-Y550 Tue 23:04:19 13-Dec-2016
[z2dn.fits[*],3]: TRES Background 1350. ap:3 beam:86

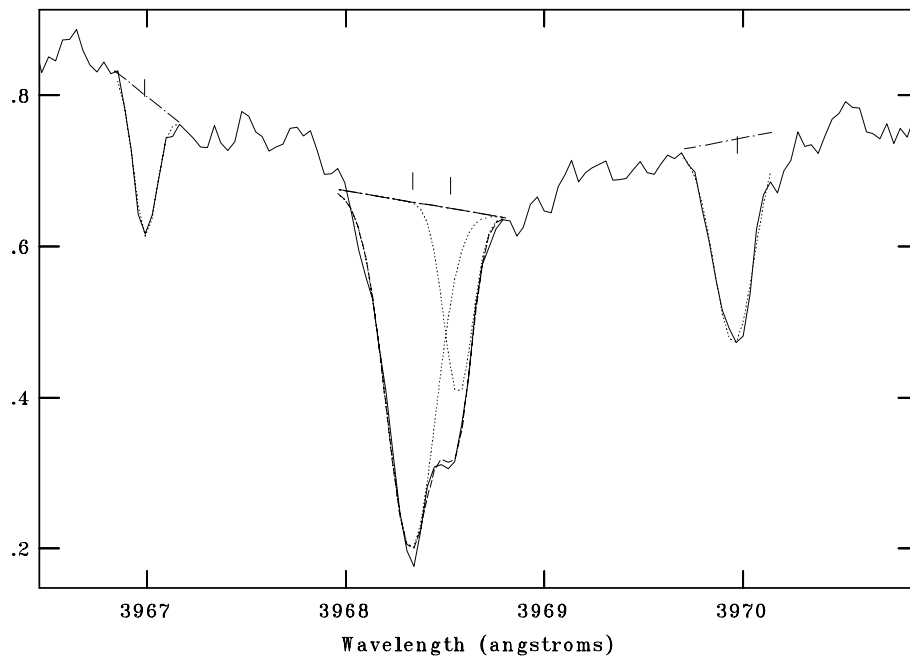
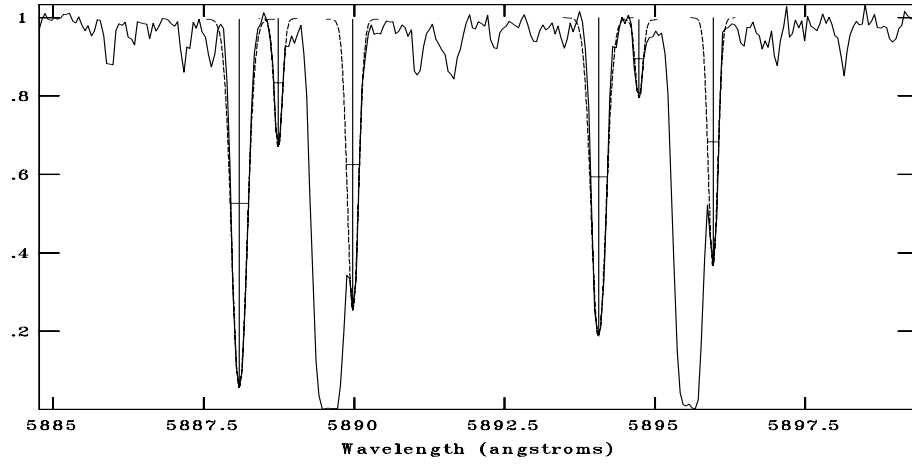
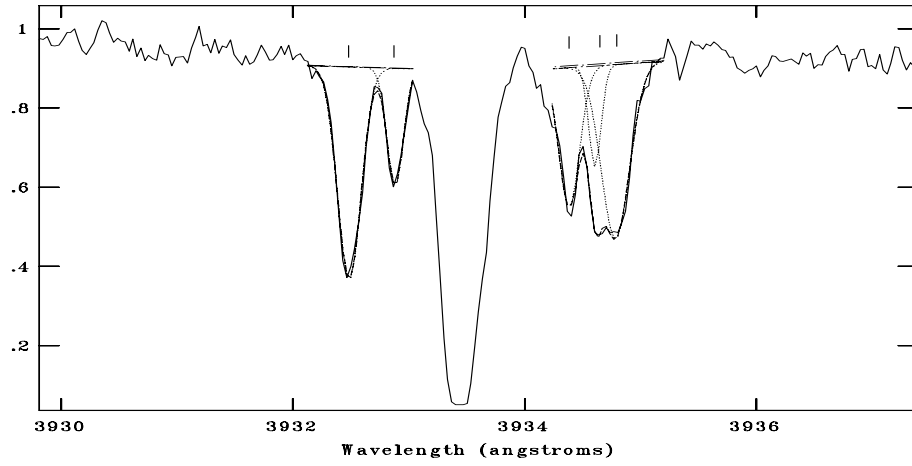


Figure B.4: High velocity gas of SNR G166.0+4.3. The Ca II-K & H lines of HD 278115.

NOAO/IRAF V2.16.1 baha@baha-Lenovo-IdeaPad-Y550 Tue 23:16:01 13-Dec-2016
[tan.fits[*],31]: TRES Background 900. ap:31 beam:58



NOAO/IRAF V2.16.1 baha@baha-Lenovo-IdeaPad-Y550 Tue 23:24:21 13-Dec-2016
[tan.fits[*],2]: TRES Background 900. ap:2 beam:87



NOAO/IRAF V2.16.1 baha@baha-Lenovo-IdeaPad-Y550 Tue 23:31:41 13-Dec-2016
[tan.fits[*],3]: TRES Background 900. ap:3 beam:86

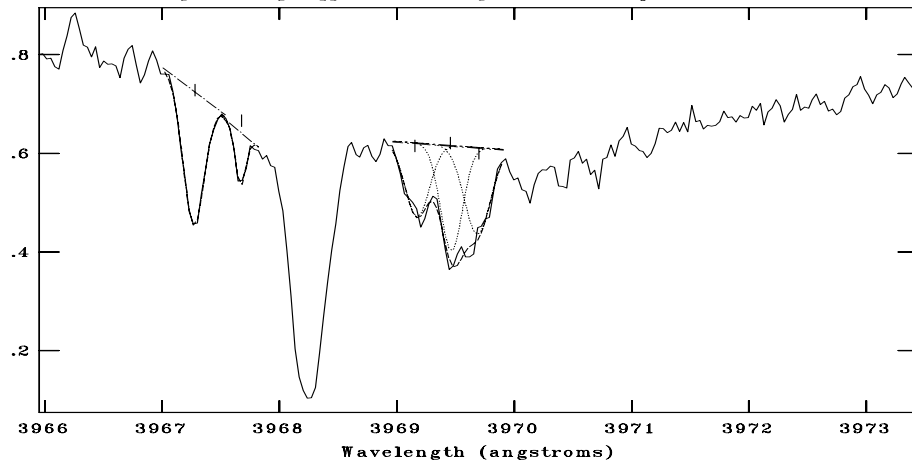


Figure B.5: High velocity gas of HB 21. The NaI, CaII-K & H lines of BD+50 3188

APPENDIX C

LOW RESOLUTION SPECTRA

In this chapter, the complete results of spectral type identification of low resolution spectroscopy are shown (Table C.1). Each spectrum is demonstrated together with the appropriate standard star spectrum. The stars shown here are classified by the host SNRs.

Table C.1: Spectral types determined from low resolution spectroscopy.

SNR	Name	RA	Dec	V	SpT	Tel
G69.0+2.7	615-089671	19:53:42.8	+32:52:26.0	13.94	F6V	C
G69.0+2.7	615-089063	19:52:40.5	+32:52:58.5	12.83	A2V	C
G78.2+2.1	653-092525	20:20:39.3	+40:31:17.6	12.59	B1V	C
G78.2+2.1	653-092507	20:20:30.7	+40:27:36.9	11.22	A6V	C
G78.2+2.1	653-092521	20:20:37.7	+40:29:37.9	13.86	B8V	C
G78.2+2.1	653-092554	20:21:03.1	+40:29:46.4	13.09	F3V	C
G82.2+5.3	678-083025	20:18:29.5	+45:35:10.4	13.65	A9V	C
G82.2+5.3	679-080132	20:18:42.5	+45:39:23.1	12.61	B9V	C
G82.2+5.3	679-080240	20:19:12.1	+45:39:39.9	13.59	F5V	C
G82.2+5.3	678-083187	20:19:22.9	+45:32:24.9	13.32	A4V	C
G82.2+5.3	679-080191	20:18:58.2	+45:39:25.6	10.88	A3V	C
G82.2+5.3	678-083207	20:19:27.3	+45:30:51.3	11.36	A0V	C
G82.2+5.3	677-080274	20:19:05.4	+45:22:19.7	12.18	B1.5V	T
G82.2+5.3	679-080132	20:18:42.5	+45:39:23.1	12.95	B9V	C
G82.2+5.3	678-083011	20:18:25.9	+45:33:44.3	10.18	A2V	C
G82.2+5.3	678-083198	20:19:24.9	+45:31:30.9	12.67	A2V	C
G82.2+5.3	678-083187	20:19:22.9	+45:32:24.9	11.80	A5V	C

...continued

SNR	Name	RA	Dec	V	SpT	Tel
G82.2+5.3	678-083207	20:19:27.3	+45:30:51.3	11.36	A0V	C
G82.2+5.3	678-083036	20:18:33.7	+45:33:48.8	11.00	F2V	C
G89.0+4.7	704-078261	20:46:10.4	+50:37:59.8	13.37	F6V	C
G89.0+4.7	703-081075	20:45:49.9	+50:30:42.4	12.44	A3V	C
G89.0+4.7	703-080795	20:44:27.6	+50:24:36.3	13.75	A1V	C
G89.0+4.7	703-081098	20:45:56.3	+50:30:50.2	13.32	A5V	C
G89.0+4.7	703-081110	20:46:00.8	+50:32:43.7	12.33	B8V	T
G89.0+4.7	703-080938	20:45:08.7	+50:33:00.3	10.22	B2V	T
G89.0+4.7	704-077771	20:43:35.0	+50:45:47.8	9.97	B8V	C
G89.0+4.7	704-078268	20:46:12.2	+50:39:08.4	10.89	A0V	C
G89.0+4.7	703-080682	20:43:55.9	+50:25:45.2	11.14	A0V	C
G89.0+4.7	704-078114	20:45:27.3	+50:40:44.4	10.91	A1V	C
G89.0+4.7	704-077723	20:43:21.5	+50:40:16.9	11.61	A3V	C
G89.0+4.7	703-080556	20:43:19.9	+50:34:51.9	11.05	F5V	C
G93.7-0.2	704-083954	21:29:23.3	+50:47:38.2	13.38	F5V	C
G93.7-0.2	705-085508	21:29:41.2	+50:54:58.9	13.72	A2V	C
G93.7-0.2	705-085345	21:28:46.9	+50:56:39.9	12.02	A3V	C
G93.7-0.2	705-085599	21:30:02.0	+50:52:36.9	12.21	A9V	C
G93.7-0.2	705-085372	21:28:59.1	+50:51:44.6	12.61	A7V	C
G93.7-0.2	705-085563	21:29:55.7	+50:53:25.2	12.75	B6V	C
G93.7-0.2	705-085461	21:29:27.9	+50:56:00.8	13.32	F0V	C
G93.7-0.2	705-085431	21:29:19.5	+50:55:58.9	13.91	A0V	C
G93.7-0.2	705-085427	21:29:18.6	+50:53:13.9	13.22	B8V	C
G93.7-0.2	704-084117	21:30:05.8	+50:45:53.4	13.42	B7V	C
G93.7-0.2	705-085447	21:29:25.2	+50:58:43.5	11.43	A3III-V	C
G93.7-0.2	704-083923	21:29:15.4	+50:45:52.7	11.86	A6V	C
G93.7-0.2	704-083991	21:29:33.3	+50:41:37.7	11.59	B9V	C
G93.7-0.2	705-085564	21:29:56.1	+50:55:20.2	13.78	B4V	C
G93.7-0.2	705-085474	21:29:31.0	+50:48:28.8	13.22	B9V	T
G93.7-0.2	704-084001	21:29:36.2	+50:46:31.2	13.24	A0V	C

... continued

SNR	Name	RA	Dec	V	SpT	Tel
G93.7-0.2	705-085595	21:30:01.0	+50:49:04.3	12.13	B9V	C
G93.7-0.2	705-085587	21:30:00.3	+50:52:43.1	10.12	B8V	C
G93.7-0.2	705-085540	21:29:50.1	+50:52:55.3	13.75	F8V	C
G93.7-0.2	705-085590	21:30:00.5	+50:53:06.8	13.64	A3III-V	C
G106.3+2.7	754-073561	22:27:23.6	+60:46:15.5	13.03	A6V	C
G106.3+2.7	754-073653	22:28:20.0	+60:43:01.1	11.56	A9V	T
G109.1-1.0	745-080772	23:01:28.4	+58:52:53.9	13.99	B7V	T
G109.1-1.0	745-080881	23:01:50.7	+58:52:56.9	12.75	A3V	C
G109.1-1.0	745-080935	23:02:04.3	+58:52:44.0	11.77	B7V	T
G109.1-1.0	745-080787	23:01:32.5	+58:55:07.8	11.99	A1V	C
G109.1-1.0	745-080774	23:01:29.5	+58:53:57.5	13.52	A3V	C
G109.1-1.0	745-080963	23:02:10.6	+58:53:30.2	12.16	F1V	C
G109.1-1.0	745-080849	23:01:45.6	+58:48:13.5	11.52	A3V	C
G114.3+0.3	760-074418	23:37:09.1	+61:57:34.7	13.60	A3V	C
G114.3+0.3	760-074536	23:38:03.2	+61:55:25.9	12.52	B1V	C
G114.3+0.3	761-072876	23:38:08.3	+62:00:31.1	11.77	A0V	C
G114.3+0.3	761-072674	23:36:25.9	+62:03:58.2	11.94	B8V	T
G114.3+0.3	761-072827	23:38:43.5	+62:03:21.1	13.40	B6V	T
G114.3+0.3	759-074519	23:37:22.7	+61:40:23.9	10.86	B2V	T
G116.9+0.2	762-075495	23:59:06.1	+62:20:01.3	12.86	B5V	C
G116.9+0.2	763-076928	23:58:37.5	+62:27:59.0	12.62	B5V	C
G116.9+0.2	763-077172	23:59:29.4	+62:30:44.2	12.29	A1V	C
G116.9+0.2	762-075534	23:59:13.1	+62:23:04.5	13.95	F0V	C
G116.9+0.2	762-075377	23:58:40.6	+62:21:18.8	13.73	A2V	C
G116.9+0.2	763-077093	23:59:11.3	+62:30:49.7	13.84	A2V	C
G116.9+0.2	763-077125	23:59:18.3	+62:28:41.8	13.13	F0V	C
G116.9+0.2	763-077195	23:59:36.0	+62:26:36.0	13.16	A5V	C
G116.9+0.2	763-077148	23:59:24.1	+62:30:22.8	13.32	A2V	C
G116.9+0.2	762-075588	23:59:24.6	+62:20:47.2	9.69	B9V	C
G116.9+0.2	763-077153	23:59:24.9	+62:29:03.7	13.24	B9V	C

...continued

SNR	Name	RA	Dec	V	SpT	Tel
G116.9+0.2	763-077012	23:58:51.7	+62:27:25.8	13.75	B8V	C
G116.9+0.2	763-077202	23:59:38.9	+62:35:19.2	12.72	B7V	C
G116.9+0.2	762-000129	00:00:29.6	+62:16:20.9	12.13	B9V	C
G116.9+0.2	763-076740	23:58:00.9	+62:28:29.3	12.78	B9V	C
G116.9+0.2	762-000278	00:01:01.3	+62:21:52.7	12.72	B9V	C
G116.9+0.2	763-000154	00:00:36.5	+62:35:41.5	11.78	B7V	C
G116.9+0.2	762-075659	23:59:42.2	+62:18:22.0	12.26	B4V	C
G116.9+0.2	763-077199	23:59:38.1	+62:30:37.0	10.61	A7V	T
G116.9+0.2	762-075426	23:58:49.9	+62:23:44.8	11.46	A0V	T
G126.2+1.6	772-009343	01:21:37.6	+64:12:37.2	13.03	A3V	C
G126.2+1.6	772-009483	01:22:48.1	+64:18:52.8	13.47	F2V	C
G126.2+1.6	772-009430	01:22:14.3	+64:17:58.1	12.78	B2V	T
G126.2+1.6	772-009467	01:22:39.3	+64:16:53.3	13.64	B1V	C
G126.2+1.6	771-009610	01:22:45.6	+64:07:11.1	13.52	A2V	C
G126.2+1.6	772-009227	01:20:45.7	+64:23:53.0	11.61	B9V	C
G126.2+1.6	771-009642	01:23:17.6	+64:09:17.6	13.15	A8V	C
G126.2+1.6	772-009224	01:20:43.8	+64:15:56.6	11.71	A2V	C
G126.2+1.6	772-009499	01:22:57.0	+64:12:29.6	11.36	A8V	C
G126.2+1.6	772-009451	01:22:29.9	+64:12:47.3	13.26	F7V	C
G126.2+1.6	772-009418	01:22:08.6	+64:17:48.4	11.99	F1V	C
G127.1+0.5	767-013562	01:28:03.1	+63:16:57.2	9.13	B0V	C
G127.1+0.5	767-013623	01:28:21.1	+63:13:12.5	11.07	B8V	T
G127.1+0.5	766-013622	01:27:16.8	+63:08:55.8	11.54	B7V	C
G127.1+0.5	766-013684	01:27:49.5	+63:04:35.0	12.13	A1V	C
G127.1+0.5	767-013562	01:28:03.1	+63:16:57.1	9.13	B0V	C
G127.1+0.5	767-013673	01:28:36.6	+63:12:28.0	13.95	A1V	C
G127.1+0.5	766-013734	01:28:12.4	+63:09:12.6	13.82	A2V	C
G132.7+1.3	764-021210	02:16:52.1	+62:39:58.8	13.80	A8V	C
G132.7+1.3	765-021792	02:17:12.3	+62:51:51.0	13.59	B7V	C
G132.7+1.3	764-021329	02:18:00.2	+62:45:48.3	12.33	F5V	C

... continued

SNR	Name	RA	Dec	V	SpT	Tel
G132.7+1.3	764-021331	02:18:00.4	+62:41:19.6	13.74	A4V	C
G132.7+1.3	764-021370	02:18:25.7	+62:44:44.0	13.65	B8V	C
G132.7+1.3	764-021388	02:18:35.7	+62:43:49.7	12.36	B9V	C
G132.7+1.3	765-021781	02:17:08.2	+62:57:18.6	11.50	B7V	C
G132.7+1.3	765-021812	02:17:22.3	+62:53:52.4	12.37	B3V	C
G132.7+1.3	764-021488	02:19:29.6	+62:43:31.3	12.93	F5V	C
G132.7+1.3	764-021273	02:17:28.4	+62:38:24.1	13.35	G5V	C
G132.7+1.3	764-021254	02:17:17.6	+62:41:41.6	13.83	A4V	C
G132.7+1.3	764-021397	02:18:39.9	+62:45:24.7	13.64	F6e	C
G132.7+1.3	765-021722	02:16:36.7	+62:53:36.9	13.50	F6V	C
G156.2+5.7	710-035795	04:59:55.1	+51:53:33.6	11.28	A1V	C
G156.2+5.7	710-035809	05:00:09.0	+51:58:09.7	12.89	A0V	C
G156.2+5.7	710-035810	05:00:08.5	+51:59:30.1	12.56	B8V	C
G156.2+5.7	710-035713	04:58:20.0	+51:48:14.6	13.66	A1V	C
G156.2+5.7	709-034542	04:59:10.4	+51:47:39.9	13.16	F5V	C
G156.2+5.7	710-035782	04:59:35.9	+51:53:47.7	13.33	F2V	C
G156.2+5.7	710-035744	04:58:57.2	+51:57:54.1	13.63	F0V	C
G160.9+2.6	683-034093	05:00:31.2	+46:33:27.2	11.19	A1V	C
G160.9+2.6	683-034211	05:01:15.9	+46:33:21.6	10.93	A2V	C
G160.9+2.6	683-034148	05:00:53.9	+46:30:00.6	11.53	A3V	C
G160.9+2.6	685-033089	04:59:09.9	+46:53:35.9	10.63	A0V	C
G160.9+2.6	684-032395	04:59:17.5	+46:47:15.6	10.78	A0V	C
G160.9+2.6	684-032951	05:03:00.9	+46:39:44.1	10.81	A0V	C
G166.0+4.3	666-037743	05:26:37.5	+43:01:10.9	10.12	B0.5V	T
G166.0+4.3	665-037654	05:25:37.1	+42:56:52.4	13.63	A0V	C
G166.0+4.3	665-037919	05:27:02.9	+42:51:47.5	13.97	F4V	C
G166.0+4.3	666-037784	05:26:48.8	+43:00:40.5	12.35	B9V	C
G166.0+4.3	666-037842	05:27:06.4	+43:01:57.2	12.72	A0V	C
G166.0+4.3	665-037914	05:27:01.2	+42:53:20.6	13.62	A1V	C
G166.0+4.3	665-037712	05:25:55.7	+42:48:27.7	13.37	A3V	C

...continued

SNR	Name	RA	Dec	V	SpT	Tel
G166.0+4.3	665-037733	05:26:01.3	+42:58:03.7	13.59	B9V	C
G166.0+4.3	665-037801	05:26:24.8	+42:53:49.7	12.20	A0V	C
G166.0+4.3	665-037807	05:26:26.9	+42:51:32.2	11.93	A0V	C
G166.0+4.3	666-037742	05:26:37.3	+43:00:29.7	13.93	A9V	C
G166.0+4.3	666-037753	05:26:41.5	+43:02:29.0	13.18	F3V	C
G166.0+4.3	665-037911	05:27:00.1	+42:49:42.7	12.87	F5V	C
G166.0+4.3	666-037857	05:27:10.4	+43:02:31.4	13.81	G2V	C
G180.0-1.7	590-020323	05:37:33.3	+27:56:14.5	10.41	F6V	C
G180.0-1.7	590-020251	05:37:5.07	+27:53:12.3	11.05	G2V	C
G180.0-1.7	591-020517	05:38:19.5	+28:05:12.7	11.09	F7V	C
G180.0-1.7	587-019374	05:39:31.7	+27:23:00.9	11.26	F0V	C
G180.0-1.7	588-020228	05:39:11.6	+27:24:35.1	11.29	F2V	C
G180.0-1.7	590-020733	05:40:27.5	+27:51:41.1	11.31	A5V	C
G180.0-1.7	592-020035	05:39:04.3	+28:14:56.9	11.52	A7V	C
G180.0-1.7	589-019826	05:37:14.1	+27:47:25.9	11.72	F2V	C
G180.0-1.7	592-020103	05:39:31.0	+28:18:26.2	11.79	F6V	C
G180.0-1.7	589-019783	05:36:59.5	+27:44:19.5	11.92	F7V	C
G180.0-1.7	589-020390	05:40:33.9	+27:42:29.3	12.18	F4V	C
G180.0-1.7	591-020513	05:38:19.3	+28:07:37.6	11.28	A1V	C
G180.0-1.7	589-020158	05:39:04.4	+27:44:37.2	11.25	B9.5V	T
G180.0-1.7	589-020119	05:38:52.3	+27:44:39.0	11.29	B9.5V	T
G189.1+3.0	563-026606	06:16:50.0	+22:32:02.3	13.97	G3V	C
G189.1+3.0	563-026625	06:16:58.8	+22:35:58.4	13.41	B3V	C
G189.1+3.0	563-026556	06:16:24.8	+22:26:25.3	12.24	A1V	C
G189.1+3.0	563-026710	06:17:31.7	+22:24:56.7	13.42	B6V	C
G189.1+3.0	564-025691	06:17:07.8	+22:42:20.3	13.00	B5V	C
G189.1+3.0	563-026587	06:16:39.2	+22:27:49.9	12.92	F0V	C
G189.1+3.0	564-025653	06:16:53.3	+22:44:27.2	11.70	B2V	C
G189.1+3.0	563-026583	06:16:37.8	+22:32:23.5	11.47	G0V	C
G189.1+3.0	562-026666	06:16:47.3	+22:22:54.4	12.38	G3V	C

...continued

SNR	Name	RA	Dec	V	SpT	Tel
G189.1+3.0	564-025656	06:16:54.8	+22:40:39.1	12.82	F4V	C
G189.1+3.0	564-025691	06:17:07.8	+22:42:20.2	13.01	B5V	C
G189.1+3.0	564-025754	06:17:29.3	+22:43:38.7	13.07	G3V	C
G189.1+3.0	563-026599	06:16:48.4	+22:31:57.3	12.65	A2V	T
G189.1+3.0	563-026616	06:16:56.2	+22:29:46.6	12.55	A1V	T

C.1 G069.0+2.7

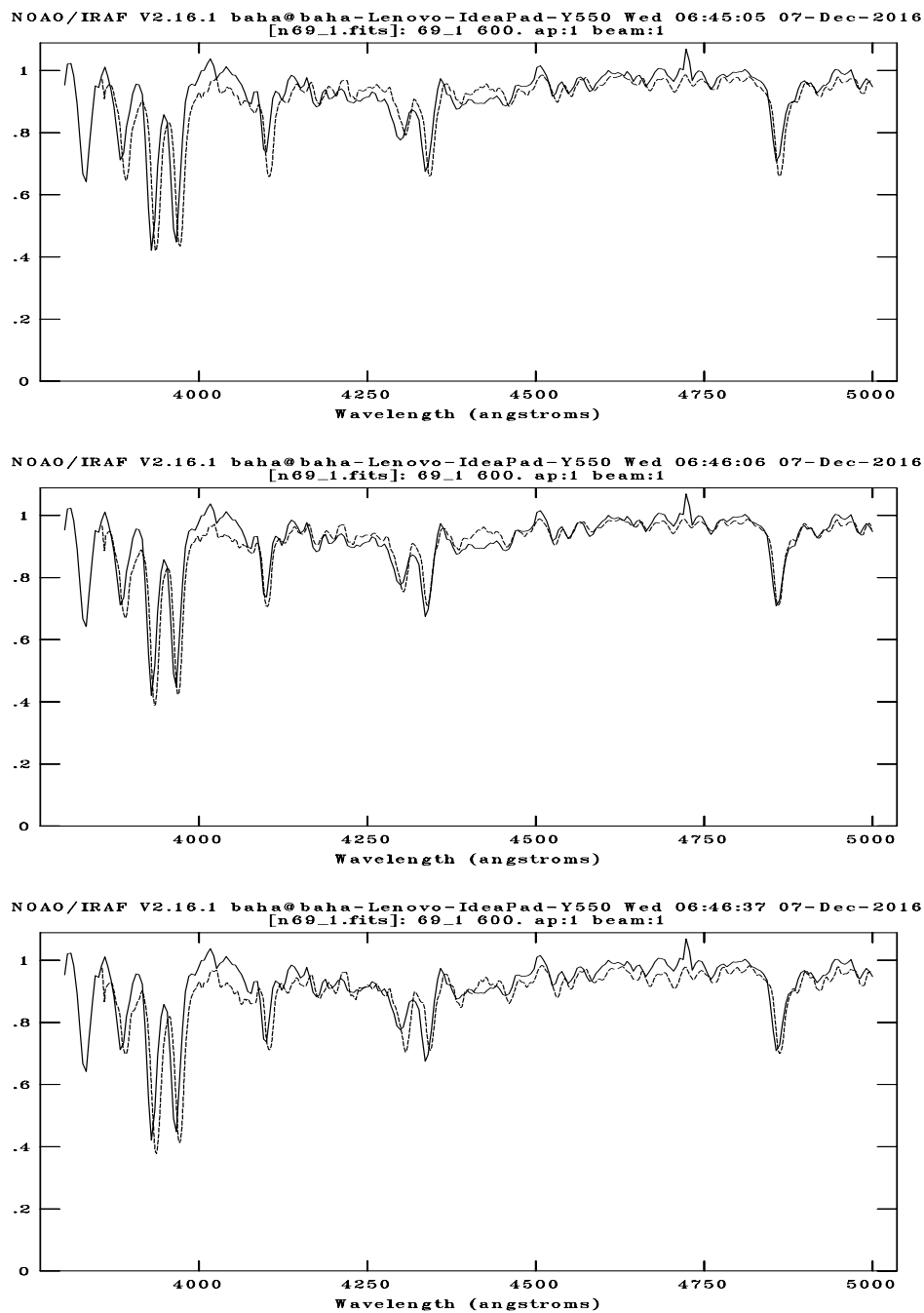
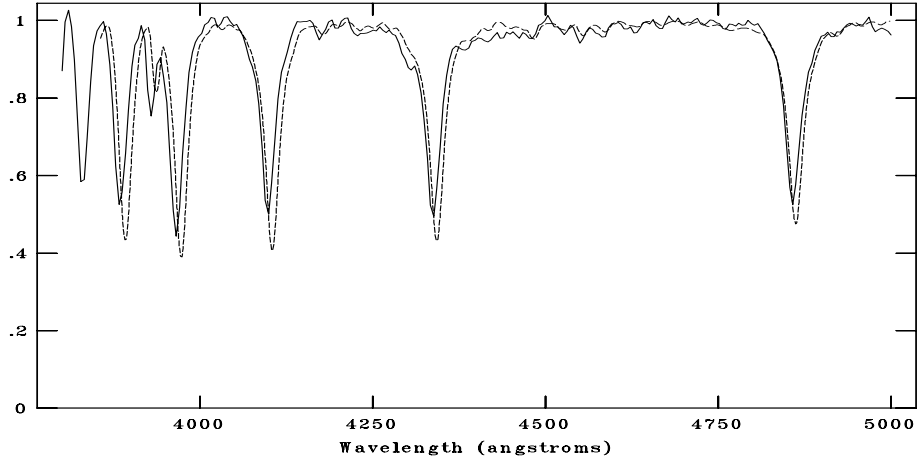
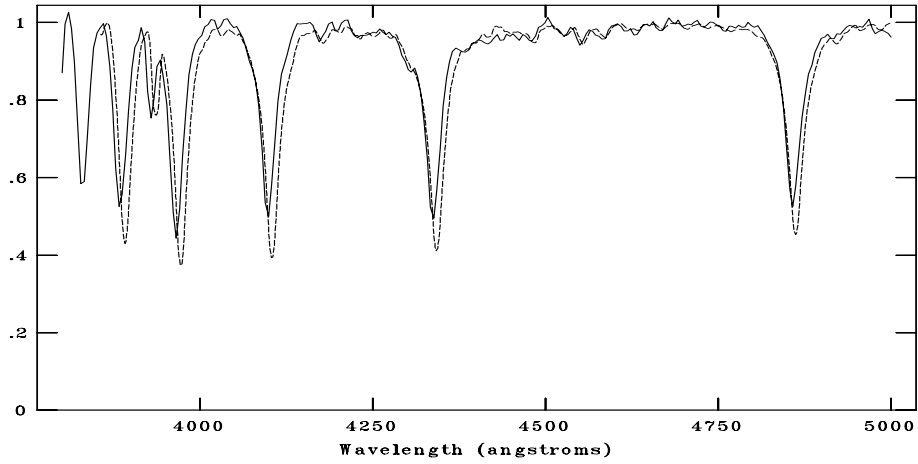


Figure C.1: CAFOS spectrum of 615-089671 compared with F5V, F6V, F8V respectively. The standard spectra are shown with dotted line. The spectral type is assigned as F6V.

NOAO/IRAF V2.16.1 baha@baha-Lenovo-IdeaPad-Y550 Mon 15:20:48 05-Dec-2016
[n069_b.fits]: 069_b 300. ap:1 beam:1



NOAO/IRAF V2.16.1 baha@baha-Lenovo-IdeaPad-Y550 Mon 15:21:12 05-Dec-2016
[n069_b.fits]: 069_b 300. ap:1 beam:1



NOAO/IRAF V2.16.1 baha@baha-Lenovo-IdeaPad-Y550 Mon 15:21:26 05-Dec-2016
[n069_b.fits]: 069_b 300. ap:1 beam:1

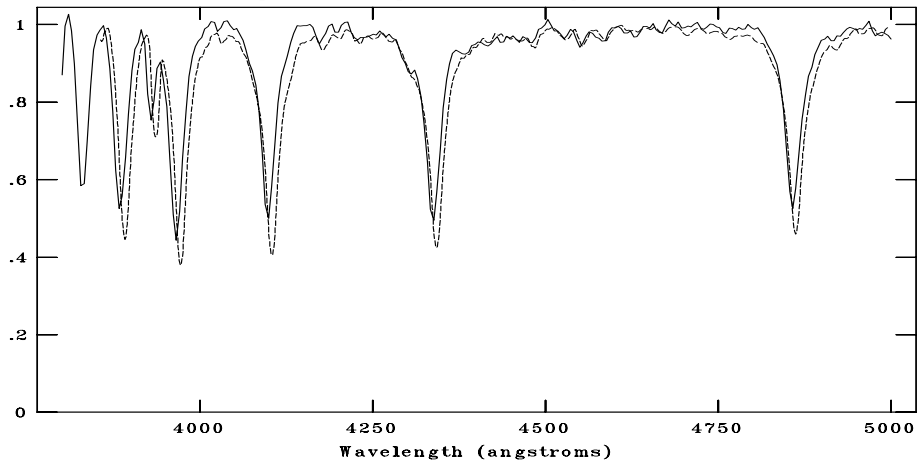


Figure C.2: CAFOS spectrum of 615-089063 compared with A1V, A3V, A5V respectively. The standard spectra are shown with dotted line. The spectral type is assigned as A2V.

C.2 G078.2+2.1

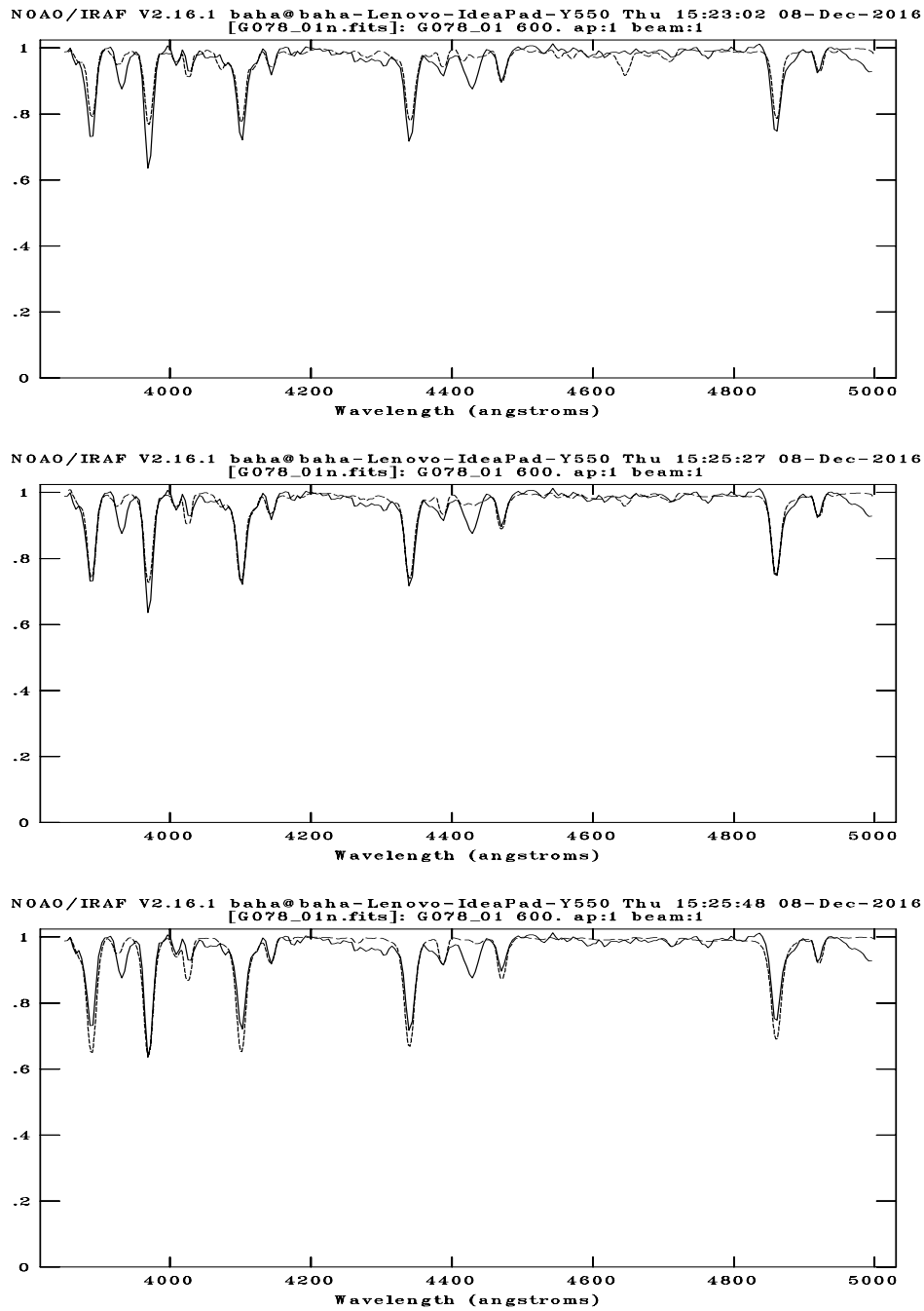
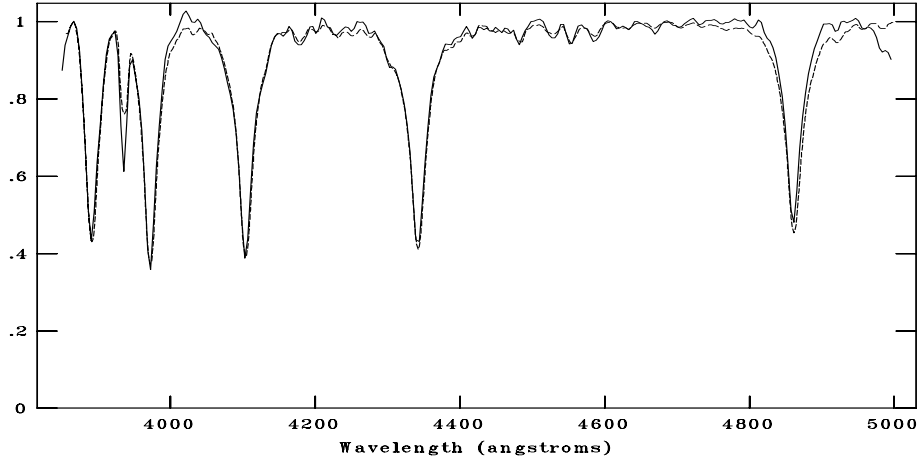
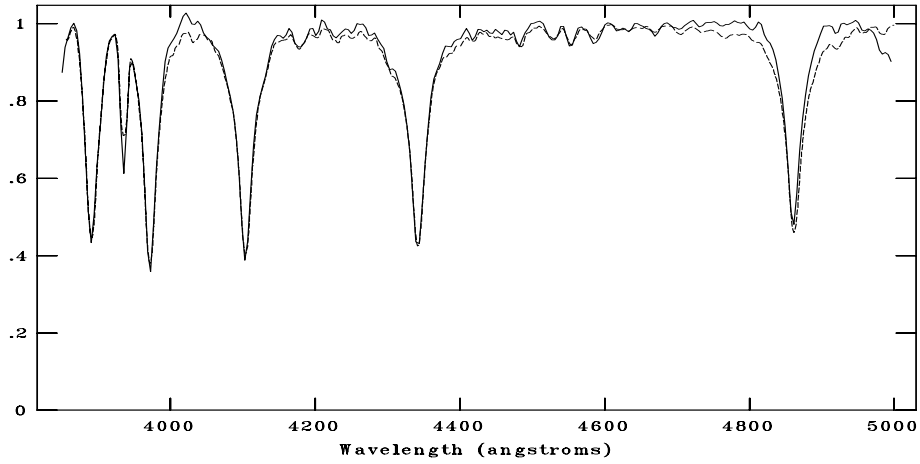


Figure C.3: CAFOS spectrum of 653-092525 compared with B0.5III, B1V, B2V respectively. The standard spectra are shown with dotted line. The spectral type is assigned as B1V.

NOAO/IRAF V2.16.1 baha@baha-Lenovo-IdeaPad-Y550 Thu 15:26:37 08-Dec-2016
[G078_02n.fits]: G078_02 240. ap:1 beam:1



NOAO/IRAF V2.16.1 baha@baha-Lenovo-IdeaPad-Y550 Thu 15:26:24 08-Dec-2016
[G078_02n.fits]: G078_02 240. ap:1 beam:1



NOAO/IRAF V2.16.1 baha@baha-Lenovo-IdeaPad-Y550 Thu 15:26:49 08-Dec-2016
[G078_02n.fits]: G078_02 240. ap:1 beam:1

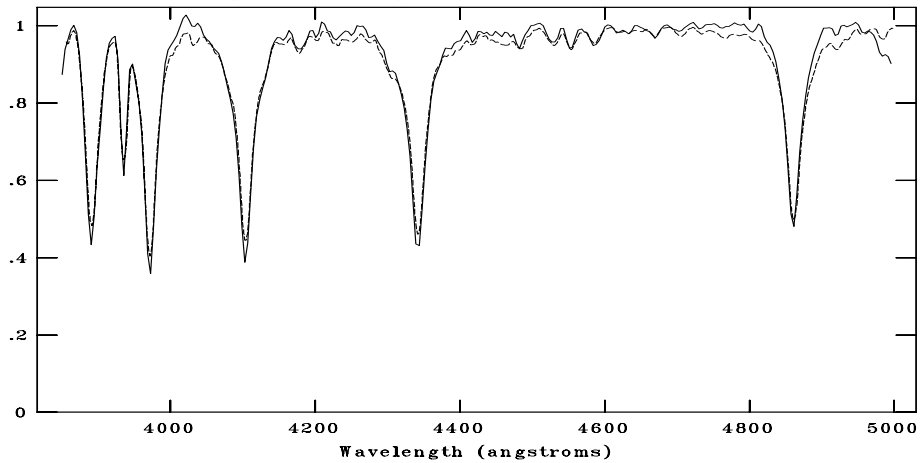
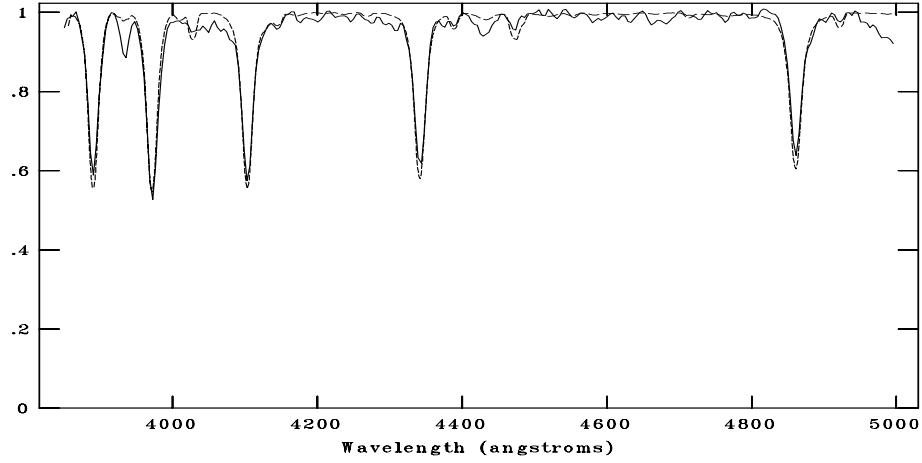
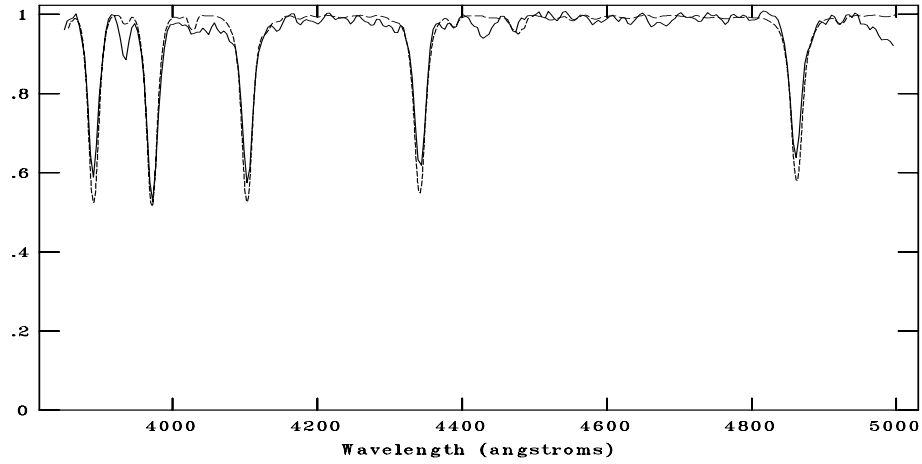


Figure C.4: CAFOS spectrum of 653-092507 compared with A3V, A5V, A7V respectively. The standard spectra are shown with dotted line. The spectral type is assigned as A6V.

NOAO/IRAF V2.16.1 baha@baha-Lenovo-IdeaPad-Y550 Thu 15:28:11 08-Dec-2016
[G078_03n.fits]: G078_03 1200. ap:1 beam:1



NOAO/IRAF V2.16.1 baha@baha-Lenovo-IdeaPad-Y550 Thu 15:27:51 08-Dec-2016
[G078_03n.fits]: G078_03 1200. ap:1 beam:1



NOAO/IRAF V2.16.1 baha@baha-Lenovo-IdeaPad-Y550 Thu 15:28:46 08-Dec-2016
[G078_03n.fits]: G078_03 1200. ap:1 beam:1

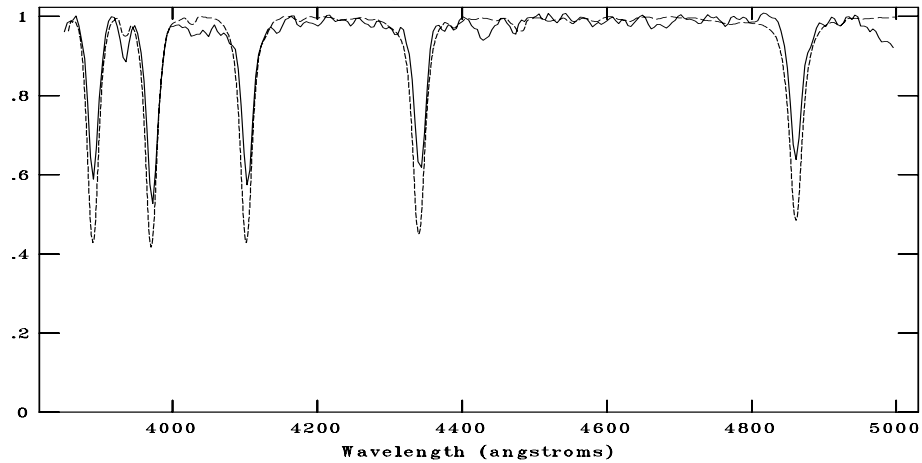
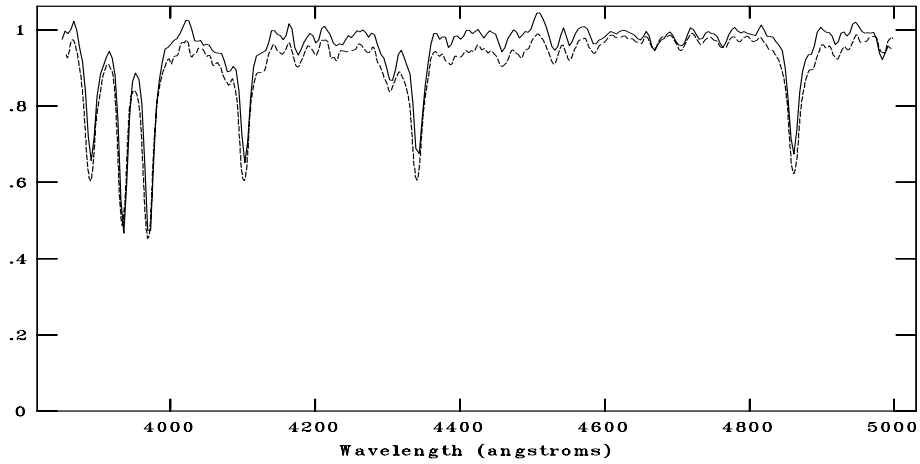
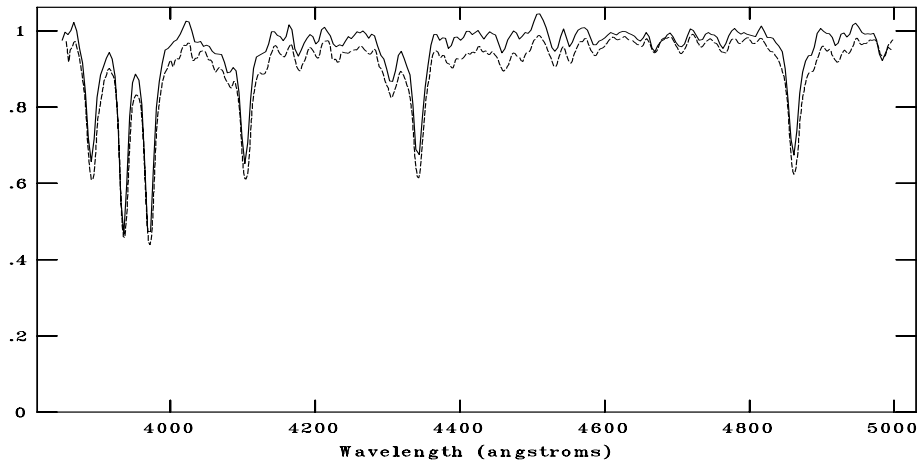


Figure C.5: CAFOS spectrum of 653-092521 compared with , , respectively. The standard spectra are shown with dotted line. The spectral type is assigned as B8V.

NOAO/IRAF V2.16.1 baha@baha-Lenovo-IdeaPad-Y550 Thu 16:01:58 08-Dec-2016
[G078_04n.fits]: G078_04 900. ap:1 beam:1



NOAO/IRAF V2.16.1 baha@baha-Lenovo-IdeaPad-Y550 Thu 16:02:23 08-Dec-2016
[G078_04n.fits]: G078_04 900. ap:1 beam:1



NOAO/IRAF V2.16.1 baha@baha-Lenovo-IdeaPad-Y550 Thu 16:02:37 08-Dec-2016
[G078_04n.fits]: G078_04 900. ap:1 beam:1

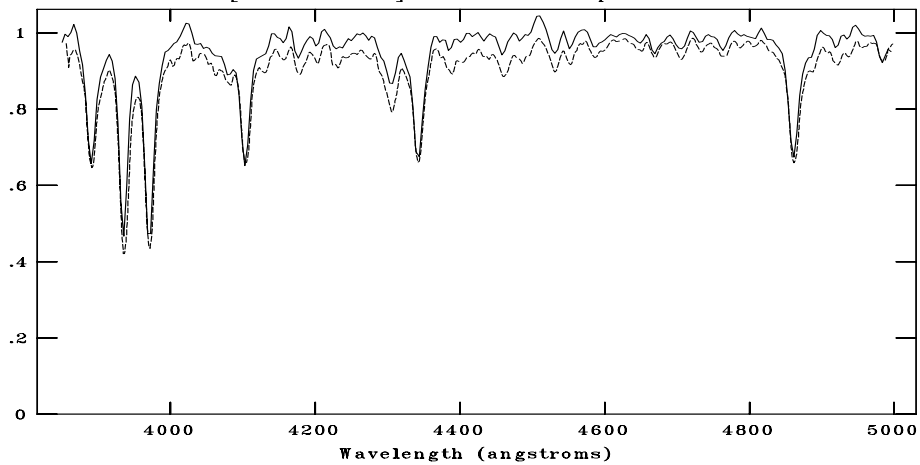


Figure C.6: CAFOS spectrum of 653-092554 compared with , , respectively. The standard spectra are shown with dotted line. The spectral type is assigned as F3V.

C.3 G082.2+5.3

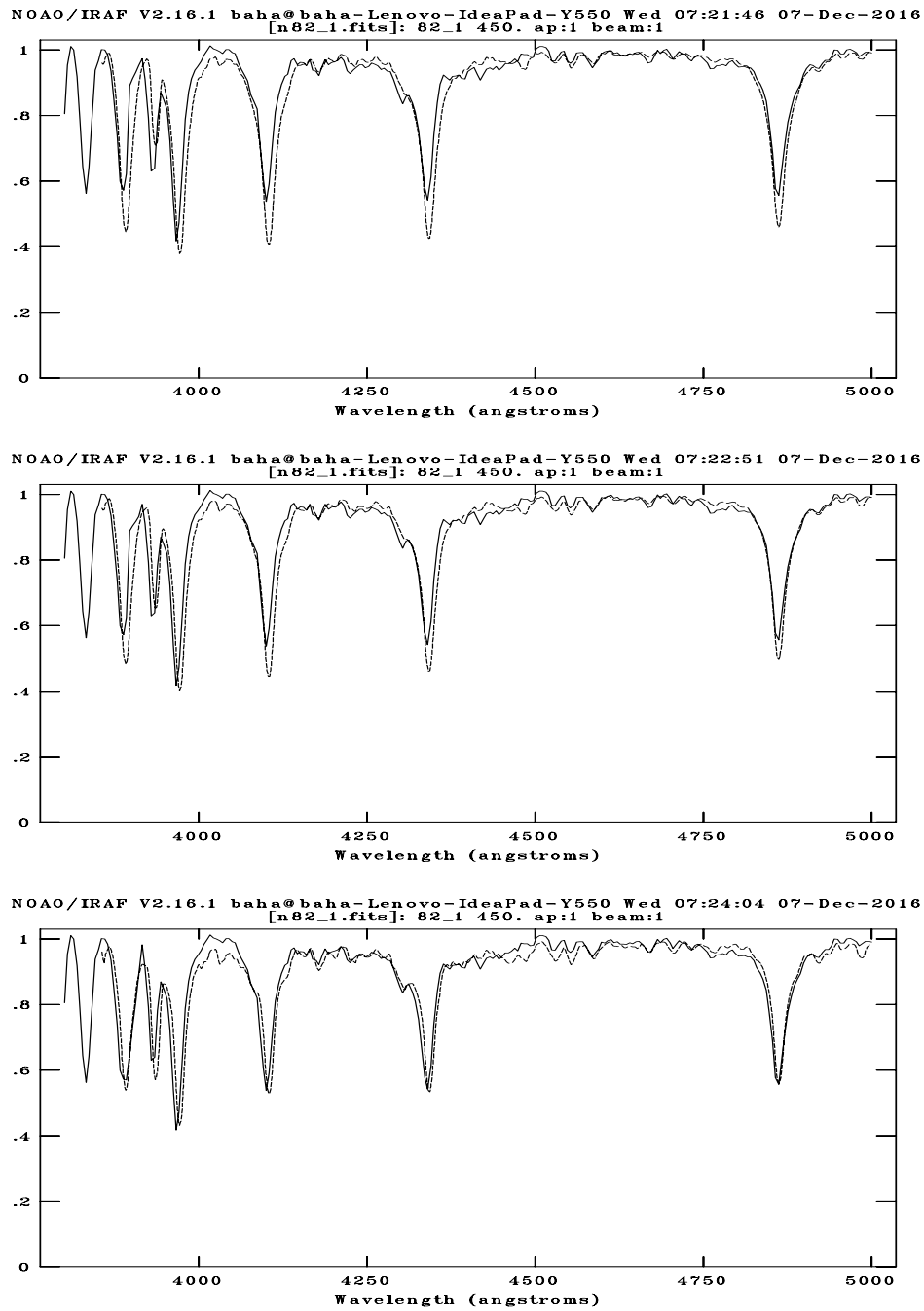
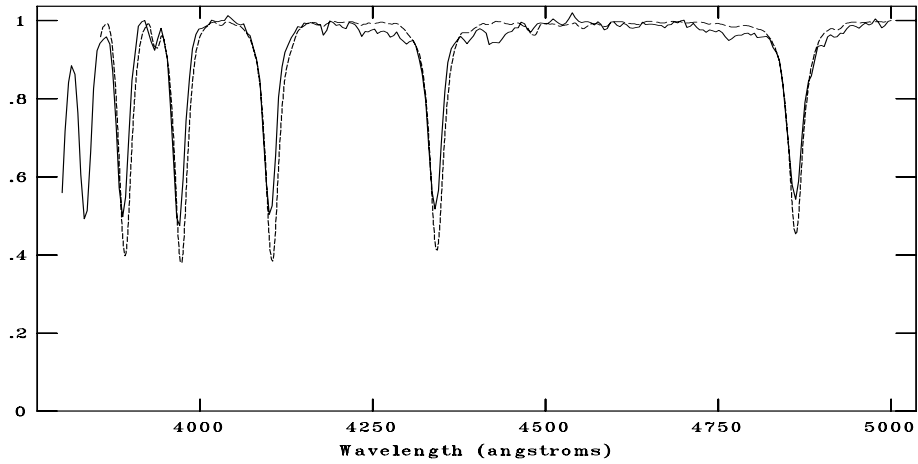
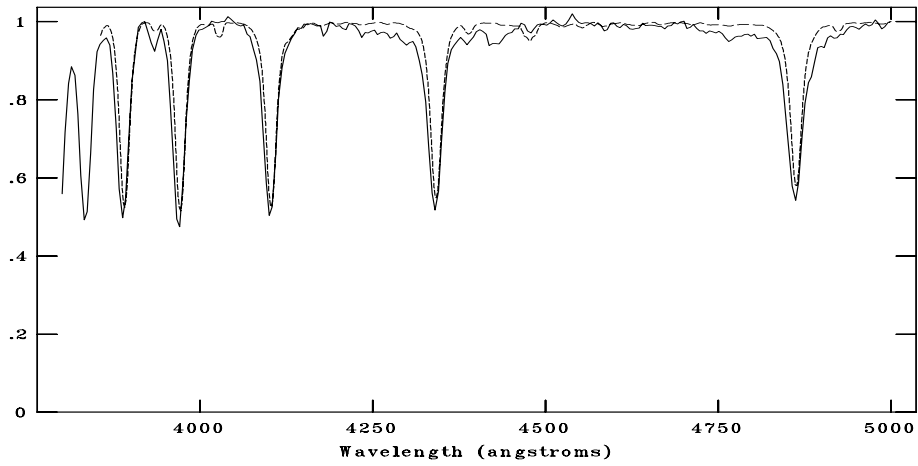


Figure C.7: CAFOS spectrum of 678-083025 compared with A5V, A7V, F0V respectively. The standard spectra are shown with dotted line. The spectral type is assigned as A9V.

NOAO/IRAF V2.16.1 baha@baha-Lenovo-IdeaPad-Y550 Wed 07:26:19 07-Dec-2016
[n82_2.fits]: 82_2 300. ap:1 beam:1



NOAO/IRAF V2.16.1 baha@baha-Lenovo-IdeaPad-Y550 Wed 07:26:53 07-Dec-2016
[n82_2.fits]: 82_2 300. ap:1 beam:1



NOAO/IRAF V2.16.1 baha@baha-Lenovo-IdeaPad-Y550 Wed 07:25:45 07-Dec-2016
[n82_2.fits]: 82_2 300. ap:1 beam:1

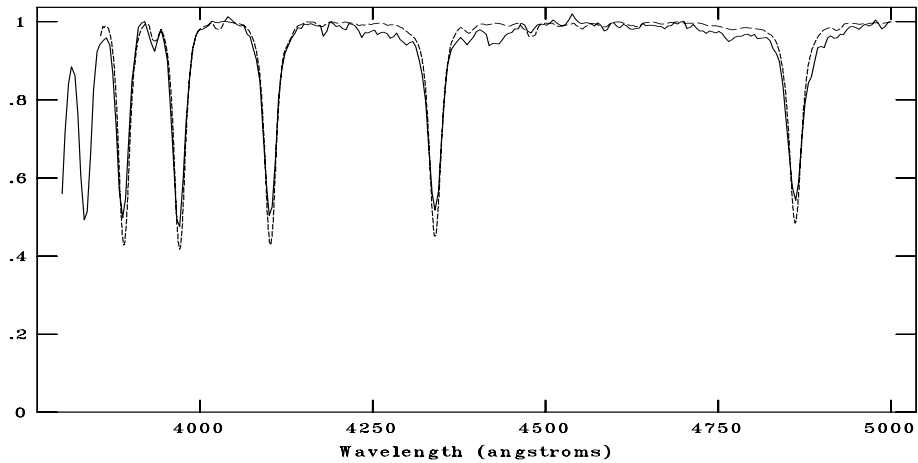
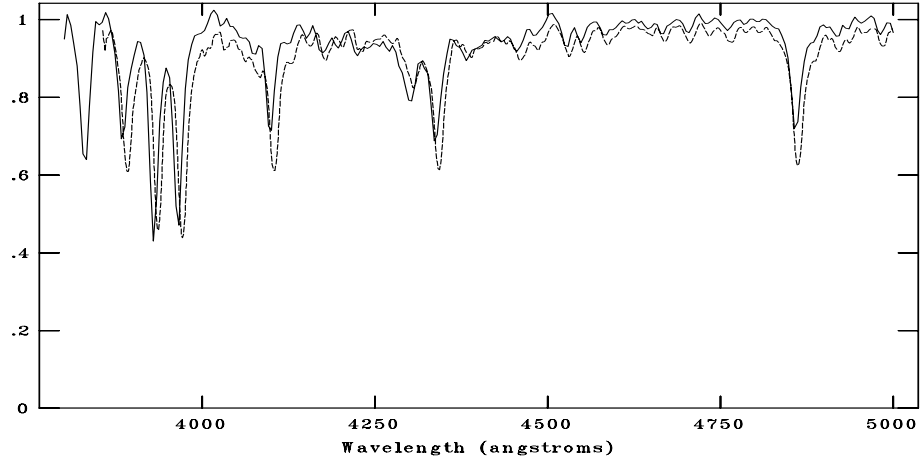
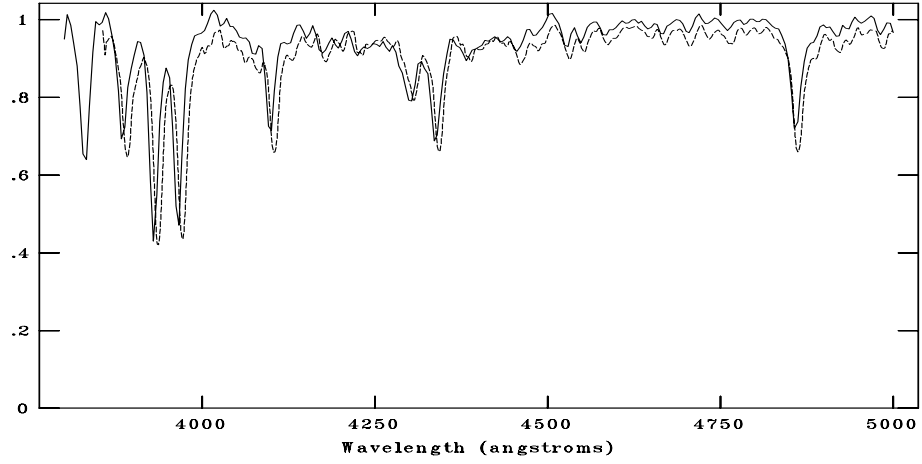


Figure C.8: CAFOS spectrum of 679-080132 compared with A0V, B8V, B9V respectively. The standard spectra are shown with dotted line. The spectral type is assigned as B9V.

NOAO/IRAF V2.16.1 baha@baha-Lenovo-IdeaPad-Y550 Wed 07:30:37 07-Dec-2016
[n82_3.fits]: 82_3 450. ap:1 beam:1



NOAO/IRAF V2.16.1 baha@baha-Lenovo-IdeaPad-Y550 Wed 07:27:26 07-Dec-2016
[n82_3.fits]: 82_3 450. ap:1 beam:1



NOAO/IRAF V2.16.1 baha@baha-Lenovo-IdeaPad-Y550 Wed 07:28:44 07-Dec-2016
[n82_3.fits]: 82_3 450. ap:1 beam:1

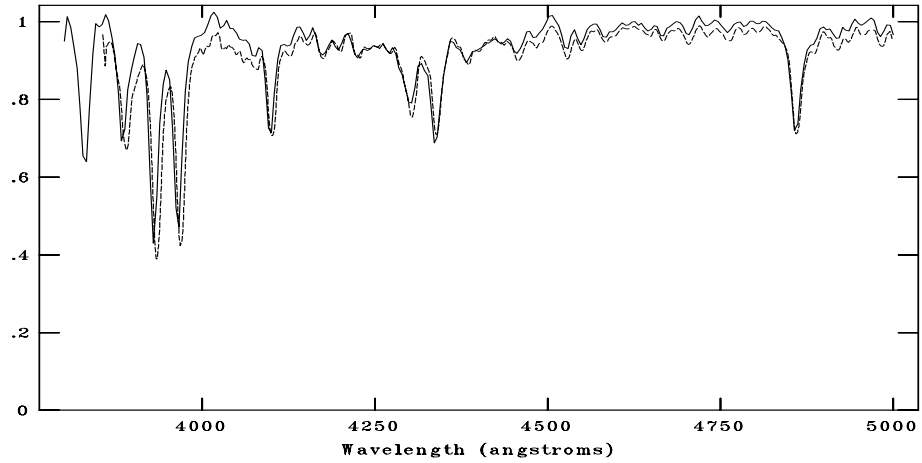
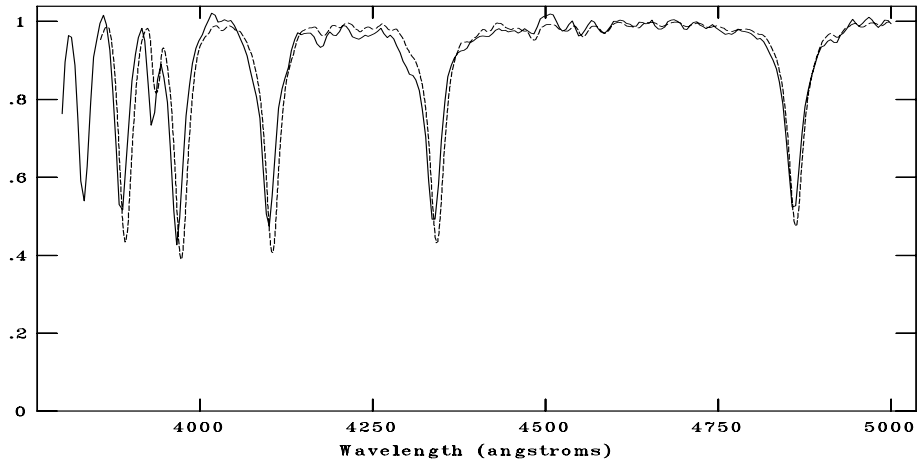
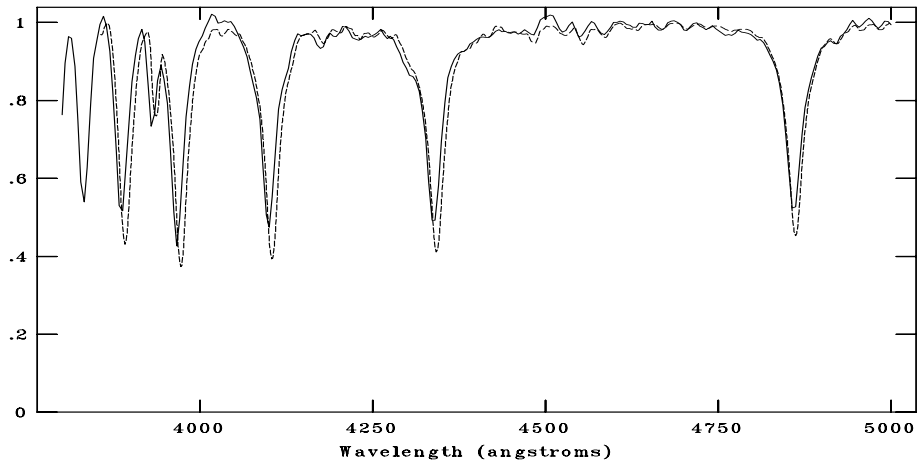


Figure C.9: CAFOS spectrum of 679-080240 compared with F3V, F5V, F6V respectively. The standard spectra are shown with dotted line. The spectral type is assigned as F5V.

NOAO/IRAF V2.16.1 baha@baha-Lenovo-IdeaPad-Y550 Wed 07:31:52 07-Dec-2016
[n82_4.fits]: 82_4 400. ap:1 beam:1



NOAO/IRAF V2.16.1 baha@baha-Lenovo-IdeaPad-Y550 Wed 07:32:16 07-Dec-2016
[n82_4.fits]: 82_4 400. ap:1 beam:1



NOAO/IRAF V2.16.1 baha@baha-Lenovo-IdeaPad-Y550 Wed 07:32:37 07-Dec-2016
[n82_4.fits]: 82_4 400. ap:1 beam:1

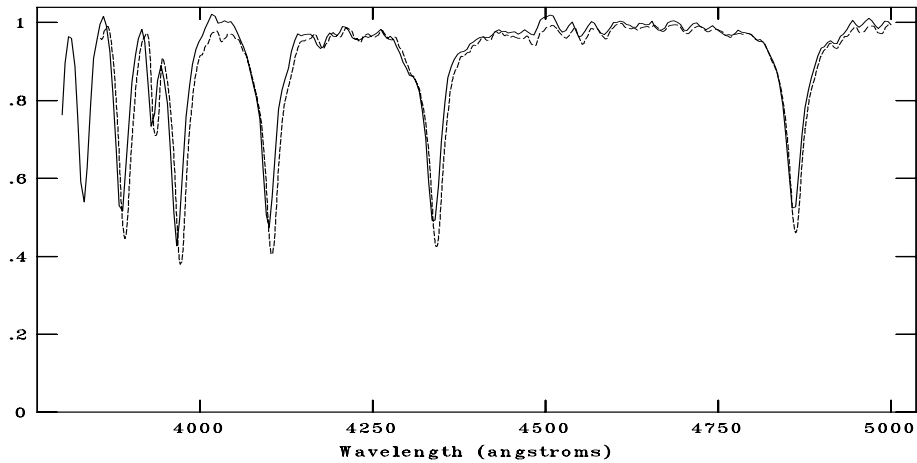
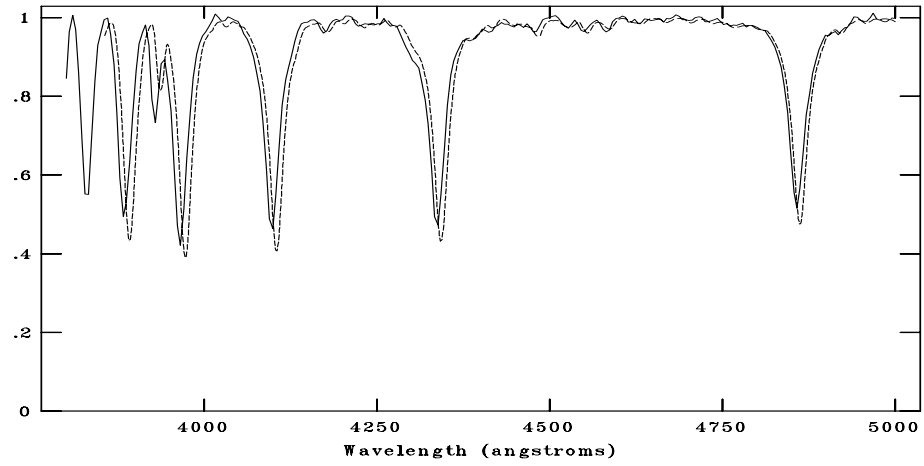
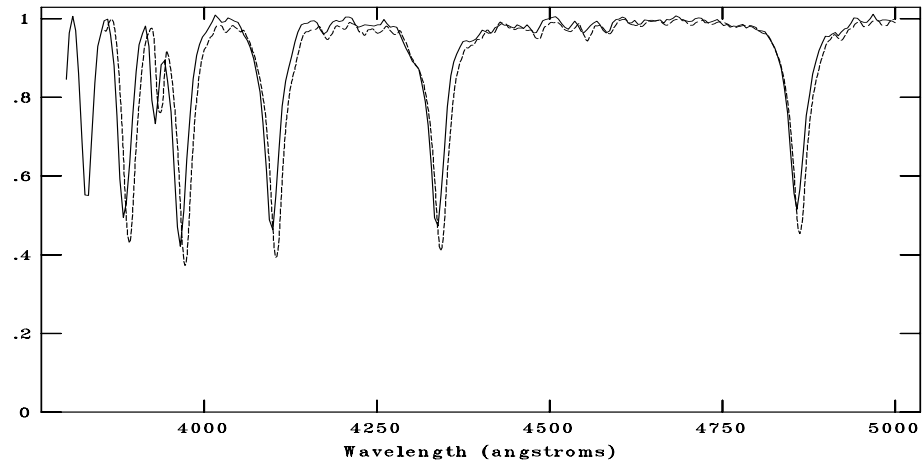


Figure C.10: CAFOS spectrum of 678-083187 compared with A1V, A3V, A5V respectively. The standard spectra are shown with dotted line. The spectral type is assigned as A4V.

NOAO/IRAF V2.16.1 baha@baha-Lenovo-IdeaPad-Y550 Mon 15:10:13 05-Dec-2016
[n082_a.fits]: 082_a 90. ap:1 beam:1



NOAO/IRAF V2.16.1 baha@baha-Lenovo-IdeaPad-Y550 Mon 15:09:38 05-Dec-2016
[n082_a.fits]: 082_a 90. ap:1 beam:1



NOAO/IRAF V2.16.1 baha@baha-Lenovo-IdeaPad-Y550 Mon 15:10:40 05-Dec-2016
[n082_a.fits]: 082_a 90. ap:1 beam:1

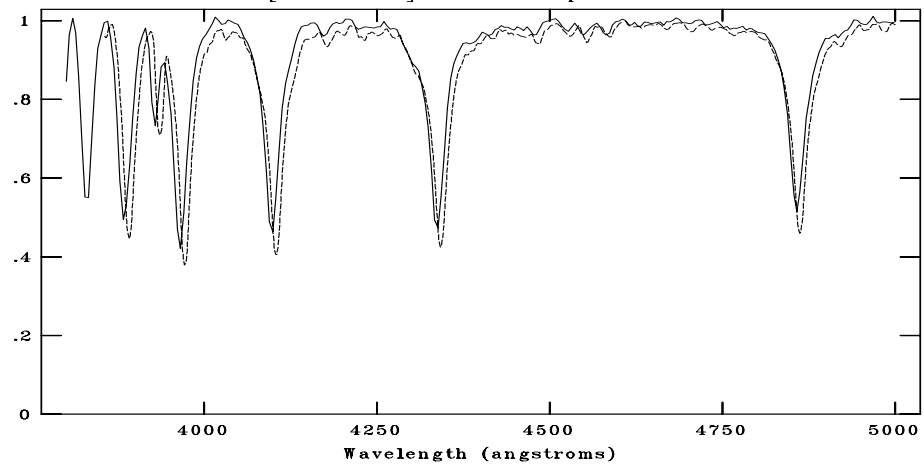
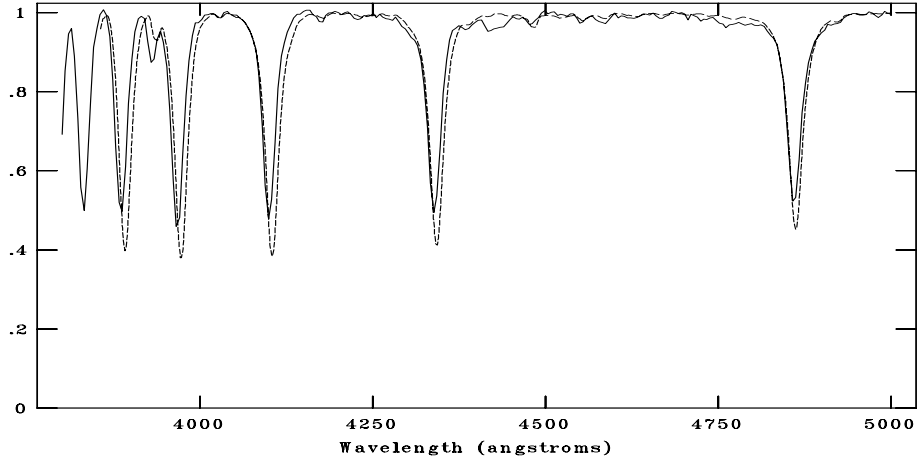
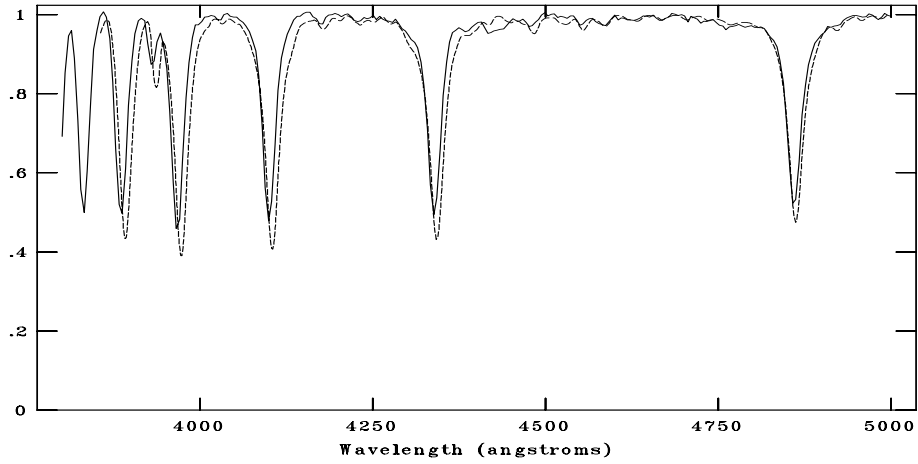


Figure C.11: CAFOS spectrum of 679-080191 compared with A1V, A3V, A5V respectively. The standard spectra are shown with dotted line. The spectral type is assigned as A3V.

NOAO/IRAF V2.16.1 baha@baha-Lenovo-IdeaPad-Y550 Mon 15:12:19 05-Dec-2016
[n082_b.fits]: 082_b 120. ap:1 beam:1



NOAO/IRAF V2.16.1 baha@baha-Lenovo-IdeaPad-Y550 Mon 15:12:46 05-Dec-2016
[n082_b.fits]: 082_b 120. ap:1 beam:1



NOAO/IRAF V2.16.1 baha@baha-Lenovo-IdeaPad-Y550 Mon 15:12:05 05-Dec-2016
[n082_b.fits]: 082_b 120. ap:1 beam:1

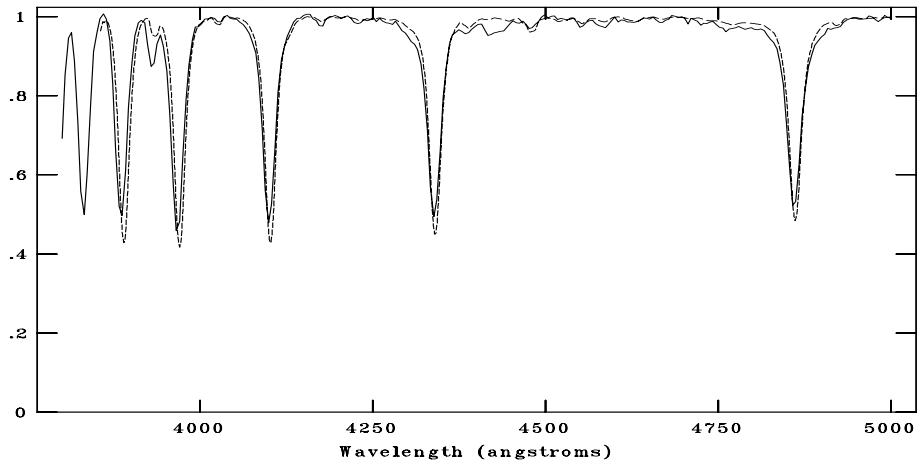
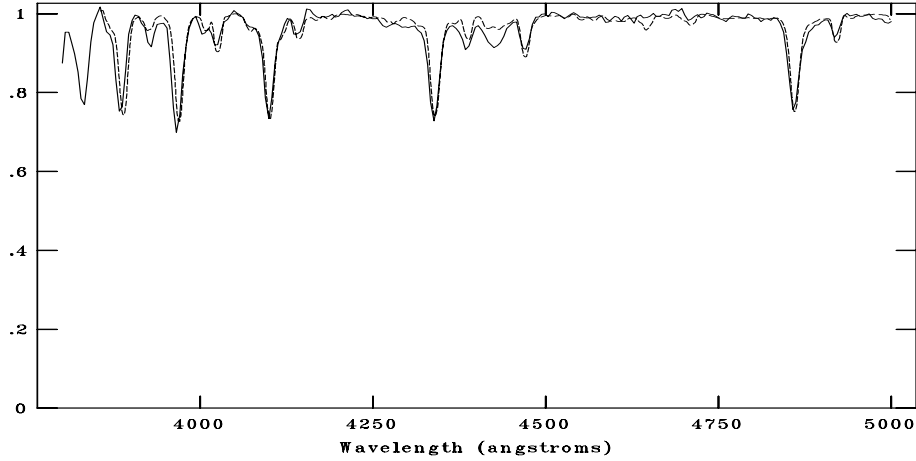
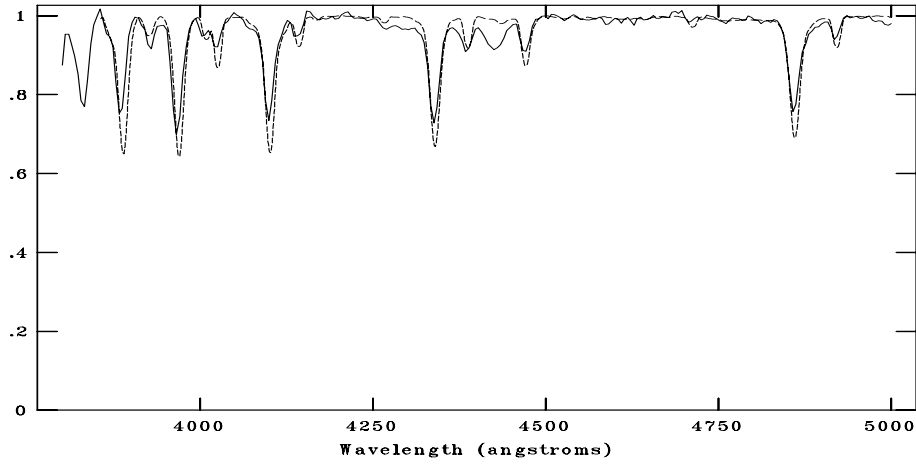


Figure C.12: CAFOS spectrum of 678-083207 compared with A0V, A1V, B9V respectively. The standard spectra are shown with dotted line. The spectral type is assigned as A0V.

NOAO/IRAF V2.16.1 baha@baha-Lenovo-IdeaPad-Y550 Mon 15:16:03 05-Dec-2016
[n082_c.fits]: 082_c 240. ap:1 beam:1



NOAO/IRAF V2.16.1 baha@baha-Lenovo-IdeaPad-Y550 Mon 15:16:39 05-Dec-2016
[n082_c.fits]: 082_c 240. ap:1 beam:1



NOAO/IRAF V2.16.1 baha@baha-Lenovo-IdeaPad-Y550 Mon 15:17:19 05-Dec-2016
[n082_c.fits]: 082_c 240. ap:1 beam:1

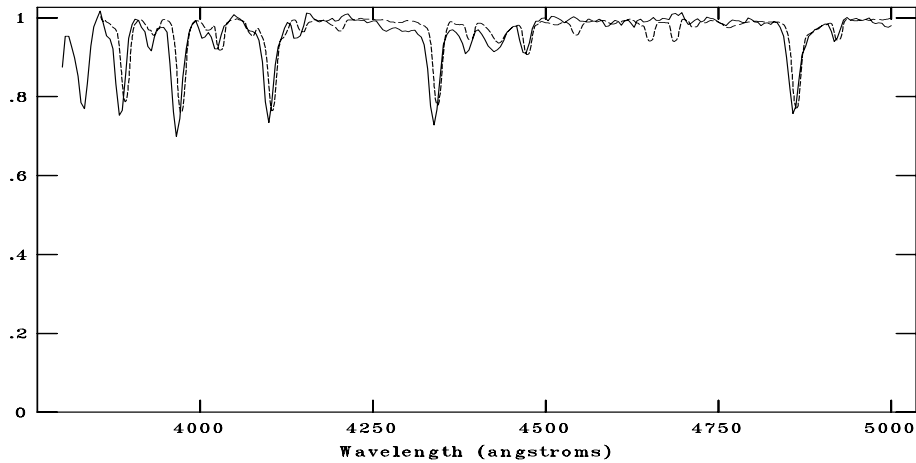
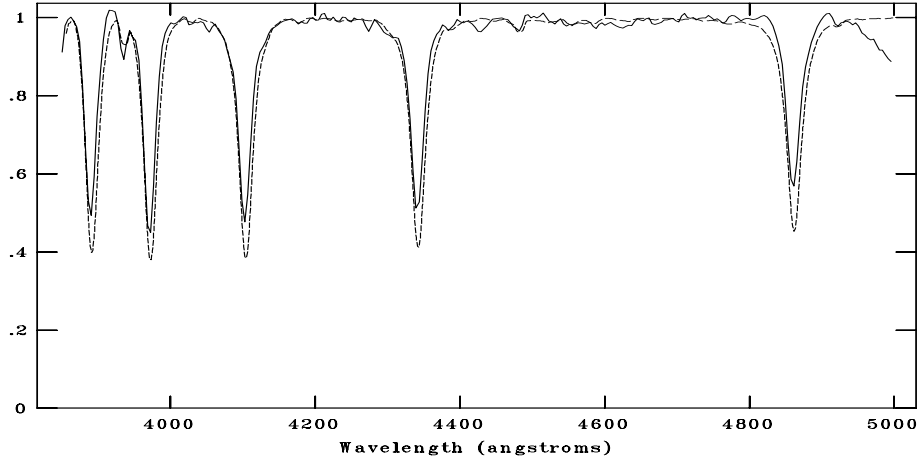
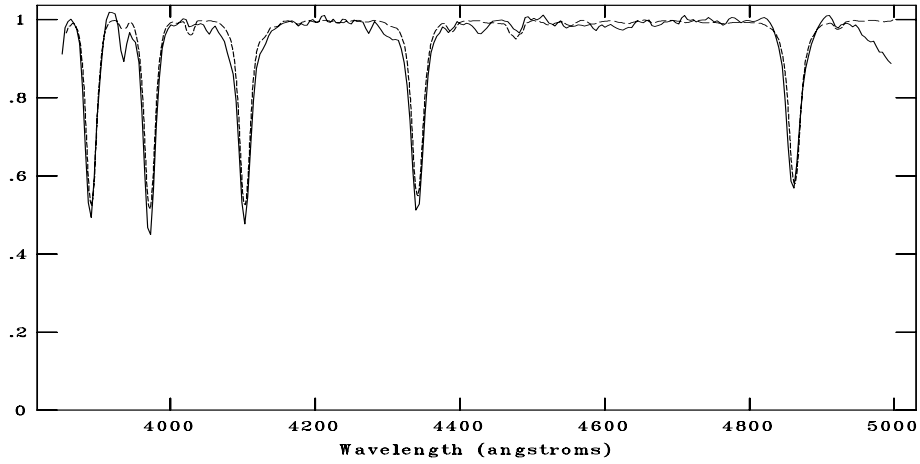


Figure C.13: CAFOS spectrum of 677-080274 compared with B1V, B2V, O9V respectively. The standard spectra are shown with dotted line. The spectral type is assigned as B1V.

NOAO/IRAF V2.16.1 baha@baha-Lenovo-IdeaPad-Y550 Thu 16:04:18 08-Dec-2016
[G082_01n.fits]: G082_01 900. ap:1 beam:1



NOAO/IRAF V2.16.1 baha@baha-Lenovo-IdeaPad-Y550 Thu 16:03:47 08-Dec-2016
[G082_01n.fits]: G082_01 900. ap:1 beam:1



NOAO/IRAF V2.16.1 baha@baha-Lenovo-IdeaPad-Y550 Thu 16:04:03 08-Dec-2016
[G082_01n.fits]: G082_01 900. ap:1 beam:1

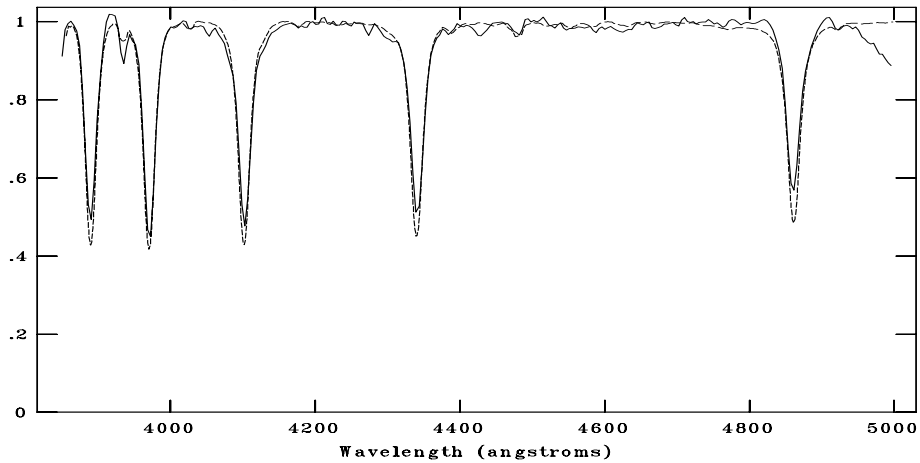
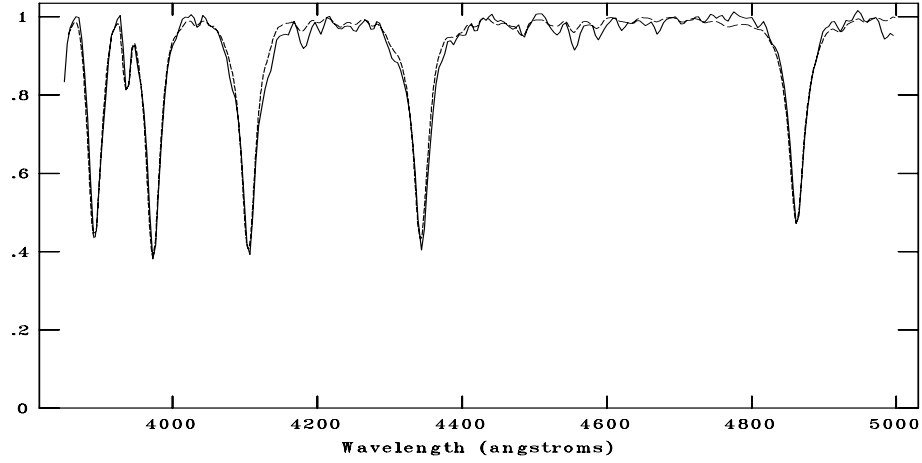
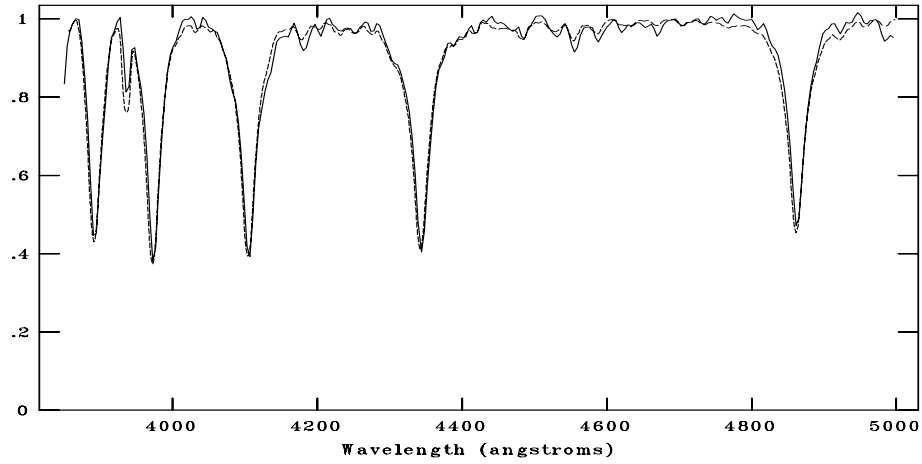


Figure C.14: CAFOS spectrum of 679-080132 compared with A0V, B8V, B9V respectively. The standard spectra are shown with dotted line. The spectral type is assigned as B9V.

NOAO/IRAF V2.16.1 baha@baha-Lenovo-IdeaPad-Y550 Thu 16:05:52 08-Dec-2016
[G082_02n.fits]: G082_02 90. ap:1 beam:1



NOAO/IRAF V2.16.1 baha@baha-Lenovo-IdeaPad-Y550 Thu 16:06:53 08-Dec-2016
[G082_02n.fits]: G082_02 90. ap:1 beam:1



NOAO/IRAF V2.16.1 baha@baha-Lenovo-IdeaPad-Y550 Thu 16:07:19 08-Dec-2016
[G082_02n.fits]: G082_02 90. ap:1 beam:1

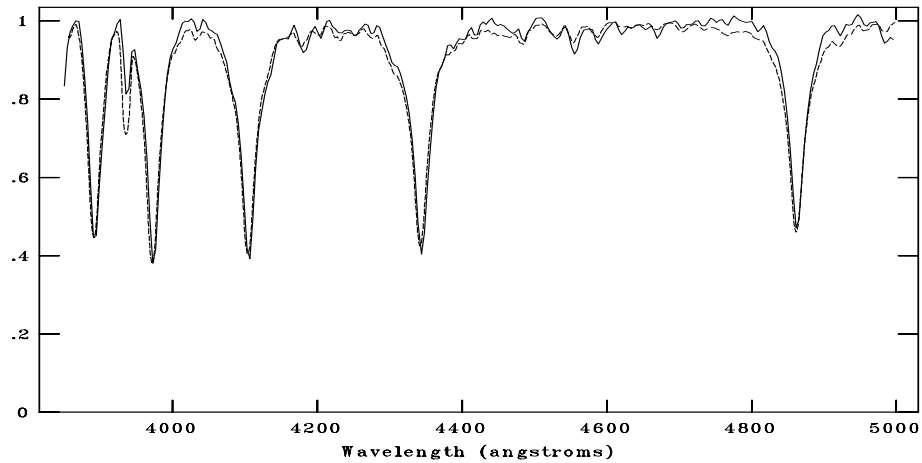
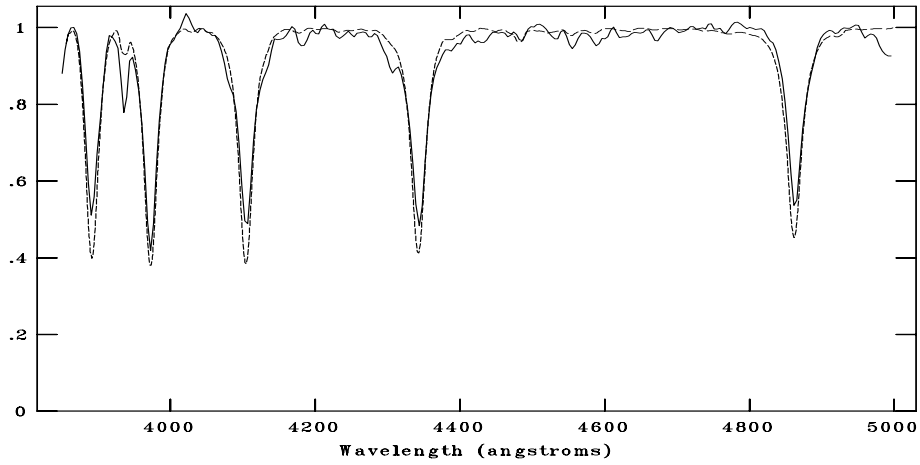


Figure C.15: CAFOS spectrum of 678-083011 compared with A1V, A3V, A5V respectively. The standard spectra are shown with dotted line. The spectral type is assigned as A2V.

NOAO/IRAF V2.16.1 baha@baha-Lenovo-IdeaPad-Y550 Thu 16:09:42 08-Dec-2016
[G082_03n.fits]: G082_03 720. ap:1 beam:1



NOAO/IRAF V2.16.1 baha@baha-Lenovo-IdeaPad-Y550 Thu 16:09:09 08-Dec-2016
[G082_03n.fits]: G082_03 720. ap:1 beam:1

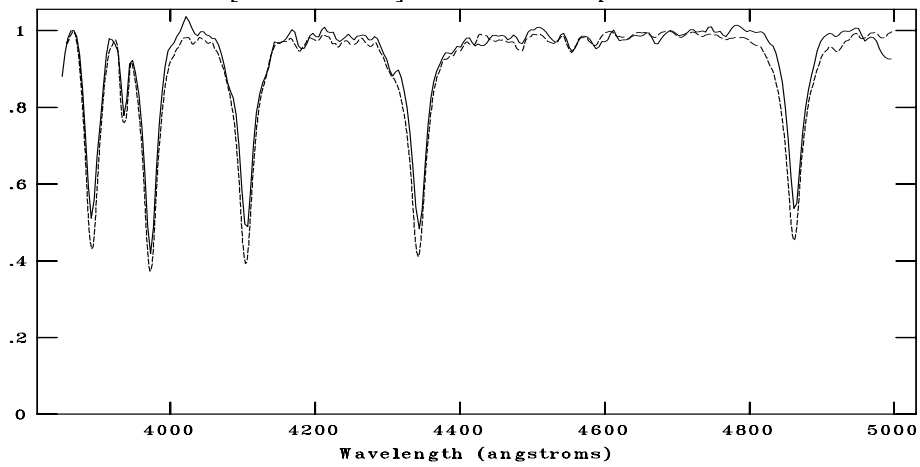
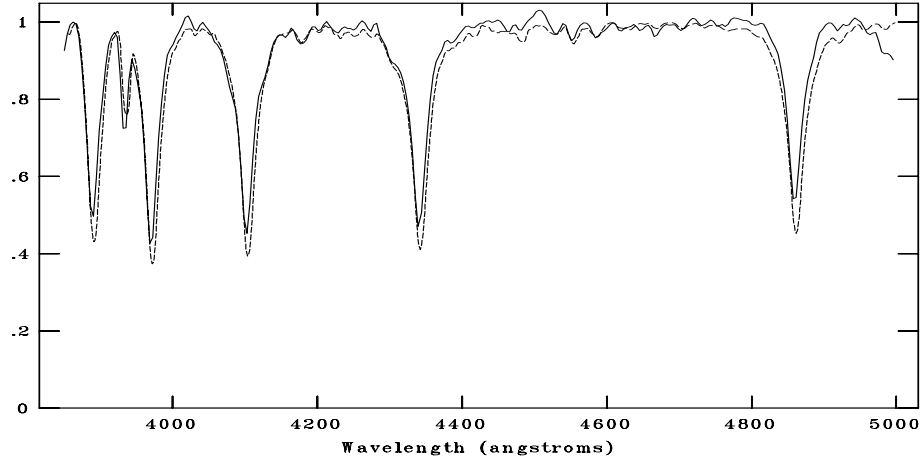
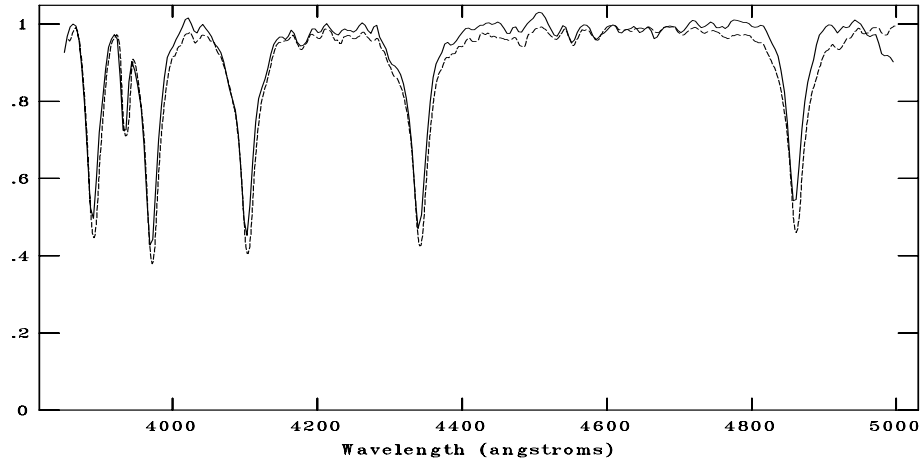


Figure C.16: CAFOS spectrum of 678-083198 compared with A1V and A3V respectively. The standard spectra are shown with dotted line. The spectral type is assigned as A2V.

NOAO/IRAF V2.16.1 baha@baha-Lenovo-IdeaPad-Y550 Thu 16:10:48 08-Dec-2016
[G082_04n.fits]: G082_04 360. ap:1 beam:1



NOAO/IRAF V2.16.1 baha@baha-Lenovo-IdeaPad-Y550 Thu 16:10:09 08-Dec-2016
[G082_04n.fits]: G082_04 360. ap:1 beam:1



NOAO/IRAF V2.16.1 baha@baha-Lenovo-IdeaPad-Y550 Thu 16:10:30 08-Dec-2016
[G082_04n.fits]: G082_04 360. ap:1 beam:1

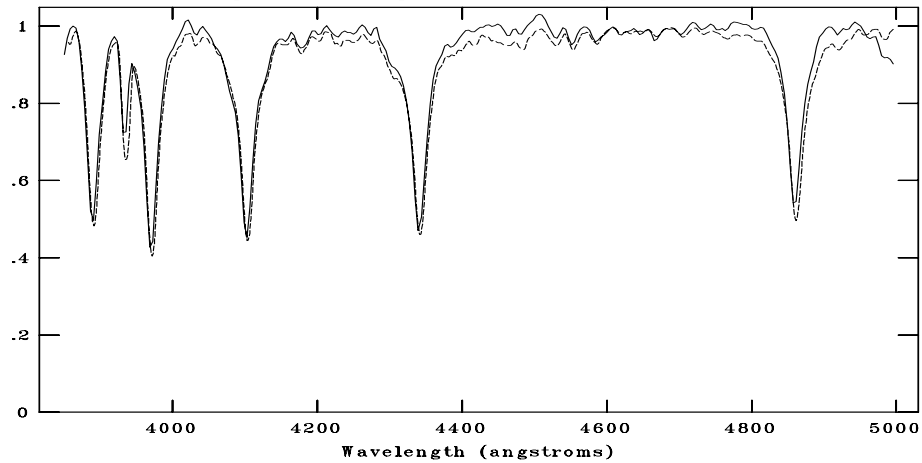
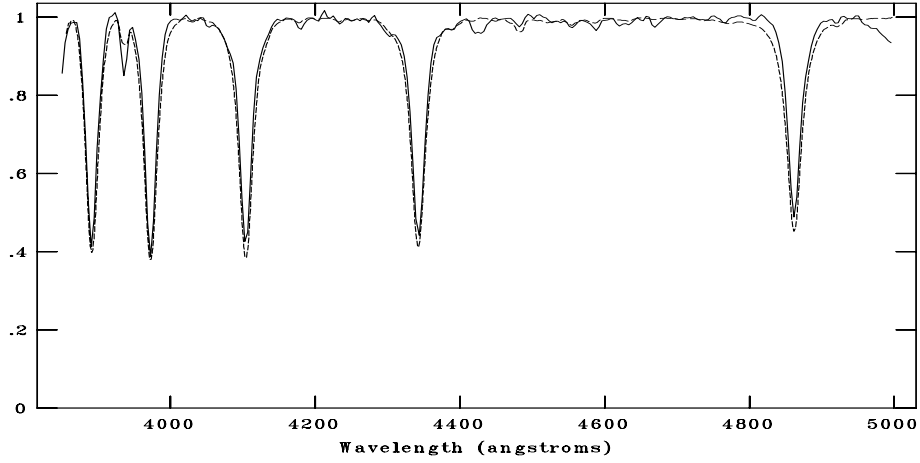
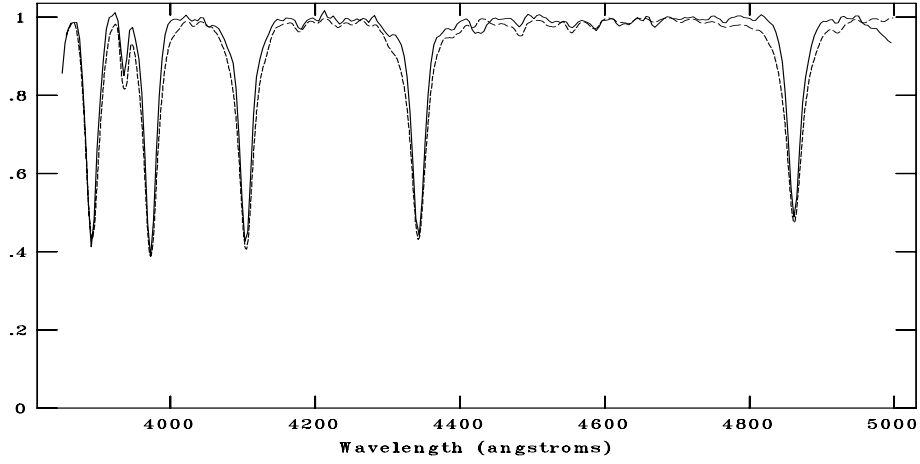


Figure C.17: CAFOS spectrum of 678-083187 compared with A3V, A5V, A7V respectively. The standard spectra are shown with dotted line. The spectral type is assigned as A5V.

NOAO/IRAF V2.16.1 baha@baha-Lenovo-IdeaPad-Y550 Thu 16:12:18 08-Dec-2016
[G082_05n.fits]: G082_05 240. ap:1 beam:1



NOAO/IRAF V2.16.1 baha@baha-Lenovo-IdeaPad-Y550 Thu 16:12:56 08-Dec-2016
[G082_05n.fits]: G082_05 240. ap:1 beam:1



NOAO/IRAF V2.16.1 baha@baha-Lenovo-IdeaPad-Y550 Thu 16:12:42 08-Dec-2016
[G082_05n.fits]: G082_05 240. ap:1 beam:1

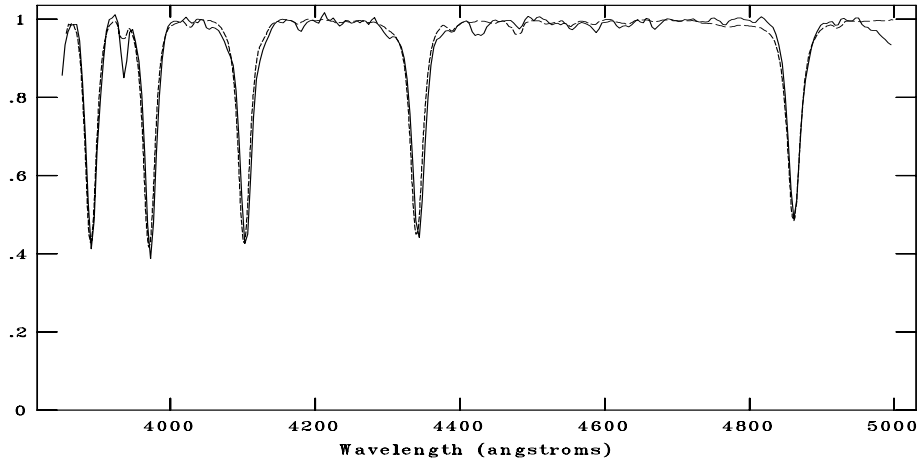
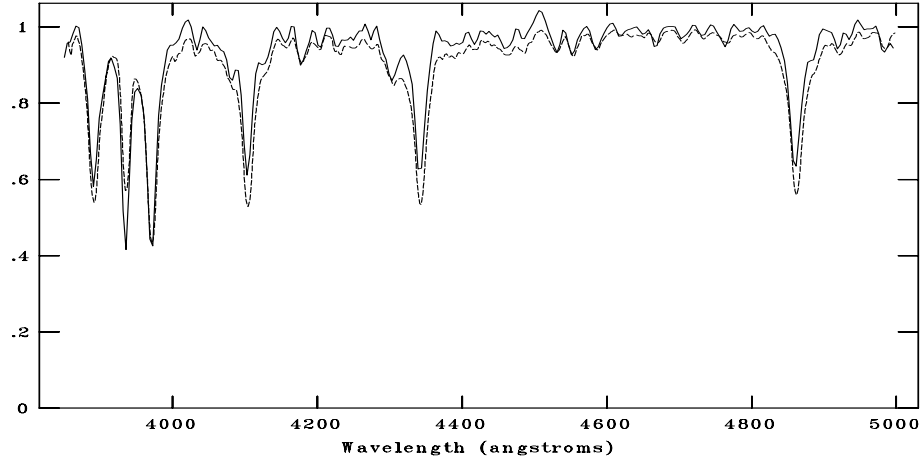
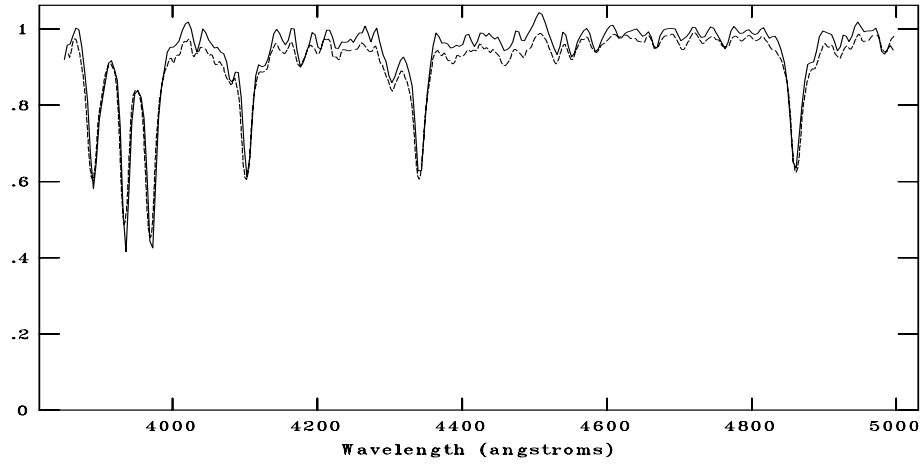


Figure C.18: CAFOS spectrum of 678-083207 compared with A0V, A1V, B9V respectively. The standard spectra are shown with dotted line. The spectral type is assigned as A0V.

NOAO/IRAF V2.16.1 baha@baha-Lenovo-IdeaPad-Y550 Thu 16:13:55 08-Dec-2016
[G082_06n.fits]: G082_06 150. ap:1 beam:1



NOAO/IRAF V2.16.1 baha@baha-Lenovo-IdeaPad-Y550 Thu 16:14:10 08-Dec-2016
[G082_06n.fits]: G082_06 150. ap:1 beam:1



NOAO/IRAF V2.16.1 baha@baha-Lenovo-IdeaPad-Y550 Thu 16:14:28 08-Dec-2016
[G082_06n.fits]: G082_06 150. ap:1 beam:1

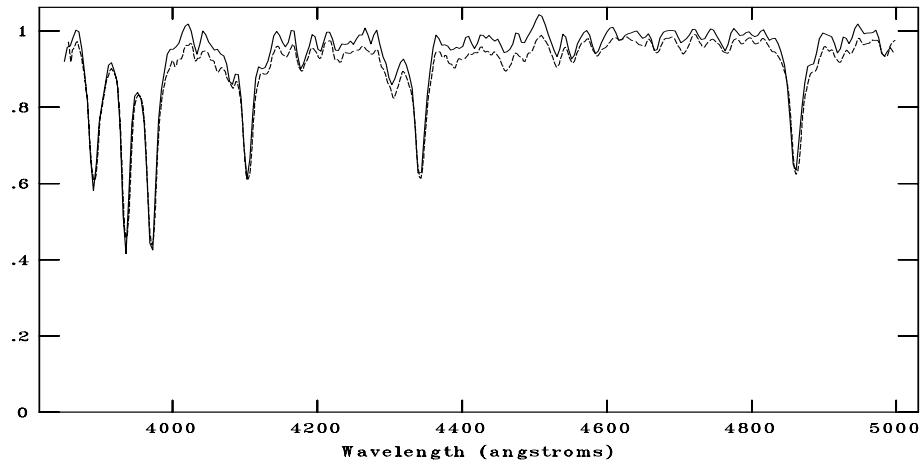
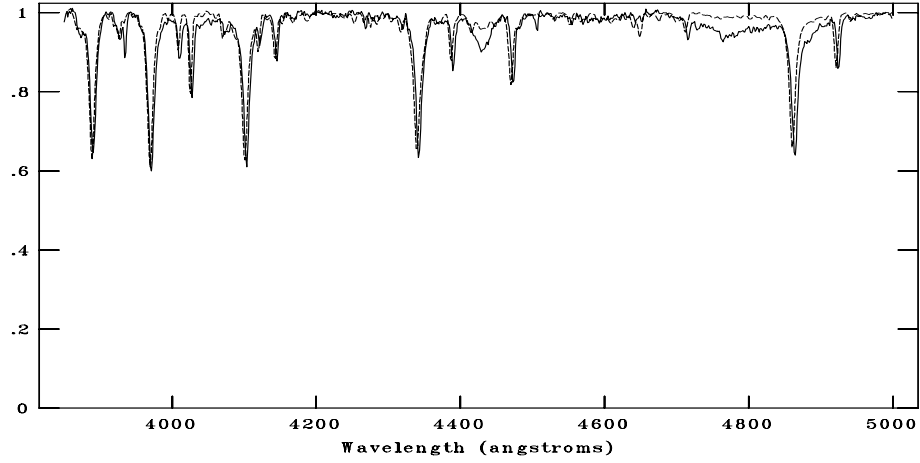
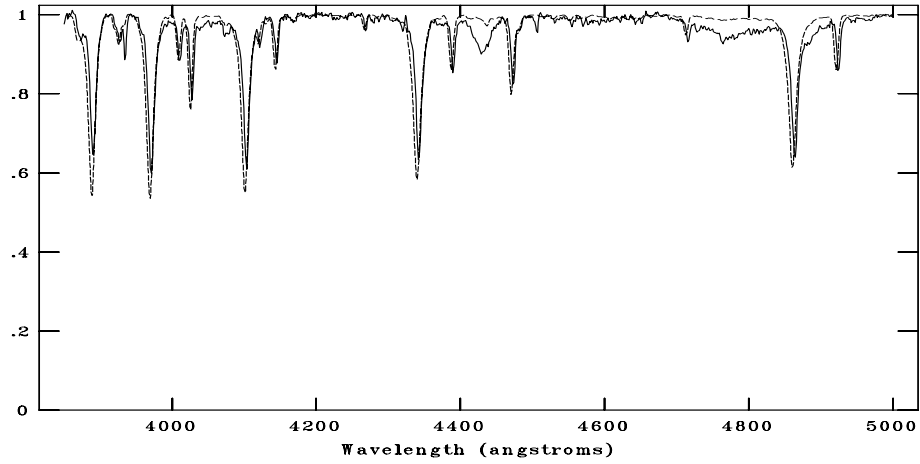


Figure C.19: CAFOS spectrum of 678-083036 compared with F0V, F2V, F3V respectively. The standard spectra are shown with dotted line. The spectral type is assigned as F2V.

NOAO/IRAF V2.16.1 baha@baha-Lenovo-IdeaPad-Y550 Wed 00:26:36 04-Jan-2017
[g82n.fits]: g82_1 1800. ap:1 beam:1



NOAO/IRAF V2.16.1 baha@baha-Lenovo-IdeaPad-Y550 Wed 00:26:01 04-Jan-2017
[g82n.fits]: g82_1 1800. ap:1 beam:1



NOAO/IRAF V2.16.1 baha@baha-Lenovo-IdeaPad-Y550 Wed 00:27:19 04-Jan-2017
[g82n.fits]: g82_1 1800. ap:1 beam:1

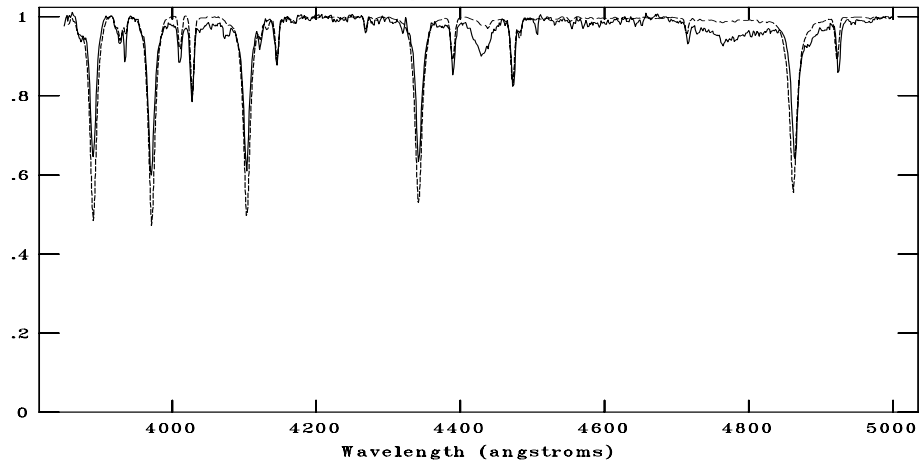


Figure C.20: TFOSC spectrum of 677-080274 compared with B1V, B2V, B3V respectively. The standard spectra are shown with dotted line. The spectral type is assigned as B1.5V.

C.4 G089.0+4.7

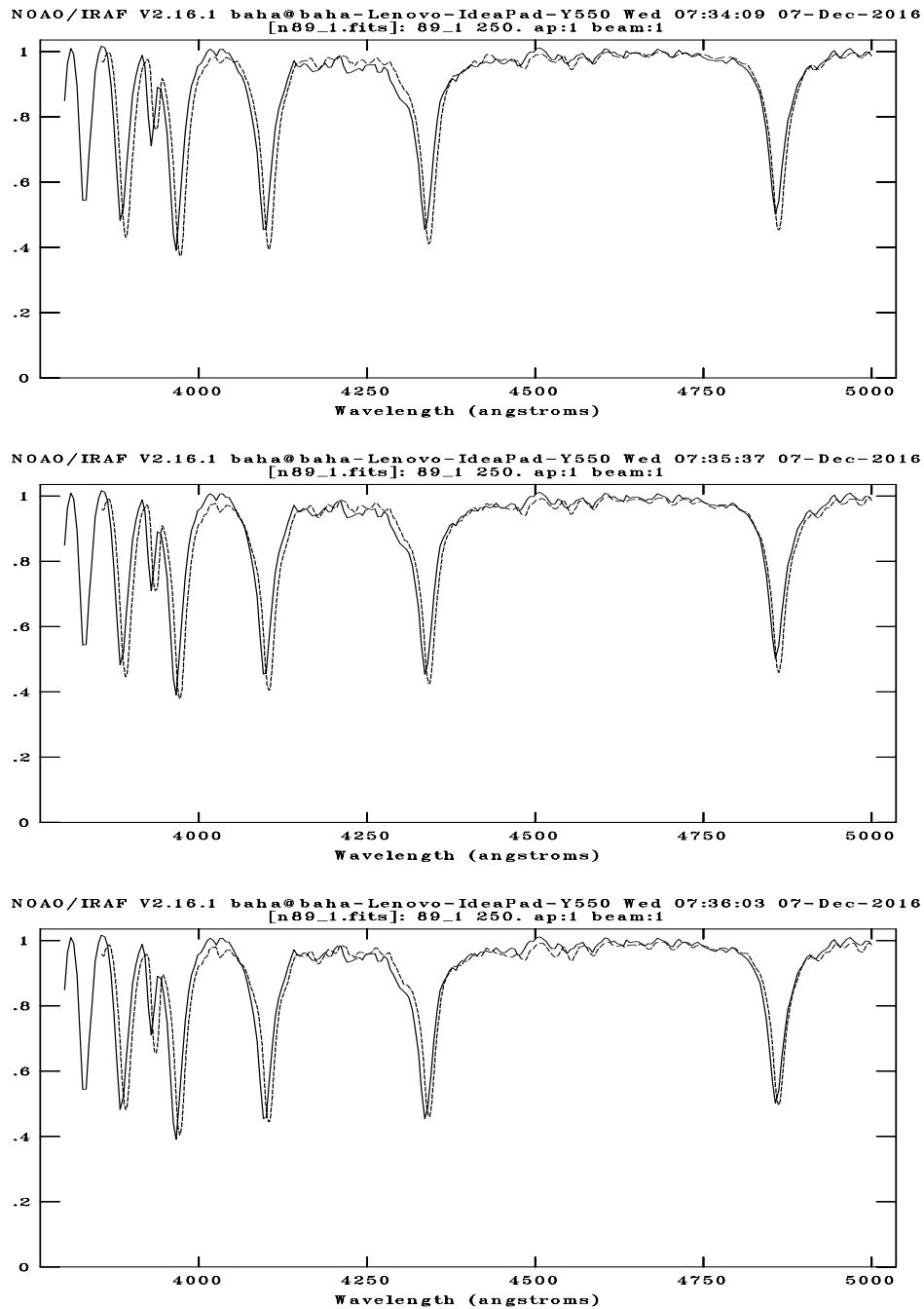
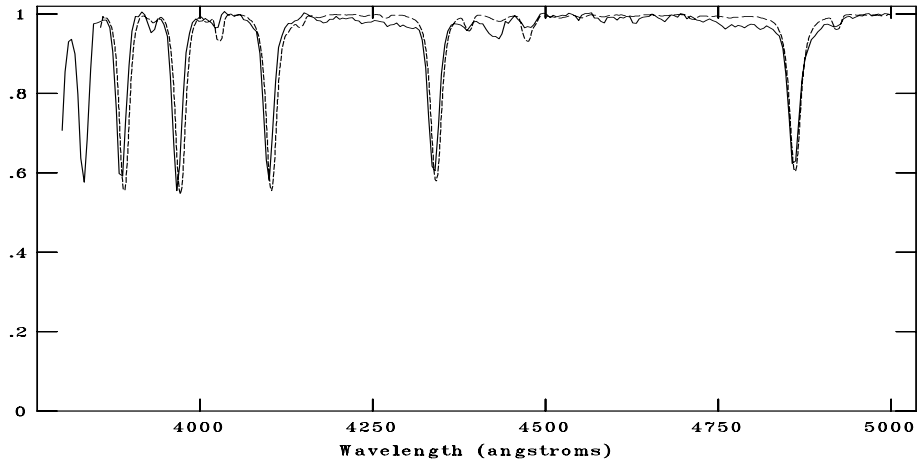
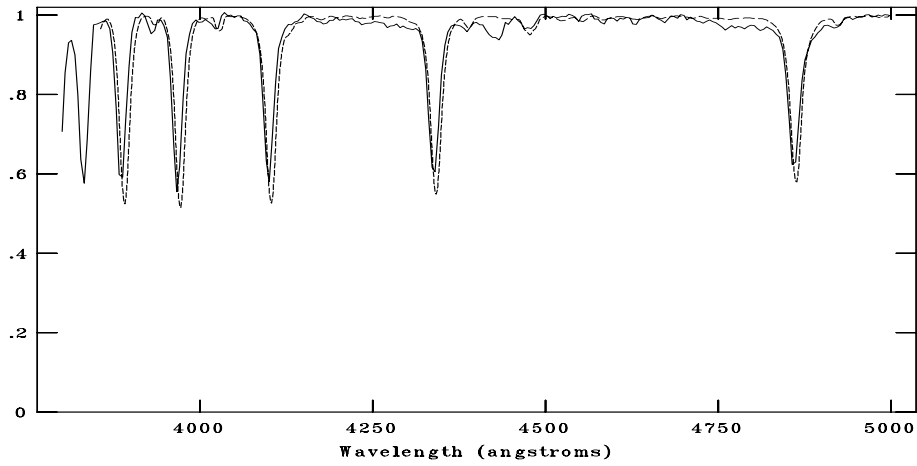


Figure C.21: CAFOS spectrum of 703-081098 compared with A3V, A5V, A7V respectively. The standard spectra are shown with dotted line. The spectral type is assigned as A4V.

NOAO/IRAF V2.16.1 baha@baha-Lenovo-IdeaPad-Y550 Wed 07:36:43 07-Dec-2016
[n89_2.fits]: 89_2 200. ap:1 beam:1



NOAO/IRAF V2.16.1 baha@baha-Lenovo-IdeaPad-Y550 Wed 07:37:41 07-Dec-2016
[n89_2.fits]: 89_2 200. ap:1 beam:1



NOAO/IRAF V2.16.1 baha@baha-Lenovo-IdeaPad-Y550 Wed 07:38:21 07-Dec-2016
[n89_2.fits]: 89_2 200. ap:1 beam:1

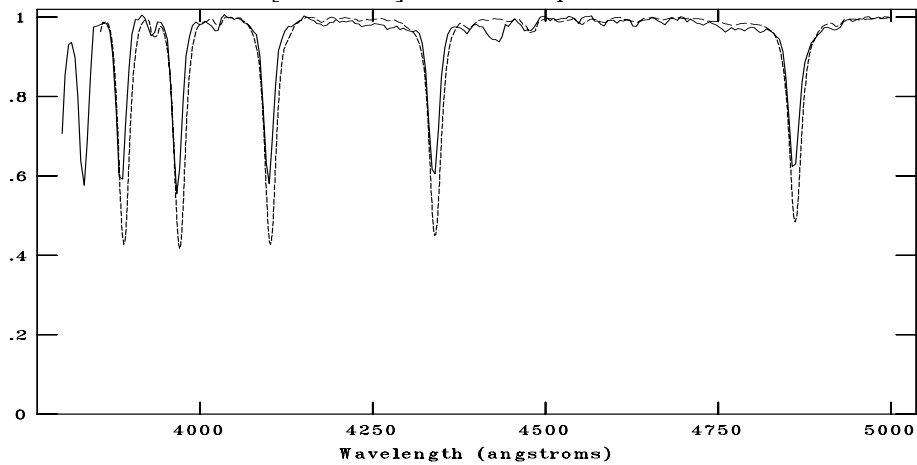
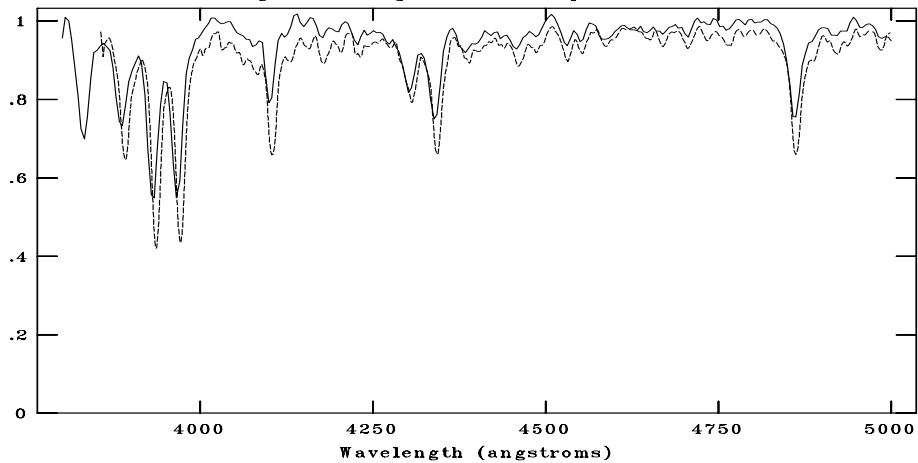
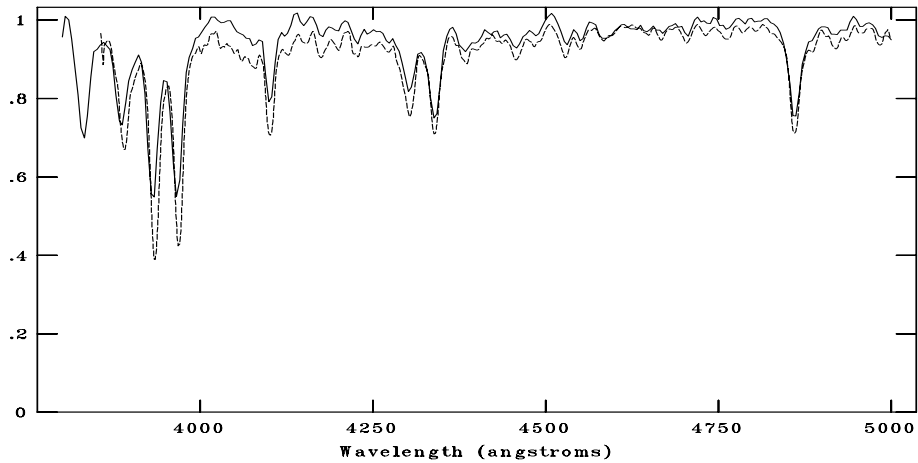


Figure C.22: CAFOS spectrum of 703-081110 compared with B7V, B8V, B9V respectively. The standard spectra are shown with dotted line. The spectral type is assigned as B8V.

NOAO/IRAF V2.16.1 baha@baha-Lenovo-IdeaPad-Y550 Mon 15:23:28 05-Dec-2016
[n089_a.fits]: 089_a 420. ap:1 beam:1



NOAO/IRAF V2.16.1 baha@baha-Lenovo-IdeaPad-Y550 Mon 15:23:15 05-Dec-2016
[n089_a.fits]: 089_a 420. ap:1 beam:1



NOAO/IRAF V2.16.1 baha@baha-Lenovo-IdeaPad-Y550 Mon 15:22:53 05-Dec-2016
[n089_a.fits]: 089_a 420. ap:1 beam:1

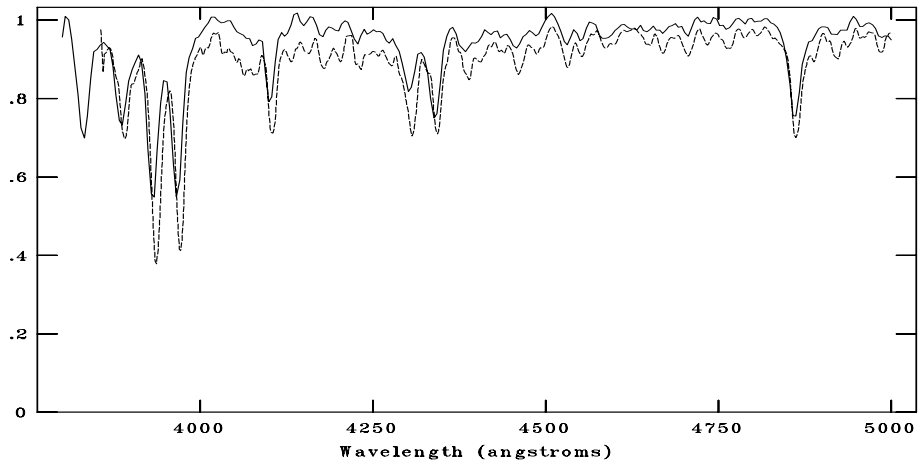
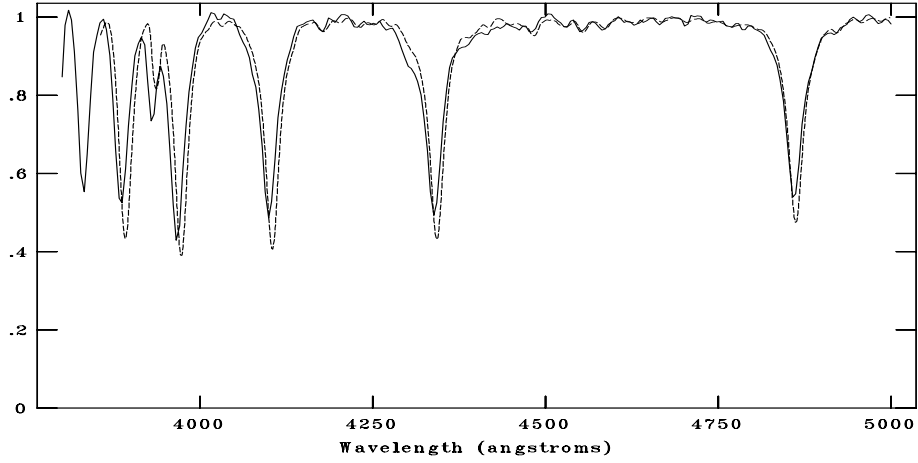
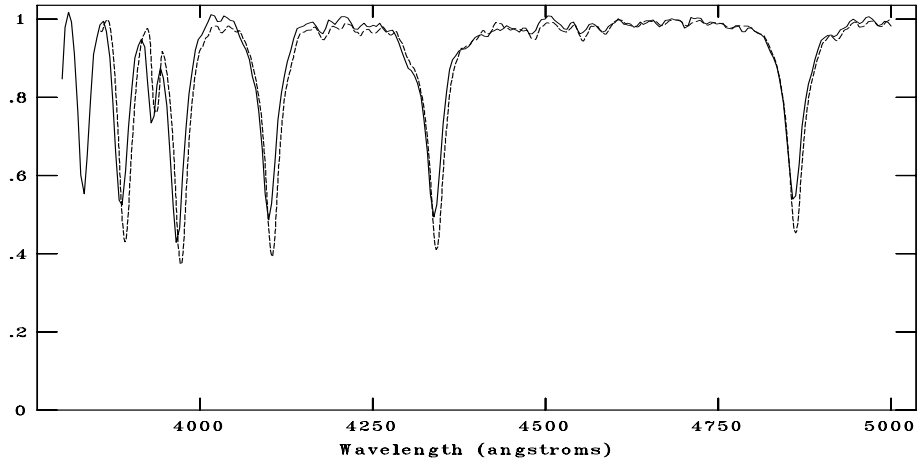


Figure C.23: CAFOS spectrum of 704-078261 compared with F5V, F6V, F8V respectively. The standard spectra are shown with dotted line. The spectral type is assigned as F6V.

NOAO/IRAF V2.16.1 baha@baha-Lenovo-IdeaPad-Y550 Mon 15:28:32 05-Dec-2016
[n089_b.fits]: 089_b 500. ap:1 beam:1



NOAO/IRAF V2.16.1 baha@baha-Lenovo-IdeaPad-Y550 Mon 15:28:52 05-Dec-2016
[n089_b.fits]: 089_b 500. ap:1 beam:1



NOAO/IRAF V2.16.1 baha@baha-Lenovo-IdeaPad-Y550 Mon 15:29:25 05-Dec-2016
[n089_b.fits]: 089_b 500. ap:1 beam:1

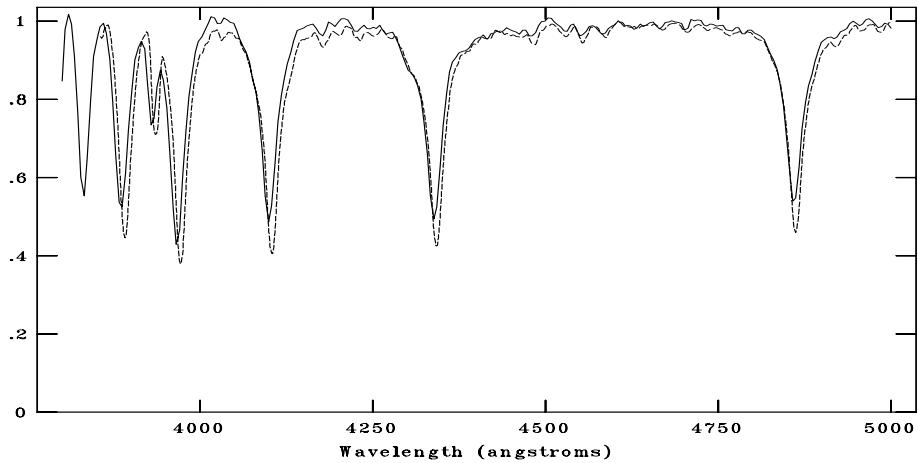
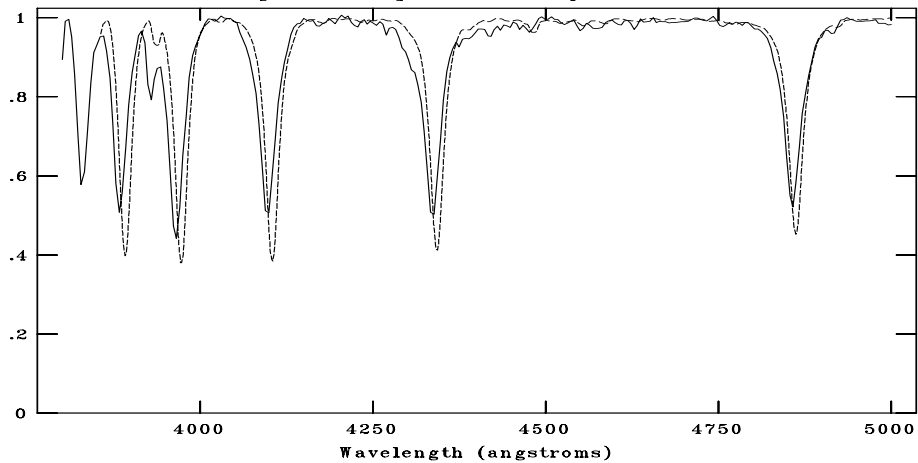
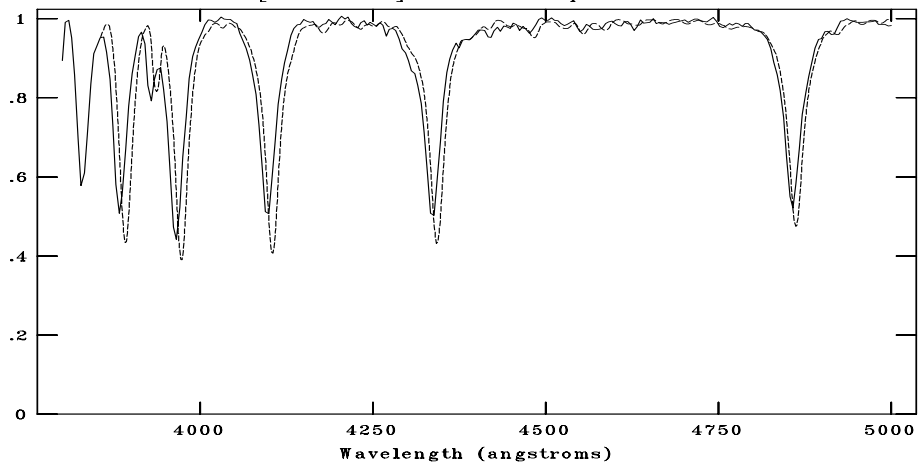


Figure C.24: CAFOS spectrum of 703-081075 compared with A1V, A3V, A5V respectively. The standard spectra are shown with dotted line. The spectral type is assigned as A3V.

NOAO/IRAF V2.16.1 baha@baha-Lenovo-IdeaPad-Y550 Mon 15:30:55 05-Dec-2016
[n089_c.fits]: 089_c 500. ap:1 beam:1



NOAO/IRAF V2.16.1 baha@baha-Lenovo-IdeaPad-Y550 Mon 15:30:36 05-Dec-2016
[n089_c.fits]: 089_c 500. ap:1 beam:1



NOAO/IRAF V2.16.1 baha@baha-Lenovo-IdeaPad-Y550 Mon 15:31:22 05-Dec-2016
[n089_c.fits]: 089_c 500. ap:1 beam:1

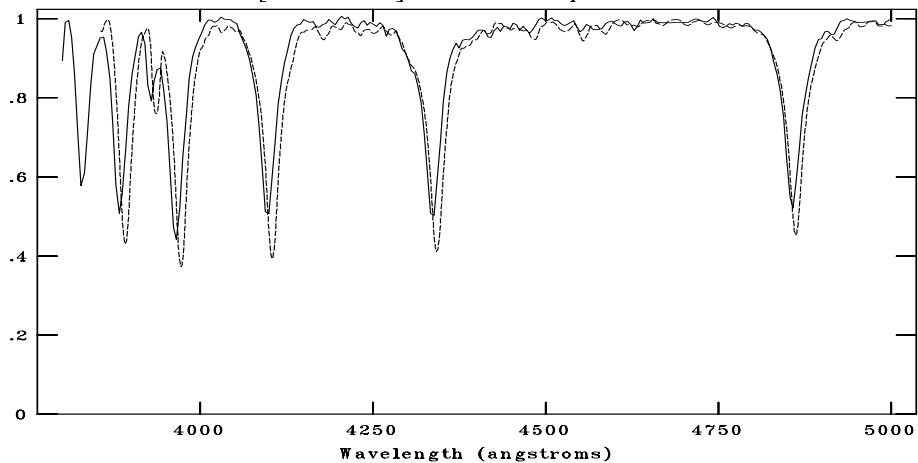
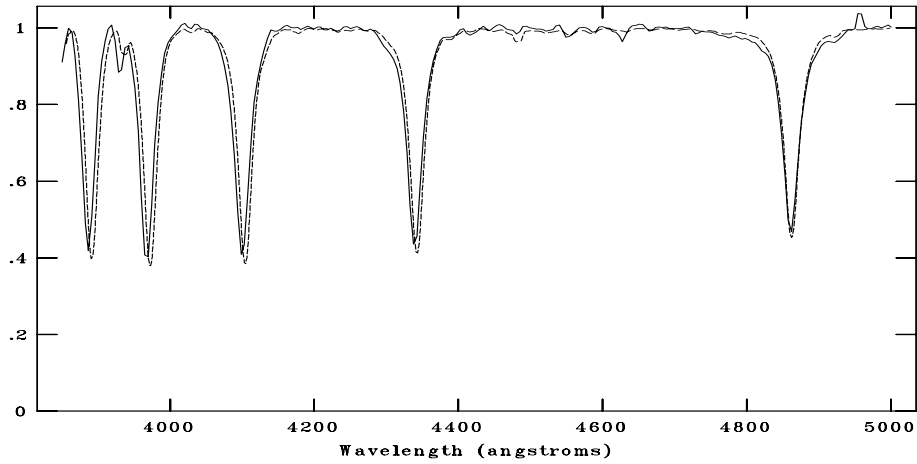
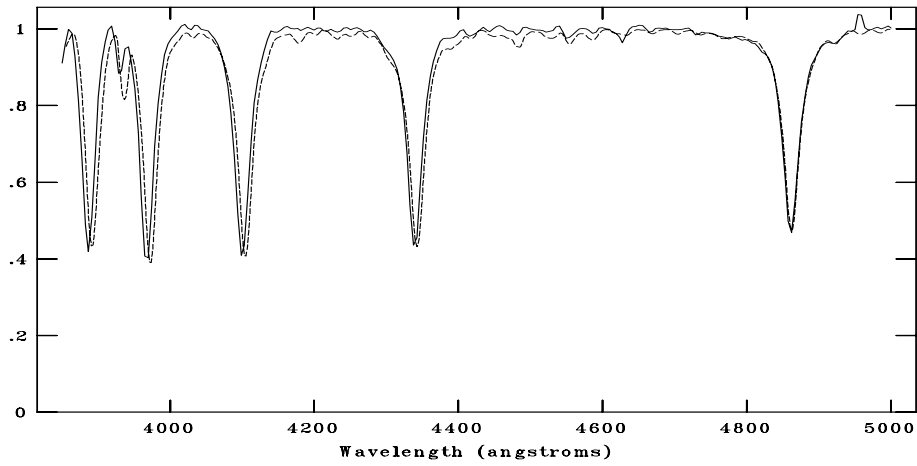


Figure C.25: CAFOS spectrum of 703-080795 compared with A0V, A1V, A3V respectively. The standard spectra are shown with dotted line. The spectral type is assigned as A1V.

NOAO/IRAF V2.16.1 baha@baha-Lenovo-IdeaPad-Y550 Wed 22:03:56 07-Dec-2016
[cg089_01A1.fits]: G089_1 150. ap:1 beam:1



NOAO/IRAF V2.16.1 baha@baha-Lenovo-IdeaPad-Y550 Wed 22:04:27 07-Dec-2016
[cg089_01A1.fits]: G089_1 150. ap:1 beam:1



NOAO/IRAF V2.16.1 baha@baha-Lenovo-IdeaPad-Y550 Wed 22:04:48 07-Dec-2016
[cg089_01A1.fits]: G089_1 150. ap:1 beam:1

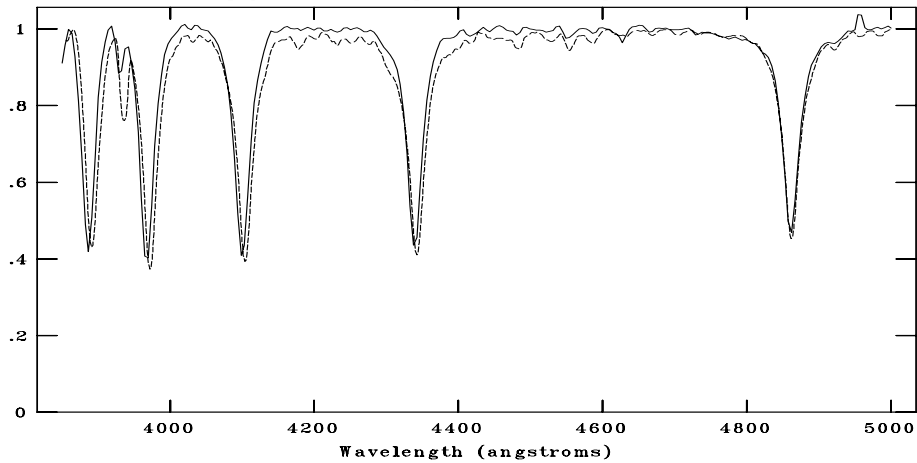
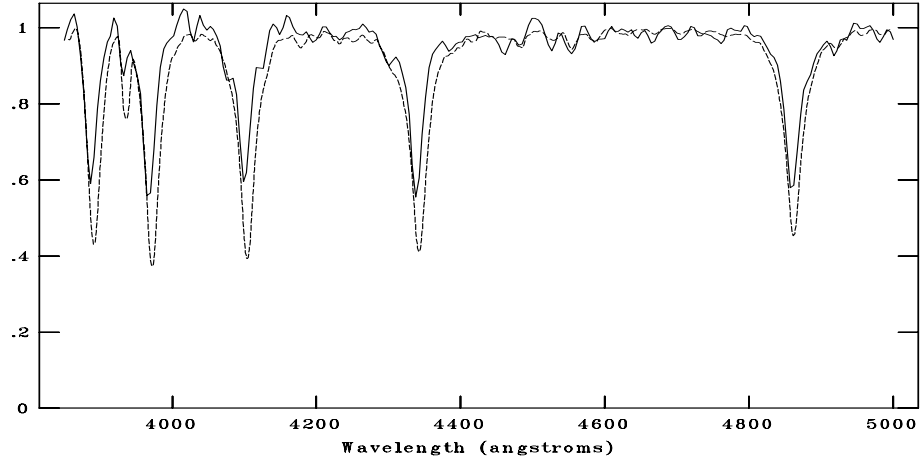
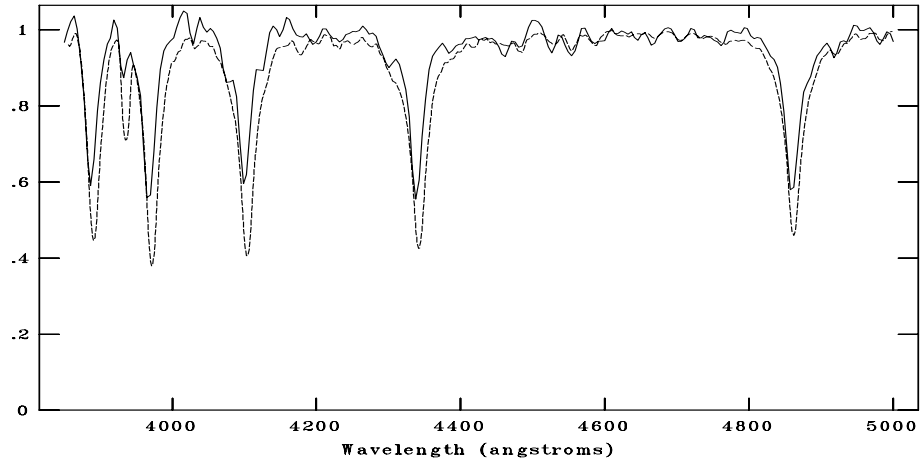


Figure C.26: CAFOS spectrum of 704-078114 compared with A0V, A1V, A3V respectively. The standard spectra are shown with dotted line. The spectral type is assigned as A1V.

NOAO/IRAF V2.16.1 baha@baha-Lenovo-IdeaPad-Y550 Wed 22:06:25 07-Dec-2016
[cg089_02_2A3.fits]: G089_2 180. ap:1 beam:1



NOAO/IRAF V2.16.1 baha@baha-Lenovo-IdeaPad-Y550 Wed 22:07:22 07-Dec-2016
[cg089_02_2A3.fits]: G089_2 180. ap:1 beam:1



NOAO/IRAF V2.16.1 baha@baha-Lenovo-IdeaPad-Y550 Wed 22:05:20 07-Dec-2016
[cg089_02_2A3.fits]: G089_2 180. ap:1 beam:1

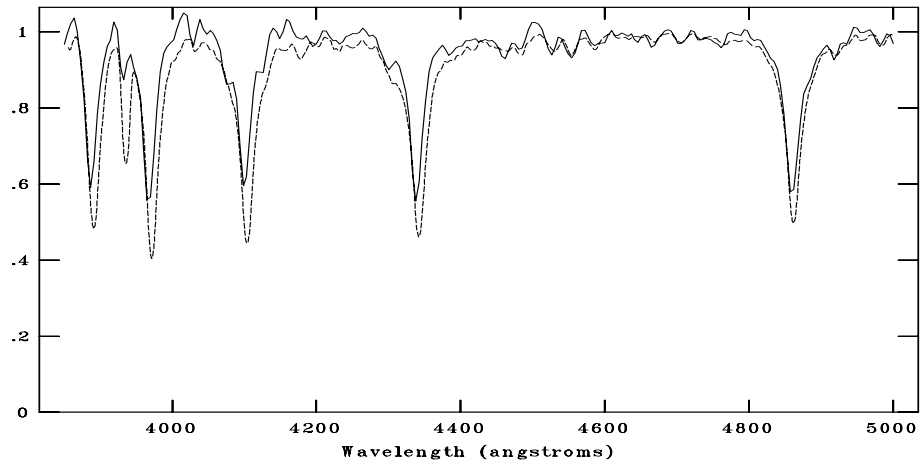
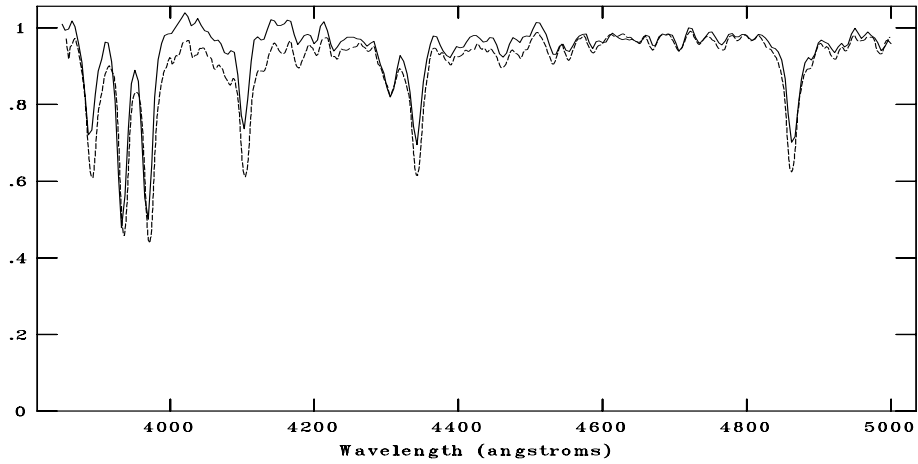
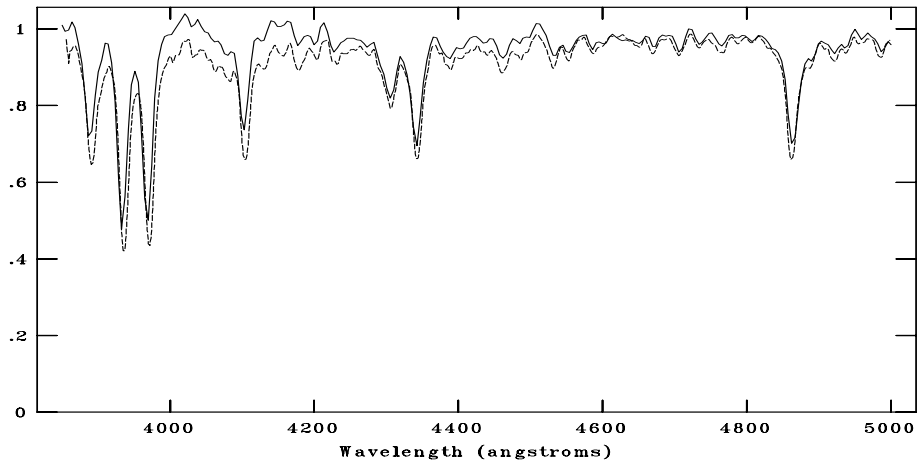


Figure C.27: CAFOS spectrum of 704-077723 compared with A3V, A5V, A7V respectively. The standard spectra are shown with dotted line. The spectral type is assigned as A3V.

NOAO/IRAF V2.16.1 baha@baha-Lenovo-IdeaPad-Y550 Wed 22:08:10 07-Dec-2016
[cg089_03F5.fits]: G089_3 120. ap:1 beam:1



NOAO/IRAF V2.16.1 baha@baha-Lenovo-IdeaPad-Y550 Wed 22:08:37 07-Dec-2016
[cg089_03F5.fits]: G089_3 120. ap:1 beam:1



NOAO/IRAF V2.16.1 baha@baha-Lenovo-IdeaPad-Y550 Wed 22:09:01 07-Dec-2016
[cg089_03F5.fits]: G089_3 120. ap:1 beam:1

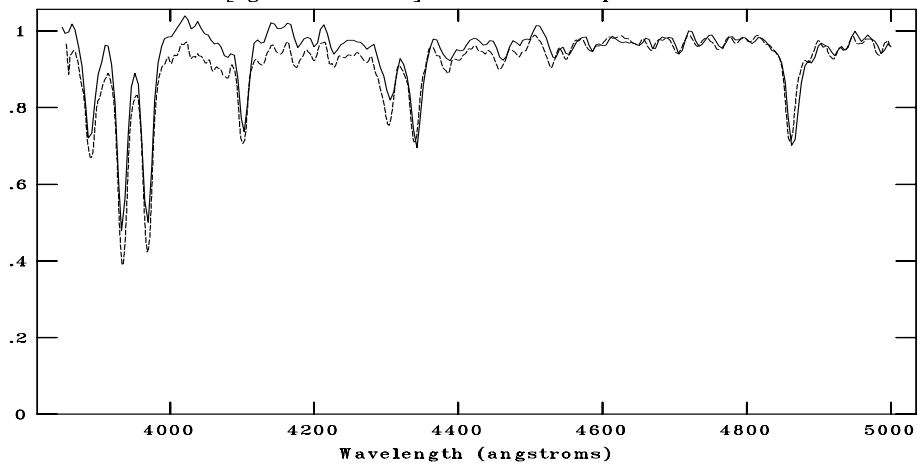
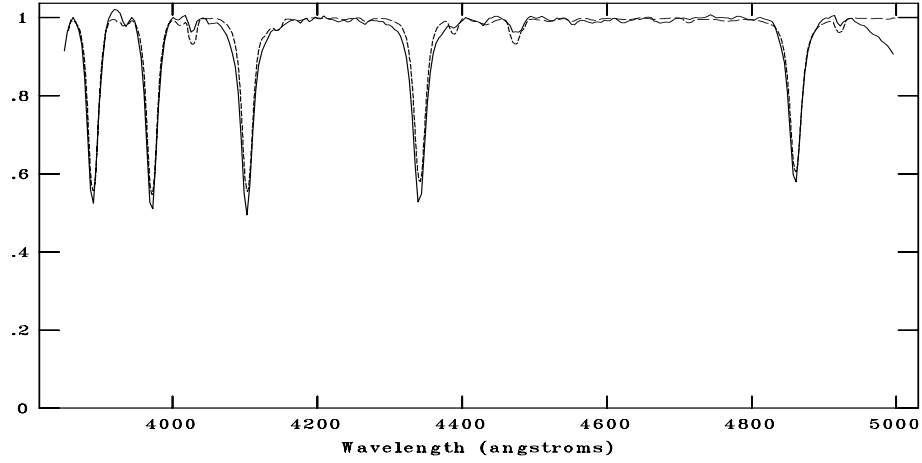
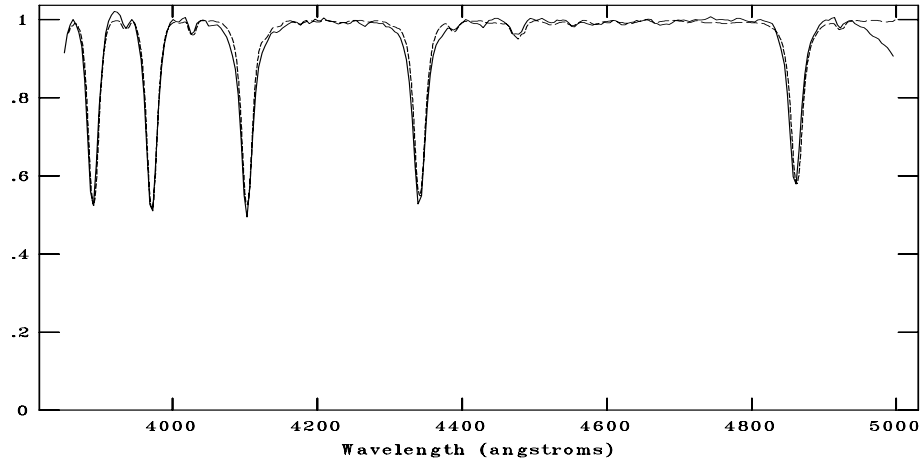


Figure C.28: CAFOS spectrum of 703-080556 compared with F3V, F5V, F6V respectively. The standard spectra are shown with dotted line. The spectral type is assigned as F5V.

NOAO/IRAF V2.16.1 baha@baha-Lenovo-IdeaPad-Y550 Thu 16:16:01 08-Dec-2016
[G089_01n.fits]: G089_01 90. ap:1 beam:1



NOAO/IRAF V2.16.1 baha@baha-Lenovo-IdeaPad-Y550 Thu 16:16:13 08-Dec-2016
[G089_01n.fits]: G089_01 90. ap:1 beam:1



NOAO/IRAF V2.16.1 baha@baha-Lenovo-IdeaPad-Y550 Thu 16:16:22 08-Dec-2016
[G089_01n.fits]: G089_01 90. ap:1 beam:1

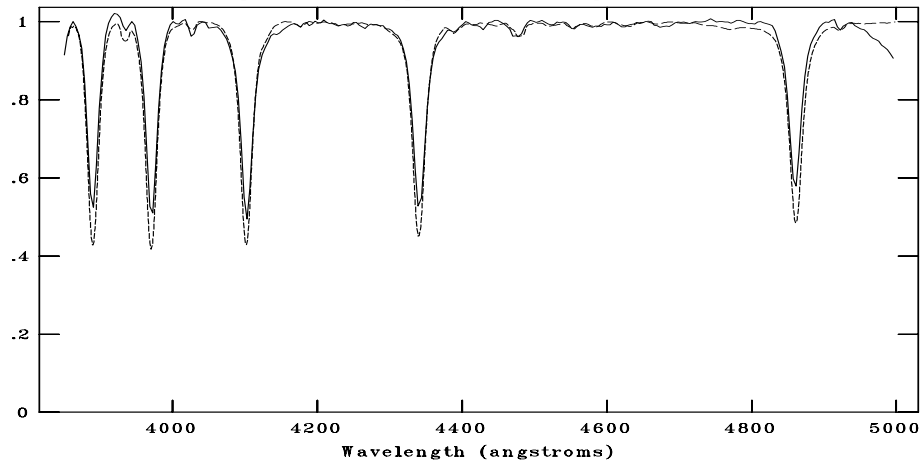
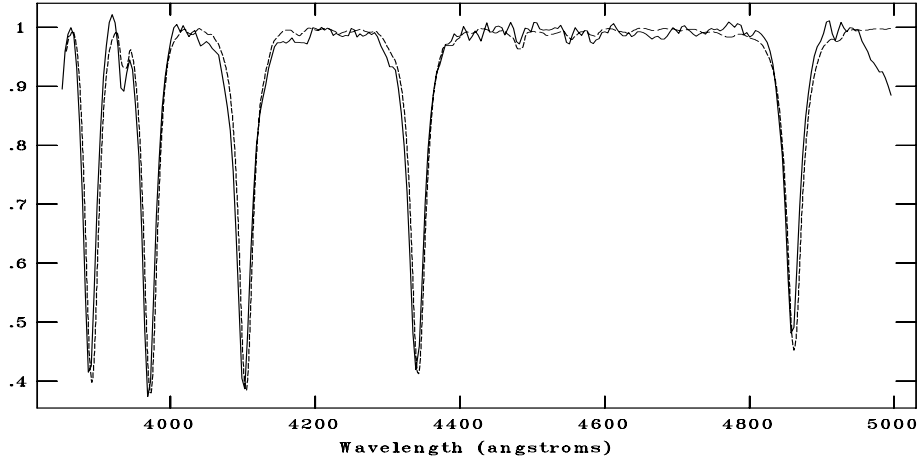
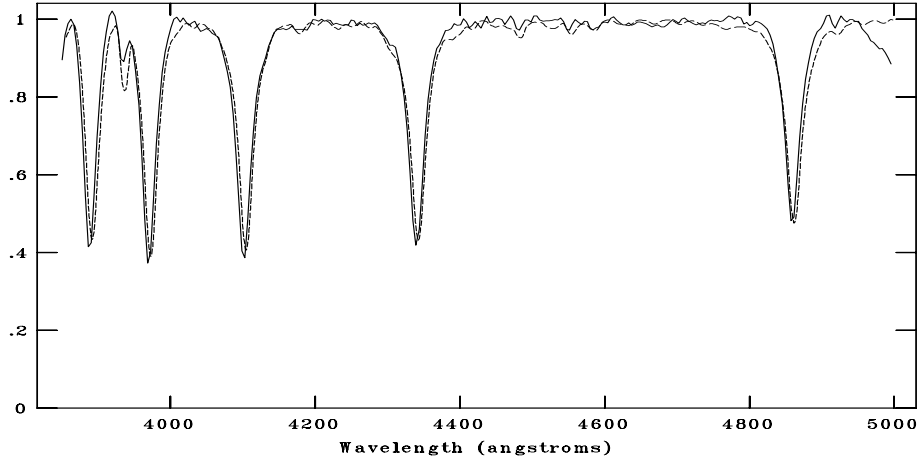


Figure C.29: CAFOS spectrum of 704-07771 compared with , , respectively. The standard spectra are shown with dotted line. The spectral type is assigned as B8V.

NOAO/IRAF V2.16.1 baha@baha-Lenovo-IdeaPad-Y550 Thu 16:18:19 08-Dec-2016
[G089_02n.fits]: G089_02 150. ap:1 beam:1



NOAO/IRAF V2.16.1 baha@baha-Lenovo-IdeaPad-Y550 Thu 16:18:32 08-Dec-2016
[G089_02n.fits]: G089_02 150. ap:1 beam:1



NOAO/IRAF V2.16.1 baha@baha-Lenovo-IdeaPad-Y550 Thu 16:18:05 08-Dec-2016
[G089_02n.fits]: G089_02 150. ap:1 beam:1

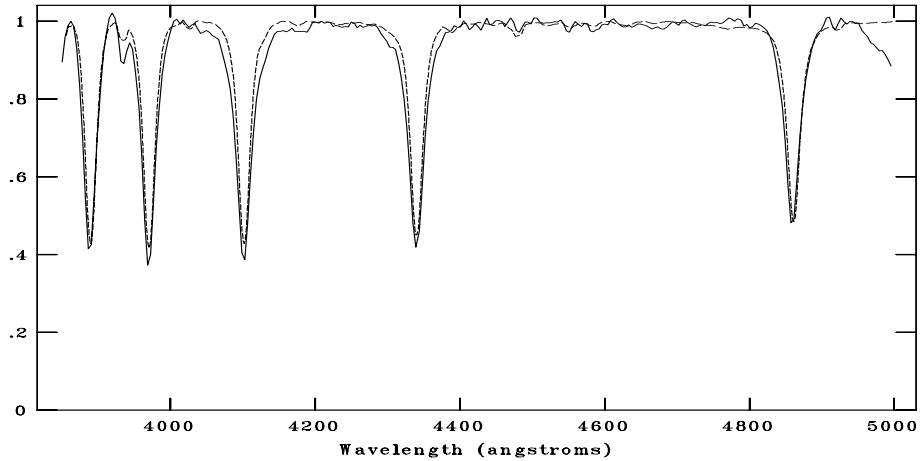
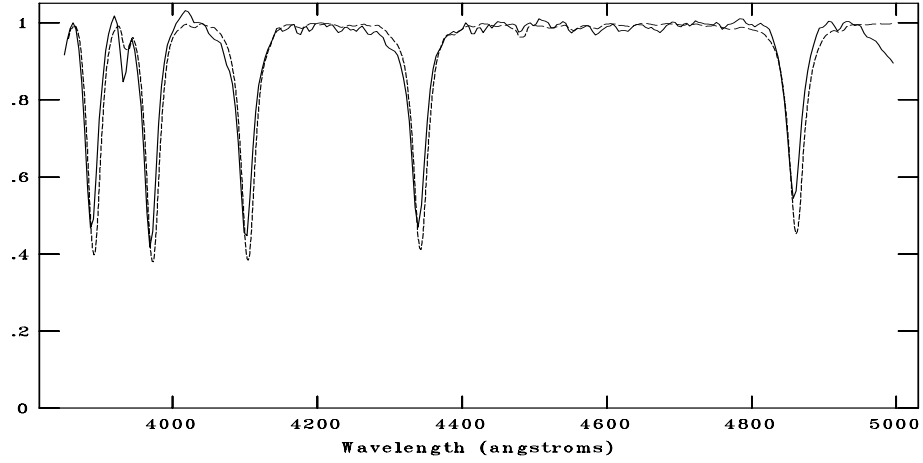
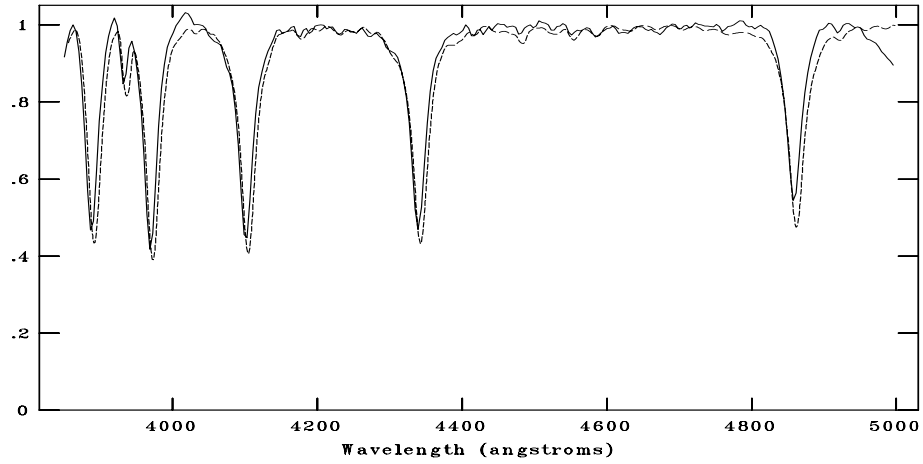


Figure C.30: CAFOS spectrum of 704-078268 compared with A0V, A1V, B9V respectively. The standard spectra are shown with dotted line. The spectral type is assigned as A0V.

NOAO/IRAF V2.16.1 baha@baha-Lenovo-IdeaPad-Y550 Thu 16:20:54 08-Dec-2016
[G089_04n.fits]: G089_04 240. ap:1 beam:1



NOAO/IRAF V2.16.1 baha@baha-Lenovo-IdeaPad-Y550 Thu 16:21:05 08-Dec-2016
[G089_04n.fits]: G089_04 240. ap:1 beam:1



NOAO/IRAF V2.16.1 baha@baha-Lenovo-IdeaPad-Y550 Thu 16:21:15 08-Dec-2016
[G089_04n.fits]: G089_04 240. ap:1 beam:1

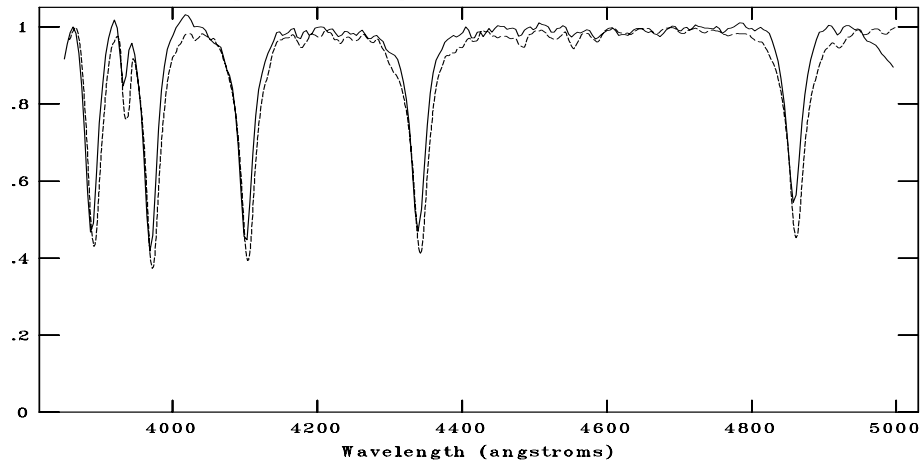
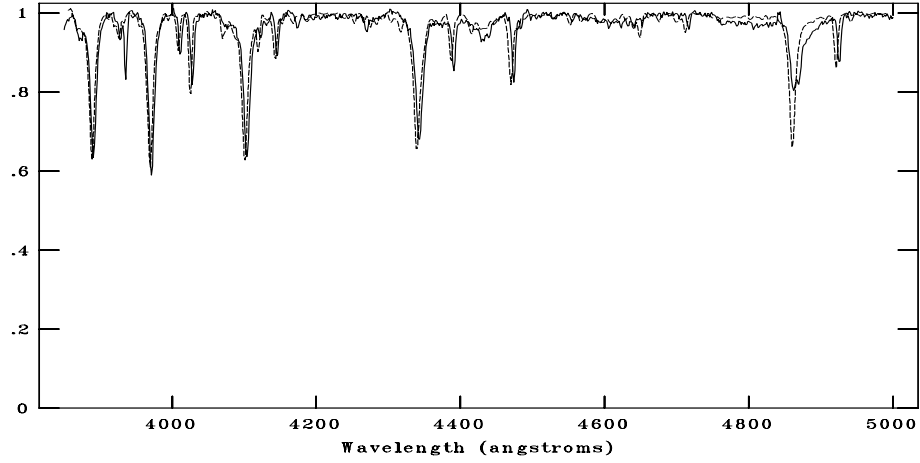
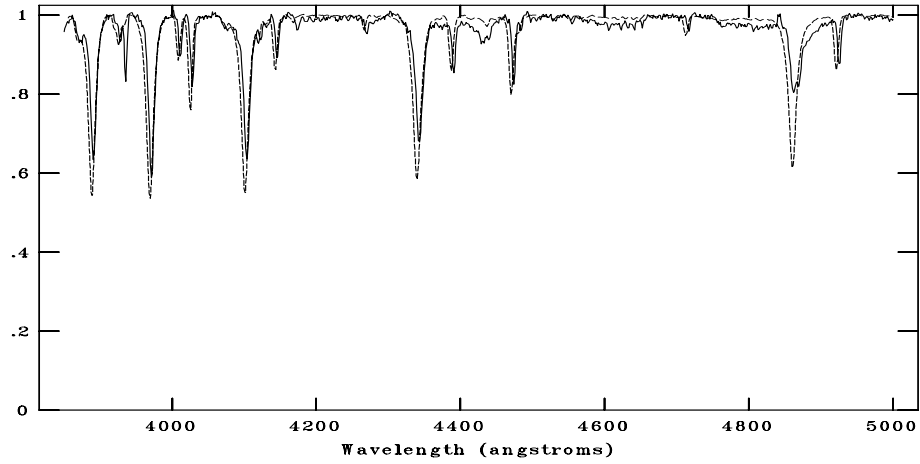


Figure C.31: CAFOS spectrum of 703-080682 compared with A0V, A1V, A3V respectively. The standard spectra are shown with dotted line. The spectral type is assigned as A0V.

NOAO/IRAF V2.16.1 baha@baha-Lenovo-IdeaPad-Y550 Wed 00:31:28 04-Jan-2017
[g89b2.fits]: g89_1 420. ap:1 beam:1



NOAO/IRAF V2.16.1 baha@baha-Lenovo-IdeaPad-Y550 Wed 00:30:11 04-Jan-2017
[g89b2.fits]: g89_1 420. ap:1 beam:1



NOAO/IRAF V2.16.1 baha@baha-Lenovo-IdeaPad-Y550 Wed 00:32:14 04-Jan-2017
[g89b2.fits]: g89_1 420. ap:1 beam:1

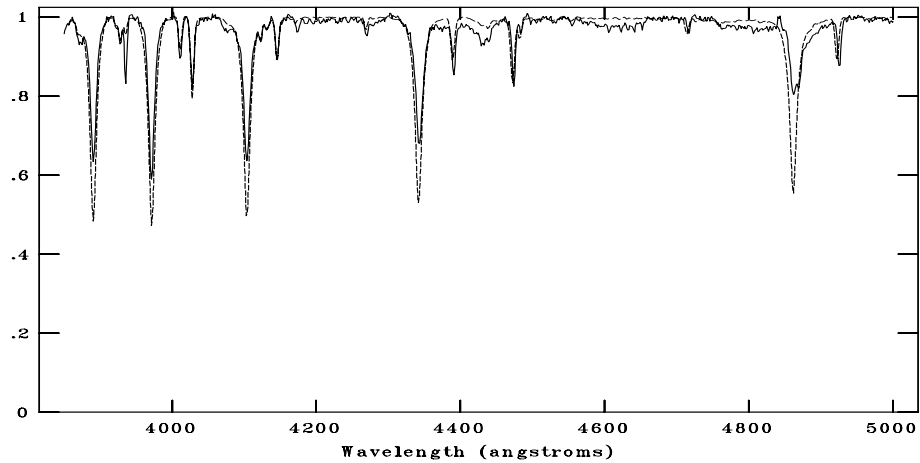
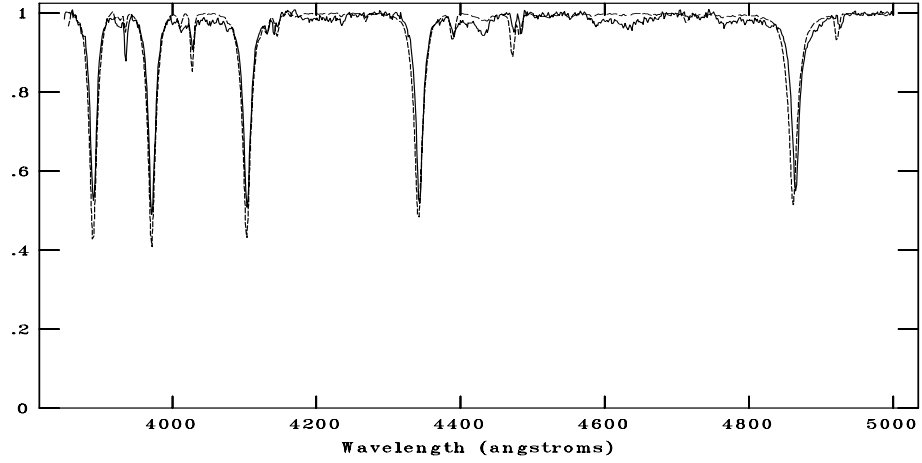
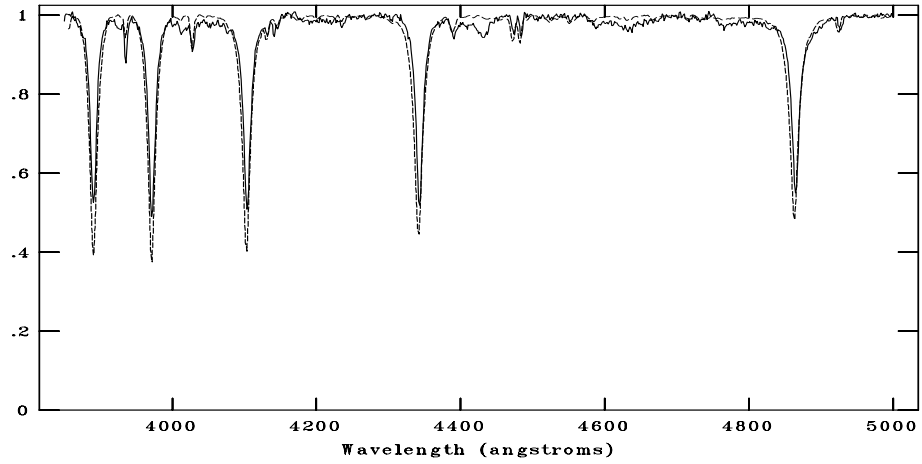


Figure C.32: TFOSC spectrum of 703-080938 compared with B1V, B2V, B3V respectively. The standard spectra are shown with dotted line. The spectral type is assigned as B2V.

NOAO/IRAF V2.16.1 baha@baha-Lenovo-IdeaPad-Y550 Wed 00:36:21 04-Jan-2017
[g892n.fits]: g89_2 1200. ap:1 beam:1



NOAO/IRAF V2.16.1 baha@baha-Lenovo-IdeaPad-Y550 Wed 00:35:56 04-Jan-2017
[g892n.fits]: g89_2 1200. ap:1 beam:1



NOAO/IRAF V2.16.1 baha@baha-Lenovo-IdeaPad-Y550 Wed 00:36:44 04-Jan-2017
[g892n.fits]: g89_2 1200. ap:1 beam:1

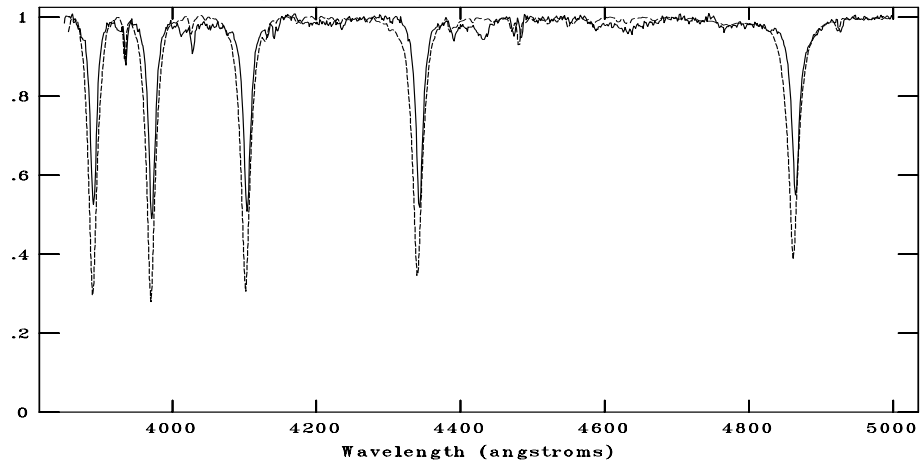


Figure C.33: TFOSC spectrum of 703-081110 compared with B7V, B8V, B9V respectively. The standard spectra are shown with dotted line. The spectral type is assigned as B8V.

C.5 G093.7-0.2

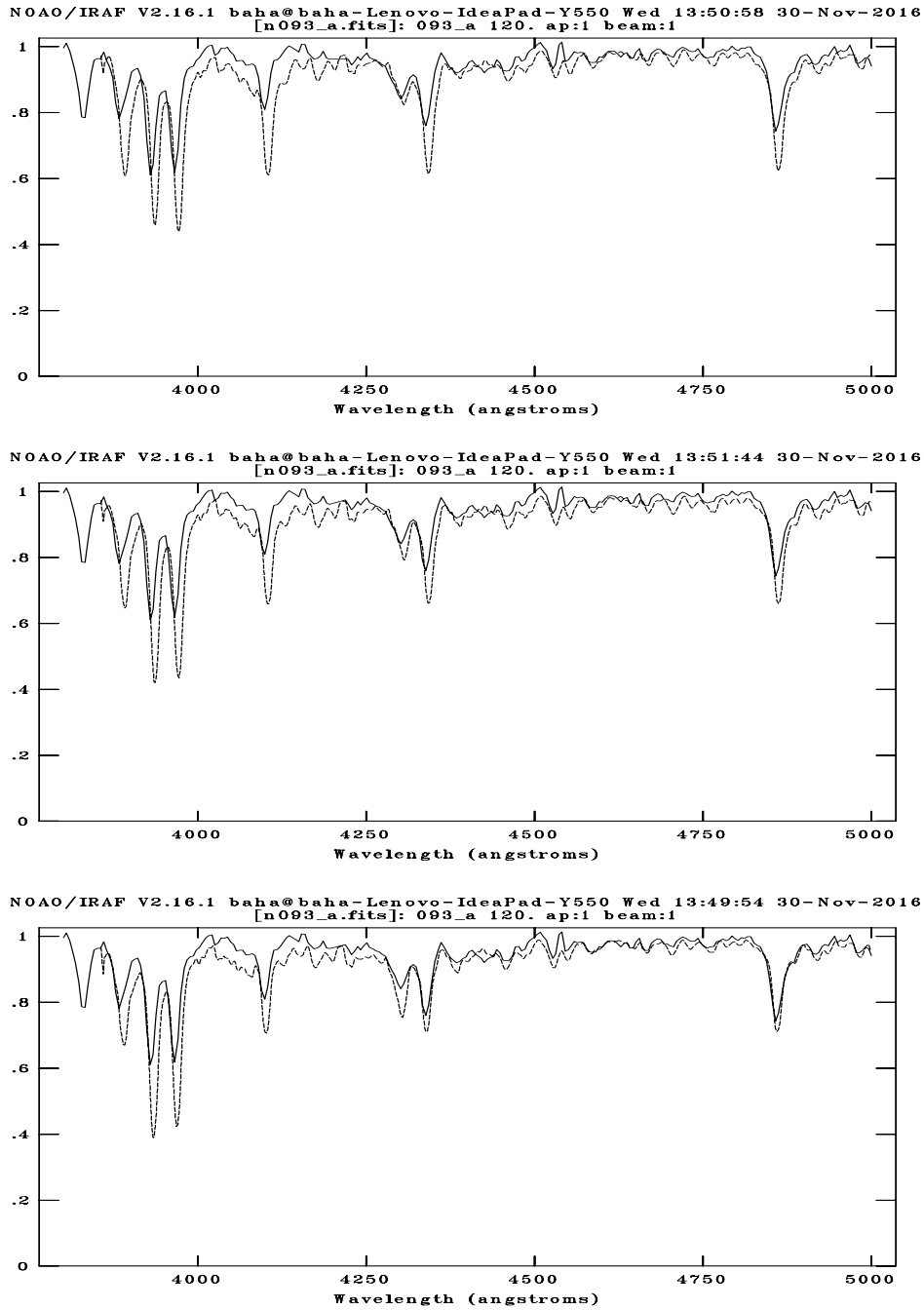
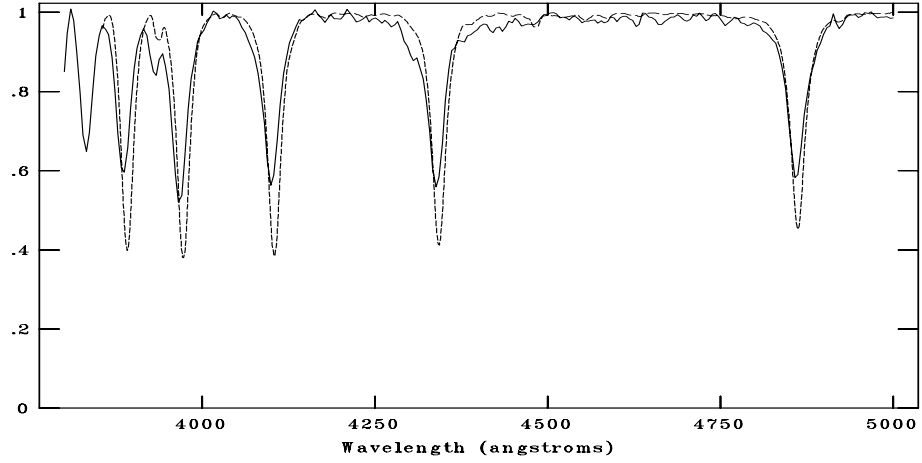
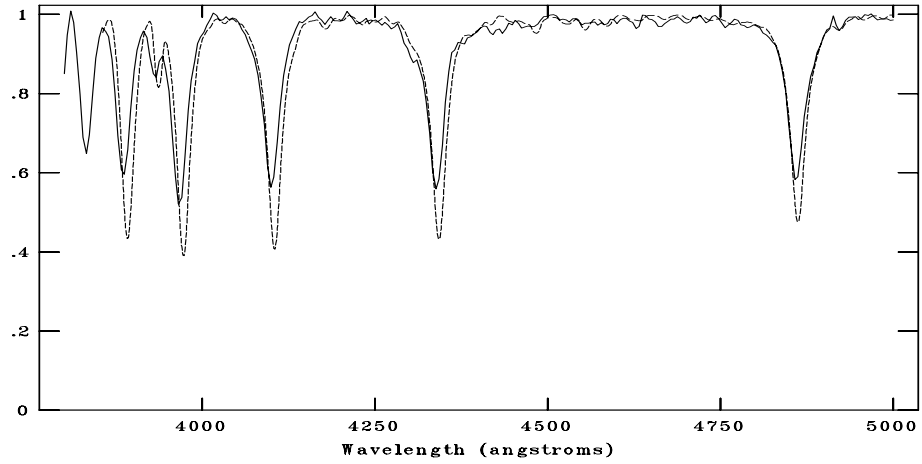


Figure C.34: CAFOS spectrum of 704-083954 compared with F3V, F5V and F6V respectively. The standard spectra are shown with dotted line. The spectral type is assigned as F5V.

NOAO/IRAF V2.16.1 baha@baha-Lenovo-IdeaPad-Y550 Wed 13:54:24 30-Nov-2016
[n093_b.fits]: 093_b 180. ap:1 beam:1



NOAO/IRAF V2.16.1 baha@baha-Lenovo-IdeaPad-Y550 Wed 13:55:36 30-Nov-2016
[n093_b.fits]: 093_b 180. ap:1 beam:1



NOAO/IRAF V2.16.1 baha@baha-Lenovo-IdeaPad-Y550 Wed 13:59:55 30-Nov-2016
[n093_b.fits]: 093_b 180. ap:1 beam:1

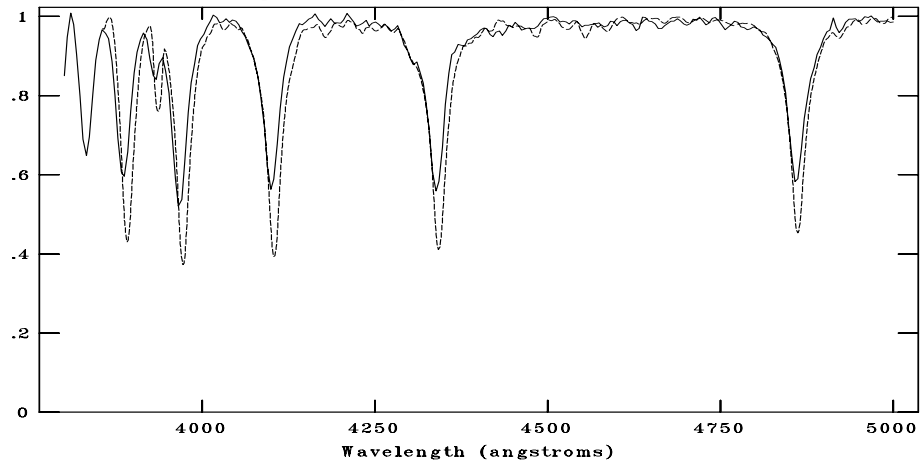
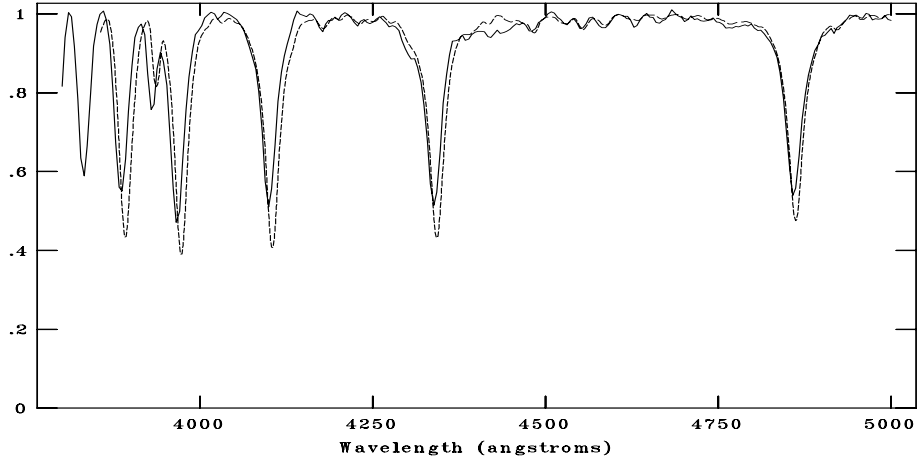
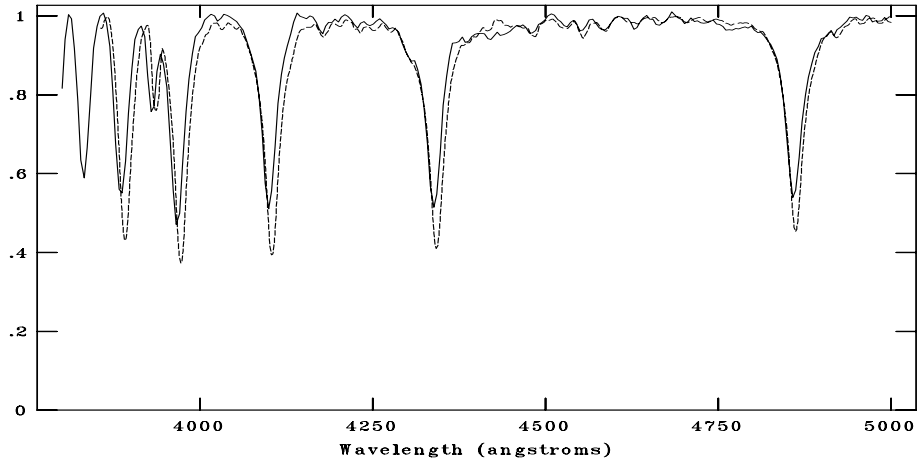


Figure C.35: CAFOS spectrum of 704-083954 compared with A0V, A1V and A3V respectively. The standard spectra are shown with dotted line. The spectral type is assigned as F5V.

NOAO/IRAF V2.16.1 baha@baha-Lenovo-IdeaPad-Y550 Wed 14:43:13 30-Nov-2016
[n093_c.fits]: 093_c 300. ap:1 beam:1



NOAO/IRAF V2.16.1 baha@baha-Lenovo-IdeaPad-Y550 Wed 14:42:27 30-Nov-2016
[n093_c.fits]: 093_c 300. ap:1 beam:1



NOAO/IRAF V2.16.1 baha@baha-Lenovo-IdeaPad-Y550 Wed 14:44:03 30-Nov-2016
[n093_c.fits]: 093_c 300. ap:1 beam:1

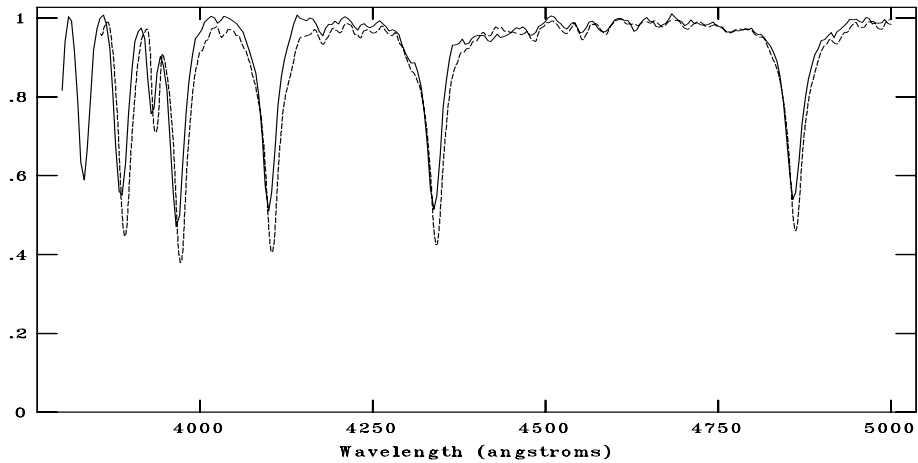
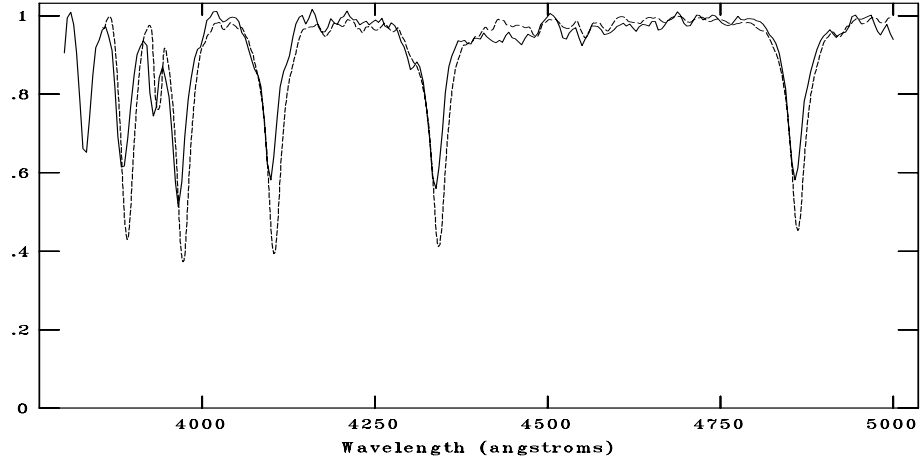
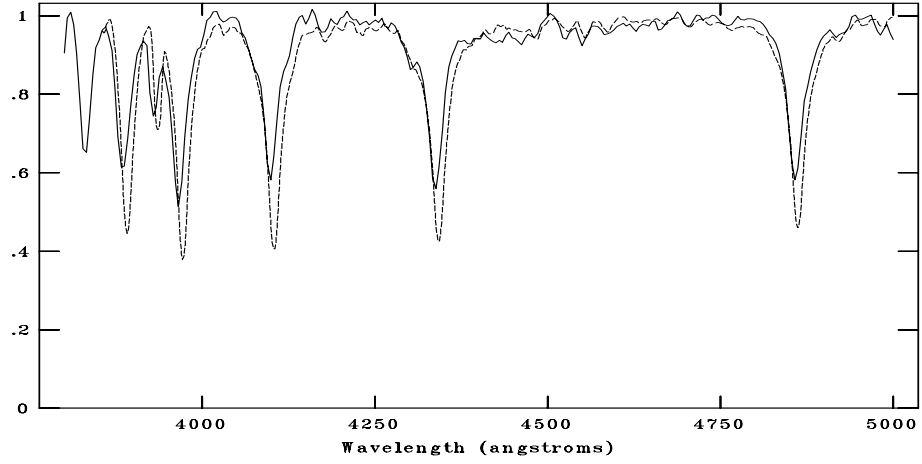


Figure C.36: CAFOS spectrum of 704-083954 compared with A1V, A3V, A5V respectively. The standard spectra are shown with dotted line. The spectral type is assigned as F5V.

NOAO/IRAF V2.16.1 baha@baha-Lenovo-IdeaPad-Y550 Wed 14:47:08 30-Nov-2016
[n093_e.fits]: 093_e 300. ap:1 beam:1



NOAO/IRAF V2.16.1 baha@baha-Lenovo-IdeaPad-Y550 Wed 14:47:43 30-Nov-2016
[n093_e.fits]: 093_e 300. ap:1 beam:1



NOAO/IRAF V2.16.1 baha@baha-Lenovo-IdeaPad-Y550 Wed 14:50:31 30-Nov-2016
[n093_d.fits]: 093_d 250. ap:1 beam:1

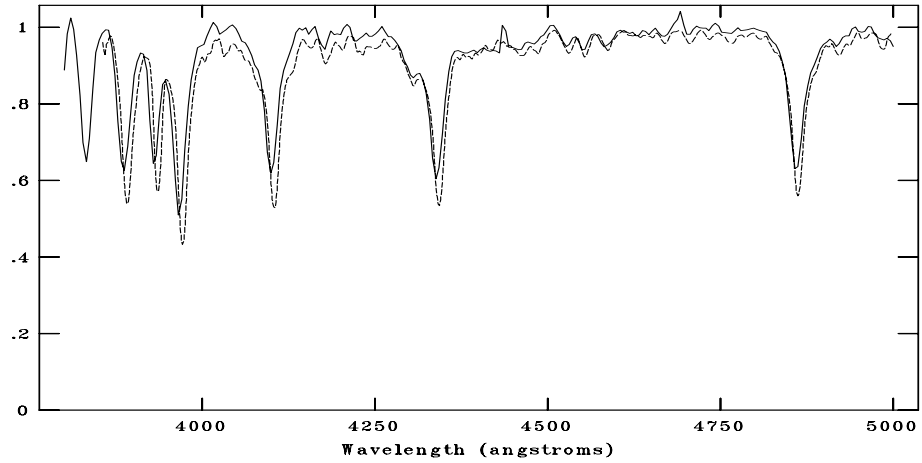
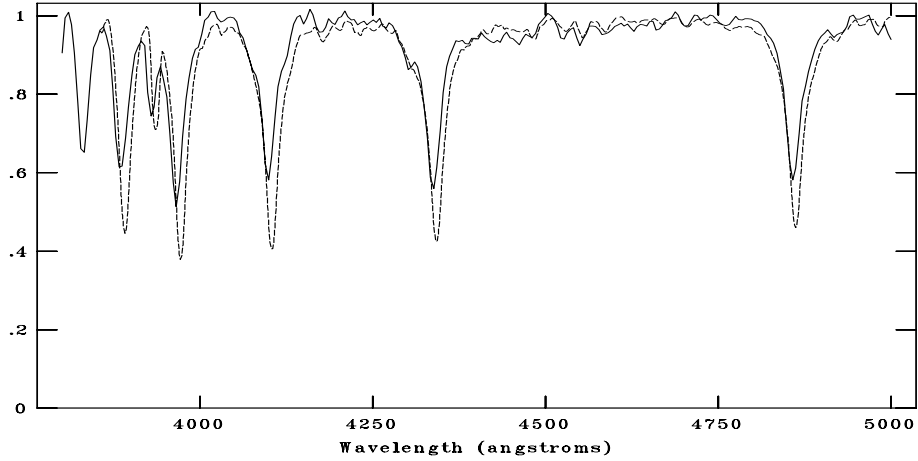
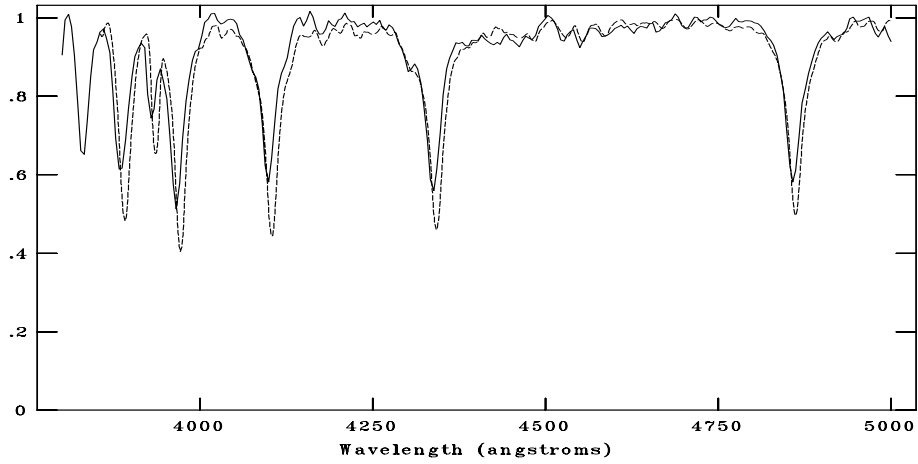


Figure C.37: CAFOS spectrum of 704-083954 compared with A3V, A5V, F0V respectively. The standard spectra are shown with dotted line. The spectral type is assigned as F5V.

NOAO/IRAF V2.16.1 baha@baha-Lenovo-IdeaPad-Y550 Wed 14:54:40 30-Nov-2016
[n093_e.fits]: 093_e 300. ap:1 beam:1



NOAO/IRAF V2.16.1 baha@baha-Lenovo-IdeaPad-Y550 Wed 14:52:36 30-Nov-2016
[n093_e.fits]: 093_e 300. ap:1 beam:1



NOAO/IRAF V2.16.1 baha@baha-Lenovo-IdeaPad-Y550 Wed 14:53:36 30-Nov-2016
[n093_e.fits]: 093_e 300. ap:1 beam:1

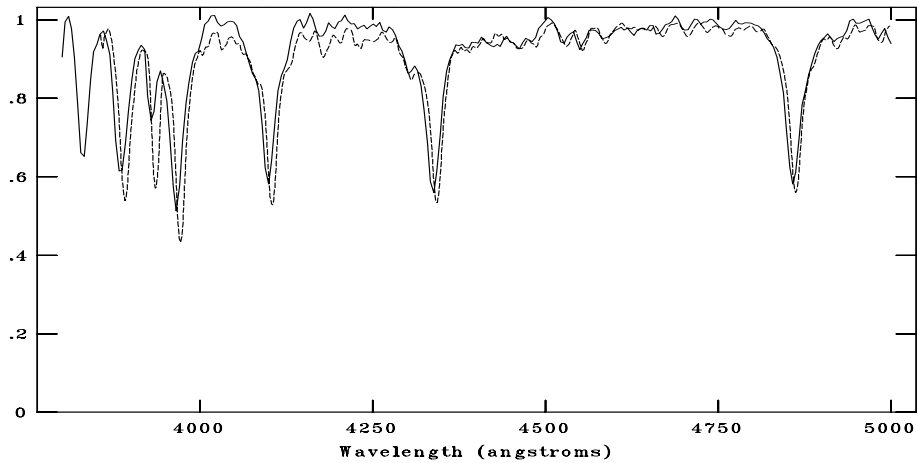
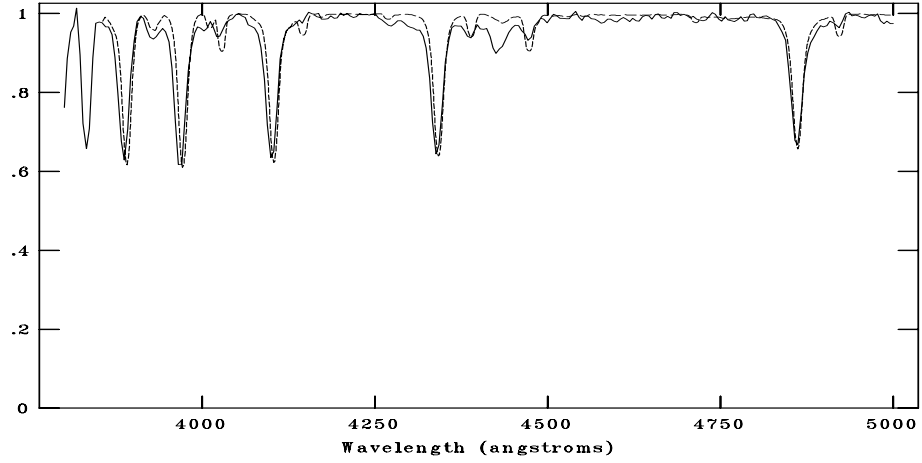
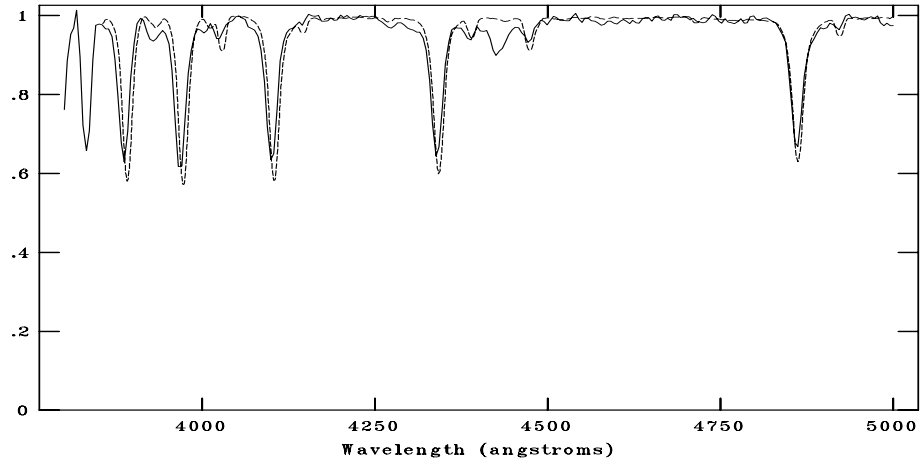


Figure C.38: CAFOS spectrum of 704-083954 compared with A5V, A7V, F0V respectively. The standard spectra are shown with dotted line. The spectral type is assigned as F5V.

NOAO/IRAF V2.16.1 baha@baha-Lenovo-IdeaPad-Y550 Wed 14:57:57 30-Nov-2016
[n093_f.fits]: 093_f 350. ap:1 beam:1



NOAO/IRAF V2.16.1 baha@baha-Lenovo-IdeaPad-Y550 Wed 14:55:26 30-Nov-2016
[n093_f.fits]: 093_f 350. ap:1 beam:1



NOAO/IRAF V2.16.1 baha@baha-Lenovo-IdeaPad-Y550 Wed 14:56:16 30-Nov-2016
[n093_f.fits]: 093_f 350. ap:1 beam:1

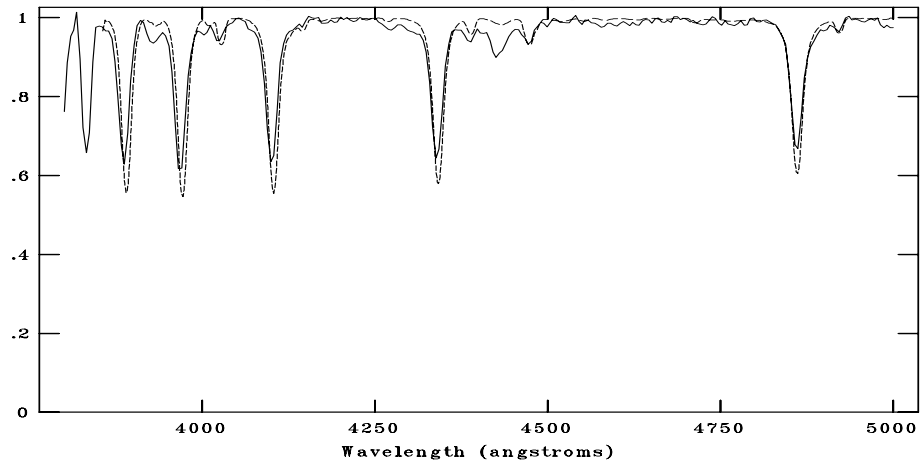
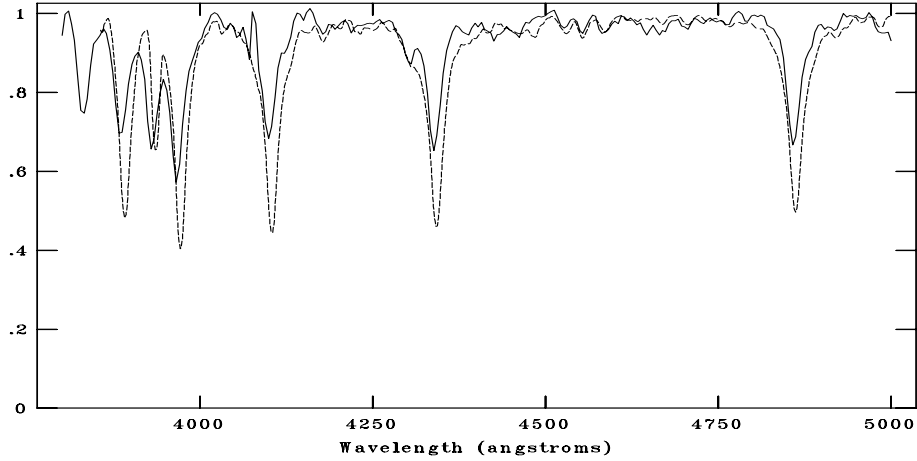
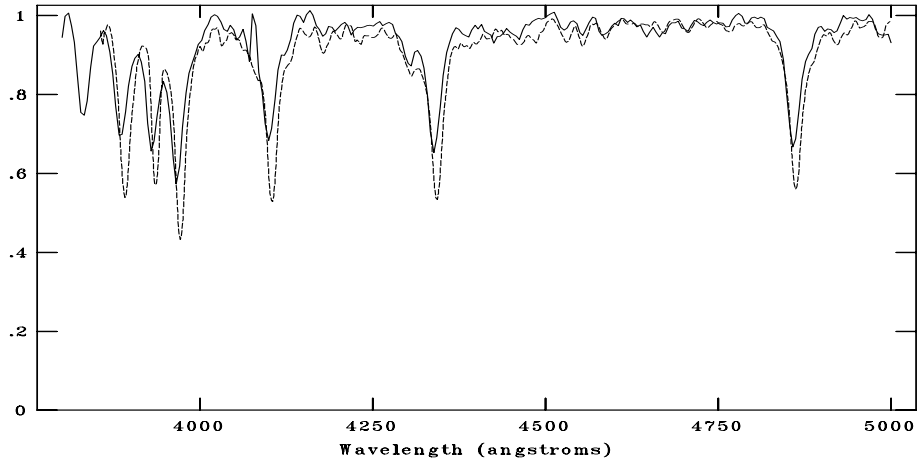


Figure C.39: CAFOS spectrum of 704-083954 compared with B3V, B5V, B7V respectively. The standard spectra are shown with dotted line. The spectral type is assigned as B6V.

NOAO/IRAF V2.16.1 baha@baha-Lenovo-IdeaPad-Y550 Wed 15:19:23 30-Nov-2016
[n093_g.fits]: 093_g 350. ap:1 beam:1



NOAO/IRAF V2.16.1 baha@baha-Lenovo-IdeaPad-Y550 Wed 14:58:46 30-Nov-2016
[n093_g.fits]: 093_g 350. ap:1 beam:1



NOAO/IRAF V2.16.1 baha@baha-Lenovo-IdeaPad-Y550 Wed 15:17:46 30-Nov-2016
[n093_g.fits]: 093_g 350. ap:1 beam:1

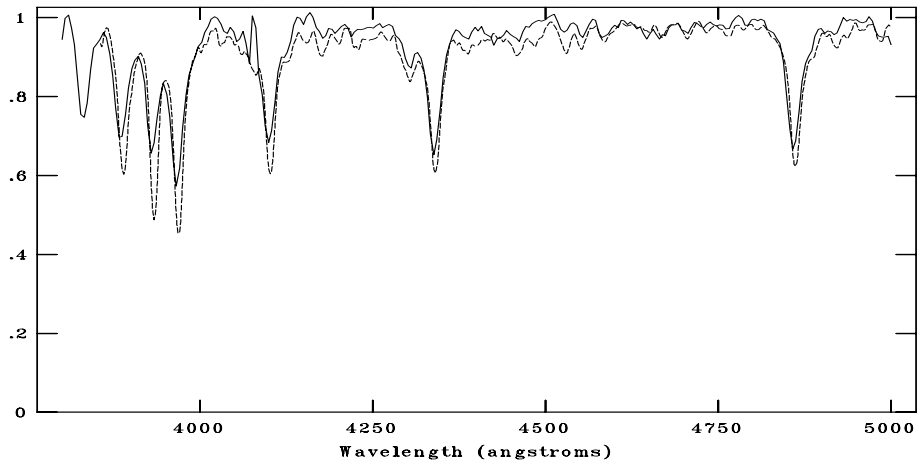
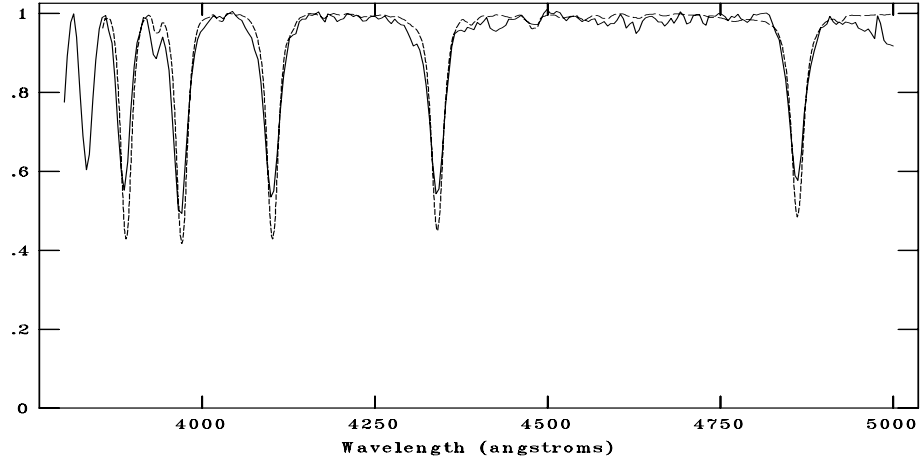
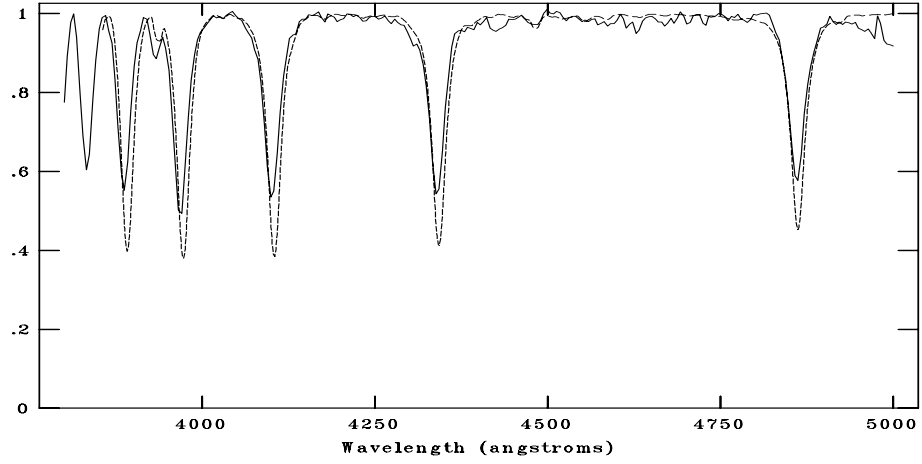


Figure C.40: CAFOS spectrum of 704-083954 compared with A7V, F0V, F2V respectively. The standard spectra are shown with dotted line. The spectral type is assigned as F5V.

NOAO/IRAF V2.16.1 baha@baha-Lenovo-IdeaPad-Y550 Wed 15:20:00 30-Nov-2016
[n093_h.fits]: 093_h 400. ap:1 beam:1



NOAO/IRAF V2.16.1 baha@baha-Lenovo-IdeaPad-Y550 Wed 15:22:21 30-Nov-2016
[n093_h.fits]: 093_h 400. ap:1 beam:1



NOAO/IRAF V2.16.1 baha@baha-Lenovo-IdeaPad-Y550 Wed 15:23:56 30-Nov-2016
[n093_h.fits]: 093_h 400. ap:1 beam:1

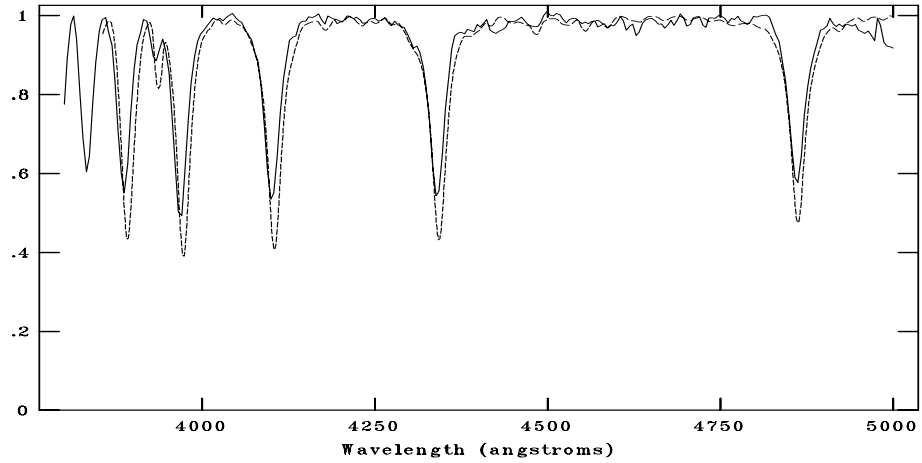
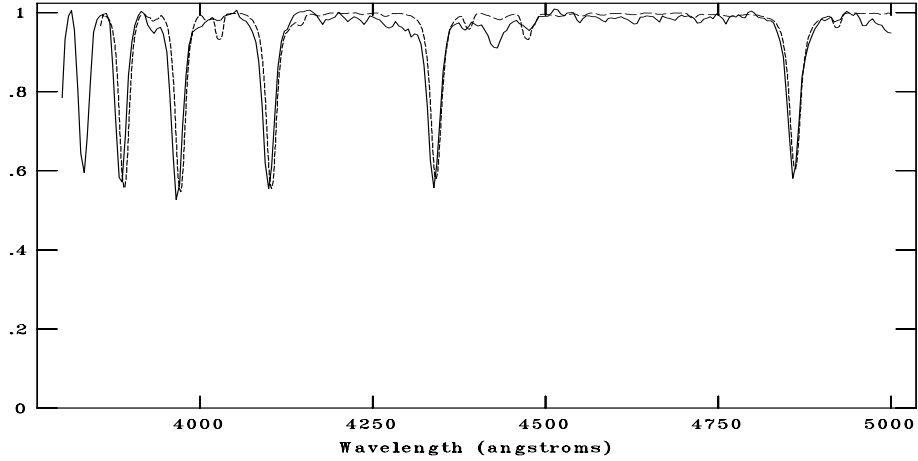
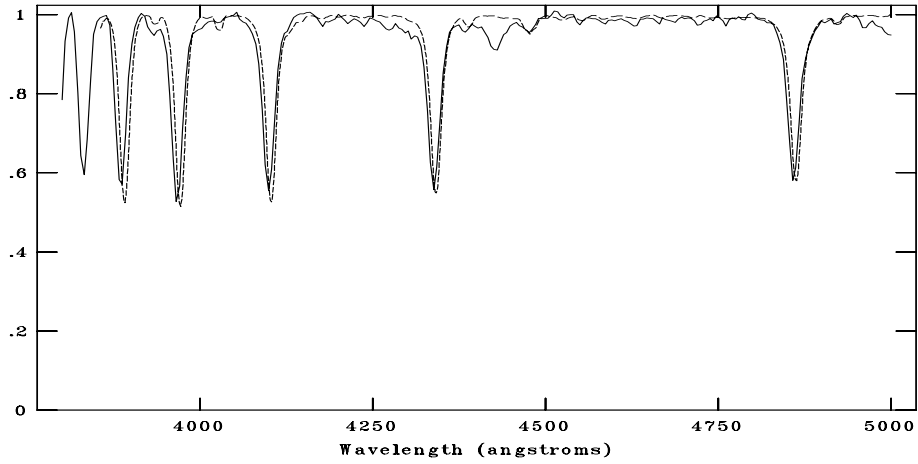


Figure C.41: CAFOS spectrum of 704-083954 compared with B9V, A0V, A1V respectively. The standard spectra are shown with dotted line. The spectral type is assigned as F5V.

NOAO/IRAF V2.16.1 baha@baha-Lenovo-IdeaPad-Y550 Wed 15:27:18 30-Nov-2016
[n093_i.fits]: 093_i 400. ap:1 beam:1



NOAO/IRAF V2.16.1 baha@baha-Lenovo-IdeaPad-Y550 Wed 15:26:09 30-Nov-2016
[n093_i.fits]: 093_i 400. ap:1 beam:1



NOAO/IRAF V2.16.1 baha@baha-Lenovo-IdeaPad-Y550 Wed 15:27:43 30-Nov-2016
[n093_i.fits]: 093_i 400. ap:1 beam:1

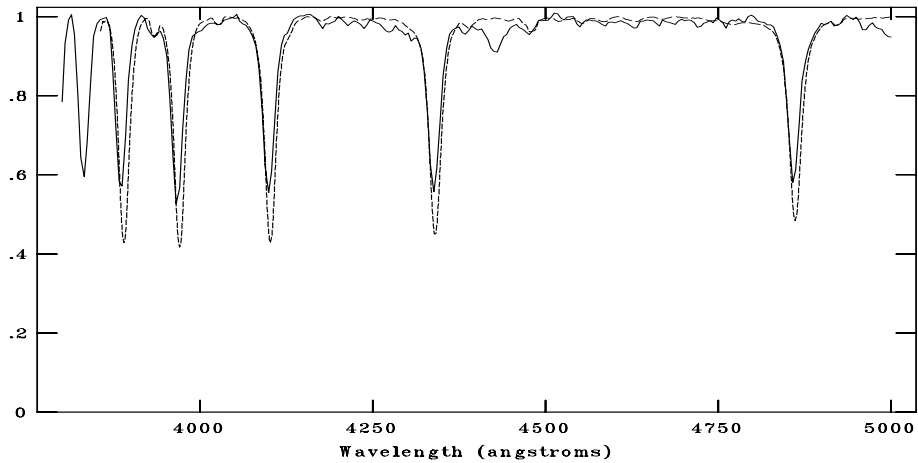
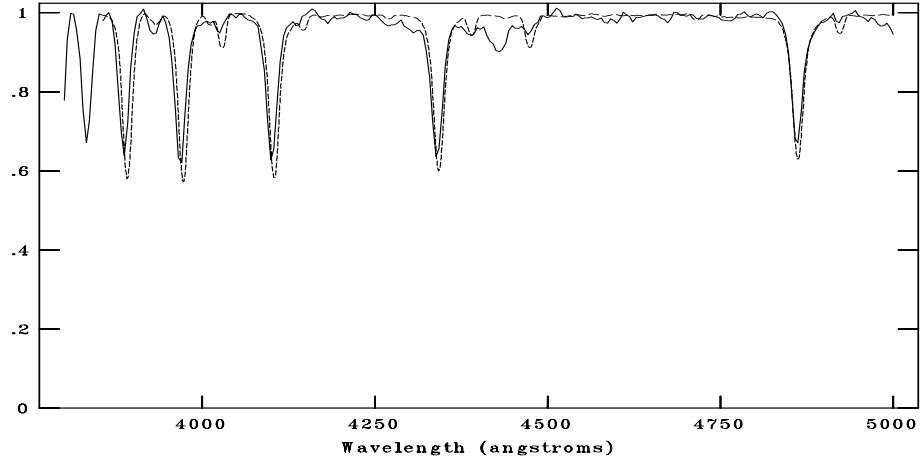
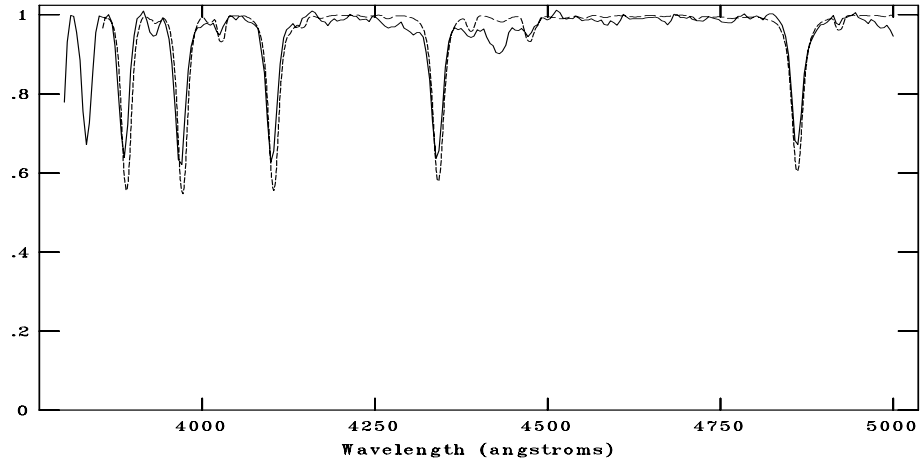


Figure C.42: CAFOS spectrum of 704-083954 compared with B7V, B8V and B9V respectively. The standard spectra are shown with dotted line. The spectral type is assigned as B8V.

NOAO/IRAF V2.16.1 baha@baha-Lenovo-IdeaPad-Y550 Wed 15:31:05 30-Nov-2016
[n093_j.fits]: 093_j 420. ap:1 beam:1



NOAO/IRAF V2.16.1 baha@baha-Lenovo-IdeaPad-Y550 Wed 15:30:16 30-Nov-2016
[n093_j.fits]: 093_j 420. ap:1 beam:1



NOAO/IRAF V2.16.1 baha@baha-Lenovo-IdeaPad-Y550 Wed 15:29:25 30-Nov-2016
[n093_j.fits]: 093_j 420. ap:1 beam:1

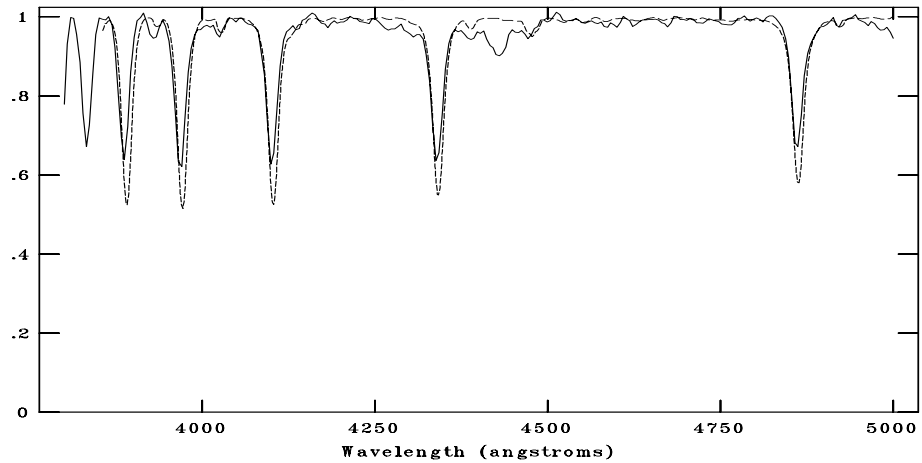
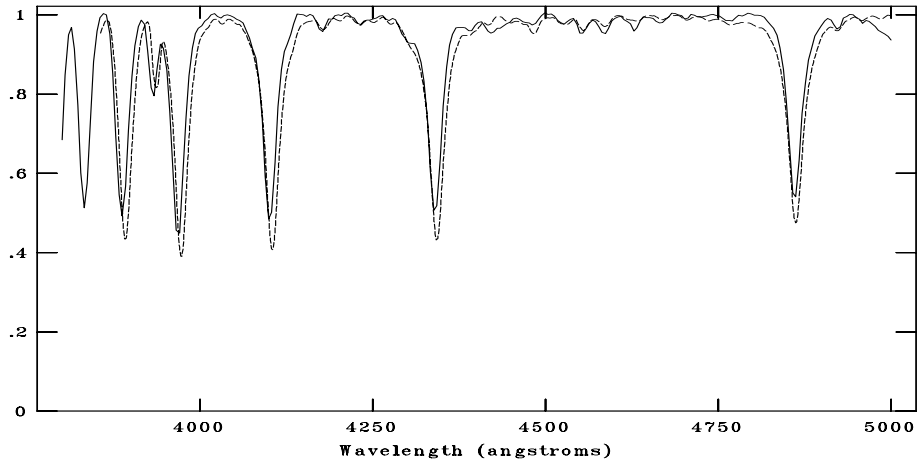
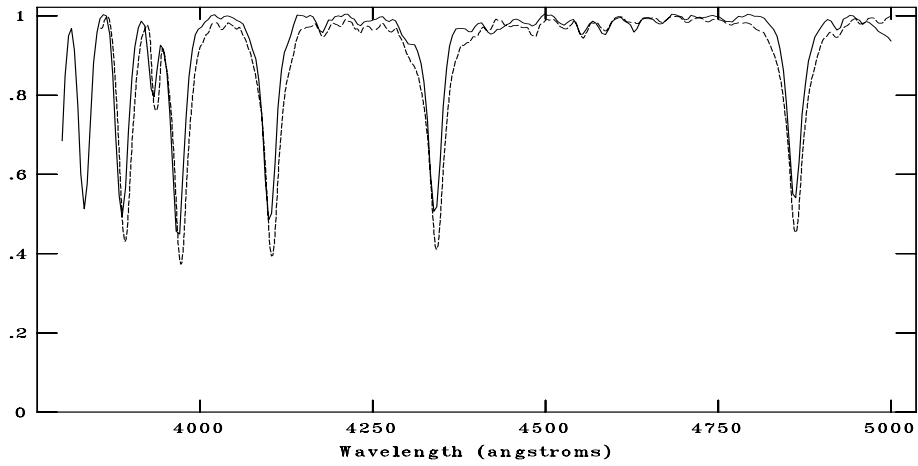


Figure C.43: CAFOS spectrum of 704-083954 compared with B5V, B7V, B8V respectively. The standard spectra are shown with dotted line. The spectral type is assigned as B7V.

NOAO/IRAF V2.16.1 baha@baha-Lenovo-IdeaPad-Y550 Wed 15:34:11 30-Nov-2016
[n093_k.fits]: 093_k 420. ap:1 beam:1



NOAO/IRAF V2.16.1 baha@baha-Lenovo-IdeaPad-Y550 Wed 15:32:44 30-Nov-2016
[n093_k.fits]: 093_k 420. ap:1 beam:1



NOAO/IRAF V2.16.1 baha@baha-Lenovo-IdeaPad-Y550 Wed 15:33:34 30-Nov-2016
[n093_k.fits]: 093_k 420. ap:1 beam:1

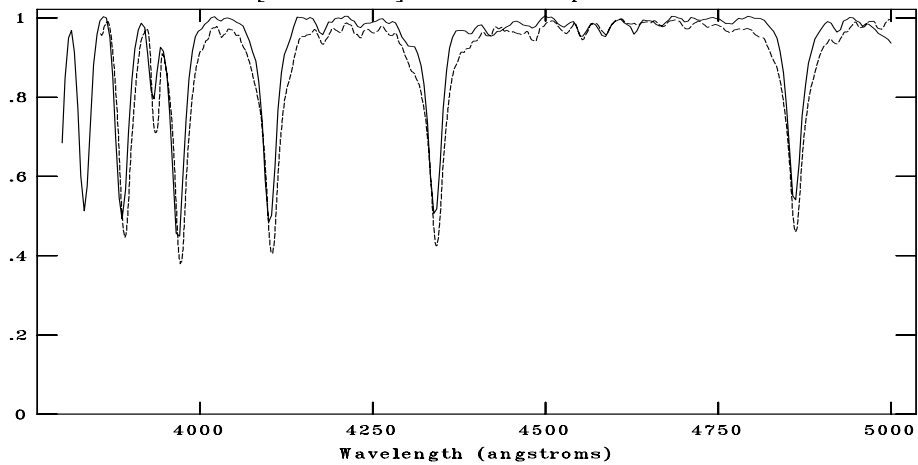
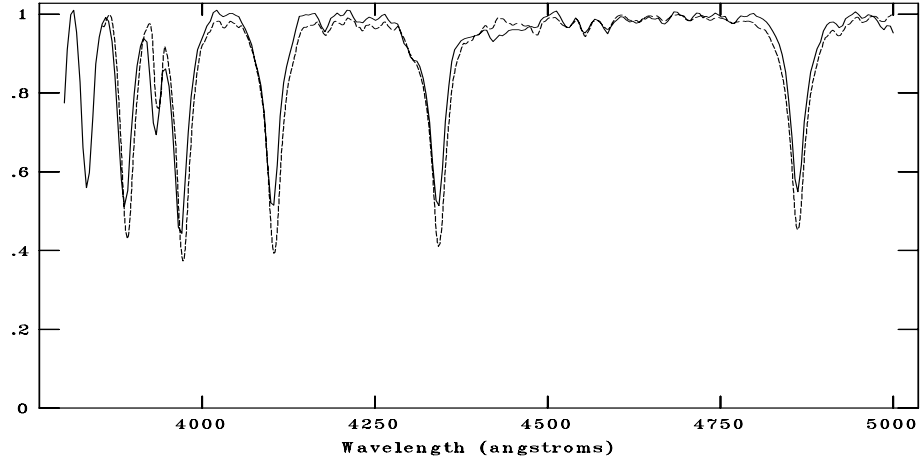
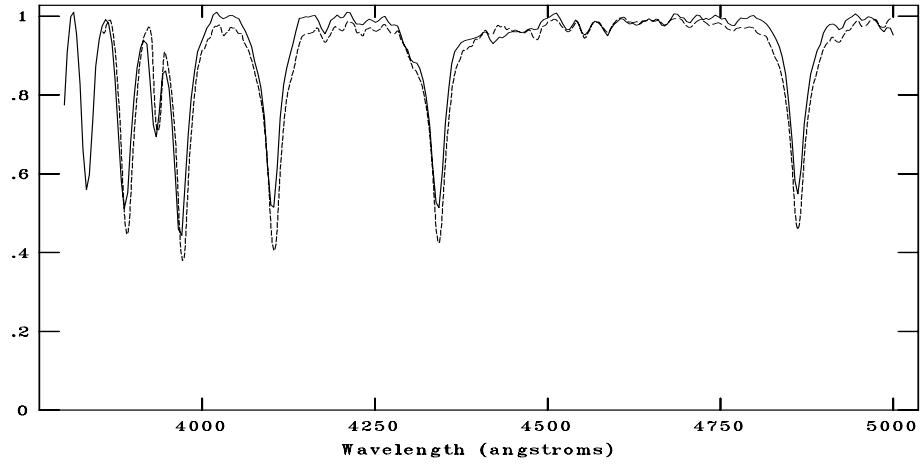


Figure C.44: CAFOS spectrum of 704-083954 compared with A1V, A3V, A5V respectively. The standard spectra are shown with dotted line. The spectral type is assigned as A3V.

NOAO/IRAF V2.16.1 baha@baha-Lenovo-IdeaPad-Y550 Wed 15:35:44 30-Nov-2016
[n093_l.fits]: 093_l 480. ap:1 beam:1



NOAO/IRAF V2.16.1 baha@baha-Lenovo-IdeaPad-Y550 Wed 15:36:11 30-Nov-2016
[n093_l.fits]: 093_l 480. ap:1 beam:1



NOAO/IRAF V2.16.1 baha@baha-Lenovo-IdeaPad-Y550 Wed 15:36:34 30-Nov-2016
[n093_l.fits]: 093_l 480. ap:1 beam:1

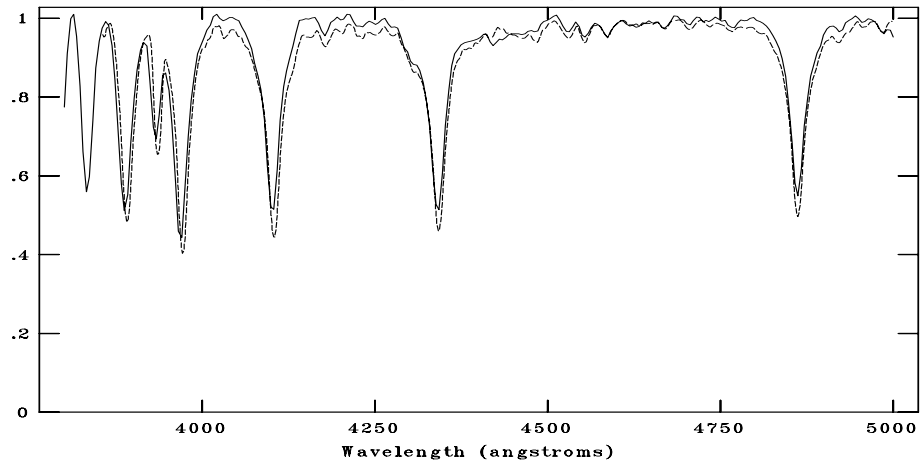
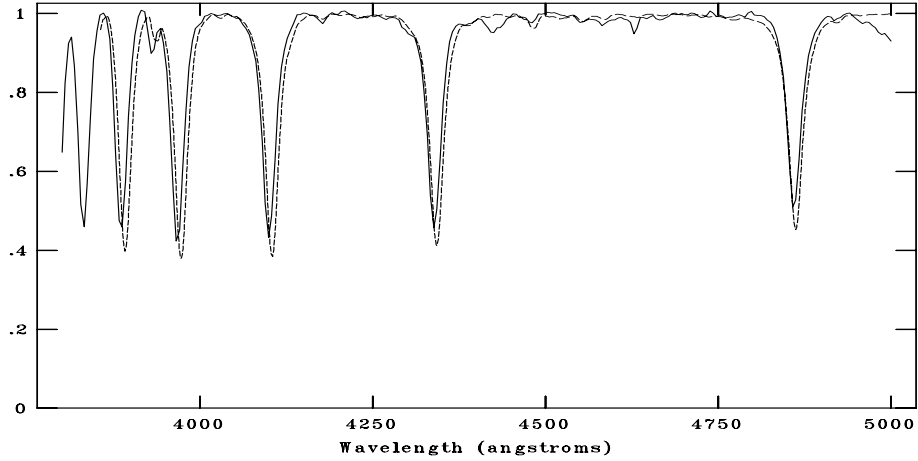
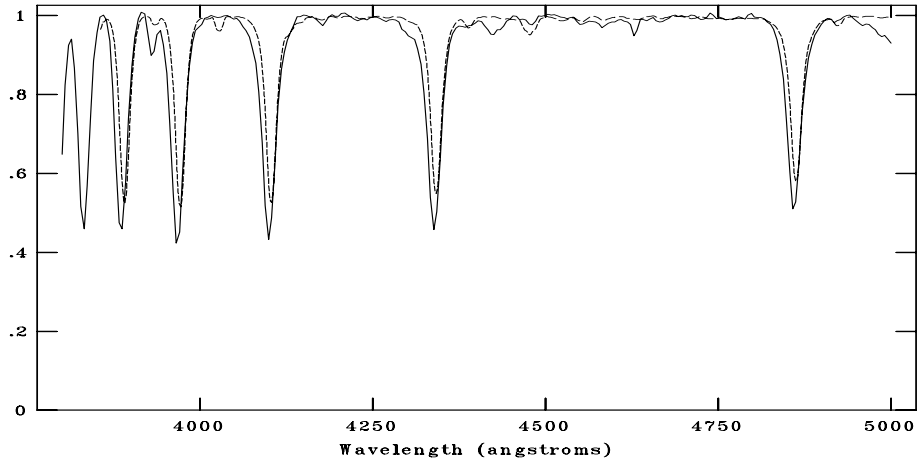


Figure C.45: CAFOS spectrum of 704-083954 compared with A3V, A5V, A7V respectively. The standard spectra are shown with dotted line. The spectral type is assigned as A5V.

NOAO/IRAF V2.16.1 baha@baha-Lenovo-IdeaPad-Y550 Wed 15:41:17 30-Nov-2016
[n093_m.fits]: 093_m 500. ap:1 beam:1



NOAO/IRAF V2.16.1 baha@baha-Lenovo-IdeaPad-Y550 Wed 15:51:30 30-Nov-2016
[n093_m.fits]: 093_m 500. ap:1 beam:1



NOAO/IRAF V2.16.1 baha@baha-Lenovo-IdeaPad-Y550 Wed 15:41:48 30-Nov-2016
[n093_m.fits]: 093_m 500. ap:1 beam:1

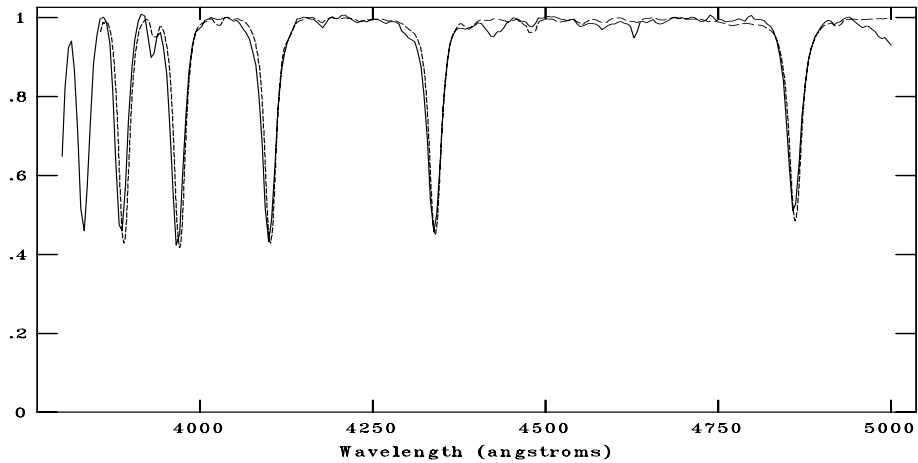
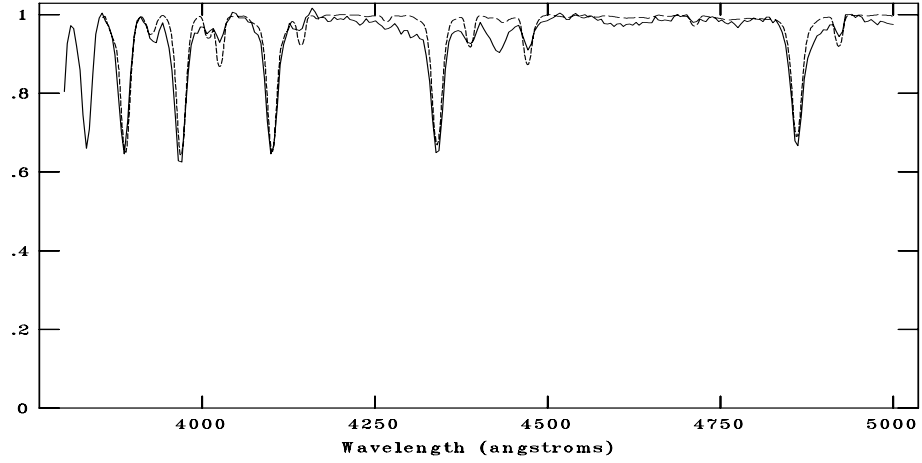
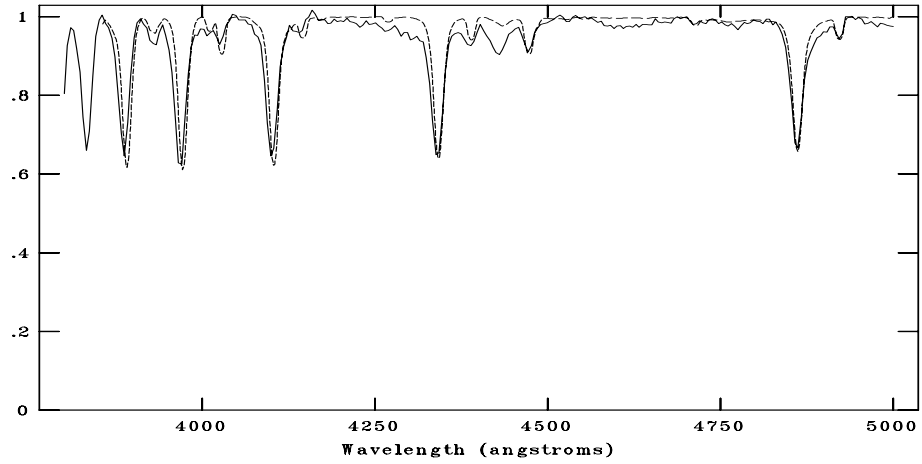


Figure C.46: CAFOS spectrum of 704-083954 compared with A0V,B8V,B9V respectively. The standard spectra are shown with dotted line. The spectral type is assigned as B9V.

NOAO/IRAF V2.16.1 baha@baha-Lenovo-IdeaPad-Y550 Wed 15:53:26 30-Nov-2016
[n093_n.fits]: 093_n 550. ap:1 beam:1



NOAO/IRAF V2.16.1 baha@baha-Lenovo-IdeaPad-Y550 Wed 15:52:39 30-Nov-2016
[n093_n.fits]: 093_n 550. ap:1 beam:1



NOAO/IRAF V2.16.1 baha@baha-Lenovo-IdeaPad-Y550 Wed 15:53:55 30-Nov-2016
[n093_n.fits]: 093_n 550. ap:1 beam:1

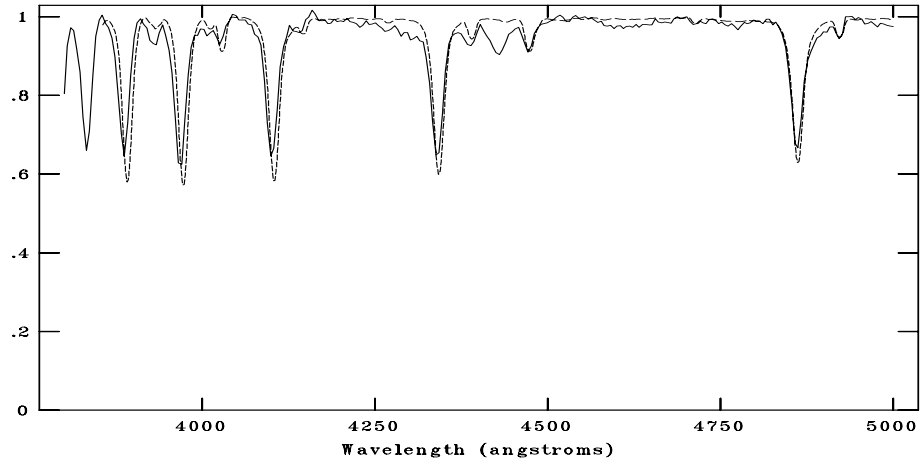
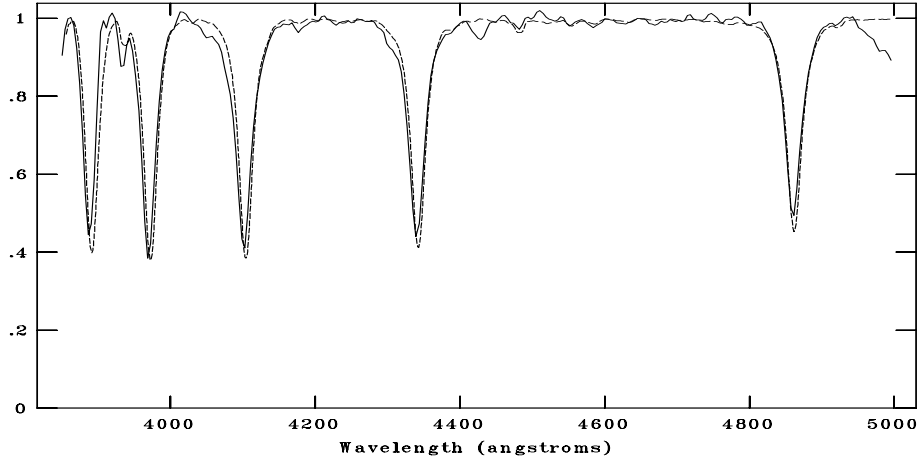
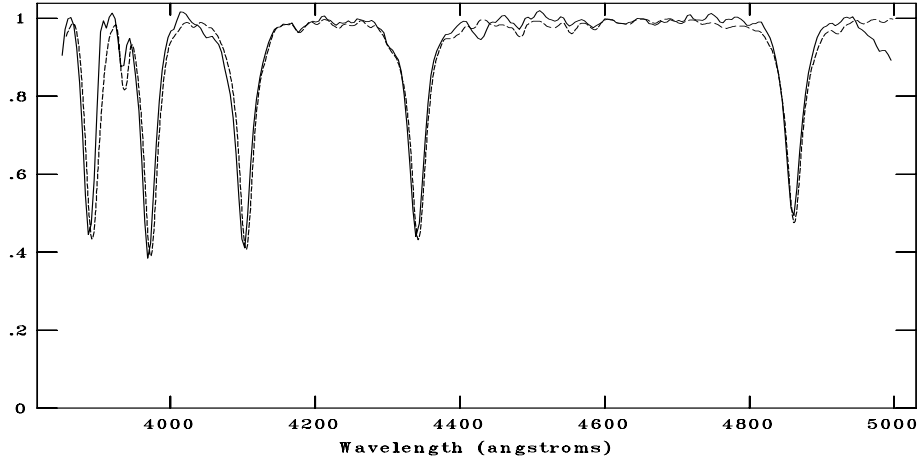


Figure C.47: CAFOS spectrum of 704-083954 compared with B2V,B3V,B5V respectively. The standard spectra are shown with dotted line. The spectral type is assigned as B4V.

NOAO/IRAF V2.16.1 baha@baha-Lenovo-IdeaPad-Y550 Wed 19:08:19 30-Nov-2016
[G093_01n.fits]: G093_01 960. ap:1 beam:1



NOAO/IRAF V2.16.1 baha@baha-Lenovo-IdeaPad-Y550 Wed 19:10:10 30-Nov-2016
[G093_01n.fits]: G093_01 960. ap:1 beam:1



NOAO/IRAF V2.16.1 baha@baha-Lenovo-IdeaPad-Y550 Wed 19:09:44 30-Nov-2016
[G093_01n.fits]: G093_01 960. ap:1 beam:1

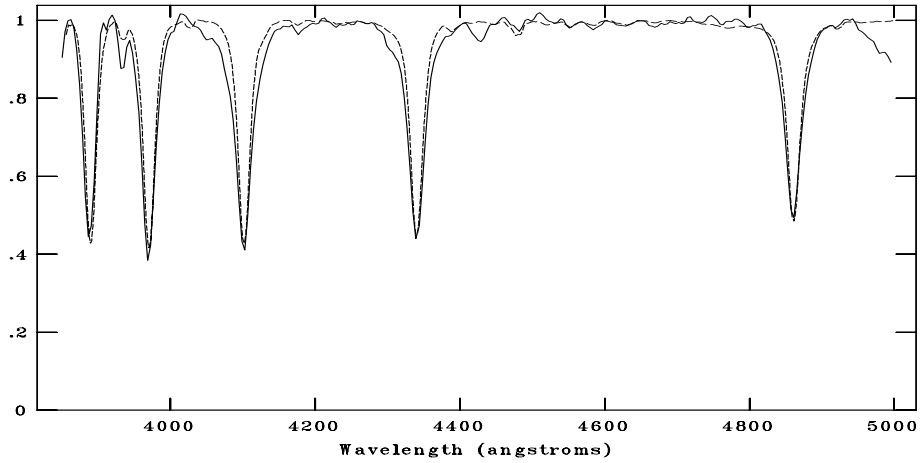
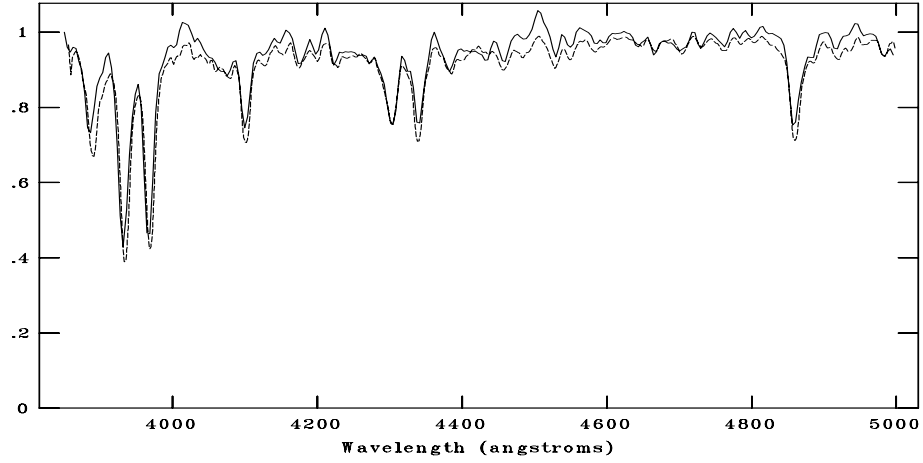
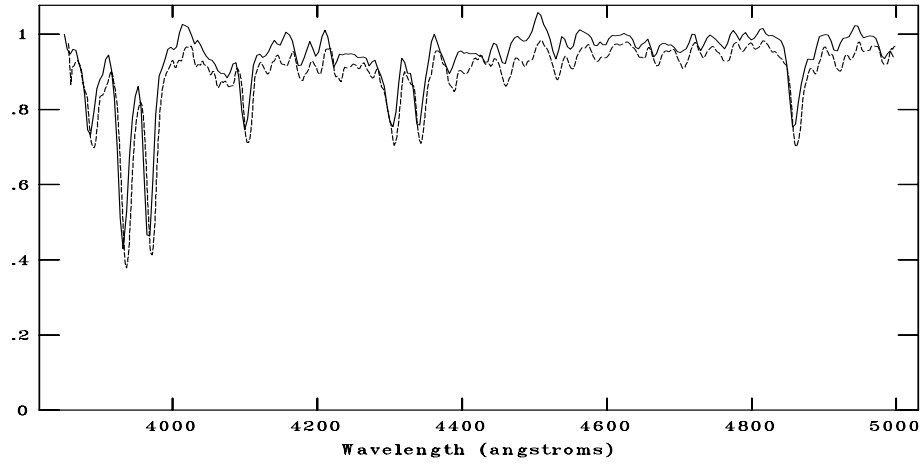


Figure C.48: CAFOS spectrum of 704-084001 compared with A0V, A1V, B9V respectively. The standard spectra are shown with dotted line. The spectral type is assigned as A0V.

NOAO/IRAF V2.16.1 baha@baha-Lenovo-IdeaPad-Y550 Wed 19:11:41 30-Nov-2016
[G093_02n.fits]: G093_02 1200. ap:1 beam:1



NOAO/IRAF V2.16.1 baha@baha-Lenovo-IdeaPad-Y550 Wed 19:10:48 30-Nov-2016
[G093_02n.fits]: G093_02 1200. ap:1 beam:1



NOAO/IRAF V2.16.1 baha@baha-Lenovo-IdeaPad-Y550 Wed 19:11:11 30-Nov-2016
[G093_02n.fits]: G093_02 1200. ap:1 beam:1

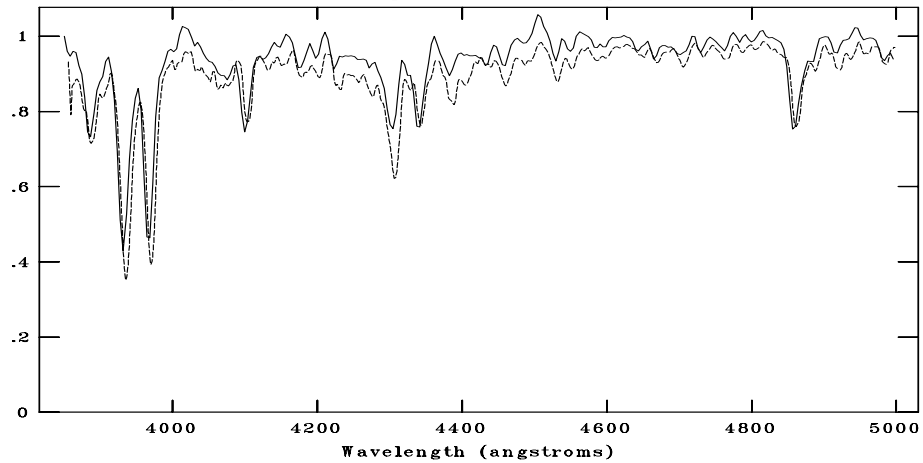
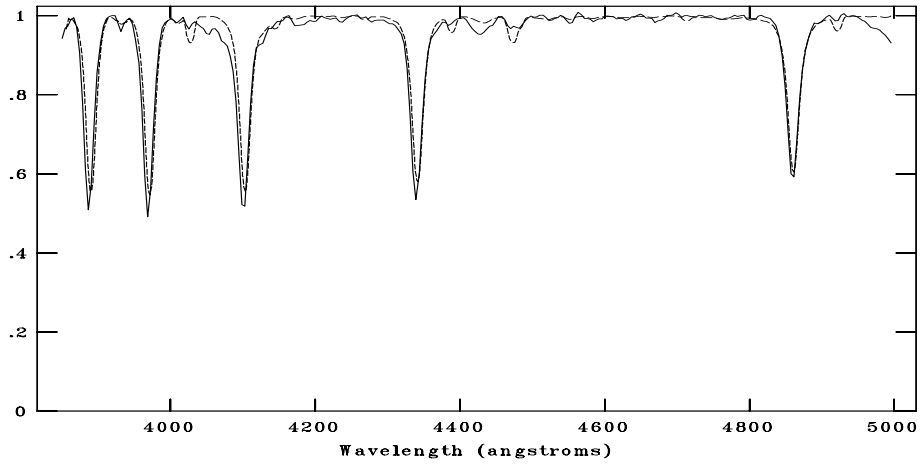
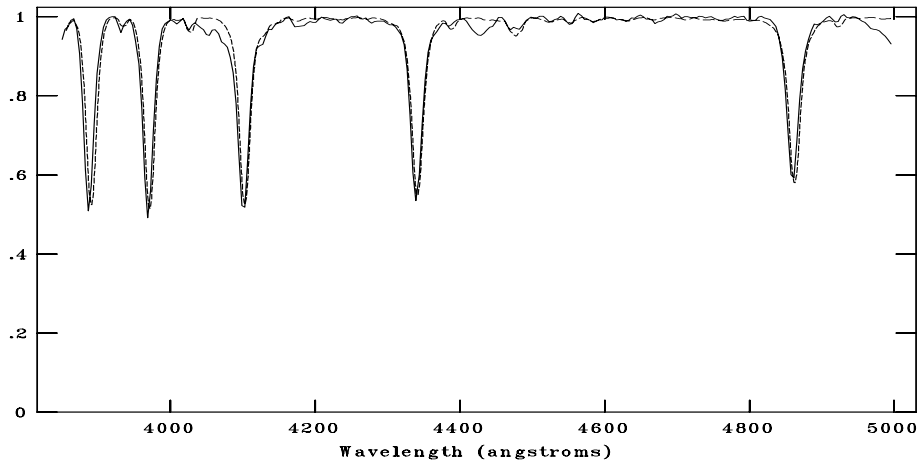


Figure C.49: CAFOS spectrum of 705-085540 compared with F6V, F8V, G0V respectively. The standard spectra are shown with dotted line. The spectral type is assigned as F8V.

NOAO/IRAF V2.16.1 baha@baha-Lenovo-IdeaPad-Y550 Wed 19:13:15 30-Nov-2016
[G093_03n.fits]: G093_03 90. ap:1 beam:1



NOAO/IRAF V2.16.1 baha@baha-Lenovo-IdeaPad-Y550 Wed 19:12:07 30-Nov-2016
[G093_03n.fits]: G093_03 90. ap:1 beam:1



NOAO/IRAF V2.16.1 baha@baha-Lenovo-IdeaPad-Y550 Wed 19:12:43 30-Nov-2016
[G093_03n.fits]: G093_03 90. ap:1 beam:1

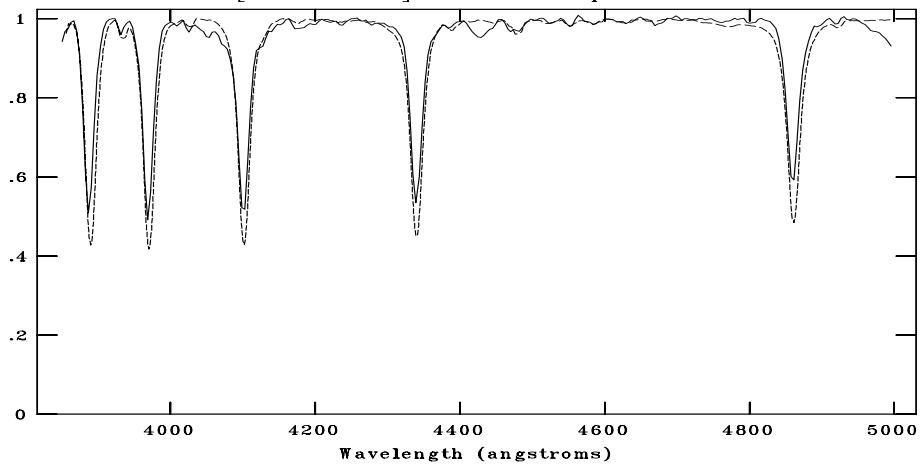
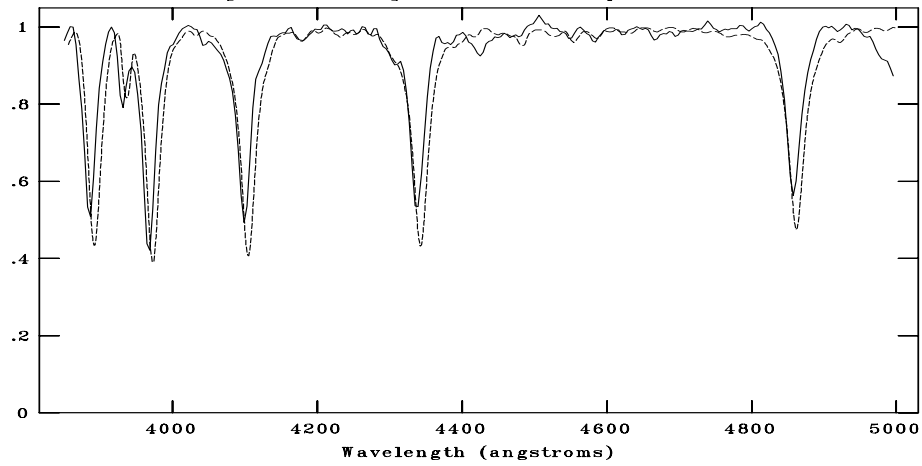
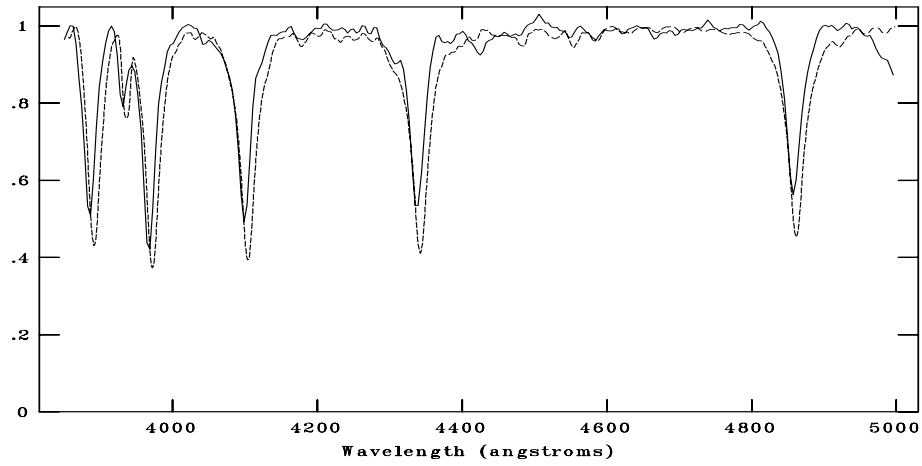


Figure C.50: CAFOS spectrum of 705-085587 compared with B7V, B8V, B9V respectively. The standard spectra are shown with dotted line. The spectral type is assigned as B8V.

NOAO/IRAF V2.16.1 baha@baha-Lenovo-IdeaPad-Y550 Wed 19:14:32 30-Nov-2016
[G093_04n.fits]: G093_04 1080. ap:1 beam:1



NOAO/IRAF V2.16.1 baha@baha-Lenovo-IdeaPad-Y550 Wed 19:15:42 30-Nov-2016
[G093_04n.fits]: G093_04 1080. ap:1 beam:1



NOAO/IRAF V2.16.1 baha@baha-Lenovo-IdeaPad-Y550 Wed 19:34:46 30-Nov-2016
[G093_04n.fits]: G093_04 1080. ap:1 beam:1

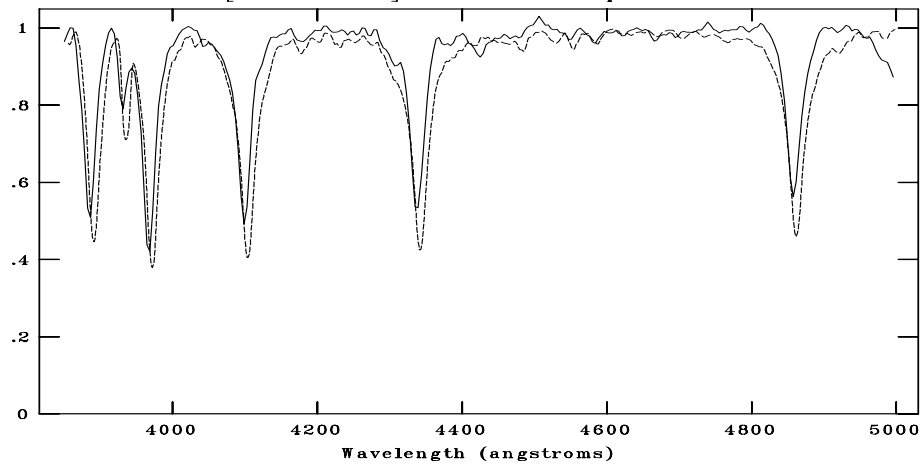
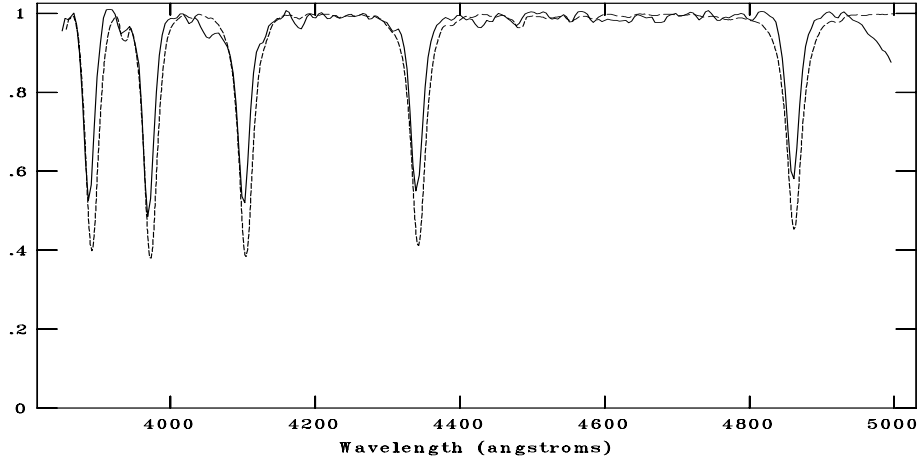
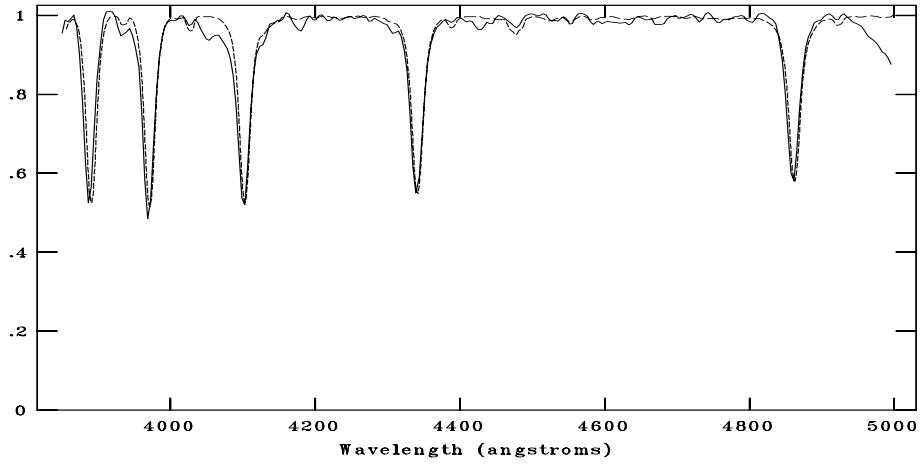


Figure C.51: CAFOS spectrum of 705-085590 compared with A1V, A3V, A5V respectively. The standard spectra are shown with dotted line. The spectral type is assigned as A5V. Due to the S/N, the identification is not accurate.

NOAO/IRAF V2.16.1 baha@baha-Lenovo-IdeaPad-Y550 Wed 19:36:20 30-Nov-2016
[G093_05n.fits]: G093_05 360. ap:1 beam:1



NOAO/IRAF V2.16.1 baha@baha-Lenovo-IdeaPad-Y550 Wed 19:37:15 30-Nov-2016
[G093_05n.fits]: G093_05 360. ap:1 beam:1



NOAO/IRAF V2.16.1 baha@baha-Lenovo-IdeaPad-Y550 Wed 19:36:53 30-Nov-2016
[G093_05n.fits]: G093_05 360. ap:1 beam:1

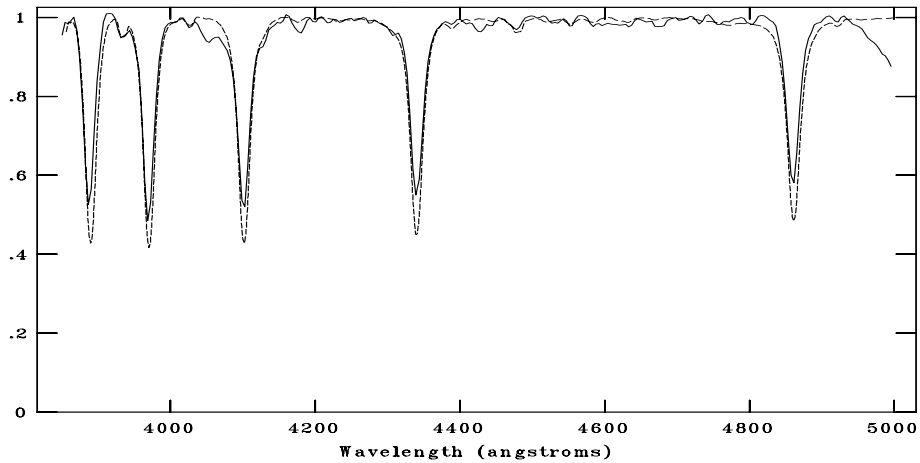
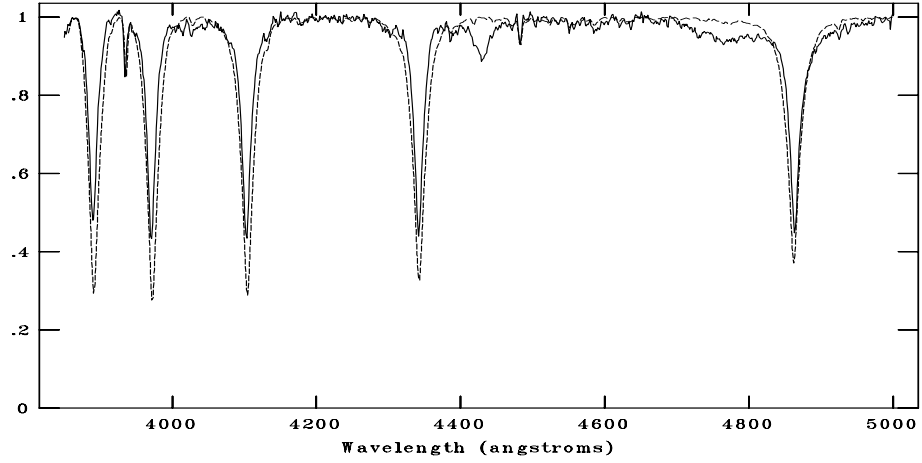
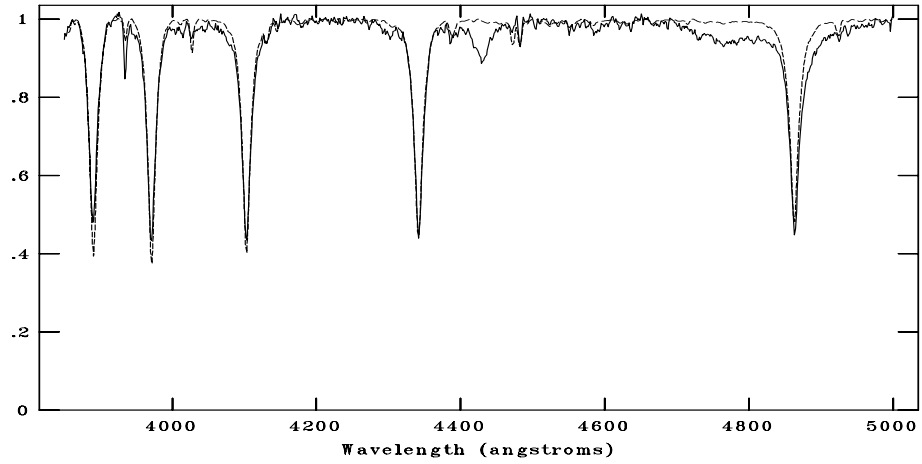


Figure C.52: CAFOS spectrum of 705-085595 compared with A0V, B8V, B9V respectively. The standard spectra are shown with dotted line. The spectral type is assigned as B9V.

NOAO/IRAF V2.16.1 baha@baha-Lenovo-IdeaPad-Y550 Wed 00:43:09 04-Jan-2017
[g932A0V.fits]: g93_2 2700. ap:1 beam:1



NOAO/IRAF V2.16.1 baha@baha-Lenovo-IdeaPad-Y550 Wed 00:43:31 04-Jan-2017
[g932A0V.fits]: g93_2 2700. ap:1 beam:1



NOAO/IRAF V2.16.1 baha@baha-Lenovo-IdeaPad-Y550 Wed 00:41:43 04-Jan-2017
[g932A0V.fits]: g93_2 2700. ap:1 beam:1

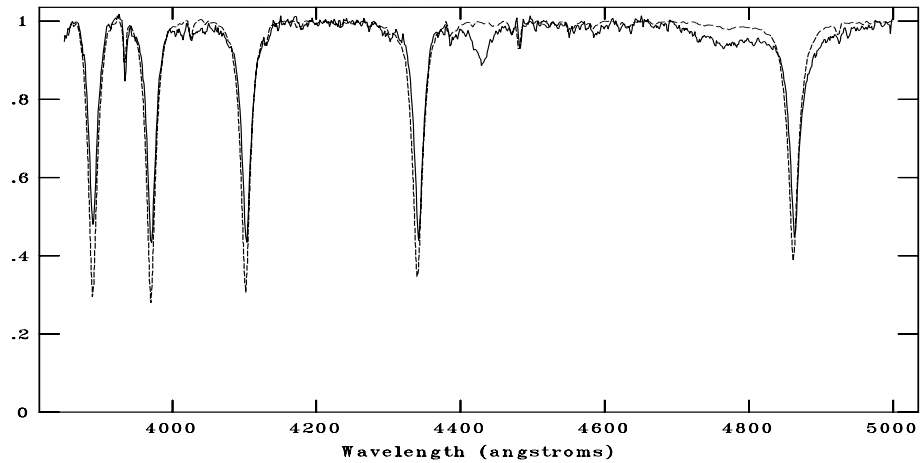


Figure C.53: TFOSC spectrum of 705-085474 compared with A0V, B8V, B9V respectively. The standard spectra are shown with dotted line. The spectral type is assigned as B9V.

C.6 G109.1-1.0

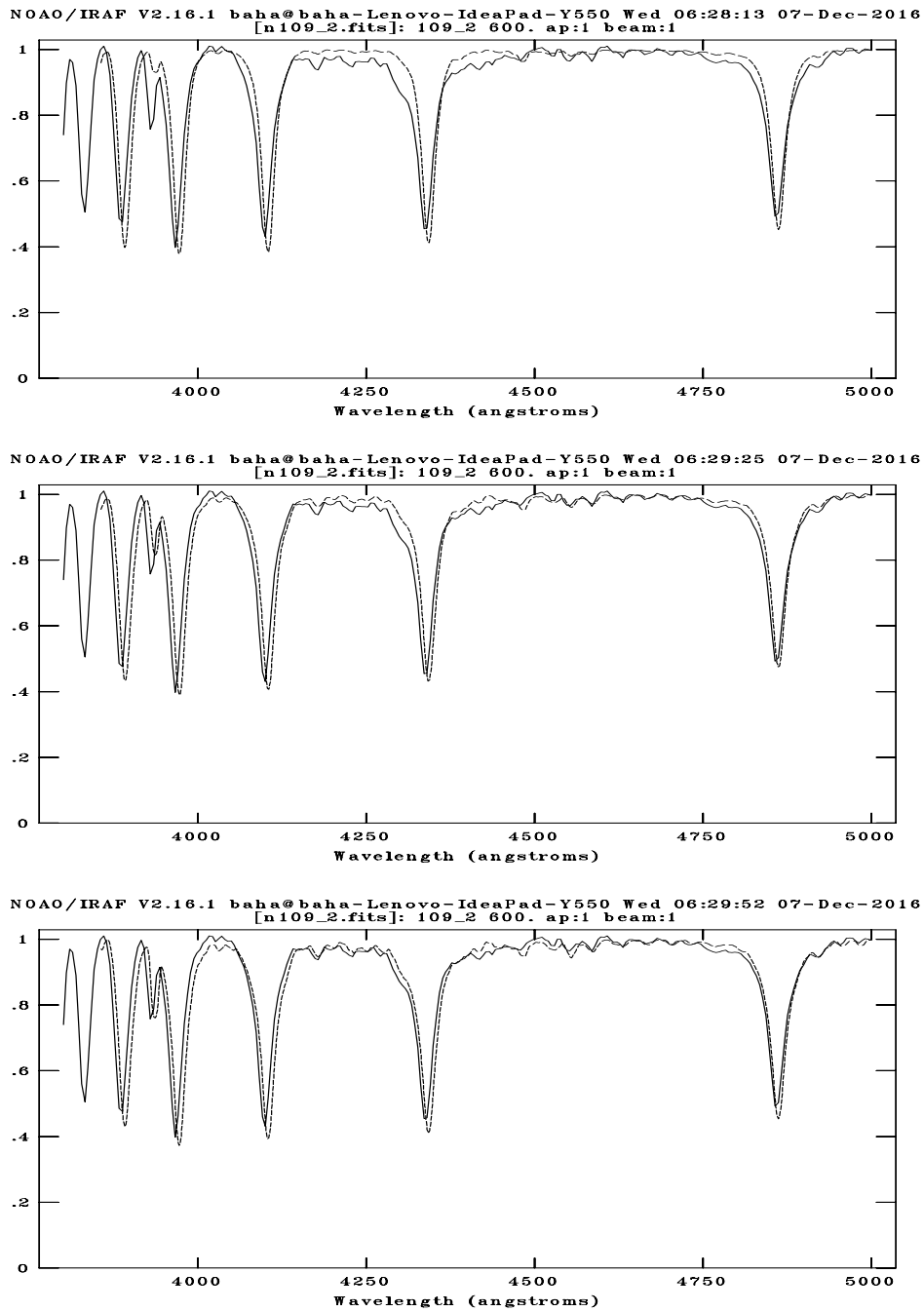
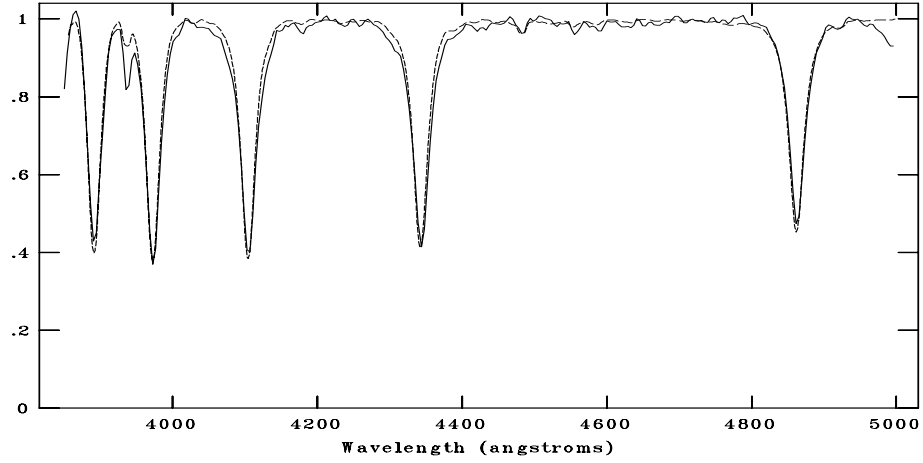
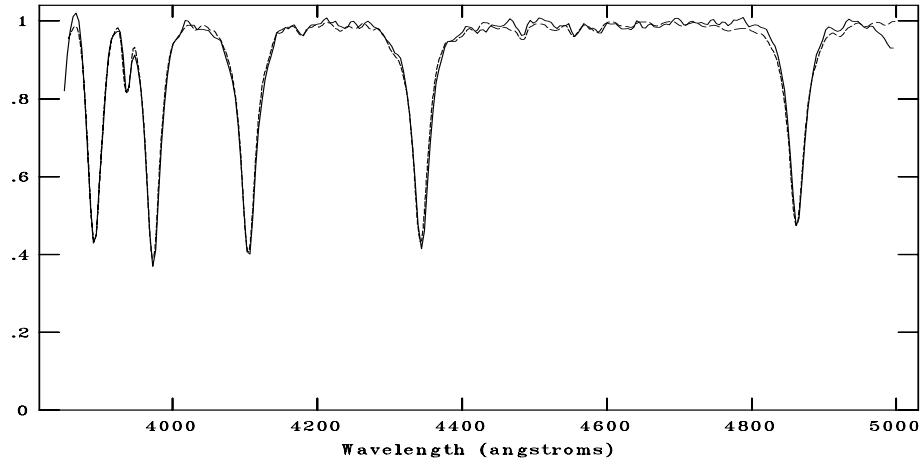


Figure C.54: CAFOS spectrum of 745-080881 compared with A0V, A1V, A3V respectively. The standard spectra are shown with dotted line. The spectral type is assigned as A3V.

NOAO/IRAF V2.16.1 baha@baha-Lenovo-IdeaPad-Y550 Thu 16:23:14 08-Dec-2016
[G109_02n.fits]: G109_02 360. ap:1 beam:1



NOAO/IRAF V2.16.1 baha@baha-Lenovo-IdeaPad-Y550 Thu 16:23:27 08-Dec-2016
[G109_02n.fits]: G109_02 360. ap:1 beam:1



NOAO/IRAF V2.16.1 baha@baha-Lenovo-IdeaPad-Y550 Thu 16:23:42 08-Dec-2016
[G109_02n.fits]: G109_02 360. ap:1 beam:1

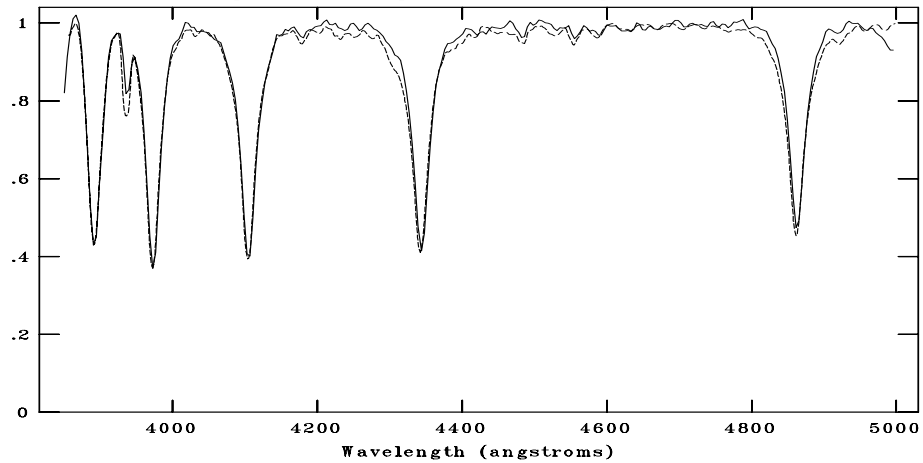
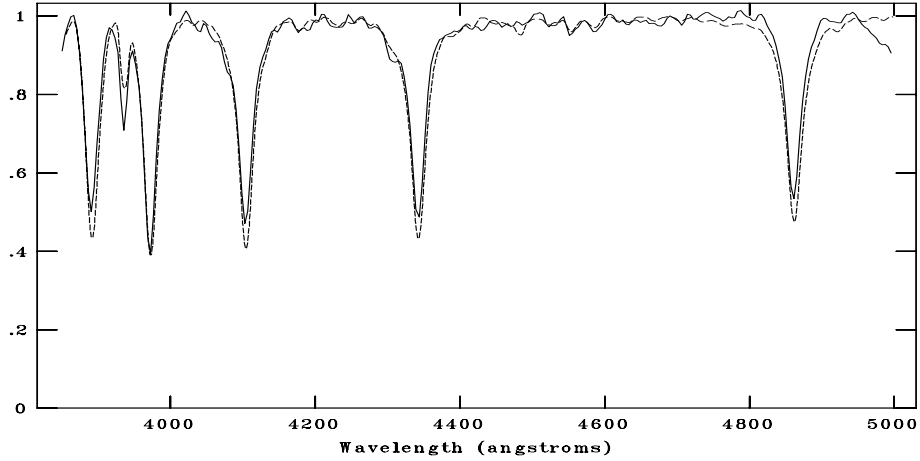
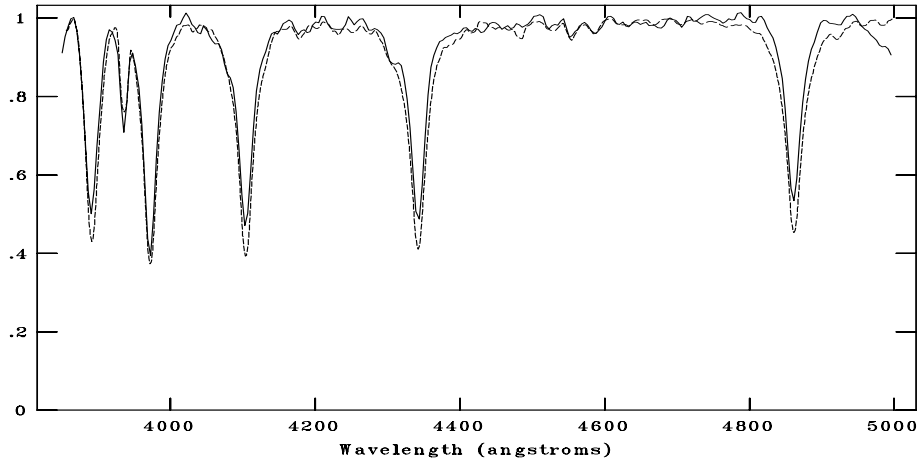


Figure C.55: CAFOS spectrum of 745-080787 compared with A0V, A1V, A3V respectively. The standard spectra are shown with dotted line. The spectral type is assigned as A1V.

NOAO/IRAF V2.16.1 baha@baha-Lenovo-IdeaPad-Y550 Thu 16:31:02 08-Dec-2016
[G109_03A3.fits]: G109_03 1080. ap:1 beam:1



NOAO/IRAF V2.16.1 baha@baha-Lenovo-IdeaPad-Y550 Thu 16:31:25 08-Dec-2016
[G109_03A3.fits]: G109_03 1080. ap:1 beam:1



NOAO/IRAF V2.16.1 baha@baha-Lenovo-IdeaPad-Y550 Thu 16:31:35 08-Dec-2016
[G109_03A3.fits]: G109_03 1080. ap:1 beam:1

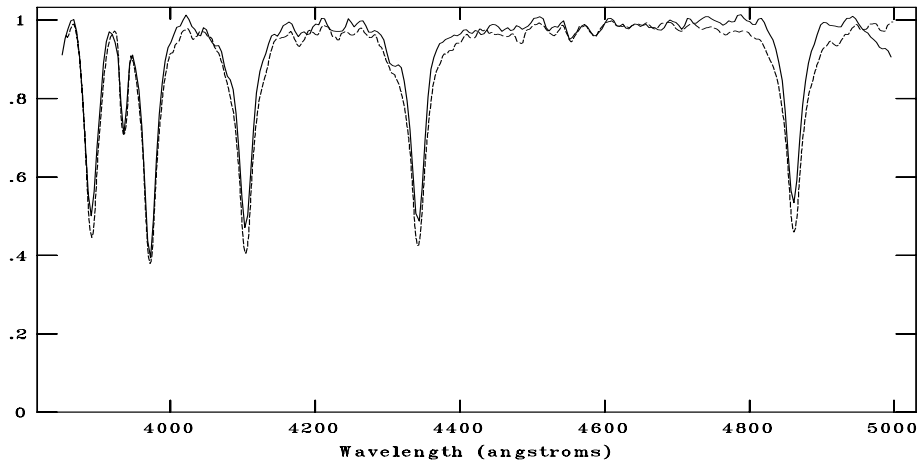
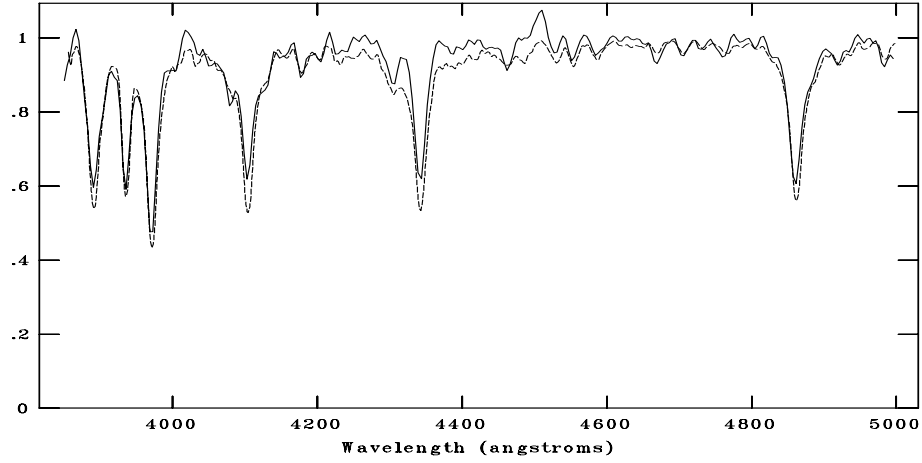
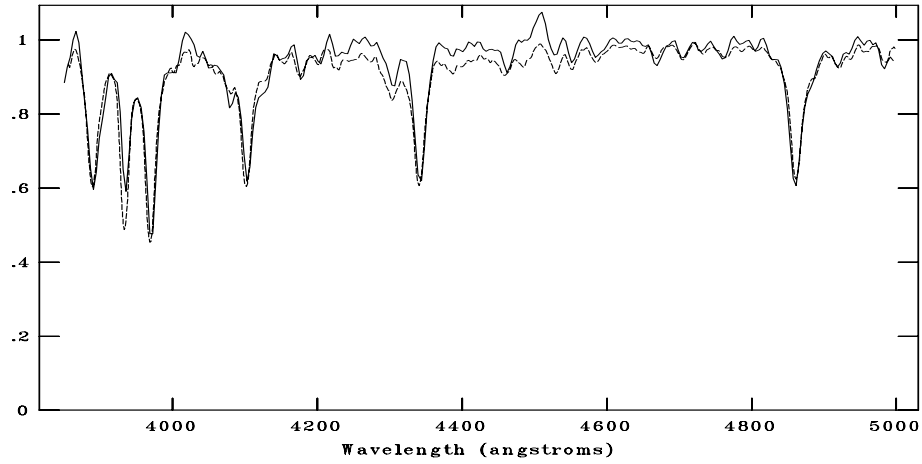


Figure C.56: CAFOS spectrum of 745-080774 compared with A1V, A3V, A5V respectively. The standard spectra are shown with dotted line. The spectral type is assigned as A3V.

NOAO/IRAF V2.16.1 baha@baha-Lenovo-IdeaPad-Y550 Thu 16:28:35 08-Dec-2016
[G109_04n.fits]: G109_04 360. ap:1 beam:1



NOAO/IRAF V2.16.1 baha@baha-Lenovo-IdeaPad-Y550 Thu 16:27:56 08-Dec-2016
[G109_04n.fits]: G109_04 360. ap:1 beam:1



NOAO/IRAF V2.16.1 baha@baha-Lenovo-IdeaPad-Y550 Thu 16:27:39 08-Dec-2016
[G109_04n.fits]: G109_04 360. ap:1 beam:1

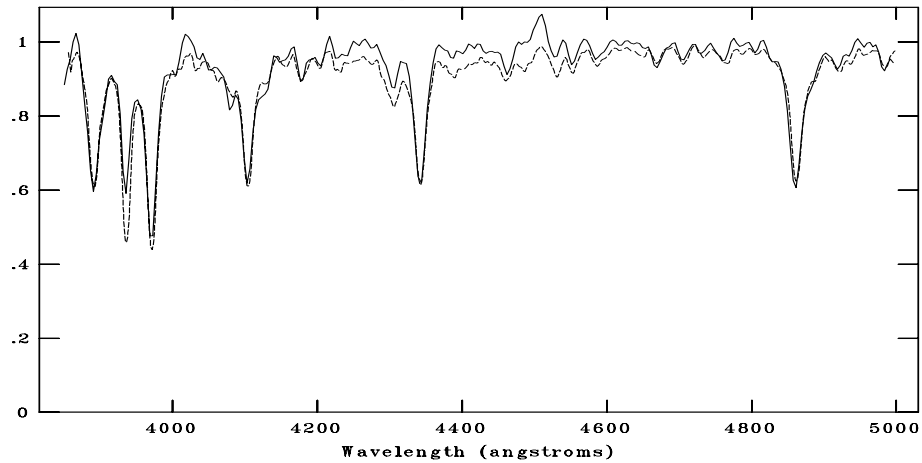
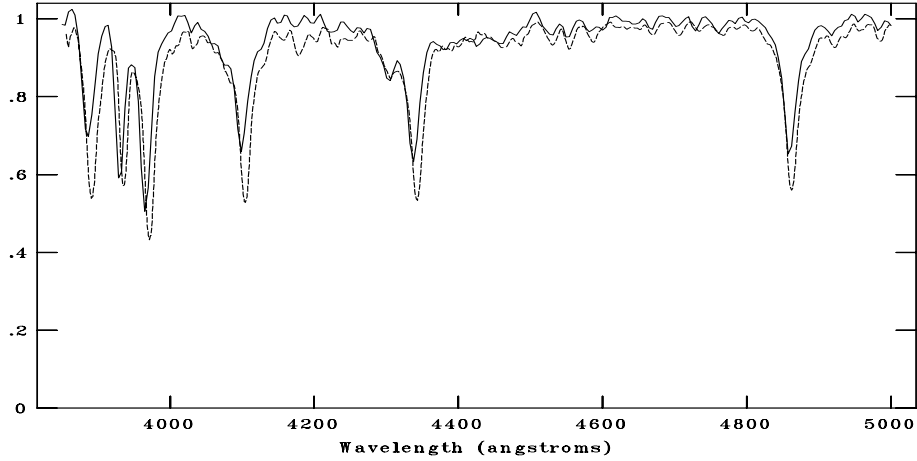
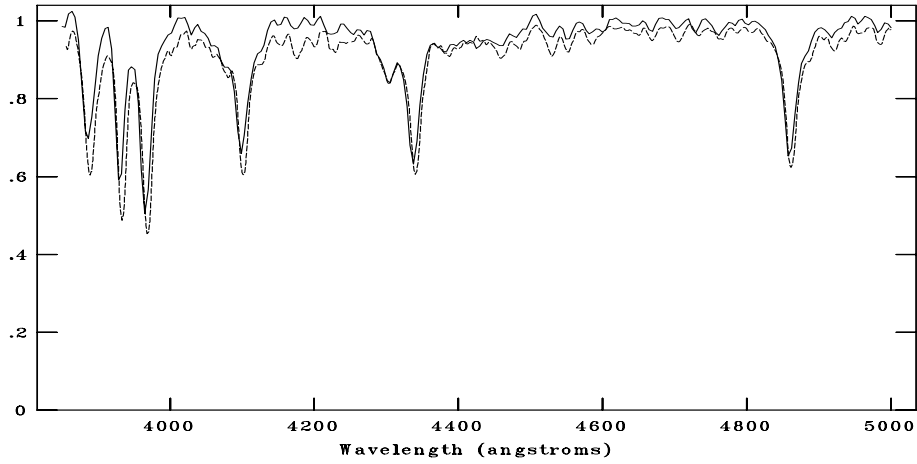


Figure C.57: CAFOS spectrum of 745-080963 compared with F0V, F2V, F3V respectively. The standard spectra are shown with dotted line. The spectral type is assigned as F1V.

NOAO/IRAF V2.16.1 baha@baha-Lenovo-IdeaPad-Y550 Wed 22:12:43 07-Dec-2016
[cg109_02_1A7.fits]: G109_2 720. ap:1 beam:1



NOAO/IRAF V2.16.1 baha@baha-Lenovo-IdeaPad-Y550 Wed 22:11:21 07-Dec-2016
[cg109_02_1A7.fits]: G109_2 720. ap:1 beam:1



NOAO/IRAF V2.16.1 baha@baha-Lenovo-IdeaPad-Y550 Wed 22:13:24 07-Dec-2016
[cg109_02_1A7.fits]: G109_2 720. ap:1 beam:1

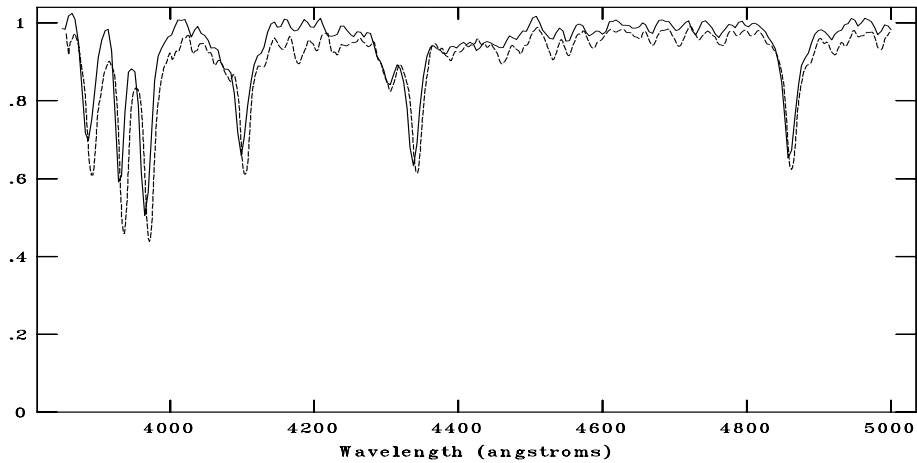
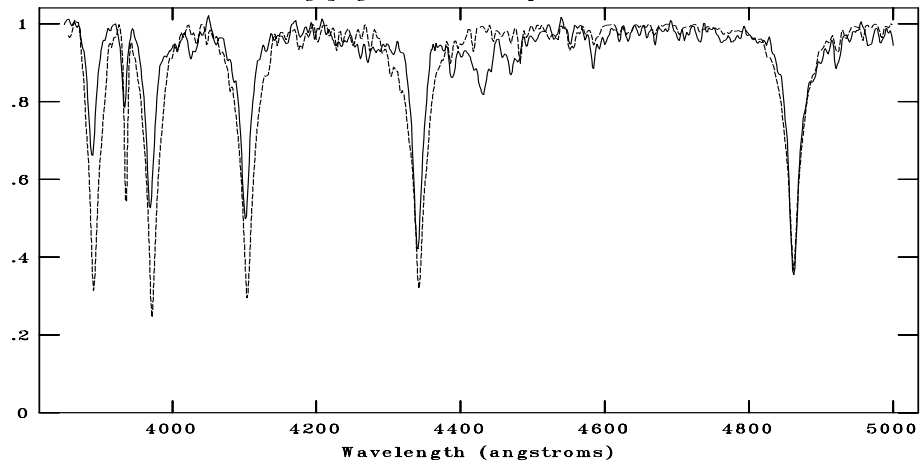
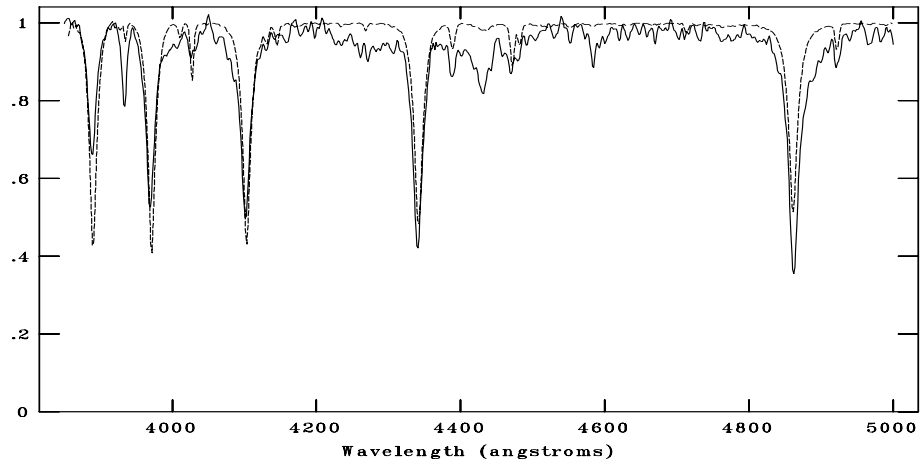


Figure C.58: CAFOS spectrum of 745-080963 compared with F0V, F2V, F3V respectively. The standard spectra are shown with dotted line. The spectral type is assigned as F1V.

NOAO/IRAF V2.16.1 baha@baha-Lenovo-IdeaPad-Y550 Tue 22:24:46 03-Jan-2017
[c]: g109_1 1800. ap:1 beam:1



NOAO/IRAF V2.16.1 baha@baha-Lenovo-IdeaPad-Y550 Tue 22:26:31 03-Jan-2017
[c]: g109_1 1800. ap:1 beam:1



NOAO/IRAF V2.16.1 baha@baha-Lenovo-IdeaPad-Y550 Tue 22:25:35 03-Jan-2017
[c]: g109_1 1800. ap:1 beam:1

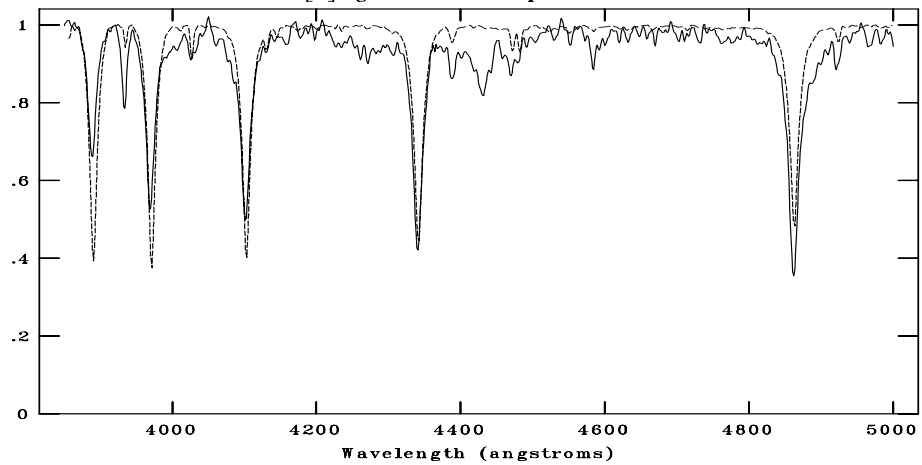
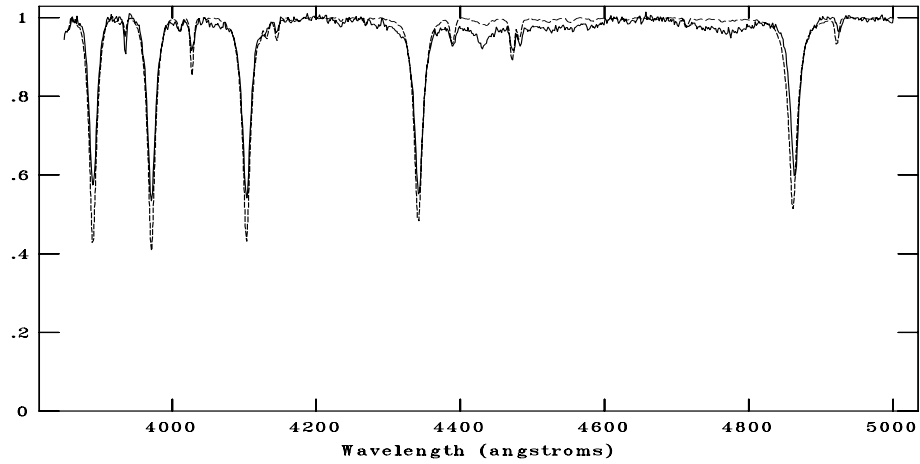
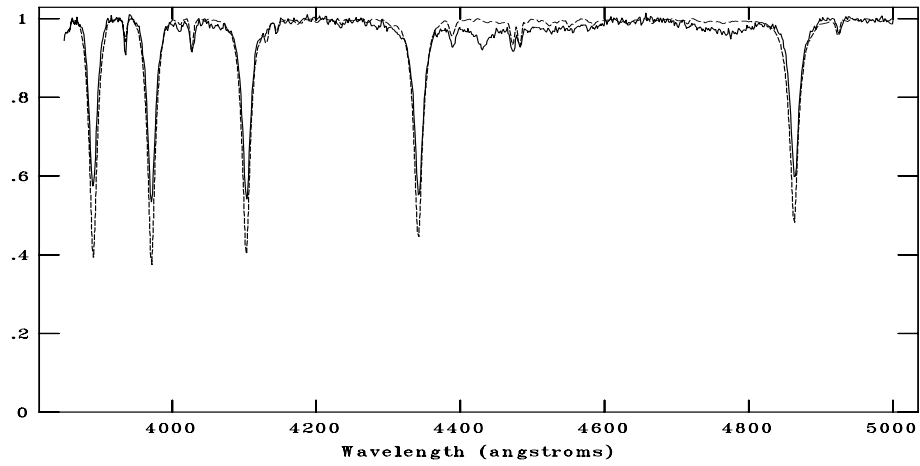


Figure C.59: TFOSC spectrum of 745-080772 compared with A3V, B7V, B8V respectively. The standard spectra are shown with dotted line. The spectral type is assigned as a value between B7V–A3V. The accuracy is low due to the low S/N.

NOAO/IRAF V2.16.1 baha@baha-Lenovo-IdeaPad-Y550 Tue 21:59:15 03-Jan-2017
[g109B8.fits]: g109_2 900. ap:1 beam:1



NOAO/IRAF V2.16.1 baha@baha-Lenovo-IdeaPad-Y550 Tue 21:57:51 03-Jan-2017
[g109B8.fits]: g109_2 900. ap:1 beam:1



NOAO/IRAF V2.16.1 baha@baha-Lenovo-IdeaPad-Y550 Tue 22:12:23 03-Jan-2017
[g109B8.fits]: g109_2 900. ap:1 beam:1

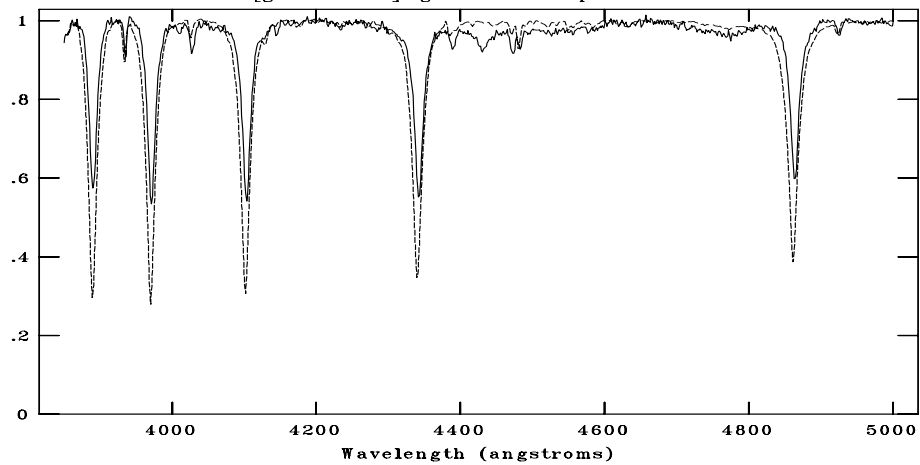


Figure C.60: TFOSC spectrum of 745-080935 compared with B7V, B8V, B9V respectively. The standard spectra are shown with dotted line. The spectral type is assigned as B8V.

C.7 G114.3+0.3

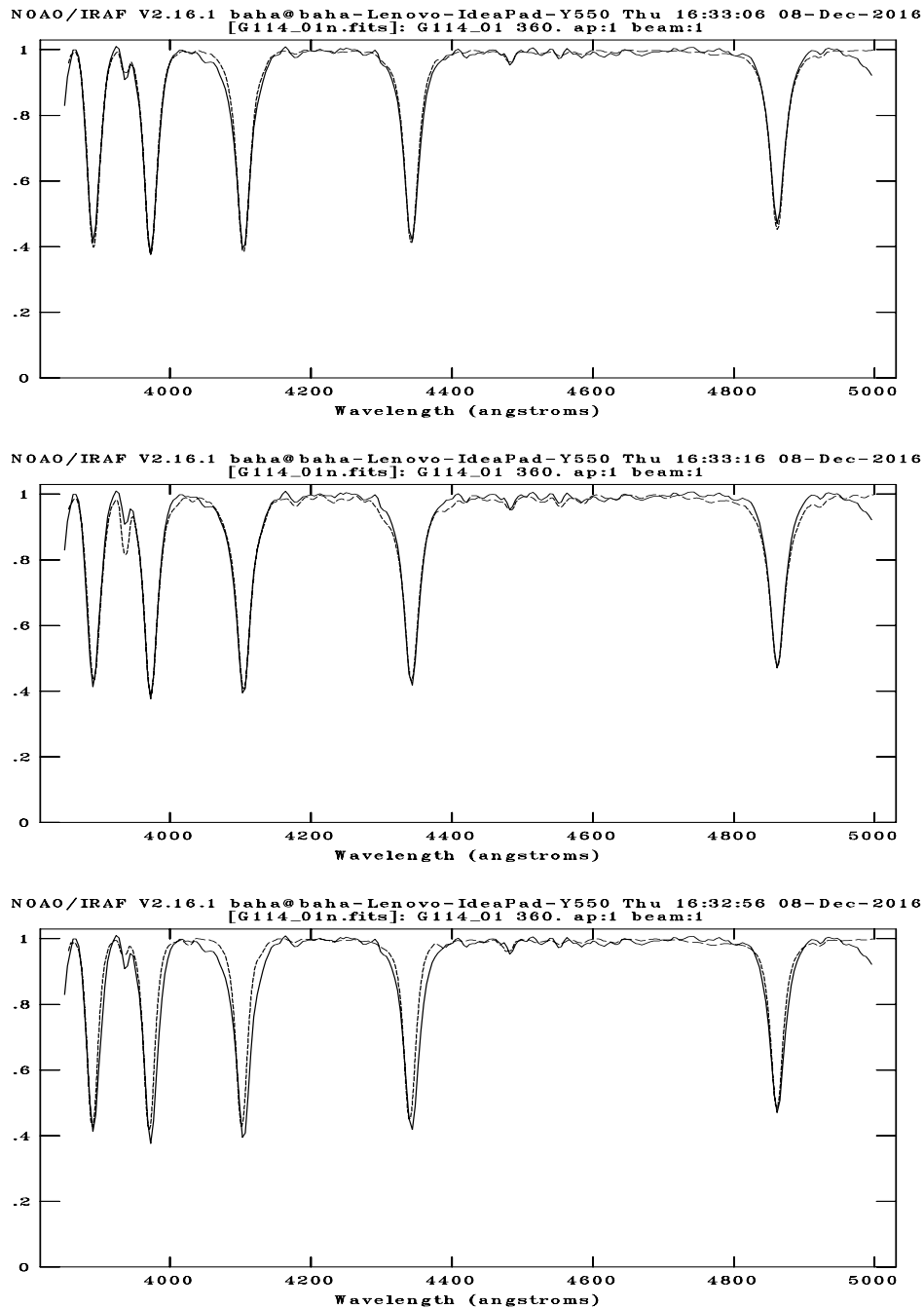
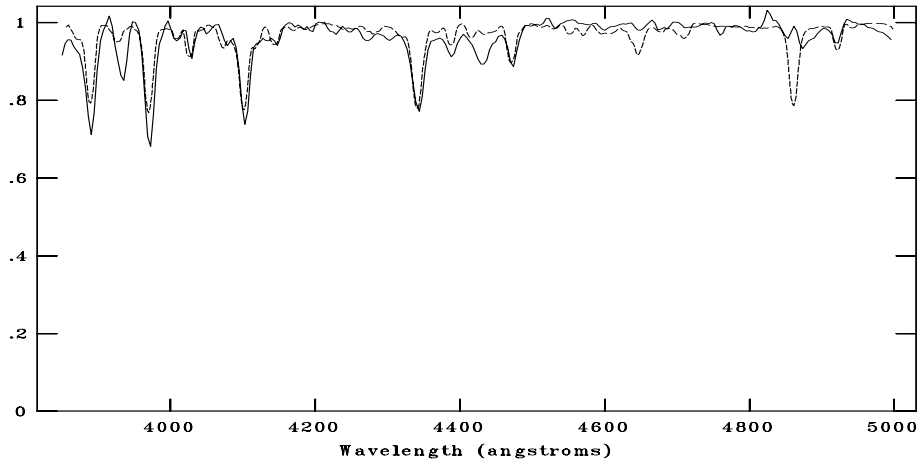
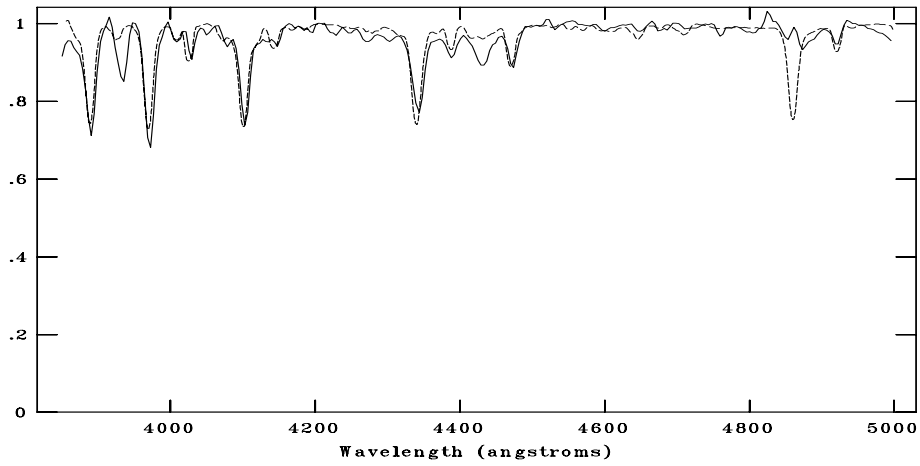


Figure C.61: CAFOS spectrum of 761-072876 compared with A0V, A1V, B9V respectively. The standard spectra are shown with dotted line. The spectral type is assigned as A0V.

NOAO/IRAF V2.16.1 baha@baha-Lenovo-IdeaPad-Y550 Thu 16:34:41 08-Dec-2016
[G114_02n.fits]: G114_02 600. ap:1 beam:1



NOAO/IRAF V2.16.1 baha@baha-Lenovo-IdeaPad-Y550 Thu 16:35:24 08-Dec-2016
[G114_02n.fits]: G114_02 600. ap:1 beam:1



NOAO/IRAF V2.16.1 baha@baha-Lenovo-IdeaPad-Y550 Thu 16:35:40 08-Dec-2016
[G114_02n.fits]: G114_02 600. ap:1 beam:1

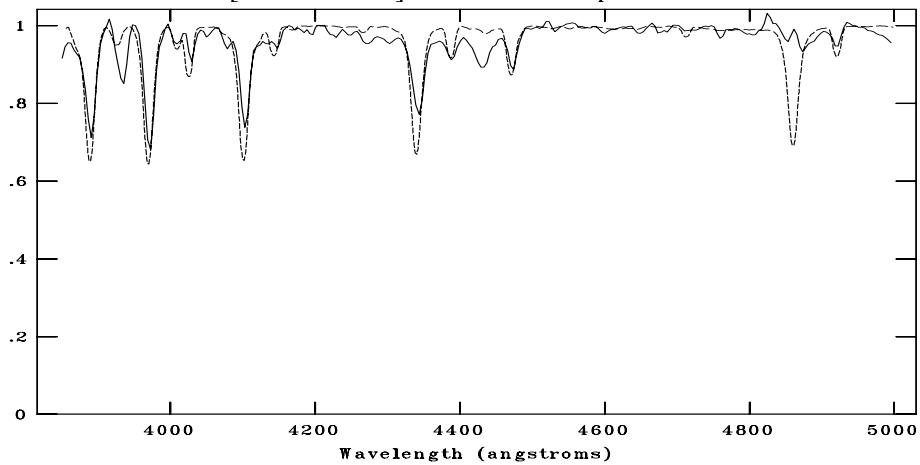
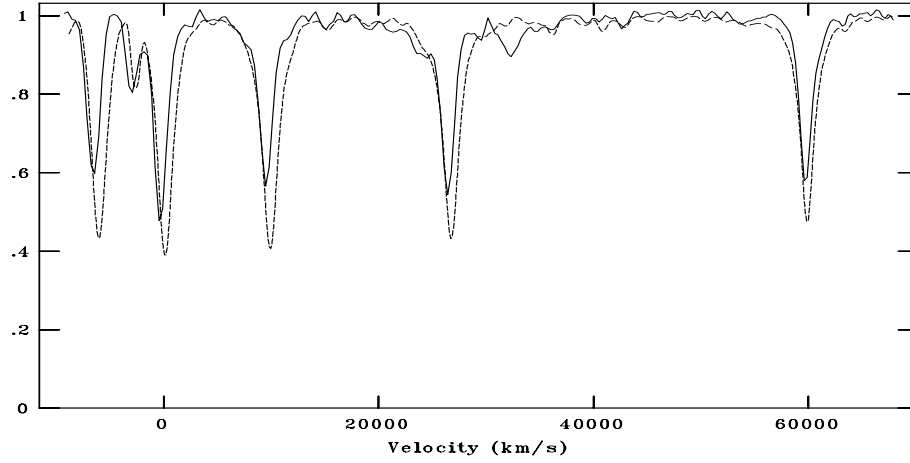
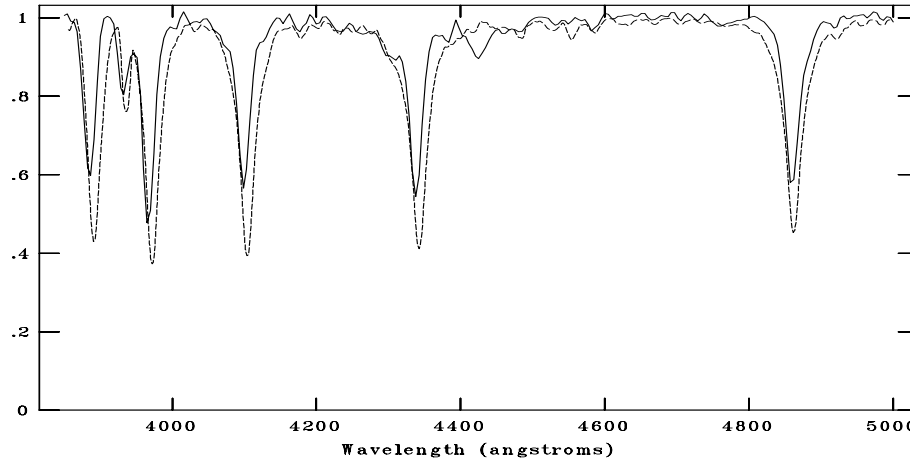


Figure C.62: CAFOS spectrum of 760-074536 compared with B0.5III, B1V, B2V respectively. The standard spectra are shown with dotted line. The spectral type is assigned as B1V.

NOAO/IRAF V2.16.1 baha@baha-Lenovo-IdeaPad-Y550 Wed 22:14:32 07-Dec-2016
[cg114_01A3.fits]: G114_1 1020. ap:1 beam:1



NOAO/IRAF V2.16.1 baha@baha-Lenovo-IdeaPad-Y550 Wed 22:15:39 07-Dec-2016
[cg114_01A3.fits]: G114_1 1020. ap:1 beam:1



NOAO/IRAF V2.16.1 baha@baha-Lenovo-IdeaPad-Y550 Thu 00:22:02 08-Dec-2016
[cg114_01A3.fits]: G114_1 1020. ap:1 beam:1

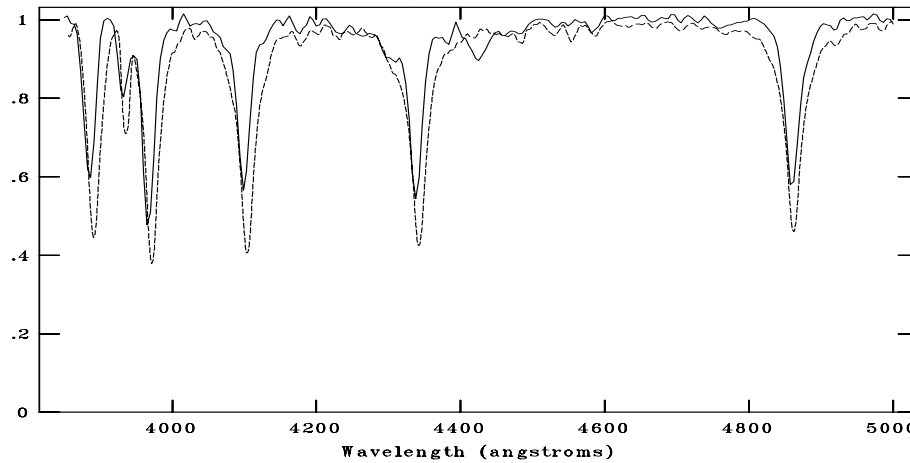
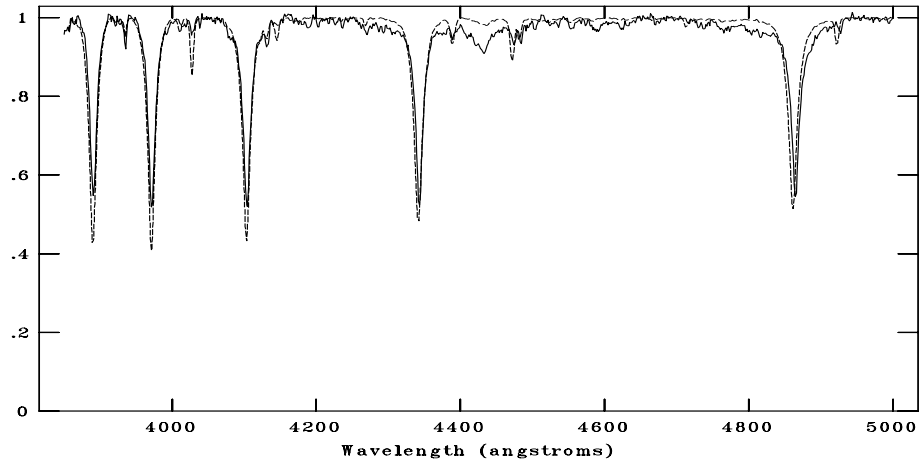
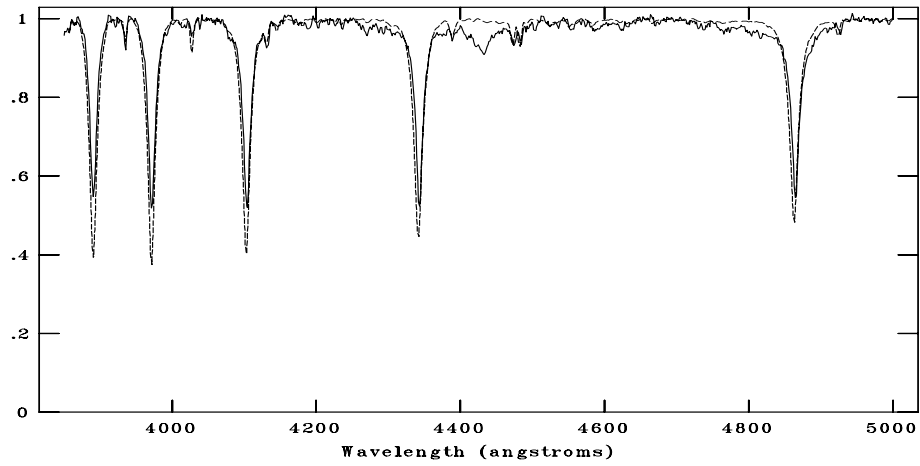


Figure C.63: CAFOS spectrum of 760-074418 compared with A1V, A3V, A5V respectively. The standard spectra are shown with dotted line. The spectral type is assigned as A3V.

NOAO/IRAF V2.16.1 baha@baha-Lenovo-IdeaPad-Y550 Tue 23:56:48 03-Jan-2017
[g1142n.fits]: g114_1 1200. ap:1 beam:1



NOAO/IRAF V2.16.1 baha@baha-Lenovo-IdeaPad-Y550 Tue 23:23:29 03-Jan-2017
[g1142n.fits]: g114_1 1200. ap:1 beam:1



NOAO/IRAF V2.16.1 baha@baha-Lenovo-IdeaPad-Y550 Tue 23:57:49 03-Jan-2017
[1142_2n.fits]: g114_1 1200. ap:1 beam:1

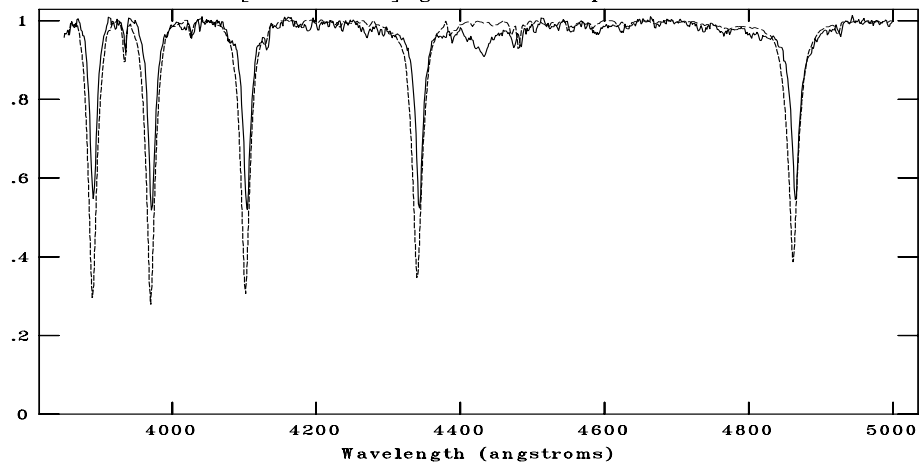
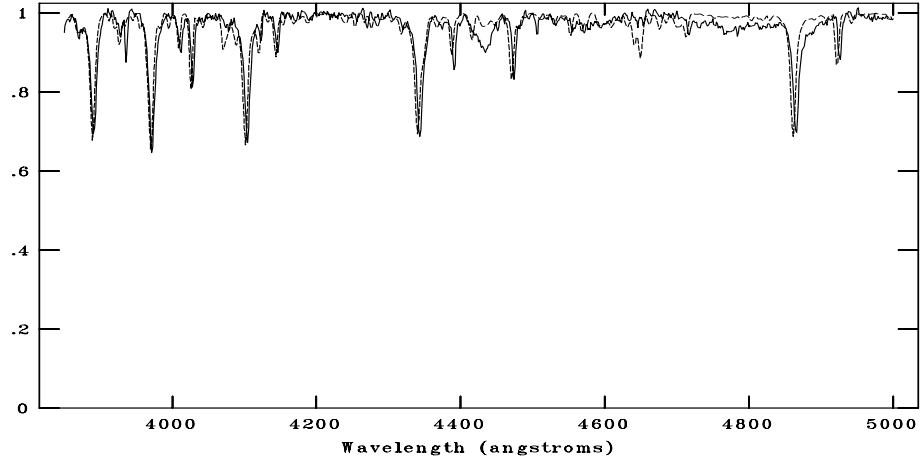
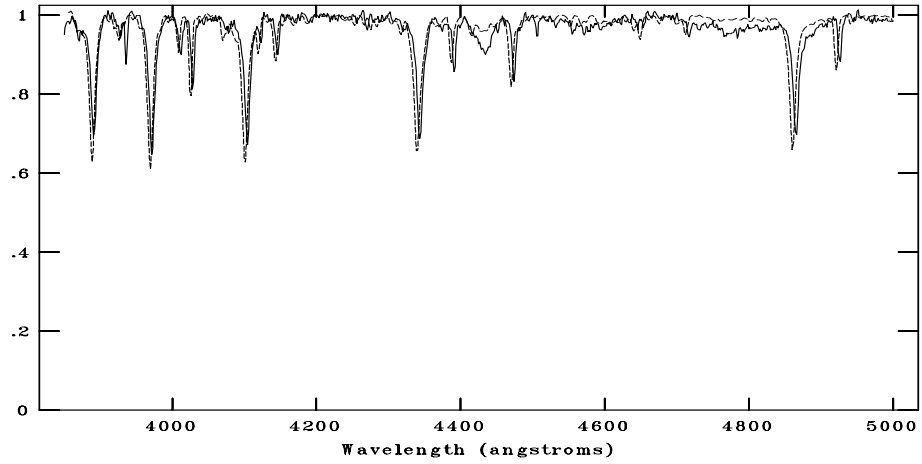


Figure C.64: TFOSC spectrum of 761-072674 compared with B7V, B8V, B9V respectively. The standard spectra are shown with dotted line. The spectral type is assigned as B8V.

NOAO/IRAF V2.16.1 baha@baha-Lenovo-IdeaPad-Y550 Tue 23:58:38 03-Jan-2017
[g1144n.fits]: g114_3 1500. ap:1 beam:1



NOAO/IRAF V2.16.1 baha@baha-Lenovo-IdeaPad-Y550 Tue 23:59:44 03-Jan-2017
[g1144n.fits]: g114_3 1500. ap:1 beam:1



NOAO/IRAF V2.16.1 baha@baha-Lenovo-IdeaPad-Y550 Wed 00:00:15 04-Jan-2017
[g1144n.fits]: g114_3 1500. ap:1 beam:1

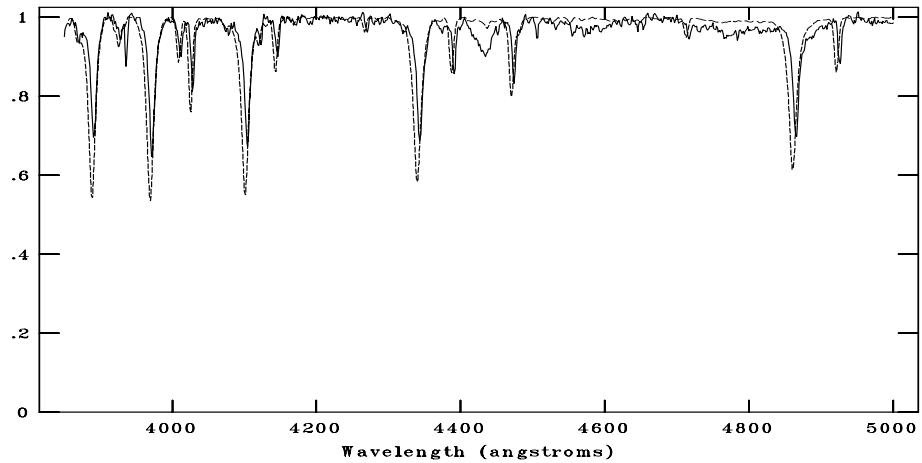
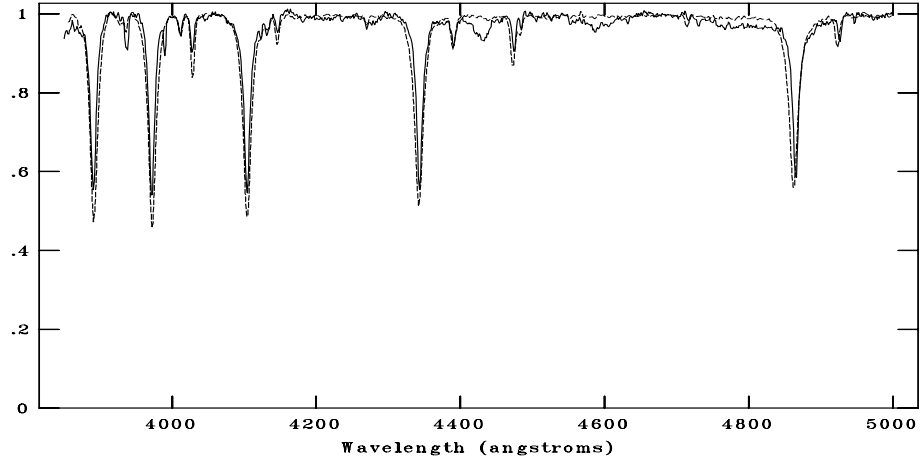
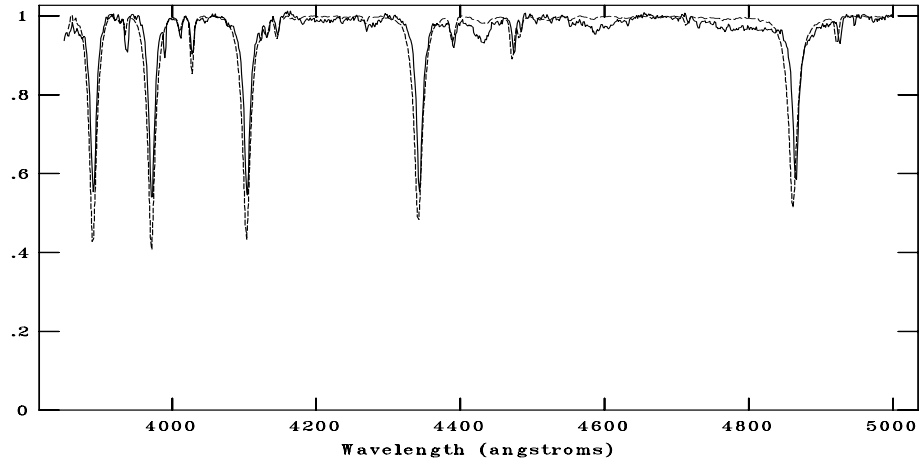


Figure C.65: TFOSC spectrum of 759-074519 compared with B0.5III, B1V, B2V respectively. The standard spectra are shown with dotted line. The spectral type is assigned as B1.5V.

NOAO/IRAF V2.16.1 baha@baha-Lenovo-IdeaPad-Y550 Wed 00:02:19 04-Jan-2017
[g1146n.fits]: g114_2 600. ap:1 beam:1



NOAO/IRAF V2.16.1 baha@baha-Lenovo-IdeaPad-Y550 Wed 00:01:00 04-Jan-2017
[g1146n.fits]: g114_2 600. ap:1 beam:1



NOAO/IRAF V2.16.1 baha@baha-Lenovo-IdeaPad-Y550 Wed 00:01:27 04-Jan-2017
[g1146n.fits]: g114_2 600. ap:1 beam:1

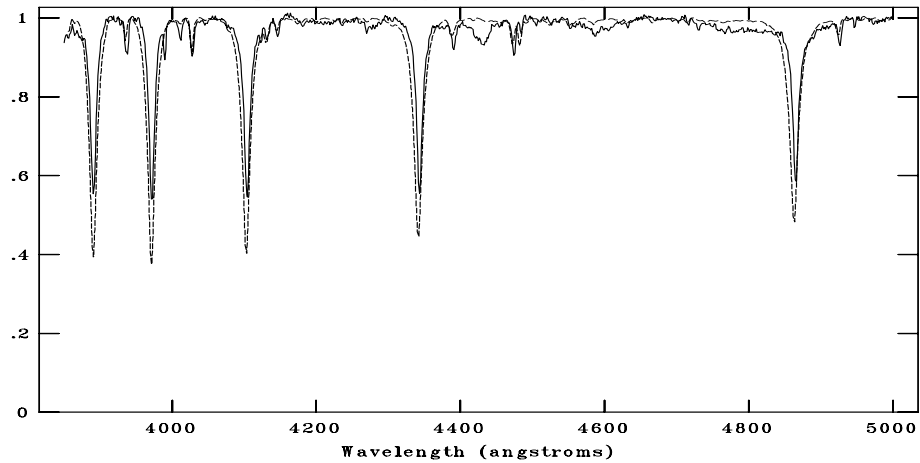


Figure C.66: TFOSC spectrum of 761-072827 compared with B5V, B7V, B8V respectively. The standard spectra are shown with dotted line. The spectral type is assigned as B6V.

C.8 G116.9+0.2

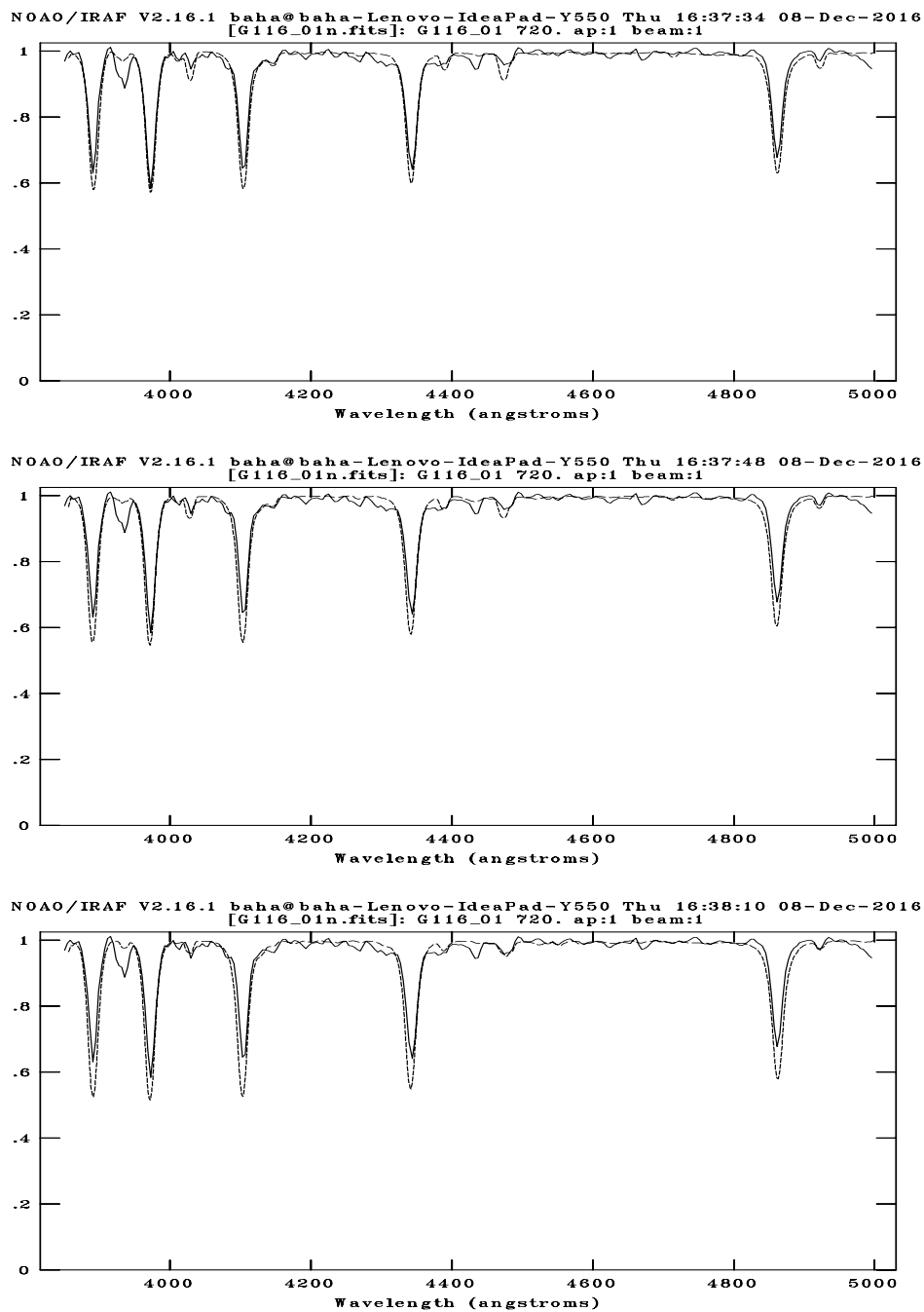
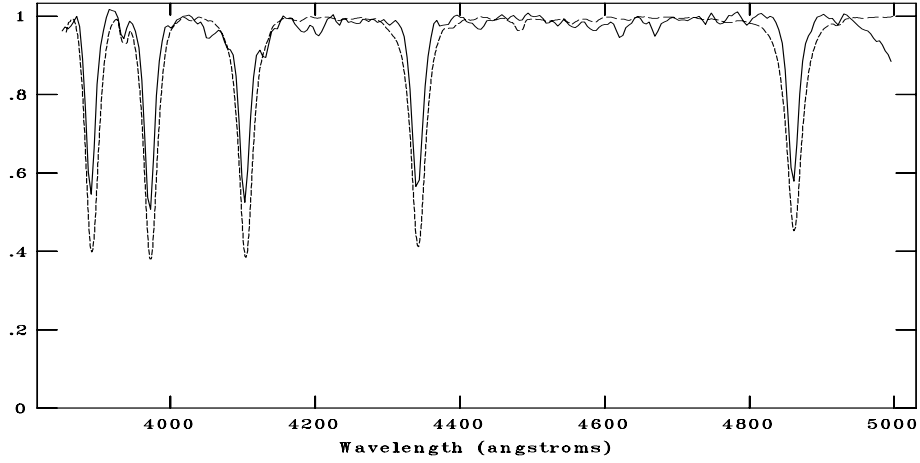
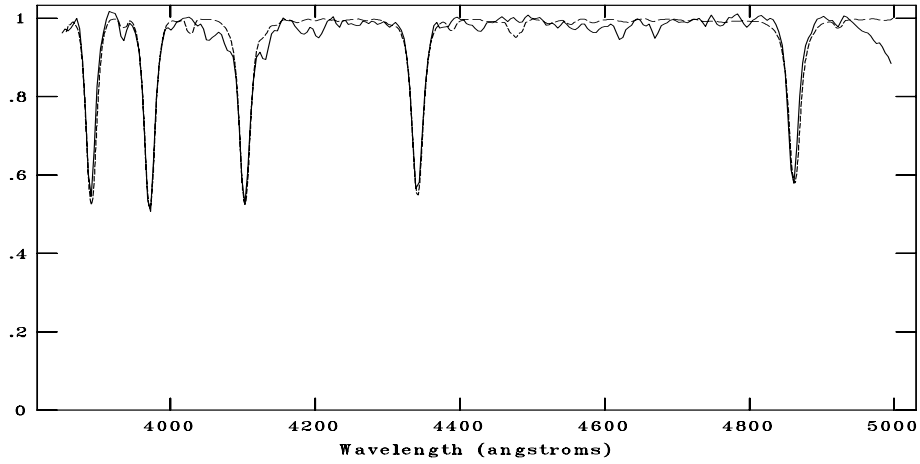


Figure C.67: CAFOS spectrum of 763-077202 compared with B5V, B7V, B8V respectively. The standard spectra are shown with dotted line. The spectral type is assigned as B7V.

NOAO/IRAF V2.16.1 baha@baha-Lenovo-IdeaPad-Y550 Thu 16:48:42 08-Dec-2016
[G116_02n.fits]: G116_02 360. ap:1 beam:1



NOAO/IRAF V2.16.1 baha@baha-Lenovo-IdeaPad-Y550 Thu 16:48:25 08-Dec-2016
[G116_02n.fits]: G116_02 360. ap:1 beam:1



NOAO/IRAF V2.16.1 baha@baha-Lenovo-IdeaPad-Y550 Thu 16:48:11 08-Dec-2016
[G116_02n.fits]: G116_02 360. ap:1 beam:1

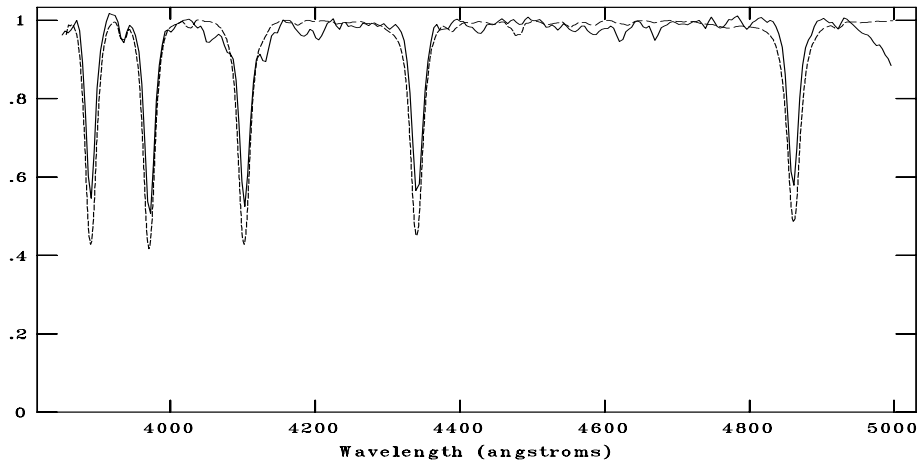
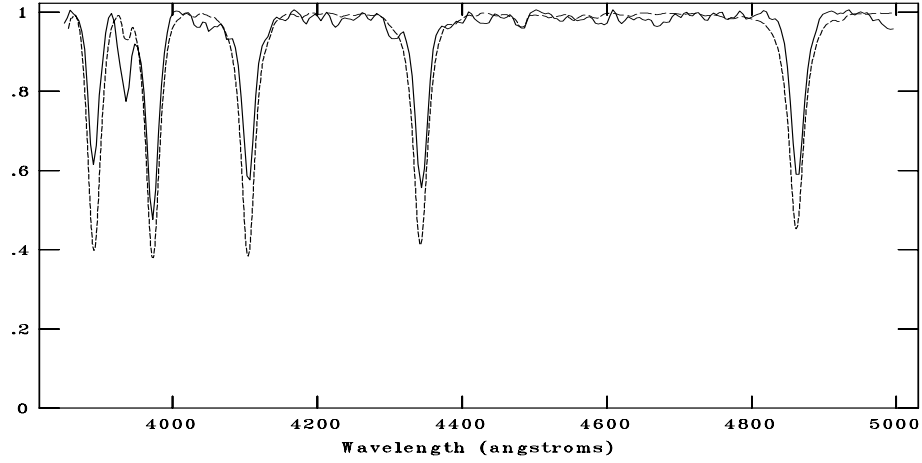
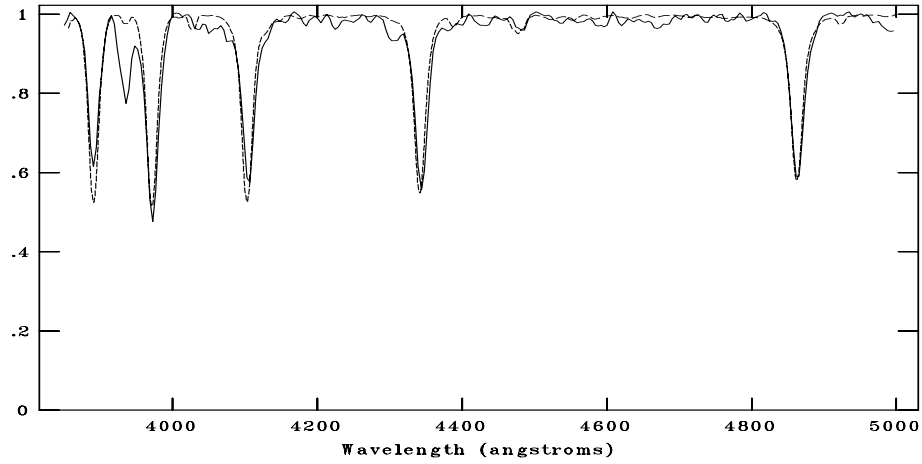


Figure C.68: CAFOS spectrum of 762-000129 compared with A0V, B8V, B9V respectively. The standard spectra are shown with dotted line. The spectral type is assigned as B9V.

NOAO/IRAF V2.16.1 baha@baha-Lenovo-IdeaPad-Y550 Thu 16:52:35 08-Dec-2016
[G116_03n.fits]: G116_03 720. ap:1 beam:1



NOAO/IRAF V2.16.1 baha@baha-Lenovo-IdeaPad-Y550 Thu 16:50:23 08-Dec-2016
[G116_03n.fits]: G116_03 720. ap:1 beam:1



NOAO/IRAF V2.16.1 baha@baha-Lenovo-IdeaPad-Y550 Thu 16:50:34 08-Dec-2016
[G116_03n.fits]: G116_03 720. ap:1 beam:1

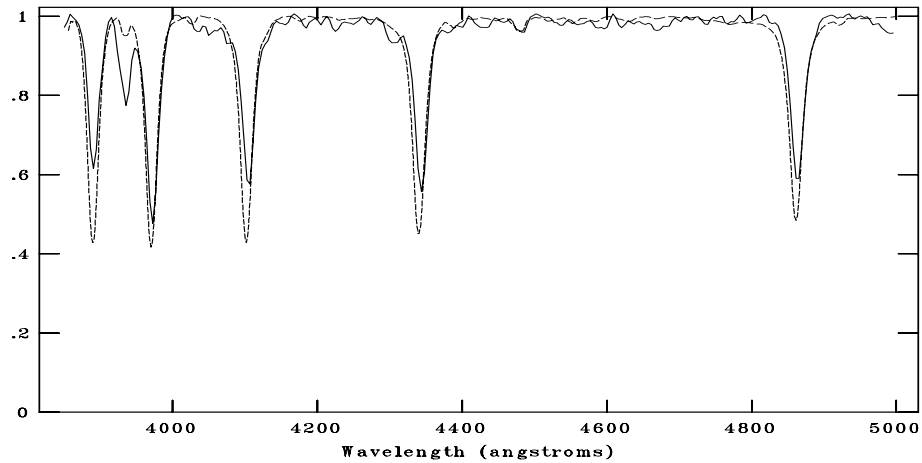
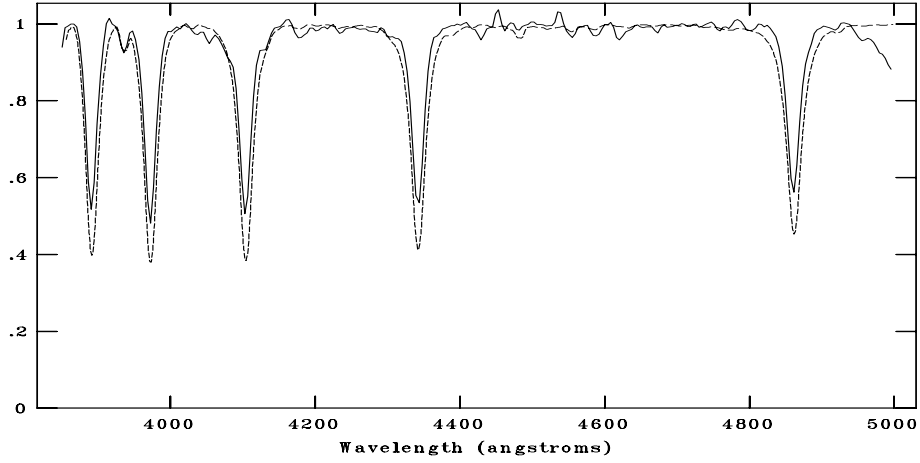
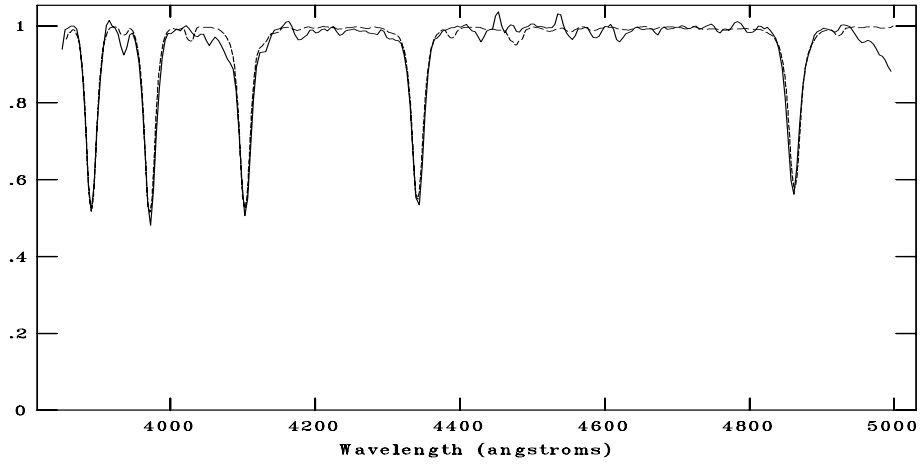


Figure C.69: CAFOS spectrum of 763-076740 compared with A0V, B8V, B9V respectively. The standard spectra are shown with dotted line. The spectral type is assigned as B9V.

NOAO/IRAF V2.16.1 baha@baha-Lenovo-IdeaPad-Y550 Thu 17:01:00 08-Dec-2016
[G116_04n.fits]: G116_04 720. ap:1 beam:1



NOAO/IRAF V2.16.1 baha@baha-Lenovo-IdeaPad-Y550 Thu 17:00:14 08-Dec-2016
[G116_04n.fits]: G116_04 720. ap:1 beam:1



NOAO/IRAF V2.16.1 baha@baha-Lenovo-IdeaPad-Y550 Thu 17:00:51 08-Dec-2016
[G116_04n.fits]: G116_04 720. ap:1 beam:1

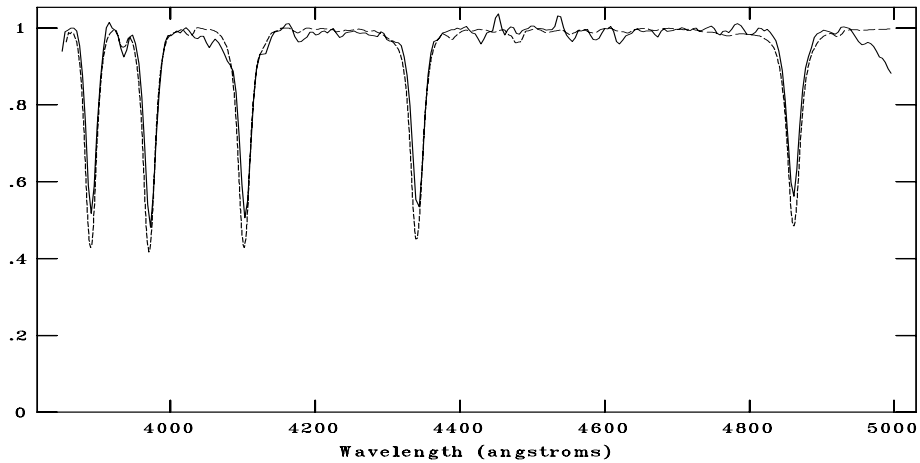
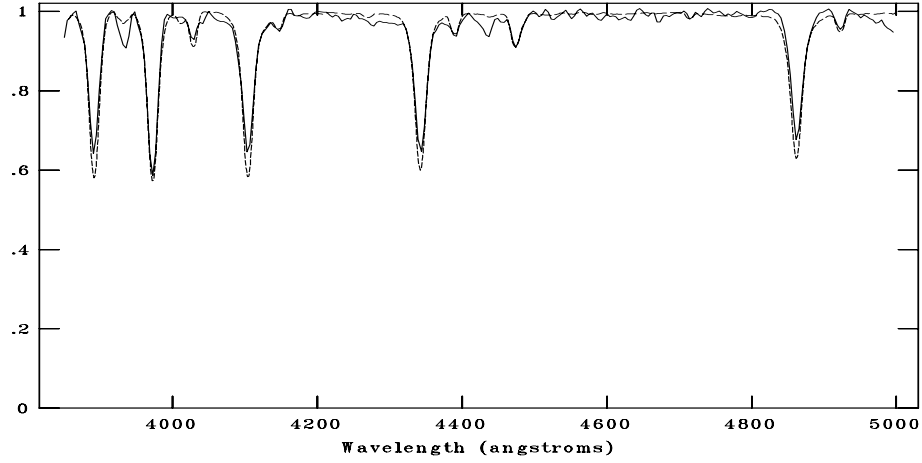
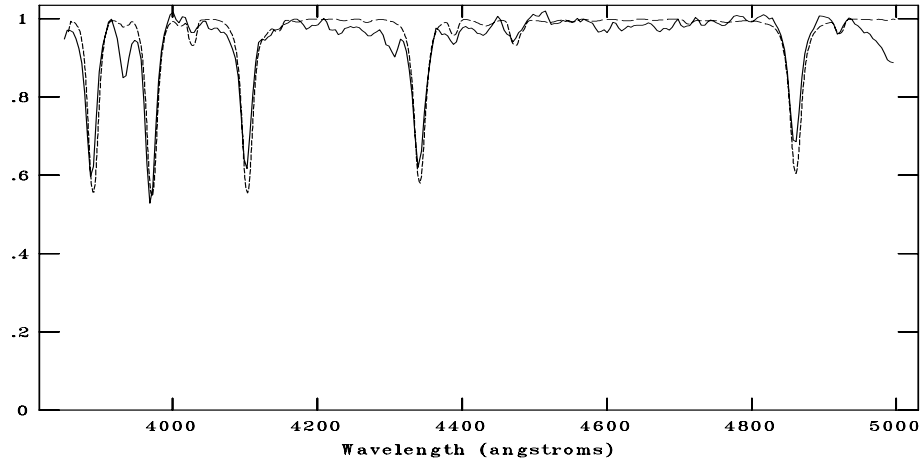


Figure C.70: CAFOS spectrum of 762-000278 compared with A0V, B8V, B9V respectively. The standard spectra are shown with dotted line. The spectral type is assigned as B9V.

NOAO/IRAF V2.16.1 baha@baha-Lenovo-IdeaPad-Y550 Thu 17:04:15 08-Dec-2016
[G116_06n.fits]: G116_06 420. ap:1 beam:1



NOAO/IRAF V2.16.1 baha@baha-Lenovo-IdeaPad-Y550 Thu 17:02:43 08-Dec-2016
[G116_05n.fits]: G116_05 360. ap:1 beam:1



NOAO/IRAF V2.16.1 baha@baha-Lenovo-IdeaPad-Y550 Thu 17:02:21 08-Dec-2016
[G116_05n.fits]: G116_05 360. ap:1 beam:1

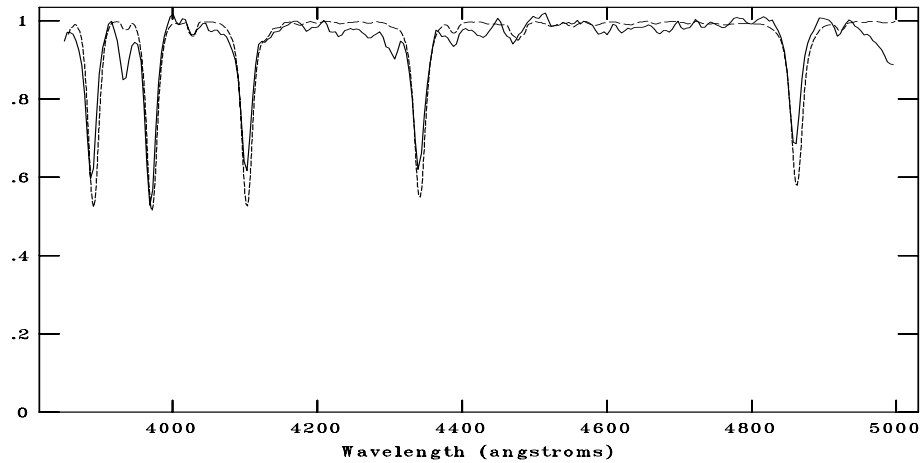
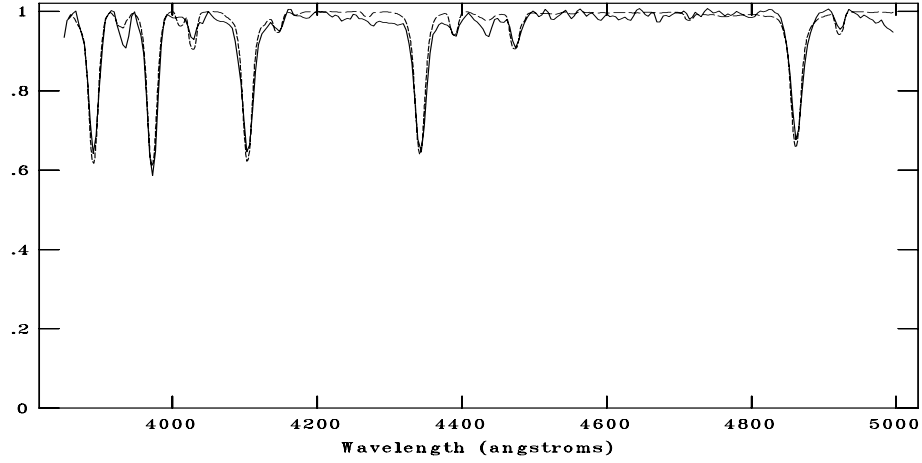
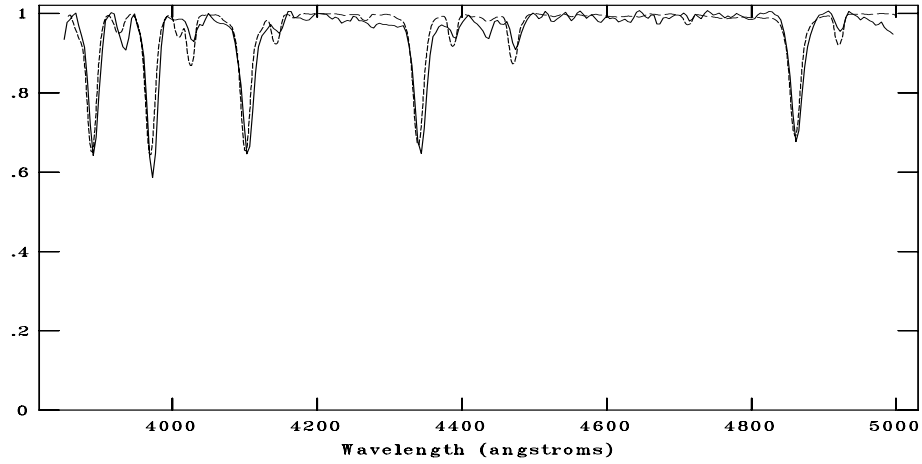


Figure C.71: CAFOS spectrum of 763-000154 compared with B5V, B7V, B8V respectively. The standard spectra are shown with dotted line. The spectral type is assigned as B7V.

NOAO/IRAF V2.16.1 baha@baha-Lenovo-IdeaPad-Y550 Tue 00:51:59 03-Jan-2017
[G116_06B4.fits]: G116_06 420. ap:1 beam:1



NOAO/IRAF V2.16.1 baha@baha-Lenovo-IdeaPad-Y550 Tue 00:52:34 03-Jan-2017
[G116_06B4.fits]: G116_06 420. ap:1 beam:1



NOAO/IRAF V2.16.1 baha@baha-Lenovo-IdeaPad-Y550 Tue 00:52:50 03-Jan-2017
[G116_06B4.fits]: G116_06 420. ap:1 beam:1

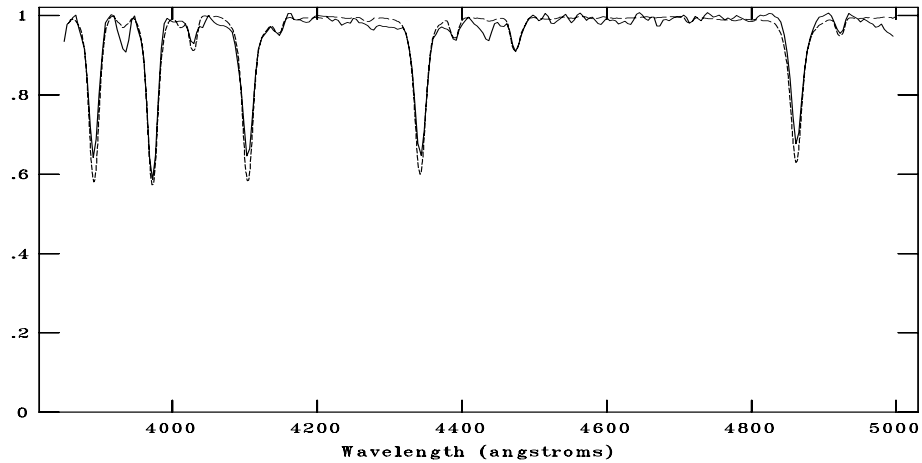
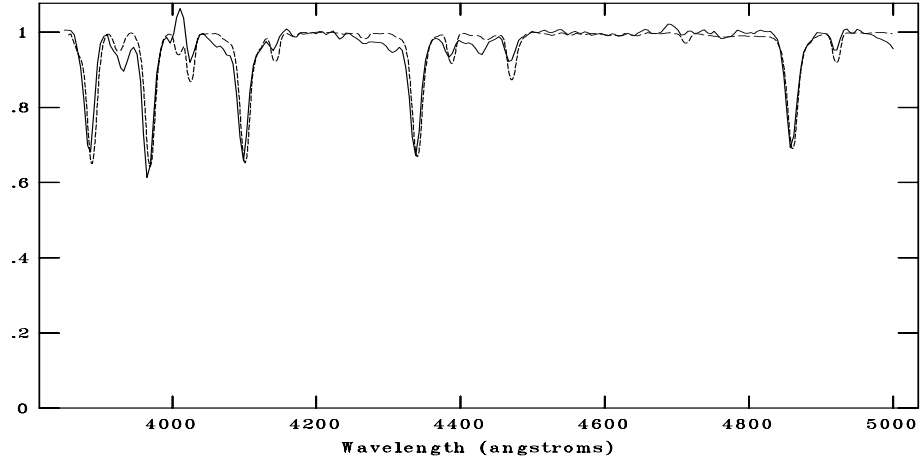
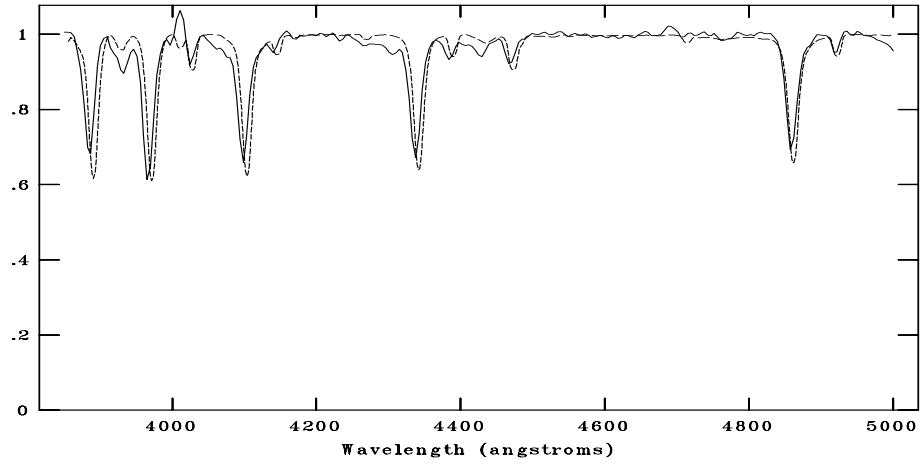


Figure C.72: CAFOS spectrum of 762-075659 compared with B3V, B2V, B5V respectively. The standard spectra are shown with dotted line. The spectral type is assigned as B4V.

NOAO/IRAF V2.16.1 baha@baha-Lenovo-IdeaPad-Y550 Thu 00:28:56 08-Dec-2016
[cg116_01B5.fits]: G116_1 720. ap:1 beam:1



NOAO/IRAF V2.16.1 baha@baha-Lenovo-IdeaPad-Y550 Thu 00:28:29 08-Dec-2016
[cg116_01B5.fits]: G116_1 720. ap:1 beam:1



NOAO/IRAF V2.16.1 baha@baha-Lenovo-IdeaPad-Y550 Thu 00:27:50 08-Dec-2016
[cg116_01B5.fits]: G116_1 720. ap:1 beam:1

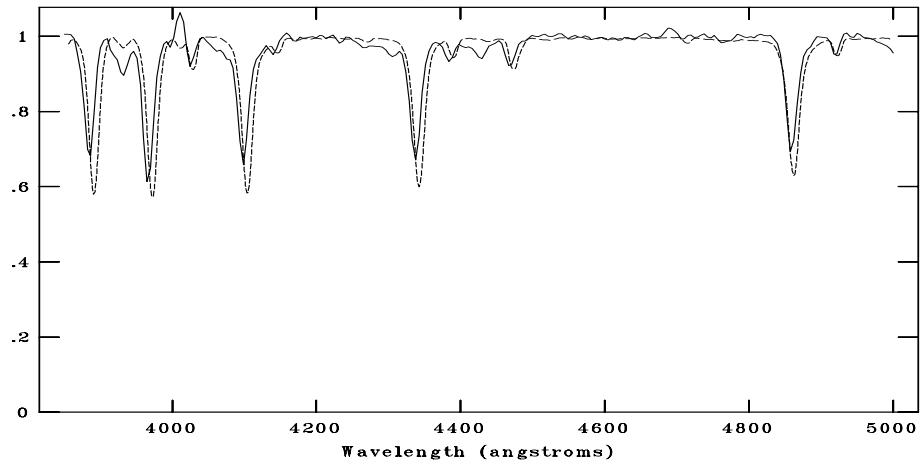
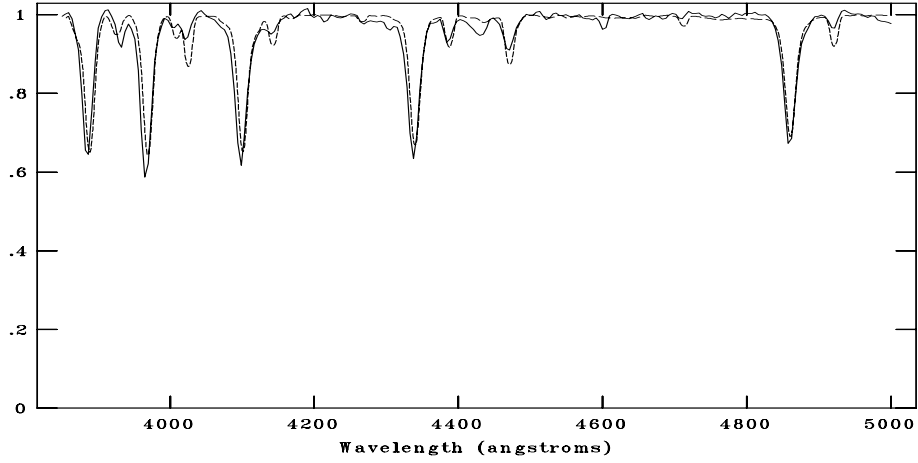
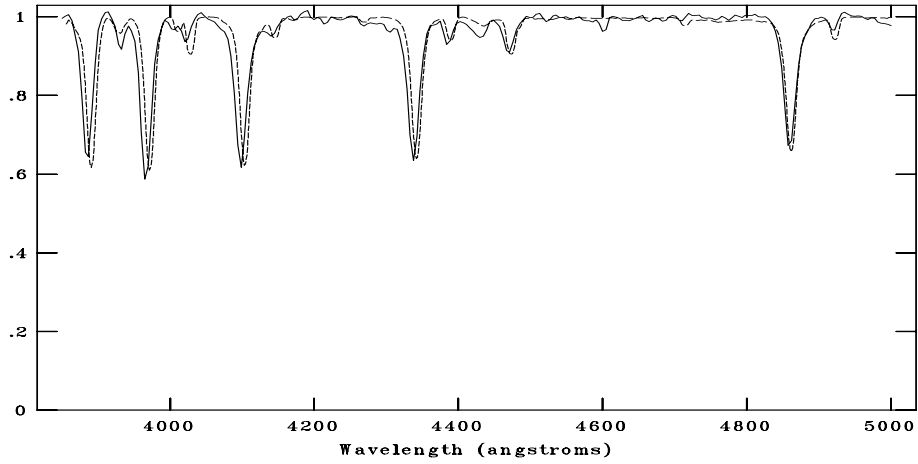


Figure C.73: CAFOS spectrum of 762-075495 compared with B2V, B3V, B5V respectively. The standard spectra are shown with dotted line. The spectral type is assigned as B5V.

NOAO/IRAF V2.16.1 baha@baha-Lenovo-IdeaPad-Y550 Thu 00:29:17 08-Dec-2016
[cg116_02B5.fits]: G116_2 540. ap:1 beam:1



NOAO/IRAF V2.16.1 baha@baha-Lenovo-IdeaPad-Y550 Thu 00:29:33 08-Dec-2016
[cg116_02B5.fits]: G116_2 540. ap:1 beam:1



NOAO/IRAF V2.16.1 baha@baha-Lenovo-IdeaPad-Y550 Thu 00:30:01 08-Dec-2016
[cg116_02B5.fits]: G116_2 540. ap:1 beam:1

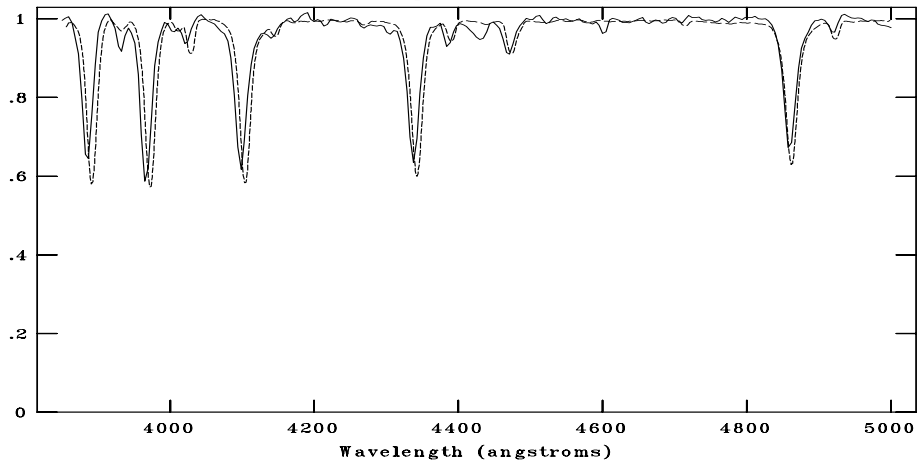
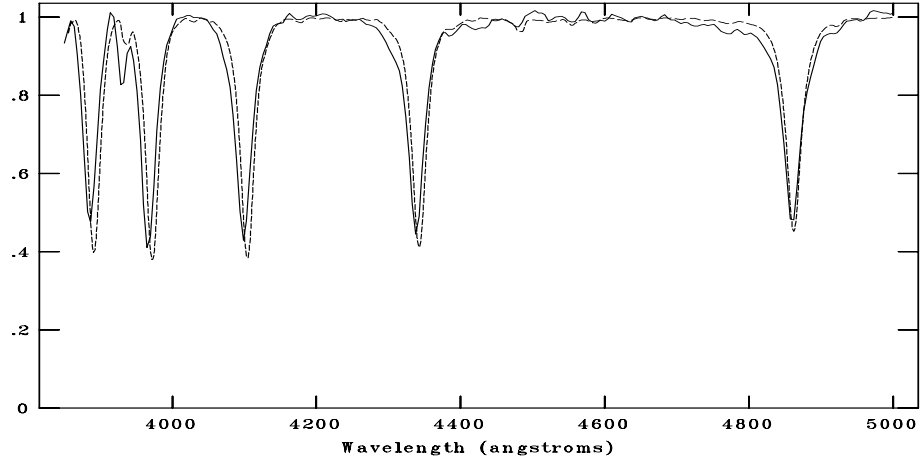
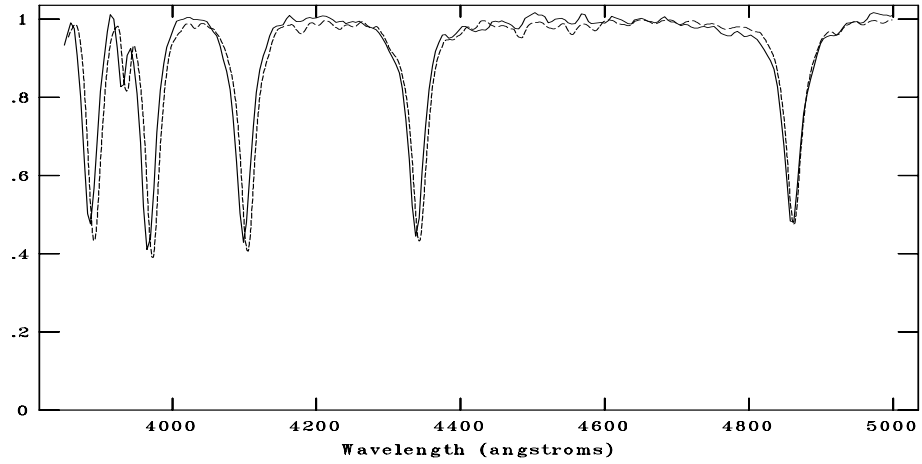


Figure C.74: CAFOS spectrum of 763-076928 compared with B2V, B3V, B5V respectively. The standard spectra are shown with dotted line. The spectral type is assigned as B5V.

NOAO/IRAF V2.16.1 baha@baha-Lenovo-IdeaPad-Y550 Thu 00:30:33 08-Dec-2016
[cg116_03A1.fits]: G116_3 360. ap:1 beam:1



NOAO/IRAF V2.16.1 baha@baha-Lenovo-IdeaPad-Y550 Thu 00:31:30 08-Dec-2016
[cg116_03A1.fits]: G116_3 360. ap:1 beam:1



NOAO/IRAF V2.16.1 baha@baha-Lenovo-IdeaPad-Y550 Thu 00:30:52 08-Dec-2016
[cg116_03A1.fits]: G116_3 360. ap:1 beam:1

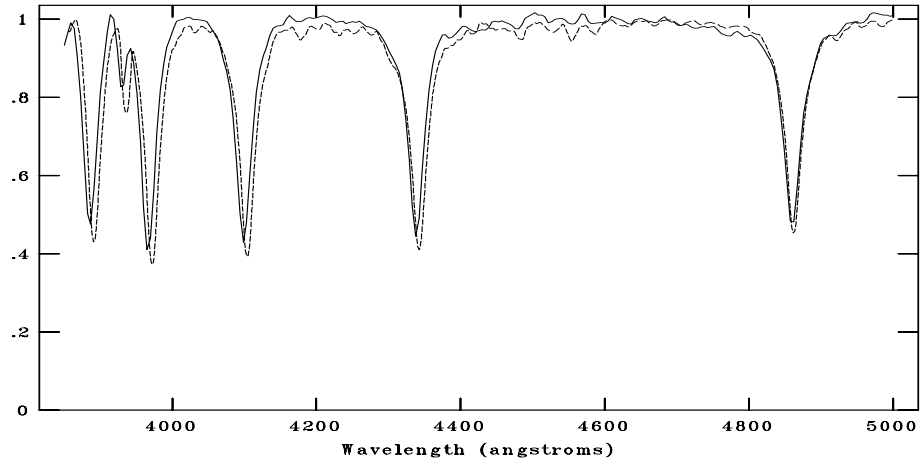
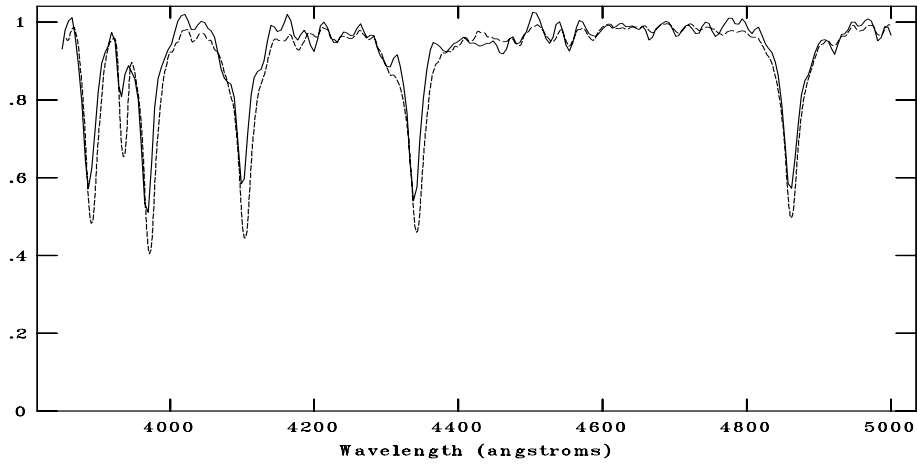
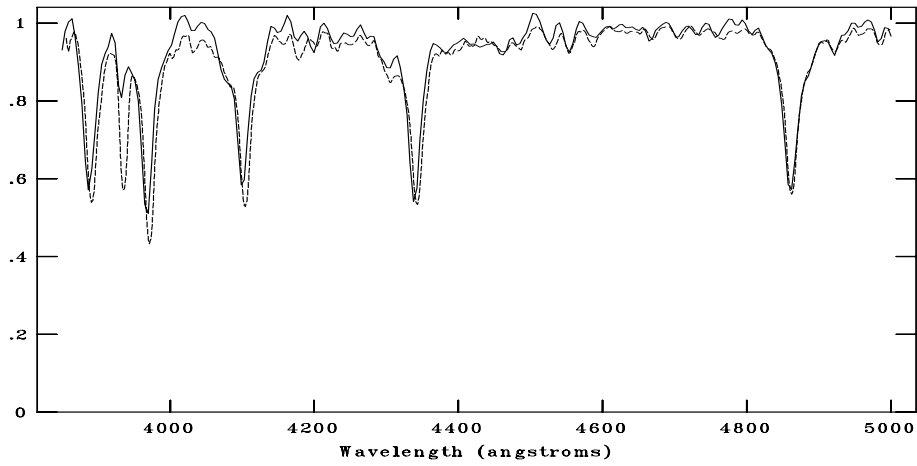


Figure C.75: CAFOS spectrum of 763-077172 compared with A0V, A1V, A3V respectively. The standard spectra are shown with dotted line. The spectral type is assigned as A1V.

NOAO/IRAF V2.16.1 baha@baha-Lenovo-IdeaPad-Y550 Thu 00:33:16 08-Dec-2016
[cg116_04A3.fits]: G116_4 1200. ap:1 beam:1



NOAO/IRAF V2.16.1 baha@baha-Lenovo-IdeaPad-Y550 Thu 00:31:57 08-Dec-2016
[cg116_04A3.fits]: G116_4 1200. ap:1 beam:1



NOAO/IRAF V2.16.1 baha@baha-Lenovo-IdeaPad-Y550 Thu 00:32:48 08-Dec-2016
[cg116_04A3.fits]: G116_4 1200. ap:1 beam:1

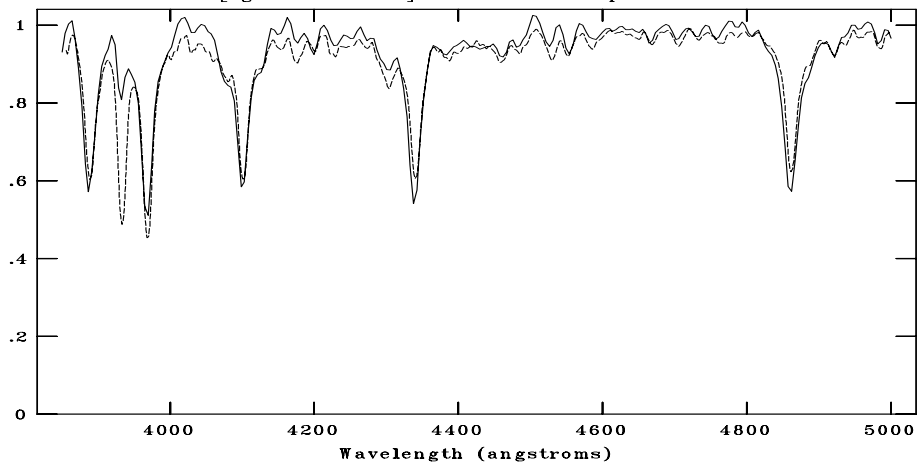
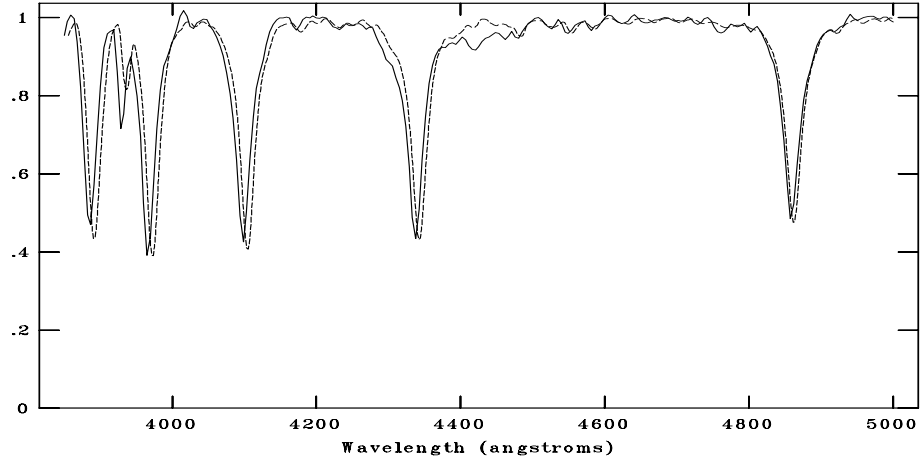
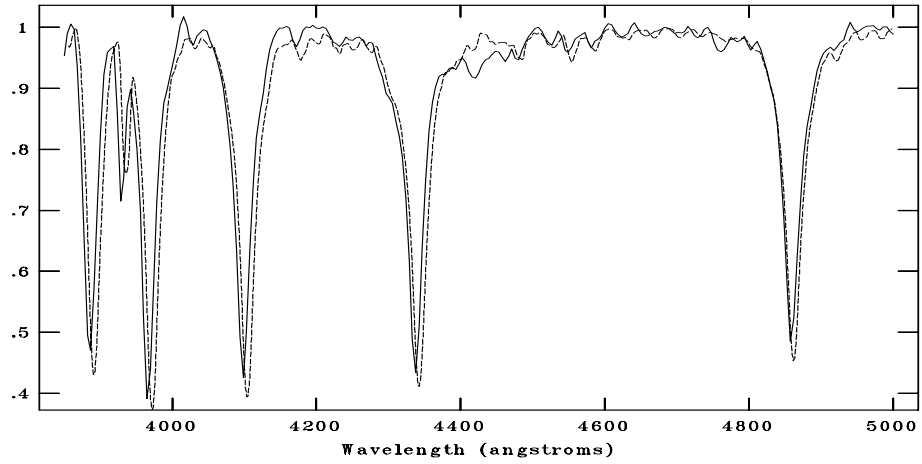


Figure C.76: CAFOS spectrum of 762-075534 compared with A7V, F0V, F2V respectively. The standard spectra are shown with dotted line. The spectral type is assigned as F0V.

NOAO/IRAF V2.16.1 baha@baha-Lenovo-IdeaPad-Y550 Thu 00:34:20 08-Dec-2016
[cg116_05A2.fits]: G116_5 1080. ap:1 beam:1



NOAO/IRAF V2.16.1 baha@baha-Lenovo-IdeaPad-Y550 Thu 00:34:31 08-Dec-2016
[cg116_05A2.fits]: G116_5 1080. ap:1 beam:1



NOAO/IRAF V2.16.1 baha@baha-Lenovo-IdeaPad-Y550 Thu 00:34:47 08-Dec-2016
[cg116_05A2.fits]: G116_5 1080. ap:1 beam:1

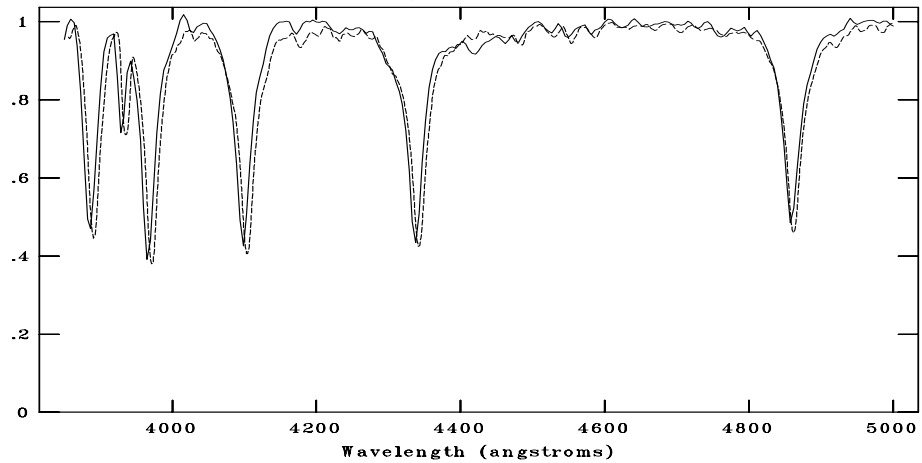
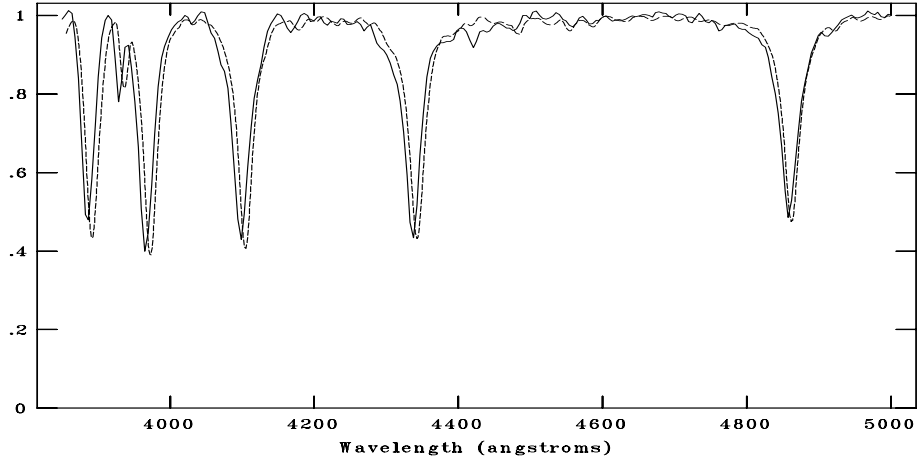
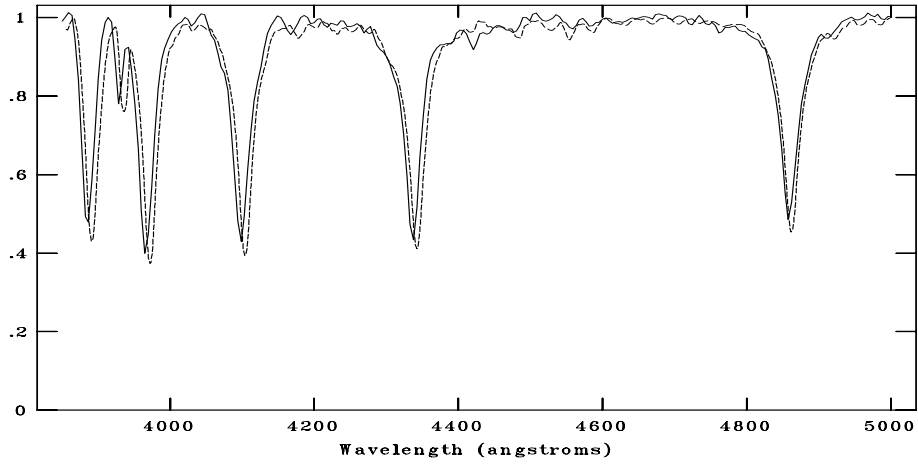


Figure C.77: CAFOS spectrum of 762-075377 compared with A1V, A3V, A5V respectively. The standard spectra are shown with dotted line. The spectral type is assigned as A2V.

NOAO/IRAF V2.16.1 baha@baha-Lenovo-IdeaPad-Y550 Thu 00:36:35 08-Dec-2016
[cg116_06A2.fits]: G116_6 1080. ap:1 beam:1



NOAO/IRAF V2.16.1 baha@baha-Lenovo-IdeaPad-Y550 Thu 00:36:52 08-Dec-2016
[cg116_06A2.fits]: G116_6 1080. ap:1 beam:1



NOAO/IRAF V2.16.1 baha@baha-Lenovo-IdeaPad-Y550 Thu 00:37:06 08-Dec-2016
[cg116_06A2.fits]: G116_6 1080. ap:1 beam:1

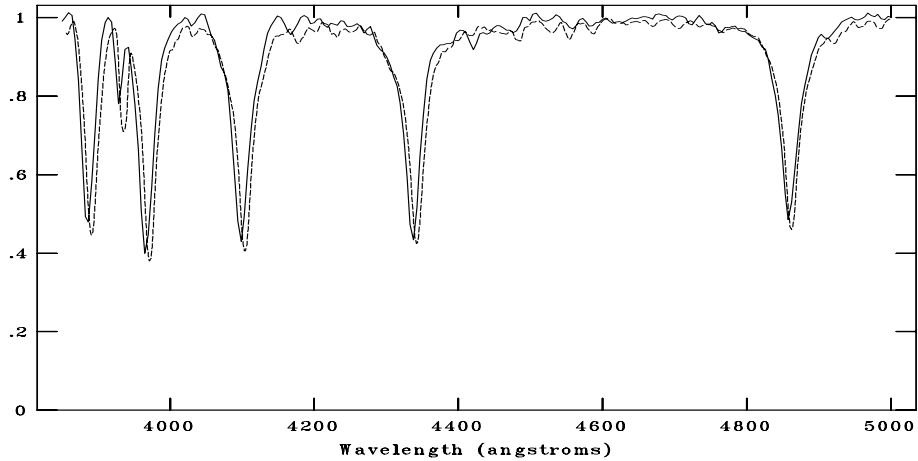
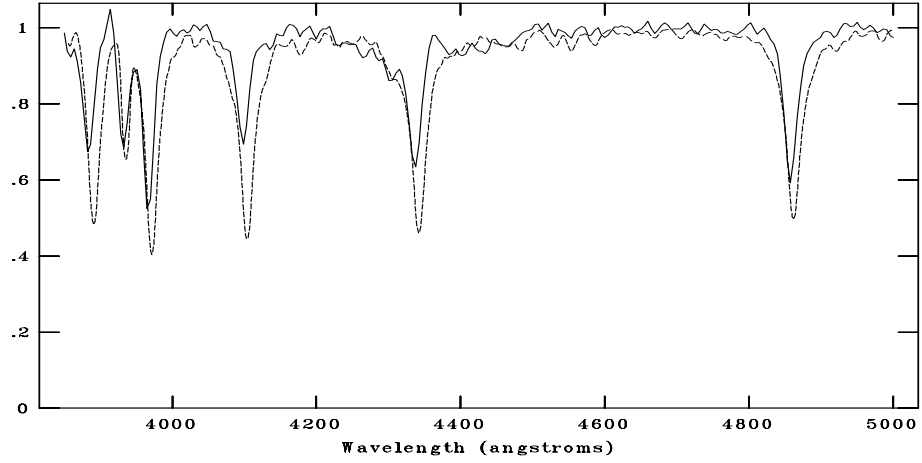
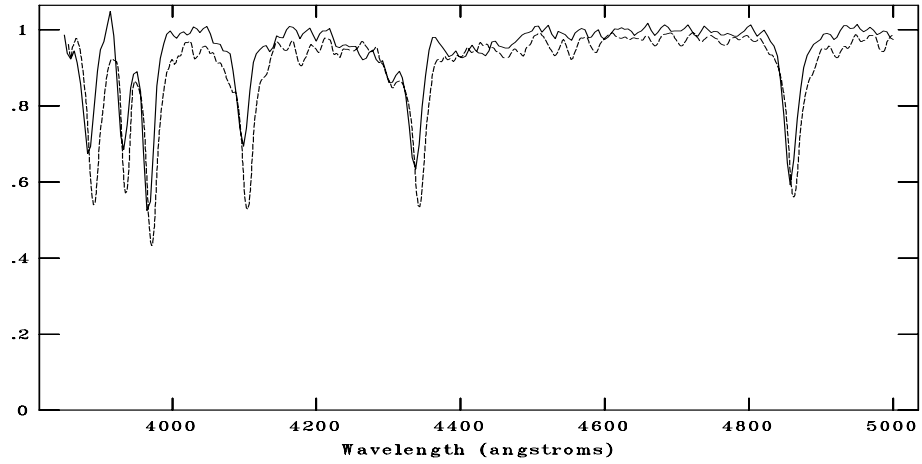


Figure C.78: CAFOS spectrum of 763-077093 compared with A1V, A3V, A5V respectively. The standard spectra are shown with dotted line. The spectral type is assigned as A2V.

NOAO/IRAF V2.16.1 baha@baha-Lenovo-IdeaPad-Y550 Thu 00:37:50 08-Dec-2016
[cg116_07A5.fits]: G116_7 720. ap:1 beam:1



NOAO/IRAF V2.16.1 baha@baha-Lenovo-IdeaPad-Y550 Thu 00:38:15 08-Dec-2016
[cg116_07A5.fits]: G116_7 720. ap:1 beam:1



NOAO/IRAF V2.16.1 baha@baha-Lenovo-IdeaPad-Y550 Thu 00:39:09 08-Dec-2016
[cg116_07A5.fits]: G116_7 720. ap:1 beam:1

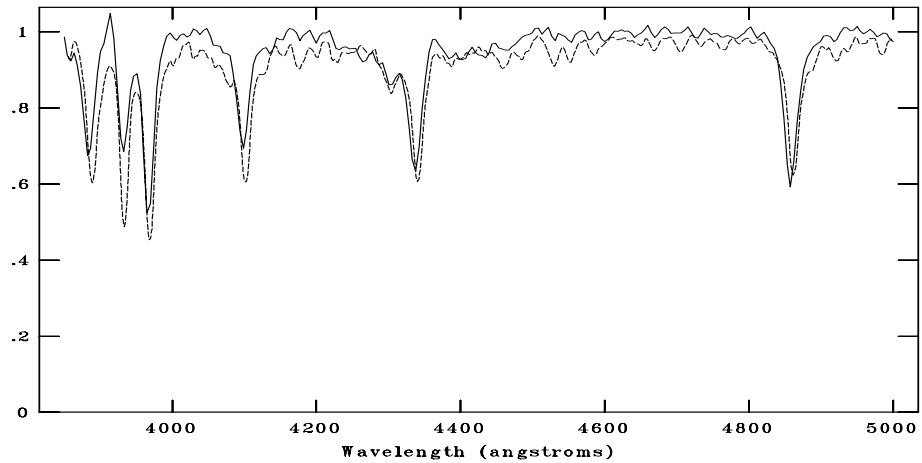
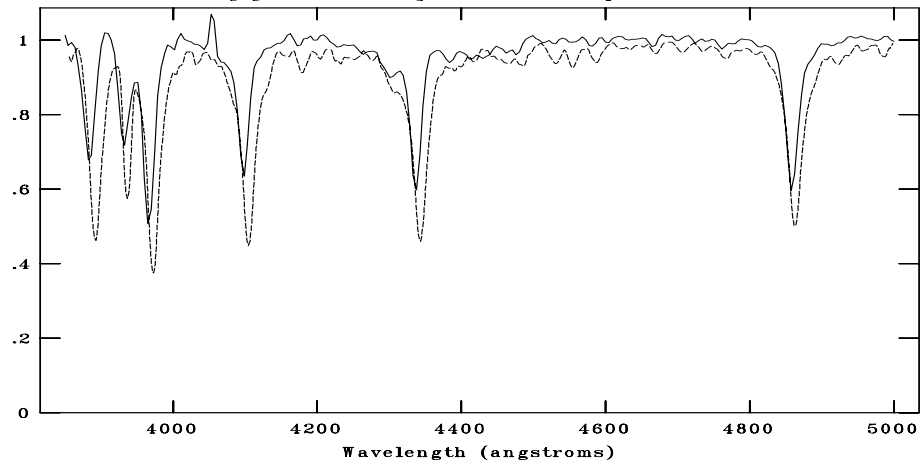
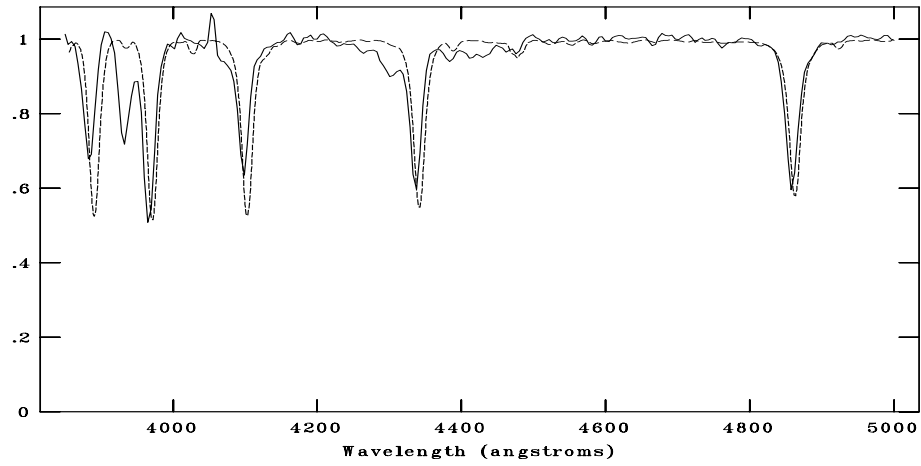


Figure C.79: CAFOS spectrum of 763-07125 compared with A7V, F0V, F2V respectively. The standard spectra are shown with dotted line. The spectral type is assigned as F0V.

NOAO/IRAF V2.16.1 baha@baha-Lenovo-IdeaPad-Y550 Thu 00:44:48 08-Dec-2016
[cg116_08A5.fits]: G116_8 900. ap:1 beam:1



NOAO/IRAF V2.16.1 baha@baha-Lenovo-IdeaPad-Y550 Thu 00:43:01 08-Dec-2016
[cg116_08A5.fits]: G116_8 900. ap:1 beam:1



NOAO/IRAF V2.16.1 baha@baha-Lenovo-IdeaPad-Y550 Thu 00:43:39 08-Dec-2016
[cg116_08A5.fits]: G116_8 900. ap:1 beam:1

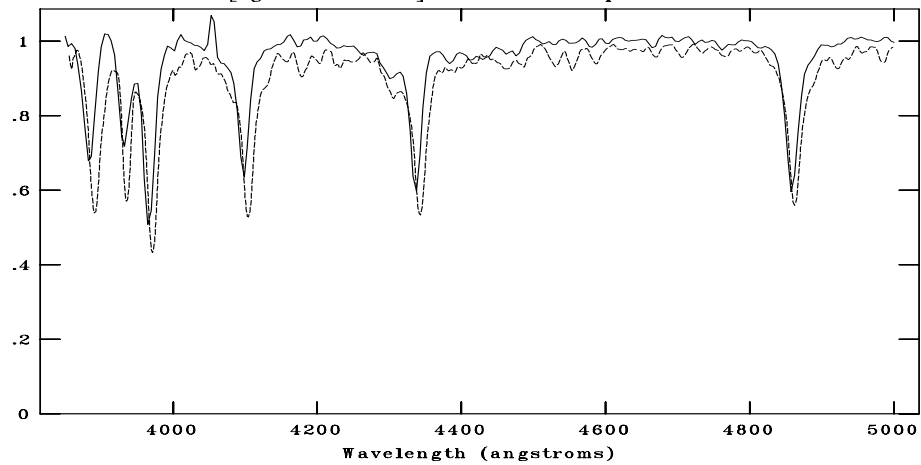
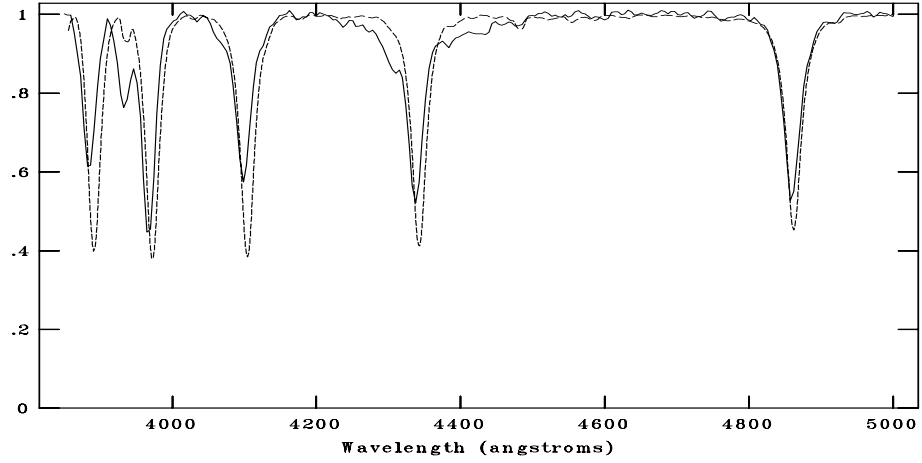
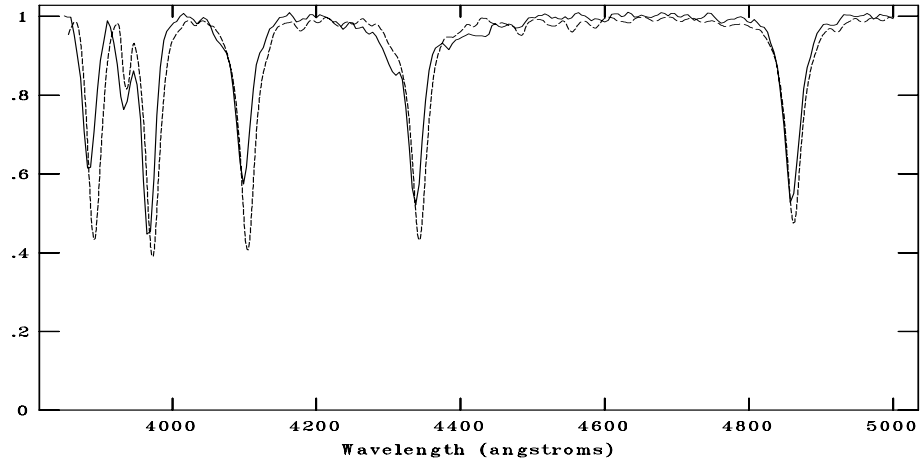


Figure C.80: CAFOS spectrum of 763-077195 compared with A7III, B8V, F0V respectively. The standard spectra are shown with dotted line. The spectral type is assigned as A5V. The spectral type identification is not reliable.

NOAO/IRAF V2.16.1 baha@baha-Lenovo-IdeaPad-Y550 Thu 00:47:41 08-Dec-2016
[cg116_09A2.fits]: G116_9 900. ap:1 beam:1



NOAO/IRAF V2.16.1 baha@baha-Lenovo-IdeaPad-Y550 Thu 00:47:13 08-Dec-2016
[cg116_09A2.fits]: G116_9 900. ap:1 beam:1



NOAO/IRAF V2.16.1 baha@baha-Lenovo-IdeaPad-Y550 Thu 00:46:58 08-Dec-2016
[cg116_09A2.fits]: G116_9 900. ap:1 beam:1

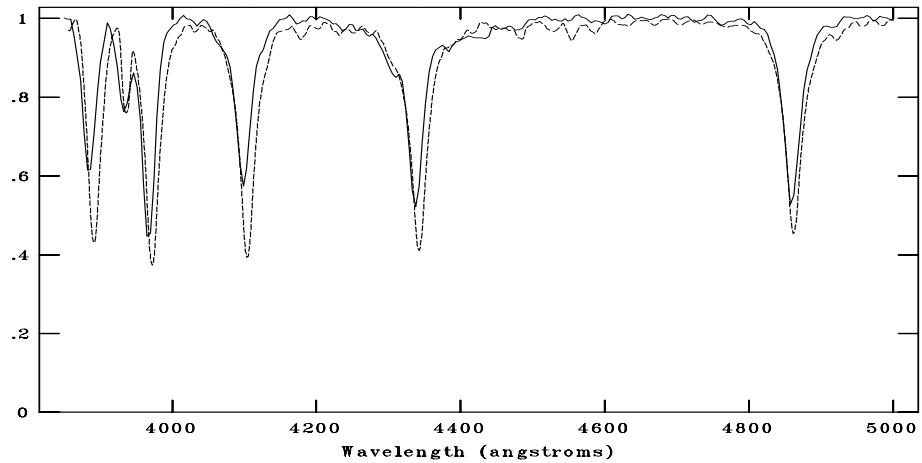
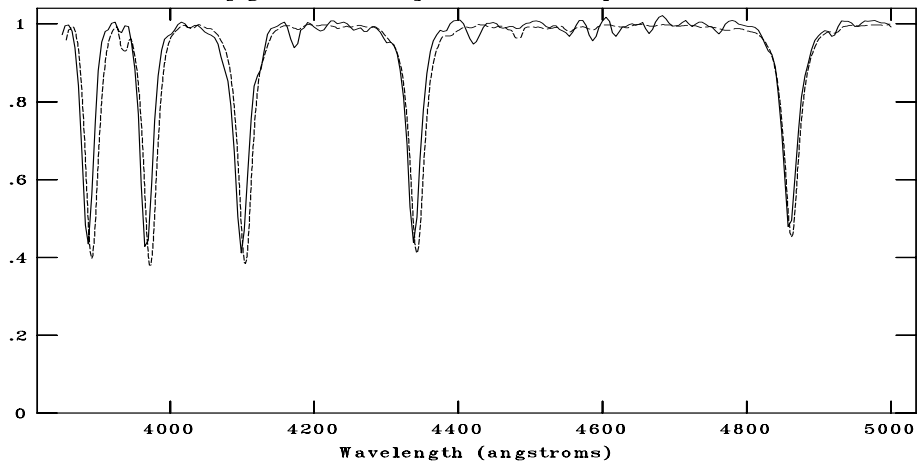
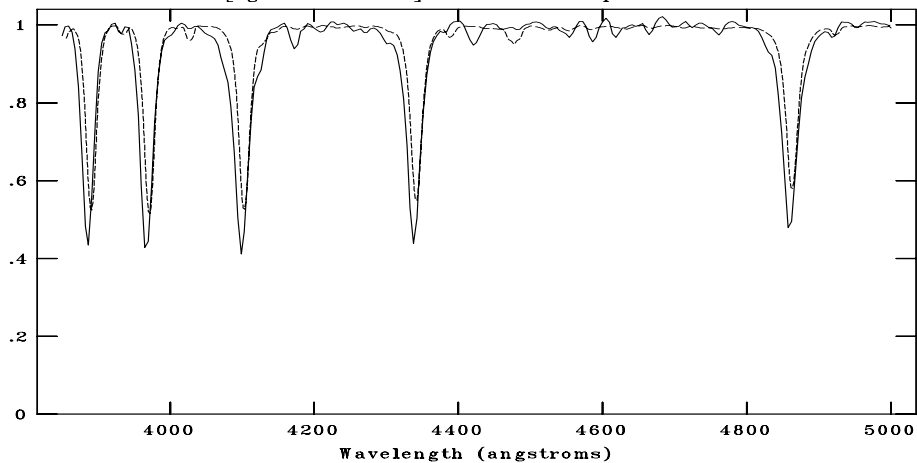


Figure C.81: CAFOS spectrum of 763-077148 compared with A0V, A1V, A3V respectively. The standard spectra are shown with dotted line. The spectral type is assigned as A2V.

NOAO/IRAF V2.16.1 baha@baha-Lenovo-IdeaPad-Y550 Thu 00:50:28 08-Dec-2016
[cg116_11B9.fits]: G116_01 90. ap:1 beam:1



NOAO/IRAF V2.16.1 baha@baha-Lenovo-IdeaPad-Y550 Thu 00:50:12 08-Dec-2016
[cg116_11B9.fits]: G116_01 90. ap:1 beam:1



NOAO/IRAF V2.16.1 baha@baha-Lenovo-IdeaPad-Y550 Thu 00:49:50 08-Dec-2016
[cg116_11B9.fits]: G116_01 90. ap:1 beam:1

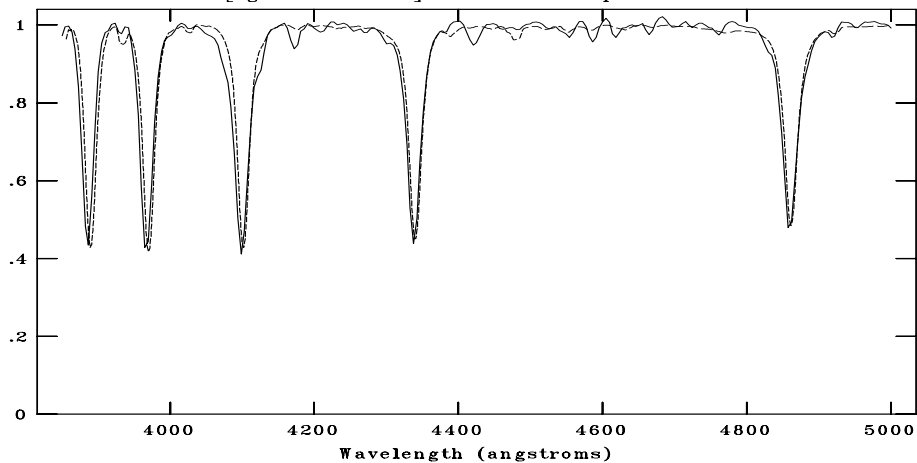
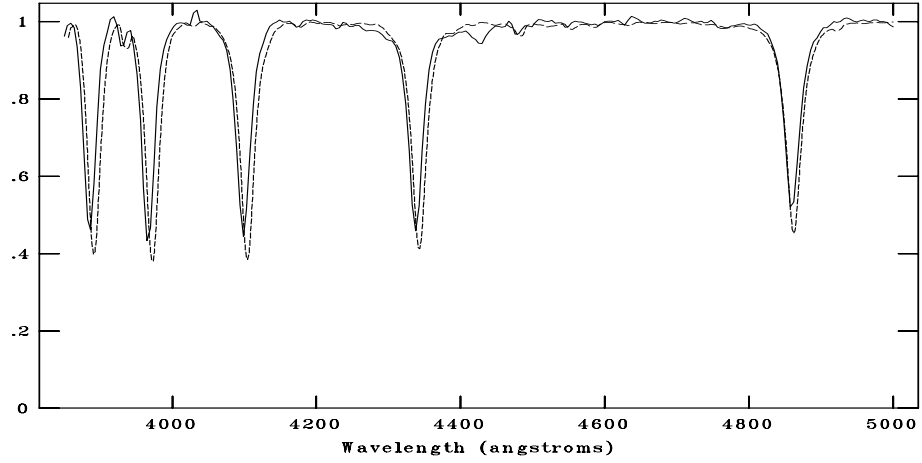
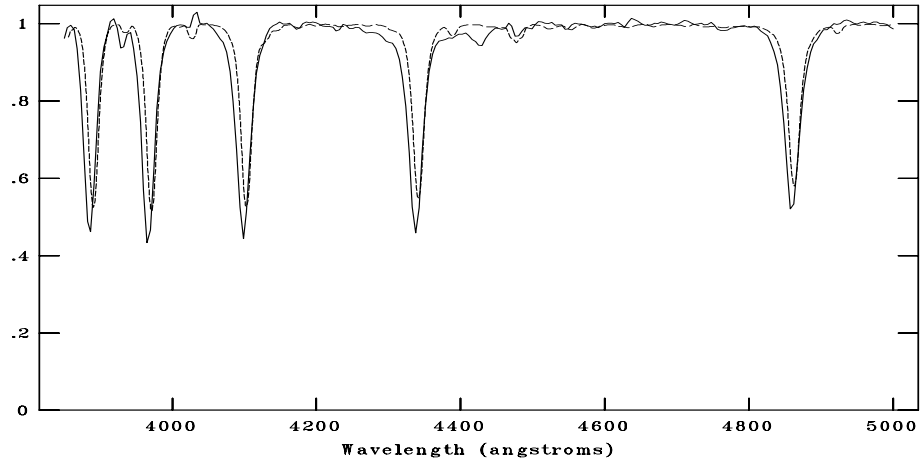


Figure C.82: CAFOS spectrum of 762-075588 compared with A0V, B8V, B9V respectively. The standard spectra are shown with dotted line. The spectral type is assigned as B9V.

NOAO/IRAF V2.16.1 baha@baha-Lenovo-IdeaPad-Y550 Thu 02:21:30 08-Dec-2016
[cg116_12B9.fits]: G116_02 960. ap:1 beam:1



NOAO/IRAF V2.16.1 baha@baha-Lenovo-IdeaPad-Y550 Thu 02:20:59 08-Dec-2016
[cg116_12B9.fits]: G116_02 960. ap:1 beam:1



NOAO/IRAF V2.16.1 baha@baha-Lenovo-IdeaPad-Y550 Thu 02:21:18 08-Dec-2016
[cg116_12B9.fits]: G116_02 960. ap:1 beam:1

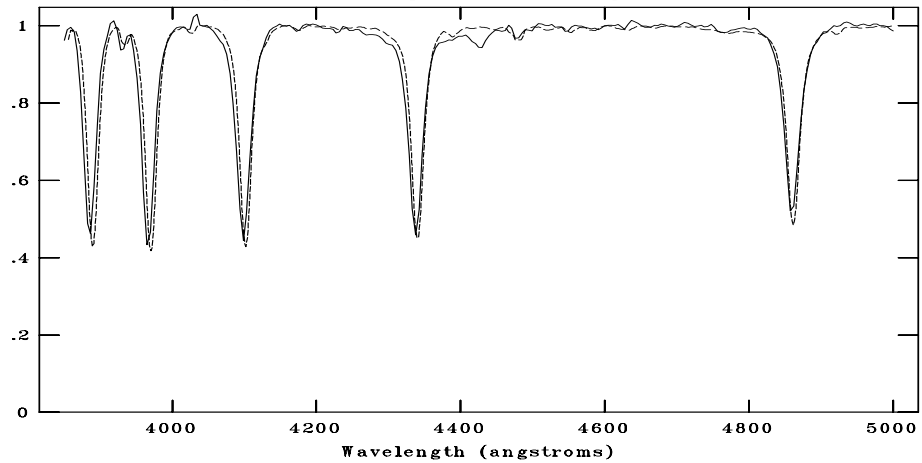
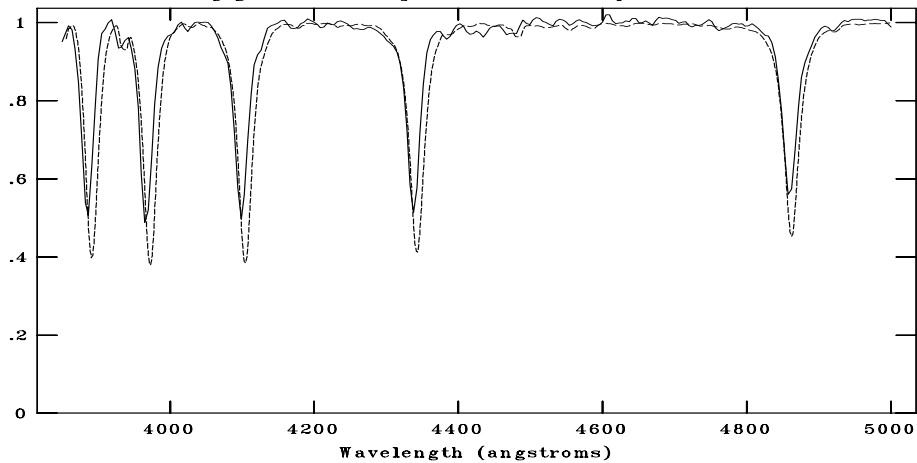
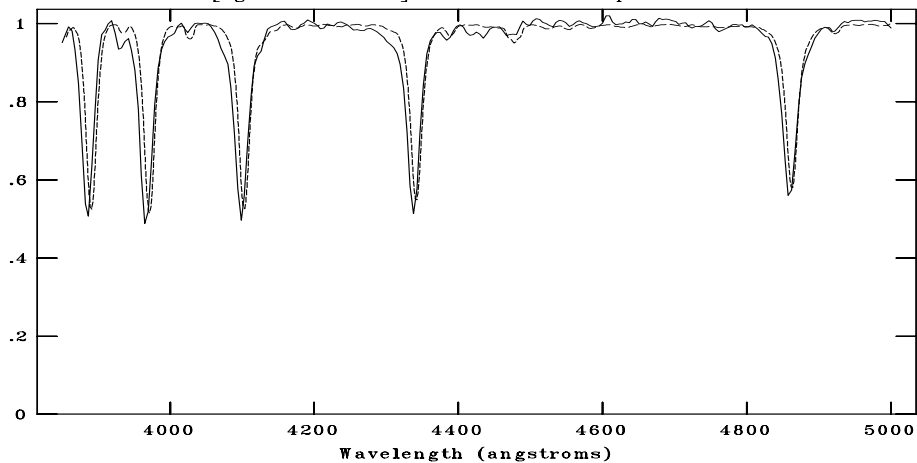


Figure C.83: CAFOS spectrum of 763-077153 compared with A0V, B8V, B9V respectively. The standard spectra are shown with dotted line. The spectral type is assigned as B9V.

NOAO/IRAF V2.16.1 baha@baha-Lenovo-IdeaPad-Y550 Thu 02:23:15 08-Dec-2016
[cg116_13B9.fits]: G116_03 1080. ap:1 beam:1



NOAO/IRAF V2.16.1 baha@baha-Lenovo-IdeaPad-Y550 Thu 02:22:22 08-Dec-2016
[cg116_13B9.fits]: G116_03 1080. ap:1 beam:1



NOAO/IRAF V2.16.1 baha@baha-Lenovo-IdeaPad-Y550 Thu 02:22:50 08-Dec-2016
[cg116_13B9.fits]: G116_03 1080. ap:1 beam:1

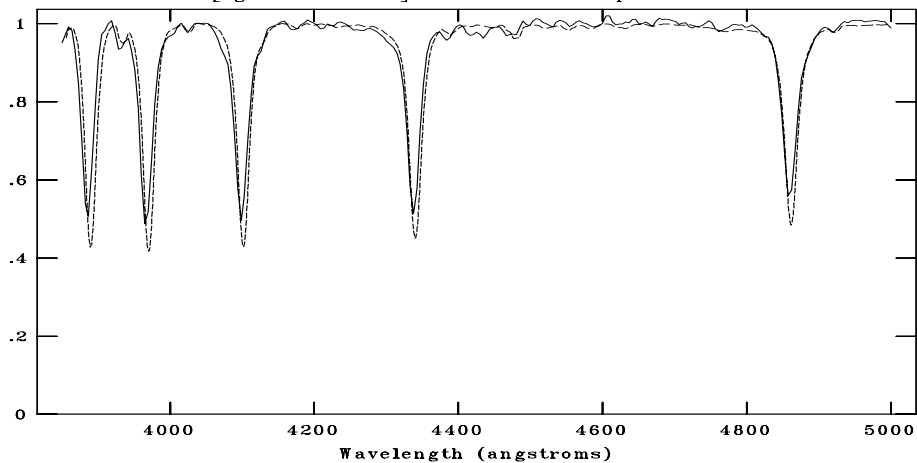


Figure C.84: CAFOS spectrum of 763-077012 compared with A0V, B8V, B9V respectively. The standard spectra are shown with dotted line. The spectral type is assigned as B9V.

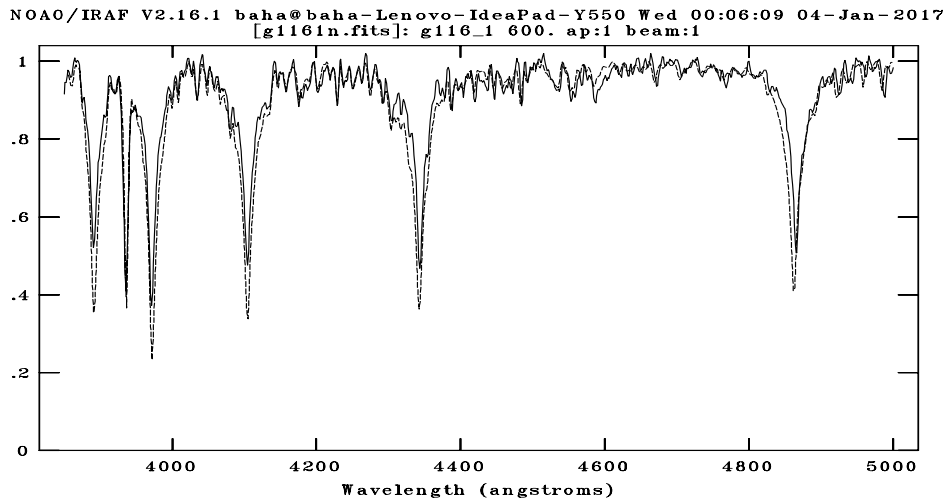
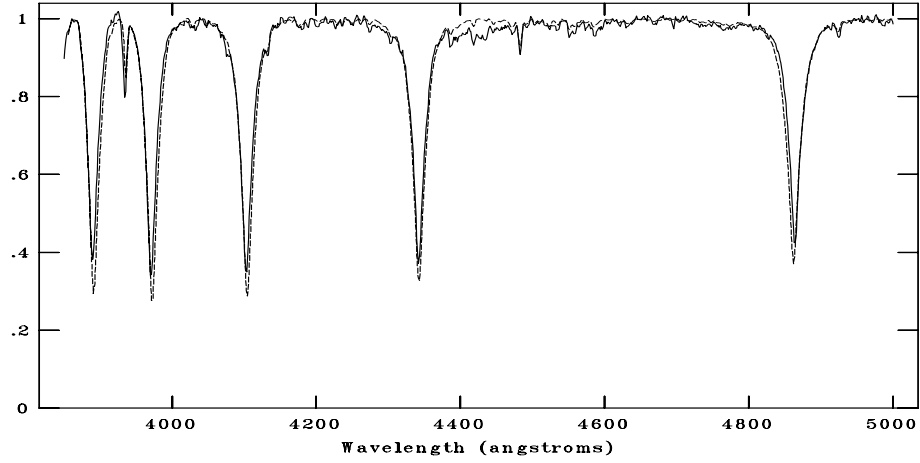
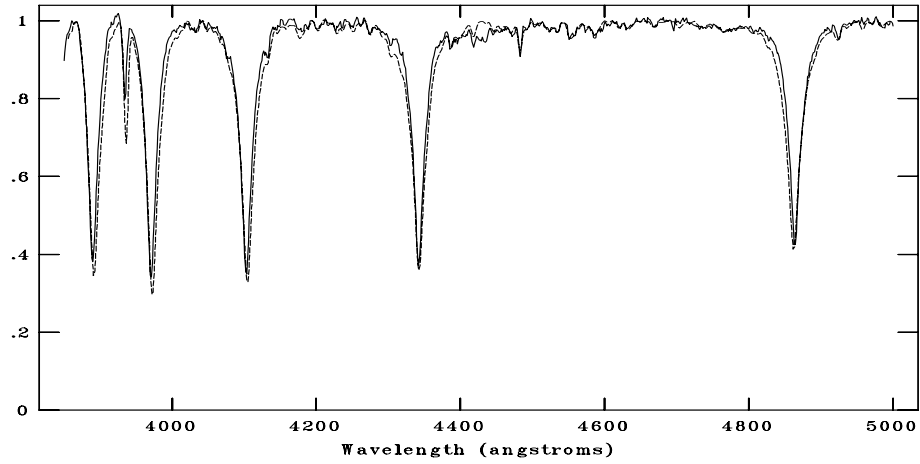


Figure C.85: TFOSC spectrum of 763-077199 compared with A7V. The spectral type is assigned as A7V.

NOAO/IRAF V2.16.1 baha@baha-Lenovo-IdeaPad-Y550 Wed 00:08:18 04-Jan-2017
[g1164n.fits]: g116_2 420. ap:1 beam:1



NOAO/IRAF V2.16.1 baha@baha-Lenovo-IdeaPad-Y550 Wed 00:08:47 04-Jan-2017
[g1164n.fits]: g116_2 420. ap:1 beam:1



NOAO/IRAF V2.16.1 baha@baha-Lenovo-IdeaPad-Y550 Wed 00:06:58 04-Jan-2017
[g1164n.fits]: g116_2 420. ap:1 beam:1

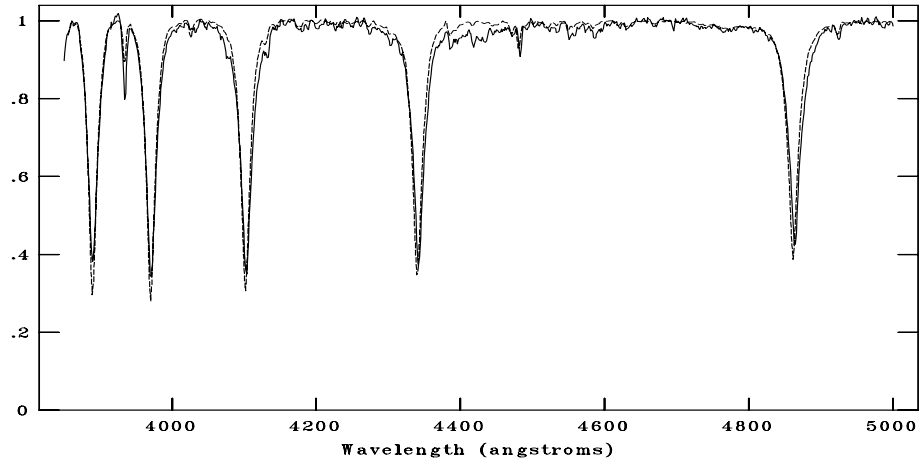


Figure C.86: TFOSC spectrum of 762-075426 compared with A0V, A1V, B9V respectively. The standard spectra are shown with dotted line. The spectral type is assigned as A0V.

C.9 G126.2+1.6

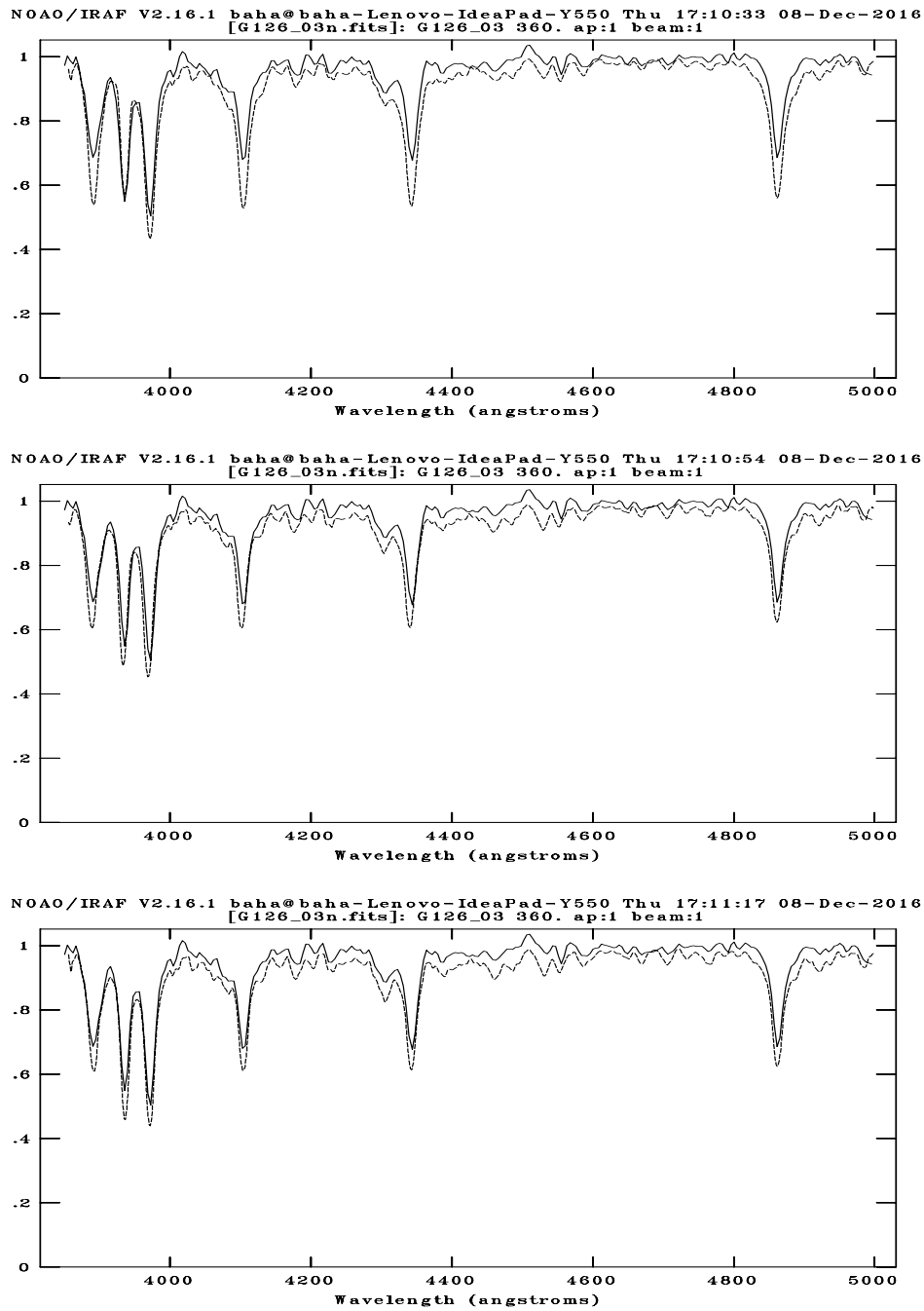
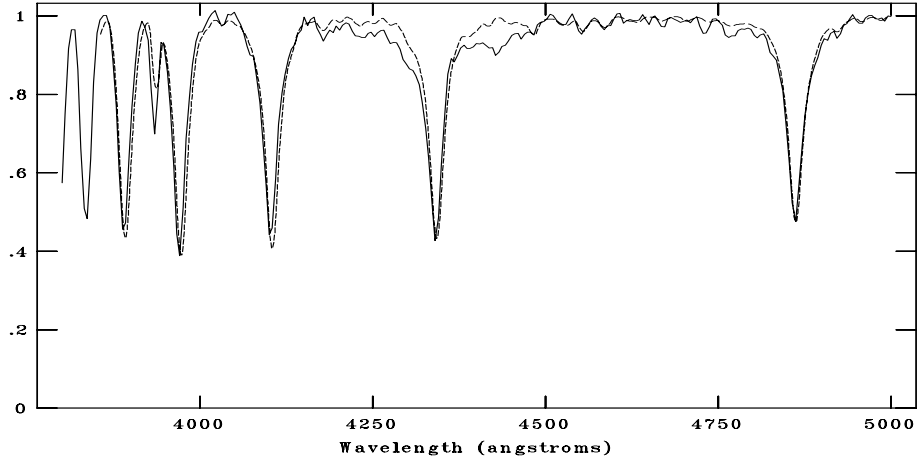
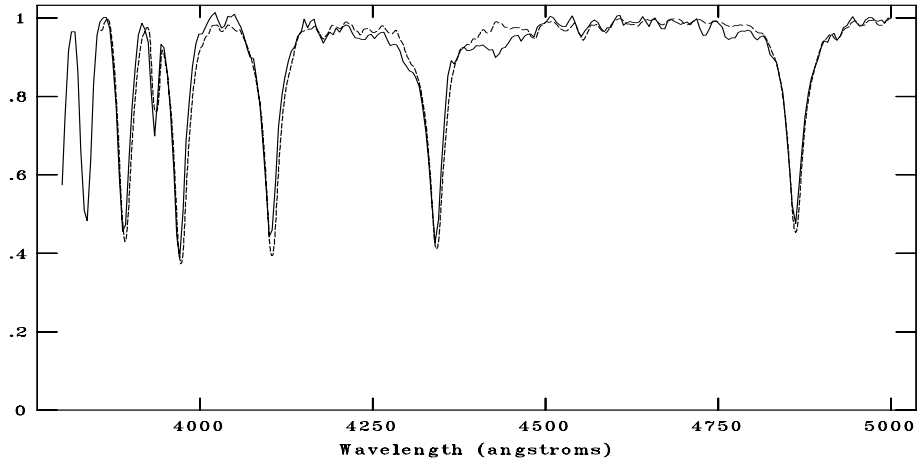


Figure C.87: CAFOS spectrum of 772-009418 compared with F0V, F2V, F3V respectively. The standard spectra are shown with dotted line. The spectral type is assigned as F1V.

NOAO/IRAF V2.16.1 baha@baha-Lenovo-IdeaPad-Y550 Wed 06:30:52 07-Dec-2016
[n126_1.fits]: 126_1 300. ap:1 beam:1



NOAO/IRAF V2.16.1 baha@baha-Lenovo-IdeaPad-Y550 Wed 06:31:41 07-Dec-2016
[n126_1.fits]: 126_1 300. ap:1 beam:1



NOAO/IRAF V2.16.1 baha@baha-Lenovo-IdeaPad-Y550 Wed 06:32:49 07-Dec-2016
[n126_1.fits]: 126_1 300. ap:1 beam:1

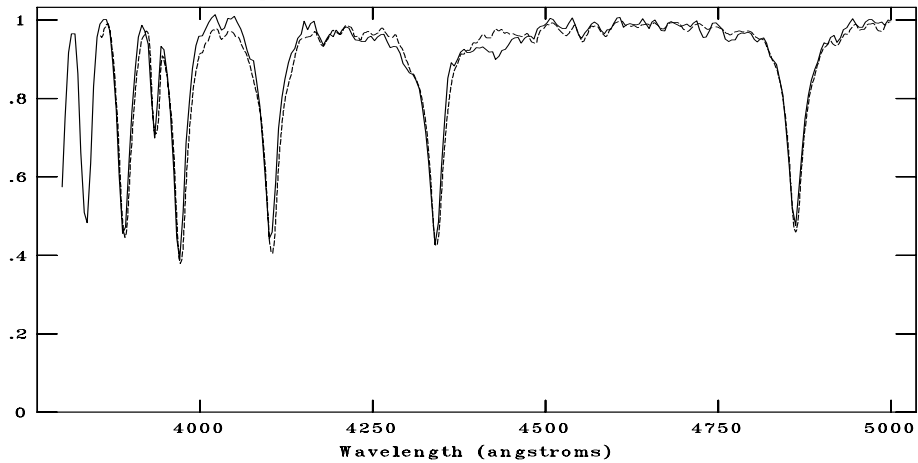
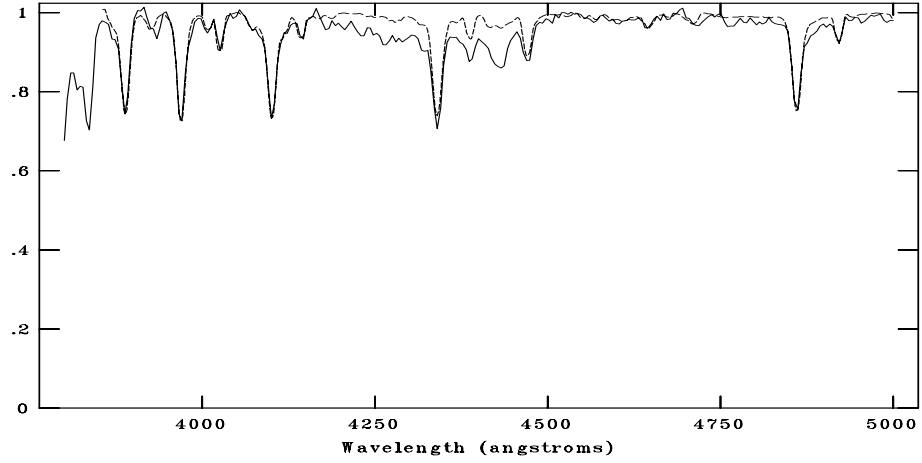
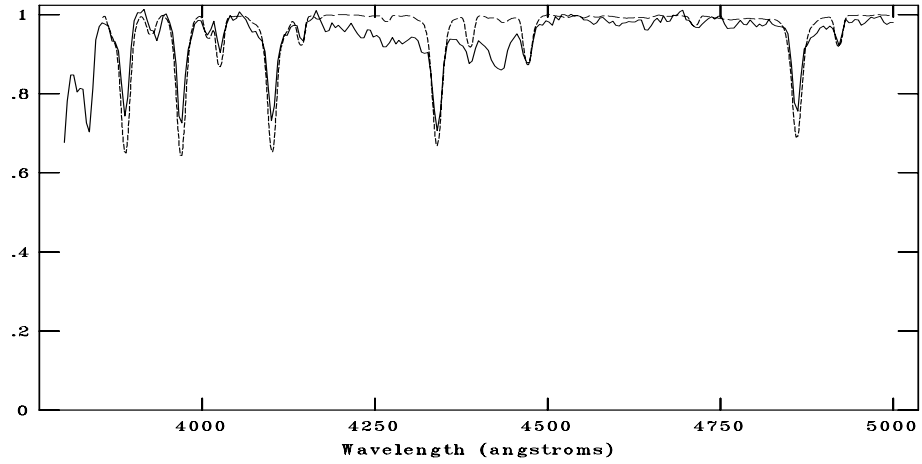


Figure C.88: CAFOS spectrum of 772-009343 compared with A1V, A3V, A5V respectively. The standard spectra are shown with dotted line. The spectral type is assigned as A3V.

NOAO/IRAF V2.16.1 baha@baha-Lenovo-IdeaPad-Y550 Wed 06:33:41 07-Dec-2016
[n126_2.fits]: 126_2 150. ap:1 beam:1



NOAO/IRAF V2.16.1 baha@baha-Lenovo-IdeaPad-Y550 Wed 06:35:06 07-Dec-2016
[n126_2.fits]: 126_2 150. ap:1 beam:1



NOAO/IRAF V2.16.1 baha@baha-Lenovo-IdeaPad-Y550 Wed 06:34:16 07-Dec-2016
[n126_2.fits]: 126_2 150. ap:1 beam:1

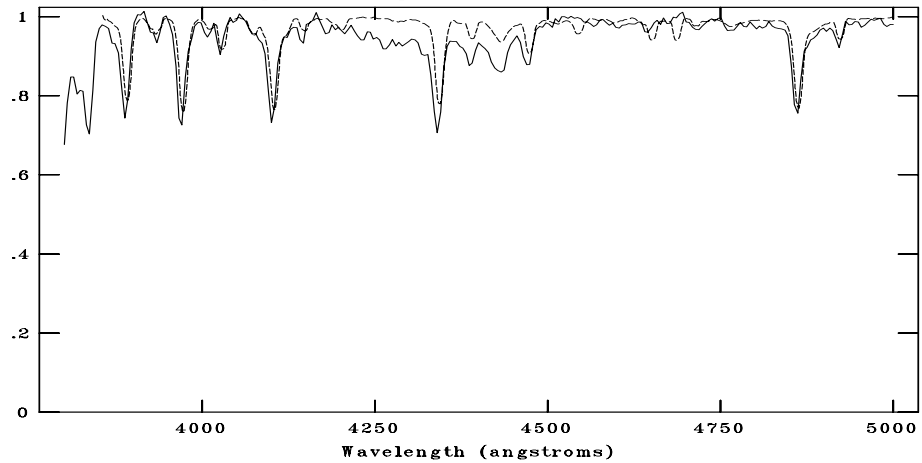
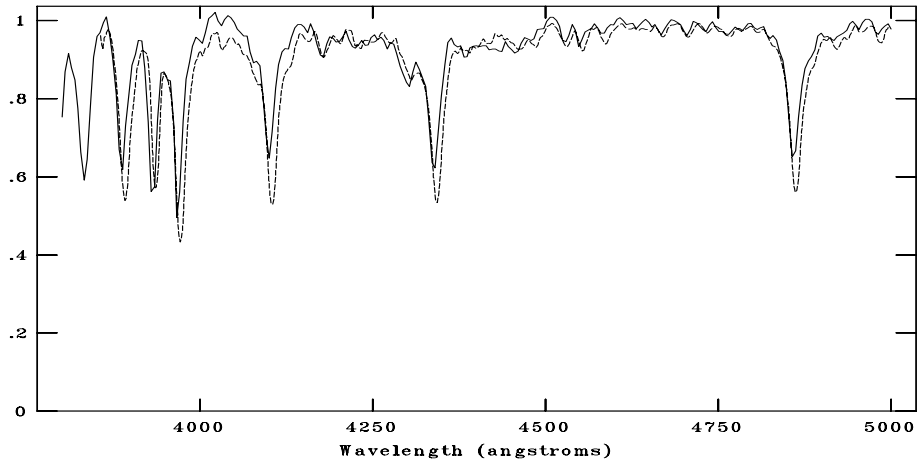
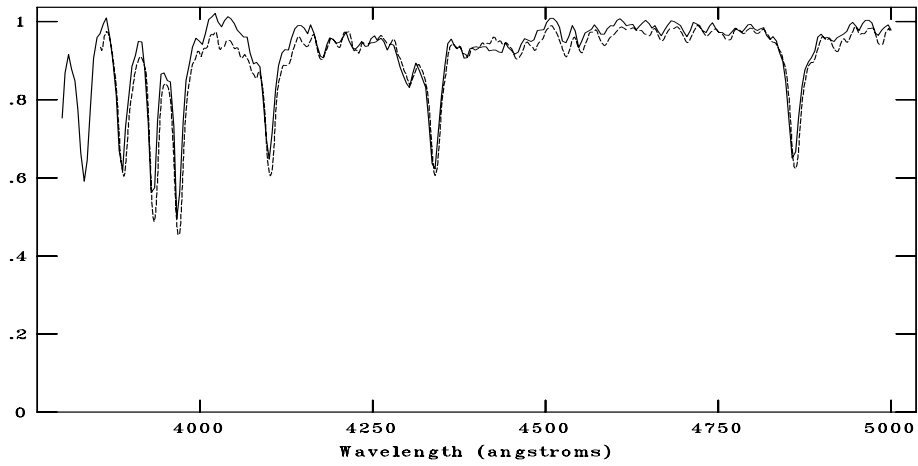


Figure C.89: CAFOS spectrum of 772-009430 compared with B1V, B2V, O9V respectively. The standard spectra are shown with dotted line. The spectral type is assigned as B1V.

NOAO/IRAF V2.16.1 baha@baha-Lenovo-IdeaPad-Y550 Wed 06:36:21 07-Dec-2016
[n126_3.fits]: 126_3 450. ap:1 beam:1



NOAO/IRAF V2.16.1 baha@baha-Lenovo-IdeaPad-Y550 Wed 06:36:55 07-Dec-2016
[n126_3.fits]: 126_3 450. ap:1 beam:1



NOAO/IRAF V2.16.1 baha@baha-Lenovo-IdeaPad-Y550 Wed 06:37:16 07-Dec-2016
[n126_3.fits]: 126_3 450. ap:1 beam:1

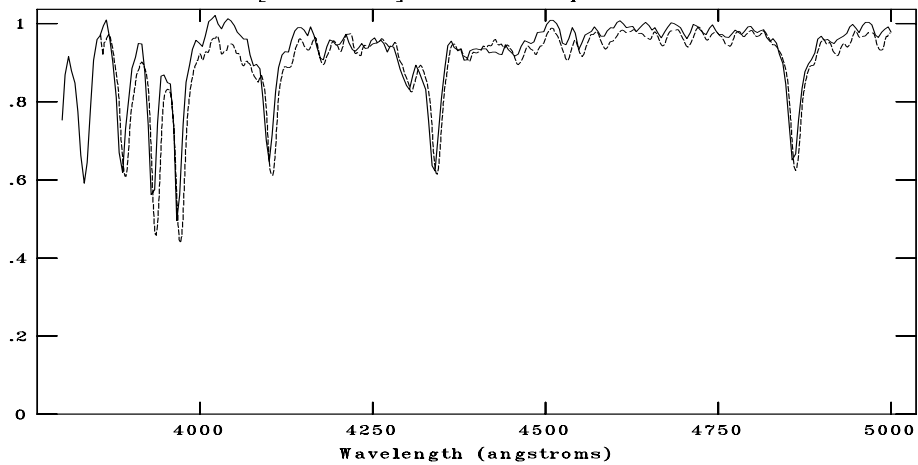
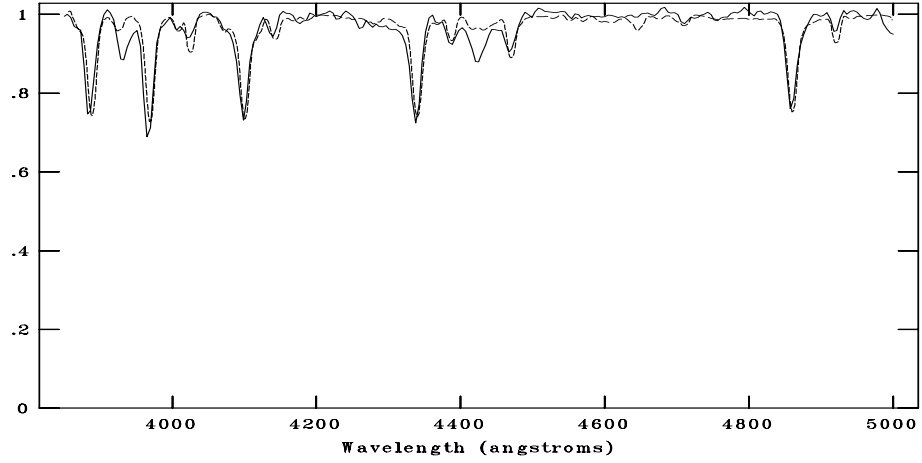
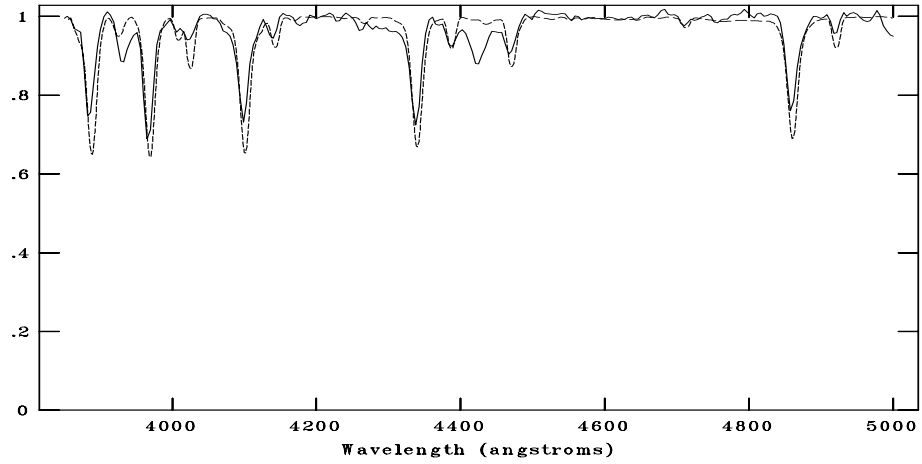


Figure C.90: CAFOS spectrum of 772-009483 compared with F0V, F2V, F3V respectively. The standard spectra are shown with dotted line. The spectral type is assigned as F2V.

NOAO/IRAF V2.16.1 baha@baha-Lenovo-IdeaPad-Y550 Thu 02:25:22 08-Dec-2016
[cg126_01B0.fits]: G126_1 960. ap:1 beam:1



NOAO/IRAF V2.16.1 baha@baha-Lenovo-IdeaPad-Y550 Thu 02:26:16 08-Dec-2016
[cg126_01B0.fits]: G126_1 960. ap:1 beam:1



NOAO/IRAF V2.16.1 baha@baha-Lenovo-IdeaPad-Y550 Thu 02:25:01 08-Dec-2016
[cg126_01B0.fits]: G126_1 960. ap:1 beam:1

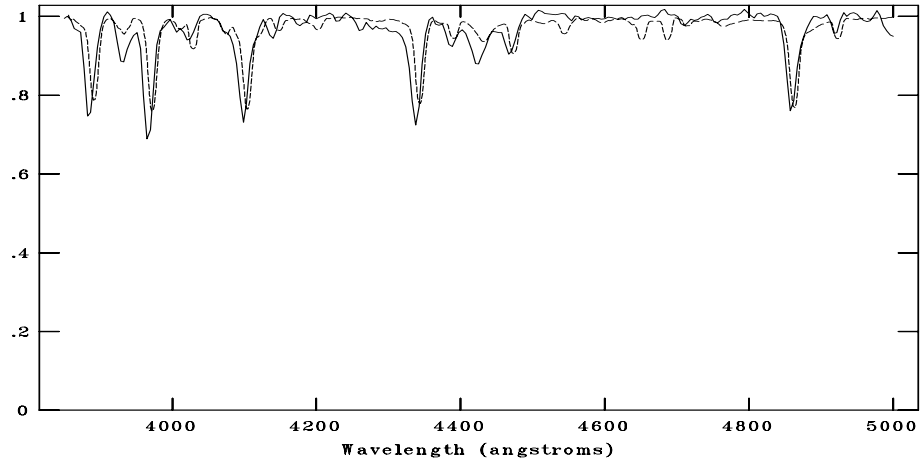
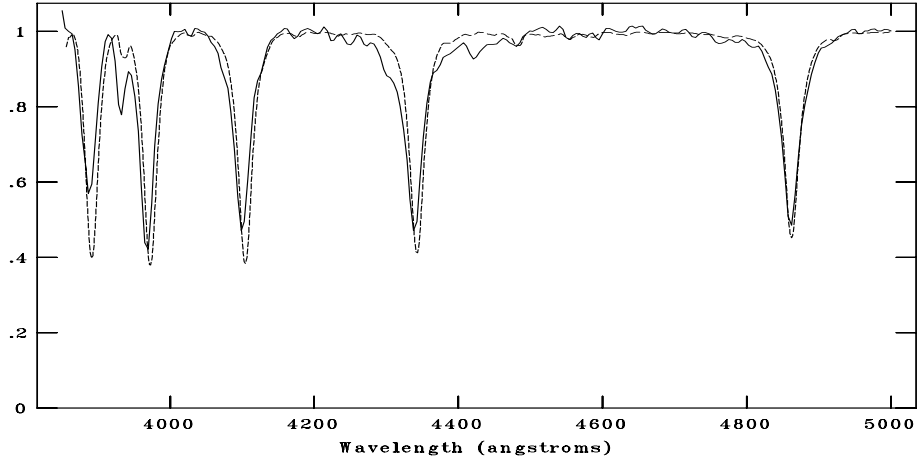
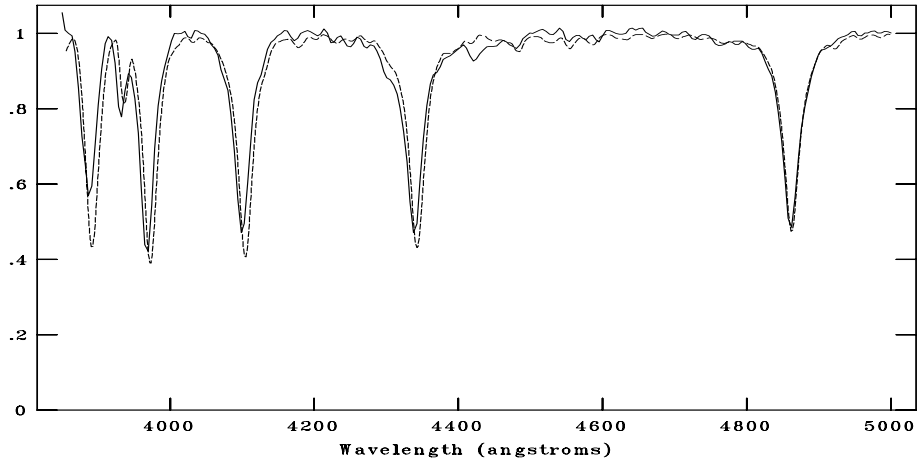


Figure C.91: CAFOS spectrum of 772-009467 compared with B1V, B2V, O9V respectively. The standard spectra are shown with dotted line. The spectral type is assigned as B1V.

NOAO/IRAF V2.16.1 baha@baha-Lenovo-IdeaPad-Y550 Thu 02:27:21 08-Dec-2016
[cg126_02A2.fits]: G126_02 960. ap:1 beam:1



NOAO/IRAF V2.16.1 baha@baha-Lenovo-IdeaPad-Y550 Thu 02:27:37 08-Dec-2016
[cg126_02A2.fits]: G126_02 960. ap:1 beam:1



NOAO/IRAF V2.16.1 baha@baha-Lenovo-IdeaPad-Y550 Thu 02:27:51 08-Dec-2016
[cg126_02A2.fits]: G126_02 960. ap:1 beam:1

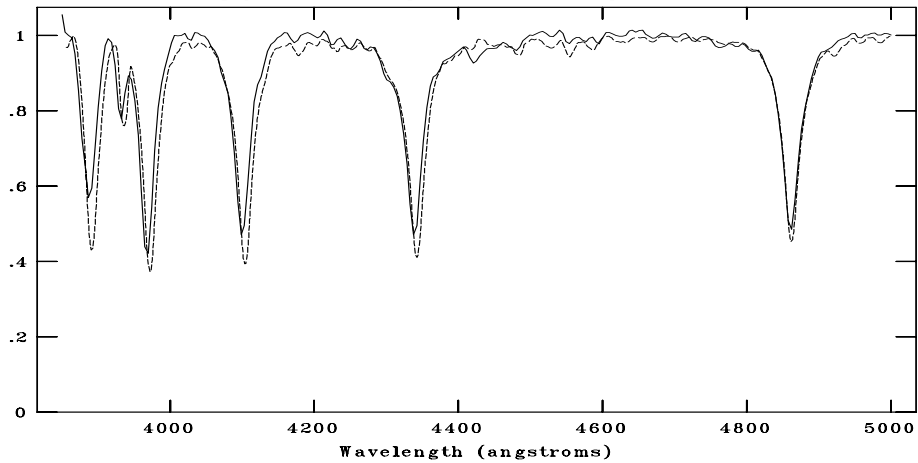
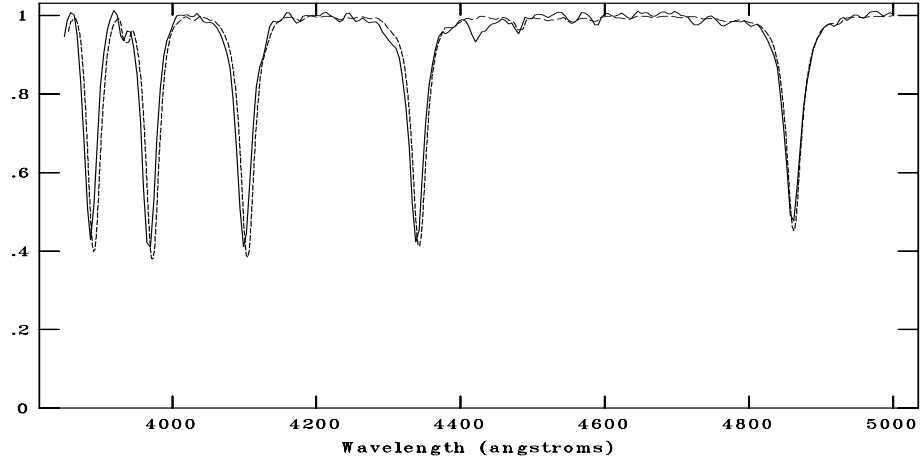
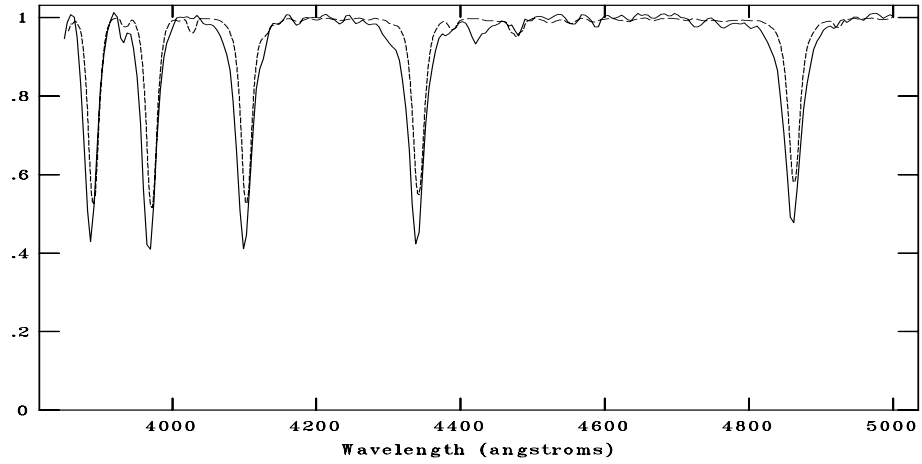


Figure C.92: CAFOS spectrum of 771-009610 compared with A0V, A1V, A3V respectively. The standard spectra are shown with dotted line. The spectral type is assigned as A2V.

NOAO/IRAF V2.16.1 baha@baha-Lenovo-IdeaPad-Y550 Thu 02:29:05 08-Dec-2016
[cg126_03B9.fits]: G126_3 240. ap:1 beam:1



NOAO/IRAF V2.16.1 baha@baha-Lenovo-IdeaPad-Y550 Thu 02:28:44 08-Dec-2016
[cg126_03B9.fits]: G126_3 240. ap:1 beam:1



NOAO/IRAF V2.16.1 baha@baha-Lenovo-IdeaPad-Y550 Thu 02:28:56 08-Dec-2016
[cg126_03B9.fits]: G126_3 240. ap:1 beam:1

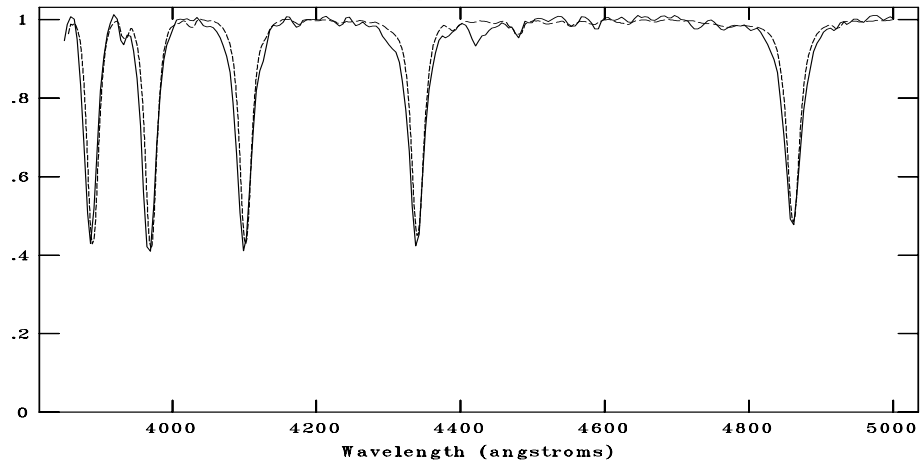
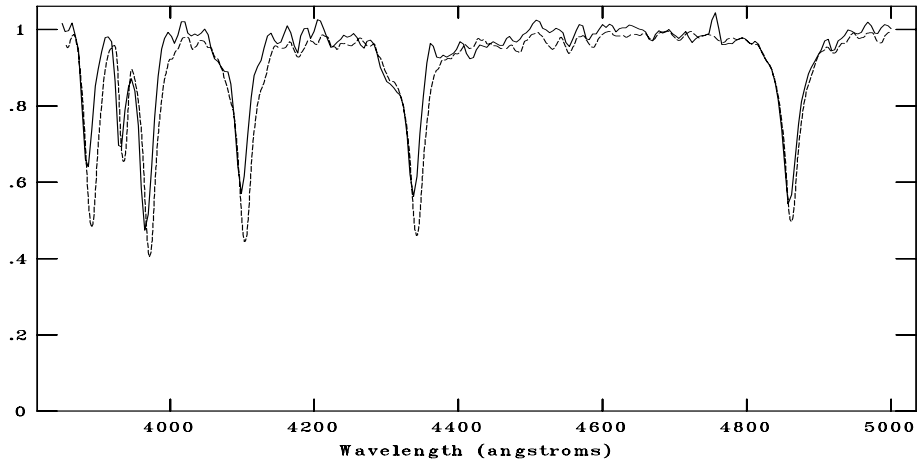
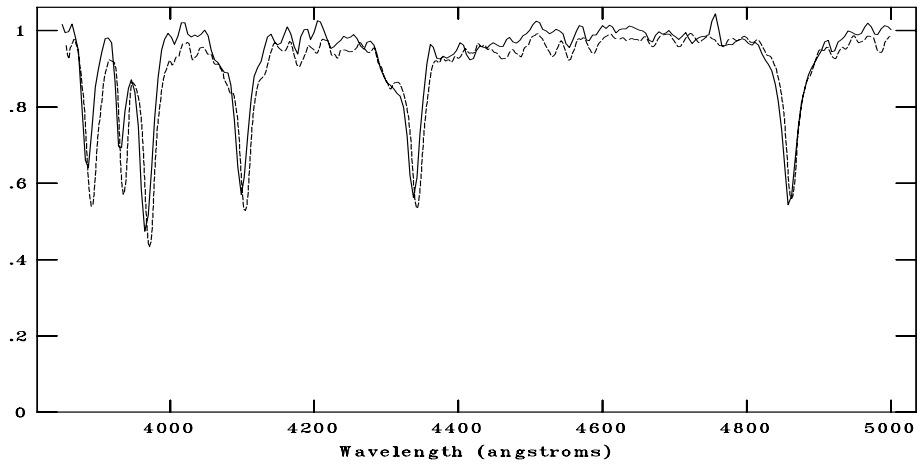


Figure C.93: CAFOS spectrum of 772-009227 compared with A0V, B8V, B9V respectively. The standard spectra are shown with dotted line. The spectral type is assigned as B9V.

NOAO/IRAF V2.16.1 baha@baha-Lenovo-IdeaPad-Y550 Thu 02:31:03 08-Dec-2016
[cg126_4A5.fits]: G126_4 720. ap:1 beam:1



NOAO/IRAF V2.16.1 baha@baha-Lenovo-IdeaPad-Y550 Thu 02:30:44 08-Dec-2016
[cg126_4A5.fits]: G126_4 720. ap:1 beam:1



NOAO/IRAF V2.16.1 baha@baha-Lenovo-IdeaPad-Y550 Thu 02:31:21 08-Dec-2016
[cg126_4A5.fits]: G126_4 720. ap:1 beam:1

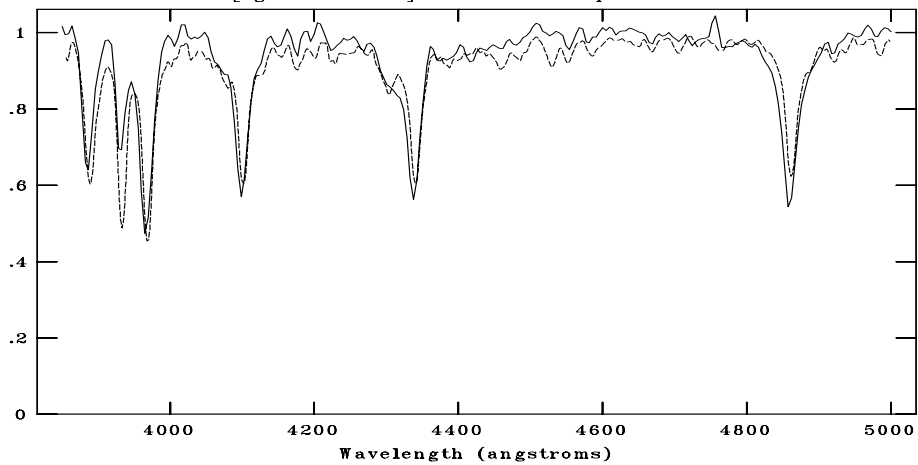
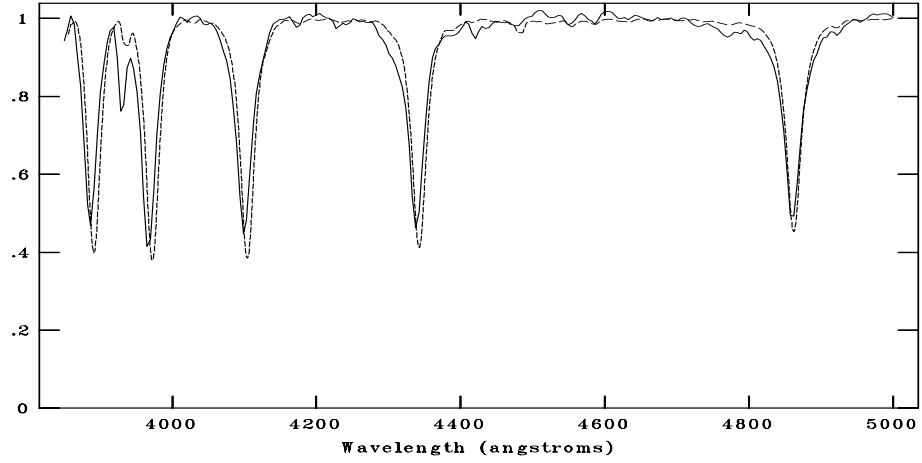
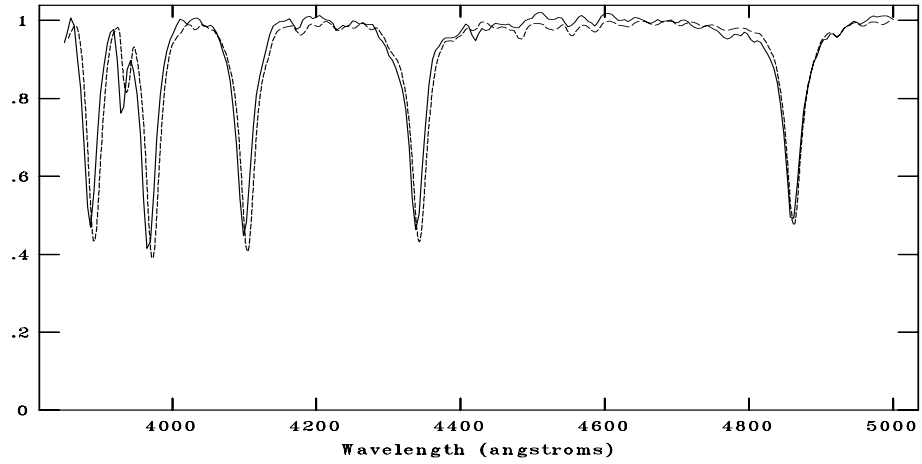


Figure C.94: CAFOS spectrum of 771-009642 compared with A7V, F0V, F2V respectively. The standard spectra are shown with dotted line. The spectral type is assigned as A8V.

NOAO/IRAF V2.16.1 baha@baha-Lenovo-IdeaPad-Y550 Thu 02:33:35 08-Dec-2016
[cg126_11A2.fits]: G126_01 240. ap:1 beam:1



NOAO/IRAF V2.16.1 baha@baha-Lenovo-IdeaPad-Y550 Thu 02:33:00 08-Dec-2016
[cg126_11A2.fits]: G126_01 240. ap:1 beam:1



NOAO/IRAF V2.16.1 baha@baha-Lenovo-IdeaPad-Y550 Thu 02:33:52 08-Dec-2016
[cg126_11A2.fits]: G126_01 240. ap:1 beam:1

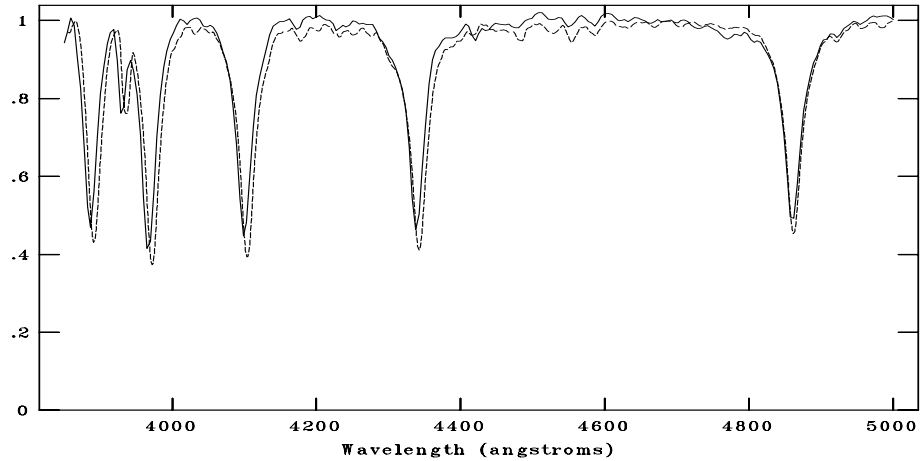
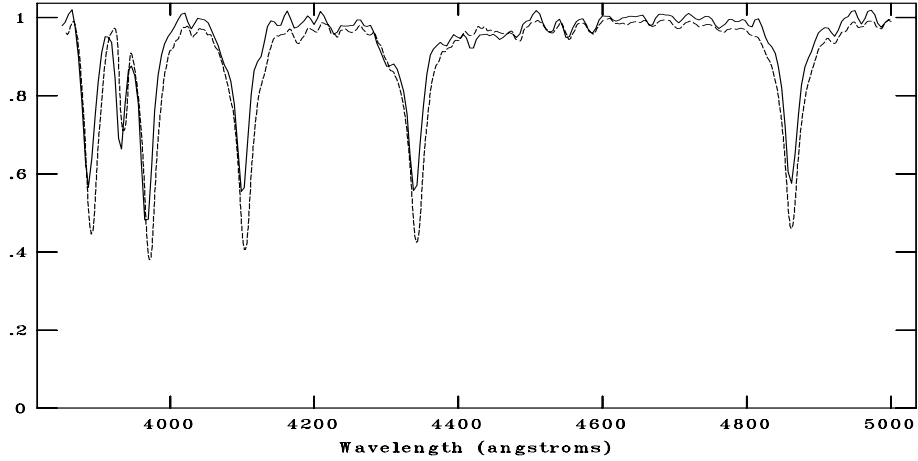
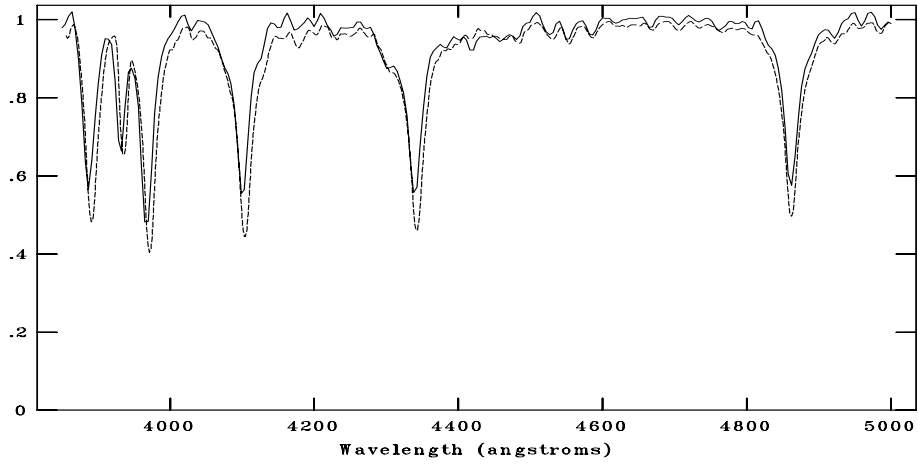


Figure C.95: CAFOS spectrum of 772-009224 compared with A0V, A1V, A3V respectively. The standard spectra are shown with dotted line. The spectral type is assigned as A2V.

NOAO/IRAF V2.16.1 baha@baha-Lenovo-IdeaPad-Y550 Thu 02:35:03 08-Dec-2016
[cg126_12A5.fits]: G126_02 240. ap:1 beam:1



NOAO/IRAF V2.16.1 baha@baha-Lenovo-IdeaPad-Y550 Thu 02:35:28 08-Dec-2016
[cg126_12A5.fits]: G126_02 240. ap:1 beam:1



NOAO/IRAF V2.16.1 baha@baha-Lenovo-IdeaPad-Y550 Thu 02:36:03 08-Dec-2016
[cg126_12A5.fits]: G126_02 240. ap:1 beam:1

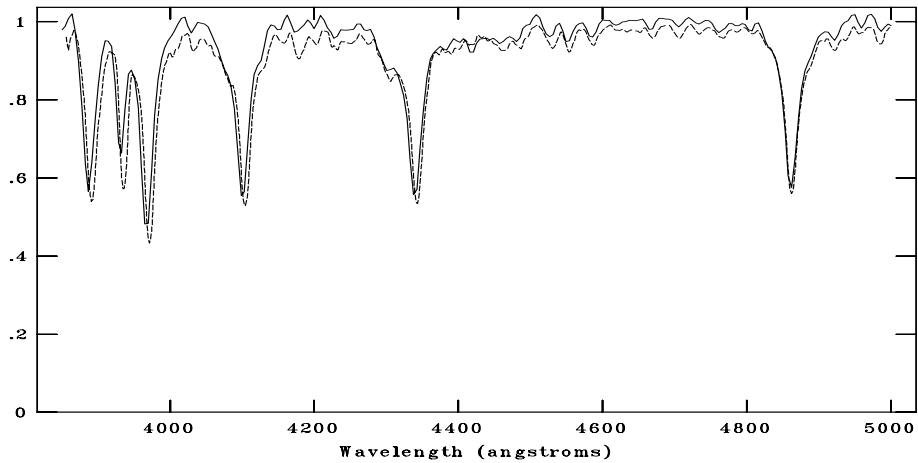
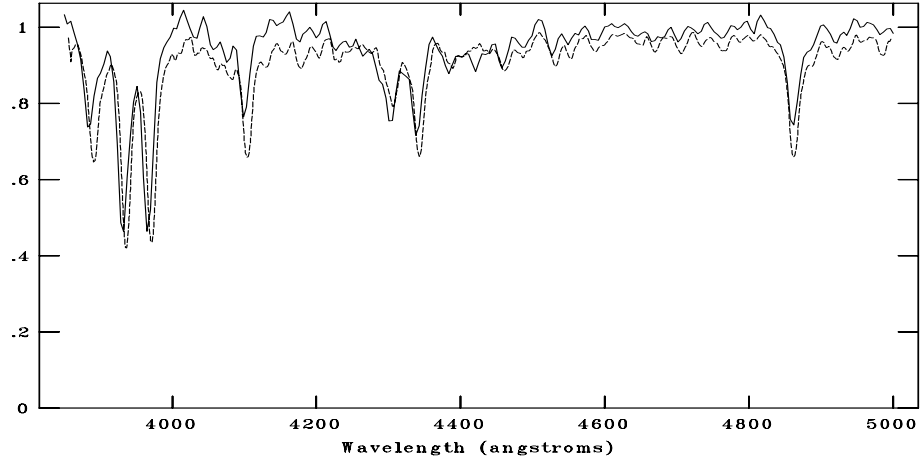
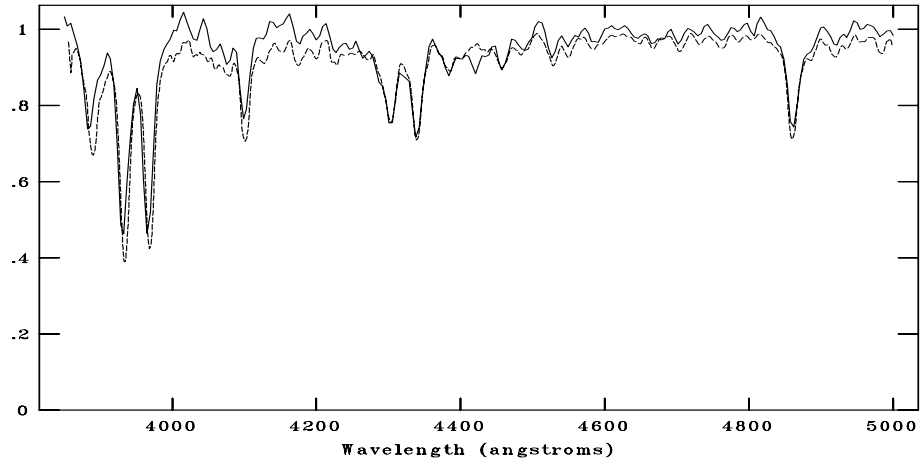


Figure C.96: CAFOS spectrum of 772-009499 compared with A5V, A7V, F0V respectively. The standard spectra are shown with dotted line. The spectral type is assigned as A8V.

NOAO/IRAF V2.16.1 baha@baha-Lenovo-IdeaPad-Y550 Thu 02:39:00 08-Dec-2016
[cg126_13G0.fits]: G126_03 900. ap:1 beam:1



NOAO/IRAF V2.16.1 baha@baha-Lenovo-IdeaPad-Y550 Thu 02:38:32 08-Dec-2016
[cg126_13G0.fits]: G126_03 900. ap:1 beam:1



NOAO/IRAF V2.16.1 baha@baha-Lenovo-IdeaPad-Y550 Thu 02:38:08 08-Dec-2016
[cg126_13G0.fits]: G126_03 900. ap:1 beam:1

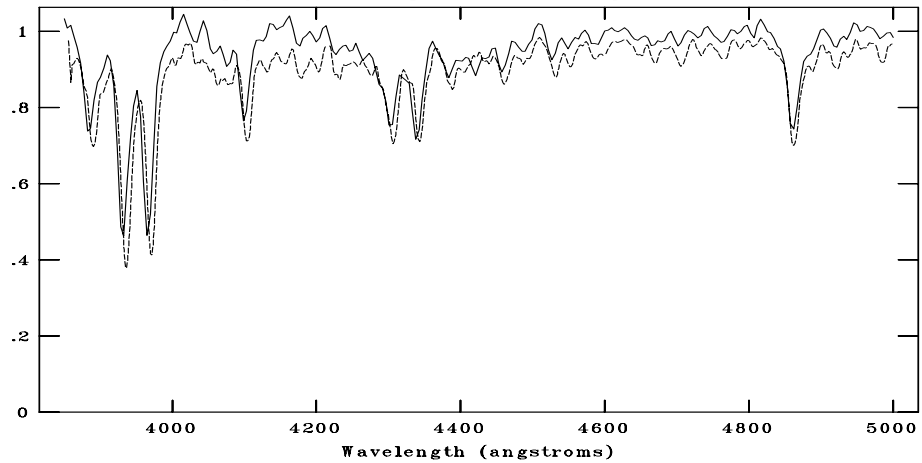
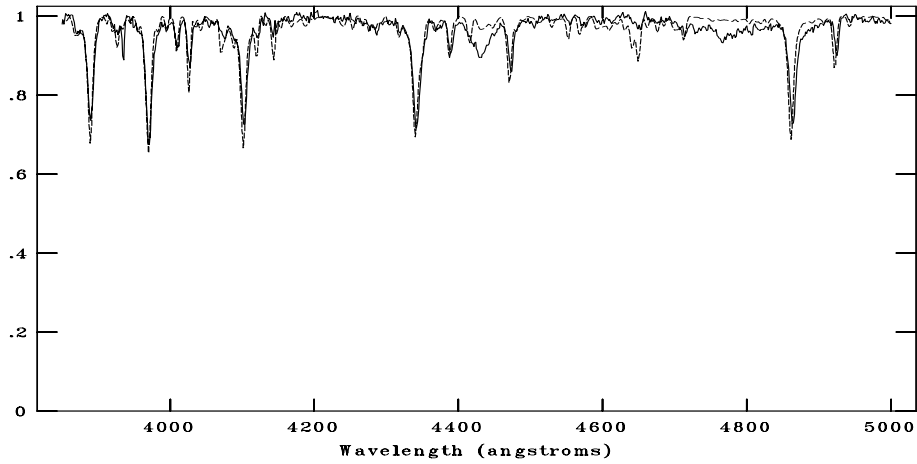
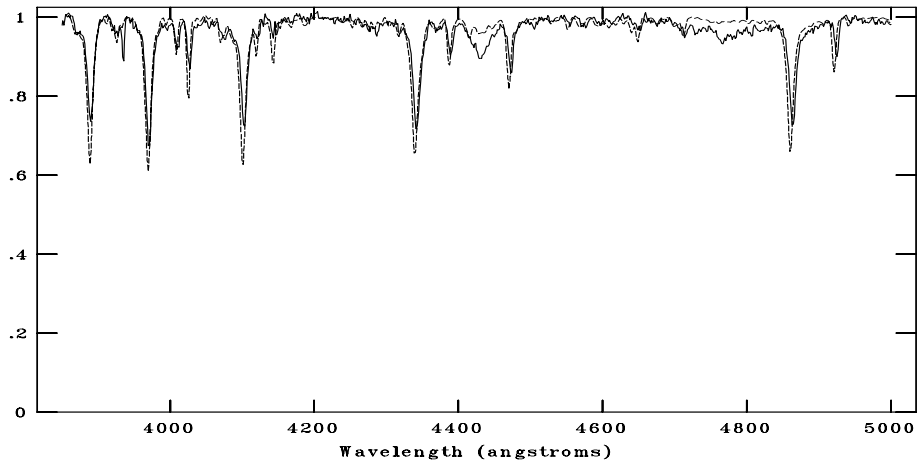


Figure C.97: CAFOS spectrum of 772-009451 compared with F5V, F6V, F8V respectively. The standard spectra are shown with dotted line. The spectral type is assigned as F7V.

NOAO/IRAF V2.16.1 baha@baha-Lenovo-IdeaPad-Y550 Wed 00:11:55 04-Jan-2017
[g126n.fits]: g126_1 1800. ap:1 beam:1



NOAO/IRAF V2.16.1 baha@baha-Lenovo-IdeaPad-Y550 Wed 00:09:49 04-Jan-2017
[g126n.fits]: g126_1 1800. ap:1 beam:1



NOAO/IRAF V2.16.1 baha@baha-Lenovo-IdeaPad-Y550 Wed 00:10:39 04-Jan-2017
[g126n.fits]: g126_1 1800. ap:1 beam:1

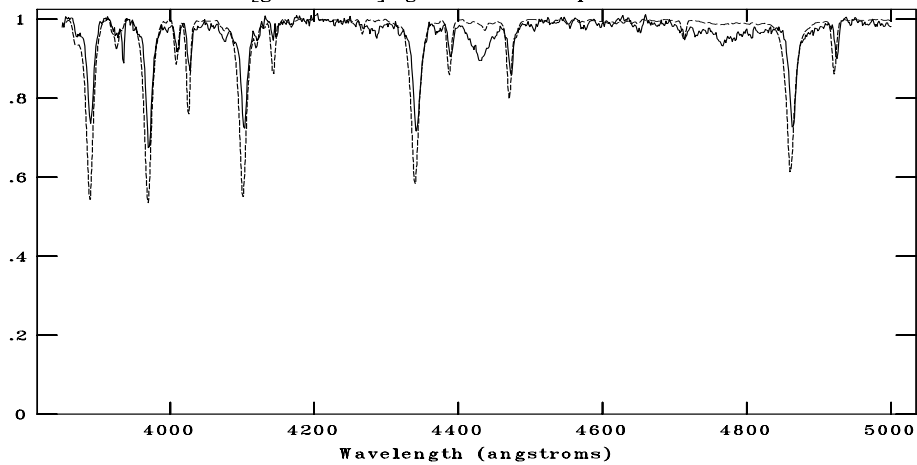


Figure C.98: TFOSC spectrum of 772-009430 compared with B0.5III, B1V, B2V respectively. The standard spectra are shown with dotted line. The spectral type is assigned as B1V.

C.10 G127.1+0.5

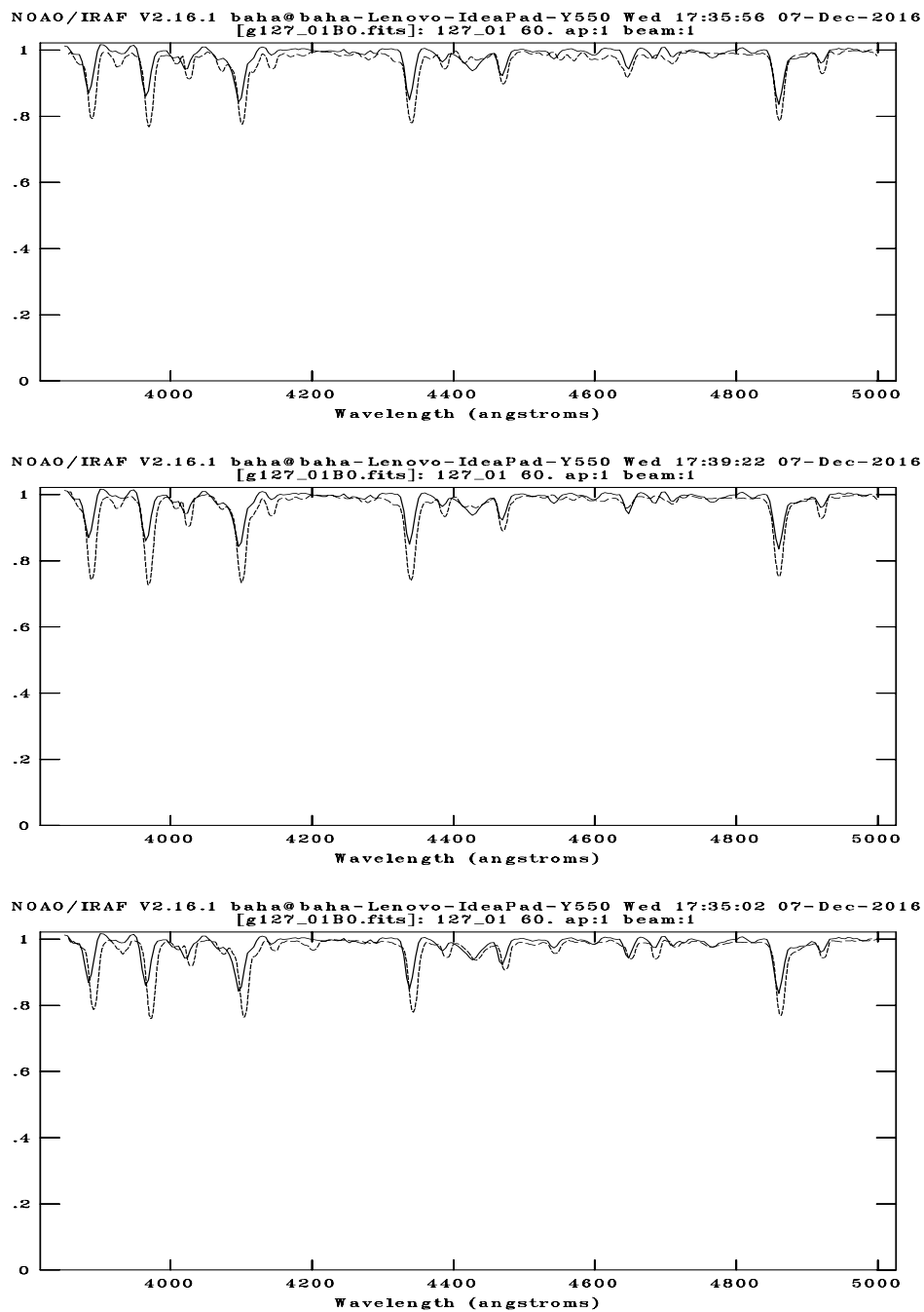
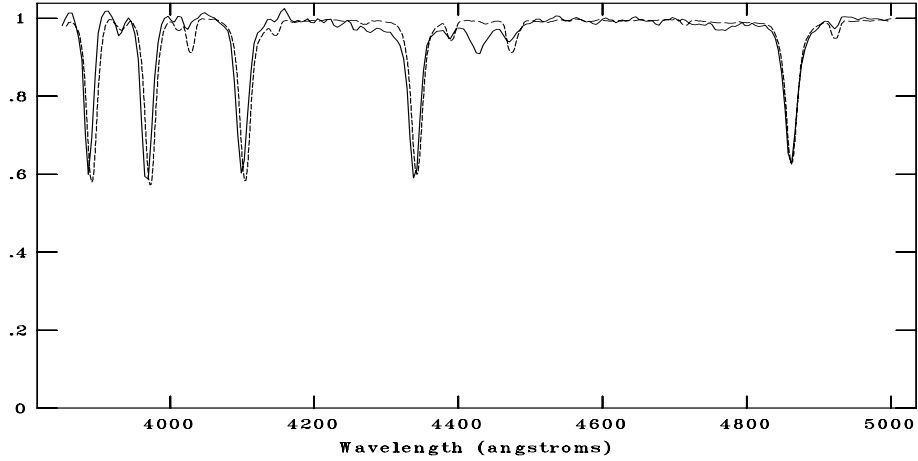
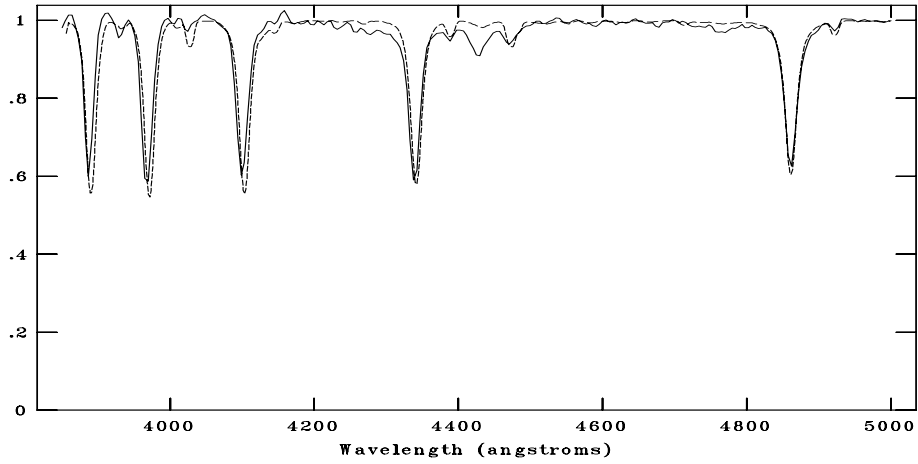


Figure C.99: CAFOS spectrum of 767-013562 compared with B0.5III, B1V, O9V respectively. The standard spectra are shown with dotted line. The spectral type is assigned as B0V.

NOAO/IRAF V2.16.1 baha@baha-Lenovo-IdeaPad-Y550 Thu 02:39:30 08-Dec-2016
[cg127_01B7.fits]: G127_1 240. ap:1 beam:1



NOAO/IRAF V2.16.1 baha@baha-Lenovo-IdeaPad-Y550 Thu 02:39:56 08-Dec-2016
[cg127_01B7.fits]: G127_1 240. ap:1 beam:1



NOAO/IRAF V2.16.1 baha@baha-Lenovo-IdeaPad-Y550 Thu 02:40:26 08-Dec-2016
[cg127_01B7.fits]: G127_1 240. ap:1 beam:1

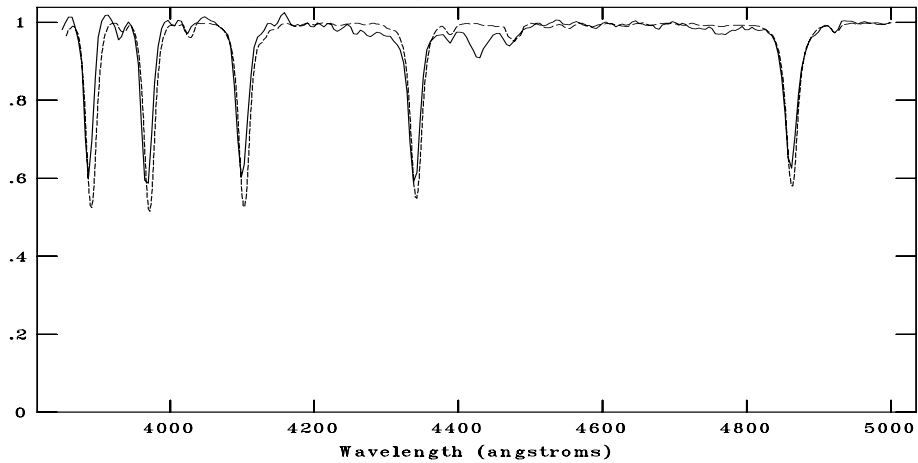
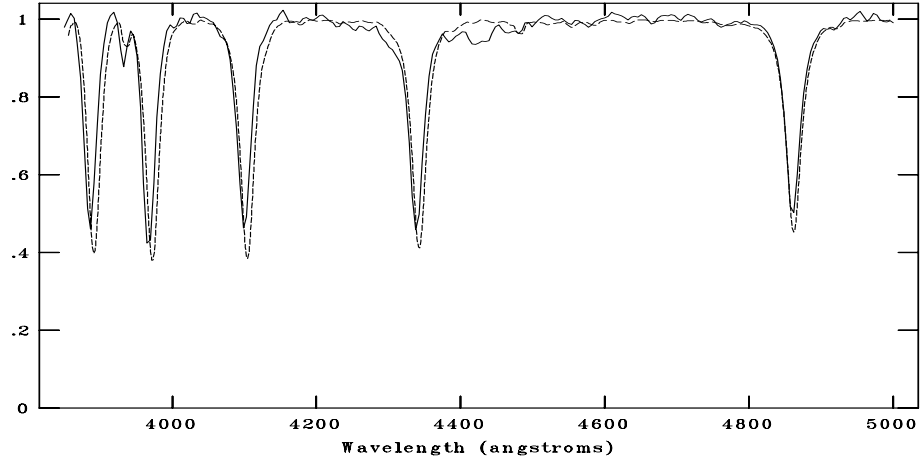
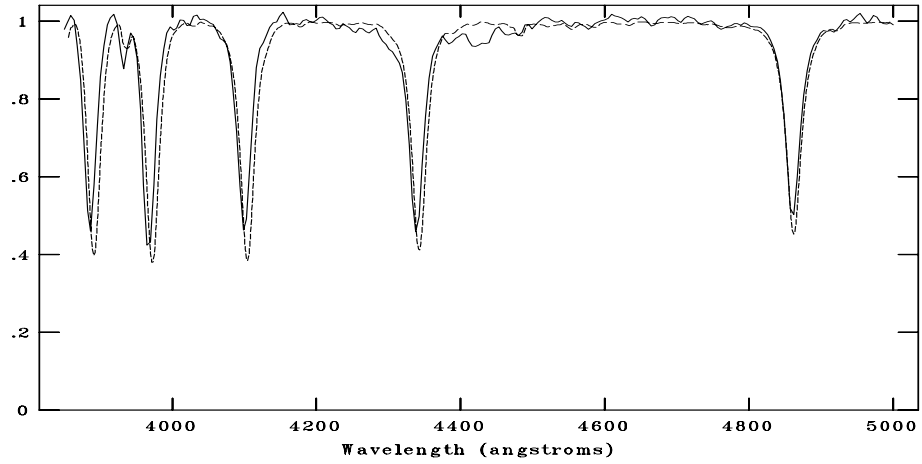


Figure C.100: CAFOS spectrum of 766-013622 compared with B5V, B7V, B8V respectively. The standard spectra are shown with dotted line. The spectral type is assigned as B7V.

NOAO/IRAF V2.16.1 baha@baha-Lenovo-IdeaPad-Y550 Thu 02:40:45 08-Dec-2016
[cg127_02A1.fits]: G127_2 300. ap:1 beam:1



NOAO/IRAF V2.16.1 baha@baha-Lenovo-IdeaPad-Y550 Thu 02:40:58 08-Dec-2016
[cg127_02A1.fits]: G127_2 300. ap:1 beam:1



NOAO/IRAF V2.16.1 baha@baha-Lenovo-IdeaPad-Y550 Thu 02:41:08 08-Dec-2016
[cg127_02A1.fits]: G127_2 300. ap:1 beam:1

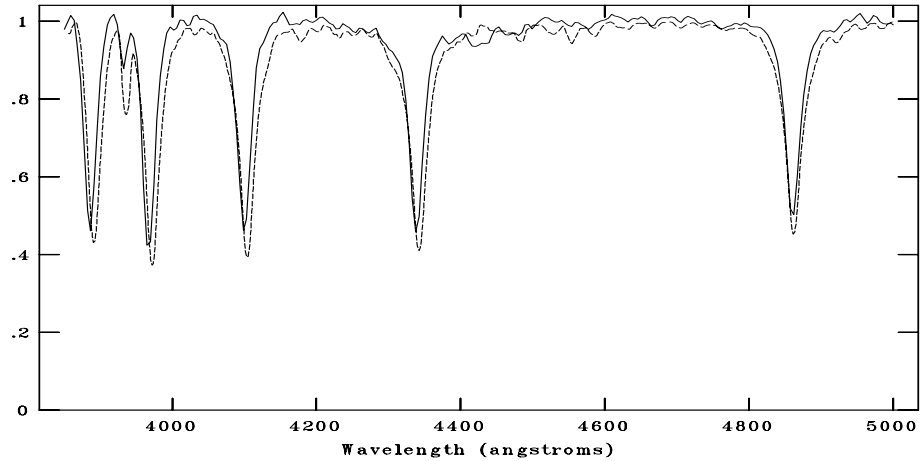
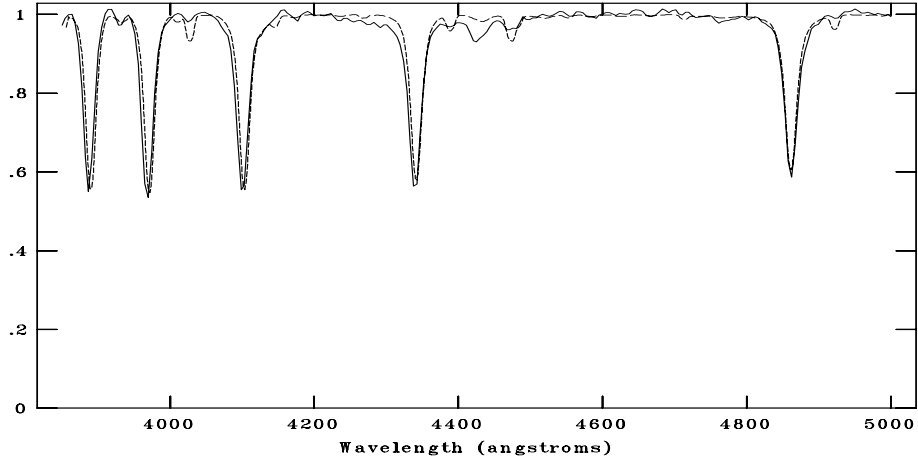
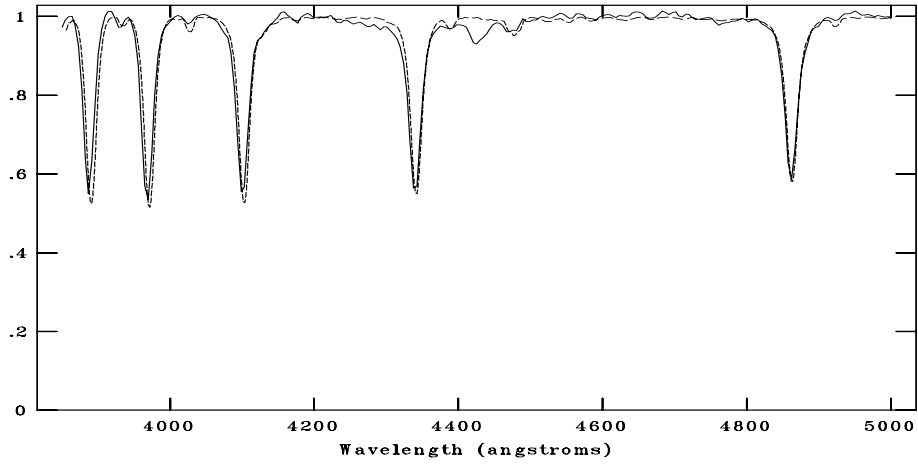


Figure C.101: CAFOS spectrum of 766-013684 compared with A0V, A1V, A3V respectively. The standard spectra are shown with dotted line. The spectral type is assigned as A1V.

NOAO/IRAF V2.16.1 baha@baha-Lenovo-IdeaPad-Y550 Thu 02:41:50 08-Dec-2016
[cg127_11B8.fits]: G127_01 240. ap:1 beam:1



NOAO/IRAF V2.16.1 baha@baha-Lenovo-IdeaPad-Y550 Thu 02:42:22 08-Dec-2016
[cg127_11B8.fits]: G127_01 240. ap:1 beam:1



NOAO/IRAF V2.16.1 baha@baha-Lenovo-IdeaPad-Y550 Thu 02:43:31 08-Dec-2016
[cg127_11B8.fits]: G127_01 240. ap:1 beam:1

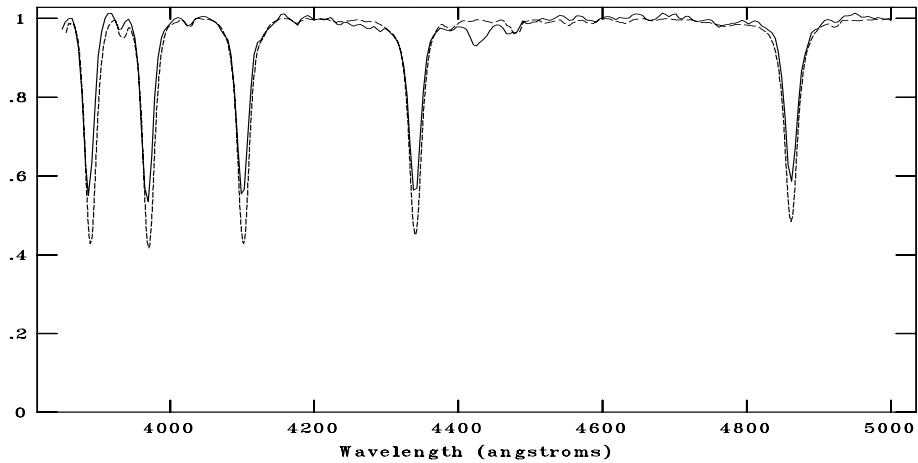
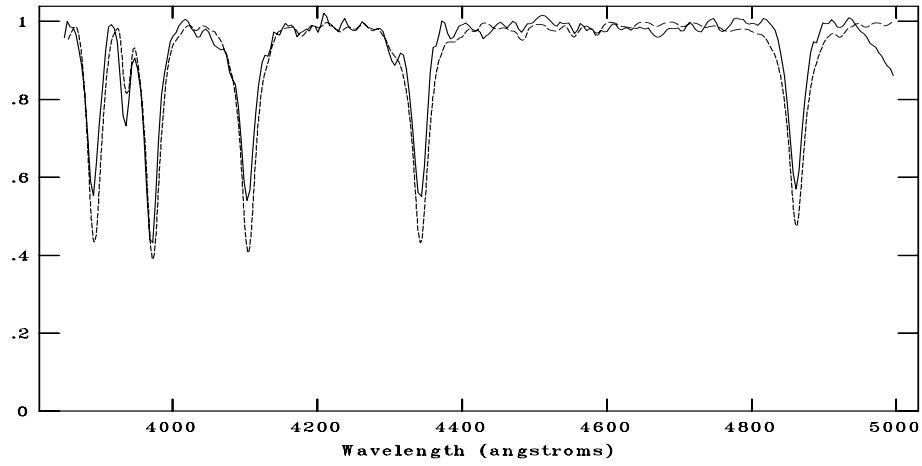
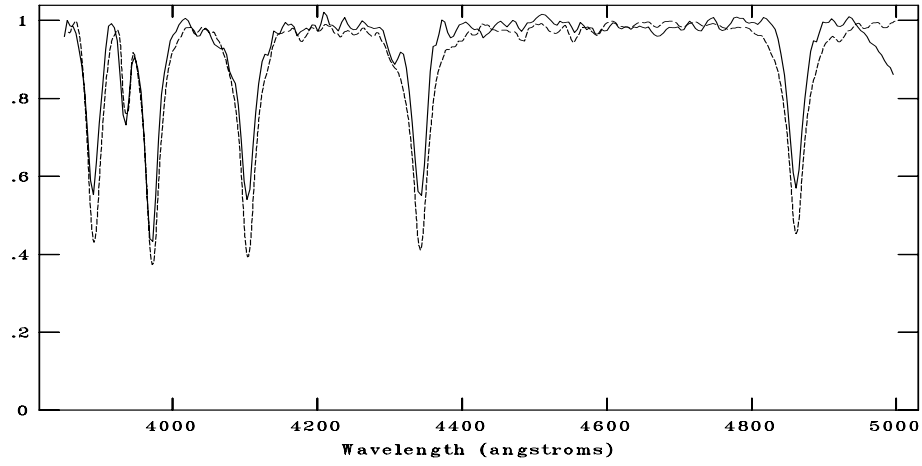


Figure C.102: CAFOS spectrum of 767-013623 compared with B7V, B8V, B9V respectively. The standard spectra are shown with dotted line. The spectral type is assigned as B8V.

NOAO/IRAF V2.16.1 baha@baha-Lenovo-IdeaPad-Y550 Thu 17:12:14 08-Dec-2016
[G127_01n.fits]: G127_01 1200. ap:1 beam:1



NOAO/IRAF V2.16.1 baha@baha-Lenovo-IdeaPad-Y550 Thu 17:13:32 08-Dec-2016
[G127_01n.fits]: G127_01 1200. ap:1 beam:1



NOAO/IRAF V2.16.1 baha@baha-Lenovo-IdeaPad-Y550 Thu 17:16:22 08-Dec-2016
[G127_01n.fits]: G127_01 1200. ap:1 beam:1

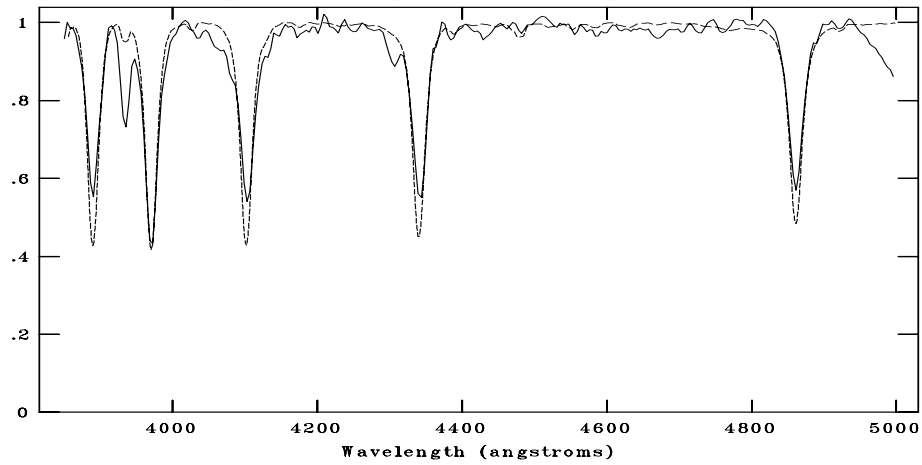
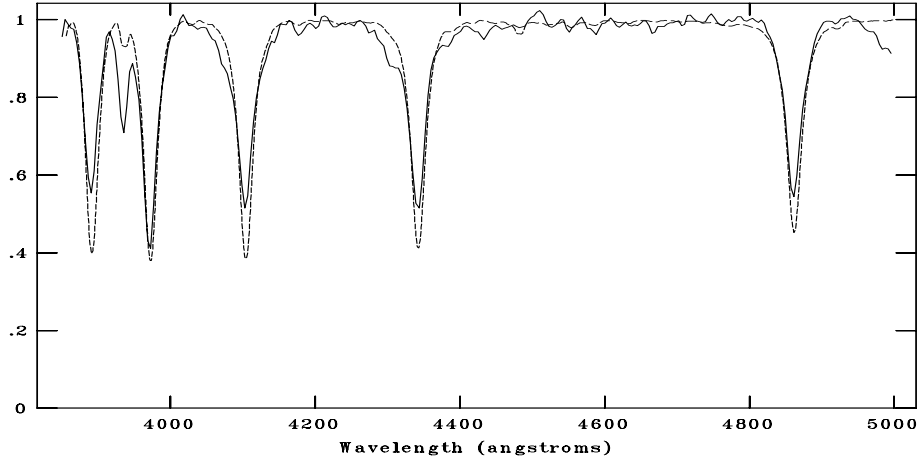
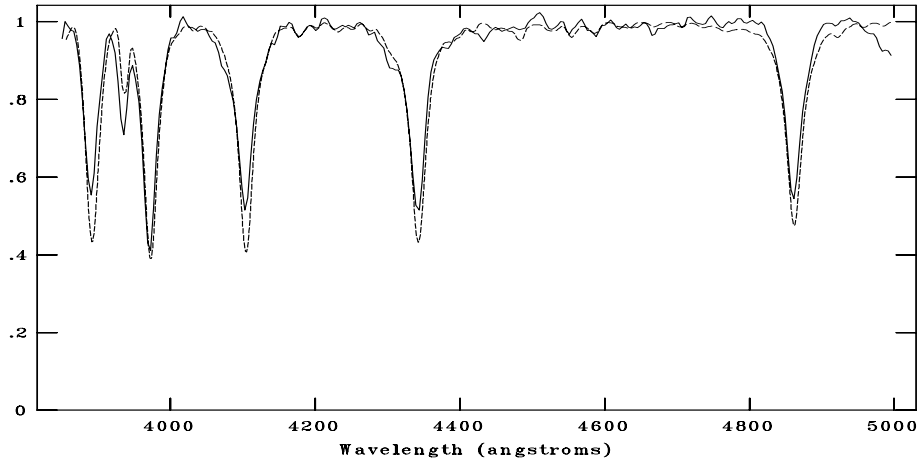


Figure C.103: CAFOS spectrum of 767-013673 compared with A1V, A3V, B9V respectively. The standard spectra are shown with dotted line. The spectral type is assigned as A1V.

NOAO/IRAF V2.16.1 baha@baha-Lenovo-IdeaPad-Y550 Thu 17:20:45 08-Dec-2016
[G127_02n.fits]: G127_02 1200. ap:1 beam:1



NOAO/IRAF V2.16.1 baha@baha-Lenovo-IdeaPad-Y550 Thu 17:19:59 08-Dec-2016
[G127_02n.fits]: G127_02 1200. ap:1 beam:1



NOAO/IRAF V2.16.1 baha@baha-Lenovo-IdeaPad-Y550 Thu 17:21:22 08-Dec-2016
[G127_02n.fits]: G127_02 1200. ap:1 beam:1

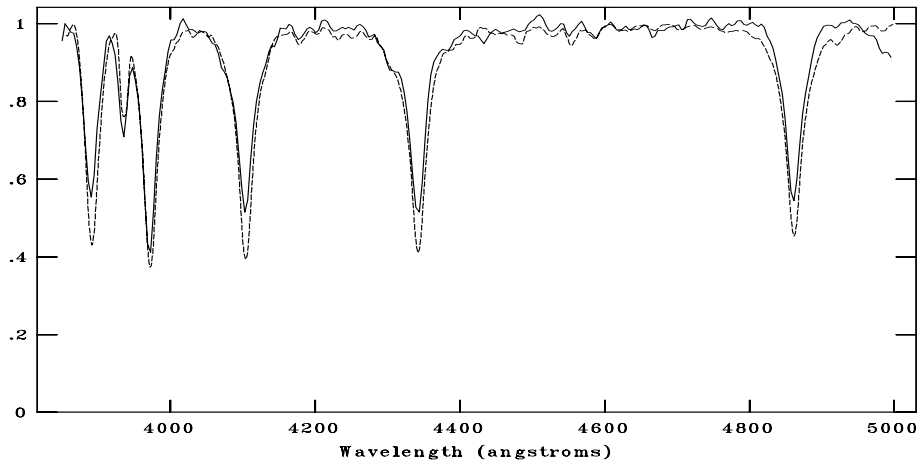
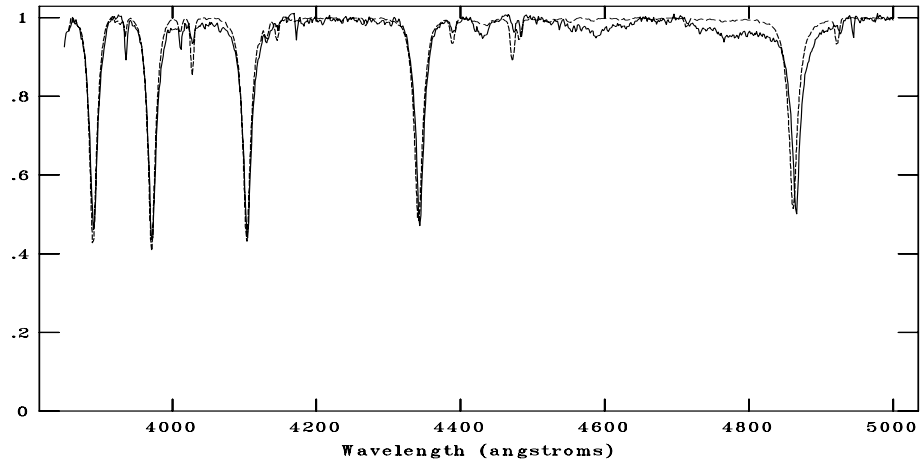
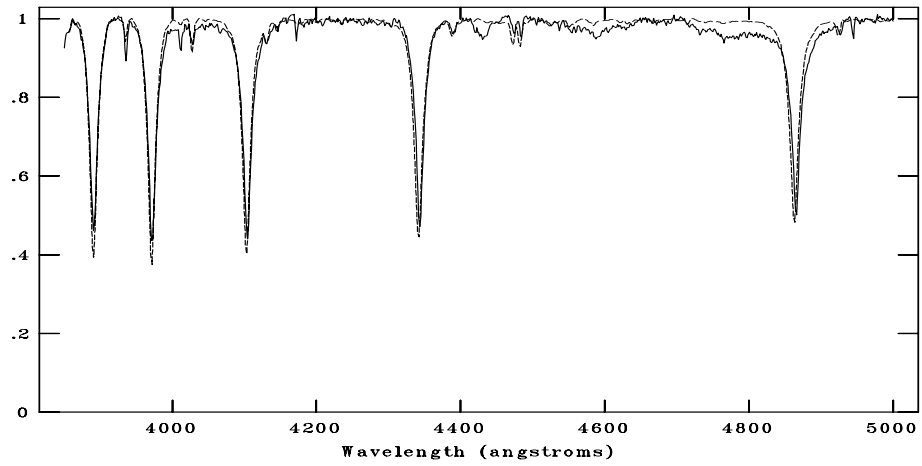


Figure C.104: CAFOS spectrum of 766-013734 compared with A0V, A1V, A3V respectively. The standard spectra are shown with dotted line. The spectral type is assigned as A2V.

NOAO/IRAF V2.16.1 baha@baha-Lenovo-IdeaPad-Y550 Wed 00:16:41 04-Jan-2017
[g127n.fits]: g127_1 750. ap:1 beam:1



NOAO/IRAF V2.16.1 baha@baha-Lenovo-IdeaPad-Y550 Wed 00:14:33 04-Jan-2017
[g127n.fits]: g127_1 750. ap:1 beam:1



NOAO/IRAF V2.16.1 baha@baha-Lenovo-IdeaPad-Y550 Wed 00:18:31 04-Jan-2017
[g127n.fits]: g127_1 750. ap:1 beam:1

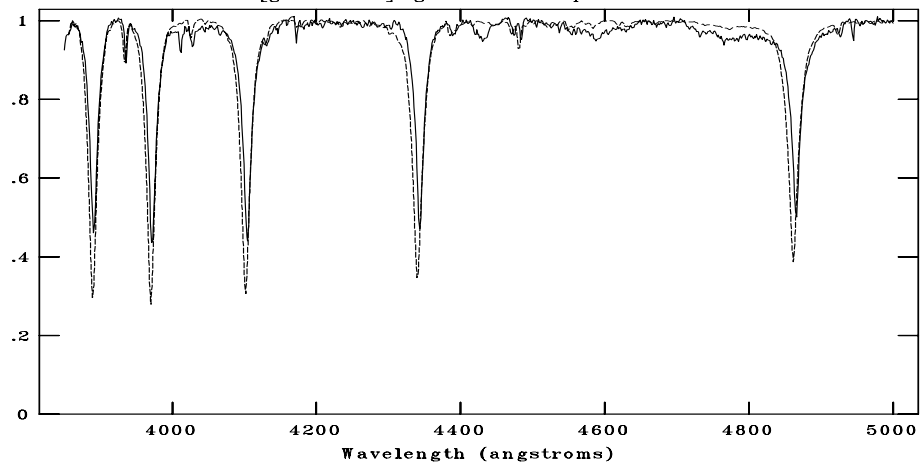


Figure C.105: TFOSC spectrum of 767-013623 compared with B7V, B8V, B9V respectively. The standard spectra are shown with dotted line. The spectral type is assigned as B8V.

C.11 G132.7+1.3

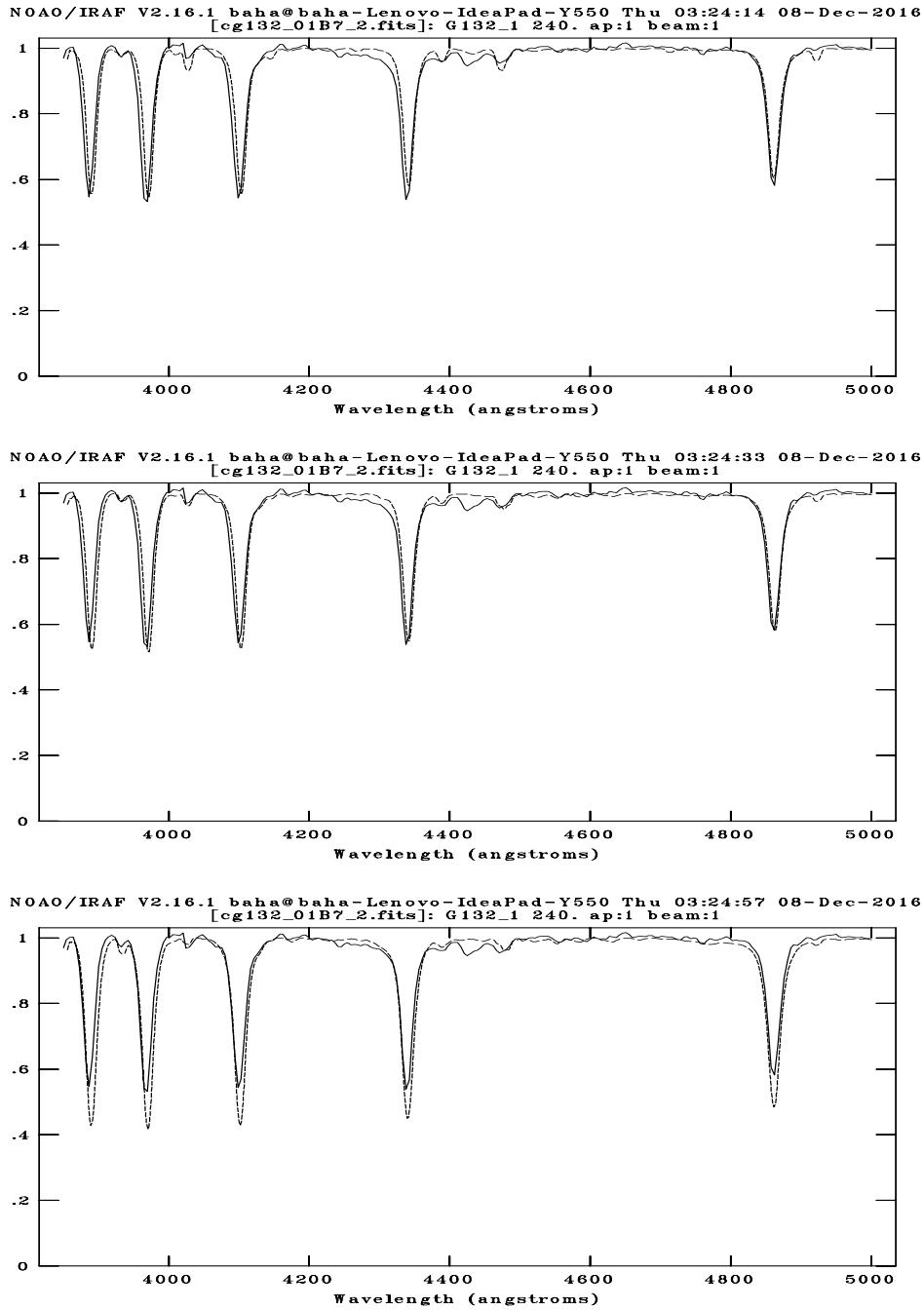
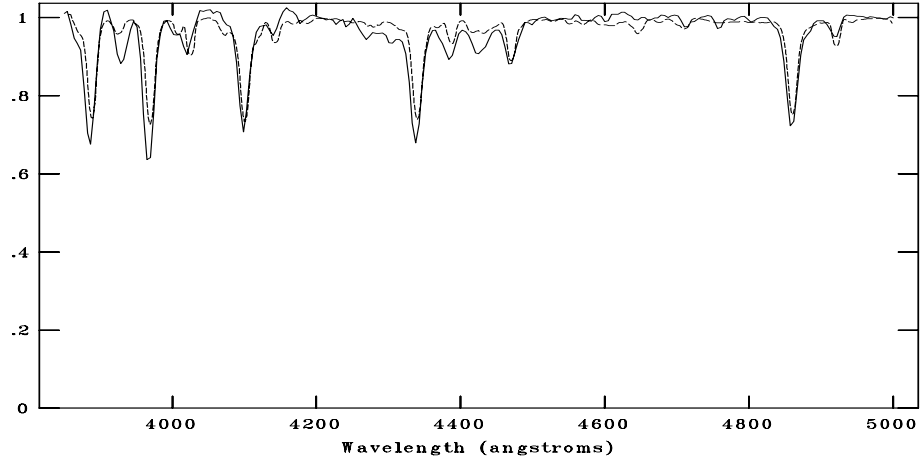
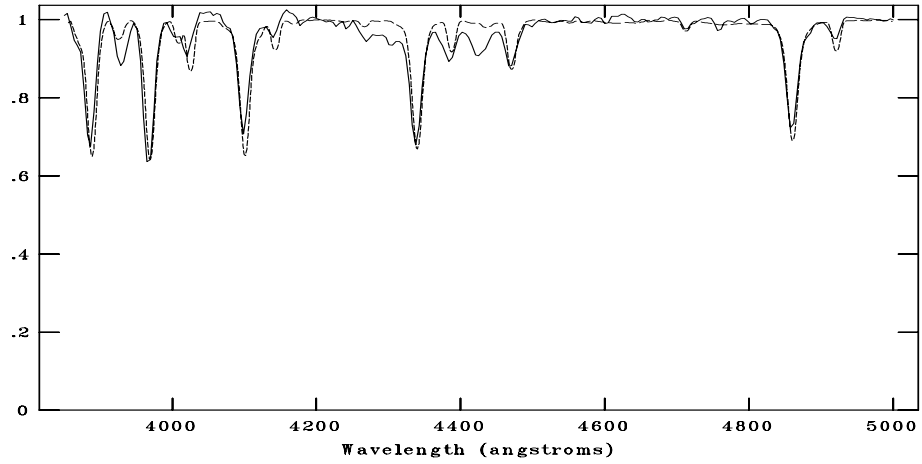


Figure C.106: CAFOS spectrum of 765-021781 compared with B7V, B8V, B9V respectively. The standard spectra are shown with dotted line. The spectral type is assigned as B7V.

NOAO/IRAF V2.16.1 baha@baha-Lenovo-IdeaPad-Y550 Thu 03:27:09 08-Dec-2016
[cg132_02_2B3.fits]: G132_2 600. ap:1 beam:1



NOAO/IRAF V2.16.1 baha@baha-Lenovo-IdeaPad-Y550 Thu 03:26:01 08-Dec-2016
[cg132_02_2B3.fits]: G132_2 600. ap:1 beam:1



NOAO/IRAF V2.16.1 baha@baha-Lenovo-IdeaPad-Y550 Thu 03:26:29 08-Dec-2016
[cg132_02_2B3.fits]: G132_2 600. ap:1 beam:1

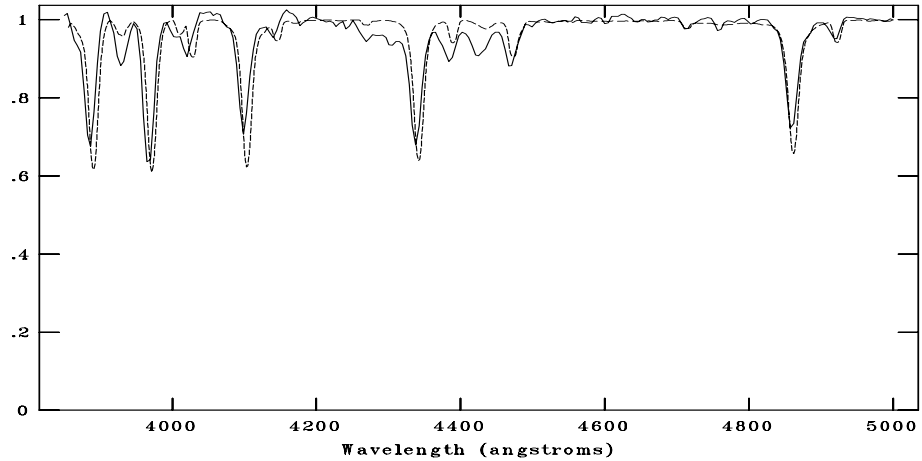
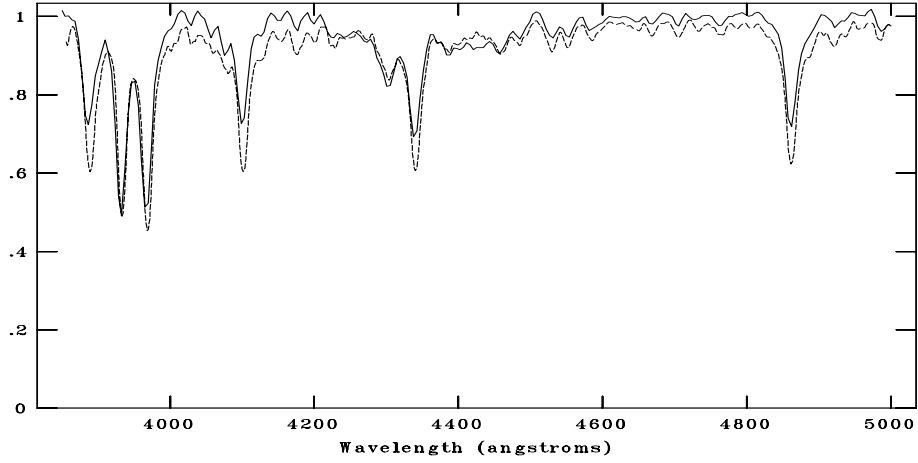
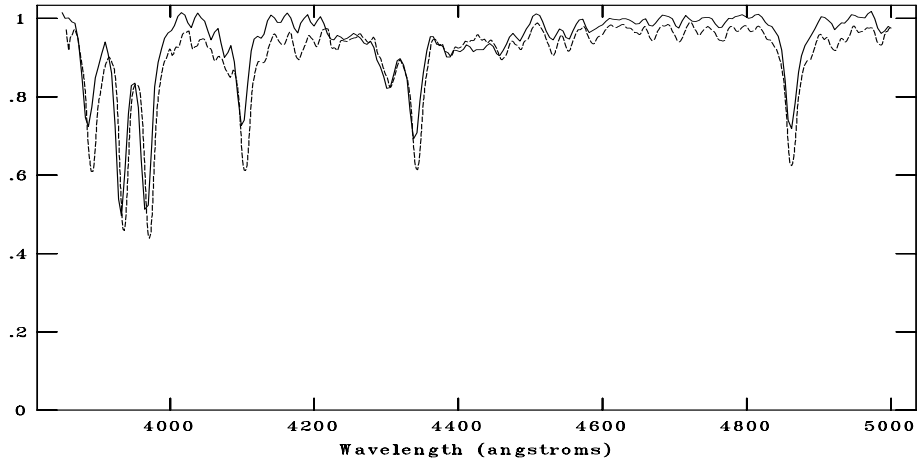


Figure C.107: CAFOS spectrum of 765-021812 compared with B1V, B2V, B3V respectively. The standard spectra are shown with dotted line. The spectral type is assigned as B3V.

NOAO/IRAF V2.16.1 baha@baha-Lenovo-IdeaPad-Y550 Thu 03:28:05 08-Dec-2016
[cg132_03F5.fits]: G132_3 720. ap:1 beam:1



NOAO/IRAF V2.16.1 baha@baha-Lenovo-IdeaPad-Y550 Thu 03:28:33 08-Dec-2016
[cg132_03F5.fits]: G132_3 720. ap:1 beam:1



NOAO/IRAF V2.16.1 baha@baha-Lenovo-IdeaPad-Y550 Thu 03:28:55 08-Dec-2016
[cg132_03F5.fits]: G132_3 720. ap:1 beam:1

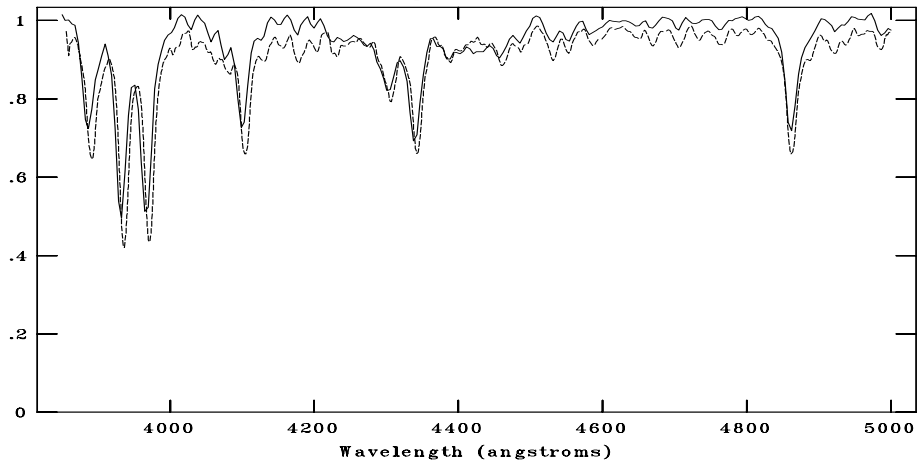
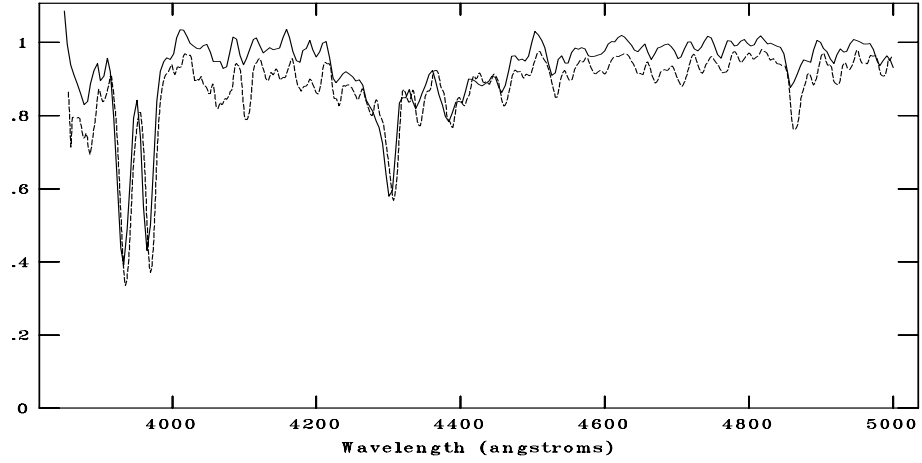
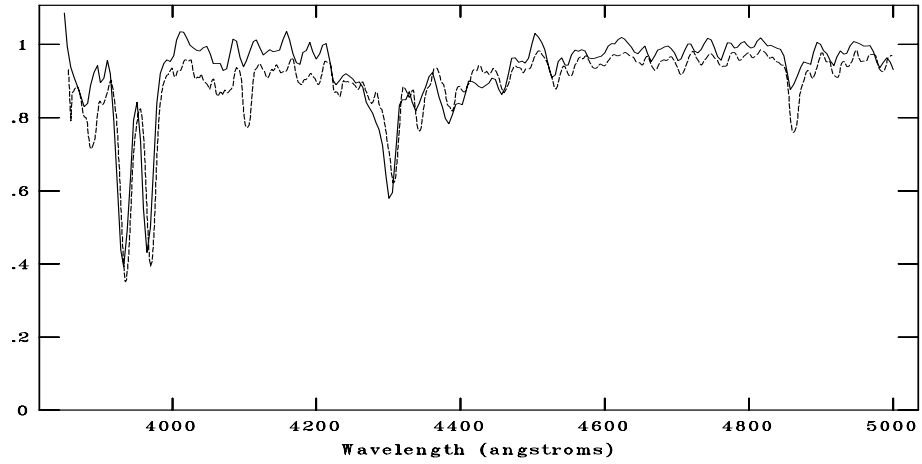


Figure C.108: CAFOS spectrum of 764-021488 compared with F2V, F3V, F5V respectively. The standard spectra are shown with dotted line. The spectral type is assigned as F5V.

NOAO/IRAF V2.16.1 baha@baha-Lenovo-IdeaPad-Y550 Thu 03:41:40 08-Dec-2016
[cg132_04K.fits]: G132_4 1080. ap:1 beam:1



NOAO/IRAF V2.16.1 baha@baha-Lenovo-IdeaPad-Y550 Thu 03:41:58 08-Dec-2016
[cg132_04K.fits]: G132_4 1080. ap:1 beam:1



NOAO/IRAF V2.16.1 baha@baha-Lenovo-IdeaPad-Y550 Thu 03:42:18 08-Dec-2016
[cg132_04K.fits]: G132_4 1080. ap:1 beam:1

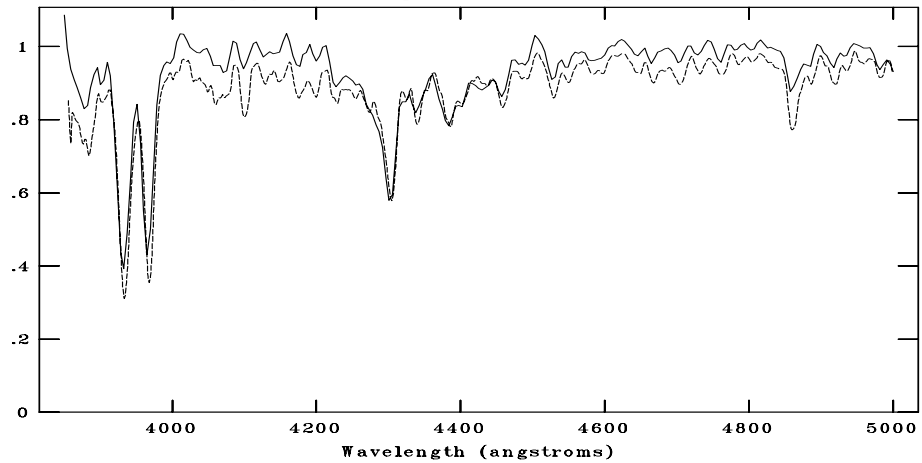
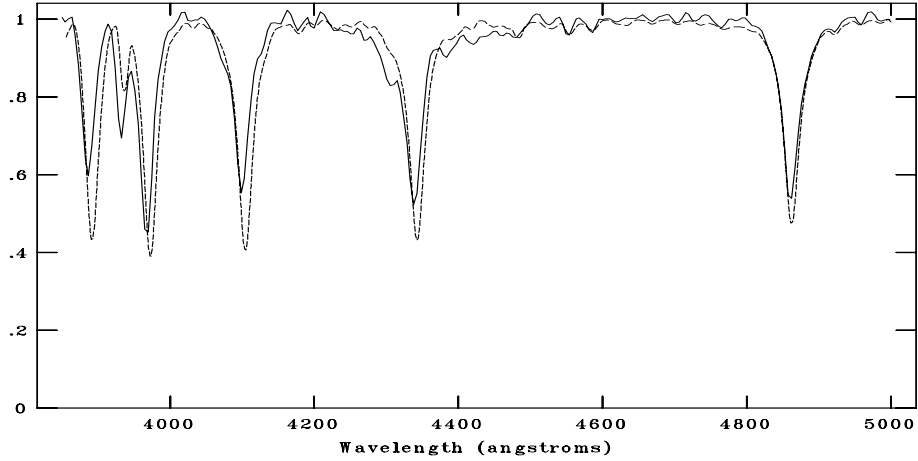
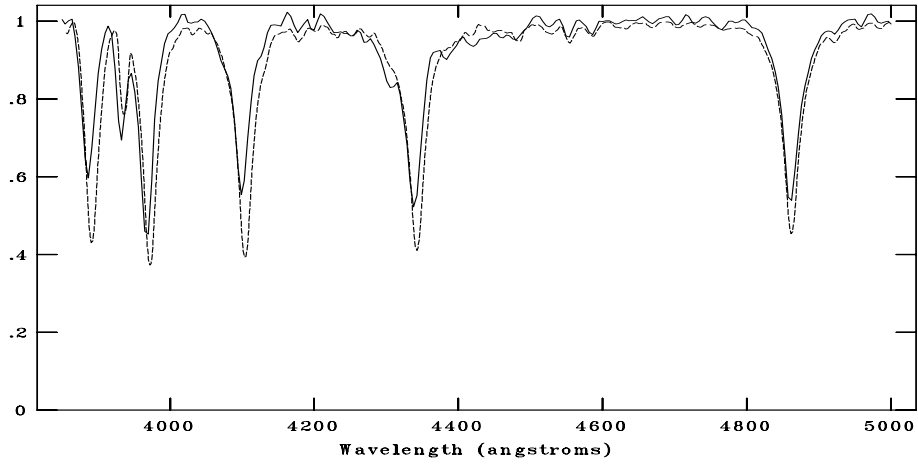


Figure C.109: CAFOS spectrum of 764-021273 compared with G2V, G3V, G5V respectively. The standard spectra are shown with dotted line. The spectral type is assigned as G5V.

NOAO/IRAF V2.16.1 baha@baha-Lenovo-IdeaPad-Y550 Thu 03:42:38 08-Dec-2016
[cg13205_05A5.fits]: G132_5 1380. ap:1 beam:1



NOAO/IRAF V2.16.1 baha@baha-Lenovo-IdeaPad-Y550 Thu 03:44:19 08-Dec-2016
[cg13205_05A5.fits]: G132_5 1380. ap:1 beam:1



NOAO/IRAF V2.16.1 baha@baha-Lenovo-IdeaPad-Y550 Thu 03:44:48 08-Dec-2016
[cg13205_05A5.fits]: G132_5 1380. ap:1 beam:1

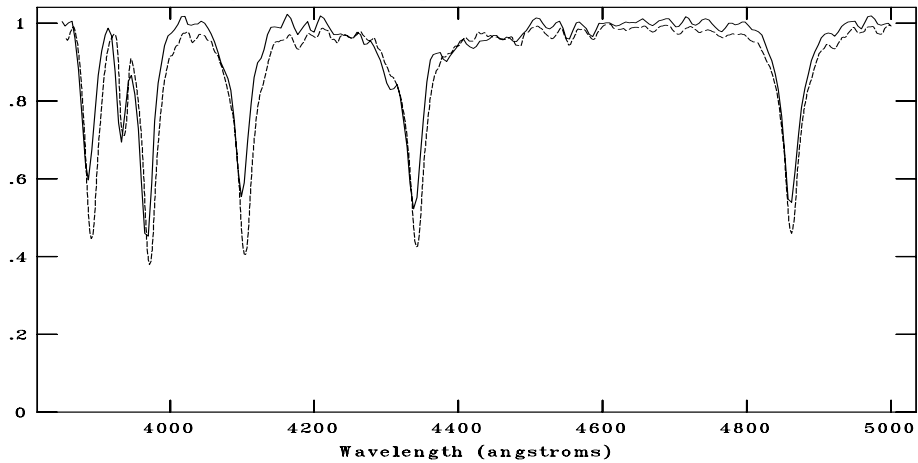


Figure C.110: CAFOS spectrum of 764-021254 compared with A1V, A3V, A5V respectively. The standard spectra are shown with dotted line. The spectral type is assigned as A4V.

NOAO/IRAF V2.16.1 baha@baha-Lenovo-IdeaPad-Y550 Thu 03:46:52 08-Dec-2016
[cg132_11FG.fits]: G132_01 1080. ap:1 beam:1

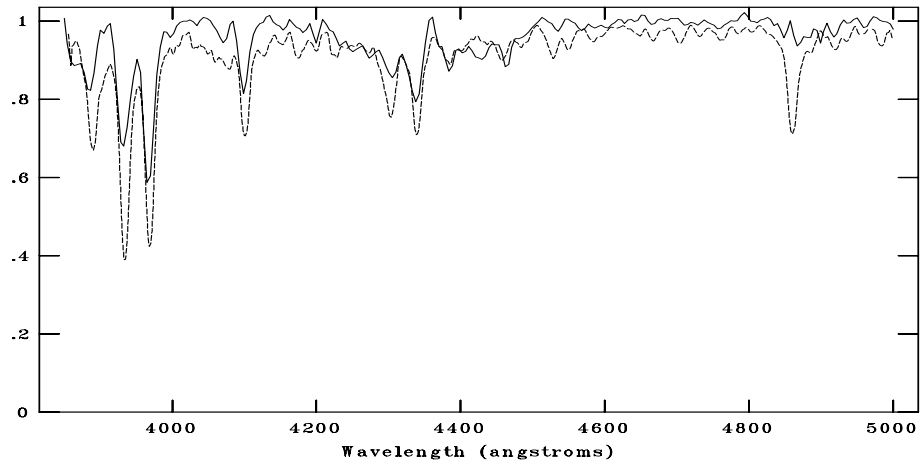
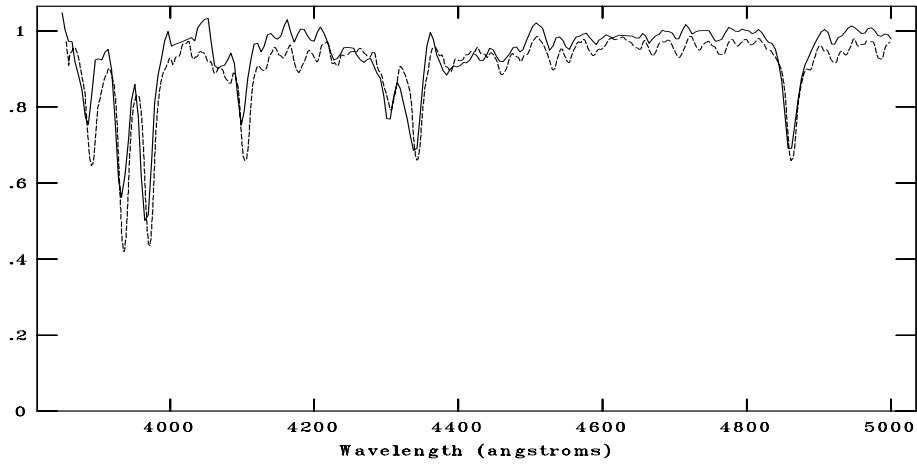
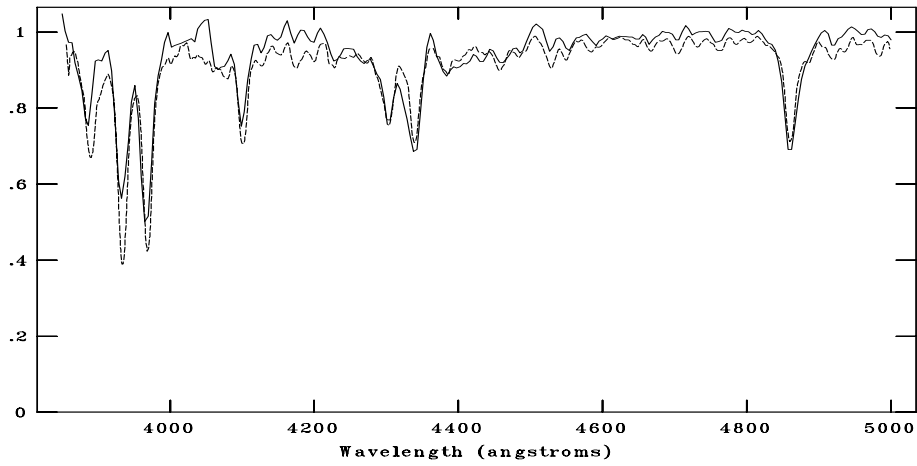


Figure C.111: CAFOS spectrum of 764-021397 compared with F6V. The spectral type is assigned as F6e. As the H lines are in emission, the spectral type identification is not accurate.

NOAO/IRAF V2.16.1 baha@baha-Lenovo-IdeaPad-Y550 Thu 03:48:05 08-Dec-2016
[cg132_12F8.fits]: G132_02 900. ap:1 beam:1



NOAO/IRAF V2.16.1 baha@baha-Lenovo-IdeaPad-Y550 Thu 03:48:41 08-Dec-2016
[cg132_12F8.fits]: G132_02 900. ap:1 beam:1



NOAO/IRAF V2.16.1 baha@baha-Lenovo-IdeaPad-Y550 Thu 03:49:25 08-Dec-2016
[cg132_12F8.fits]: G132_02 900. ap:1 beam:1

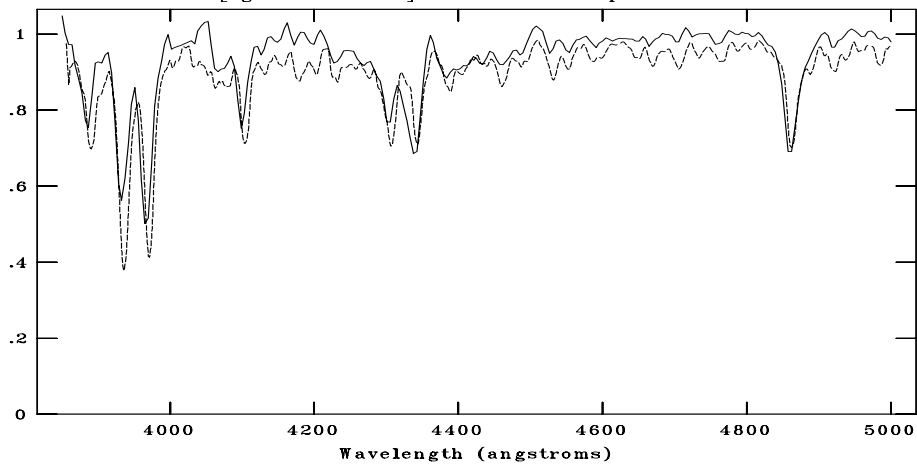
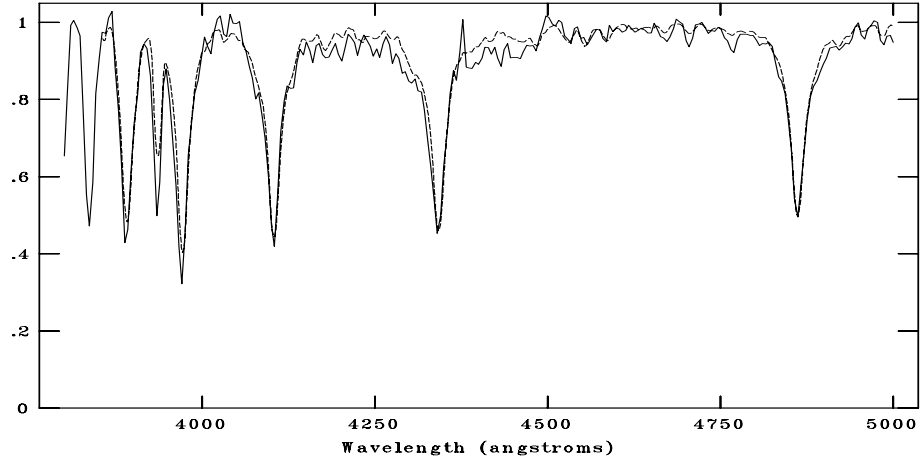
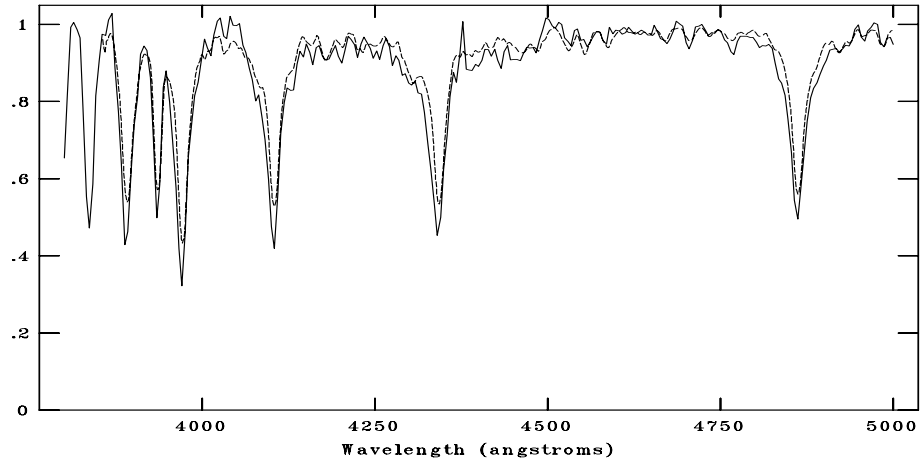


Figure C.112: CAFOS spectrum of 765-021722 compared with F5V, F6V, F8V respectively. The standard spectra are shown with dotted line. The spectral type is assigned as F6V.

NOAO/IRAF V2.16.1 baha@baha-Lenovo-IdeaPad-Y550 Wed 08:20:27 07-Dec-2016
[n132_1.fits]: 132_1 200. ap:1 beam:1



NOAO/IRAF V2.16.1 baha@baha-Lenovo-IdeaPad-Y550 Wed 08:21:03 07-Dec-2016
[n132_1.fits]: 132_1 200. ap:1 beam:1



NOAO/IRAF V2.16.1 baha@baha-Lenovo-IdeaPad-Y550 Wed 08:21:36 07-Dec-2016
[n132_1.fits]: 132_1 200. ap:1 beam:1

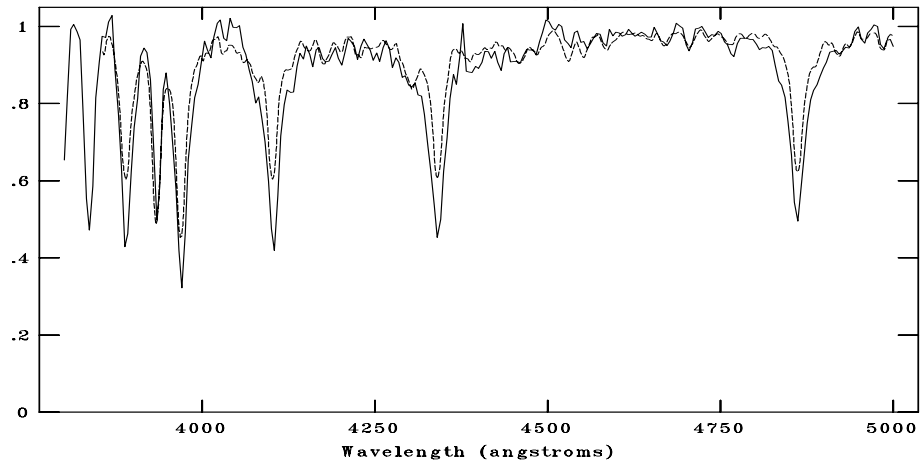
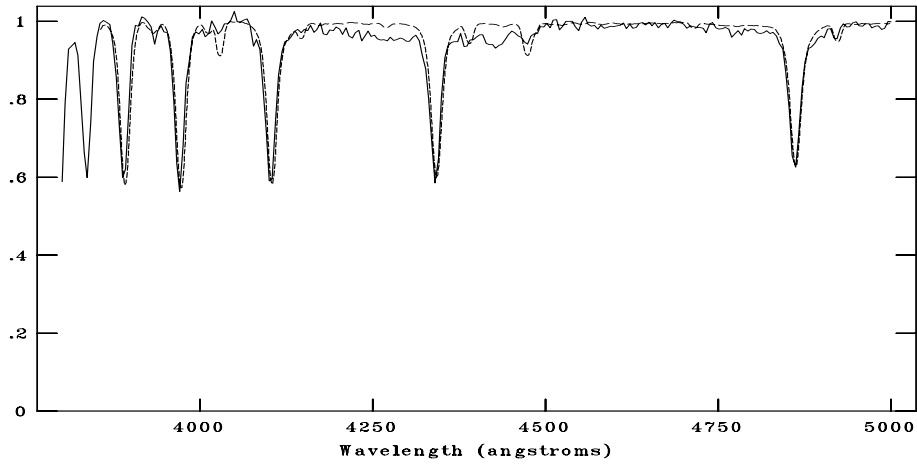
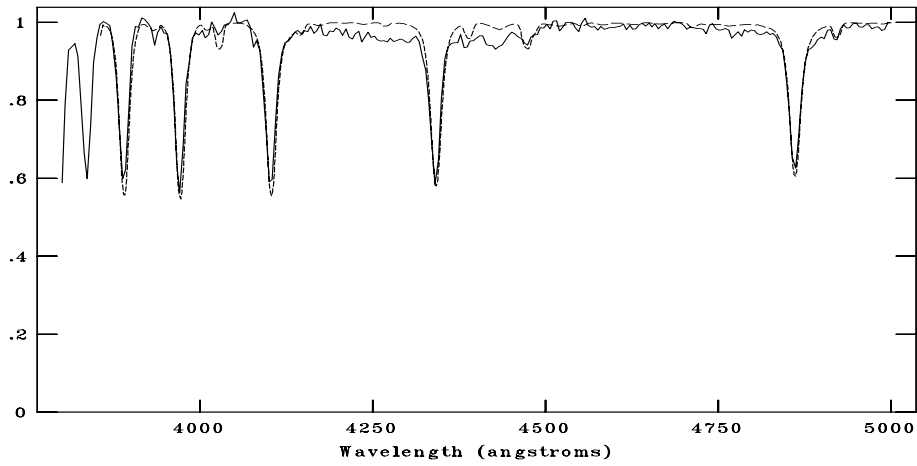


Figure C.113: CAFOS spectrum of 764-021210 compared with A7V, F0V, F2V respectively. The standard spectra are shown with dotted line. The spectral type is assigned as A8V.

NOAO/IRAF V2.16.1 baha@baha-Lenovo-IdeaPad-Y550 Wed 08:23:51 07-Dec-2016
[n132_2.fits]: 132_2 300. ap:1 beam:1



NOAO/IRAF V2.16.1 baha@baha-Lenovo-IdeaPad-Y550 Wed 08:22:04 07-Dec-2016
[n132_2.fits]: 132_2 300. ap:1 beam:1



NOAO/IRAF V2.16.1 baha@baha-Lenovo-IdeaPad-Y550 Wed 08:23:05 07-Dec-2016
[n132_2.fits]: 132_2 300. ap:1 beam:1

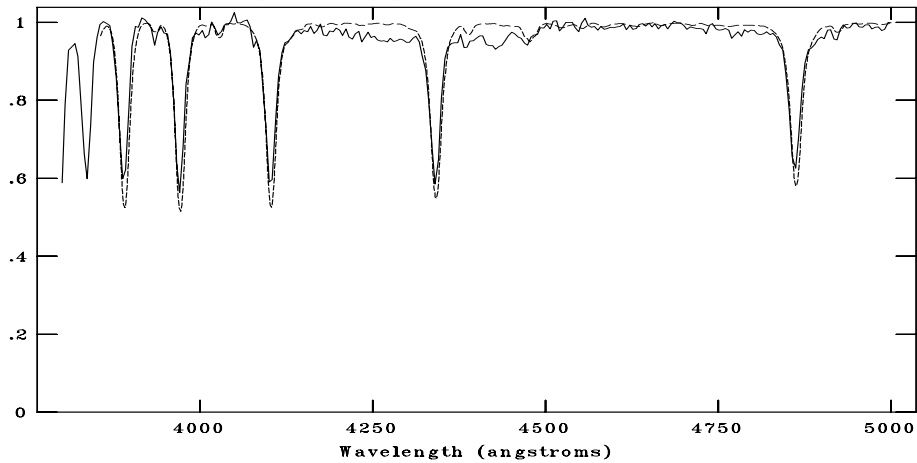
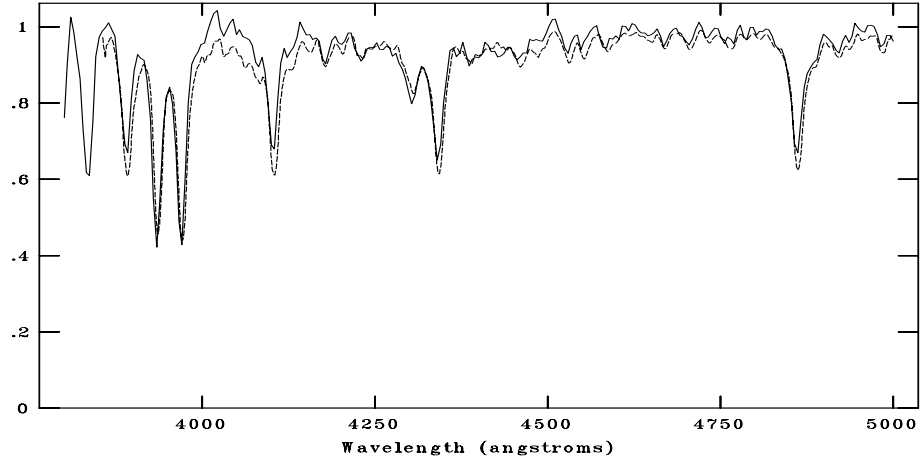
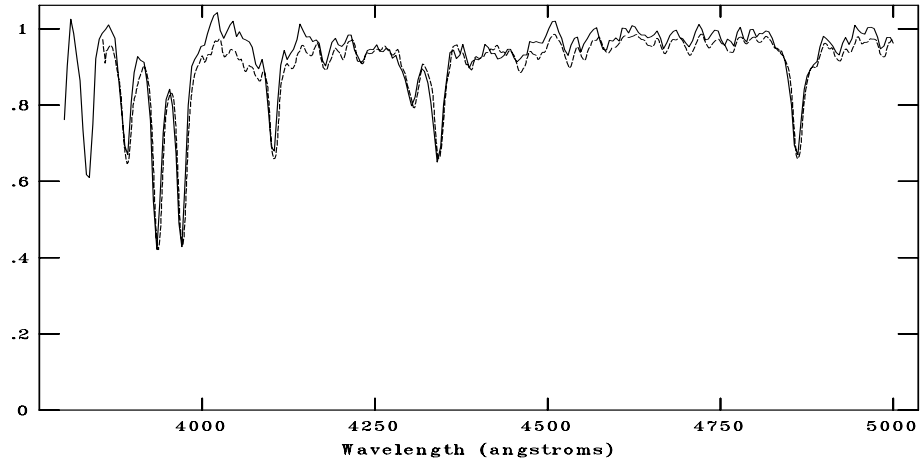


Figure C.114: CAFOS spectrum of 765-021792 compared with B5V, B7V, B8V respectively. The standard spectra are shown with dotted line. The spectral type is assigned as B7V.

NOAO/IRAF V2.16.1 baha@baha-Lenovo-IdeaPad-Y550 Wed 08:25:28 07-Dec-2016
[n132_3.fits]: 132_3 90. ap:1 beam:1



NOAO/IRAF V2.16.1 baha@baha-Lenovo-IdeaPad-Y550 Wed 08:24:32 07-Dec-2016
[n132_3.fits]: 132_3 90. ap:1 beam:1



NOAO/IRAF V2.16.1 baha@baha-Lenovo-IdeaPad-Y550 Wed 08:25:02 07-Dec-2016
[n132_3.fits]: 132_3 90. ap:1 beam:1

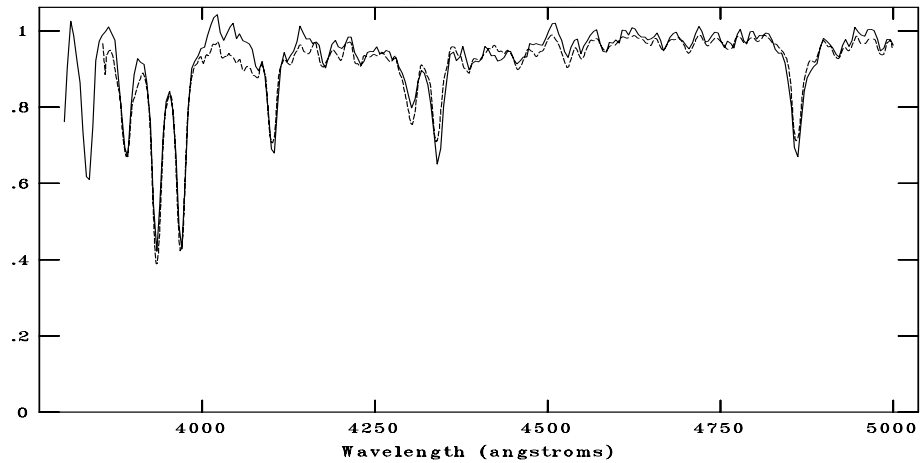
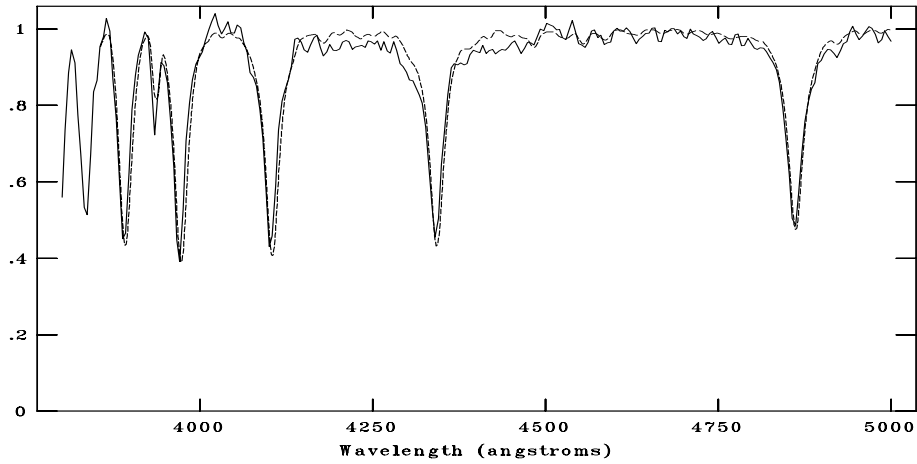
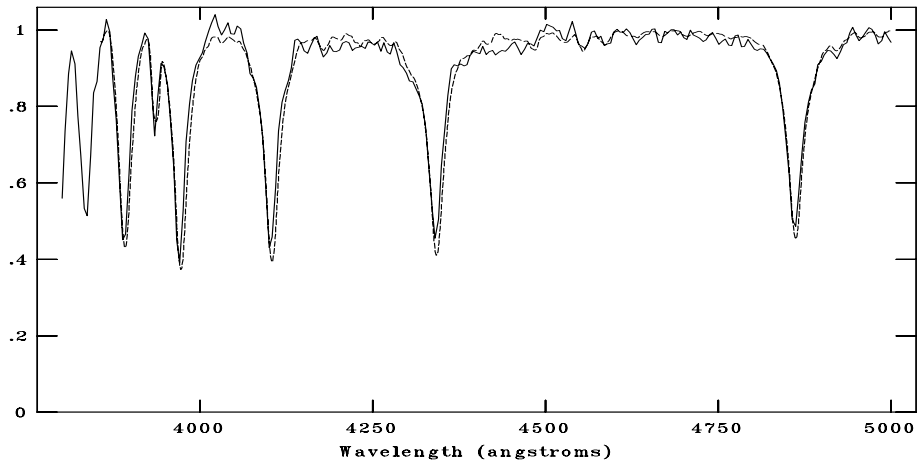


Figure C.115: CAFOS spectrum of 764-021329 compared with F3V, F5V, F6V respectively. The standard spectra are shown with dotted line. The spectral type is assigned as F5V.

NOAO/IRAF V2.16.1 baha@baha-Lenovo-IdeaPad-Y550 Mon 23:40:06 02-Jan-2017
[132_4awsn.fits]: 132_4 500. ap:1 beam:1



NOAO/IRAF V2.16.1 baha@baha-Lenovo-IdeaPad-Y550 Mon 23:41:48 02-Jan-2017
[132_4awsn.fits]: 132_4 500. ap:1 beam:1



NOAO/IRAF V2.16.1 baha@baha-Lenovo-IdeaPad-Y550 Mon 23:40:35 02-Jan-2017
[132_4awsn.fits]: 132_4 500. ap:1 beam:1

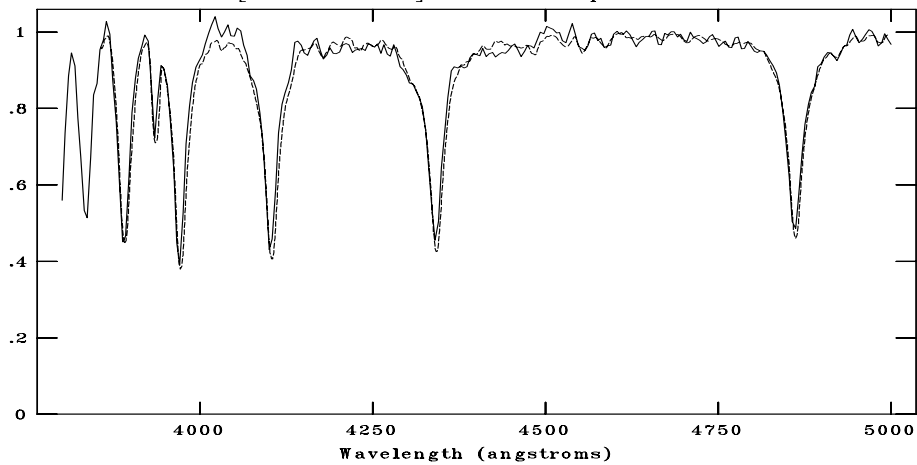
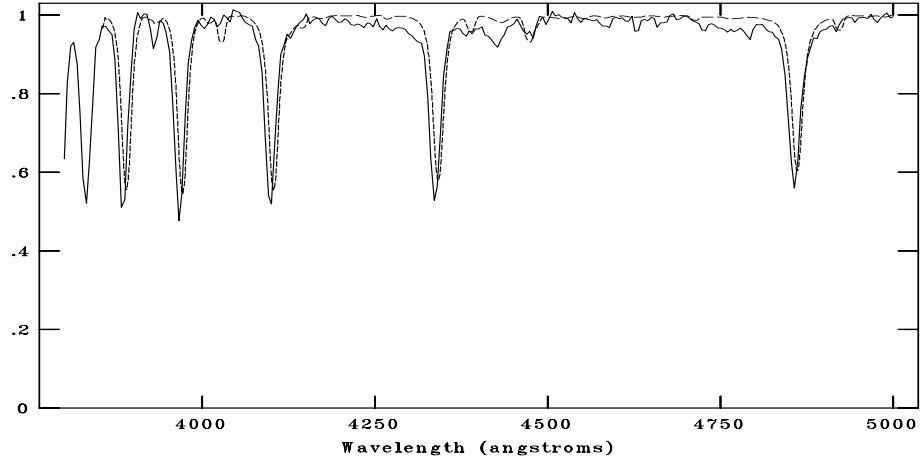
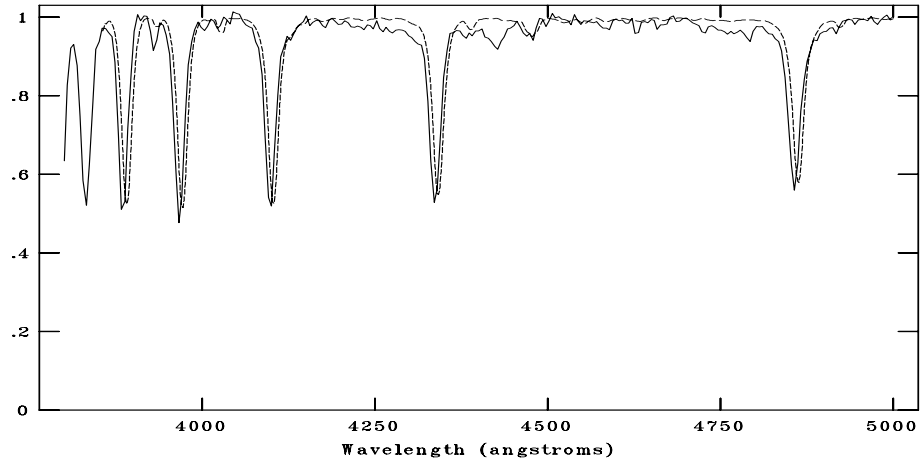


Figure C.116: CAFOS spectrum of 764-021331 compared with A1V, A3V, A5V respectively. The standard spectra are shown with dotted line. The spectral type is assigned as A4V.

NOAO/IRAF V2.16.1 baha@baha-Lenovo-IdeaPad-Y550 Wed 08:26:03 07-Dec-2016
[n132_5.fits]: 132_5 350. ap:1 beam:1



NOAO/IRAF V2.16.1 baha@baha-Lenovo-IdeaPad-Y550 Wed 08:26:53 07-Dec-2016
[n132_5.fits]: 132_5 350. ap:1 beam:1



NOAO/IRAF V2.16.1 baha@baha-Lenovo-IdeaPad-Y550 Wed 08:27:10 07-Dec-2016
[n132_5.fits]: 132_5 350. ap:1 beam:1

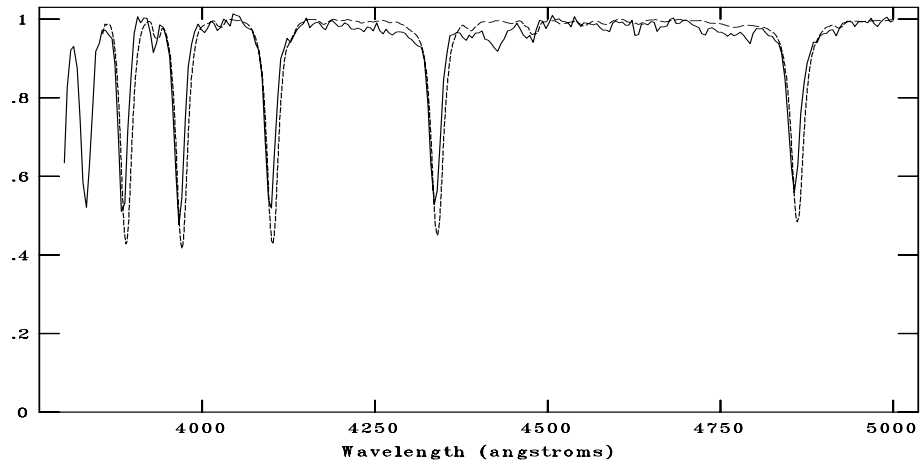
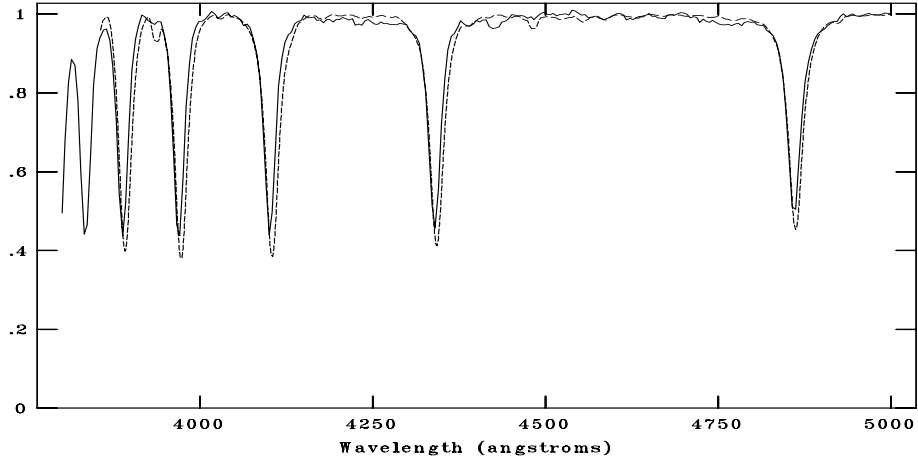
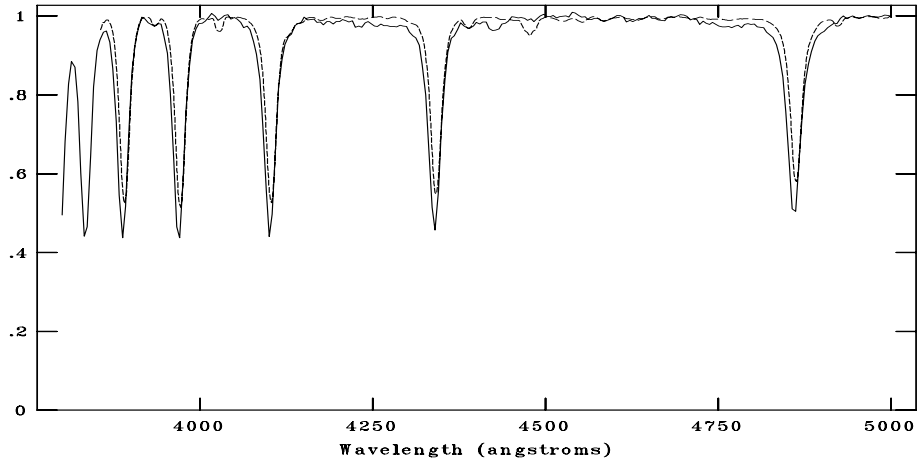


Figure C.117: CAFOS spectrum of 764-021370 compared with B7V, B8V, B9V respectively. The standard spectra are shown with dotted line. The spectral type is assigned as B8V.

NOAO/IRAF V2.16.1 baha@baha-Lenovo-IdeaPad-Y550 Wed 08:28:22 07-Dec-2016
[n132_6.fits]: 132_6 250. ap:1 beam:1



NOAO/IRAF V2.16.1 baha@baha-Lenovo-IdeaPad-Y550 Wed 08:29:04 07-Dec-2016
[n132_6.fits]: 132_6 250. ap:1 beam:1



NOAO/IRAF V2.16.1 baha@baha-Lenovo-IdeaPad-Y550 Wed 08:27:58 07-Dec-2016
[n132_6.fits]: 132_6 250. ap:1 beam:1

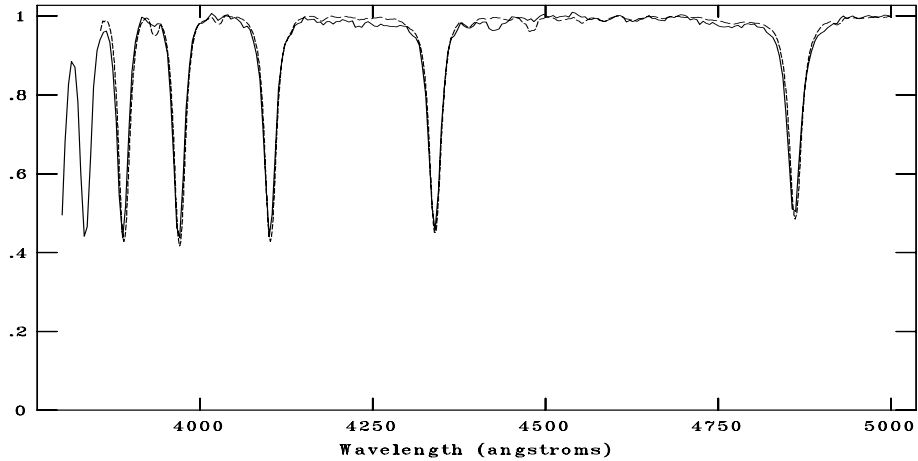


Figure C.118: CAFOS spectrum of 764-021388 compared with A0V, B8V, B9V respectively. The standard spectra are shown with dotted line. The spectral type is assigned as B9V.

C.12 G156.2+5.7

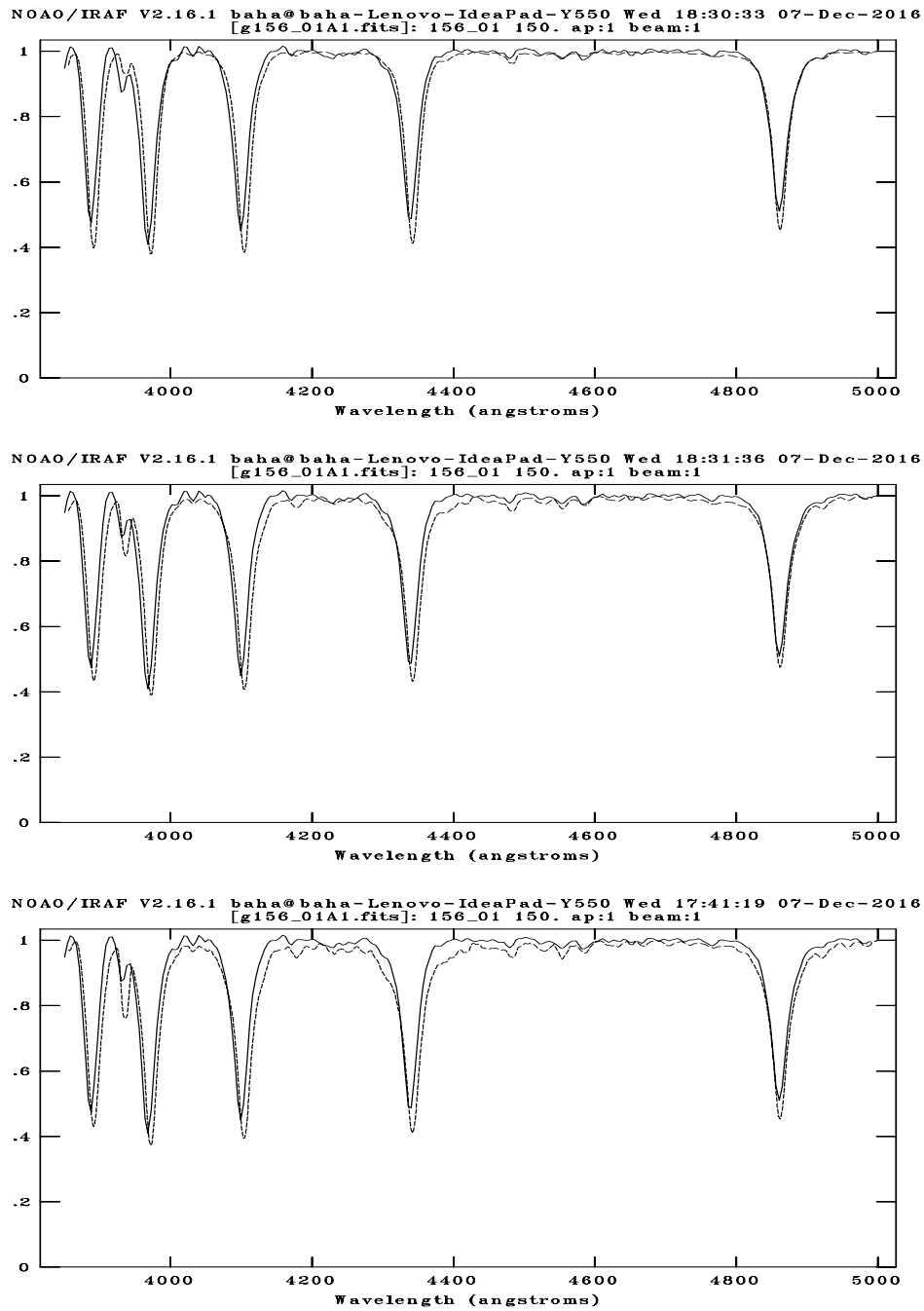
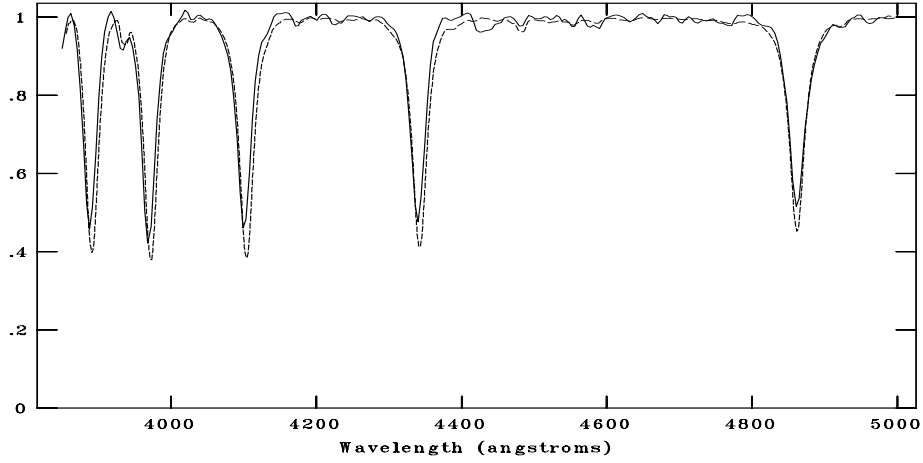
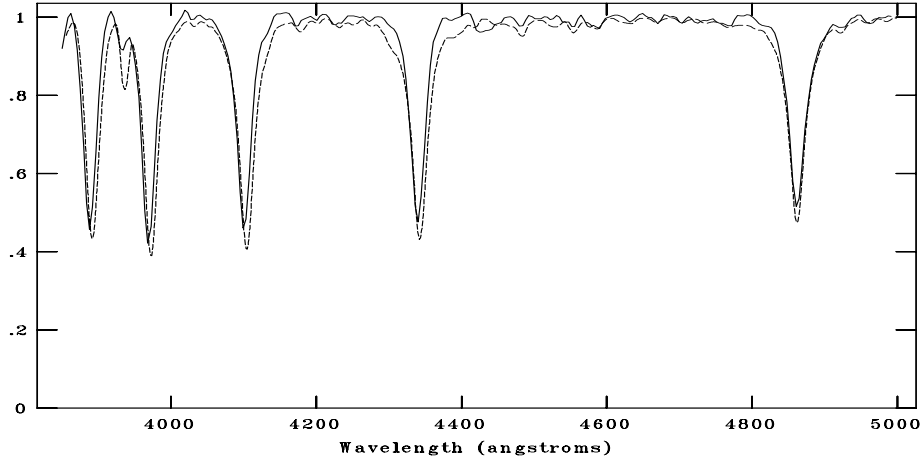


Figure C.119: CAFOS spectrum of 710-035795 compared with A0V, A1V, A3V respectively. The standard spectra are shown with dotted line. The spectral type is assigned as A1V.

NOAO/IRAF V2.16.1 baha@baha-Lenovo-IdeaPad-Y550 Wed 18:32:13 07-Dec-2016
[g156_02A0.fits]: 156_02 300. ap:1 beam:1



NOAO/IRAF V2.16.1 baha@baha-Lenovo-IdeaPad-Y550 Wed 18:32:39 07-Dec-2016
[g156_02A0.fits]: 156_02 300. ap:1 beam:1



NOAO/IRAF V2.16.1 baha@baha-Lenovo-IdeaPad-Y550 Wed 17:41:50 07-Dec-2016
[g156_02A0.fits]: 156_02 300. ap:1 beam:1

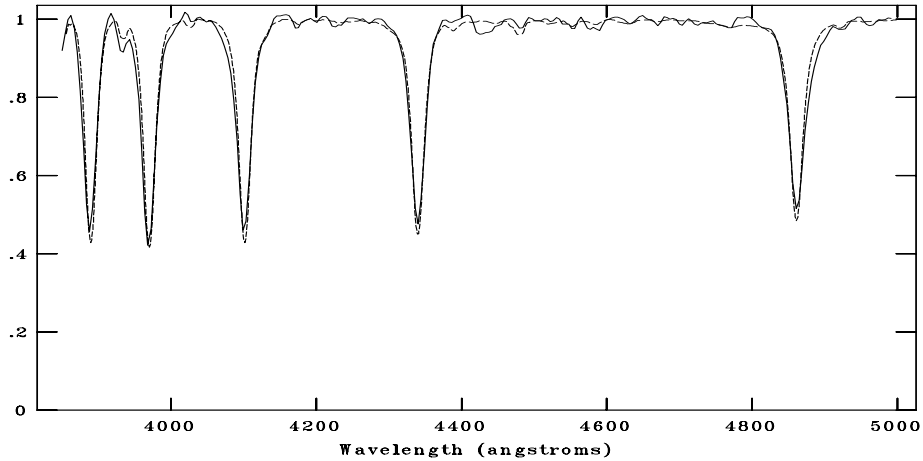
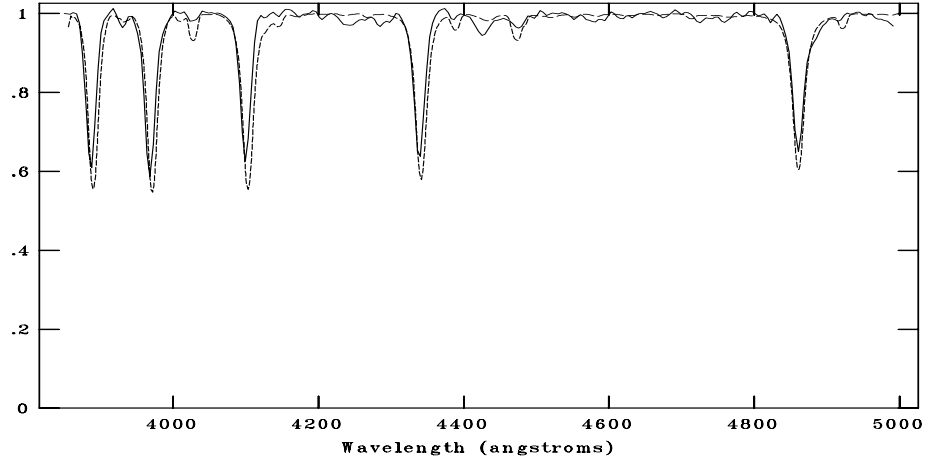
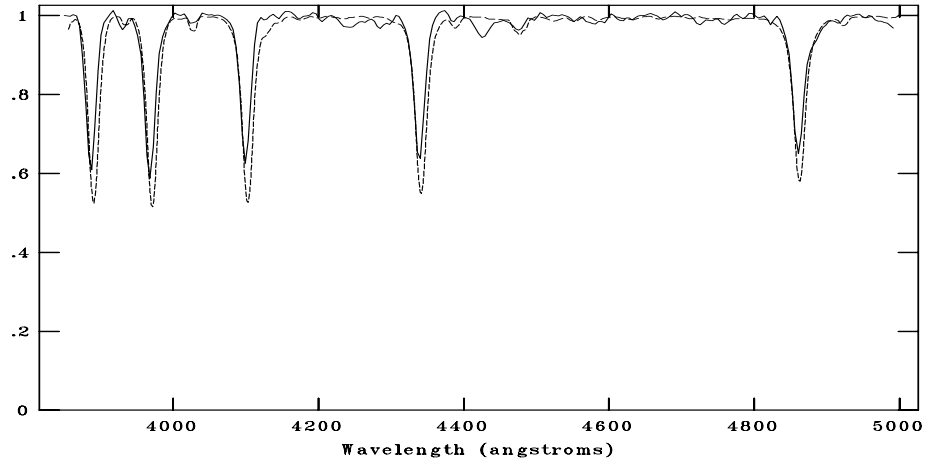


Figure C.120: CAFOS spectrum of 710-03589 compared with A0V, A1V, B9V respectively. The standard spectra are shown with dotted line. The spectral type is assigned as A0V.

NOAO/IRAF V2.16.1 baha@baha-Lenovo-IdeaPad-Y550 Wed 18:33:15 07-Dec-2016
[g156_03B8.fits]: 156_03 400. ap:1 beam:1



NOAO/IRAF V2.16.1 baha@baha-Lenovo-IdeaPad-Y550 Wed 18:33:45 07-Dec-2016
[g156_03B8.fits]: 156_03 400. ap:1 beam:1



NOAO/IRAF V2.16.1 baha@baha-Lenovo-IdeaPad-Y550 Wed 18:34:15 07-Dec-2016
[g156_03B8.fits]: 156_03 400. ap:1 beam:1

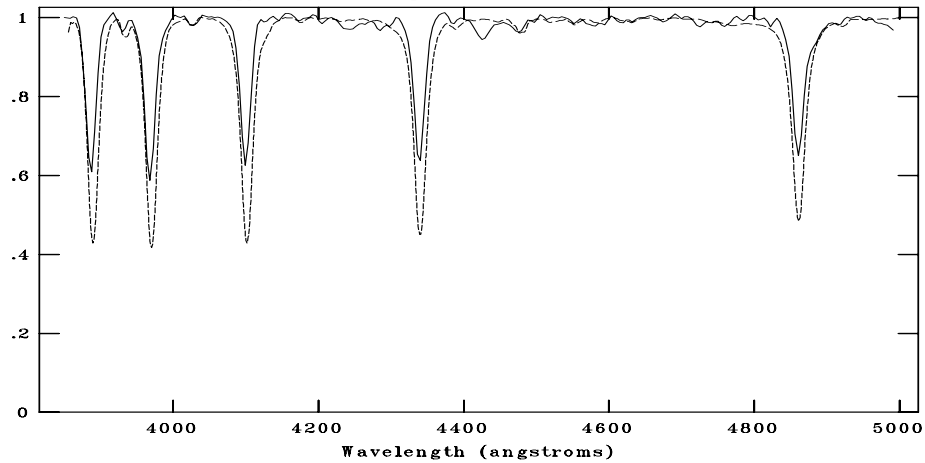
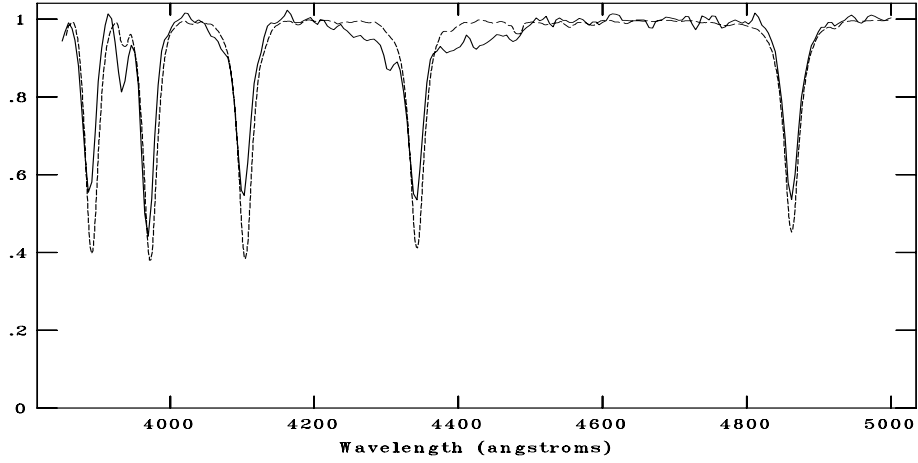
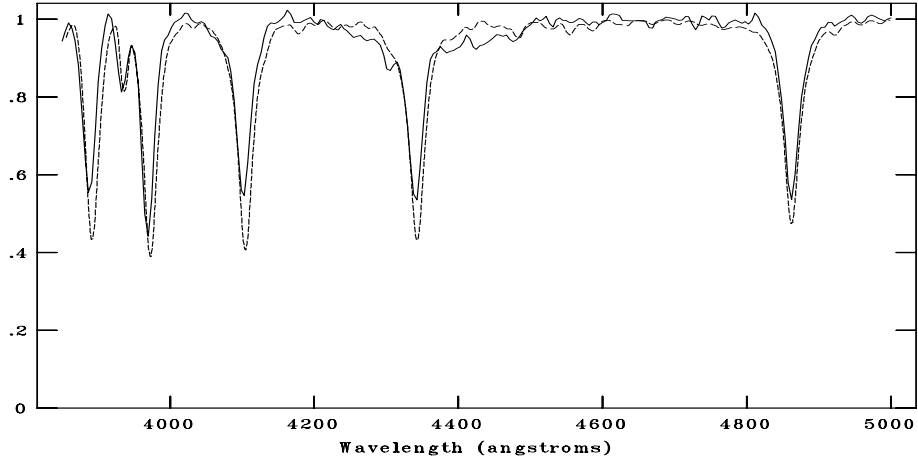


Figure C.121: CAFOS spectrum of 710-035810 compared with B7V, B8V, B9V respectively. The standard spectra are shown with dotted line. The spectral type is assigned as B8V.

NOAO/IRAF V2.16.1 baha@baha-Lenovo-IdeaPad-Y550 Thu 03:50:17 08-Dec-2016
[cg156_01A2.fits]: G156_1 960. ap:1 beam:1



NOAO/IRAF V2.16.1 baha@baha-Lenovo-IdeaPad-Y550 Thu 03:50:28 08-Dec-2016
[cg156_01A2.fits]: G156_1 960. ap:1 beam:1



NOAO/IRAF V2.16.1 baha@baha-Lenovo-IdeaPad-Y550 Thu 03:50:56 08-Dec-2016
[cg156_01A2.fits]: G156_1 960. ap:1 beam:1

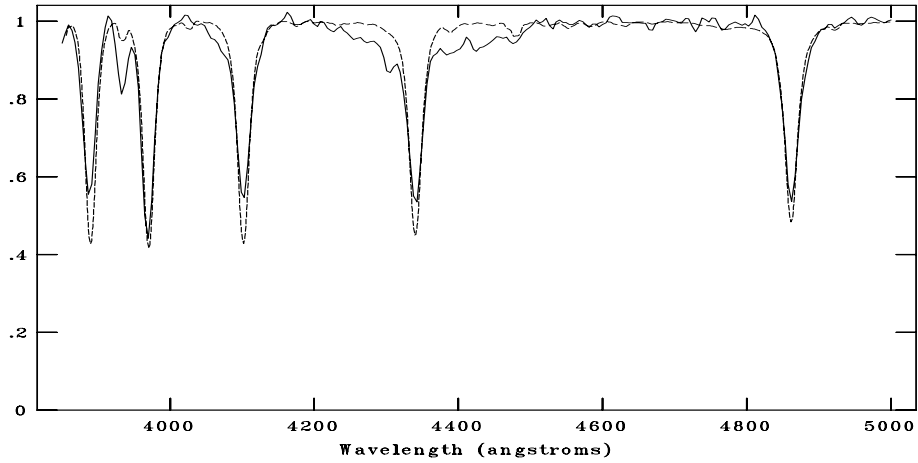
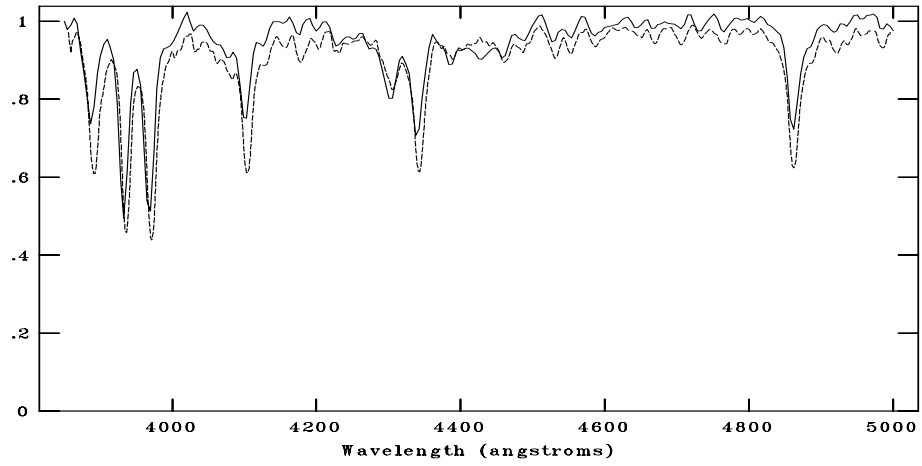
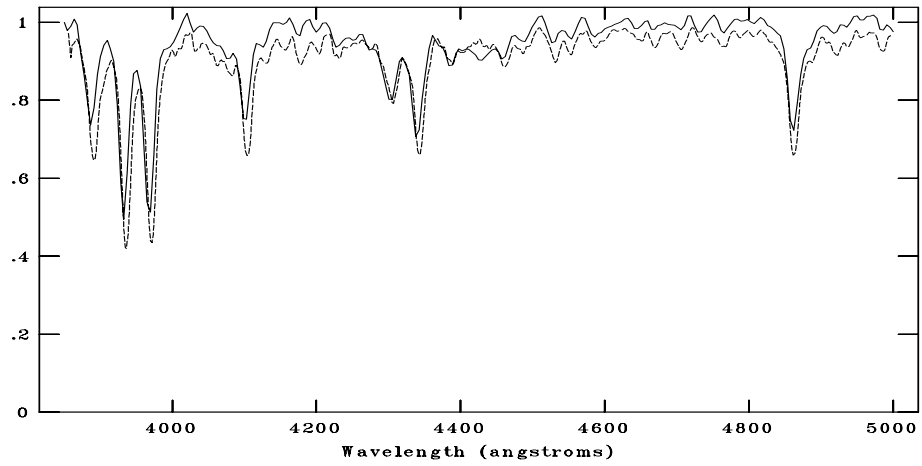


Figure C.122: CAFOS spectrum of 710-035713 compared with A0V, A1V, B9V respectively. The standard spectra are shown with dotted line. The spectral type is assigned as A1V.

NOAO/IRAF V2.16.1 baha@baha-Lenovo-IdeaPad-Y550 Tue 00:20:10 03-Jan-2017
[nn15603.fits]: G156_3 720. ap:1 beam:1



NOAO/IRAF V2.16.1 baha@baha-Lenovo-IdeaPad-Y550 Tue 00:21:15 03-Jan-2017
[nn15603.fits]: G156_3 720. ap:1 beam:1



NOAO/IRAF V2.16.1 baha@baha-Lenovo-IdeaPad-Y550 Tue 00:21:44 03-Jan-2017
[nn15603.fits]: G156_3 720. ap:1 beam:1

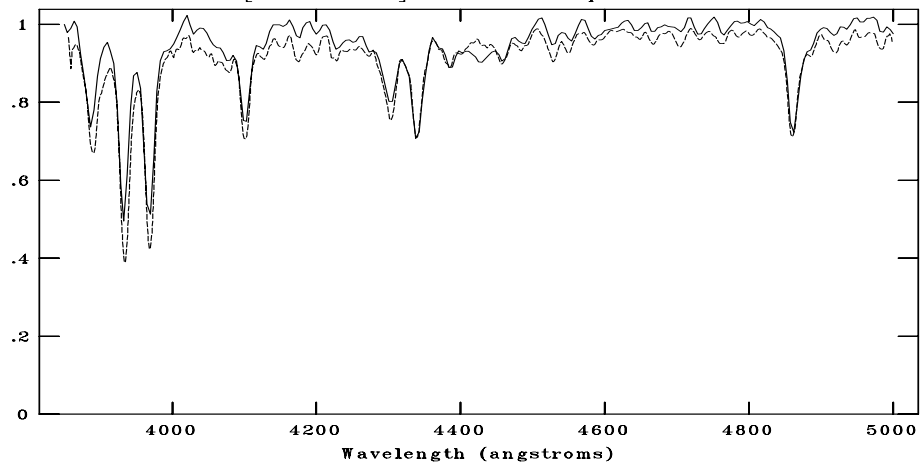
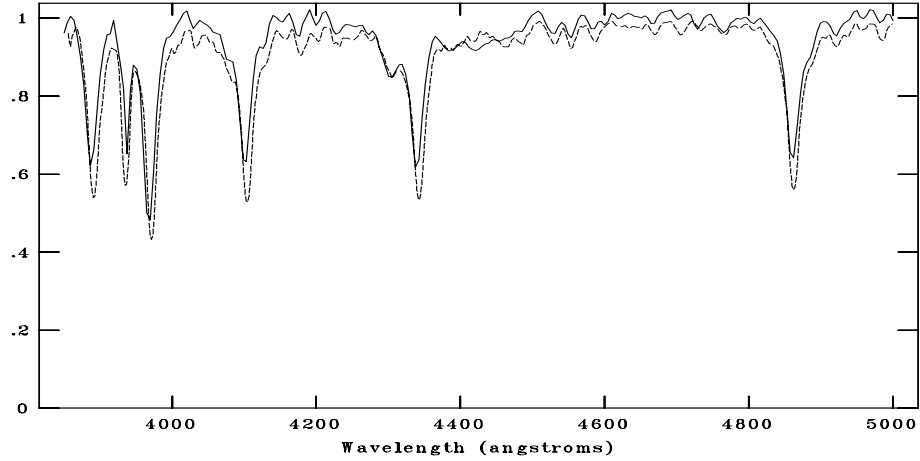
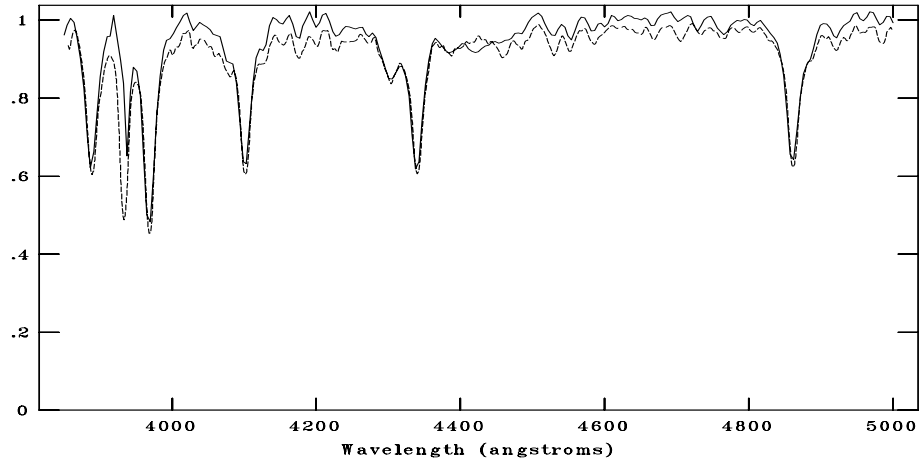


Figure C.123: CAFOS spectrum of 710-035782 compared with F3V, F5V, F6V respectively. The standard spectra are shown with dotted line. The spectral type is assigned as F5V.

NOAO/IRAF V2.16.1 baha@baha-Lenovo-IdeaPad-Y550 Tue 00:25:38 03-Jan-2017
[nn15602.fits]: G156_2 780. ap:1 beam:1



NOAO/IRAF V2.16.1 baha@baha-Lenovo-IdeaPad-Y550 Tue 00:26:38 03-Jan-2017
[nn15602.fits]: G156_2 780. ap:1 beam:1



NOAO/IRAF V2.16.1 baha@baha-Lenovo-IdeaPad-Y550 Tue 00:27:14 03-Jan-2017
[nn15602.fits]: G156_2 780. ap:1 beam:1

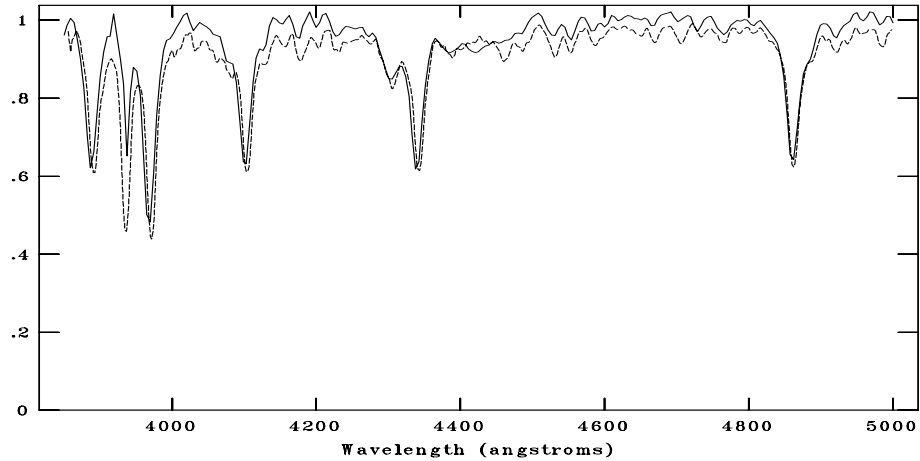
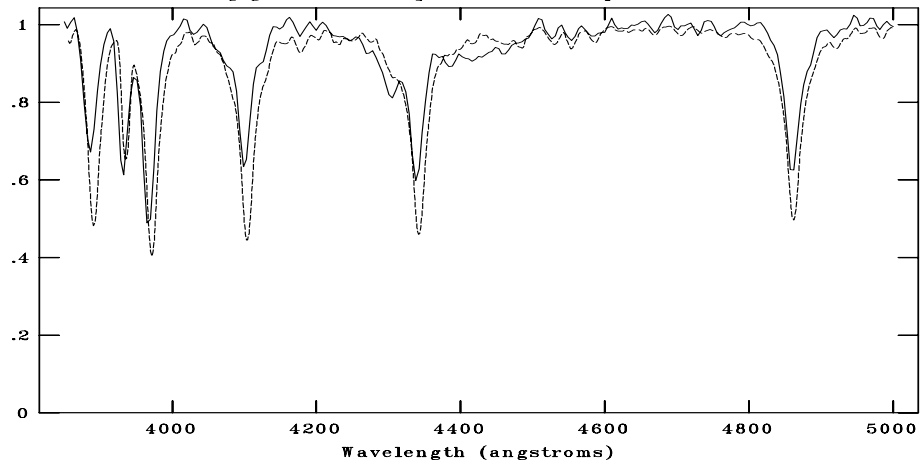
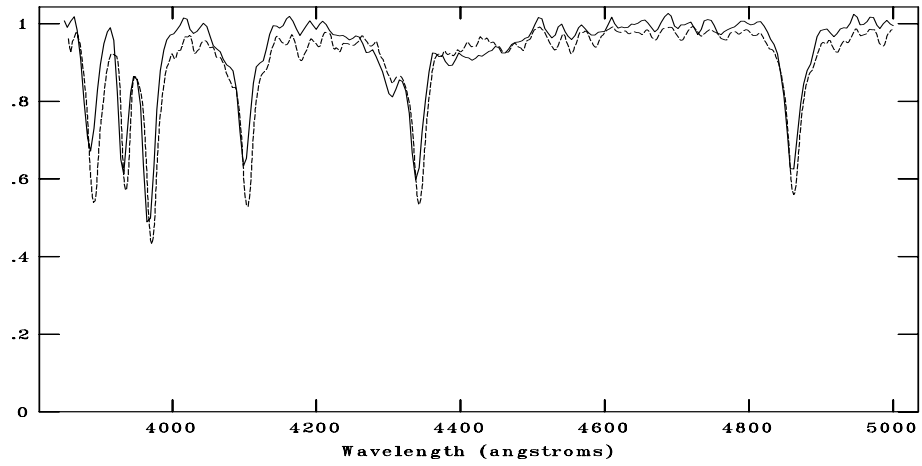


Figure C.124: CAFOS spectrum of 709-034542 compared with F0V, F2V, F3V respectively. The standard spectra are shown with dotted line. The spectral type is assigned as F2V.

NOAO/IRAF V2.16.1 baha@baha-Lenovo-IdeaPad-Y550 Thu 03:53:46 08-Dec-2016
[cg156_04A5.fits]: G156_4 960. ap:1 beam:1



NOAO/IRAF V2.16.1 baha@baha-Lenovo-IdeaPad-Y550 Thu 03:54:46 08-Dec-2016
[cg156_04A5.fits]: G156_4 960. ap:1 beam:1



NOAO/IRAF V2.16.1 baha@baha-Lenovo-IdeaPad-Y550 Thu 03:54:22 08-Dec-2016
[cg156_04A5.fits]: G156_4 960. ap:1 beam:1

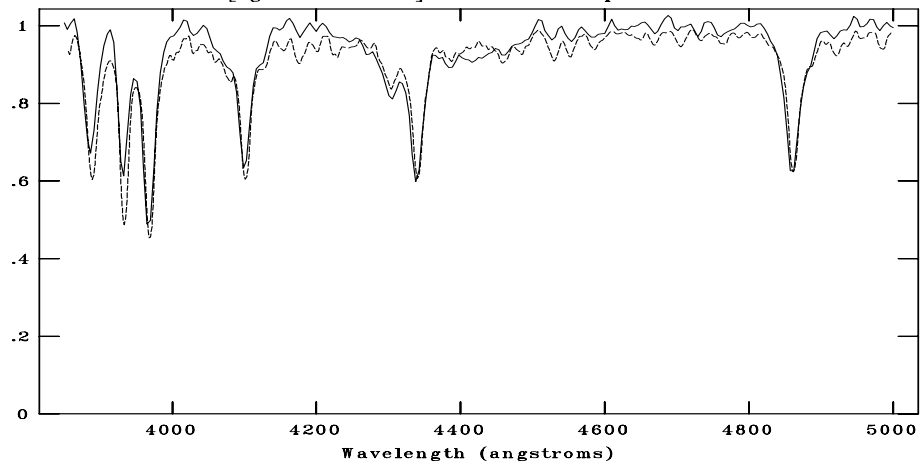


Figure C.125: CAFOS spectrum of 710-035744 compared with A7V, F0V, F2V respectively. The standard spectra are shown with dotted line. The spectral type is assigned as F0V. The identification is not accurate due to the weakness of Ca II-K line.

C.13 G160.9+2.6

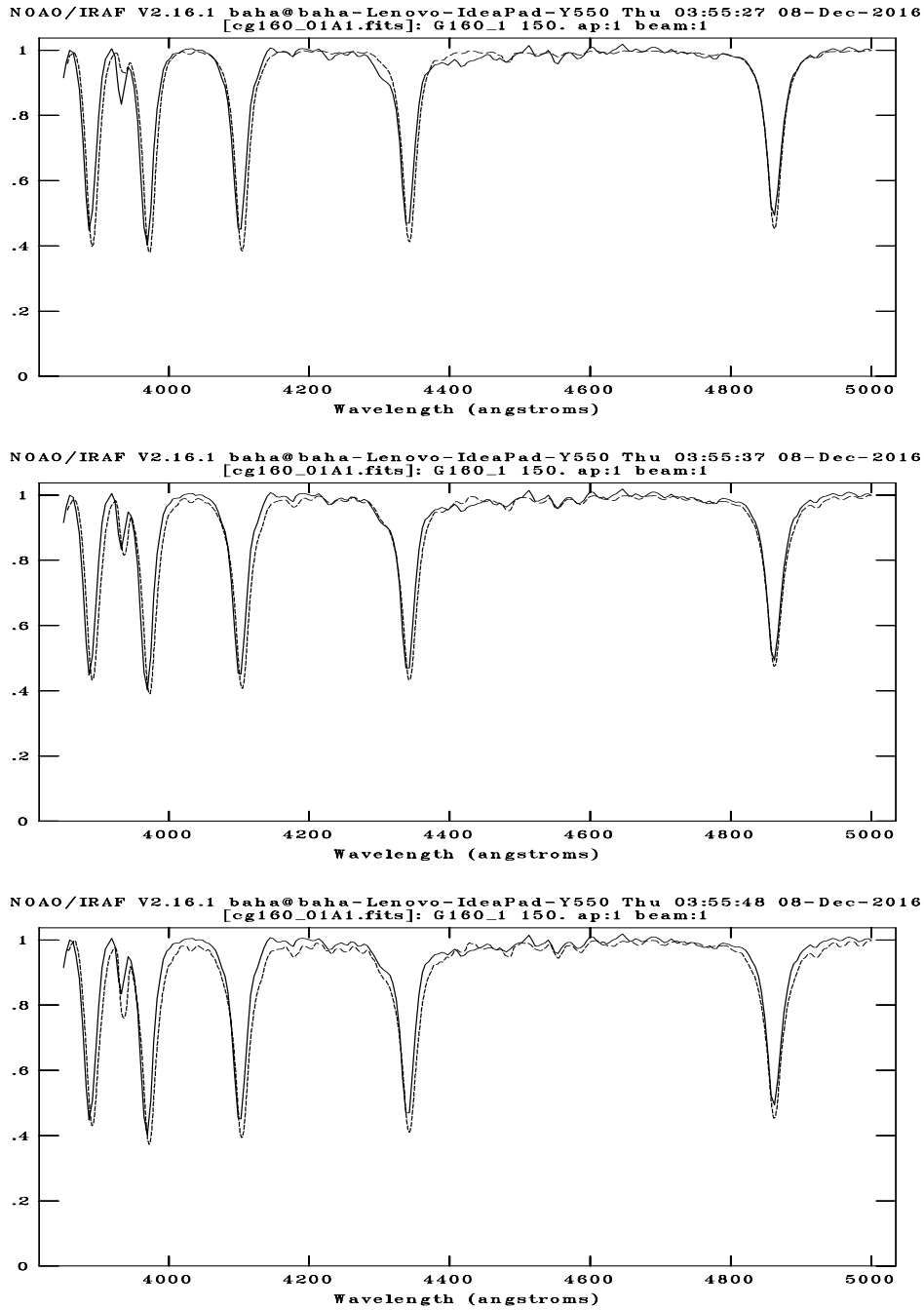
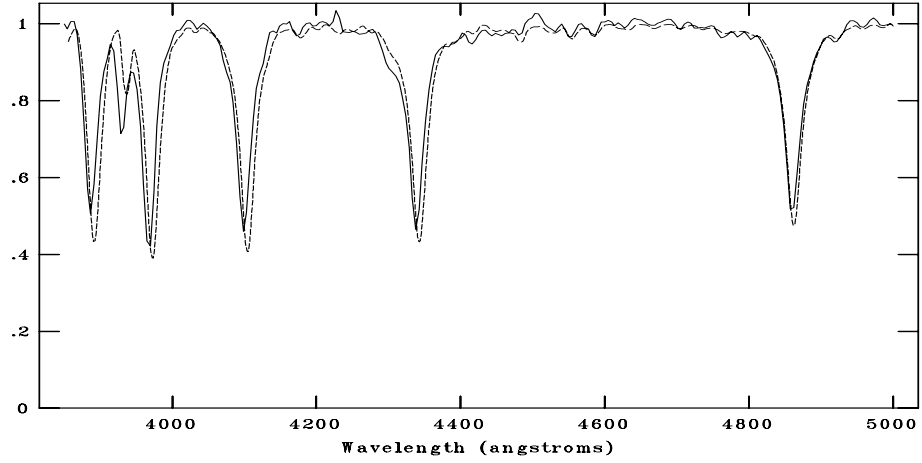
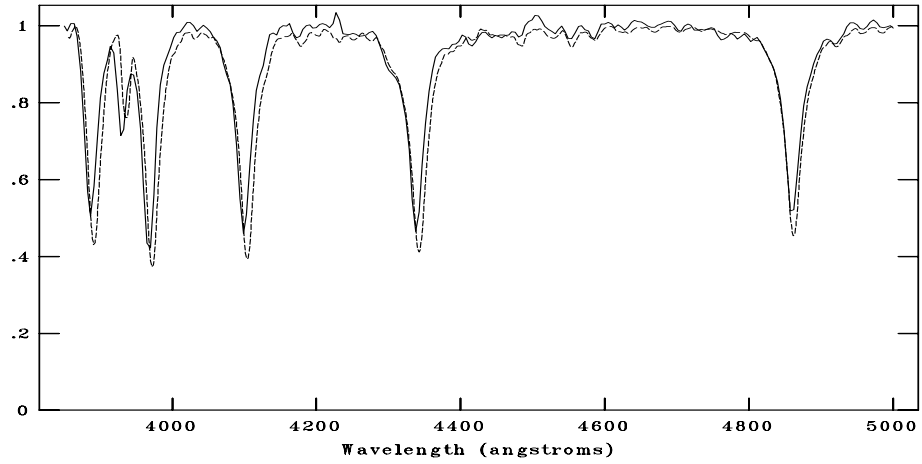


Figure C.126: CAFOS spectrum of 683-034093 compared with A0V, A1V, A3V respectively. The standard spectra are shown with dotted line. The spectral type is assigned as A1V.

NOAO/IRAF V2.16.1 baha@baha-Lenovo-IdeaPad-Y550 Thu 03:57:50 08-Dec-2016
[cg160_02A2.fits]: G160_2 150. ap:1 beam:1



NOAO/IRAF V2.16.1 baha@baha-Lenovo-IdeaPad-Y550 Thu 03:57:20 08-Dec-2016
[cg160_02A2.fits]: G160_2 150. ap:1 beam:1



NOAO/IRAF V2.16.1 baha@baha-Lenovo-IdeaPad-Y550 Thu 03:57:33 08-Dec-2016
[cg160_02A2.fits]: G160_2 150. ap:1 beam:1

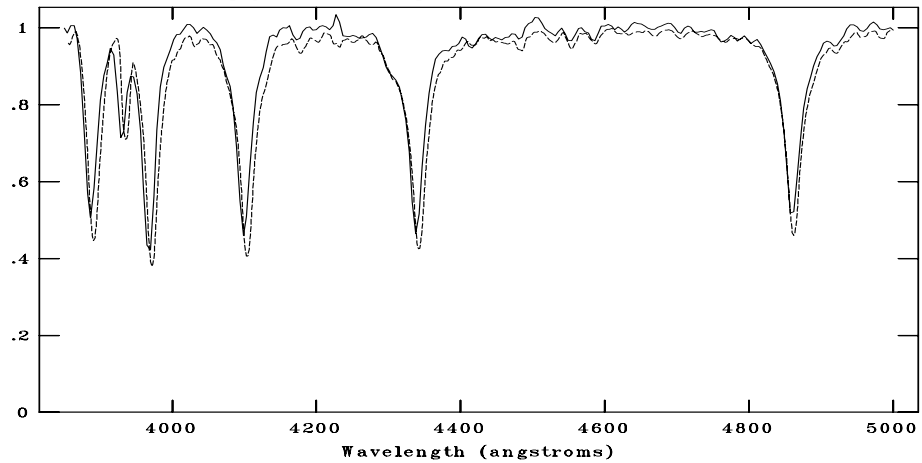
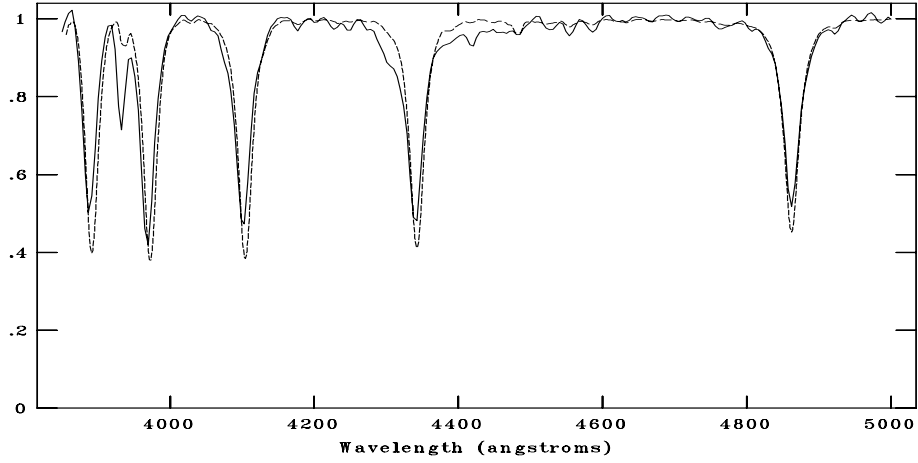
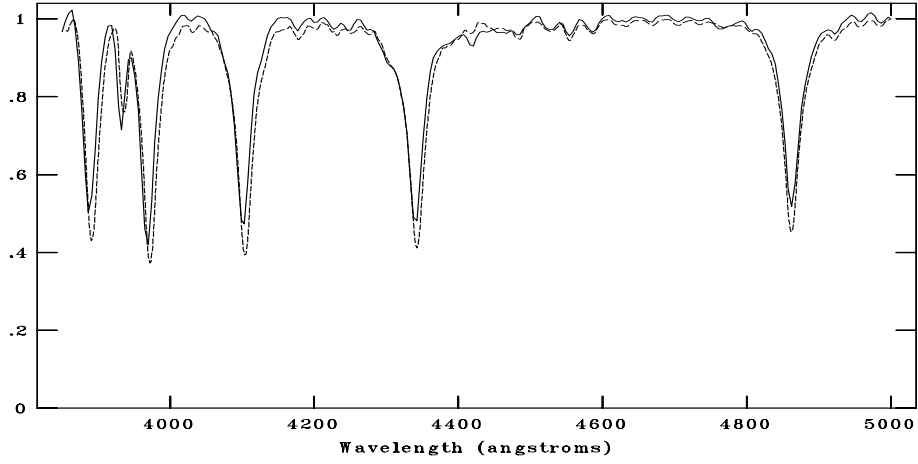


Figure C.127: CAFOS spectrum of 683-034211 compared with A1V, A3V, A5V respectively. The standard spectra are shown with dotted line. The spectral type is assigned as A2V.

NOAO/IRAF V2.16.1 baha@baha-Lenovo-IdeaPad-Y550 Thu 03:58:32 08-Dec-2016
[cg160_03A3.fits]: G160_3 300. ap:1 beam:1



NOAO/IRAF V2.16.1 baha@baha-Lenovo-IdeaPad-Y550 Thu 03:58:48 08-Dec-2016
[cg160_03A3.fits]: G160_3 300. ap:1 beam:1



NOAO/IRAF V2.16.1 baha@baha-Lenovo-IdeaPad-Y550 Thu 03:59:03 08-Dec-2016
[cg160_03A3.fits]: G160_3 300. ap:1 beam:1

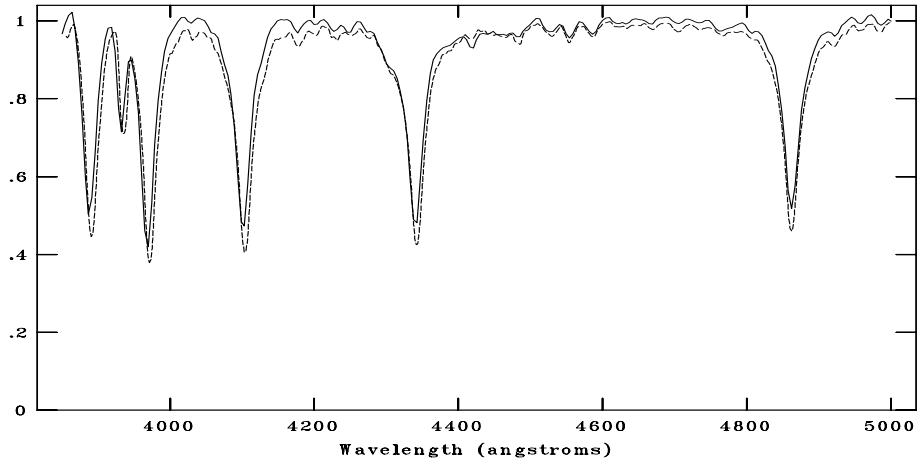
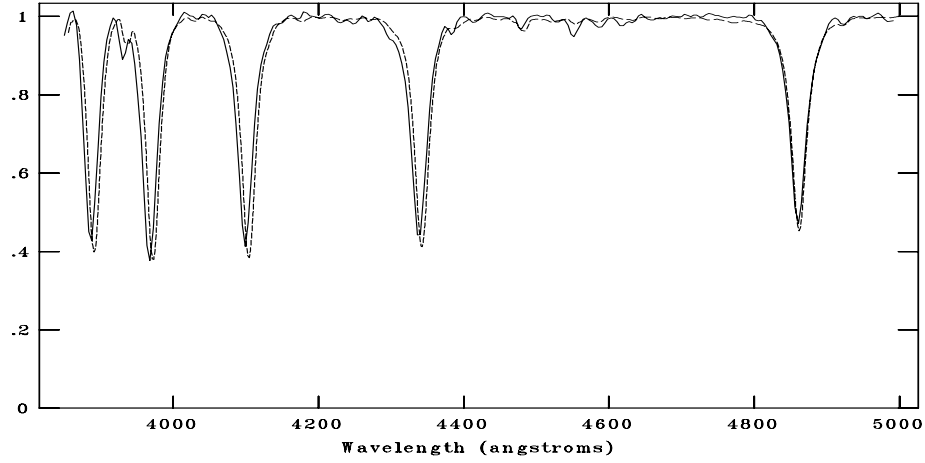
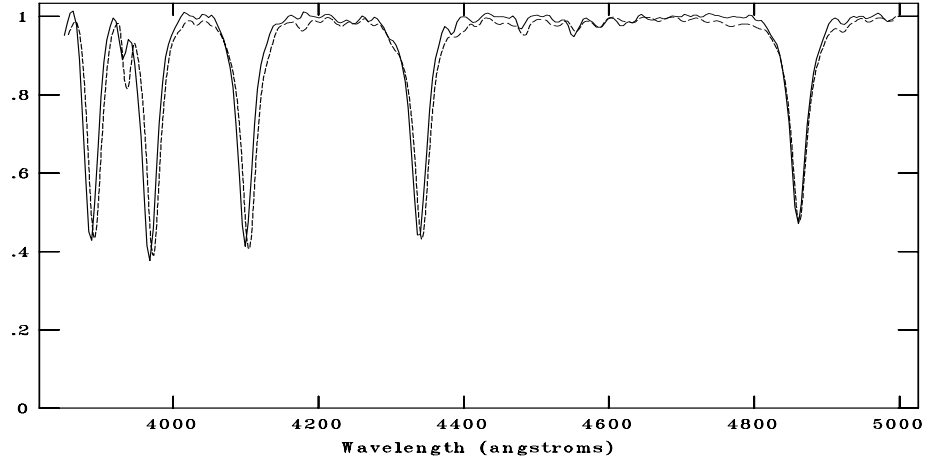


Figure C.128: CAFOS spectrum of 683-034148 compared with A1V, A3V, A5V respectively. The standard spectra are shown with dotted line. The spectral type is assigned as A3V.

NOAO/IRAF V2.16.1 baha@baha-Lenovo-IdeaPad-Y550 Wed 18:35:07 07-Dec-2016
[g160_01A0.fits]: 160_01 100. ap:1 beam:1



NOAO/IRAF V2.16.1 baha@baha-Lenovo-IdeaPad-Y550 Wed 18:35:42 07-Dec-2016
[g160_01A0.fits]: 160_01 100. ap:1 beam:1



NOAO/IRAF V2.16.1 baha@baha-Lenovo-IdeaPad-Y550 Wed 18:34:45 07-Dec-2016
[g160_01A0.fits]: 160_01 100. ap:1 beam:1

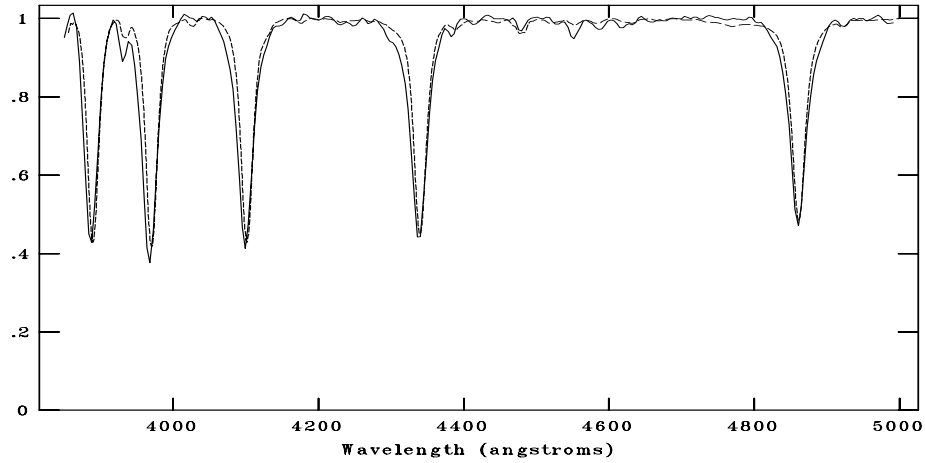
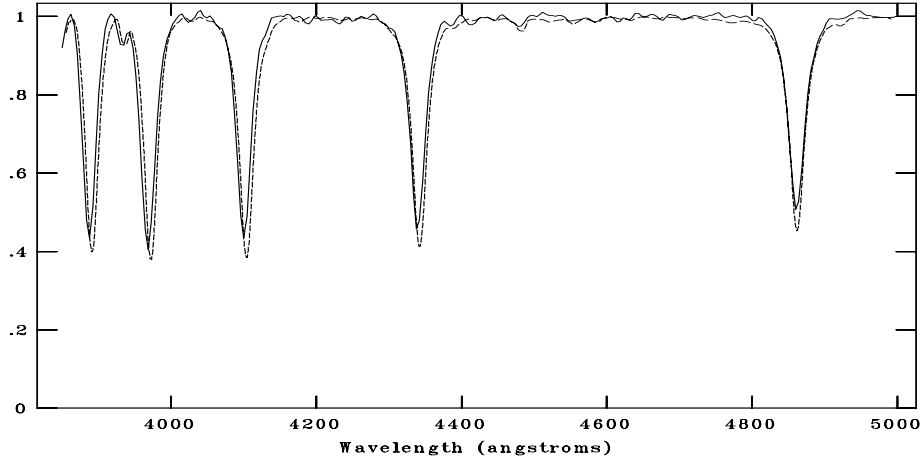
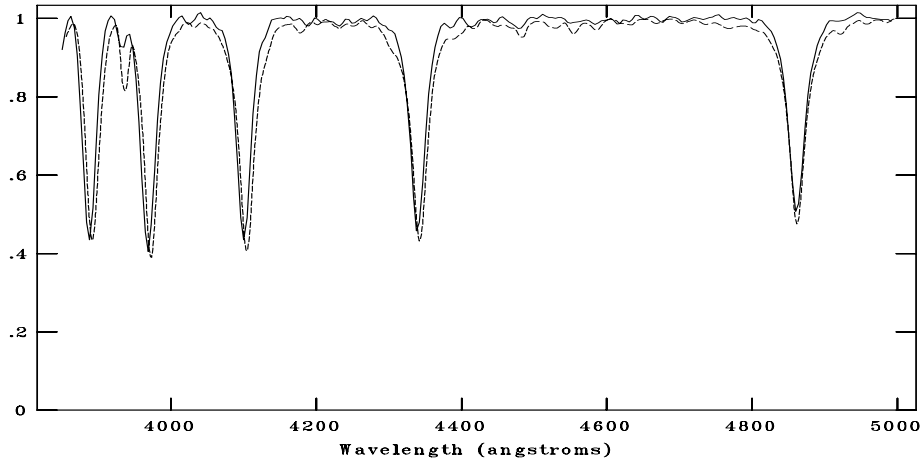


Figure C.129: CAFOS spectrum of 685-033089 compared with A0V, A1V, B9V respectively. The standard spectra are shown with dotted line. The spectral type is assigned as A0V.

NOAO/IRAF V2.16.1 baha@baha-Lenovo-IdeaPad-Y550 Wed 18:36:43 07-Dec-2016
[g160_02A0.fits]: 160_02 100. ap:1 beam:1



NOAO/IRAF V2.16.1 baha@baha-Lenovo-IdeaPad-Y550 Wed 18:37:00 07-Dec-2016
[g160_02A0.fits]: 160_02 100. ap:1 beam:1



NOAO/IRAF V2.16.1 baha@baha-Lenovo-IdeaPad-Y550 Wed 18:36:05 07-Dec-2016
[g160_02A0.fits]: 160_02 100. ap:1 beam:1

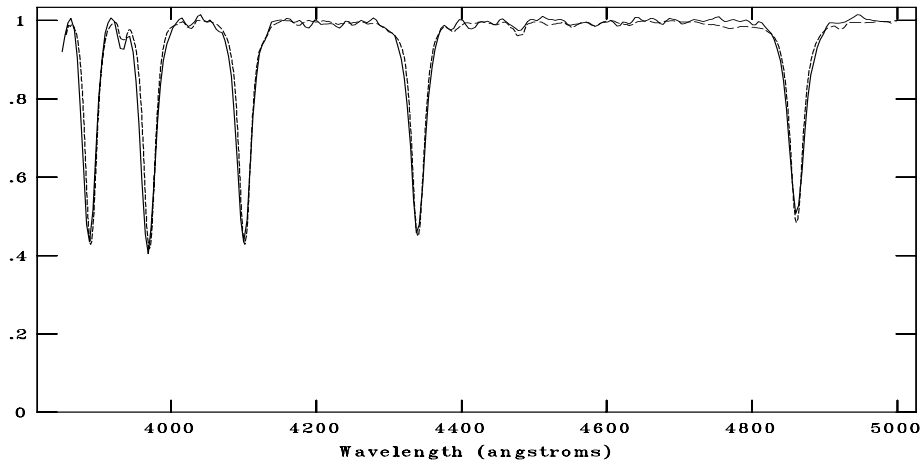
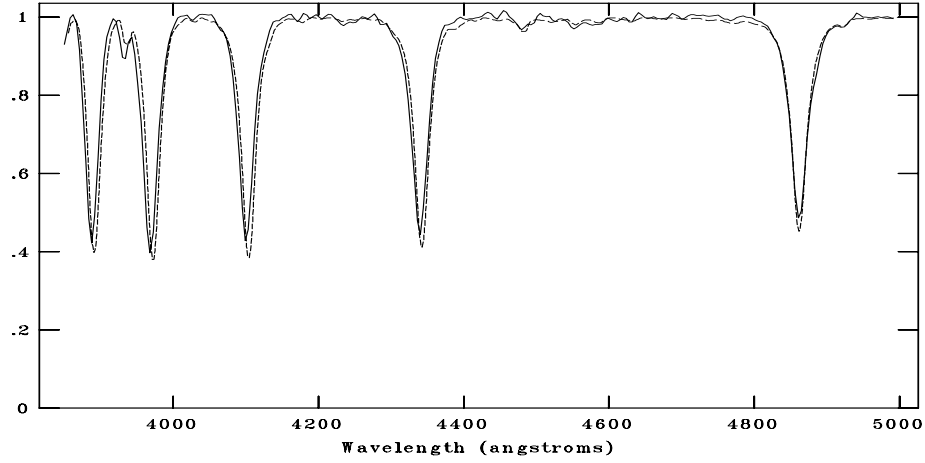
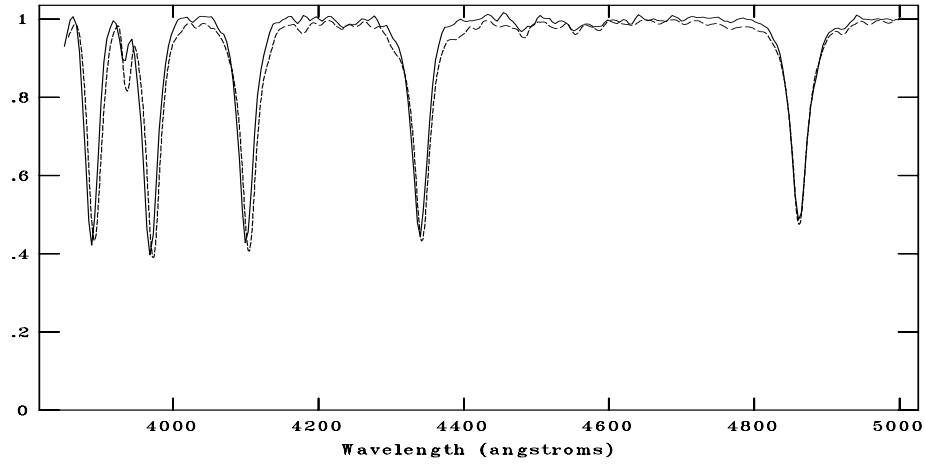


Figure C.130: CAFOS spectrum of 684-032395 compared with A0V, A1V, B9V respectively. The standard spectra are shown with dotted line. The spectral type is assigned as A0V.

NOAO/IRAF V2.16.1 baha@baha-Lenovo-IdeaPad-Y550 Wed 18:37:21 07-Dec-2016
[g160_03A1.fits]: 160_03 110. ap:1 beam:1



NOAO/IRAF V2.16.1 baha@baha-Lenovo-IdeaPad-Y550 Wed 18:37:42 07-Dec-2016
[g160_03A1.fits]: 160_03 110. ap:1 beam:1



NOAO/IRAF V2.16.1 baha@baha-Lenovo-IdeaPad-Y550 Wed 18:38:36 07-Dec-2016
[g160_03A1.fits]: 160_03 110. ap:1 beam:1

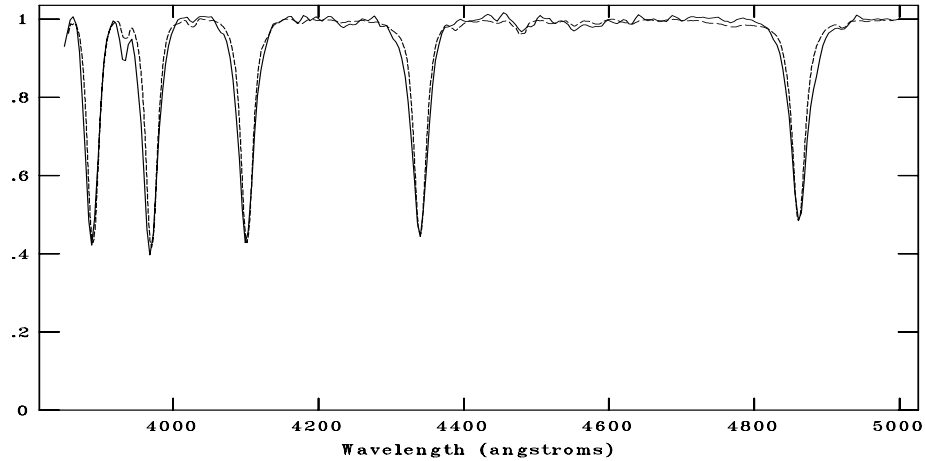


Figure C.131: CAFOS spectrum of 684-032951 compared with A0V, A1V, B9V respectively. The standard spectra are shown with dotted line. The spectral type is assigned as A0V.

C.14 G166.0+4.3

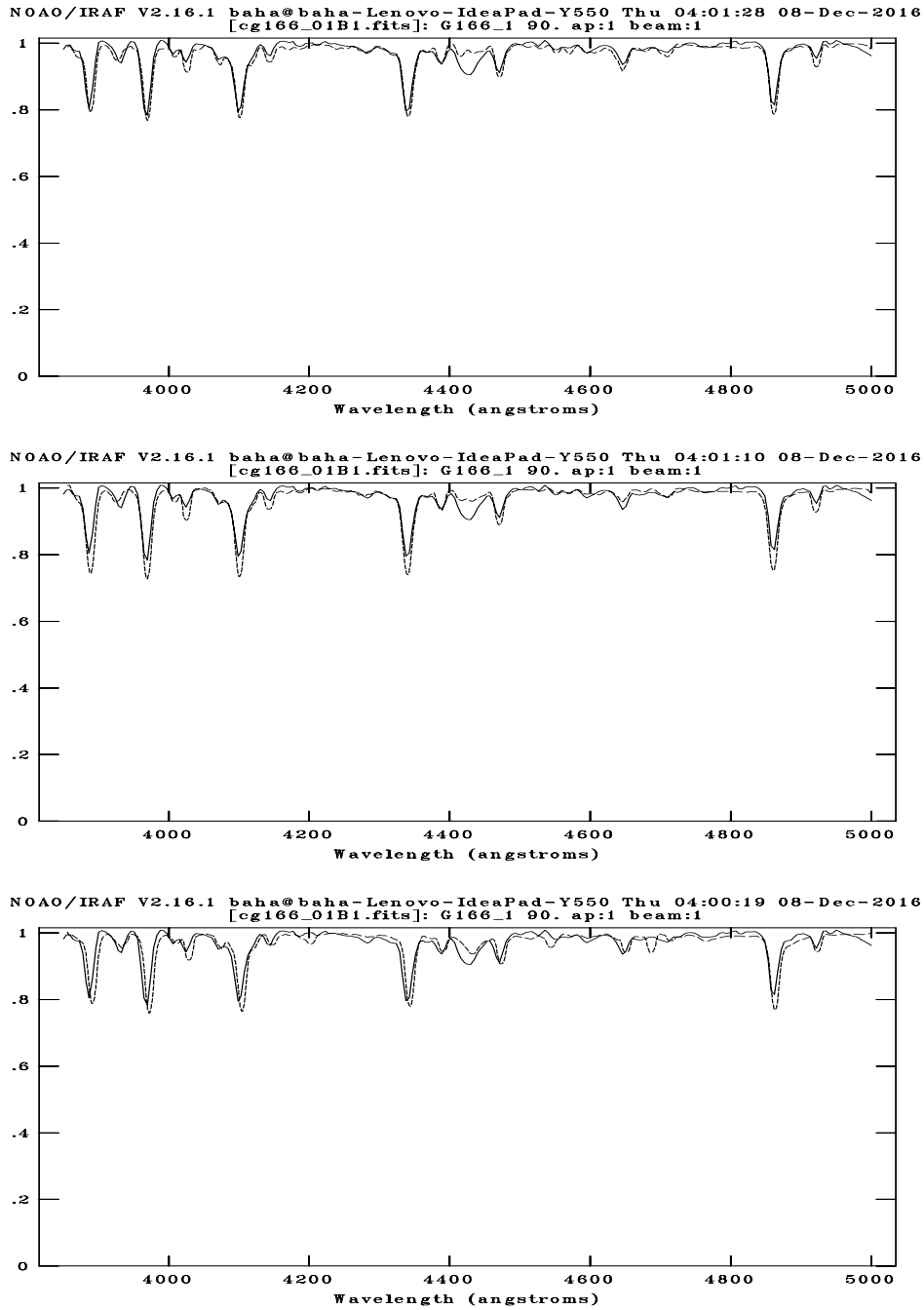
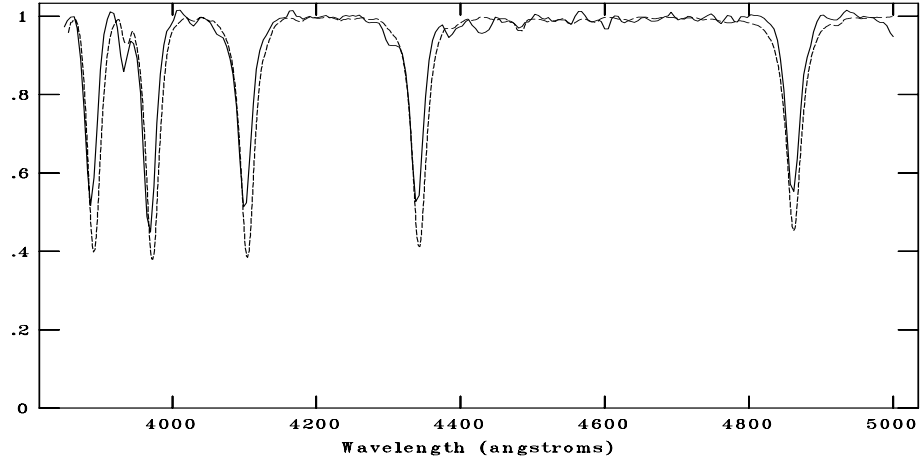
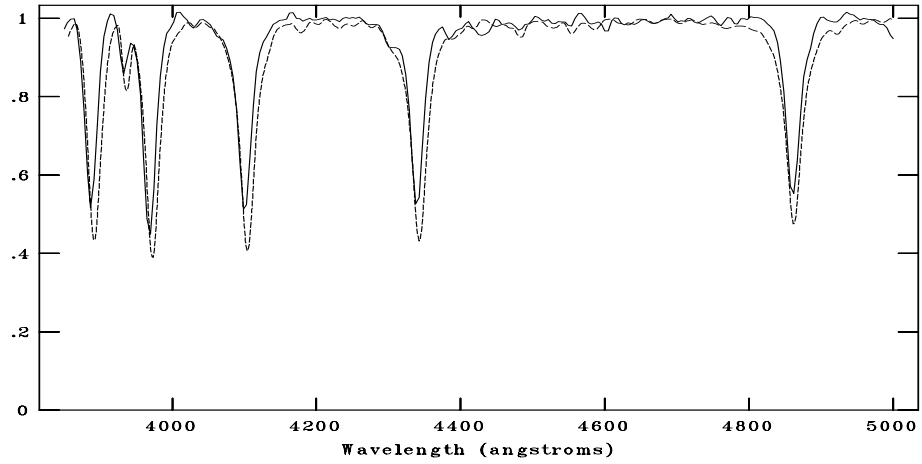


Figure C.132: CAFOS spectrum of 666-037743 compared with B0.5III, B1V, O9V respectively. The standard spectra are shown with dotted line. The spectral type is assigned as B1V.

NOAO/IRAF V2.16.1 baha@baha-Lenovo-IdeaPad-Y550 Thu 14:11:18 08-Dec-2016
[cg166_02A1.fits]: G166_2 960. ap:1 beam:1



NOAO/IRAF V2.16.1 baha@baha-Lenovo-IdeaPad-Y550 Thu 14:15:55 08-Dec-2016
[cg166_02A0.fits]: G166_2 960. ap:1 beam:1



NOAO/IRAF V2.16.1 baha@baha-Lenovo-IdeaPad-Y550 Thu 14:09:54 08-Dec-2016
[cg166_02A1.fits]: G166_2 960. ap:1 beam:1

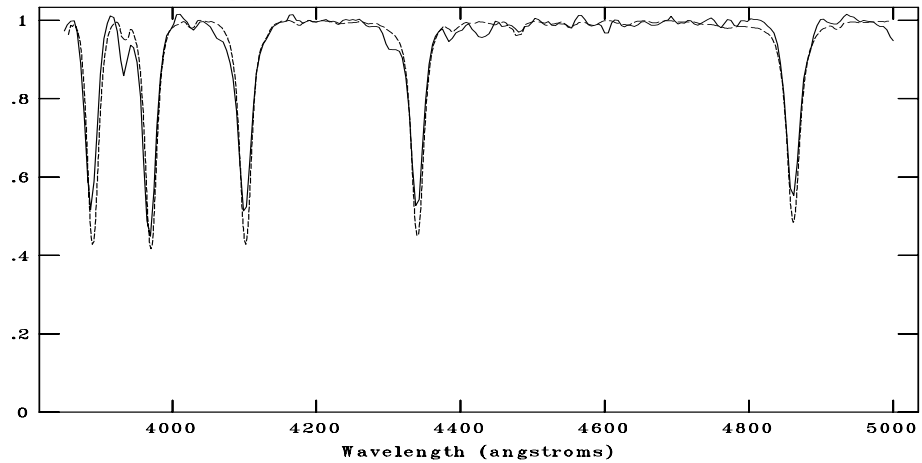
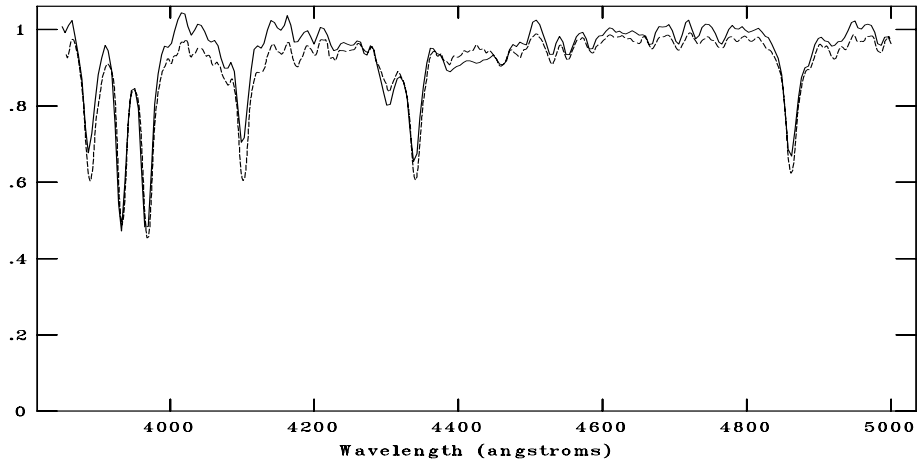
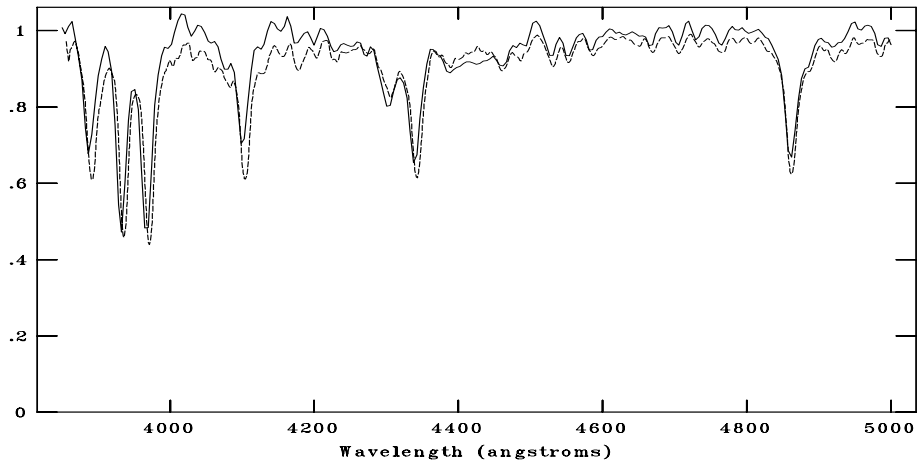


Figure C.133: CAFOS spectrum of 665-037654 compared with A0V, A1V, B9V respectively. The standard spectra are shown with dotted line. The spectral type is assigned as A0V.

NOAO/IRAF V2.16.1 baha@baha-Lenovo-IdeaPad-Y550 Thu 14:16:25 08-Dec-2016
[cg166_03F5.fits]: G166_3 1200. ap:1 beam:1



NOAO/IRAF V2.16.1 baha@baha-Lenovo-IdeaPad-Y550 Thu 14:13:18 08-Dec-2016
[cg166_03F5.fits]: G166_3 1200. ap:1 beam:1



NOAO/IRAF V2.16.1 baha@baha-Lenovo-IdeaPad-Y550 Thu 14:13:46 08-Dec-2016
[cg166_03F5.fits]: G166_3 1200. ap:1 beam:1

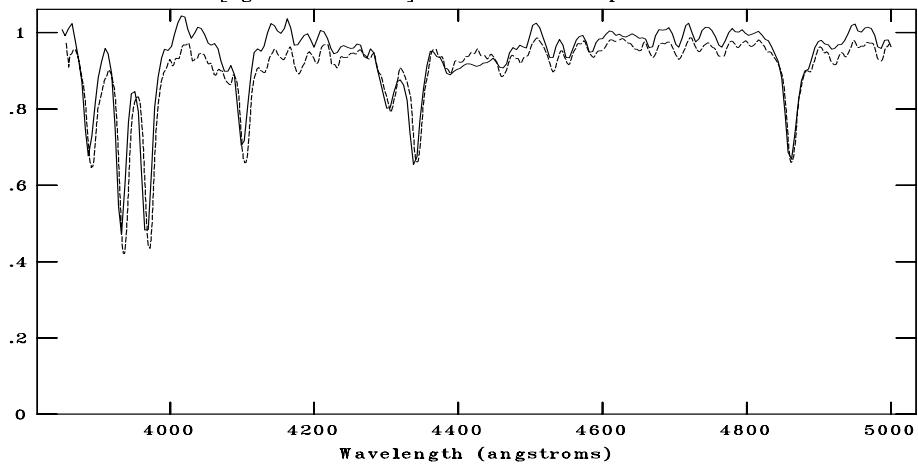
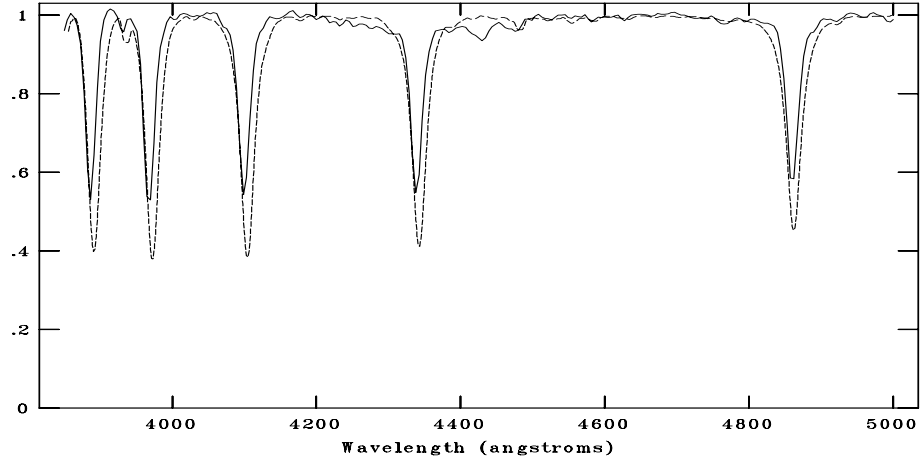
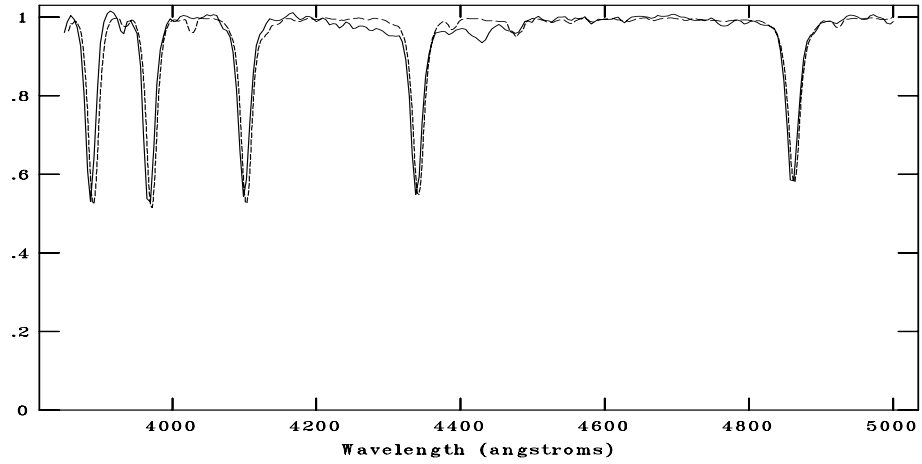


Figure C.134: CAFOS spectrum of 665-037919 compared with F2V, F3V, F5V respectively. The standard spectra are shown with dotted line. The spectral type is assigned as F4V.

NOAO/IRAF V2.16.1 baha@baha-Lenovo-IdeaPad-Y550 Thu 14:18:51 08-Dec-2016
[cg166_04B9.fits]: G166_4 360. ap:1 beam:1



NOAO/IRAF V2.16.1 baha@baha-Lenovo-IdeaPad-Y550 Thu 14:17:56 08-Dec-2016
[cg166_04B9.fits]: G166_4 360. ap:1 beam:1



NOAO/IRAF V2.16.1 baha@baha-Lenovo-IdeaPad-Y550 Thu 14:18:26 08-Dec-2016
[cg166_04B9.fits]: G166_4 360. ap:1 beam:1

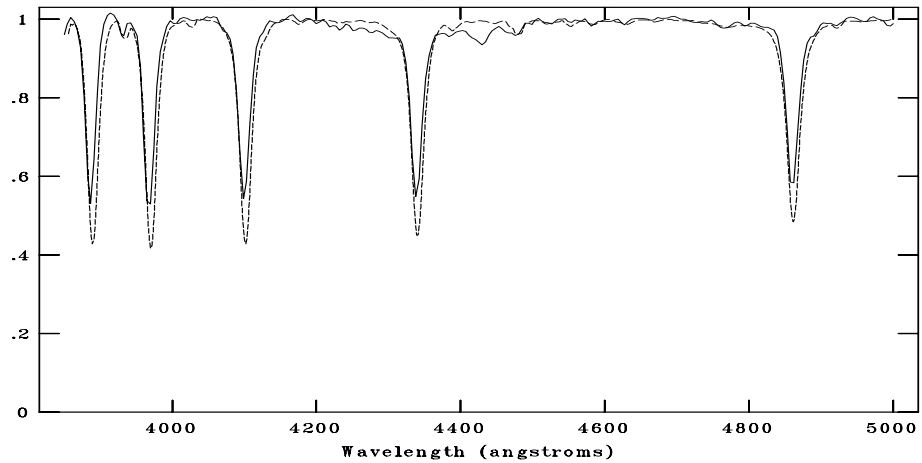
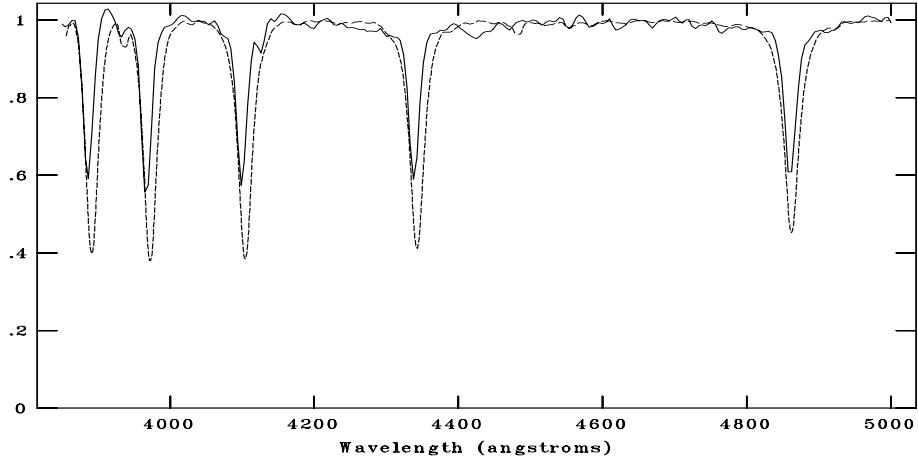
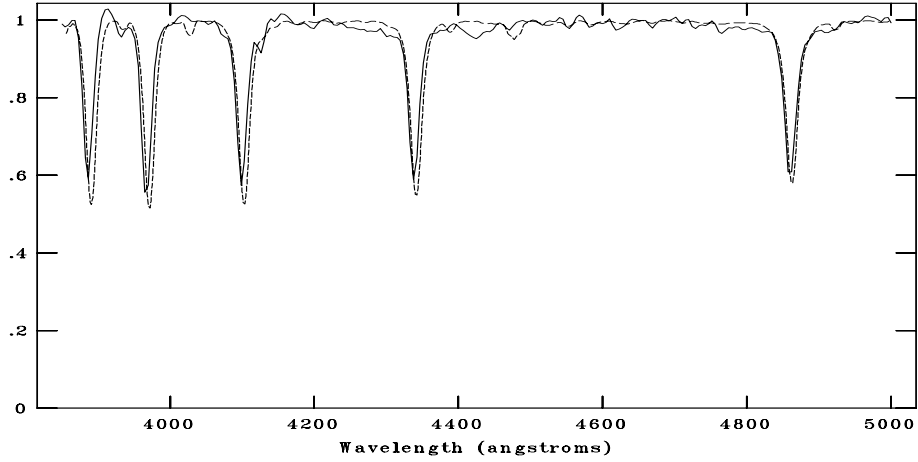


Figure C.135: CAFOS spectrum of 666-037784 compared with A0V, B8V, B9V respectively. The standard spectra are shown with dotted line. The spectral type is assigned as B9V.

NOAO/IRAF V2.16.1 baha@baha-Lenovo-IdeaPad-Y550 Thu 14:19:57 08-Dec-2016
[cg166_05A0.fits]: G166_5 540. ap:1 beam:1



NOAO/IRAF V2.16.1 baha@baha-Lenovo-IdeaPad-Y550 Thu 14:20:25 08-Dec-2016
[cg166_05A0.fits]: G166_5 540. ap:1 beam:1



NOAO/IRAF V2.16.1 baha@baha-Lenovo-IdeaPad-Y550 Thu 14:19:19 08-Dec-2016
[cg166_05A0.fits]: G166_5 540. ap:1 beam:1

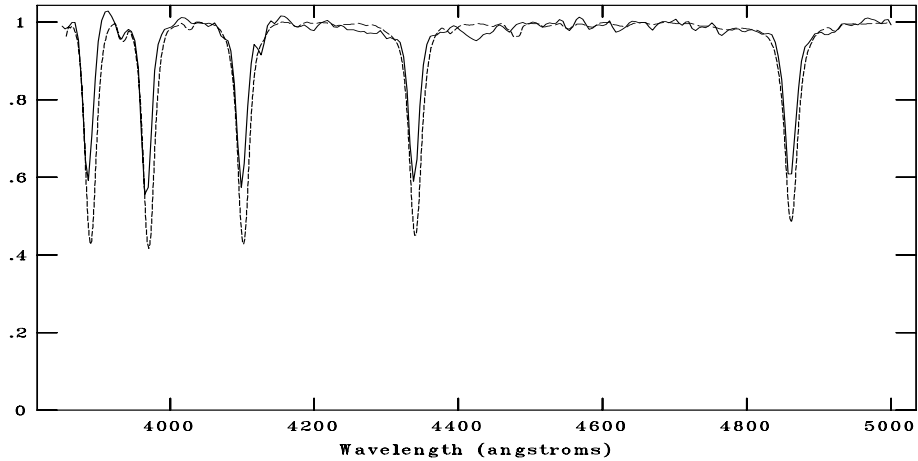
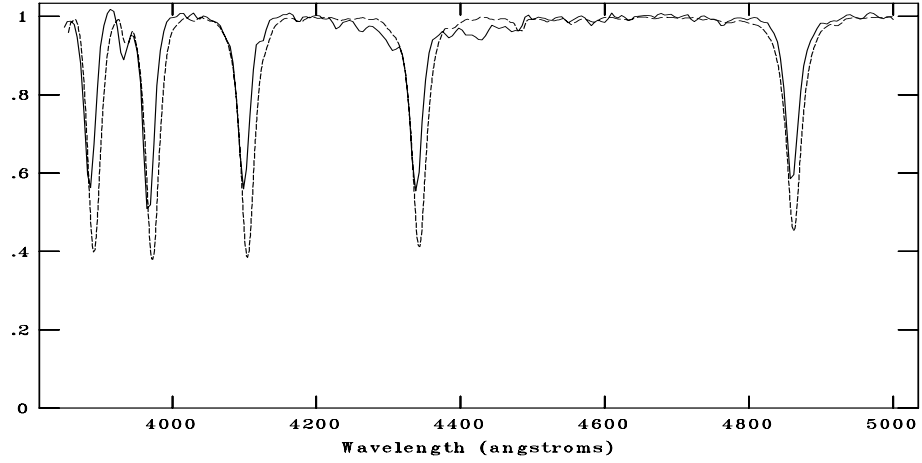
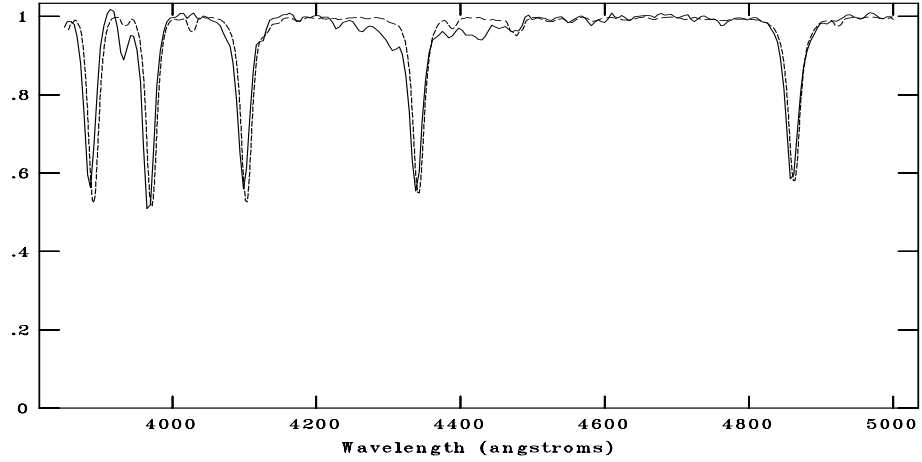


Figure C.136: CAFOS spectrum of 666-037842 compared with A0V, B8V, B9V respectively. The standard spectra are shown with dotted line. The spectral type is assigned as A0V.

NOAO/IRAF V2.16.1 baha@baha-Lenovo-IdeaPad-Y550 Thu 14:22:22 08-Dec-2016
[cg166_06A1.fits]: G166_6 960. ap:1 beam:1



NOAO/IRAF V2.16.1 baha@baha-Lenovo-IdeaPad-Y550 Thu 14:20:55 08-Dec-2016
[cg166_06A1.fits]: G166_6 960. ap:1 beam:1



NOAO/IRAF V2.16.1 baha@baha-Lenovo-IdeaPad-Y550 Thu 14:21:24 08-Dec-2016
[cg166_06A1.fits]: G166_6 960. ap:1 beam:1

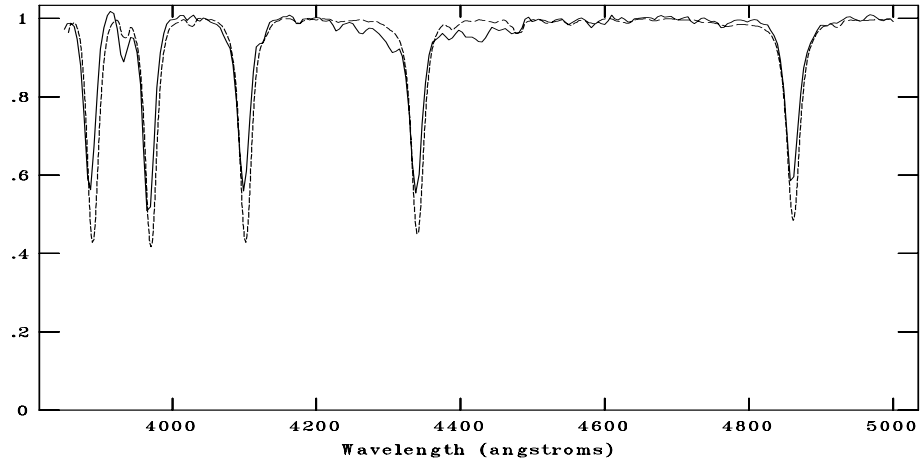
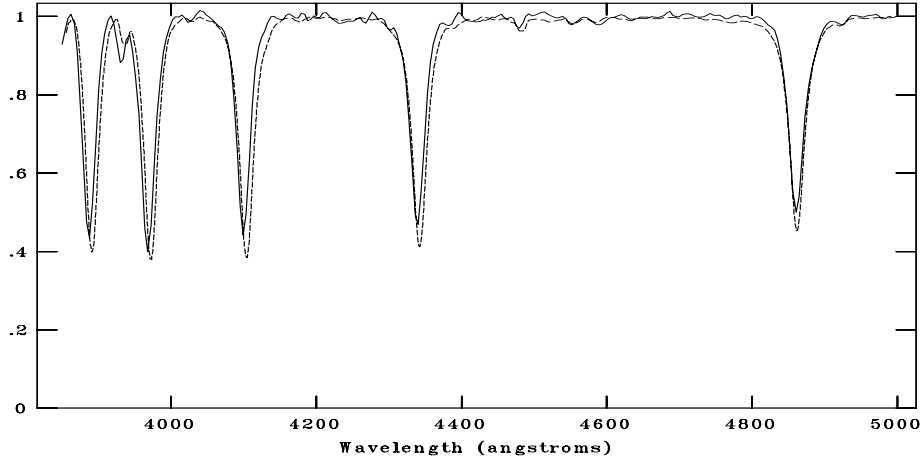
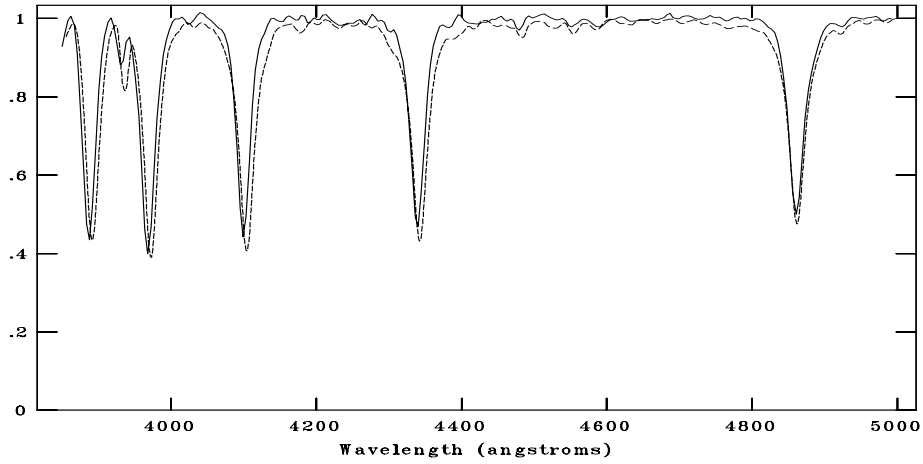


Figure C.137: CAFOS spectrum of 665-037914 compared with A0V, B8V, B9V respectively. The standard spectra are shown with dotted line. The spectral type is assigned as A1V.

NOAO/IRAF V2.16.1 baha@baha-Lenovo-IdeaPad-Y550 Wed 18:39:34 07-Dec-2016
[g166_02A1.fits]: 166_02 240. ap:1 beam:1



NOAO/IRAF V2.16.1 baha@baha-Lenovo-IdeaPad-Y550 Wed 18:51:29 07-Dec-2016
[g166_02A1.fits]: 166_02 240. ap:1 beam:1



NOAO/IRAF V2.16.1 baha@baha-Lenovo-IdeaPad-Y550 Wed 18:50:51 07-Dec-2016
[g166_02A1.fits]: 166_02 240. ap:1 beam:1

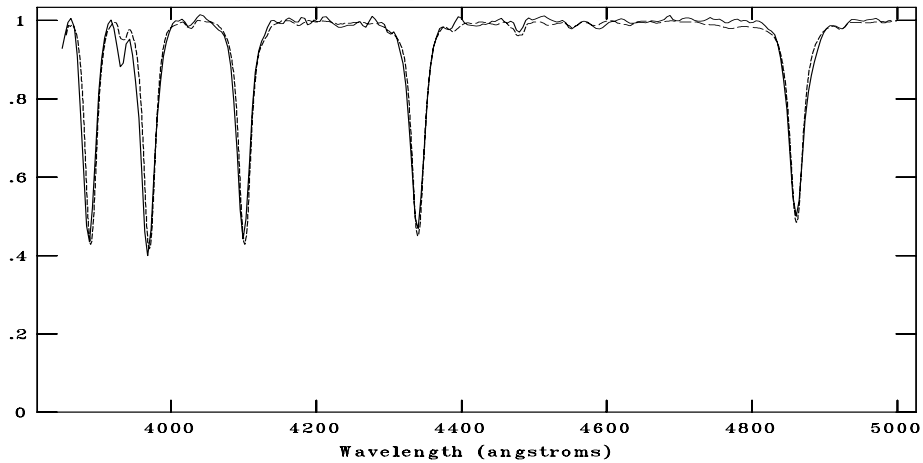
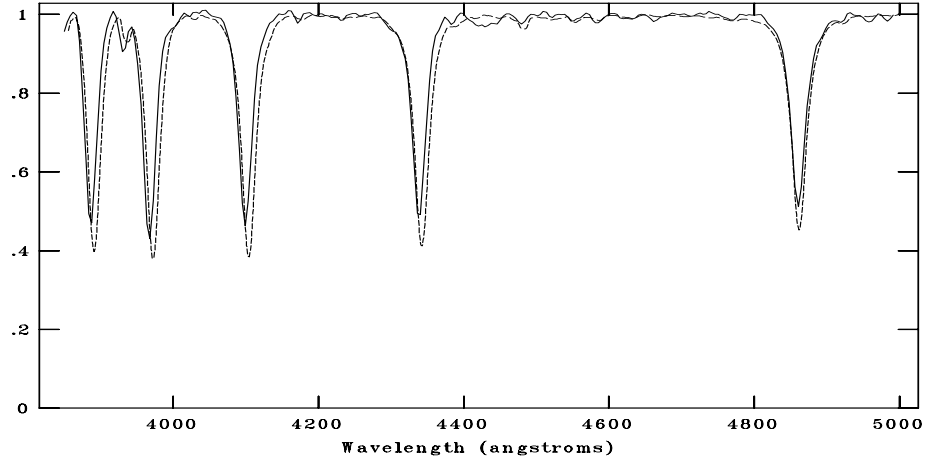
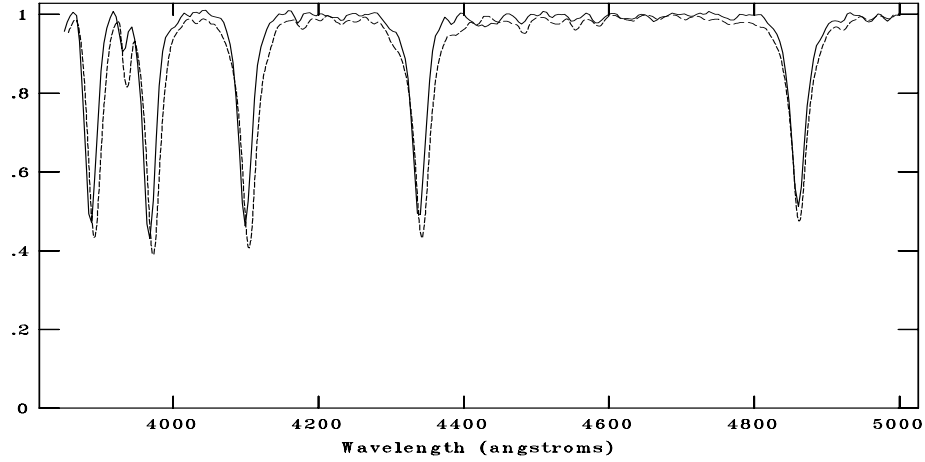


Figure C.138: CAFOS spectrum of 665-037807 compared with A0V, A1V, B9V respectively. The standard spectra are shown with dotted line. The spectral type is assigned as A0V.

NOAO/IRAF V2.16.1 baha@baha-Lenovo-IdeaPad-Y550 Wed 18:53:28 07-Dec-2016
[g166_03A1.fits]: 166_03 260. ap:1 beam:1



NOAO/IRAF V2.16.1 baha@baha-Lenovo-IdeaPad-Y550 Wed 18:53:51 07-Dec-2016
[g166_03A1.fits]: 166_03 260. ap:1 beam:1



NOAO/IRAF V2.16.1 baha@baha-Lenovo-IdeaPad-Y550 Wed 18:52:45 07-Dec-2016
[g166_03A1.fits]: 166_03 260. ap:1 beam:1

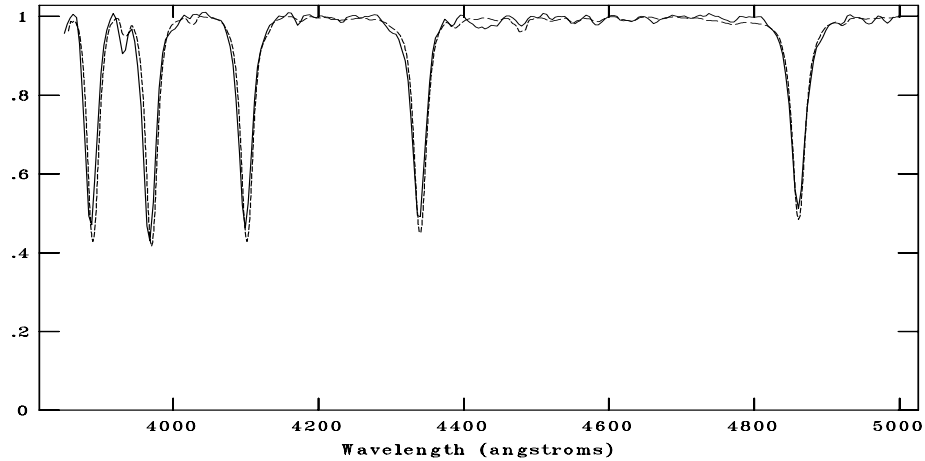
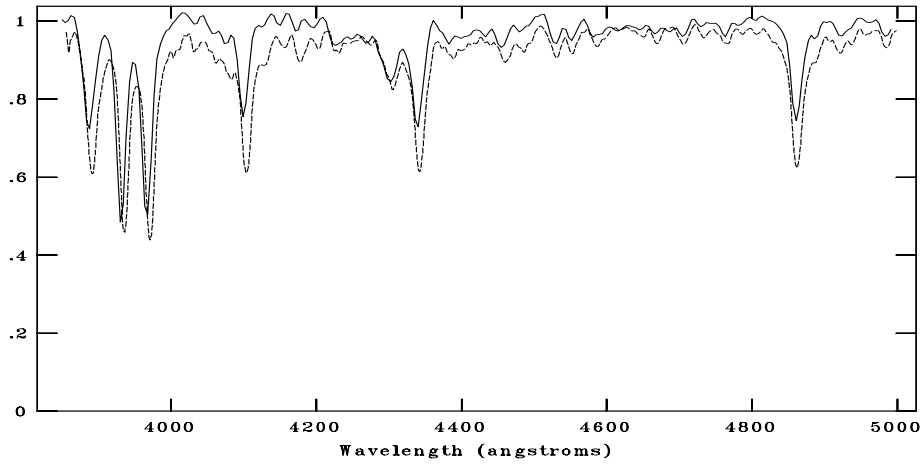
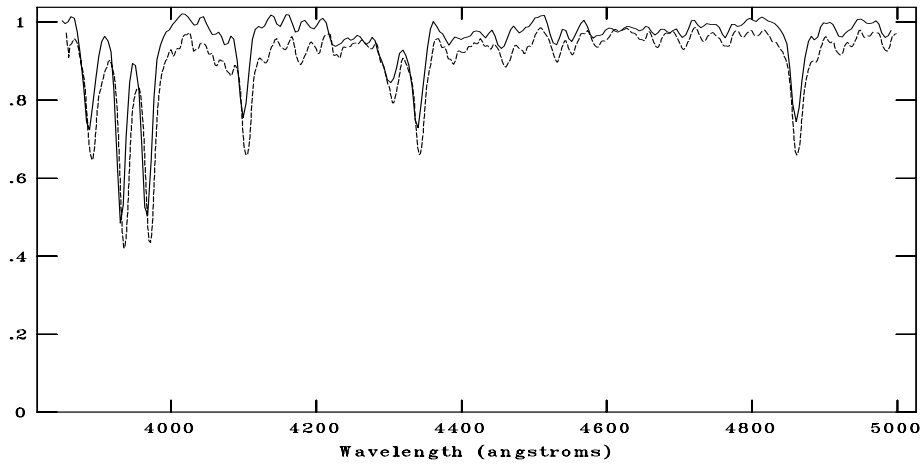


Figure C.139: CAFOS spectrum of 665-037801 compared with A0V, A1V, B9V respectively. The standard spectra are shown with dotted line. The spectral type is assigned as A0V.

NOAO/IRAF V2.16.1 baha@baha-Lenovo-IdeaPad-Y550 Wed 18:55:42 07-Dec-2016
[g166_04F7.fits]: 166_04 360. ap:1 beam:1



NOAO/IRAF V2.16.1 baha@baha-Lenovo-IdeaPad-Y550 Wed 18:54:38 07-Dec-2016
[g166_04F7.fits]: 166_04 360. ap:1 beam:1



NOAO/IRAF V2.16.1 baha@baha-Lenovo-IdeaPad-Y550 Wed 18:55:18 07-Dec-2016
[g166_04F7.fits]: 166_04 360. ap:1 beam:1

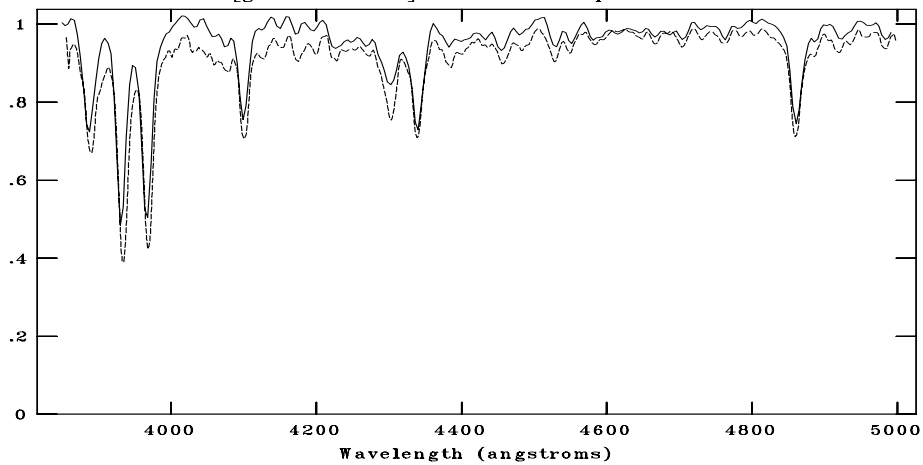
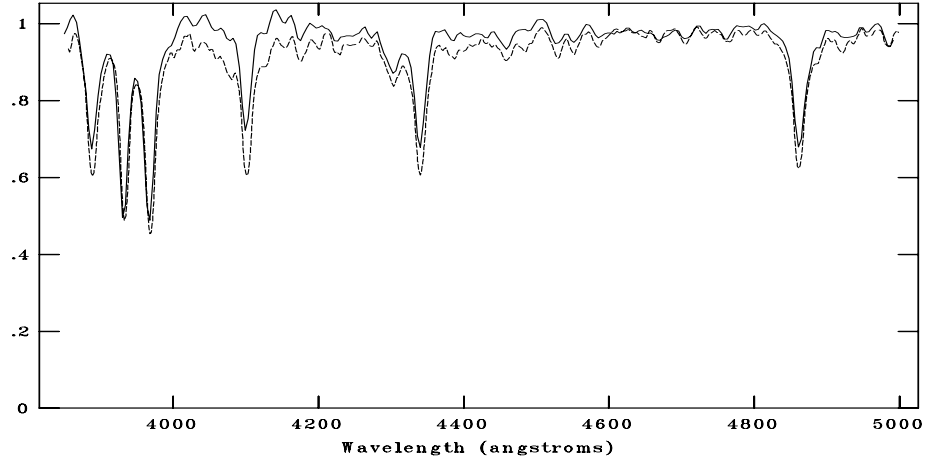
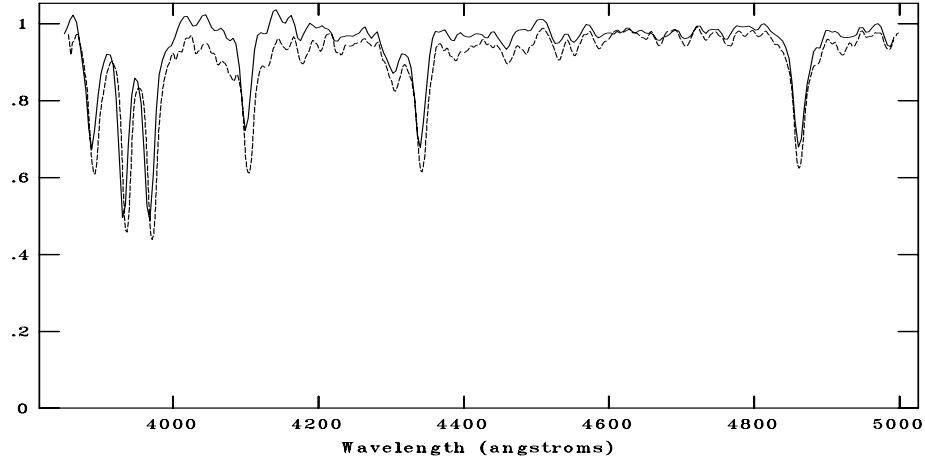


Figure C.140: CAFOS spectrum of 665-037911 compared with F3V, F5V, F6V respectively. The standard spectra are shown with dotted line. The spectral type is assigned as F5V.

NOAO/IRAF V2.16.1 baha@baha-Lenovo-IdeaPad-Y550 Wed 19:00:01 07-Dec-2016
[g166_5.fits]: 166_05 400. ap:1 beam:1



NOAO/IRAF V2.16.1 baha@baha-Lenovo-IdeaPad-Y550 Wed 18:58:41 07-Dec-2016
[g166_5.fits]: 166_05 400. ap:1 beam:1



NOAO/IRAF V2.16.1 baha@baha-Lenovo-IdeaPad-Y550 Wed 18:59:42 07-Dec-2016
[g166_5.fits]: 166_05 400. ap:1 beam:1

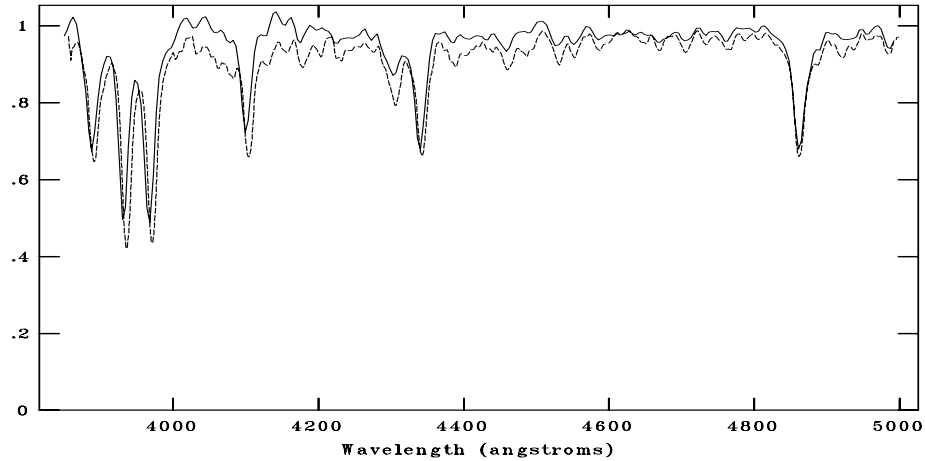
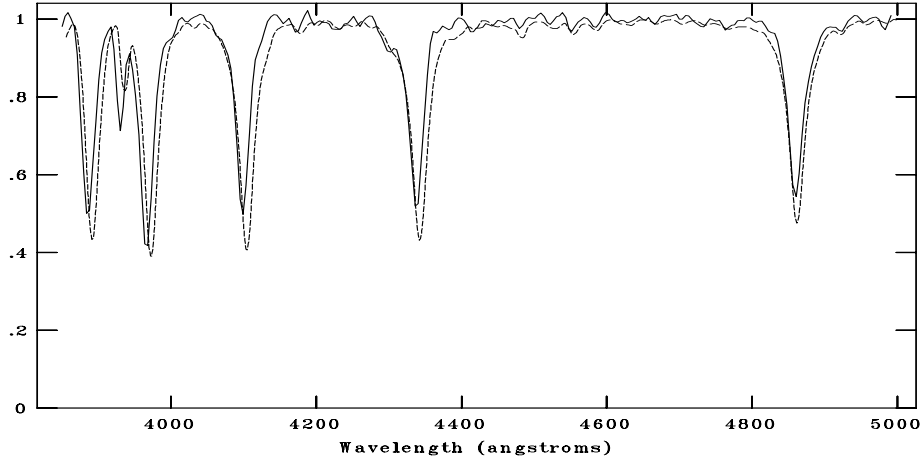
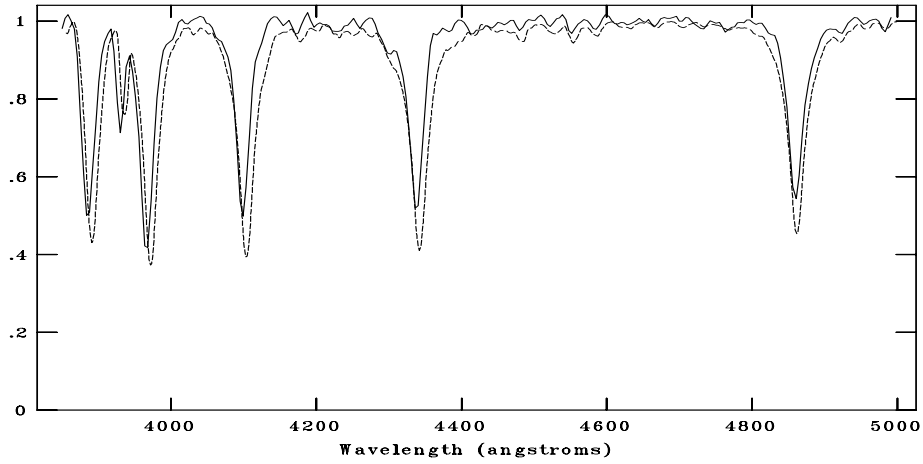


Figure C.141: CAFOS spectrum of 666-037753 compared with F2V, F3V, F5V respectively. The standard spectra are shown with dotted line. The spectral type is assigned as F3V.

NOAO/IRAF V2.16.1 baha@baha-Lenovo-IdeaPad-Y550 Wed 19:01:58 07-Dec-2016
[g166_06A3.fits]: 166_06 450. ap:1 beam:1



NOAO/IRAF V2.16.1 baha@baha-Lenovo-IdeaPad-Y550 Wed 19:01:29 07-Dec-2016
[g166_06A3.fits]: 166_06 450. ap:1 beam:1



NOAO/IRAF V2.16.1 baha@baha-Lenovo-IdeaPad-Y550 Wed 19:03:02 07-Dec-2016
[g166_06A3.fits]: 166_06 450. ap:1 beam:1

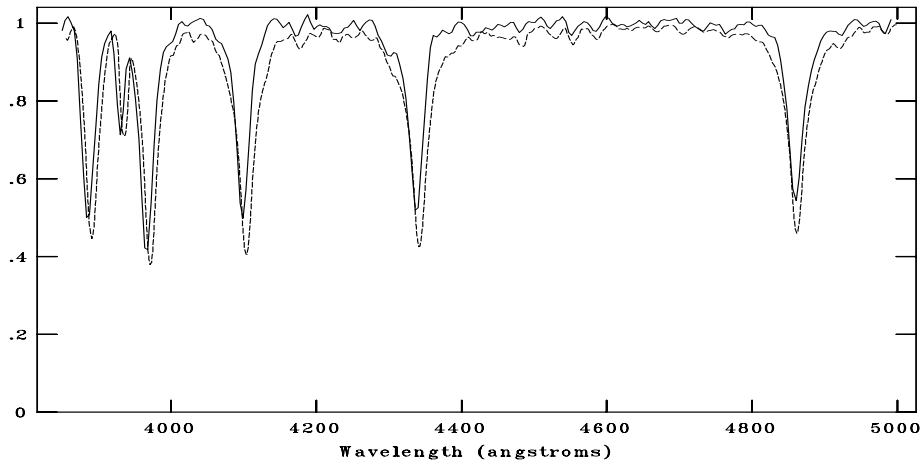
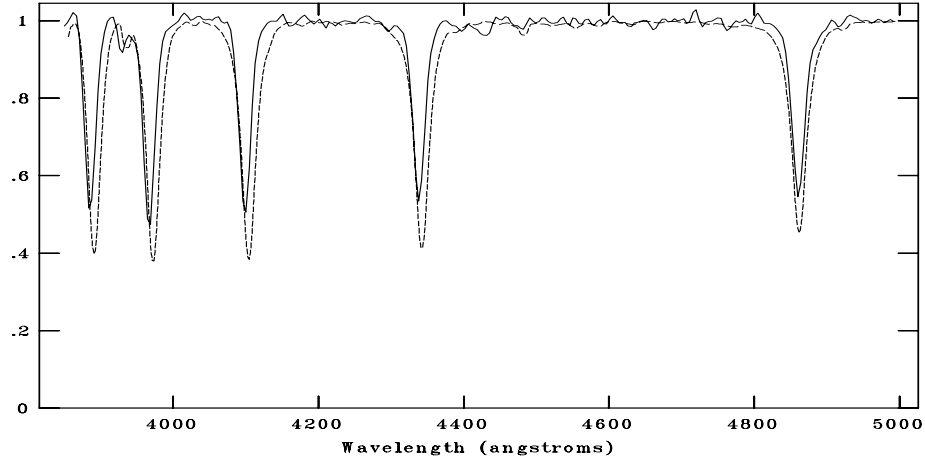
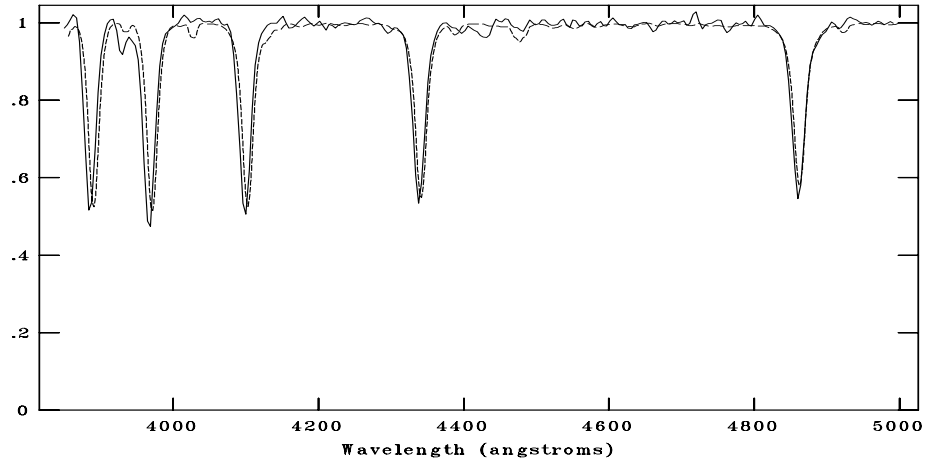


Figure C.142: CAFOS spectrum of 665-037712 compared with A1V, A3V, A5V respectively. The standard spectra are shown with dotted line. The spectral type is assigned as A3V.

NOAO/IRAF V2.16.1 baha@baha-Lenovo-IdeaPad-Y550 Wed 19:05:22 07-Dec-2016
[g166_07B9.fits]: 166_07 520. ap:1 beam:1



NOAO/IRAF V2.16.1 baha@baha-Lenovo-IdeaPad-Y550 Wed 19:03:43 07-Dec-2016
[g166_07B9.fits]: 166_07 520. ap:1 beam:1



NOAO/IRAF V2.16.1 baha@baha-Lenovo-IdeaPad-Y550 Wed 19:04:14 07-Dec-2016
[g166_07B9.fits]: 166_07 520. ap:1 beam:1

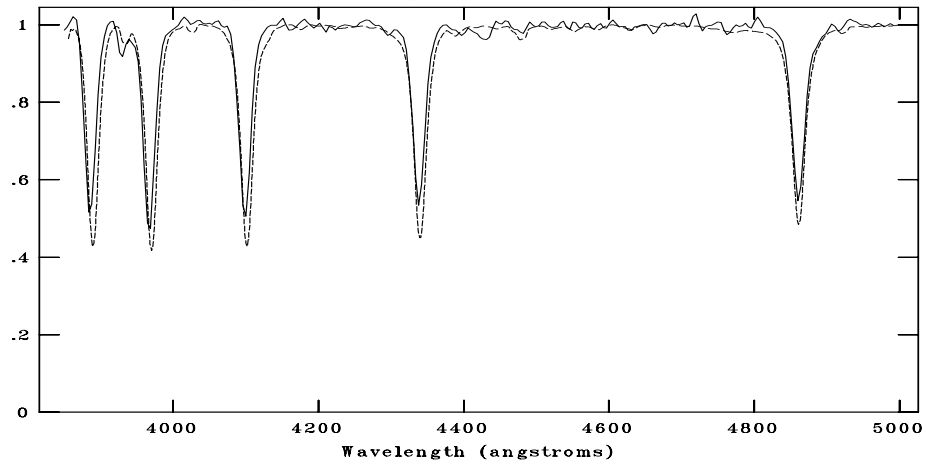
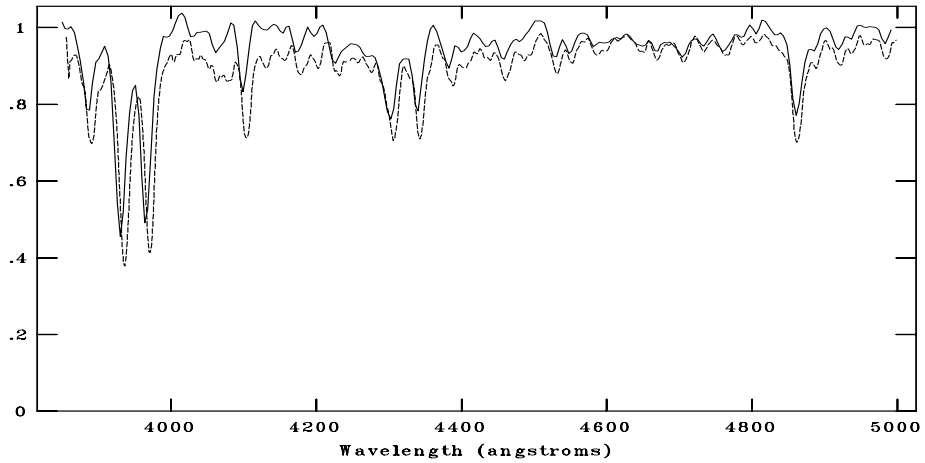


Figure C.143: CAFOS spectrum of 665-03773 compared with A0V, B8V, B9V respectively. The standard spectra are shown with dotted line. The spectral type is assigned as B9V.

NOAO/IRAF V2.16.1 baha@baha-Lenovo-IdeaPad-Y550 Wed 19:07:20 07-Dec-2016
[g166_08G2.fits]: 166_08 640. ap:1 beam:1



NOAO/IRAF V2.16.1 baha@baha-Lenovo-IdeaPad-Y550 Wed 19:09:47 07-Dec-2016
[g166_08G2.fits]: 166_08 640. ap:1 beam:1

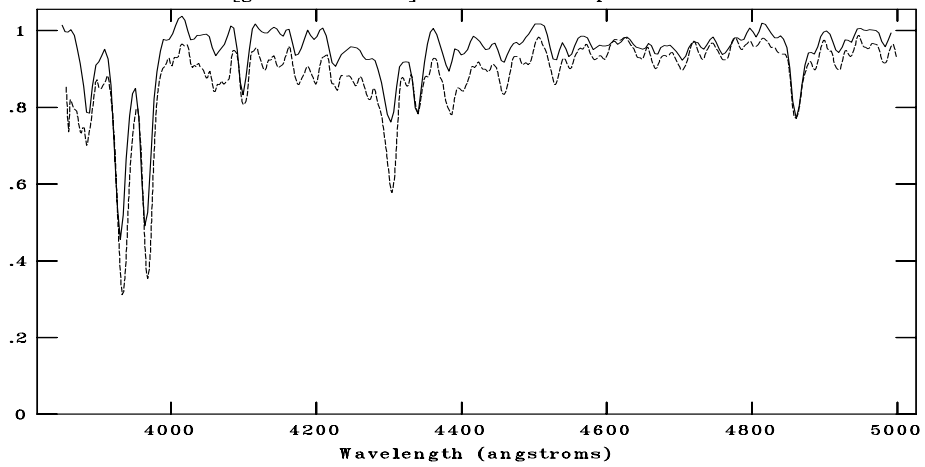
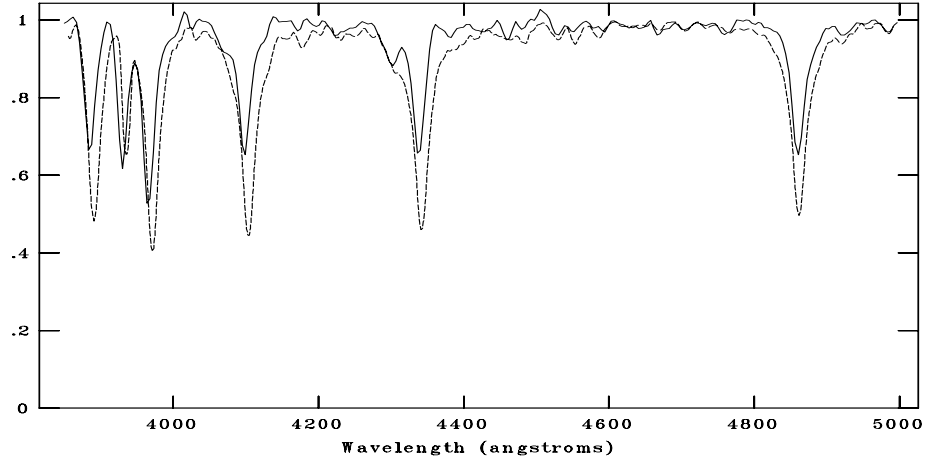
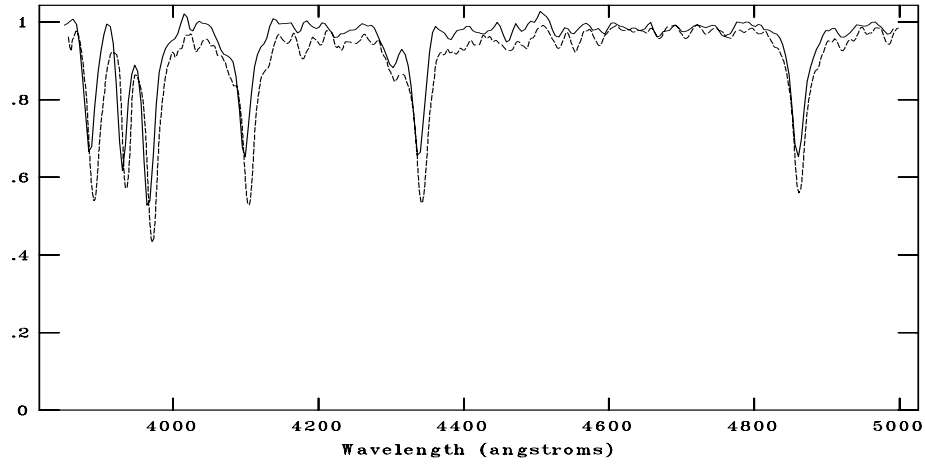


Figure C.144: CAFOS spectrum of 666-037857 compared with F8V and G2V respectively. The standard spectra are shown with dotted line. The spectral type is assigned as G2V.

NOAO/IRAF V2.16.1 baha@baha-Lenovo-IdeaPad-Y550 Wed 19:11:34 07-Dec-2016
[g166_09A7.fits]: 166_09 700. ap:1 beam:1



NOAO/IRAF V2.16.1 baha@baha-Lenovo-IdeaPad-Y550 Wed 19:10:28 07-Dec-2016
[g166_09A7.fits]: 166_09 700. ap:1 beam:1



NOAO/IRAF V2.16.1 baha@baha-Lenovo-IdeaPad-Y550 Wed 19:11:00 07-Dec-2016
[g166_09A7.fits]: 166_09 700. ap:1 beam:1

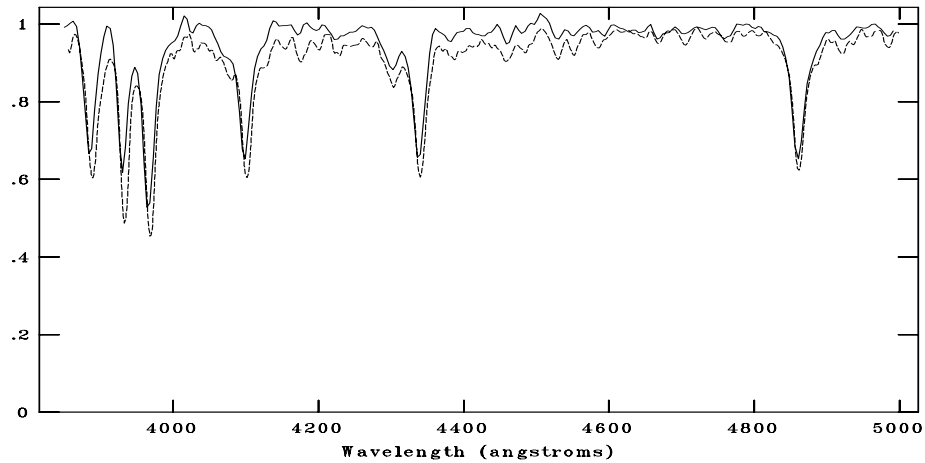
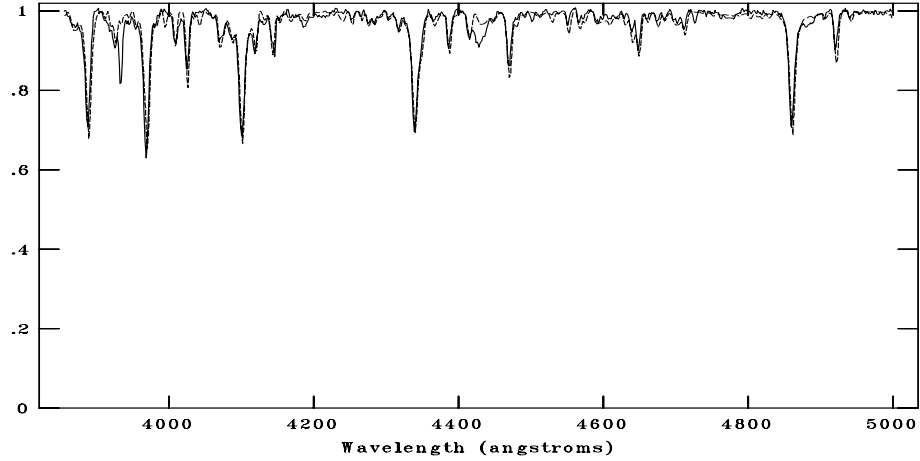
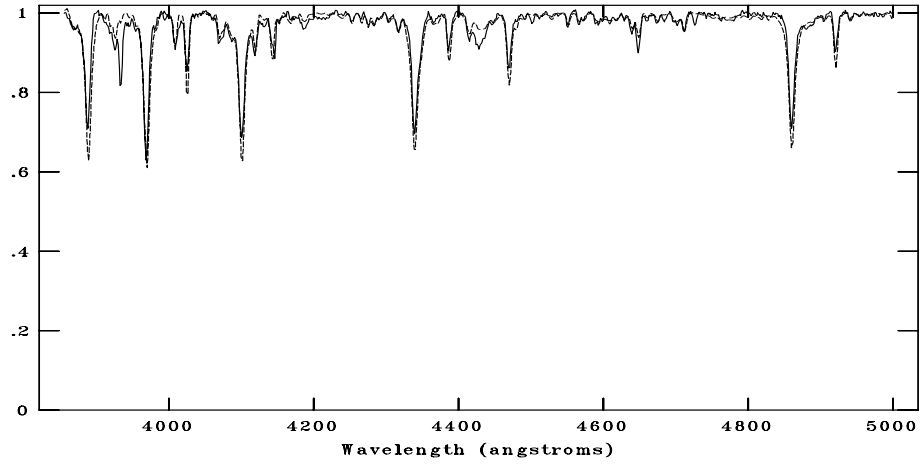


Figure C.145: CAFOS spectrum of 590-020323 compared with A7V, F0V, F2V respectively. The standard spectra are shown with dotted line. The spectral type is assigned as A9V.

NOAO/IRAF V2.16.1 baha@baha-Lenovo-IdeaPad-Y550 Tue 21:48:48 03-Jan-2017
[g166n.fits]: g78_1 600. ap:1 beam:1



NOAO/IRAF V2.16.1 baha@baha-Lenovo-IdeaPad-Y550 Tue 21:51:28 03-Jan-2017
[g166n.fits]: g78_1 600. ap:1 beam:1



NOAO/IRAF V2.16.1 baha@baha-Lenovo-IdeaPad-Y550 Tue 21:51:52 03-Jan-2017
[g166n.fits]: g78_1 600. ap:1 beam:1

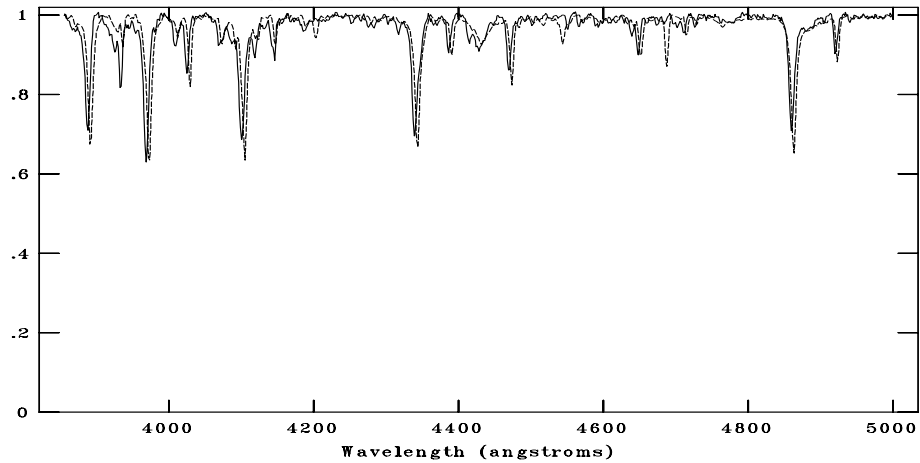


Figure C.146: TFOSC spectrum of 666-037743 compared with B0.5III, B1V, O9V respectively. The standard spectra are shown with dotted line. The spectral type is assigned as B0.5V.

C.15 G180.0-1.7

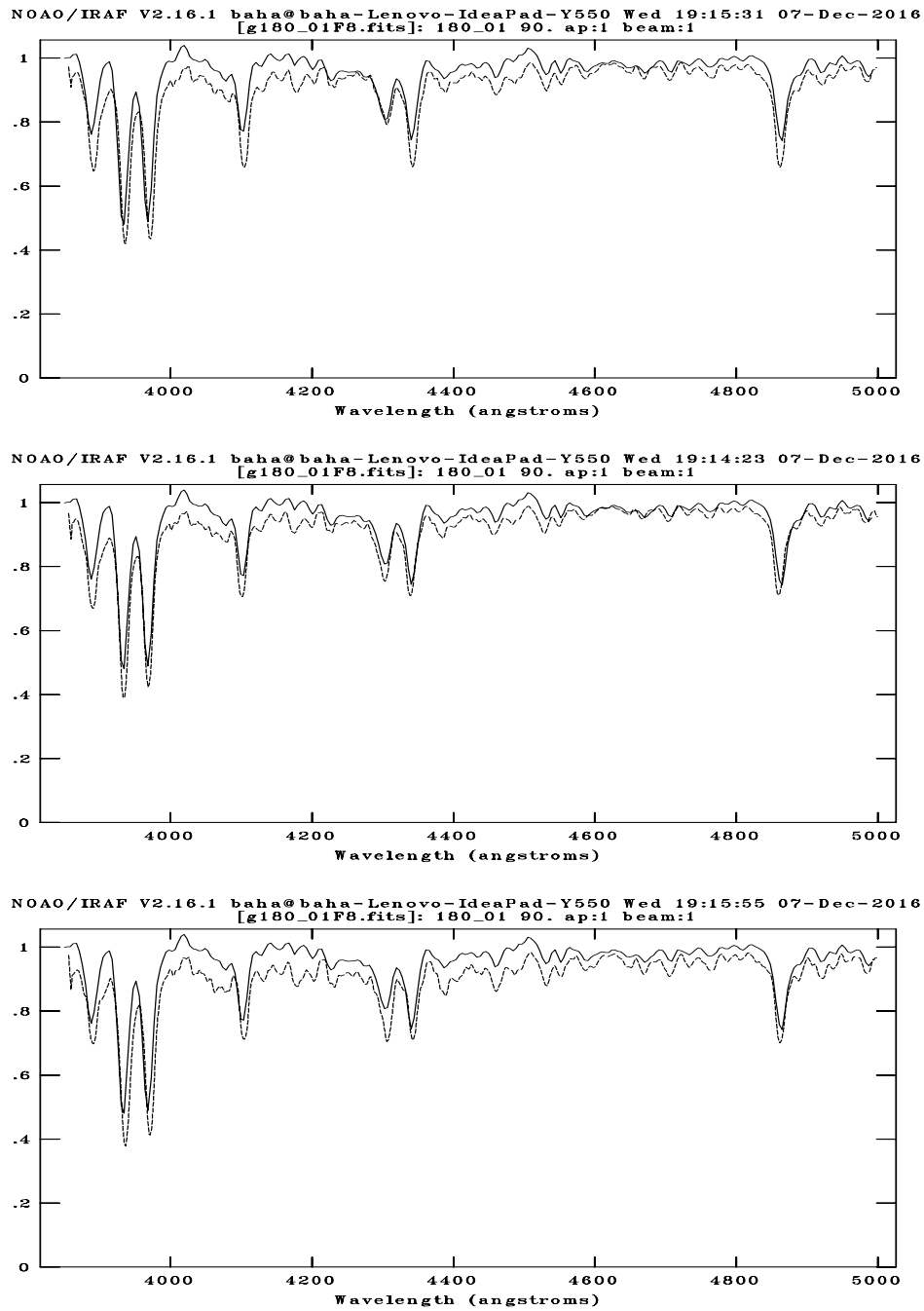
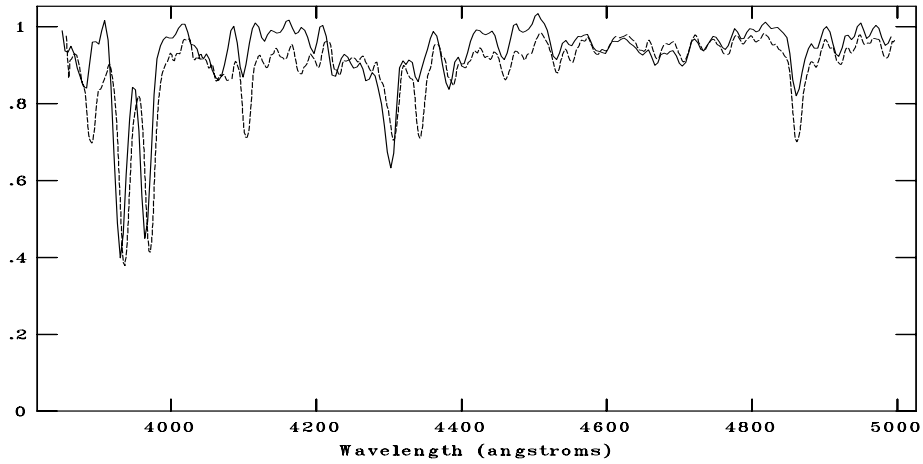
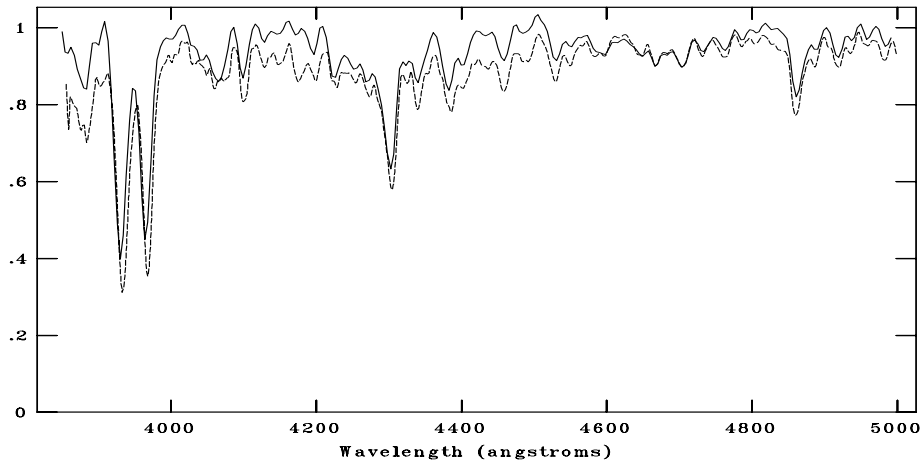


Figure C.147: CAFOS spectrum of compared with F5V, F6V, F8V respectively. The standard spectra are shown with dotted line. The spectral type is assigned as F6V.

NOAO/IRAF V2.16.1 baha@baha-Lenovo-IdeaPad-Y550 Wed 19:19:07 07-Dec-2016
[g180_02K.fits]: 180_02 160. ap:1 beam:1



NOAO/IRAF V2.16.1 baha@baha-Lenovo-IdeaPad-Y550 Wed 19:18:45 07-Dec-2016
[g180_02K.fits]: 180_02 160. ap:1 beam:1



NOAO/IRAF V2.16.1 baha@baha-Lenovo-IdeaPad-Y550 Wed 19:17:00 07-Dec-2016
[g180_02K.fits]: 180_02 160. ap:1 beam:1

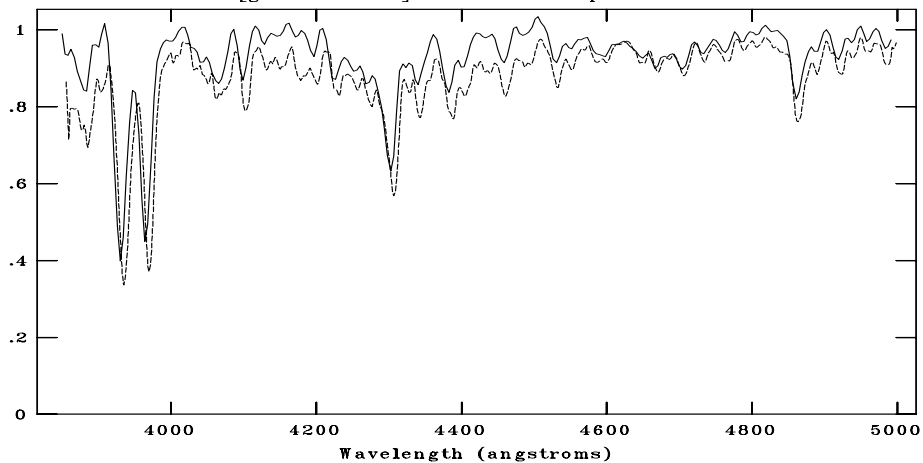
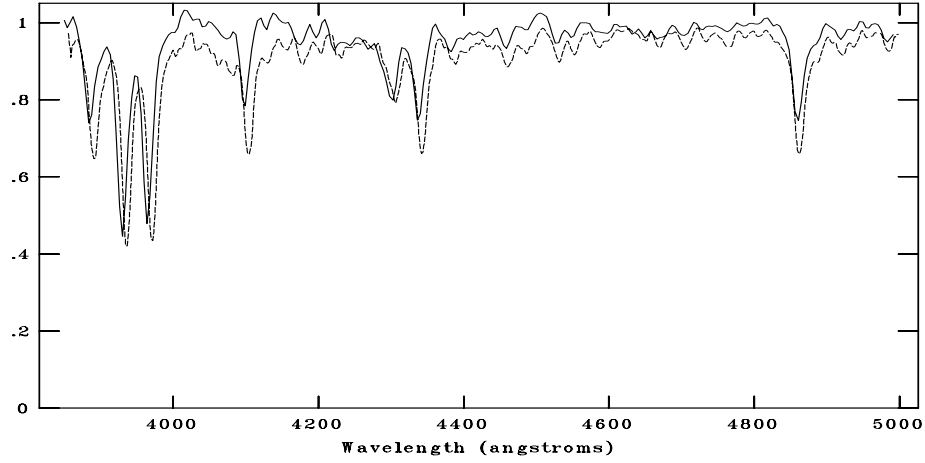
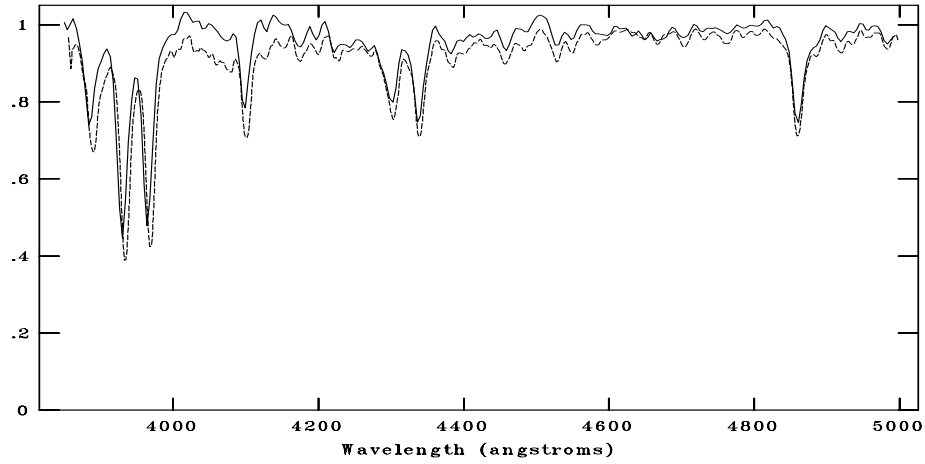


Figure C.148: CAFOS spectrum of 590-020251 compared with F8V, G2V, G3V respectively. The standard spectra are shown with dotted line. The spectral type is assigned as G2V.

NOAO/IRAF V2.16.1 baha@baha-Lenovo-IdeaPad-Y550 Wed 19:21:29 07-Dec-2016
[g180_03F8.fits]: 180_03 160. ap:1 beam:1



NOAO/IRAF V2.16.1 baha@baha-Lenovo-IdeaPad-Y550 Wed 19:19:54 07-Dec-2016
[g180_03F8.fits]: 180_03 160. ap:1 beam:1



NOAO/IRAF V2.16.1 baha@baha-Lenovo-IdeaPad-Y550 Wed 19:20:45 07-Dec-2016
[g180_03F8.fits]: 180_03 160. ap:1 beam:1

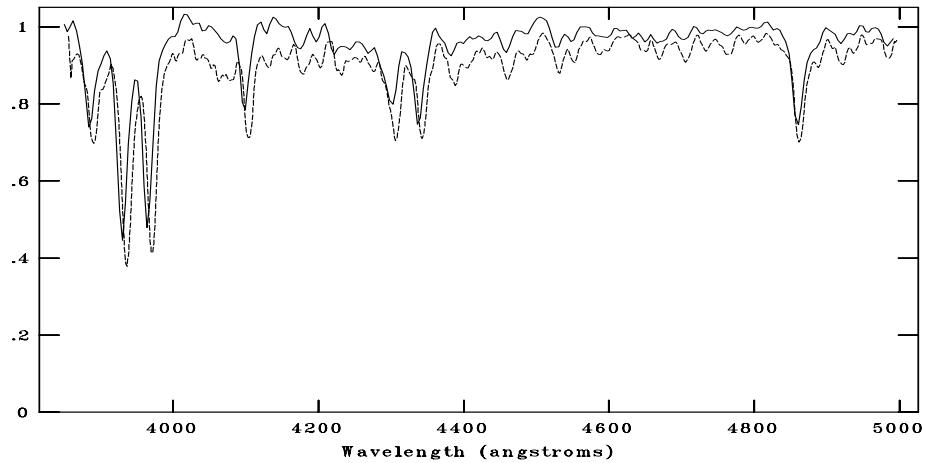
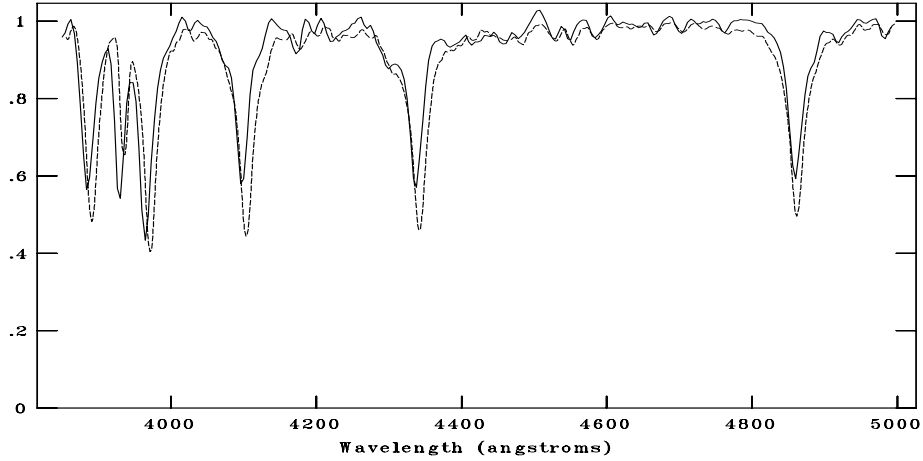
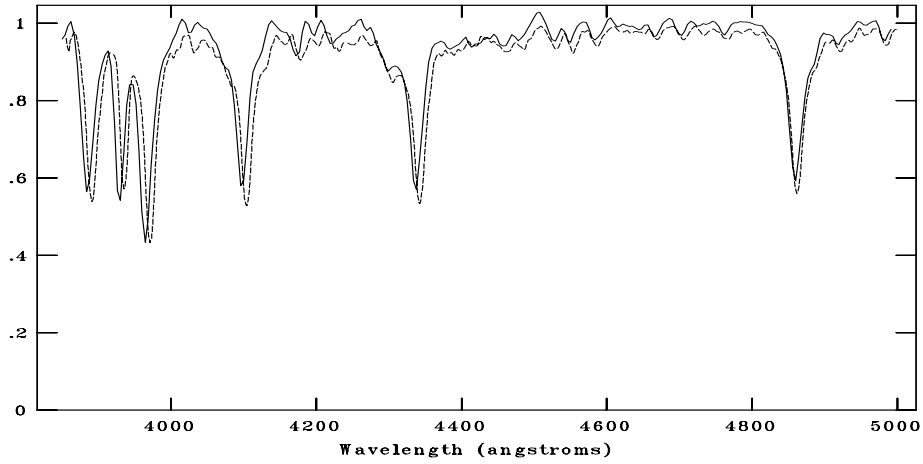


Figure C.149: CAFOS spectrum of 591-020517 compared with F5V, F6V, F8V respectively. The standard spectra are shown with dotted line. The spectral type is assigned as F7V.

NOAO/IRAF V2.16.1 baha@baha-Lenovo-IdeaPad-Y550 Wed 19:22:29 07-Dec-2016
[g180_04A8.fits]: 180_04 180. ap:1 beam:1



NOAO/IRAF V2.16.1 baha@baha-Lenovo-IdeaPad-Y550 Wed 19:22:55 07-Dec-2016
[g180_04A8.fits]: 180_04 180. ap:1 beam:1



NOAO/IRAF V2.16.1 baha@baha-Lenovo-IdeaPad-Y550 Wed 19:23:38 07-Dec-2016
[g180_04A8.fits]: 180_04 180. ap:1 beam:1

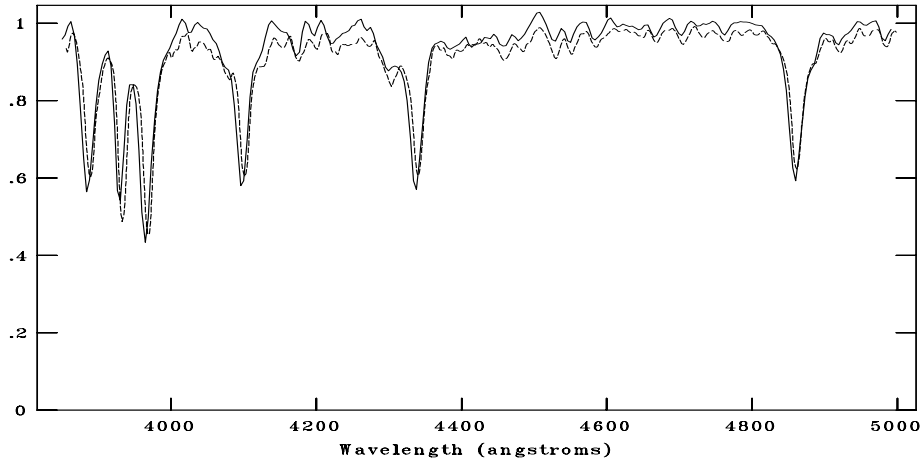
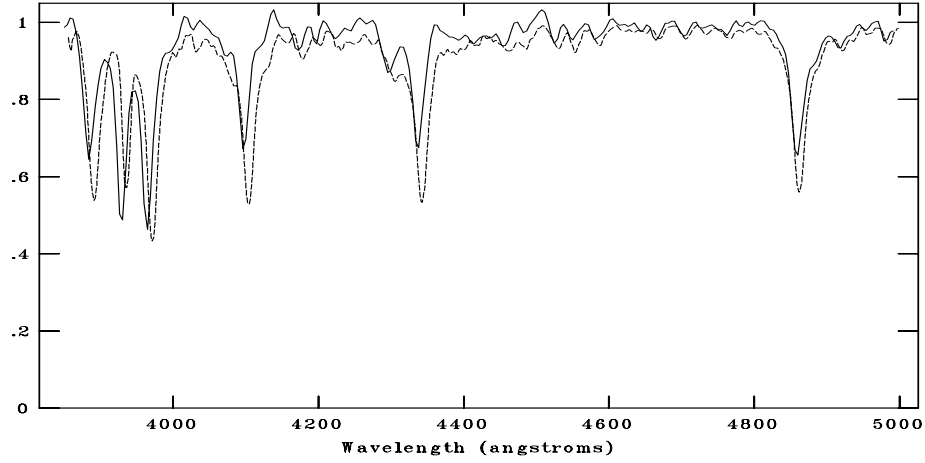
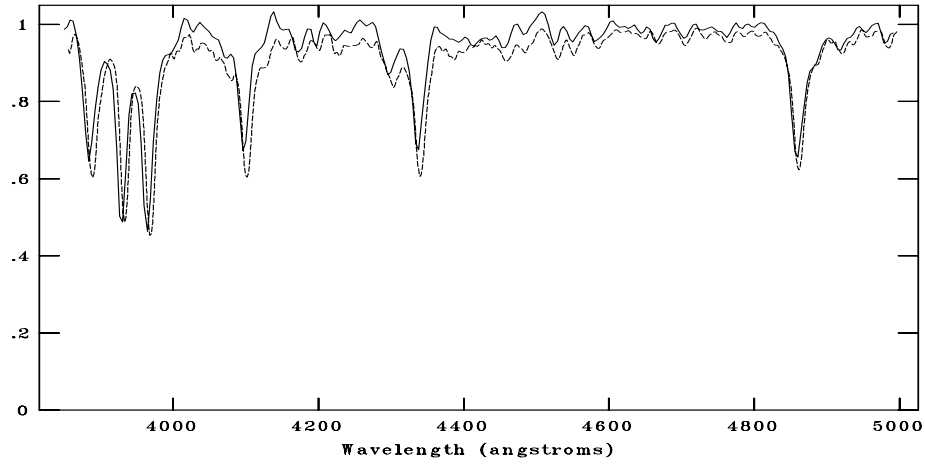


Figure C.150: CAFOS spectrum of 587-019374 compared with A7V, F0V, F2V respectively. The standard spectra are shown with dotted line. The spectral type is assigned as F0V.

NOAO/IRAF V2.16.1 baha@baha-Lenovo-IdeaPad-Y550 Wed 19:24:28 07-Dec-2016
[g180_05F2.fits]: 180_05 180. ap:1 beam:1



NOAO/IRAF V2.16.1 baha@baha-Lenovo-IdeaPad-Y550 Wed 19:24:48 07-Dec-2016
[g180_05F2.fits]: 180_05 180. ap:1 beam:1



NOAO/IRAF V2.16.1 baha@baha-Lenovo-IdeaPad-Y550 Wed 19:25:13 07-Dec-2016
[g180_05F2.fits]: 180_05 180. ap:1 beam:1

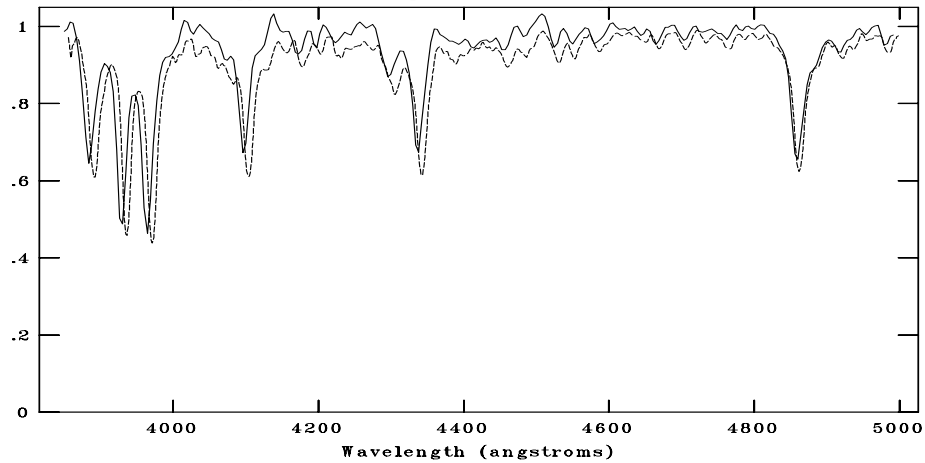
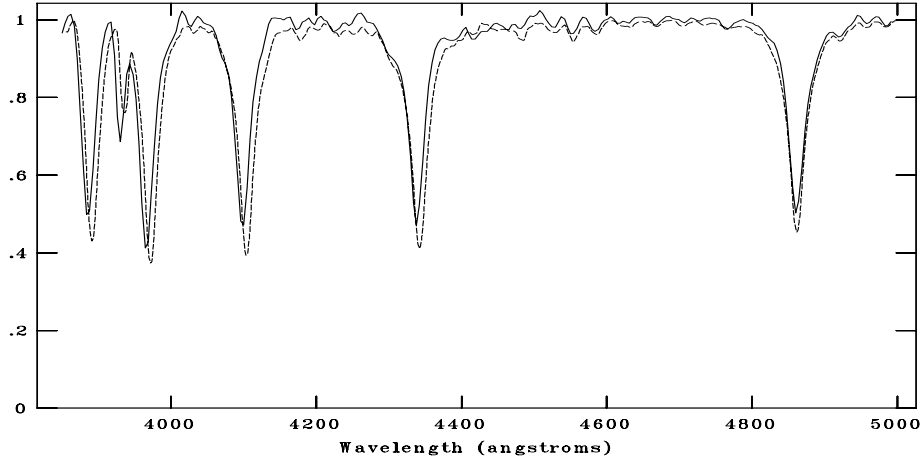
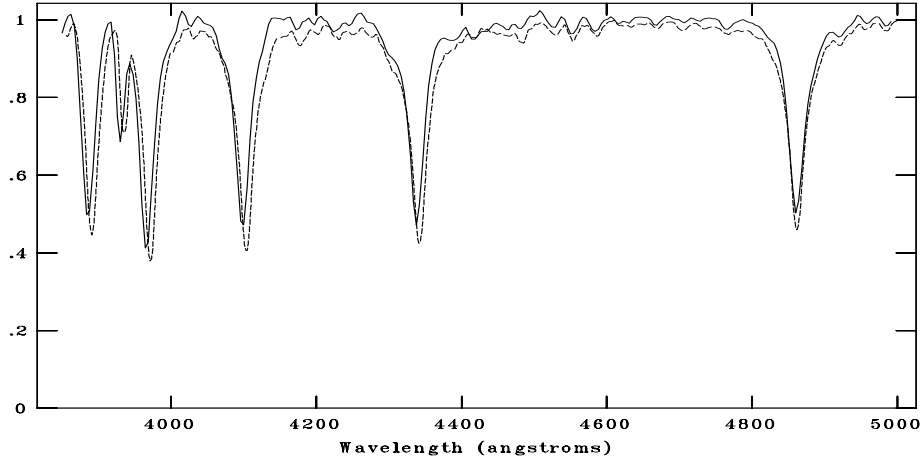


Figure C.151: CAFOS spectrum of 588-020228 compared with F0V, F2V, F3V respectively. The standard spectra are shown with dotted line. The spectral type is assigned as F2V.

NOAO/IRAF V2.16.1 baha@baha-Lenovo-IdeaPad-Y550 Wed 19:25:38 07-Dec-2016
[g180_06A5.fits]: 180_06 190. ap:1 beam:1



NOAO/IRAF V2.16.1 baha@baha-Lenovo-IdeaPad-Y550 Wed 19:26:13 07-Dec-2016
[g180_06A5.fits]: 180_06 190. ap:1 beam:1



NOAO/IRAF V2.16.1 baha@baha-Lenovo-IdeaPad-Y550 Wed 19:26:29 07-Dec-2016
[g180_06A5.fits]: 180_06 190. ap:1 beam:1

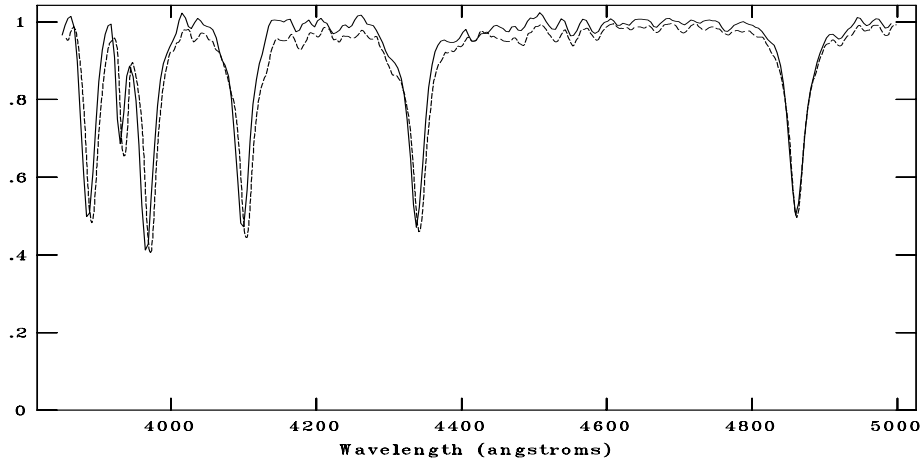
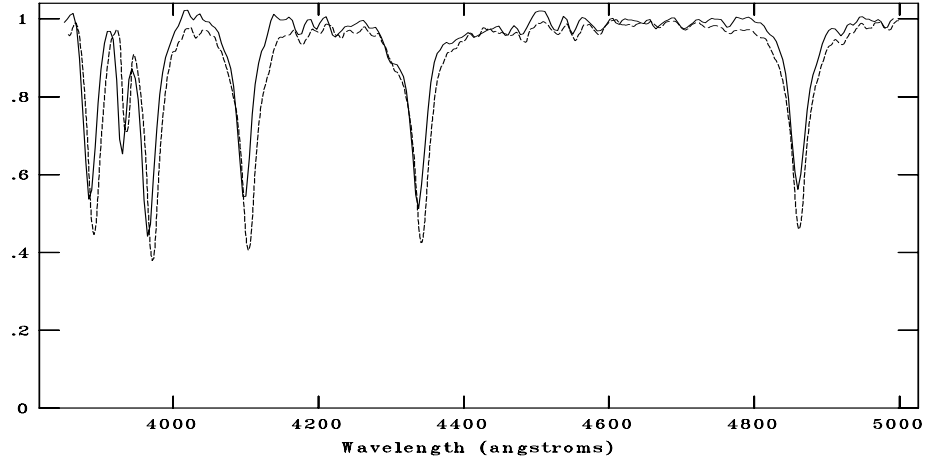
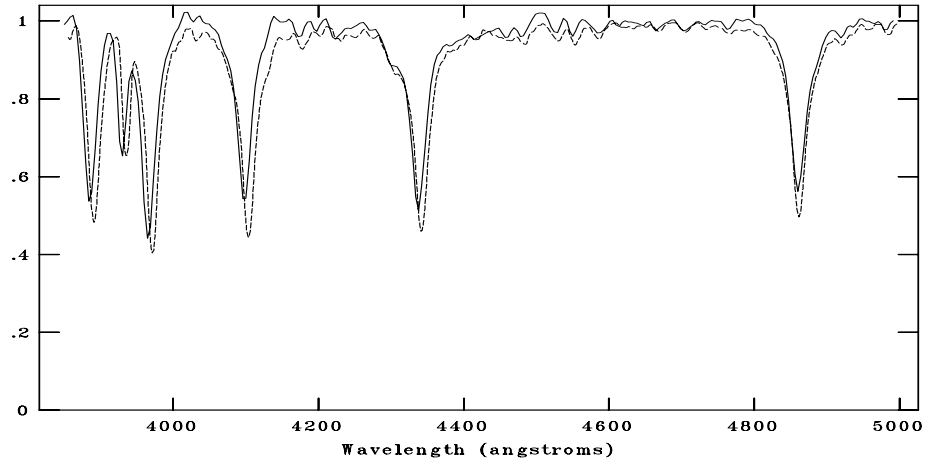


Figure C.152: CAFOS spectrum of 590-020733 compared with A3V, A5V, A7V respectively. The standard spectra are shown with dotted line. The spectral type is assigned as A5V.

NOAO/IRAF V2.16.1 baha@baha-Lenovo-IdeaPad-Y550 Wed 19:27:07 07-Dec-2016
[g180_07A5.fits]: 180_07 190. ap:1 beam:1



NOAO/IRAF V2.16.1 baha@baha-Lenovo-IdeaPad-Y550 Wed 19:27:36 07-Dec-2016
[g180_07A5.fits]: 180_07 190. ap:1 beam:1



NOAO/IRAF V2.16.1 baha@baha-Lenovo-IdeaPad-Y550 Wed 19:27:56 07-Dec-2016
[g180_07A5.fits]: 180_07 190. ap:1 beam:1

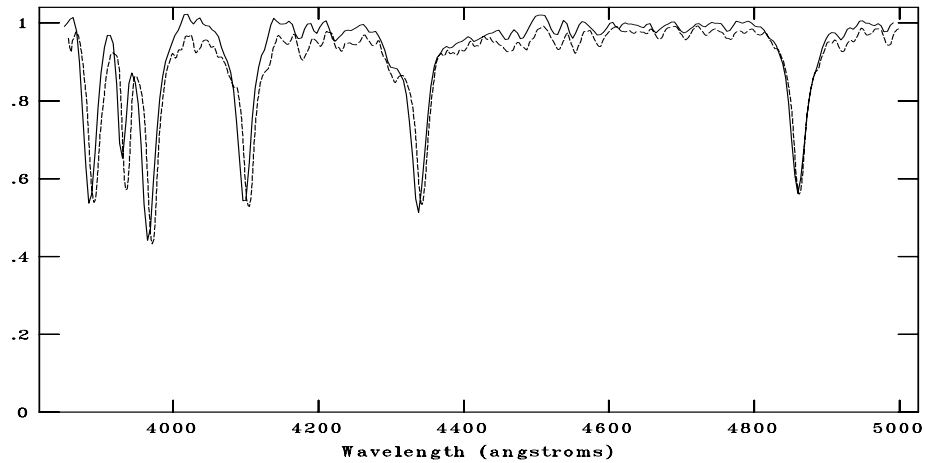
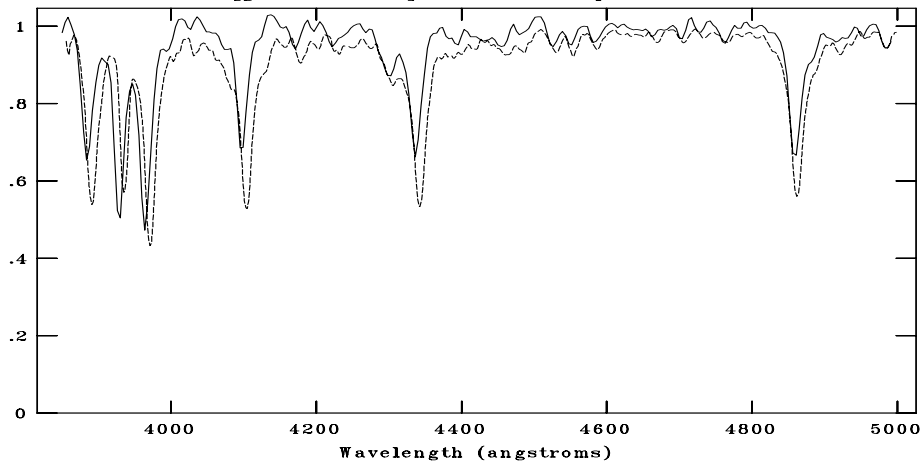
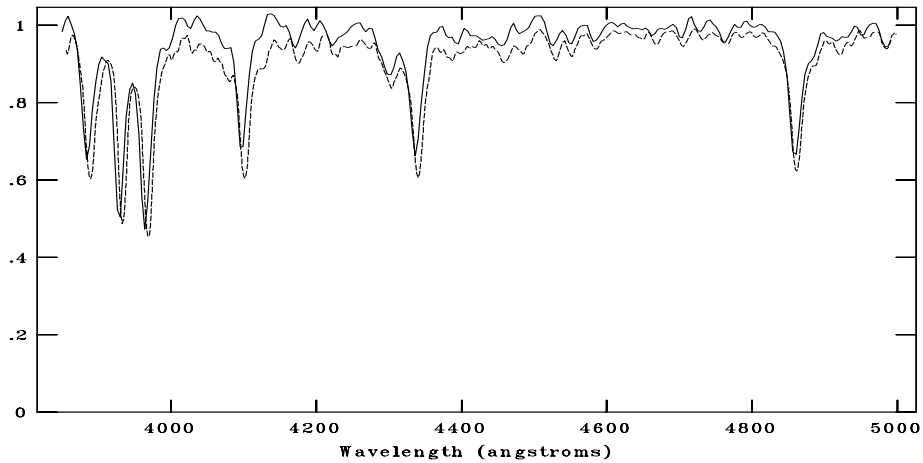


Figure C.153: CAFOS spectrum of 592-020035 compared with A5V, A7V, F0V respectively. The standard spectra are shown with dotted line. The spectral type is assigned as A7V.

NOAO/IRAF V2.16.1 baha@baha-Lenovo-IdeaPad-Y550 Wed 20:23:42 07-Dec-2016
[g180_08F0.fits]: 180_08 220. ap:1 beam:1



NOAO/IRAF V2.16.1 baha@baha-Lenovo-IdeaPad-Y550 Wed 20:24:06 07-Dec-2016
[g180_08F0.fits]: 180_08 220. ap:1 beam:1



NOAO/IRAF V2.16.1 baha@baha-Lenovo-IdeaPad-Y550 Wed 20:24:38 07-Dec-2016
[g180_08F0.fits]: 180_08 220. ap:1 beam:1

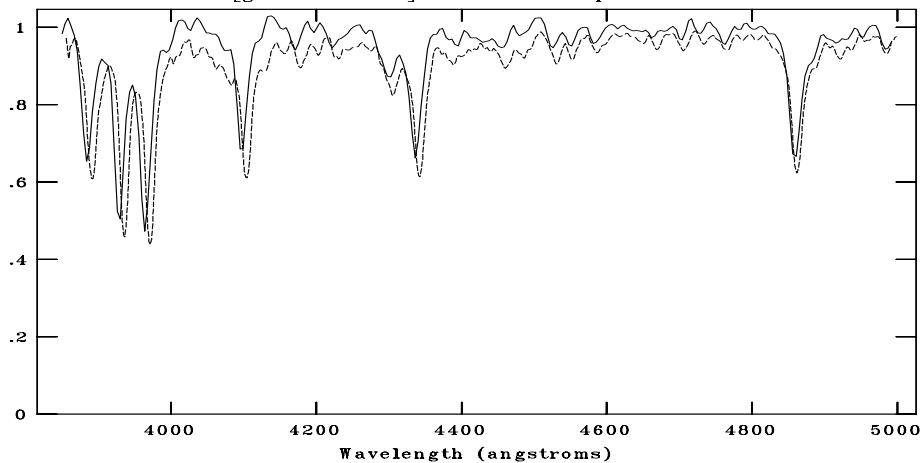
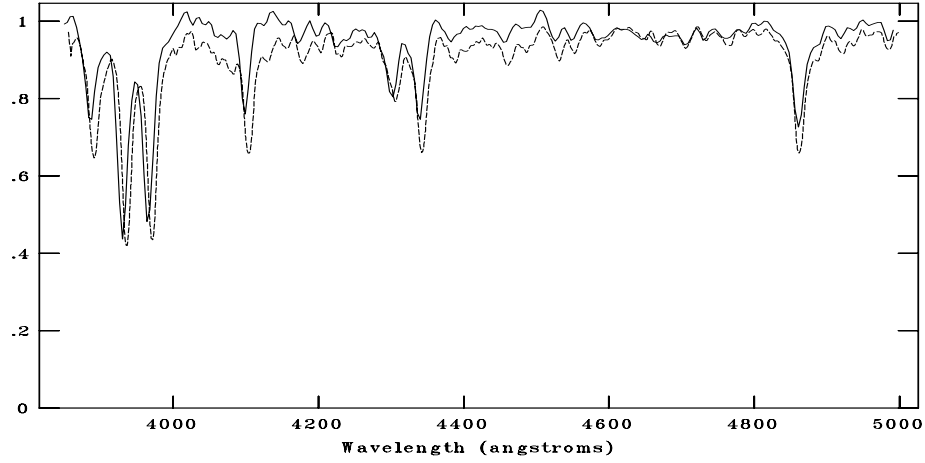
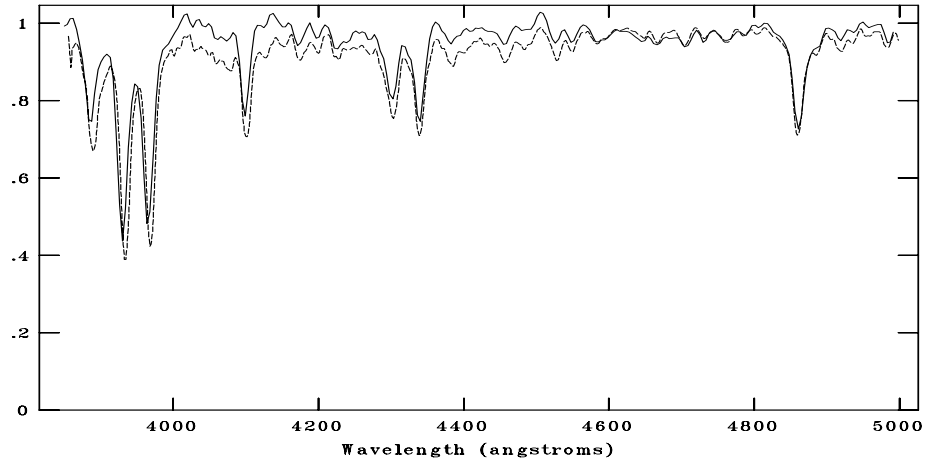


Figure C.154: CAFOS spectrum of 589-019826 compared with F0V, F2V, F3V respectively. The standard spectra are shown with dotted line. The spectral type is assigned as F2V.

NOAO/IRAF V2.16.1 baha@baha-Lenovo-IdeaPad-Y550 Wed 20:26:31 07-Dec-2016
[g180_09G0.fits]: 180_09 220. ap:1 beam:1



NOAO/IRAF V2.16.1 baha@baha-Lenovo-IdeaPad-Y550 Wed 20:26:51 07-Dec-2016
[g180_09G0.fits]: 180_09 220. ap:1 beam:1



NOAO/IRAF V2.16.1 baha@baha-Lenovo-IdeaPad-Y550 Wed 20:26:06 07-Dec-2016
[g180_09G0.fits]: 180_09 220. ap:1 beam:1

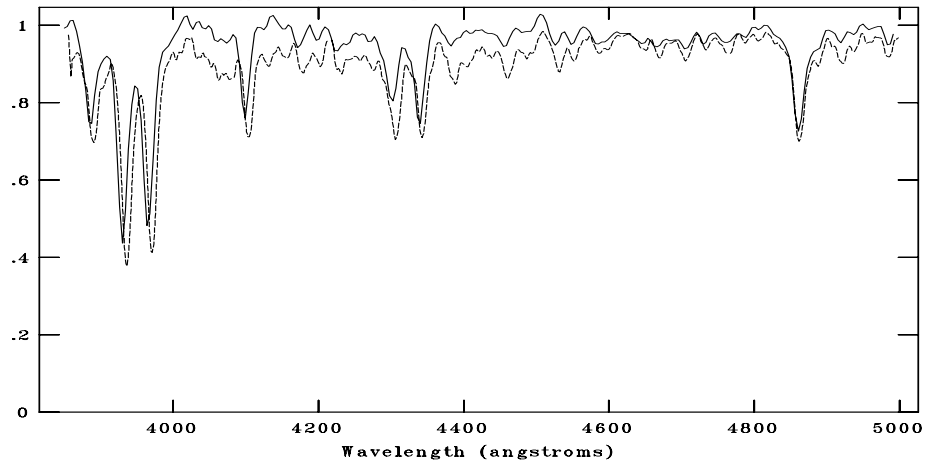
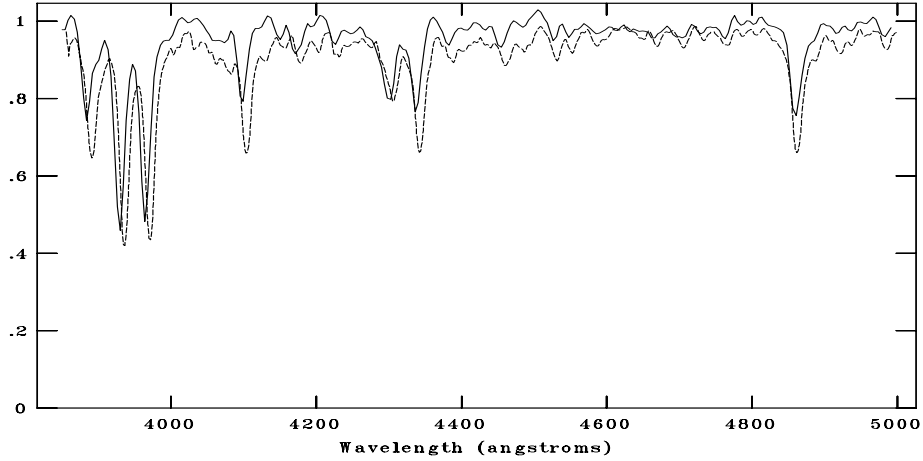
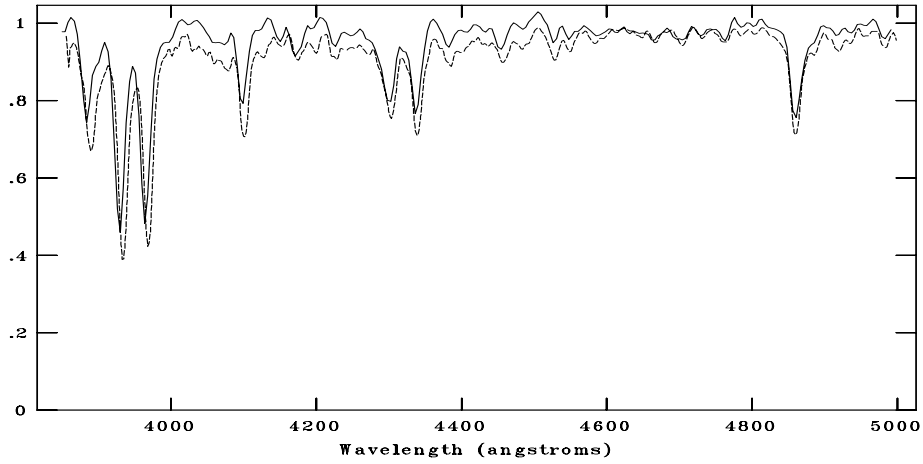


Figure C.155: CAFOS spectrum of 592-020103 compared with F5V, F6V, F8V respectively. The standard spectra are shown with dotted line. The spectral type is assigned as F6V.

NOAO/IRAF V2.16.1 baha@baha-Lenovo-IdeaPad-Y550 Wed 21:43:39 07-Dec-2016
[contin/g180_10nnn.fits]: 180_10 240. ap:1 beam:1



NOAO/IRAF V2.16.1 baha@baha-Lenovo-IdeaPad-Y550 Wed 20:28:05 07-Dec-2016
[contin/g180_10nnn.fits]: 180_10 240. ap:1 beam:1



NOAO/IRAF V2.16.1 baha@baha-Lenovo-IdeaPad-Y550 Wed 21:41:39 07-Dec-2016
[contin/g180_10nnn.fits]: 180_10 240. ap:1 beam:1

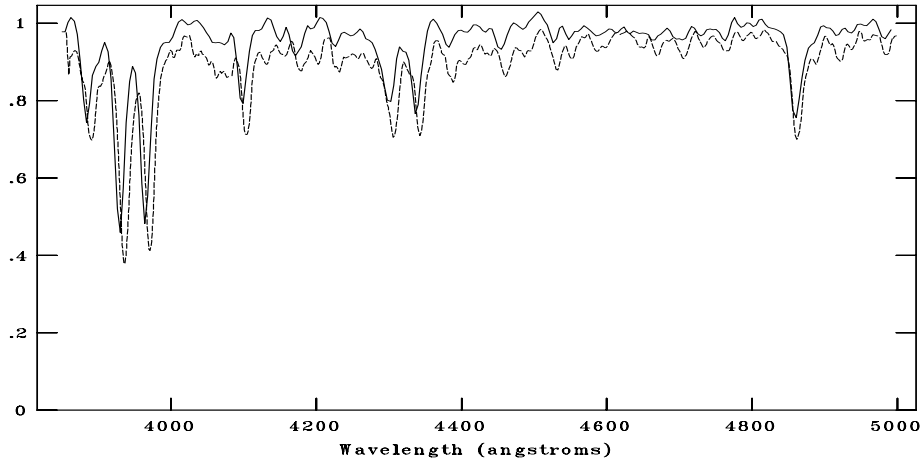
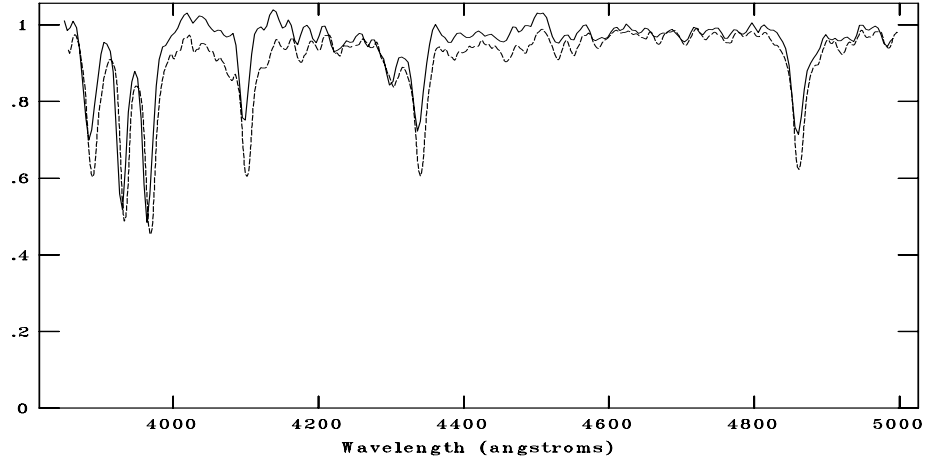
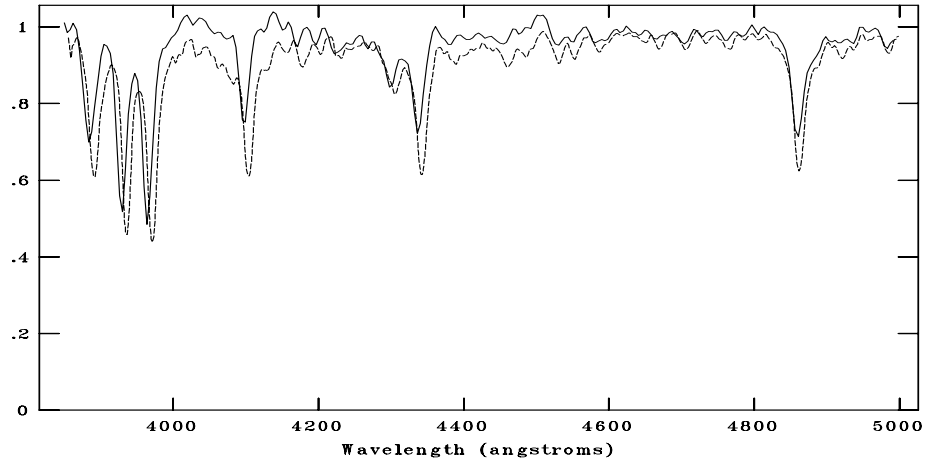


Figure C.156: CAFOS spectrum of 589-019783 compared with F5V, F6V, F8V respectively. The standard spectra are shown with dotted line. The spectral type is assigned as F7V.

NOAO/IRAF V2.16.1 baha@baha-Lenovo-IdeaPad-Y550 Wed 21:45:11 07-Dec-2016
[g180_11F5.fits]: 180_11 270. ap:1 beam:1



NOAO/IRAF V2.16.1 baha@baha-Lenovo-IdeaPad-Y550 Wed 21:45:32 07-Dec-2016
[g180_11F5.fits]: 180_11 270. ap:1 beam:1



NOAO/IRAF V2.16.1 baha@baha-Lenovo-IdeaPad-Y550 Wed 21:45:49 07-Dec-2016
[g180_11F5.fits]: 180_11 270. ap:1 beam:1

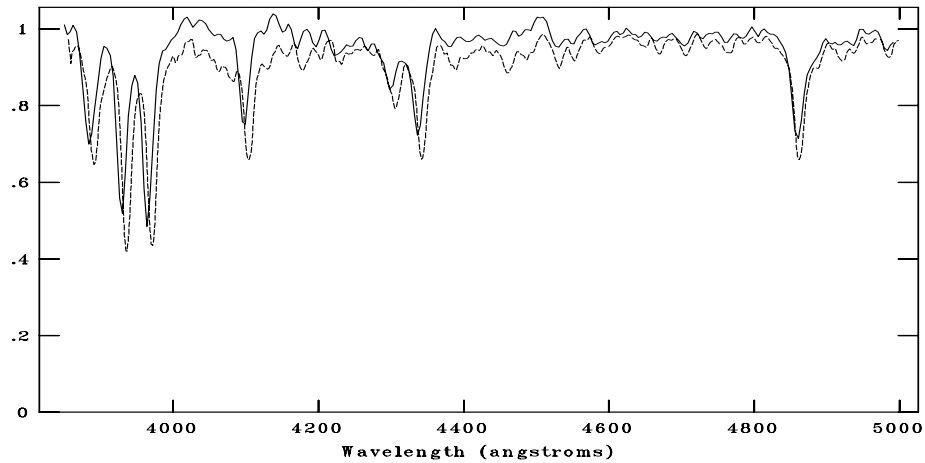
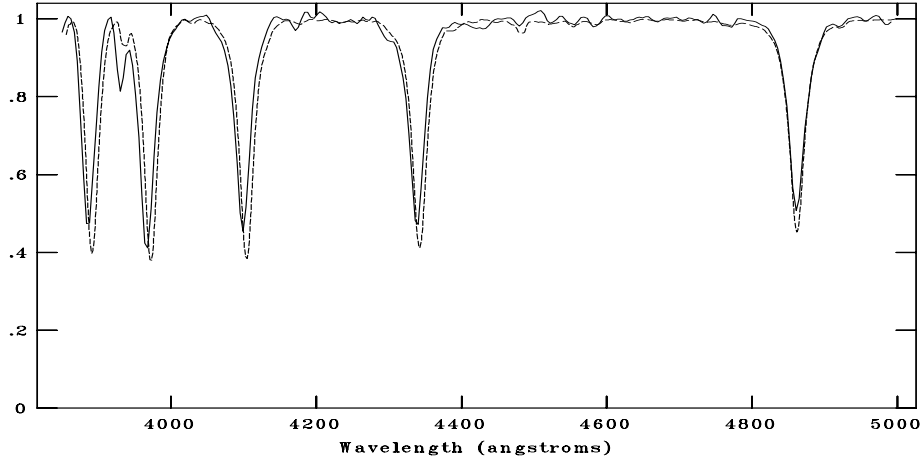
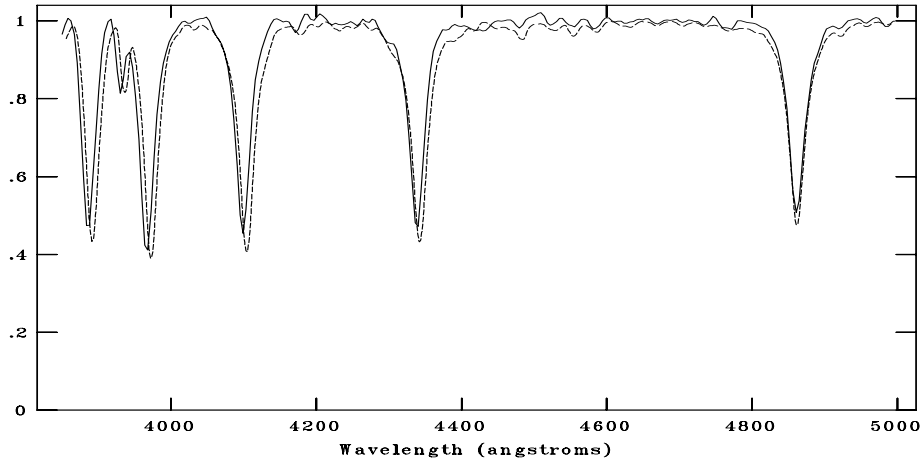


Figure C.157: CAFOS spectrum of 589-020390 compared with F2V, F3V, F5V respectively. The standard spectra are shown with dotted line. The spectral type is assigned as F4V.

NOAO/IRAF V2.16.1 baha@baha-Lenovo-IdeaPad-Y550 Wed 21:46:37 07-Dec-2016
[g180_12A2.fits]: 180_12 180. ap:1 beam:1



NOAO/IRAF V2.16.1 baha@baha-Lenovo-IdeaPad-Y550 Wed 21:47:06 07-Dec-2016
[g180_12A2.fits]: 180_12 180. ap:1 beam:1



NOAO/IRAF V2.16.1 baha@baha-Lenovo-IdeaPad-Y550 Wed 21:47:34 07-Dec-2016
[g180_12A2.fits]: 180_12 180. ap:1 beam:1

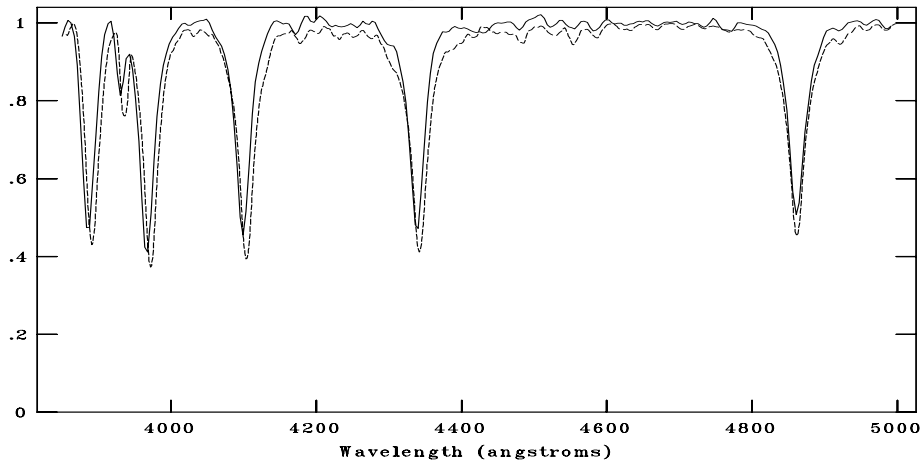
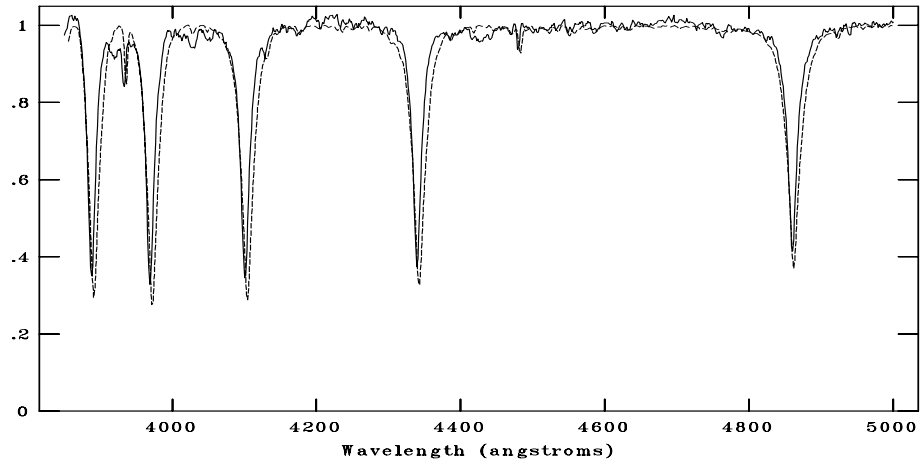
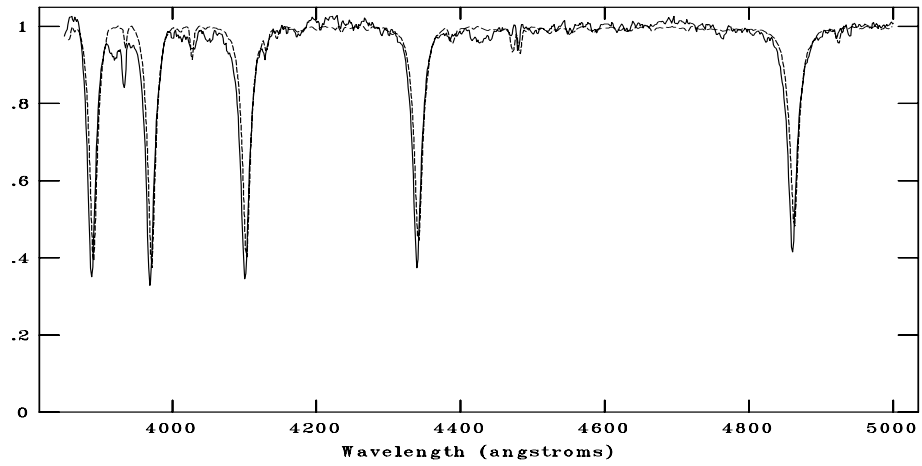


Figure C.158: CAFOS spectrum of 591-020513 compared with A0V, A1V, A3V respectively. The standard spectra are shown with dotted line. The spectral type is assigned as A1V.

NOAO/IRAF V2.16.1 baha@baha-Lenovo-IdeaPad-Y550 Wed 00:20:30 04-Jan-2017
[g180_0.fits]: g180_1 1800. ap:1 beam:1



NOAO/IRAF V2.16.1 baha@baha-Lenovo-IdeaPad-Y550 Wed 00:24:03 04-Jan-2017
[g180_0.fits]: g180_1 1800. ap:1 beam:1



NOAO/IRAF V2.16.1 baha@baha-Lenovo-IdeaPad-Y550 Wed 00:19:41 04-Jan-2017
[g180n]: g180_1 1800. ap:1 beam:1

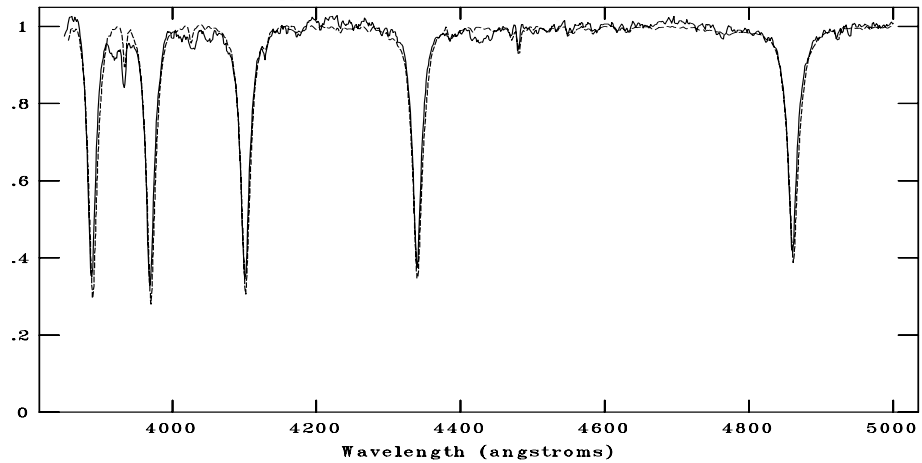


Figure C.159: TFOSC spectrum of 589-020158 compared with A0V, B8V, B9V respectively. The standard spectra are shown with dotted line. The spectral type is assigned as B9.5V.

C.16 G189.1+3.0

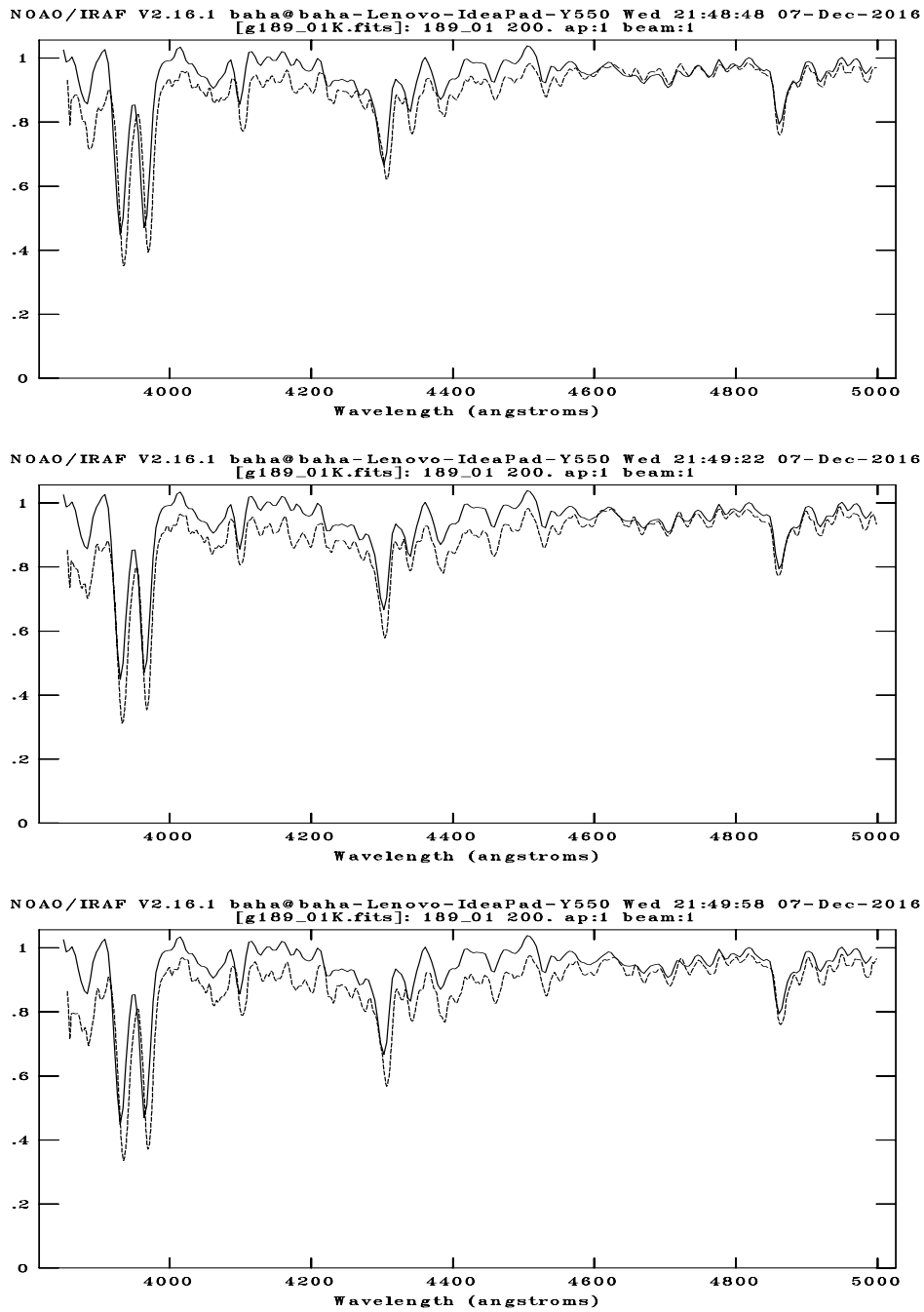
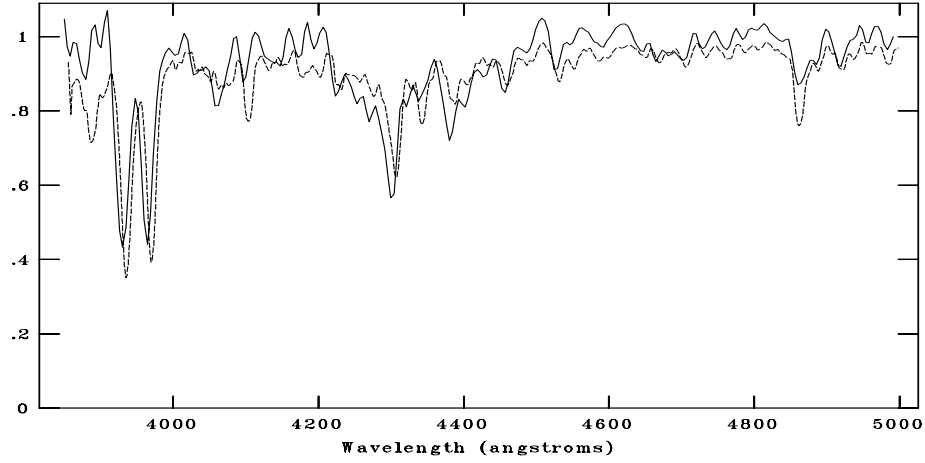
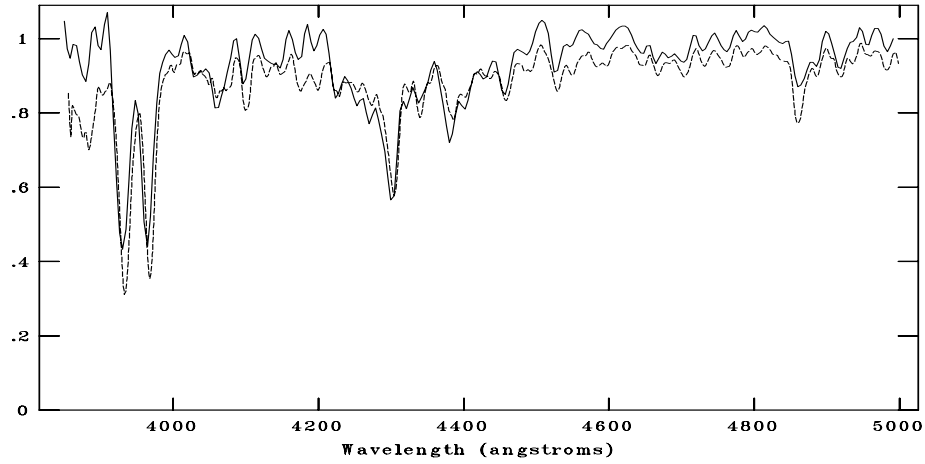


Figure C.160: CAFOS spectrum of 563-026583 compared with G0V, G2V, G3V respectively. The standard spectra are shown with dotted line. The spectral type is assigned as G0V.

NOAO/IRAF V2.16.1 baha@baha-Lenovo-IdeaPad-Y550 Wed 21:53:49 07-Dec-2016
[g189_02K.fits]: 189_02 300. ap:1 beam:1



NOAO/IRAF V2.16.1 baha@baha-Lenovo-IdeaPad-Y550 Wed 21:54:24 07-Dec-2016
[g189_02K.fits]: 189_02 300. ap:1 beam:1



NOAO/IRAF V2.16.1 baha@baha-Lenovo-IdeaPad-Y550 Wed 21:51:06 07-Dec-2016
[g189_02K.fits]: 189_02 300. ap:1 beam:1

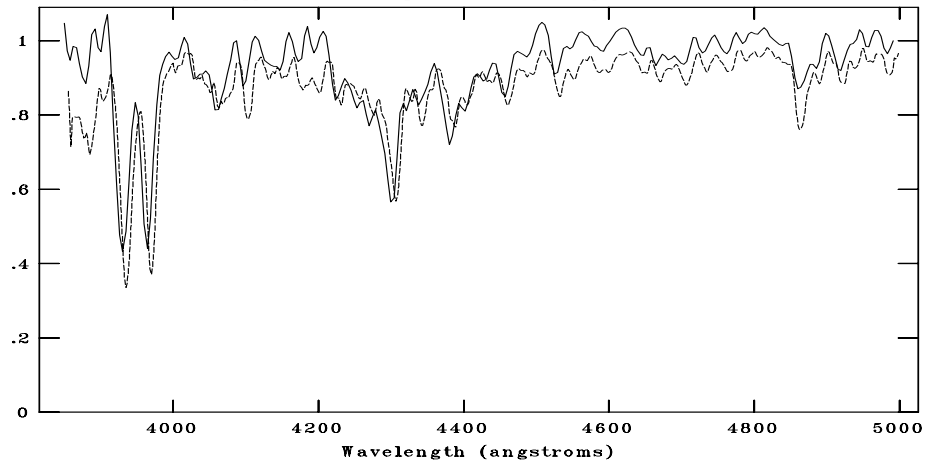
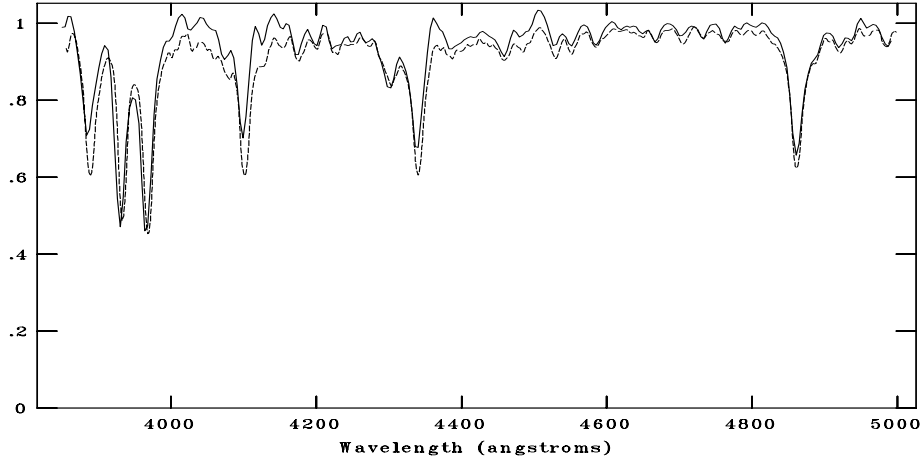
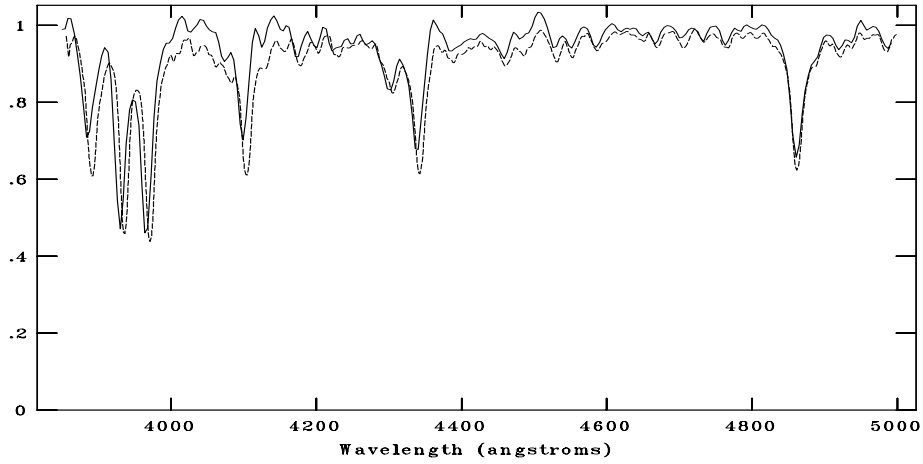


Figure C.161: CAFOS spectrum of 562-026666 compared with G0V, G2V, G3V respectively. The standard spectra are shown with dotted line. The spectral type is later than G3V.

NOAO/IRAF V2.16.1 baha@baha-Lenovo-IdeaPad-Y550 Wed 21:54:50 07-Dec-2016
[g189_03F5.fits]: 189_03 400. ap:1 beam:1



NOAO/IRAF V2.16.1 baha@baha-Lenovo-IdeaPad-Y550 Wed 21:55:25 07-Dec-2016
[g189_03F5.fits]: 189_03 400. ap:1 beam:1



NOAO/IRAF V2.16.1 baha@baha-Lenovo-IdeaPad-Y550 Wed 21:55:52 07-Dec-2016
[g189_03F5.fits]: 189_03 400. ap:1 beam:1

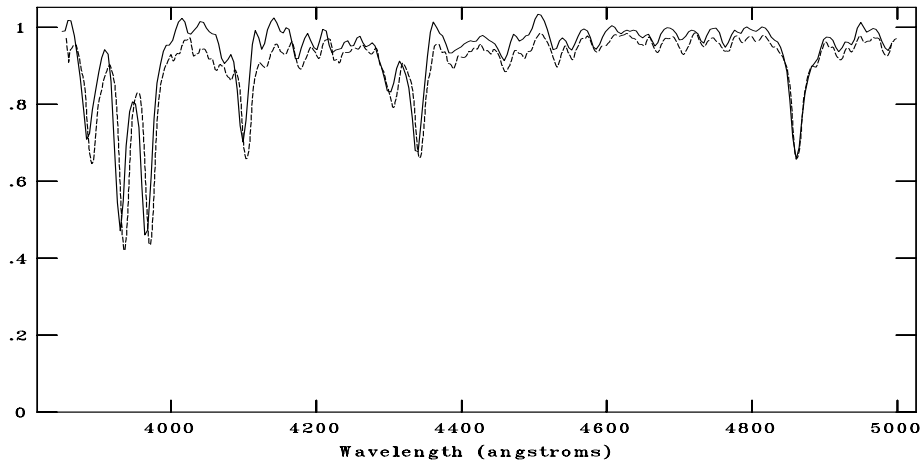
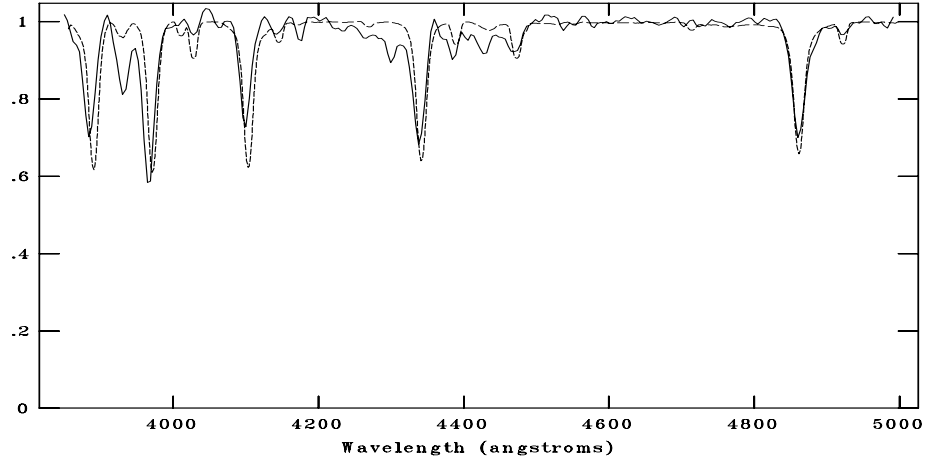
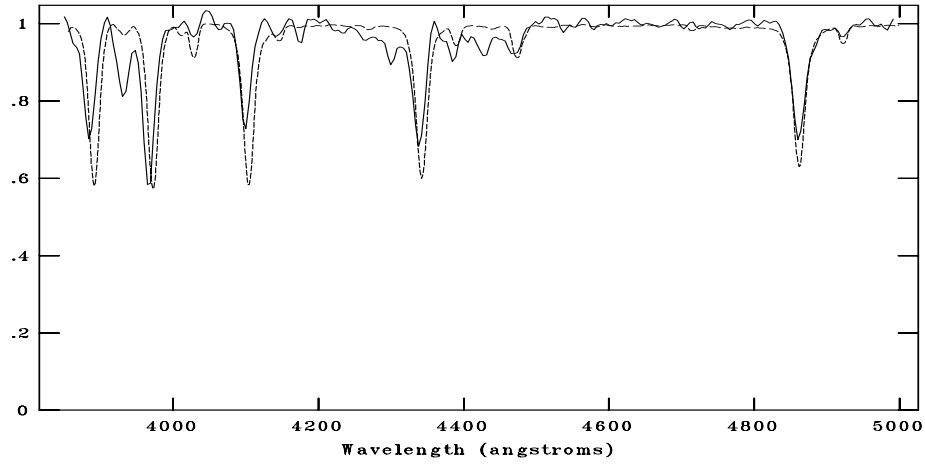


Figure C.162: CAFOS spectrum of 564-025656 compared with F2V, F3V, F5V respectively. The standard spectra are shown with dotted line. The spectral type is assigned as F4V.

NOAO/IRAF V2.16.1 baha@baha-Lenovo-IdeaPad-Y550 Wed 21:58:46 07-Dec-2016
[g189_04B5.fits]: 189_04 400. ap:1 beam:1



NOAO/IRAF V2.16.1 baha@baha-Lenovo-IdeaPad-Y550 Wed 21:56:48 07-Dec-2016
[g189_04B5.fits]: 189_04 400. ap:1 beam:1



NOAO/IRAF V2.16.1 baha@baha-Lenovo-IdeaPad-Y550 Wed 22:00:38 07-Dec-2016
[g189_04B5.fits]: 189_04 400. ap:1 beam:1

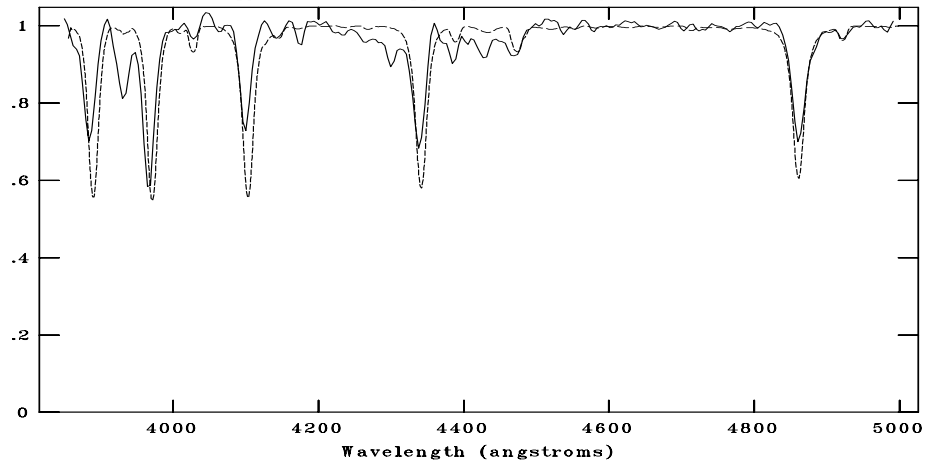
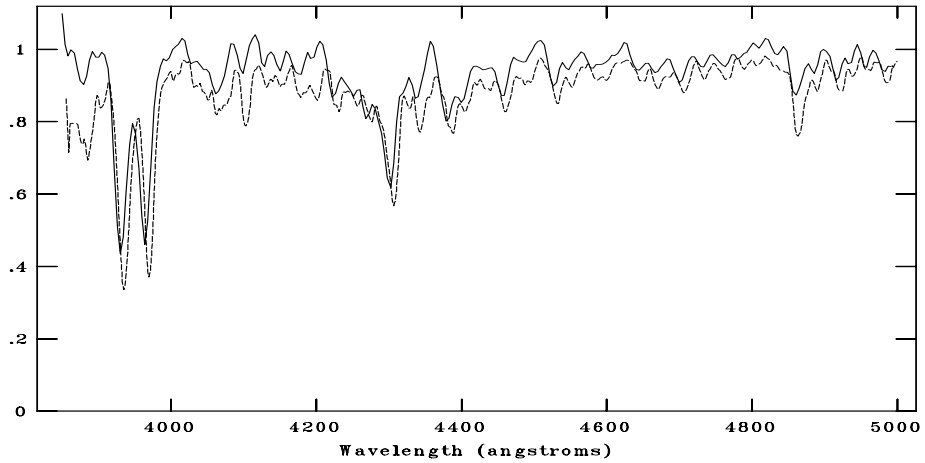


Figure C.163: CAFOS spectrum of 564-025691 compared with B3V, B5V, B7V respectively. The standard spectra are shown with dotted line. The spectral type is assigned as B5V.

NOAO/IRAF V2.16.1 baha@baha-Lenovo-IdeaPad-Y550 Wed 22:01:40 07-Dec-2016
[g189_05K.fits]: 189_05 400. ap:1 beam:1



NOAO/IRAF V2.16.1 baha@baha-Lenovo-IdeaPad-Y550 Wed 22:02:14 07-Dec-2016
[g189_05K.fits]: 189_05 400. ap:1 beam:1

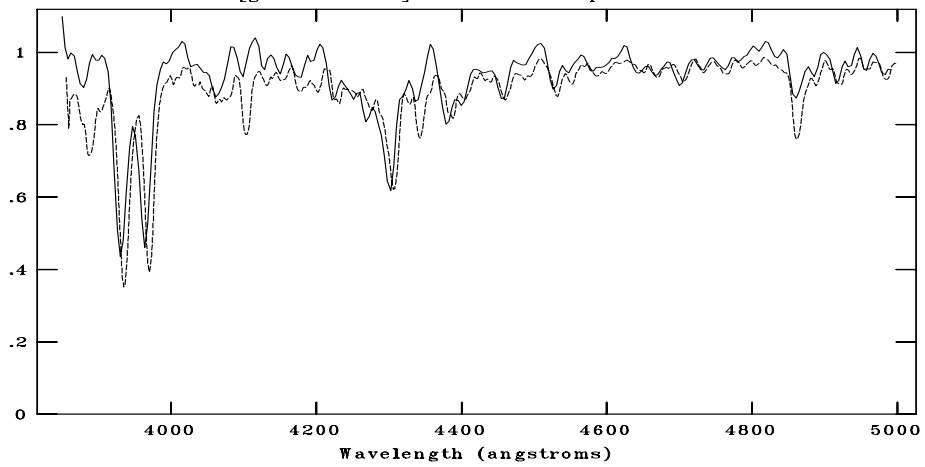
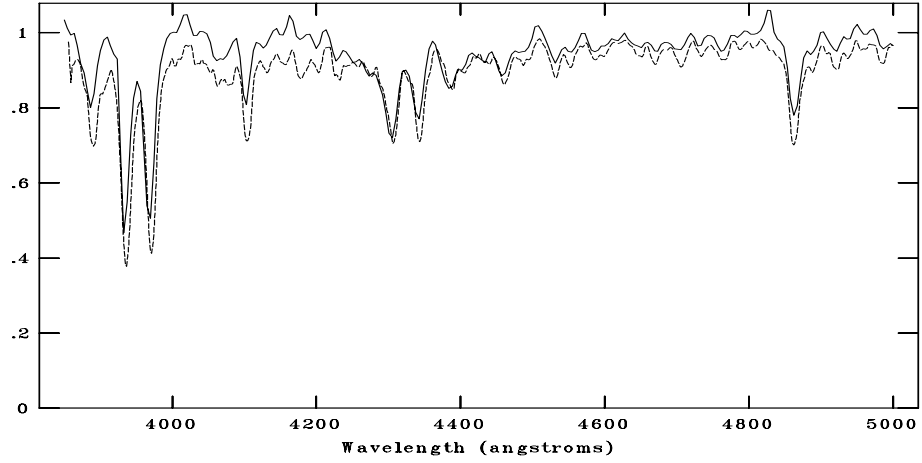
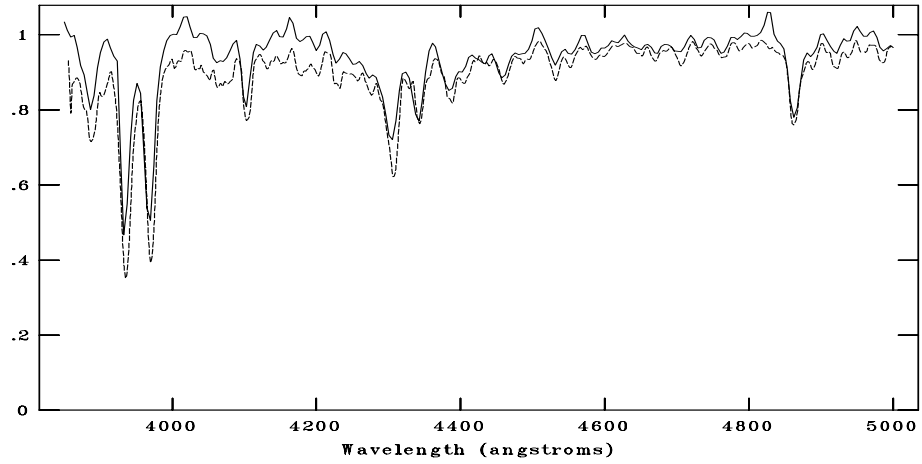


Figure C.164: CAFOS spectrum of 564-025754 compared with G3V and G5V respectively. The standard spectra are shown with dotted line. The spectral type is assigned as G3V.

NOAO/IRAF V2.16.1 baha@baha-Lenovo-IdeaPad-Y550 Thu 14:23:46 08-Dec-2016
[cg189_01G5.fits]: G189_1 1200. ap:1 beam:1



NOAO/IRAF V2.16.1 baha@baha-Lenovo-IdeaPad-Y550 Thu 14:23:14 08-Dec-2016
[cg189_01G5.fits]: G189_1 1200. ap:1 beam:1



NOAO/IRAF V2.16.1 baha@baha-Lenovo-IdeaPad-Y550 Thu 14:23:33 08-Dec-2016
[cg189_01G5.fits]: G189_1 1200. ap:1 beam:1

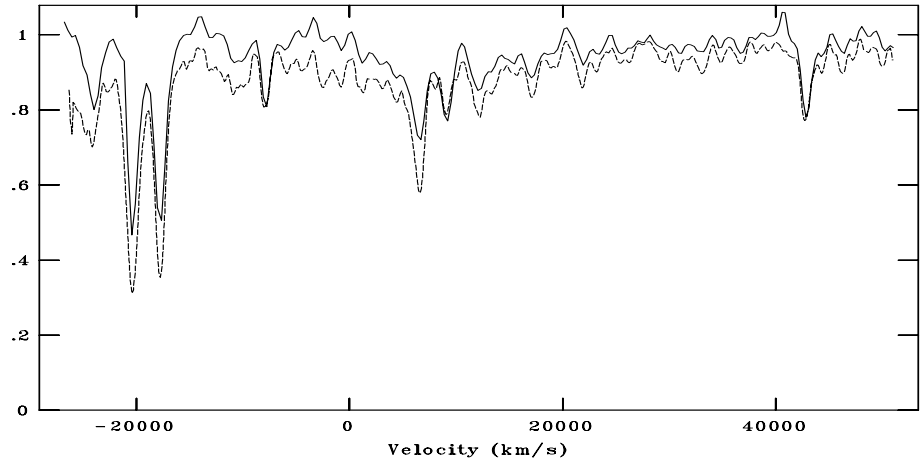
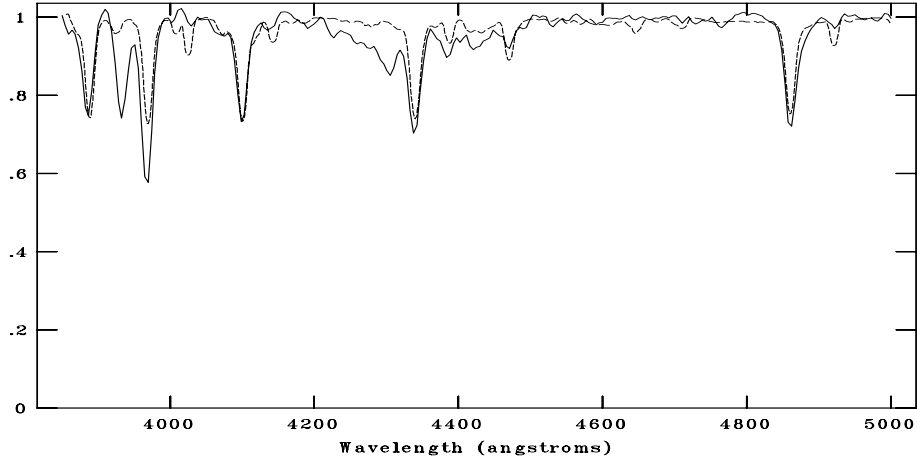
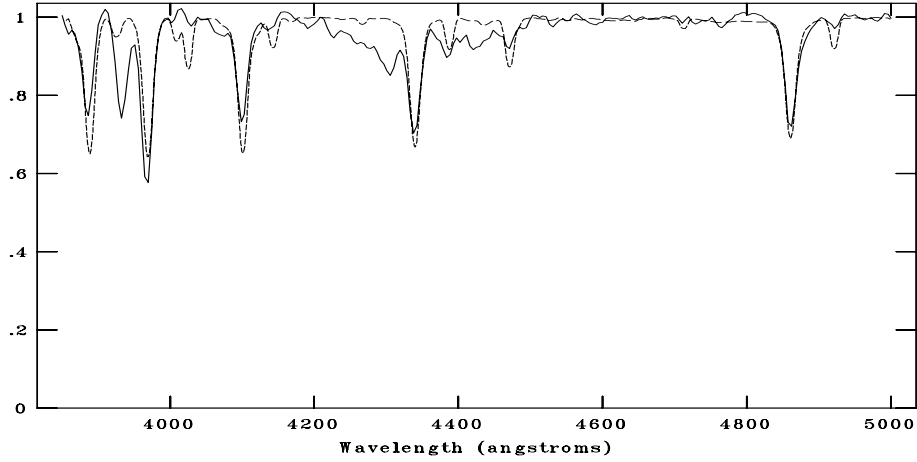


Figure C.165: CAFOS spectrum of 563-026606 compared with F8V, G0V, G2V respectively. The standard spectra are shown with dotted line. The spectral type is assigned as G3V.

NOAO/IRAF V2.16.1 baha@baha-Lenovo-IdeaPad-Y550 Thu 14:36:59 08-Dec-2016
[cg189_02FB.fits]: G189_2 960. ap:1 beam:1



NOAO/IRAF V2.16.1 baha@baha-Lenovo-IdeaPad-Y550 Thu 14:36:15 08-Dec-2016
[cg189_02FB.fits]: G189_2 960. ap:1 beam:1



NOAO/IRAF V2.16.1 baha@baha-Lenovo-IdeaPad-Y550 Thu 14:38:05 08-Dec-2016
[cg189_02FB.fits]: G189_2 960. ap:1 beam:1

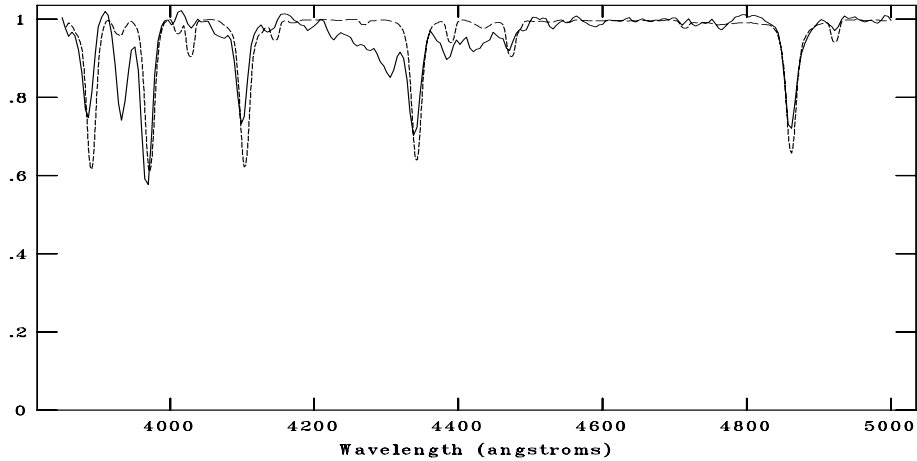
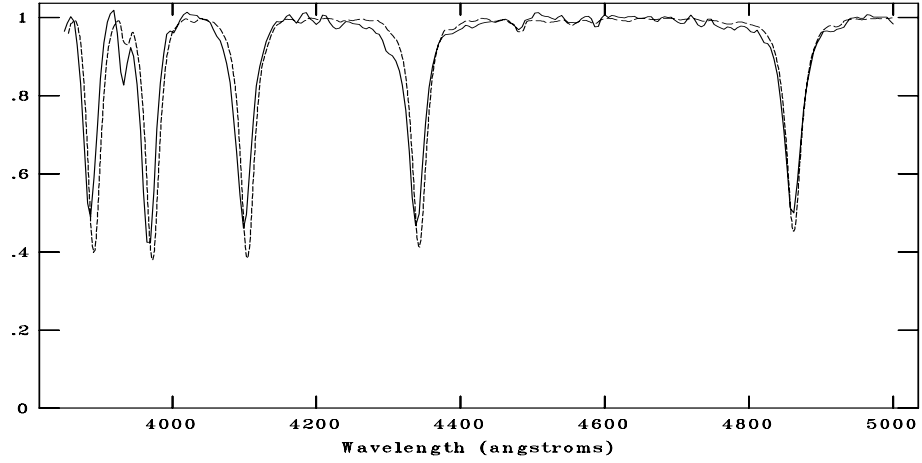
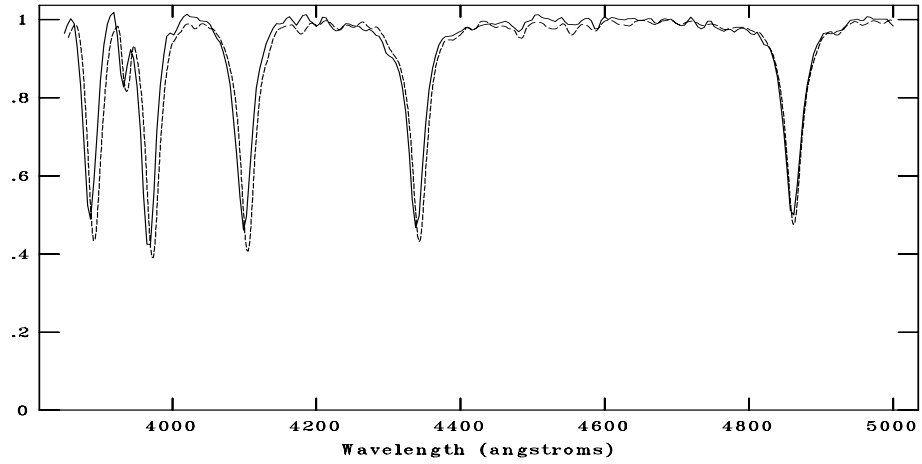


Figure C.166: CAFOS spectrum of 563-026625 compared with B1V, B2V, B3V respectively. The standard spectra are shown with dotted line. The spectral type is assigned as B3V.

NOAO/IRAF V2.16.1 baha@baha-Lenovo-IdeaPad-Y550 Thu 15:00:22 08-Dec-2016
[cg189_03A1.fits]: G189_3 360. ap:1 beam:1



NOAO/IRAF V2.16.1 baha@baha-Lenovo-IdeaPad-Y550 Thu 15:00:43 08-Dec-2016
[cg189_03A1.fits]: G189_3 360. ap:1 beam:1



NOAO/IRAF V2.16.1 baha@baha-Lenovo-IdeaPad-Y550 Thu 15:00:59 08-Dec-2016
[cg189_03A1.fits]: G189_3 360. ap:1 beam:1

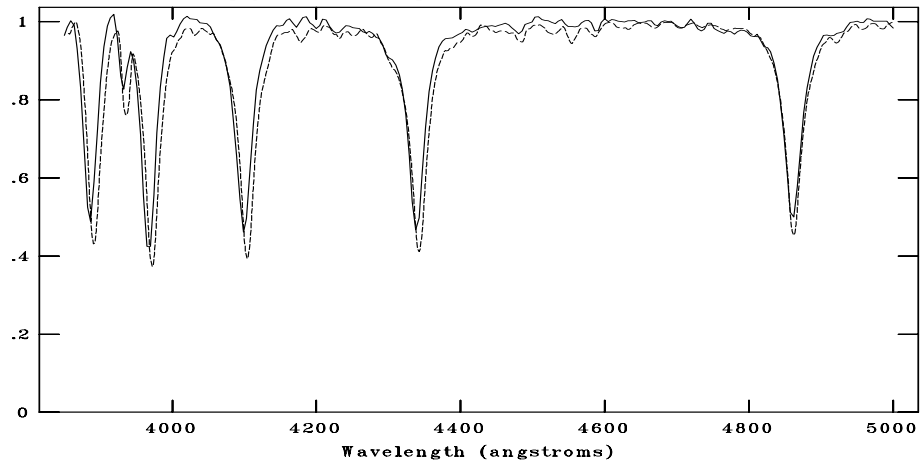
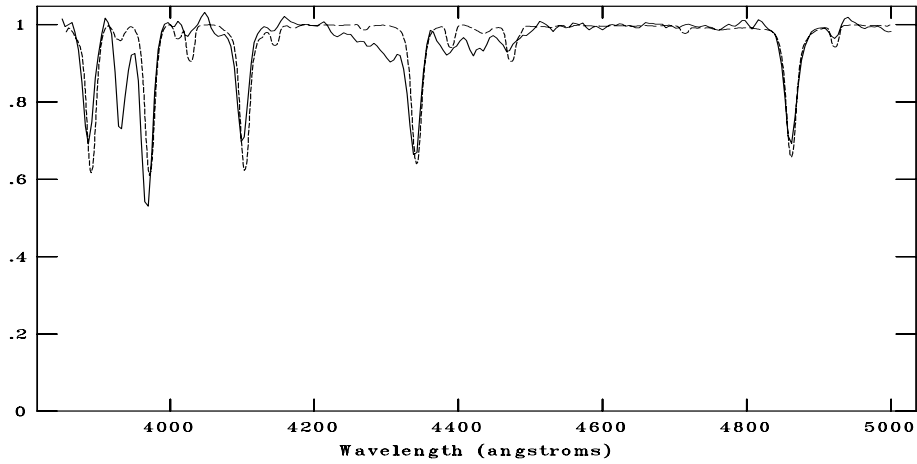
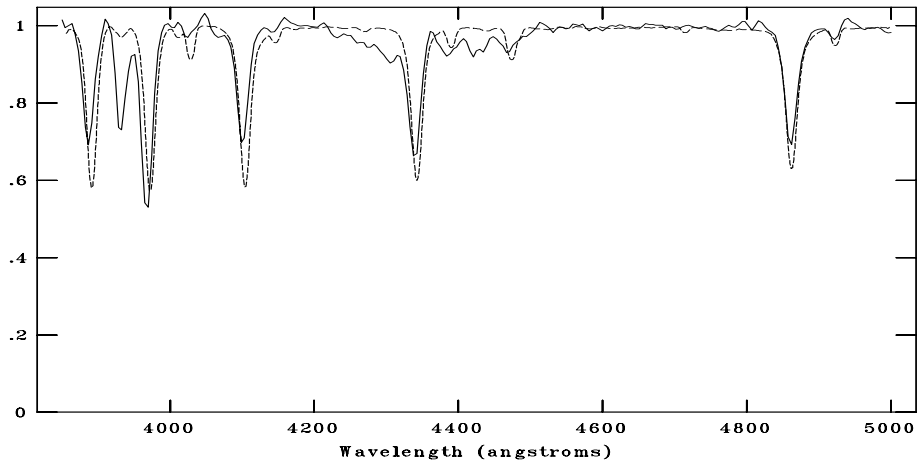


Figure C.167: CAFOS spectrum of 563-026556 compared with A0V, A1V, A3V respectively. The standard spectra are shown with dotted line. The spectral type is assigned as A1V.

NOAO/IRAF V2.16.1 baha@baha-Lenovo-IdeaPad-Y550 Thu 15:01:59 08-Dec-2016
[cg189_04FB.fits]: G189_4 1080. ap:1 beam:1



NOAO/IRAF V2.16.1 baha@baha-Lenovo-IdeaPad-Y550 Thu 15:01:17 08-Dec-2016
[cg189_04FB.fits]: G189_4 1080. ap:1 beam:1



NOAO/IRAF V2.16.1 baha@baha-Lenovo-IdeaPad-Y550 Thu 15:01:45 08-Dec-2016
[cg189_04FB.fits]: G189_4 1080. ap:1 beam:1

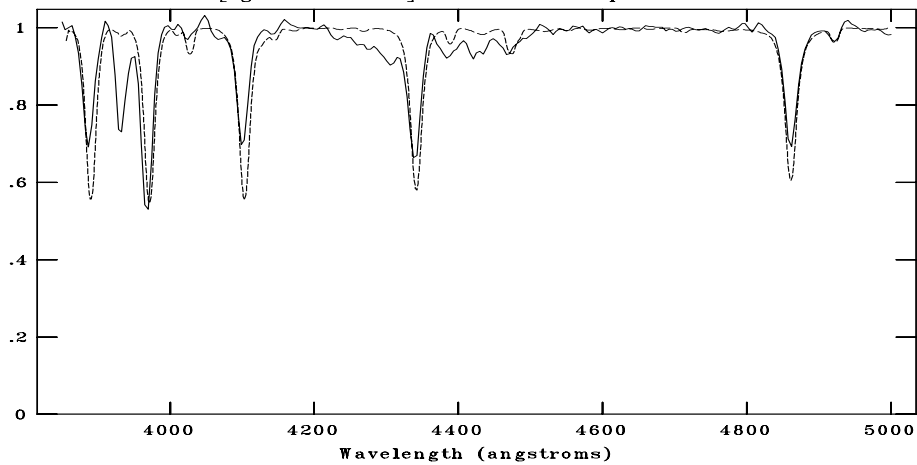
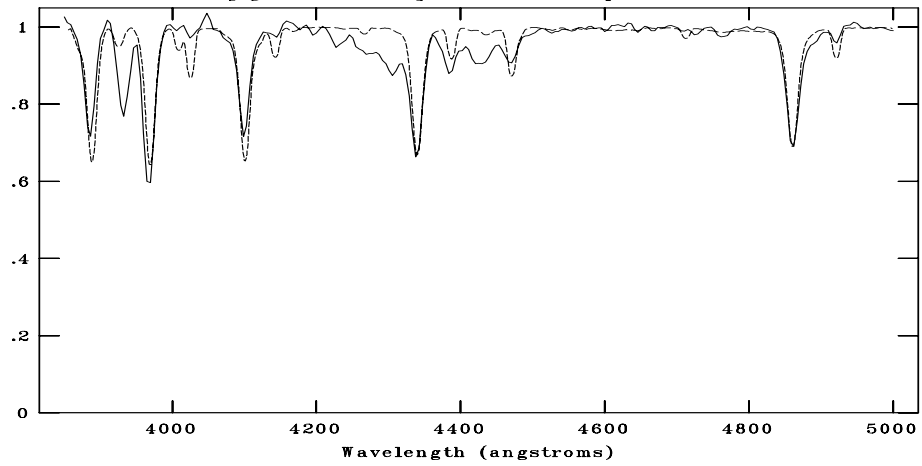
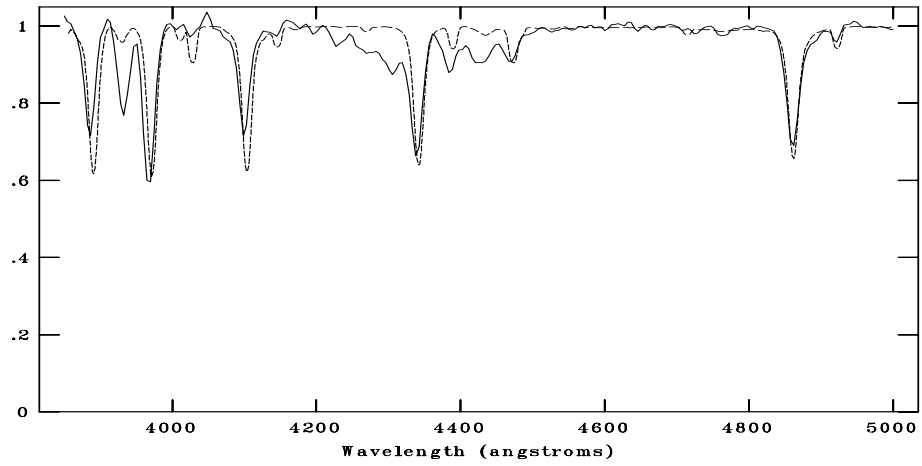


Figure C.168: CAFOS spectrum of 563-026710 compared with B3V, B5V, B7V respectively. The standard spectra are shown with dotted line. The spectral type is assigned as B6V.

NOAO/IRAF V2.16.1 baha@baha-Lenovo-IdeaPad-Y550 Thu 15:03:48 08-Dec-2016
[cg189_05FB.fits]: G189_5 900. ap:1 beam:1



NOAO/IRAF V2.16.1 baha@baha-Lenovo-IdeaPad-Y550 Thu 15:04:28 08-Dec-2016
[cg189_05FB.fits]: G189_5 900. ap:1 beam:1



NOAO/IRAF V2.16.1 baha@baha-Lenovo-IdeaPad-Y550 Thu 15:05:48 08-Dec-2016
[cg189_05FB3.fits]: G189_5 900. ap:1 beam:1

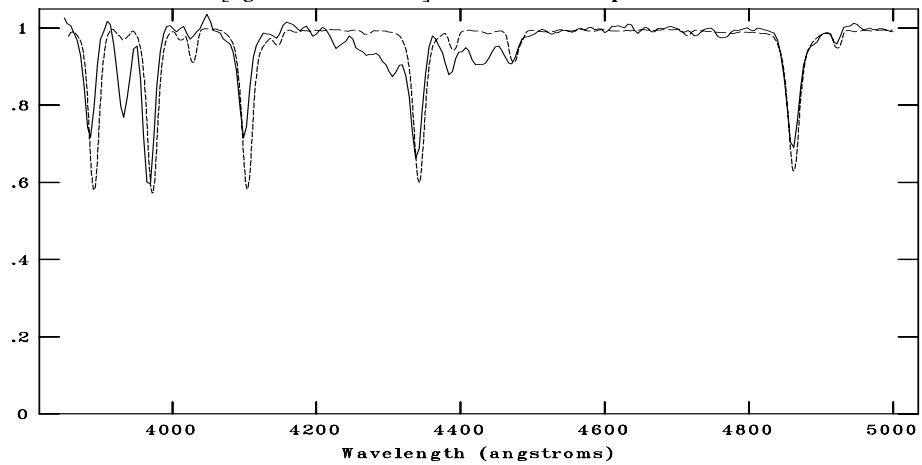
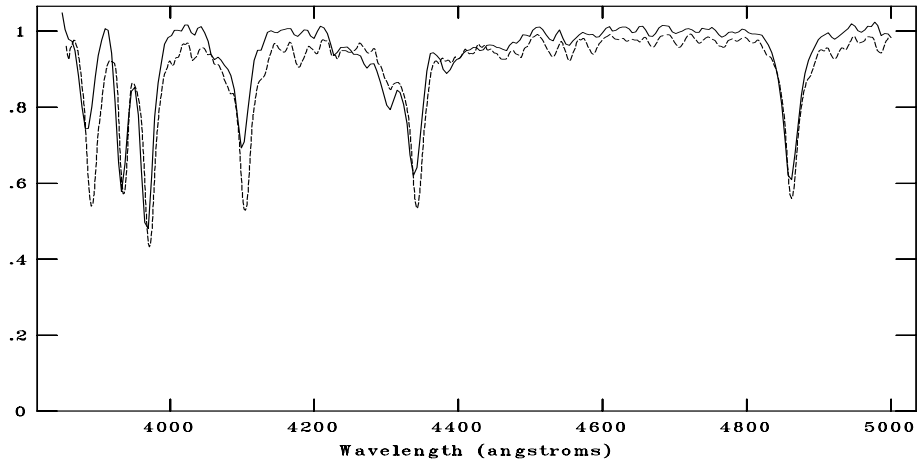
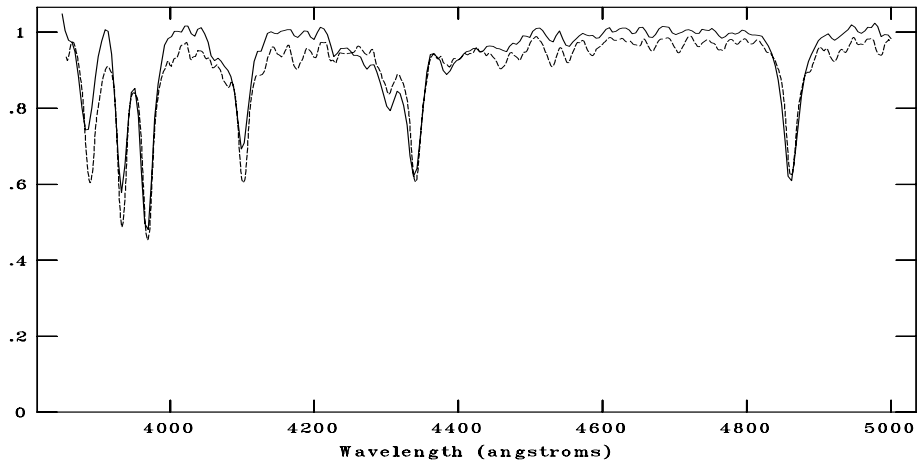


Figure C.169: CAFOS spectrum of 564-025691 compared with B2V, B3V, B5V respectively. The standard spectra are shown with dotted line. The spectral type is assigned as B5V. Due to the high S/N, the identification is not accurate.

NOAO/IRAF V2.16.1 baha@baha-Lenovo-IdeaPad-Y550 Thu 15:06:24 08-Dec-2016
[cg189_06F0.fits]: G189_6 720. ap:1 beam:1



NOAO/IRAF V2.16.1 baha@baha-Lenovo-IdeaPad-Y550 Thu 15:06:46 08-Dec-2016
[cg189_06F0.fits]: G189_6 720. ap:1 beam:1



NOAO/IRAF V2.16.1 baha@baha-Lenovo-IdeaPad-Y550 Thu 15:07:10 08-Dec-2016
[cg189_06F0.fits]: G189_6 720. ap:1 beam:1

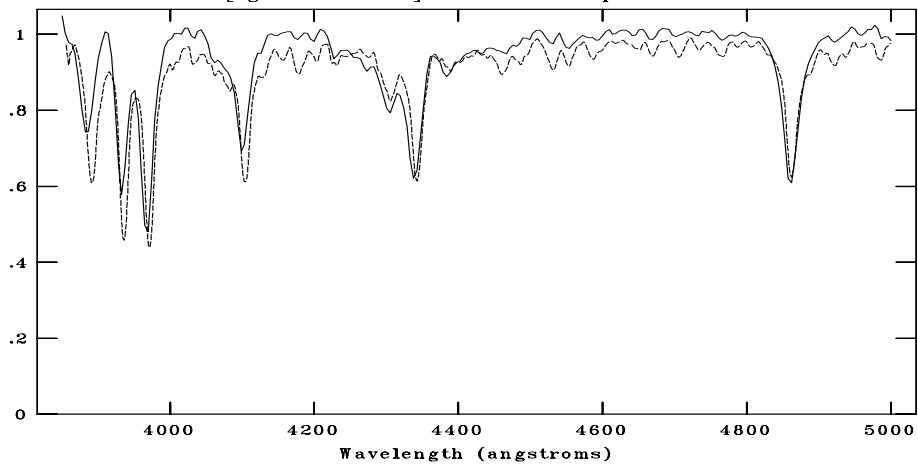
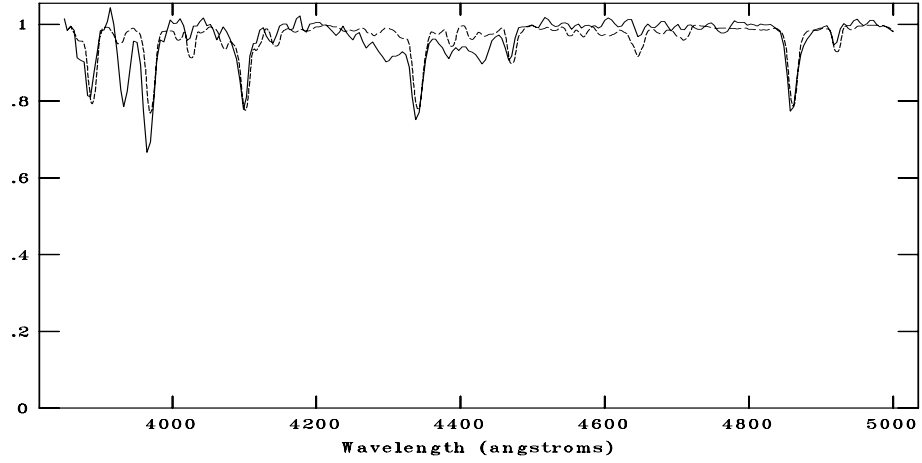
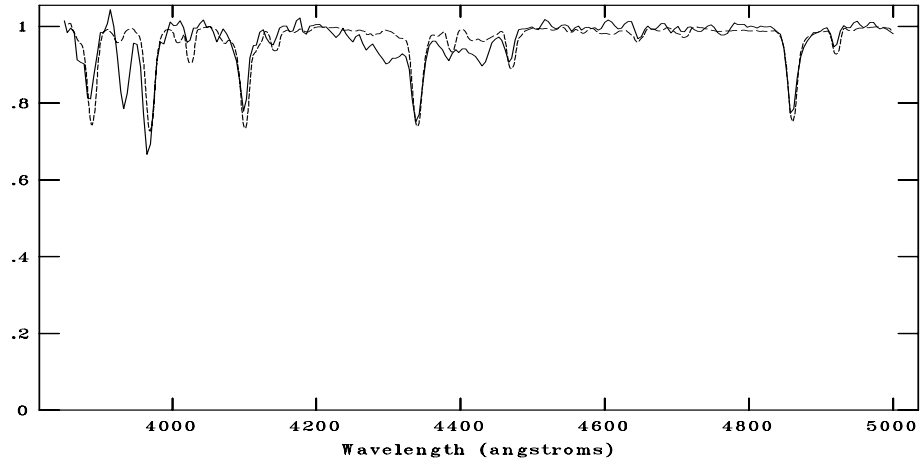


Figure C.170: CAFOS spectrum of 563-026587 compared with F0V, F2V, F3V respectively. The standard spectra are shown with dotted line. The spectral type is assigned as F0V.

NOAO/IRAF V2.16.1 baha@baha-Lenovo-IdeaPad-Y550 Thu 15:08:15 08-Dec-2016
[cg189_07_1FB.fits]: G189_7 240. ap:1 beam:1



NOAO/IRAF V2.16.1 baha@baha-Lenovo-IdeaPad-Y550 Thu 15:07:50 08-Dec-2016
[cg189_07_1FB.fits]: G189_7 240. ap:1 beam:1



NOAO/IRAF V2.16.1 baha@baha-Lenovo-IdeaPad-Y550 Thu 15:08:40 08-Dec-2016
[cg189_07_1FB.fits]: G189_7 240. ap:1 beam:1

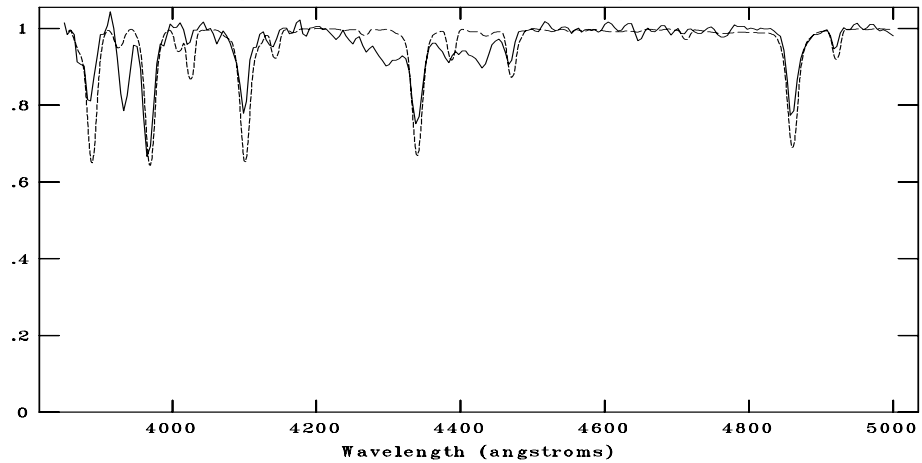


Figure C.171: CAFOS spectrum of 564-025653 compared with B0.5V, B1V, B2V respectively. The standard spectra are shown with dotted line. The spectral type is assigned as B2V.

CURRICULUM VITAE

PERSONAL INFORMATION

Surname, Name: Dincel, Baha

Nationality: Turkish (TC)

Date and Place of Birth: 29/07/1983, Salihli

Marital Status: Single

Phone: +49 174 9621988

E-mail: dincel@astro.uni-tuebingen.de

EDUCATION

Degree	Institution	Year of Graduation
M.S.	METU	2012
B.S.	METU	2009
High School	Darussafaka	2001

PROJECTS

2010–2012 "Determining the Asymmetry in Star Formation Regions (SFRs) in the Galactic Plane by Reconstructing the Pulsars and SFR Distributions", supported by The Scientific And Technological Research Council of Turkey (TUBİTAK), METU **2012–2016** "SFB TR–7:Populations of Astrophysical Sources" supported by Deutsche Forschungsgemeinschaft (DFG), FSU–Jena

Ort, Datum

Unterschrift des Verfassers

PUBLICATIONS

Dinçel, B. and Neuhäuser, R. and Yerli, S. K. and Ankaý, A. and Tetzlaff, N. and Torres, G. and Mugrauer, M. , "Discovery of an OB runaway star inside SNR S147", MNRAS, ix = "arXiv", 1501.07220, "astro-ph.SR", 2015, apr, 448, 3196-3205, 10.1093/mnras/stv124, <http://adsabs.harvard.edu/abs/2015MNRAS.448.3196D>,

Tetzlaff, N. and **Dinçel, B.** and Neuhäuser, R. and Kovtyukh, V. V., "The origin of the young pulsar PSR J0826+2637 and its possible former companion HIP 13962", MNRAS, "arXiv", 1401.4678, 2014, mar, 438, 3587-3593, 10.1093/mnras/stt2478,

Mugrauer, M. and **Dinçel, B.**, "Follow-up spectroscopic observations of HD 107148 B: A new white dwarf companion of an exoplanet host star", *Astronomische Nachrichten*, 2016, jul, 337, 627, DOI:10.1002/asna.201512306

Errmann, R. and Torres, G. and Schmidt, T. O. B. and Seeliger, M. and Howard, A. W. and Maciejewski, G. and Neuhäuser, R. and Meibom, S. and Kellerer, A. and Dimitrov, D. P. and **Dinçel, B.** and Marka, C. and Mugrauer, M. and Ginski, C. and Adam, C. and Raetz, S. and Schmidt, J. G. and Hohle, M. M. and Berndt, A. and Kitze, M. and Trepl, L. and Moualla, M. and Eisenbeiß, T. and Fiedler, S. and Dathe, A. and Graefe, C. and Pawellek, N. and Schreyer, K. and Kjurkchieva, D. P. and Radeva, V. S. and Yotov, V. and Chen, W. P. and Hu, S. C.-L. and Wu, Z.-Y. and Zhou, X. and Pribulla, T. and Budaj, J. and Vaňko, M. and Kundra, E. and Hambálek, L. and Krushevska, V. and Bukowiecki, Ł. and Nowak, G. and Marschall, L. and Terada, H. and Tomono, D. and Fernandez, M. and Sota, A. and Takahashi, H. and Oasa, Y. and Briceño, C. and Chini, R. and Broeg, C. H., "Investigation of a transiting planet candidate in Trumpler 37: An astrophysical false positive eclipsing spectroscopic binary star", *Astronomische Nachrichten*, archivePrefix = "arXiv", eprint = 1403.6020, primaryClass = "astro-ph.SR", keywords = open clusters and associations: individual (Trumpler 37), binaries: eclipsing, binaries: spectroscopic, planetary systems, stars: fundamental parameters, stars: late-type, year = 2014, volume = 335, pages = 345, doi = 10.1002/asna.201412047,

Seeliger, M. and Kitze, M. and Errmann, R. and Richter, S. and Ohlert, J. M. and Chen, W. P. and Guo, J. K. and Göğüş, E. and Güver, T. and Aydın, B. and Mottola, S. and Hellmich, S. and Fernandez, M. and Aceituno, F. J. and Dimitrov, D. and Kjurkchieva, D. and Jensen, E. and Cohen, D. and Kundra, E. and Pribulla, T. and Vaňko, M. and Budaj, J. and Mallonn, M. and Wu, Z.-Y. and Zhou, X. and Raetz, S. and Adam, C. and Schmidt, T. O. B. and Ide, A. and Mugrauer, M. and Marschall, L. and Hackstein, M. and Chini, R. and Haas, M. and Ak, T. and Güzel, E. and Özdönmez, A. and Ginski, C. and Marka, C. and Schmidt, J. G. and **Dinçel, B.** and Werner, K. and Dathe, A. and Greif, J. and Wolf, V. and Buder, S. and Pannicke, A. and Puchalski, D. and Neuhäuser, R., "Ground-based transit observations of the HAT-P-18, HAT-P-19, HAT-P-27/WASP40 and WASP-21 systems", MNRAS, "arXiv", 1508.06215, "astro-ph.EP", 2015, aug, 451, 4060-4072, 10.1093/mnras/stv1187

Garai, Z. and Pribulla, T. and Hambálek, L. and Errmann, R. and Adam, C. and Buder, S. and Butterley, T. and Dhillon, V. S. and **Dinçel, B.** and Gilbert, H. and Ginski, C. and Hardy, L. K. and Kellerer, A. and Kitze, M. and Kundra, E. and Littlefair, S. P. and Mugrauer, M. and Nedoroščík, J. and Neuhäuser, R. and Pannicke, A. and Raetz, S. and Schmidt, J. G. and Schmidt, T. O. B. and Seeliger, M. and Vaňko, M. and Wilson, R. W., "Search for transiting exoplanets and variable stars in the open cluster NGC 7243", Astronomische Nachrichten, "arXiv", 1601.04562, "astro-ph.EP", 2016, mar, 337, 261-285, 10.1002/asna.201512310

Fritzewski, D. J. and Kitze, M. and Mugrauer, M. and Neuhäuser, R. and Adam, C. and Briceño, C. and Buder, S. and Butterley, T. and Chen, W.-P. and **Dinçel, B.** and Dhillon, V. S. and Errmann, R. and Garai, Z. and Gilbert, H. F. W. and Ginski, C. and Greif, J. and Hardy, L. K. and Hernández, J. and Huang, P. C. and Kellerer, A. and Kundra, E. and Littlefair, S. P. and Mallonn, M. and Marka, C. and Pannicke, A. and Pribulla, T. and Raetz, S. and Schmidt, J. G. and Schmidt, T. O. B. and Seeliger, M. and Wilson, R. W. and Wolf, V., "Long-term photometry of IC 348 with the Young Exoplanet Transit Initiative network", MNRAS, 2016, nov, 462, 2396-2417, 10.1093/mnras/stw1797

Yeşilyaprak, C. and Yerli, S. K. and Güçsav, B. B. and Aksaker, N. and Dikicioğlu, E. and Helvacı, M. and Çoker, D. and Aydın, M. E. and **Dinçel, B.** and Uzun, N., "Long-term variations and periods of Mira stars from ROTSE-IIIId", New Astronomy 2012, jul, 504-513, 10.1016/j.newast.2011.11.010,

TEACHING & TALKS

- Neutronensterne und Supernovaüberreste, Übungsleitung, 04/2013–07/2013
- Terra–Astronomie, Übungsleitung, 04/2015–07/2015
- Stars On the Run, August 2016, Bamberg, Germany (Talk)
- Supernova Remnants: An Odyssey in Space after Stellar Death, June 2016, Chania, Greece (Talk)
- XIX. National Astronomy Congress, February, 2015, Ankara, Turkey (Talk)
- Annual Meeting of Astronomische Gesellschaft, September 2014, Bamberg, Germany (Talk)
- Supernova in the Local Universe, August 2014, Coffs Harbour, Australia (Poster)
- Formation and Evolution of Neutron Stars, March 2014, Bonn, Germany (Talk)
- SFB Meeting, December 2013, Tuebingen, Germany (Talk)
- Formation and Evolution of Neutron Stars, November 2013, Bonn, Germany
- IAUS 296: Supernova environmental impacts, January 2013, Raichak, India (Talk)
- XVIII. National Astronomy Congress, September 2012, Malatya, Turkey (Talk)
- Electromagnetic Radiation from Pulsars & Magnetars, April 2012, Zielona Gora, Poland
- 42th Saas Fee Course; Dynamics of Young Clusters & Assoc, March 2012, Villars-Sur-Ollon, Switzerland
- XVII. National Astronomy Congress, September 2010, Adana, Turkey
- Astrophysics of Neutron Stars, August 2010, Cesme, Turkey
- Astrophysics of Neutron Stars, September 2009, Istanbul, Turkey

Declaration

Ich erkläre hiermit ehrenwörtlich, dass ich die vorliegende Arbeit selbständig, ohne un- zulässige Hilfe Dritter und ohne Benutzung anderer als der angegebenen Hilfsmittel und Literatur angefertigt habe. Die aus anderen Quellen direkt oder indirekt übernommenen Daten und Konzepte sind unter Angabe der Quelle gekennzeichnet. Bei der Auswahl und Auswertung folgenden Materials haben mir die nachstehend aufge- führten Personen in der jeweils beschriebenen Weise unentgeltlich geholfen:

1. Die in Abschnitt 4.1 genannten Monte-Carlo-Simulationen wurden von Dr. Nina Tetzlaff durchgeführt. Die Ergebnisse im Abschnitt 4.1 und die Abbildung 4.3 wurden ebenfalls von ihr angefertigt.
2. Der Python-Code, den ich zur Auswahl der OB-Sternkandidaten verwendete, wurde von Dr. Ronny Errmann geschrieben.
3. Die spektroskopischen Beobachtungen und die Datenreduktion (Bias, Dunkelbild und Weisslichtbild Korrekturen und Wellenlängenkalibrierungen) mit dem Instrument TRES wurden von Guillermo Torres durchgeführt.
4. Das Mosaik von 52 photometrischen Bildern in Abbildung 4.1 wurde von Dr. Markus Mugrauer erstellt.

Weitere Personen waren an der inhaltlich-materiellen Erstellung der vorliegenden Arbeit nicht beteiligt. Insbesondere habe ich hierfür nicht die entgeltliche Hilfe von Vermittlungs- bzw.

Beratungsdiensten (Promotionsberater oder andere Personen) in Anspruch genom- men. Niemand hat von mir unmittelbar oder mittelbar geldwerte Leistungen für Arbeiten erhalten, die im Zusammenhang mit dem Inhalt der vorgelegten Dissertation stehen. Die Arbeit wurde bisher weder im In- noch im Ausland in gleicher oder ähnlicher Form einer anderen Prüfungsbehörde vorgelegt. Die geltende Promotionsordnung der Physikalisch-Astronomischen Fakultät ist mir bekannt. Ich versichere ehrenwörtlich, dass ich nach bestem Wissen die reine Wahrheit gesagt und nichts verschwiegen habe.

Ort, Datum

Unterschrift des Verfassers